College of Instrumentation & Electrical Engineering, Jilin University

Academic Practice "Six in One" Training Project

English Proceedings

2019 (First Half)

CONTENTS

Design of Traffic Light Control Based on 51 Single Chip Microcomputer Connected to USB Interface

Shipeng Wang, Xiwen Li, Zhaorun Chen, Tiehu Fan
（School of Instrument Science and Electrical Engineering, Jilin University,Changchun 130012）

***Abstract*—Nowadays, problems such as the inefficiency of traditional signal lights have seriously hindered the development of urban traffic. For solving the problem of fixed signal time, the intelligent traffic light system with flexible adjustment of transit time is the best solution at present. This design is based on a simulated traffic light designed by a 51 MCU. This system uses an infrared transmitting/receiving device to count the number of vehicles located in the waiting area of the signal, and then analyzes the statistical results to adjust the transit time in all directions. At the same time, the number of vehicles in each direction is compared, and the adjustment scheme of the signal light is further optimized to deal with dynamic and complicated traffic conditions as much as possible, and to solve the problem intelligently.**

***keywords*—Intelligent traffic light Infrared sensing technology 51 single chip microcomputer**

I. INTRODUCTION

WITH the development of social economy and the improvement of people's quality of life, private car travel has become the main mode of travel, the traffic load of the city is also increasing, and traffic problems have attracted people's attention. In today's urban road traffic, traffic lights are one of the most important components, and the control of signal lights has become an important factor affecting traffic conditions. Most of the traffic lights used today are traditional signal lights, which are fixed at artificial preset times. This lack of flexibility of signal lights often causes traffic congestion and low efficiency. Therefore, the problem of the traffic signal control system has become an urgent problem to be solved in the current urban development.

Compared with traditional signal lights, the intelligent traffic signal control system can rely on the traffic conditions of the road to timely count the number of vehicles on the road, reasonably allocate the transit time, effectively alleviate the traffic congestion caused by the signal lights, improve the operating efficiency, and facilitate people's travel. Lu Haiquan [1] used the single-chip microcomputer as the controller in the paper, and used the infrared transmitter/receiver to divide the traffic flow into three states: no car, less car, more cars, to allocate green light time; Gao Jing [2] in the thesis In the case of single-chip microcomputer as the controller, the vehicle traffic is calculated by infrared vehicle detector to realize the intelligent control of the transit time; Wen Zhida [3] uses PLC as the controller, and uses the ground-sensing coil based on the principle of electromagnetic induction to calculate the vehicle in the waiting area. The number determines the delay time of the green light. The system detects the number of vehicles in the waiting area through the ultrasonic detector and determines the transit time by comparing the number of vehicles. In order to improve the traffic efficiency of the intersection and alleviate the traffic pressure, it has certain guiding significance for solving the urban traffic congestion problem.

II. SYSTEM DESIGN

Taking the intersection as an example, the system uses 51 single-chip microcomputer as the main controller to design, and counts the number of vehicles in the waiting area through the ultrasonic transmitting and receiving device. The whole system consists of 51 MCU, ultrasonic detection module, emergency button, traffic light and countdown display module. The overall block diagram of the system is shown in Figure 1.

Fig.1. system overall block diagram

A set of ultrasonic detection modules are placed on the roads in the north, south, south and north directions. Each group includes multiple ultrasonic detectors, two for each lane, one at the intersection and the other at 100m from the intersection. The vehicles respectively count the passing vehicles, and use the difference of the counts to calculate the number of vehicles in the waiting area in each direction. At each intersection, a traffic light and a countdown display module are

respectively placed to display the transit time determined by the system after the 51 single-chip microcomputer processes the number of vehicles in the waiting area in all directions. The emergency button can also be used to manually control the traffic time of the traffic lights as an emergency solution.

III. HARDWARE DESIGN

A. Controller

This system uses STC89C52RC microcontroller as its main controller. The device has low power consumption, high performance and low price. It has 8KB of program memory, 512 bytes of data memory, 4KB of EEPROM memory, and direct download program using serial port. Ability.

B. Infrared detection module

At present, there are four main schemes for road vehicle detection: video detection, ultrasonic detection, ground sense coil detection and infrared detection. Video detection is to use the camera to analyze the input traffic image, identify passing vehicles, and calculate the number of vehicles. The advantages are easy installation and maintenance, stable operation, high recognition rate, and shortcomings are susceptible to bad weather. Ultrasonic detection uses reflection principle, through calculation The time difference between the transmission and reception of the ultrasonic wave determines whether the vehicle has passed, but at the same time is expensive, the service life may be affected by environmental factors; the ground coil detection is detected by changing the inductance value of the ground coil through the metal part of the vehicle. Whether there is a vehicle passing, this technology is accurate in counting, stable in performance, and will not be affected by the external environment, but it needs to damage the road surface during installation, and the engineering quantity is large and difficult to maintain; Infrared detection is detected by linearly arranged infrared light emission and reception. The vehicle is easy to install and is not susceptible to the weather. Compared with other technologies, the technology is easy to install, low in price, stable in performance and less affected by weather.

Therefore, this system uses an infrared sensing module. The module emits infrared light through the transmitting probe and propagates to the receiving probe through the air medium. When no vehicle passes between the transmitting probe and the receiving probe, it can be normally received. When it is unable to receive, it can be judged that the vehicle passes, and finally a certain one is judged. The number of times the vehicle passed through the fixed time. The ultrasonic detector has a longest recognition distance of up to 18m, a working length of only 125ms, an operating temperature of -25~70°C, and is resistant to dirt. It has little influence in a hazy environment and can be used in harsh environments. Normal work, in line with the conditions required for urban road detection. The infrared detection module is erected about 0.5m to the left and right of the lane and has a height of 1 meter. Two sets of infrared detection are placed in each lane, and the placement position is shown in Figure 2. When the vehicle is not used as the initial value, when the vehicle passes, the result of the infrared detection module is 0. After the vehicle passes, the distance measurement result will return to the initial value again, and the number of vehicles will be counted.

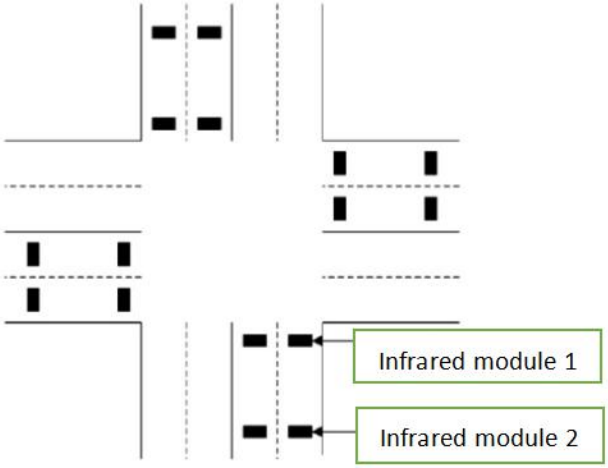

Fig.2. Infrared detection module placement location map

B. Traffic light and display module

The traffic lights of this system are traditional LED traffic lights. The display module uses a 2-digit 8-segment LED common cathode digital tube to display the remaining time of the traffic light.

C. USB interface module

As a new microcomputer bus interface specification, Universal Serial Bus (USB) has the characteristics of convenience, easy expansion, low cost, low interference, etc. USB technology is more and more widely used on PCs, and it is also very suitable as a host and The communication interface between peripherals. Due to its own functional limitations, the use of USB technology in single-chip microcomputer systems has been limited, especially in the field of industrial control, data communication still uses the traditional serial communication scheme. In order to realize the data exchange and information transmission between the microcomputer and the single-chip microcomputer, shorten the gap between the upper computer and the lower computer technology, and improve the compatibility of the system, we use the CH372 communication chip to connect the C51

single-chip microcomputer and the USB interface to realize the transmission of the CPU control function. This greatly facilitates the connection between the microcontroller and peripherals, and expands the application range of the microcontroller.

IV. SOFTWARE DESIGN

The system sets a traffic signal in the east, west, south and north directions. When the system starts, the east-west direction turns into a green light, and the north-south direction turns into a red light. After 57s, the east-west direction changes from green light to yellow light, north-south direction. After 3s, the east-west direction turns into a red light, and the north-south direction turns into a green light; after another 57s, the north-south direction turns yellow and the east-west direction does not change; after the yellow light 3s, the traffic light returns to the initial state. The initial state of the traffic lights is shown in Table 1.

TABLE 1 Traffic Light Initial Status Table

status	East-west direction	North-south direction
1	Green light 57s	Red light 60s
2	Yellow light 3s	Green light 57s
3	Red light 60s	Yellow light 3s

The system places two sets of infrared detection modules in the east, west, south and north directions. The infrared detector at each road intersection is used to count the number of vehicles leaving the waiting area. The infrared detector at the intersection 100m is used to count the vehicles entering the waiting area. The number, the difference between the number of driving and the number of driving out, is the number of vehicles in the waiting area.

The system design is based on the green light in the east-west direction. After 35s green light, if the difference between the maximum number of vehicles in the east and west waiting areas and the maximum number of vehicles in the south and north waiting areas is less than 10, the green light The duration does not change; if the maximum number of vehicles in the waiting area of the east and west is greater than the maximum number of vehicles in the waiting area of the south and north, and the difference is greater than 10 and less than 20, the green time of the east-west direction is extended by 10s; if East and West The maximum number of vehicles in the direction waiting area is greater than the maximum number of vehicles in the waiting area of the south and north, and the difference is greater than 20, which makes the green time of the east-west direction extend by 20s; if the number of vehicles in the east and west directions is less than the south and north The maximum number of vehicles in the two directions waiting area is greater than 10 and less than 20, which shortens the green time of the east-west direction by 10s; if the number of vehicles in the east and west directions is less than the maximum number of vehicles in the waiting area of the south and north If the difference is greater than 20, the green time of the east-west direction is shortened by 20s.The software design flow chart is shown in Figure 3.

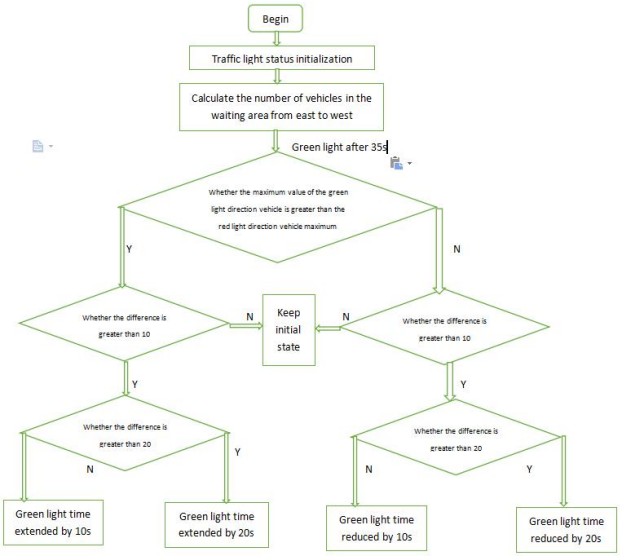

Fig.3. Software design flow chart

V. EXPERIMENTAL RESULT

According to the above design scheme, we have made a set of intelligent traffic light system, and carried out simulation experiments indoors, draw crossroads on the ground, simulate vehicles with small wooden blocks, and the infrared detection system is arranged on both sides of the road. After the traffic and other systems start working, moving the wooden blocks, through the infrared detection system, can see the time of the traffic lights change, consistent with the expected results.

VI. IN CONCLUSION

The urban intelligent transportation system is an important part of the smart city. We use the infrared sensor to obtain the traffic information of the intersection. The camera can monitor the traffic of the vehicle. The data is transmitted wirelessly to the traffic management center to let the management know the road. Real-time traffic conditions; and can remotely control the traffic lights at various intersections based on this information, making these times more reasonable, slowing traffic pressure, speeding up the

speed of vehicles passing through intersections, and saving people's time. When an accident occurs, the manager can activate the emergency mode to avoid the occurrence of a secondary accident and make people travel safer and more convenient. This is what the intelligent transportation wants to achieve and the meaning of completion.

The design of intelligent traffic lights has certain significance for the future urban traffic construction. The intelligent traffic lights designed by this system use infrared system to detect the number of vehicles in the waiting area of the road in real time, and according to this quantity, the transit time of vehicles in all directions is reasonably allocated. This can maximize the rational use of time, ease the congestion of the road, and facilitate people's travel. At the same time, the system has the advantages of small calculation amount, simple installation and low cost, and has strong practical value.

References

[1] Lu Haiquan, Li Zhijun, Yan Feifan, Wu Jianglong. Intelligent Traffic Light Control System Based on Single Chip Microcomputer[J]. Electronic Technology and Software Engineering, 2016(03): 51~53.

[2] Gao Jing, Liang Chongxi. Research on Intelligent Traffic Light Control System Based on Traffic Flow[J]. Information Technology and Informatization, 2015(02): 158~160.

[3] WEN Zhida, LIANG Guirong, CHEN Biming, GAO Suping. Intelligent traffic light control system based on traffic flow[J].Automation Technology and Application,2009,28(06):115~118.

[4] Bian Hailong, Sun Yongkui. Detailed Explanation of SCM Development and Typical Engineering Projects[J]. Electronic Industry Press, 2008,(10):143-160.

[5] Wang Weiqing, Qiu Wenxun. Selected Cases of 51 Single Chip Development Cases [J]. People's Posts and Telecommunications Press, 2001, (5): 45-47.

[6] Zhang Xin, Hua Wei, Chen Shuqian. The principle and application of single chip microcomputer [J]. Publishing House of Electronics Industry, 2008 (5).

[7] Zhang Hongrun, Zhang Yafan. Principle and Application of Single Chip Microcomputer[J]. Tsinghua University Press, 2005, (4).

[8] Huang Zhiwei. Lingyang SCM Course Design Guide[J]. Beijing Aerospace University Press, 2007, (6)

[9] Jiang Huiping, Zhou Guoxiong. Design and simulation of single-chip system based on Proteus [M]. Mechanical Industry Press, 2009.

[10] Zhang Yikun. Principle and application of single-chip microcomputer, [M] Xidian University Press, 1998

[11] Yu Xicun Cao Guohua. Principles and Interface Technology of Single Chip Microcomputer [M]. Shaanxi: Xi'an University of Electronic Science and Technology Press, 2000.7

[12] Lei Liwen et al. Microcomputer principle and interface technology [M]. Beijing: Publishing House of Electronics Industry, 1997.

[13] Zhang Meng·Single-chip application system development comprehensive example·Second Edition·Tsinghua University Press·2005

[14] He Limin·Microcontroller Application Collection·First Edition·Beijing University of Aeronautics and Astronautics Press·2004

The Design of a Acquisition System of Pulse Based on Automatic Pressure of Gas

Tang Bingyi, Yang Yang, Li Honghe, Li Suyi
(College of Instrumentation and Electrical Engineering, Jilin University,Changchun 130012)

***Abstract*—A acquisition system of pulse based on automatic pressure of gas has been developed which has least size, lower cost and more friendliness for carrying out, household using than present machines. It uses piezoelectric sensor and triaxial acceleration sensor to acquire pulse signal and wrist movement information respectively, and apply pressure by controlling the suction motor and vent valve to control the total quantity of the gas. Finally, the data acquired are uploaded to host computer for display. The system can display clear and stable pulse signal and wrist movement information in real time, and can accurately control the pressure of pulse which is meaningful for the objectification of traditional Chinese medicine pulse diagnosis and family pulse diagnosis.**

***keywords*—Pulse Mobile medical Wristband pulse diagnosis Triaxial accelerometer**

0 FOREWORD

PULSE diagnosis is the earliest diagnostic method with the unique characteristics of traditional Chinese medicine, and it has been used until now. It has been the symbol of traditional Chinese medicine since the Qin Dynasty. At present, the standard of clinical diagnosis is based on whether the body has organic lesions, lack of the evaluation of the functional status of organs[1]. But the pulse diagnosis is a direct diagnostic method, which can reflect the state of body. Whether the body is low in function or pathologically altered, pulse contains all the information, so it is also called “the language of life” by Chinese traditional medicine. The doctor uses the feeling of fingers to analyze the characteristics of the "bit, number, shape, and potential" of the pulse [2]. So observing the image of the patient's artery to judge the physiological and pathological conditions of the human body is important for judging the body condition, distinguishing the pathogenesis and inferring the prognosis[3].

Under the situation that modern advanced science technology has promoted western medicine remarkablely, especially the rapid development of diagnostic medicine and its equipment, traditional pulse diagnosis has no objective judgement index influenced by many factors such as clinical experience and subjective perception of doctors, which leads to many differences, poor accuracy and reproducibility and their limited clinical application and inheritance[4]. Therefore, the objective diagnosis of pulse diagnosis is an important part of modern pulse diagnosis research[5], which means to make the study of pulse not only stay at the stage of language description, but also to describe, analyze and discriminate objectively with waveforms and quantitative indicators[6].

In recent years, the objective diagnosis of TCM pulse diagnosis has made great progress, and various pulse diagnosis instruments have emerged. Tang Weichang from the Shanghai University of Traditional Chinese Medicine designed a three-step pulse detection system in 2005[7]. Dang Hongzhi from LanZhou University of Technology designs a manual pressure three-point pulse detection system in 2011[8]. In addition, the TD-III pulse instrument developed by Lu Xiaozuo from Tianjin University of Traditional Chinese Medicine is widely used[9]. With reference to these pulse detections, we choose the traditional pressure-applying method, the gas pressure, which can not only accurately control the pulse pressure, but also has high comfort for the patient. In addition to acquiring the pulse signal, the system also collects the three-axis acceleration signal of the wrist to describe the movement of the wrist. In order to judge the influence of the slight movement of the wrist on the acquired pulse signal.[10] The system uses the ARM microprocessor as the main controller for signal acquisition and other operations, and the host computer acts as the data receiver and the command sender. The whole system is small in size, easy to operate and convenient for home use[11].

I. OVERALL SYSTEM DESIGN

The system provides human-computer interaction function through the host computer, which control the acquisition of pulse data, and analyses information, or stores the measurement data to the SD card. The system is mainly composed of a front-end acquisition

module, a signal conditioning module, a pulse-receiving control module, a main control module, a storage module and a host computer. The overall block diagram of the system is as follows:

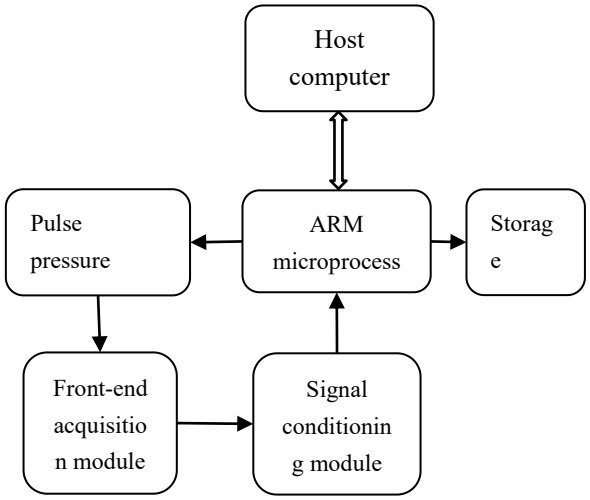

Fig.1 Diagram of the system

The system uses a 32-bit Flash microcontroller STM32F103ZET6 based on the ARM Cortex-M3 core as the main controller for the acquisition, transmission, storage and control of the pulse pressure module. The microprocessor has high integration, small package and low power consumption. It integrates three 12-bit AD converters, one USB interface module and external bus (FSMC) to expand SRAM and connect LCD. The pulse sensor adopted is HK-2000B. It is integrated by the sensitivity temperature compensation component, the force sensitive component (PVDF piezoelectric film), the temperature sensing component, and the signal conditioning circuit, and has high sensitivity with 2000uV/mmHg, strong anti-interference ability, large overload capacity, good consistency, stable and reliable performance. Its output signal is analog signal with voltage range -0.2V-0.6V. At the same time, the ADXL335 three-axis accelerometer is used to collect the motion information of the wrist in real time. The sensor is an analog signal output with small size, low power consumption and good temperature stability.

Fig.2 HK-2000B pulse sensor

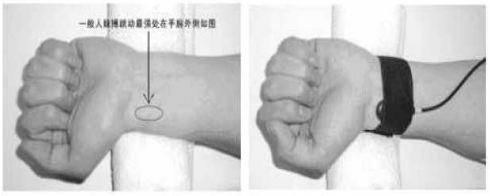

Fig.3 HK-2000B pulse sensor fixation method

II. Signal Conditioning Module Design

Pulse is one of the most important physiological parameters in human body. It contains many information reflecting human physiology and pathology, and has important physiological and clinical diagnostic reference value.However, the pulse signal belongs to the low frequency weak signal under the background of strong noise, which has the characteristics of strong randomness and low frequency. It is very vulnerable to the interference of internal noise and external stimulus (environment and temperature). It is necessary to process the detected pulse signal in a series of ways, such as filtering and amplification, in order to obtain high accuracy and undistorted pulse information, So as to provide accurate and effective pulse data source for medical analysis and research.Therefore, studying the pulse signal conditioning circuit is of great significance to the entire pulse signal detection system.

The pulse signal is taken from the surface artery of human body. The input impedance of the signal source is large, and the amplitude is small and the frequency is low. It is highly susceptible to noise interference.Therefore, the following requirements are put forward for pulse signal conditioning circuit:(1)Gain: Since the output voltage of the HK-2000B piezoelectric pulse sensor is small, in order to improve the resolution of the signal after AD sampling, the signal should be appropriately amplified.(2)Low noise: In the signal conditioning circuit, the noise is mainly the inherent thermal noise and shot noise of the electronic circuit, so it must be ensured that they do not cover the weak pulse signal;(3)Low drift: Prevent saturation distortion in the amplifier circuit;(4)Suitable bandwidth: to effectively eliminate noise interference and prevent sampling overlap;(5)High safety: to ensure that its damage to the human body is zero, mainly considering electrical safety and radiation requirements[12].

Based on the above requirements of the pulse signal, since the HK-2000B integrates a simple signal conditioning module, the external signal conditioning module consists of two modules, a signal amplification module and a voltage boosting module, to suit the needs of the selected AD converter.

Pulse Mobile medical Wristband pulse diagnosis Triaxial accelerometer

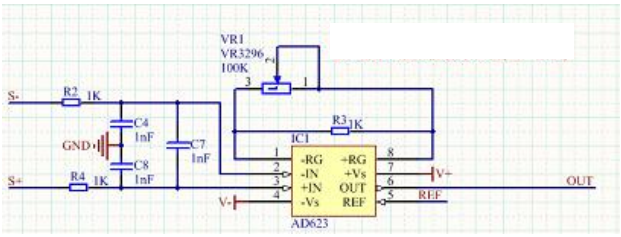

Fig.4 The principle diagram of the AD623

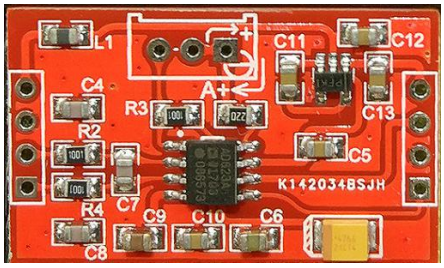

Fig.5 Physical picture of AD623 module

A. Signal amplification module

The output range of the HK-2000B piezoelectric pulse sensor is about -0.2V to 0.6V. In order to improve the resolution of the signal after AD sampling, the signal should be properly amplified.Since the input reference voltage range of the STM32F103ZET6 internal A/D converter is 0-3.3V, the amplification of the pulse signal amplifier should be adjustable within 20 times. The output signal of the HK-2000B is voltage amplified using an AD623 millivolt instrumentation amplifier module[13].The AD623 millivolt instrumentation amplifier module is a dedicated instrumentation amplifier core with rail-to-rail output, high input impedance, high common-mode rejection ratio, low offset and drift, low noise, and high closed-loop gain stability.The magnification is adjustable from 2-1000 times.The principle of AD623 is shown in Figure 4[14].

B. Voltage boost module

After the previous circuit, a relatively pure pulse signal has been obtained.However, since the pulse signal output by the HK-2000B sensor has a portion smaller than zero, the minimum conversion limit defined by the internal AD converter of the STM32F103ZET6 is 0V.In order to ensure that there is no negative peak distortion during A/D conversion, the amplified pulse signal must be passed through a voltage boosting circuit so that the level values of the pulse signals are positive.The essence of the voltage boosting circuit is the adder circuit[15].

The TL431 is a three-terminal adjustable shunt reference with good thermal stability.Its output voltage can be set to output any voltage from VREF (2.5V) to 36V with two resistors.The component's typical dynamic impedance is 0.2Ω, which can be used in many applications to replace Zener diodes.The adder circuit structure is shown in Figure 6.In order to ensure the normal operation of the TL431, a suitable resistance value should be selected to ensure that the cathode current is between 1 and 100 mA.The TL431 and potentiometer RP3 provide an adjustable voltage of 0 to 2.5V to ensure that the output voltages are all positive.Its output is:

$$U_{OUT} = 2(U_1 + U_2) \tag{1}$$

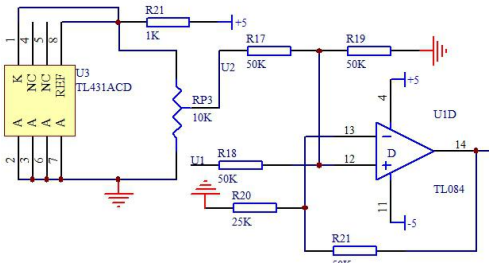

Fig.6 Adding circuit

III. Pressure Control

This paper designed a system that can accurately apply the pressure. Structure of the system is shown in figure 7.

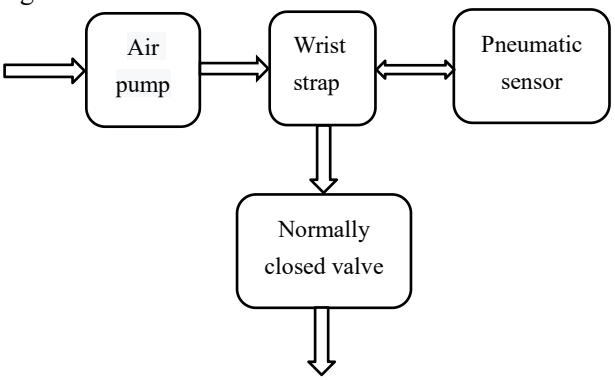

Fig.7 Pulse pressure control system（the arrow indicates the direction of the flow）

Main controller control electromagnetic relay switch by controlling the I/O voltage to the level of high or low, which resulting in suction motor and deflated solenoid valve open or close respectively. So it can control the power on time of the motor and the valve to control the gas volume in the wrist strap, thus the pressure can change in three levels of floating, medium and heavy. At the same time, the pressure volume in the wristband (reflecting the pressure) is detected by the gas sensor and fed back to the main controller to facilitate adjust the pressure.

IV. Data Acquisition, Transmission, Display and Storage

A. data collection and transmission

After the signal passes through the conditioning module, the AD converters built inside the

STM32F103ZET6 controller are used to convert the signal. The controller is with three AD converters, two of which can acquire signals simultaneously. In order to reflect the influence of wrist movement on pulse signal in real time, the signals must be acquired synchronously with these two converters to reduce delay errors. The signals are uploaded to the host computer through rs-232 (serial port to USB module) with the sampling frequency 1KHz by means of acquiring one data and then sending at once.

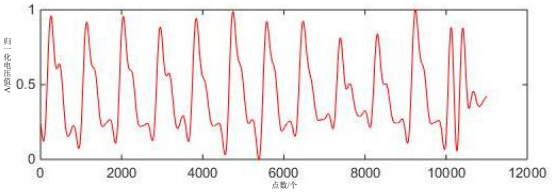

Fig.8 Collected pulse signals

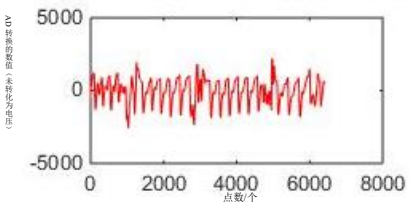

Fig.9 Triaxial accelerometer signal

B. data display

The system adopts LabVIEW software platform to draw and analyze pulse signal waveforms and sends instructions to the main controller. As shown in figure 10.

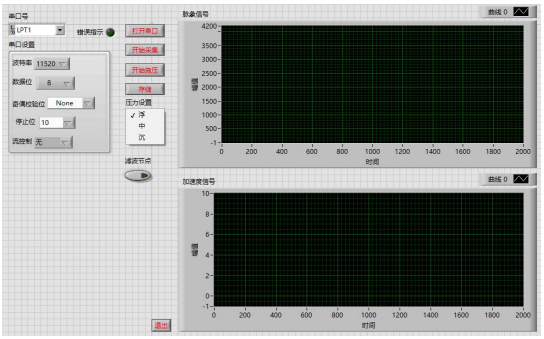

Fig.10 LabVIEW display interface

The serial port of the host computer receives the signal datas of the autonomous controller and the data of the triaxial acceleration sensor, in order to ensure that the datas are right, a transmission protocol is set as follows:

When a string is received, it is converted into a byte array, and then we detected if the frame header is in it or not. If it is, we judge whether the string contains a complete frame data according to the frame length. If it contains a complete frame data, we extract the signal data from it, and then look for the next frame header. If the frame data is incomplete, intercept the string from the frame header to the end of the string and merge it with the string received the next time for the next search. The collected data is formed into an array with 2000 data. When new data is received, the first data of the array is removed and the new data is added to the end to form a new array. The waveform will be made of the line of data connection.This method has the advantages of fast data receiving speed and high data accuracy, and forms an array for subsequent data processing.

C.data storage

Main controller not only can send the signal data to the host computer, but also store into the SD card. Upon receiving the storage instruction sent by host computer, main controller will create a new data file, which is named by the current date and time, and write the data acquried during 10s after the instruction is sent into SD card. This is convenient for the check of historical data and the horizontal comparison of pulse signal.

V. Experiment Result Analysis

The two sensors are integrated into one. Since the acceleration signal is mainly the z-axis signal, the three-axis accelerometer should be integrated directly above the pulse phase sensor. The integrated sensor is placed on the inside of the wristband, and all the electronic circuits are encapsulated in the system shell, leaving only the interface with the wristband and the host computer[16].

And then we used the system to do experiments, and the subjects were three team members, all of whom were healthy. Before the test, locate the GUAN part of the radial artery with your finger and place the sensor on it. After the state of the subject is stable, select the appropriate pulse pressure for the subject and make the system start to work.

Pulse signals and wrist movement information of the three subjects can be normally collected and displayed, which are clear, stable and continuous under the condition of small motion range of the subjects.

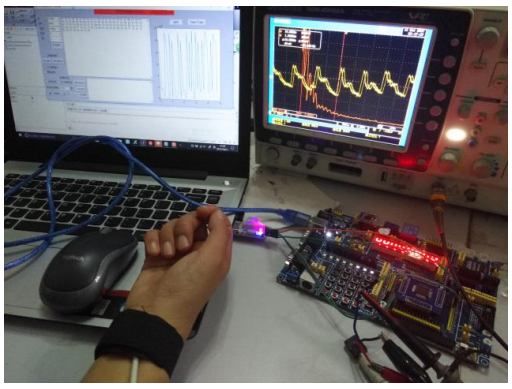

Fig.11 The whole system diagram

VI. Conclusion

This paper designed a kind of pulse condition detection system based on gas pressure, by controlling the quantity of gas inside the wristbands to apply different pulse pressure, improved the patients' comfort in diagnostic process, and can display the pulse signal and wrist movement information of patient. The use of triaxial acceleration, make pulse signal obtained more accurately. This has realized the objectification of pulse diagnosis in traditional Chinese medicine and provided specific image information for doctors' diagnosis.

References

[1] Xia mingyi. Human pulse signal acquisition and processing based on strain sensor [J]. Journal of jiangsu university (natural science edition),2016,(04):423-428.

[2] Wang xuemin, sun fei, lu xiaozuo, yu zhifeng, zhou peng. Research on portable pulse acquisition and analysis system based on mechanical compression [J]. Journal of sensor technology,2016,(11):1631-1636.

[3] Anonymous. Traditional Chinese medicine pulse diagnosis I understand [J]. Family health, 2014,(11).

[4] Li tian, liu xuemei-mei, liu yuan, lu xiaozuo. Objectification of traditional Chinese medicine pulse examination from pulse examination instrument [J]. Henan journal of traditional Chinese medicine,2017,(01):37-40.

[5] Sha hong, xu yuanjing, wang bin, ren chaoshi. Multi-channel pulse detection system based on the theory of three parts of pulse diagnosis in traditional Chinese medicine [J]. Chinese journal of traditional Chinese medicine,2006,(03):139-141.

[6] Wei hong, xu gang. Objectification of pulse diagnosis from the perspective of holistic, dynamic and balanced TCM [J]. Journal of TCM,2014,(01):25-27.

[7] Tang w c, li r. Research on three pulse detection systems [J]. Chinese journal of medical devices, 2005 (3) : 164-166.

[8] Dang hongzhi. Cun guchi pulse information detection system [D]. Lanzhou: lanzhou university of technology, 2011:7-22.

[9] Wang xuemin, Yang cheng, lu xiaozuo, et al. Design of pulse detection system based on flexible array sensor [J]. Journal of sensor technology, 2012,25 (6) : 733-737.

[10] Wang nanyue et al. Reflections on objectification of pulse examination [J]. Chinese journal of traditional Chinese medicine,2015,(08):2655.

[11] Guo shi-zhen, tian fei, yu zhi-feng, zhao jing, lu cheng, ye zhi-hua, zhang hai-fang, jiang zhi-hao, lu xiao-zuo. Overview of pulse analyzer development [J]. Abstract of papers for the 2013 academic annual meeting,2013, : 95-96

[12] Alarka Sanyal，Arijit Baral，Abhijit Lahiri. Application of Frame-

[13] let Transform in Filtering Baseline Drift from ECG Signals ［J］Procedia Technology，2012（4）：862-866.

[14] Huai Yongjin,Han Zhengsheng.Design of High Precision Array Pulse Sensor in TCM[J].Journal of Semiconduetors.2O08,4.

[15] ZHANG H X，YE W T，CHEN X W，et al.Weakmode coupling measurement with EMD-based methodinpolarization-maintaining fibers ［J］.Optics Communications，2012，285(2) :113 － 117.

[16] LIU M L,WANG K Q，SUN L J，et al．Applying empirical mode decomposition(EMD)and entropy to diagnose circuit breaker faults［J］.Optik,2015，126(20) :2338 － 2342.

Automatic Temperature Measurement Technology in Automotive Drive Axle Housing Processing

Tang Qingcheng, Sun Yongze, Xu Heyi, Sun Feng, Liu Changying
(School of Instrument Science and Electrical Engineering, Jilin University,Changchun 130012)

***Abstract*—In order to realize remote wireless transmission of data and automatic temperature measurement in the process of integral mechanical expansion forming of automotive driving axle housing, Wireless transmission of data and automatic an automatic temperature measurement technology system for automotive manual temperature measurement at high temperature, monitors the temperature and controls the process of temperature and technology data converted by sensors are obtained and stored in STM32; serial port is received and displayed (PC module and SCM interface); and PC responds the temperature and controls accordingly. Ensures safety and effectively data analysis and compensation are completed by MATLAB on PC side, and processed data are obtained on PC. The temperature range is - 50 - 300 degree C and the sampling frequency is 10 seconds. rocess of temperature and technology in. The sensor collects parameters, the MCU processes data and displays temperature, wireless data transmission, wireless transmission of data and automatic and PC responds accordingly. The operator monitors the temperature and controls the process of temperature time on the mobile phone, avoids the operator's manual temperature measurement at high temperature, ensures safety and effectively improves work efficiency.**

***Key words*—Automatic Temperature Measurement Technology Wireless transmission STM32 GSM**

0 PREFACE

IN recent years, the concept of automobile lightweight has been paid more and more attention. With the continuous development of transportation industry, the market demand of heavy vehicles and giant vehicles is expanding. Considering from the point of view of heavy vehicles, the drive axle system plays an indispensable role and is also its core component. As the main part of the whole system, it is directly related to the carrying capacity, service life and safety performance of the vehicle and other important performance indicators[1]. As far as the production of driving axle housing is concerned, the integral mechanical thermal expansion forming process of driving axle housing for heavy vehicles has unique advantages over the traditional production process. In the process of integral mechanical expansion forming of driving axle housing, it is particularly important to control the temperature accurately. Nowadays[2], infrared thermometers used in workshops are generally non-contact type.

This kind of thermometer will be applied to the new infrared technology when measuring the surface temperature of the object, so the detection is efficient and simple. There is no need to use the tedious detection of mechanical contact at all, so the measurement speed is very fast. For the measured object, the trigger can be activated first, then the LED screen can be stared at, and finally the data will be displayed. It is light in weight, small in volume, convenient in operation and easy to carry. Even for objects with high danger, hot and difficult to touch, it can also measure efficiently and accurately. Not only that, after the measurement, there will be no damage or pollution to the measured object. The non-contact instruments used in driving production need staff to read by themselves and can not work automatically, so they are not only inefficient, but also prone to errors[3]. [2]Therefore, this paper proposes a remote wireless automatic temperature control technology and system to solve the problem of material temperature measurement and control in the process of automobile driving axle housing processing.

1 OVERALL DESIGN SCHEME

1.1 Programme

This design detects and converts temperature in real time by MLX90614 sensor; STM32 stores data and completes long-distance transmission; PC serial port receives data, and finally draws temperature curve by MATLAB; mobile phone receives prompt information in the range of 50-300 C, sampling frequency once a second[4].

This design improves the principle of portable wireless thermometer on the market, and adds the following contents on the basis of the existing temperature measurement module of sensor and temperature measurement circuit: data acquisition, central control unit, wireless transmission, short message prompt.

Data acquisition includes two parts: temperature measurement and data acquisition. The main purpose of

data acquisition is to transmit the measured temperature data to the central control unit for further analysis and control. The central control unit is based on a single-chip computer and designs a control module to receive the key data of the temperature acquisition module. At the same time, it simply judges the incoming data and filters out the abnormal data. At the same time, the program of data transmission is compiled, and the temperature data is sent to the wireless data transmission port for transmission. The core goal of wireless transmission is to transfer the data processed in the central control unit to the computer through serial port, relying on the GSM module, in the previous data acquisition system of single-chip computer, the module supporting short message and data communication function is added[5], and the SIM card is allocated based on this module. The joint system achieves the function of data wireless transmission in the form of serial communication interface. Of course, it can also be transmitted directly by WiFi. The functions of the computer control terminal are as follows:

(1) Data reception: data is received and transmitted to the database through the wireless receiving device[6].

(2) Storage: Store application program, temperature data and temperature image.

(3) Temperature control: can be divided into manual control and automatic control, according to the temperature obtained for heating, cooling and other operations.

(4) Image display: provide friendly man-machine interface to form image of temperature data, and display prompt information to guide the operation process smoothly.

(5) System self-checking: This module is used to automatically check whether there are errors in the operation of the system.

1.2 System Structure Block Diagram

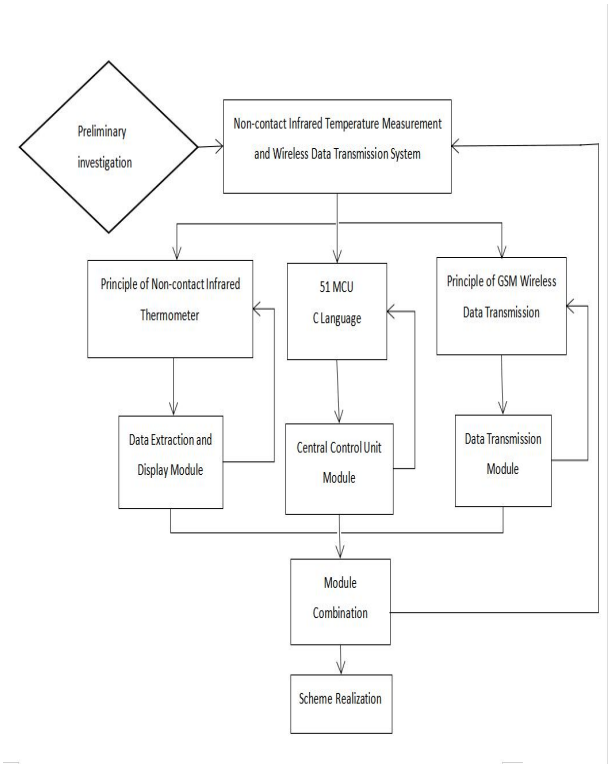

Fig.1 system overall block diagram

2 DESIGN OF EACH MODULE

2.1 STM32 LCD Display

Edit the display interface of STM32 LCD screen, the temperature can be displayed after data import, and analyze the data[7].

TFT-LCD is quite different from passive TN-LCD and STN-LCD in its simple matrix. Every pixel in its display contains thin film transistor (TFT), which can be used to suppress the crosstalk when it is not turned on, so that the static characteristics of the screen are not related to the number of scanning lines, which is of great benefit to image quality . The use process of this module can be referred to in the following figure:

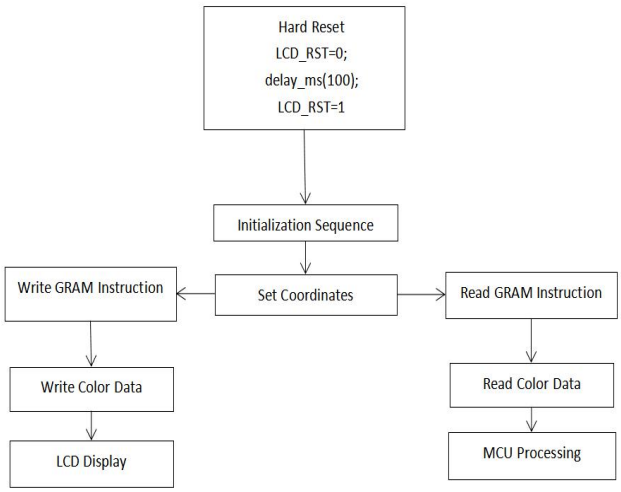

Fig.2 Flow chart of TFTLCD module

The schematic diagram of the module is shown as follows:

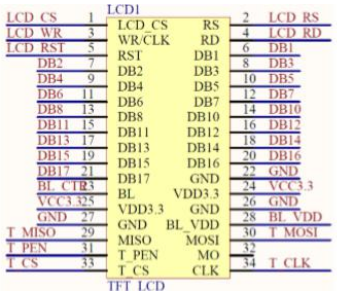

Fig.3 TFTLCD module schematic diagram

It is not difficult to find that TFTLCD uses 16-bit parallel mode to connect the external. There is no need for 8-bit format here because of the large amount of data. Especially when displaying pictures[8], 16-bit speed is more than twice as fast as 8-bit speed. That is naturally the faster the speed, the better the efficiency, the better, so the 8-bit format is abandoned here. Its 80 parallel port has the following signal lines :

CS: TFTLCD chip selection signal.

WR: Write data to TFTLCD.

RD: Read data from TFTLCD.

D[15:0]: 16-bit bidirectional data line.

RST: Hard reset TFTLCD.

RS: Command/data flag (0, read and write commands; 1, read and write data).

2.2 MLX90614 Sensor

This kind of sensor combines infrared detection thermopile chip and signal processing chip. They complement each other and are encapsulated in TO-39.

The full integration of low noise amplifier, 17 bit ADC and powerful DSP processing unit makes the sensor achieve high precision and high resolution measurement.

The measurement results of the sensors are factory calibrated, and the data interface is digital PWM and SMBus (System Management Bus) output. As a standard, the PWM is 10 bits, and the resolution is 0.14 C continuous output.

Sensors are manufactured by default and SMBus communication is used when power is restored.

Low noise amplifier (LNA) and 17-bit ADC are all integrated with excellent DSP processing units. These elements enable the sensor to achieve extremely high accuracy and resolution. The temperature and environment of the measured object are in RAM, which can be read by using two-wire serial SMBus compatibility protocol or 10-bit PWM (Pulse Width Modulated) output.

The temperature measurement value of the target under test is the average temperature of all objects in the sensor FOV field of view. The measurement accuracy of this kind of sensor at room temperature is (+0.5 C). The accuracy of medical application type sensor in human body temperature measurement is (+0.2 C）.

Temperature difference on sensor package may cause additional errors in sensor measurement. The source of temperature difference on sensor package, such as heating element, heating device or heat dissipation device beside sensor, or object with relatively hot or cold sensor, will not only heat sensor's temperature sensor, but also affect sensor's packaging temperature. Based on FOV, some of these existing thermal effects play a decisive role in its performance, such as xxC and xxF. From the sensor's own point of view, they can receive few signals, so Melexis uses a brand-new xCx sensor. In MLX90614xCx series, the sensor compensates the thermal gradient after measuring it, but the effect is only reduced, not completely removed. Therefore, in the design, the thermal gradient should be avoided as far as possible, or the sensor should be thermal isolated.

Standardly, MLX90614 is calibrated according to target emittance 1. Customers can modify according to the emittance of their target objects, ranging from 0.1 to 1.0. After modification, customers do not need to calibrate in bold. The 10-bit PWM output mode is the standard configuration for continuously outputting the temperature of the measured object, and its temperature is -20°C. The resolution is 0.14 °C in 120 °C range. By modifying the values of two units in EEPROM, PWM can actually adjust to any temperature range according to the requirements, which has no effect on the factory calibration results.

PWM pins can also be configured as thermal relays (input is To), which can achieve simple and cost-effective constant temperature controller or temperature alarm (freezing point/boiling point) applications, where the temperature threshold is programmable by users. In SMBus system, this function can be used as an interrupt signal, which triggers reading the value of the main line follower, and then verifies the accuracy condition [9].

The sensor consists of 5V or 3V voltage. Among them, 5V can also be easily modulated by external components from higher supply voltages (e.g. 8 to 16V). Optical filters (long wave transmittance) are also integrated in the sensor package, which mainly cut off visible and near infrared radiation, so as to improve the sensor's immunity to environmental light and sunlight. Optical filters can penetrate from 5.5 μm to 14μm .

The internal structure of MLX90614 is shown as follows:

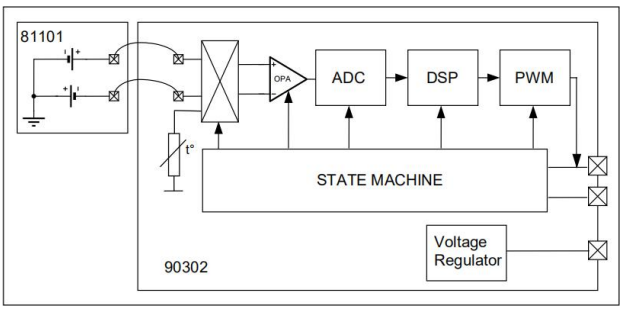

Fig.4 Internal structure of MLX90614

The MLX90614 temperature sensor is an external device. The connection circuit between MLX90614 and STM32 is shown in the figure：

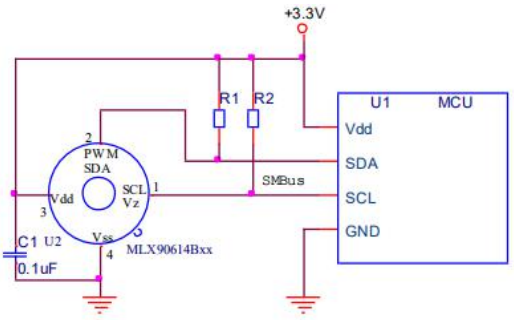

Fig.5 Connection Circuit of MLX90614 and STM32

2.3 Serial port receiving and displaying (PC module and MCU interface)

Import data from STM32 to PC.

Serial port is a general equipment communication protocol between computer and instrument equipment. Generally, computer will contain two RS232-based serial ports, not only that, GPLB also has the serial port. Through the above communication protocol, the data of remote acquisition equipment can be obtained.

Its concept is easy to understand. It completes the sending and receiving of bytes by bit. Compared with byte parallel communication, the latter is faster, but when serial port transmits data with one line, it can receive data with other lines at the same time. It can accomplish long-distance communication simply and efficiently. For example, when IEEE488 defines parallel state, it stipulates that the length of device line must be less than 20 meters, and the length between two devices must be less than 2 meters. But the length of serial port can reach 1200 meters. Typically, serial ports can transmit ASCII code characters. Apply to the ground line, send and receive the three lines to complete the work. Since its communication is not synchronous, it is transmitted from the first line and received by the second line. Other lines are used to shake hands, but this is not necessary. Among them, baud rate, data bit, stop bit and parity check play an indispensable role for serial port. When 2 ports are in communication state, the above parameters must match [10]:

(1) Baud rate: This parameter can highlight the speed of communication. It refers to the number of bits transmitted per second. For example, 250 Potter means 250 bits per second. Once the clock cycle is involved, it must satisfy the 4800 baud rate, so that the clock is 4800 Hz. Generally speaking, there are three kinds of baud rates for telephone lines: 14400, 28800 and 36600. In fact, the baud rate can be much larger than the three mentioned above, which is inversely proportional to the distance. If the distance between the two instruments is not far, the baud rate will be relatively high, for example, GPLB will meet this condition.

(2) Data bits: This refers to a parameter which can measure the actual data bits in the communication process. After the information package is sent out, the standard values of the actual data are 5, 7 and 8. It is necessary to decide which one is related to the final information. If the data is in simple text, then 7-bit data will be used. Packet refers to the byte itself, which is composed of start and stop bits, data bits, parity bits. It is closely related to the choice of communication protocol. Packets can also represent the state of all communications.

(3) Stop bit: It refers to the last bit of each packet, with typical values of 1, 1.5 and 2 bits. The final timing is based on the transmission line. Each device has its own clock. When communicating, there is a certain probability that the two devices are not fully synchronized, so the stop bit can correct the clock and keep them synchronized again. As the number of clocks increases, the tolerance of clocks increases proportionally when they are synchronized. Of course, the transmission speed becomes slower and slower.

(4) parity bits: This refers to a simple method of error detection in the communication process, which can be developed from the perspective of even, odd, high and low. For the first two kinds of cases, the serial port will set the parity bits and use a value, which will ensure that the data will have odd and even logical high bits. Whether low or high, they do not really check data, simple positioning logic high or low check. If the equipment can know the situation of a certain location, it will play a positive role in judging whether there is noise obstructing communication. At the same time, it can also judge whether the received data and the transmitted data are synchronized.

The serial port program is written by LABVIEW. The ABVIEW program block diagram of importing data from STM to PC is shown in the figure：

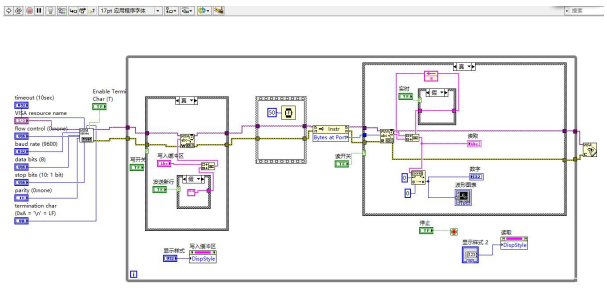

Fig.6 LabVIEW Program Block Diagram for Importing Data from STM into PC

2.4 GSM Mobile Communication

STM32 communicates with mobile phone through GSM module, and receives data and prompt information by short message.

ATK-SIM800C module is a high performance industrial GSM/GPRS module (development board) developed by ALIENTEK. It has perfect functions and is especially suitable for various fields requiring voice/short message/GPRS data/Bluetooth communication services. Its resource map is shown as follows:

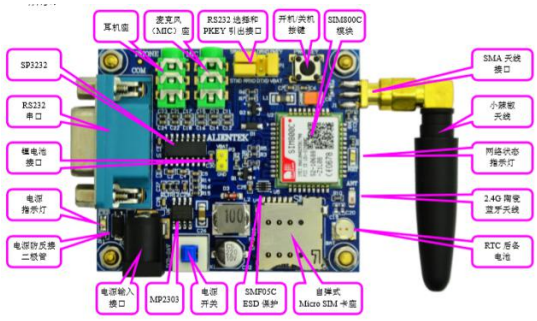

Fig.7 Resource Map of ATK-SIM800C

ATK-SIM800C module not only has beautiful appearance, but also has complete functions. The size of the module (excluding the antenna part) is 62mm*52.5mm. The module itself has the hole position for installation. It is small in size and easy to install. It has outstanding adaptability for many products.

This module can easily read and send Chinese and English short messages.The commands used for reading and sending short messages are AT+CNMI(1), AT+CMGF(2), AT+CSCSCS(3), AT+CSMP(4), AT+CMGR(5), AT+CMGS(6), AT+CPMS(7). The first instruction sets instructions for new messages. Send: AT + CNMI = 2,1 can complete, if the SIM card is not full, the above module will output data through the serial port, such as: +CMTI: "SM", 2, which is to receive new messages, and then store in the location 2 of the SIM card. The second instruction is used to set short message mode. The module supports PDU and text mode. Sending: AT + CMGF = 1, it can be set to the second mode. The third kind of instruction can set TE character set, which is IRA. When sending English short messages, AT+CSCSCS= "GSM" can be used. If sending Chinese, AT+CSCSCS= "UCS2" can be used. The fourth instruction can be used to set text mode parameters of short message. AT+CSMP=17,167,2,25 is used to send Chinese information. The fifth instruction is AT+CMGR, which is convenient for reading short messages, such as sending: AT+CMGR=1, which refers to the location of 1 in SIM. AT+CMGS is the sixth instruction. This instruction is convenient for sending information. If GSM is used as the criterion, then English words with no more than 180 words can be sent. If UCS2 is used as the criterion, AT+CPMS with no more than 70 Chinese characters can be sent, which is the last instruction. This instruction can be used to query or set up the preferred message memory. Send: AT+CPMS?, then it can be obtained. How many text messages have been stored so far, and how many can be stored at most? For example, return: +CPMS:"SM_P", "1,30", "SM_P", "1,30", "SM_P", "1,30". This can highlight up to 30 pieces of information stored, compared with only one at present. These are the instructions of SMS.

3 Test Results

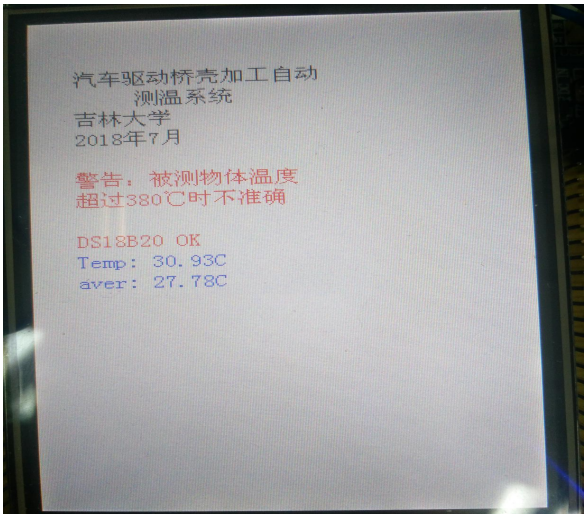

Fig.8 Main Interface of Single Chip Microcomputer

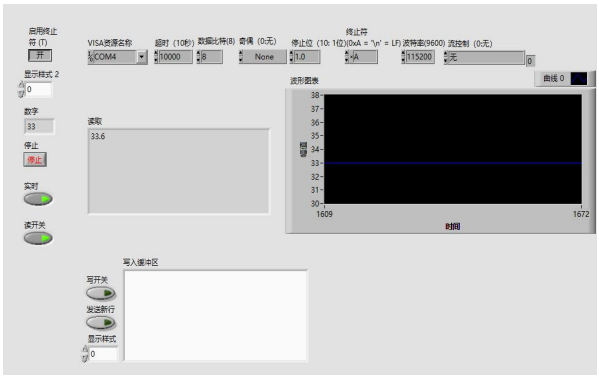

Fig. 9 Main interface of PC

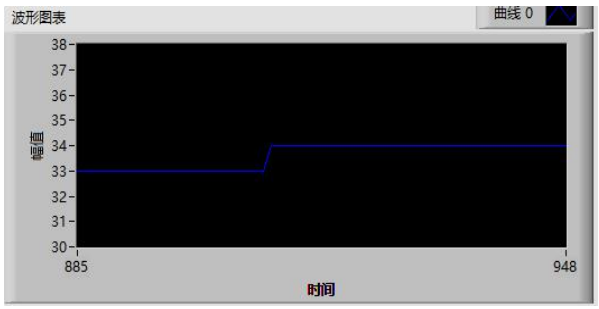

Fig. 10 Temperature Curve of PC

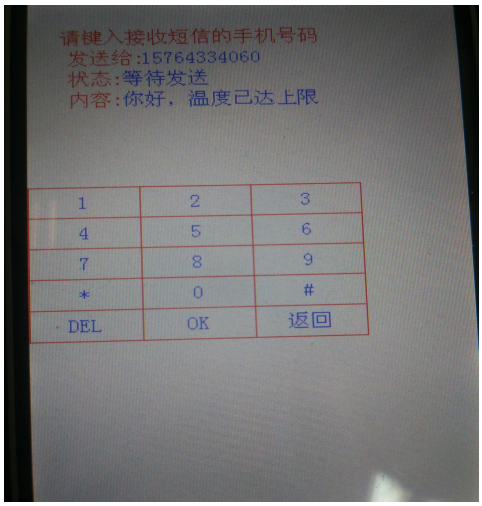

Fig.11 Temperature Control Interface of Single Chip Microcomputer

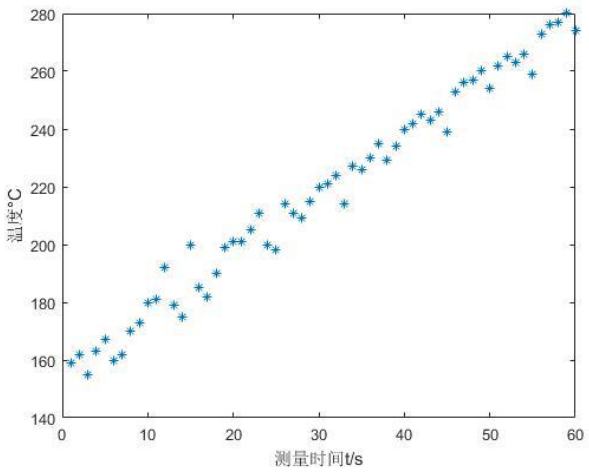

Fig.12 Temperature image in MATLAB

4 Conclusion

The non-contact infrared thermometer will be applied to the new infrared technology when measuring the surface temperature of the object, so the detection is efficient and simple. There is no need to use the tedious detection of mechanical contact at all, so the measurement speed is very fast. For the measured object, the trigger can be activated first, then the LED screen can be stared at, and finally the data will be displayed. It is light in weight, small in volume, convenient in operation and easy to carry. Even for objects with high danger, hot and difficult to touch, it can also measure efficiently and accurately. Not only that, after the measurement, there will be no damage or pollution to the measured object. The non-contact instruments used in driving production need staff to read their own data and can not work automatically [10], so they are not only inefficient, but also more likely to produce errors. Therefore, the remote wireless automatic temperature control technology and system proposed in this paper solves the problem of material temperature measurement and control in the process of automobile driving axle housing processing.

Thermal bulging processing technology of mechanical automotive drive axle housing is a new processing technology. The temperature of material is the key factor affecting the processing effect. This paper takes the automatic temperature measurement and control method as the research objective, and designs an intelligent automatic system. Temperature sensor collects parameters, MCU processes data and displays temperature, wireless data transmission, PC responds accordingly and controls the process. The whole process forms a closed-loop system, which realizes the process automation. This project can avoid manual temperature measurement by staff in high temperature environment, and work efficiency can be greatly improved. Wireless data can be used to complete the control of remote process. People only need to use mobile phones to observe the specific information of temperature in the process of monitoring, and then control the temperature. The non-contact infrared thermometer will be applied to the new infrared technology when measuring the surface temperature of the object, so the detection is efficient and simple. There is no need to use the tedious detection of mechanical contact at all, so the measurement speed is very fast. It is light in weight, small in volume, convenient in operation and easy to carry. Even for objects with high danger, hot and difficult to touch, it can also measure efficiently and accurately. Not only that, after the measurement, there will be no damage or pollution to the measured object.

Reference

[1] Jinhua Cheng, Yang Weixiu, Shuyang, Wenshixiang, Liu Dan, Chen Hongmei, Zhu Caiping. Application of non-contact infrared thermometer in pediatric ward [J]. Journal of Yangtze University (self-study edition), 2018, 15 (20): 81-83.

[2] TSFA portable non - contact infrared thermometer casting temperature measurement across [J].Casting Technology, 2018,39(07): 1548.

[3] Li E, Xia Kun, He Sheng. Design of Wearable Body Temperature Detection Device Based on Wrist Temperature Measurement [J]. Electronic Measurement Technology, 2018, 41 (13): 100-106.

[4] Chen Hailin.Application and analysis of mid-infrared temperature measurement technology in transmission line operation and maintenance [J]. Building materials and decoration, 2018 (27): 223-224.

[5] Ren Guozhong, Zhang Zhongxing, Zhao Guanzong. Research on a new non-contact ambient temperature measurement technology [J]. Sci-tech horizon, 2018 (16): 173-174.

[6] Xu Kan,Zhang Fengdeng.Design of infrared temperature measurement system based on CAN bus [J]. Electronic measurement technology, 2018, 41 (10): 55-58.

[7] Liu Yanwu.Application analysis of mid-infrared temperature measuring equipment in electrical equipment maintenanc [J].Decision-making exploration (middle), 2018 (03): 59-60.

[8] Li Yifeng, Mao Xiaobo, Yang Yihang, Zhu Feng. Design of Non-contact Infrared Thermometric Cooker Dry Burning Prevention System [J]. Journal of Zhengzhou University (Engineering Edition), 2017, 38 (05): 18-22.

[9] Sun Chuanheng.Research on temperature measurement of different parts of Holstein cows by non-contact infrared thermometer. [A]. Information Technology Branch of Chinese Society of Animal Husbandry and Veterinary Medicine. Papers of the 12th Symposium of Information Technology Branch of Chinese Society of Animal Husbandry and Veterinary Medicine [C]. Information Technology Branch of Chinese Society of Animal Husbandry and Veterinary Medicine: Chinese Society of Animal Husbandry and Veterinary Medicine, 2017:4.

[10] Yang Ying.Realization and application of non-contact infrared thermometer [J]. China Medical Device Information, 2017, 23 (11): 34-35.

Research on the pretreatment process of drilling strain data of Guzan station before Lushan earthquake

Zhang Jinlun, Zhu Meiyi, Ma Songchen
（jilin university instrument science and engineering institute,changchun,130021）

***Abstract*—In this paper, the pretreatment method and process of drilling strain data of Guzan station before 2013 Lushan earthquake is described. Based on the measured data of drilling strain from November 2008 to November 2014 in Guzan station, interpolation processing, differential reconstruction and clipping mean filter or difference are used to process it successively after analyzing its characteristics . The results excluded the influence of some non-seismic factors and the eventual relatively flat useful data can be used for follow-up research.**

***Key words*—Lushan earthquake Guzan Station Borehole strain data Pretreatment method**

I. INTRODUCTION

DUE to the enormous destructiveness of earthquake disasters, the state also attaches great importance to the monitoring and forecasting of earthquakes. An earthquake precursor network consisting mainly of crustal deformation observation, electromagnetic observation and underground fluid observation is established [1] [2] The severe geostress change is an important factor in the earthquake. [3] Therefore, real-time observation of changes in ground stress, processing of observation data, and analysis of data laws are the key to earthquake prediction research. The borehole strain observation is a two-dimensional (horizontal) strain observation. The measurement has the characteristics of high observation accuracy and good frequency response, and plays an important role in the study of earthquake precursors, focal mechanism and solid tide. Drilling strain observation has become one of the effective data for earthquake prediction analysis at home and abroad. Hiroshi Ishii [4] used borehole strain gauges in 2014 to study the 2011 northeastern Japan earthquake; Andrew J. Barbour [5] equalized 2014 analysis of the coseismic variation of the borehole strain gauges in the southern California plate boundary; Qiu Zehua [6] studied the borehole strain anomaly of the Wenchuan earthquake in Ningshan, and confirmed the authenticity of the overrun anomaly. Earthquake events are small-probability events, and the underground structure is extremely complex, so the number of major earthquakes is very small. The observations of monitoring instruments are sometimes affected by non-seismic factors such as man-made or surrounding natural environment, so data preprocessing is performed on them. After pre-processing, in order to obtain the effective information related to seismic events in the observation data, it can be further analyzed by spectrum analysis and time-frequency analysis, which is of great significance for the study of earthquakes and their detection and prediction.

Based on the measured data of borehole strain from November 2008 to November 2014 in Guyutai Station, Sichuan Province, this paper studies the data pretreatment process.

II . GUZAN SEISMIC STATION BOREHOLE MEARSURED DATA

The 2013 Lushan Ms7.0 earthquake in Sichuan was one of the most serious earthquakes in China. Due to the different positions of the stations and the epicenter and their own environmental impacts, the observation data affected by the earthquakes at different stations are also different. The Guzhen Seismic Station is one of the nearest borehole strain observation stations from the epicenter of the Lushan earthquake. The distance is only 80km, while the other stations are more than 200km away from the epicenter. It is difficult to observe obvious anomalies before the earthquake.

The observed data is recorded at a frequency of once per minute, and the resulting data is stored in a text document format. The borehole strain is observed as the deformation (that is, the spatial derivative of a point displacement) changes with time. There are three independent components. The plane strain has only three independent strain components. The four-component observation should satisfy the self-consistent equation and can be used to test the observation. Correct or not. The first component S1 of the YRY four-component borehole strain gauge of

Guyutai is 51° east to the east, and the S2 azimuth plus 45° is 81° east and south, and the S3 and S4 orientations are clockwise plus 45°. In order to study the self-consistency of the observation data, the four-component borehole strain self-consistent lines S1+S3 and S2+S4 are similar in shape, and the four-component observation data conforms to the self-consistent equation. The analysis results of the Wenchuan and Lushan earthquakes are basically consistent with the four-way component of the borehole strain of the Guyu station. Therefore, this paper mainly analyzes the borehole strain data of the South Component (S1) of the Lugu.

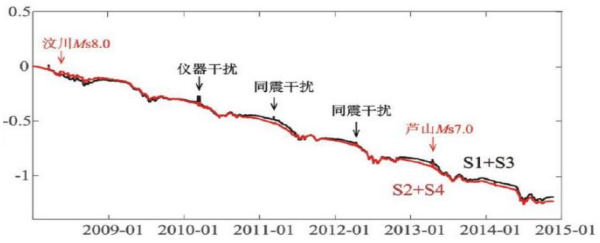

Fig.1 Comparison Curves of Strain S1+S3 and S2+S4 at Guzan Station(January 1st,2008-November 21st,2014)

The advantage of a four-component borehole strain gauge is that it does not observe a change in displacement over time compared to GPS and seismograph observations, but rather a change in the deformation (ie, the spatial derivative of a point displacement) over time, which provides two other Observing the information that cannot be provided [6]; at the same time, the single point independently gives the local deformation, effectively reducing the ground interference without reference point; compared with the telescopic instrument, it has fewer restrictions on the surface and is easy to install; the frequency response is high and the frequency can reach 100Hz. The short-cycle end is much shorter than the telescopic instrument, and is much wider than the seismograph at the long-period end; the precision high-resolution can reach 1E-10, which is at least 1-2 orders of magnitude higher than the GPS observation.

III. REMOVING NULL AND MUTATION DATA

The sampling frequency of the four-component drilling strain gauge is 1/60, that is, the data is recorded once every minute, and the monitoring data is stored as a text document, which can be read and analyzed by the software MATLAB. In order to ensure the normal operation of the instrument, the observer of the station will make adjustments to the instrument from time to time according to the operating conditions of the instrument [7]. Omissions and accidents may still occur during the monitoring process. Once the instrument fails, the character “null” will be automatically used to replace the correct observations recorded at these moments in the document. This type of character data cannot be read correctly. The software design replaces all "null" with 0 to solve the problem of missing data.

In addition to the influence of the instrument, the surrounding environment of the station will also affect the results. Affected by the changes in personnel activities around the instrument and the sensitivity of the instrument [8], the raw data has a sudden jump in the value of the individual time, although the distinction and separation of the abnormal signal and noise in the corresponding variable observation data is not completely conclusive. This error caused by non-seismic factors needs to be removed in time during the pre-processing stage. Because unknown earthquake anomalies may be submerged in some large jump anomalies, it may result in failure to get a correct conclusion, and timely removal or suppression of such abrupt anomalies may minimize their impact on post-processing. The amount of data in this study is large enough, so the Layida criterion, that is, the principle of 3 times standard deviation, can be used as a criterion for removing outliers to detect sudden jump anomalies, and the missing value and the kick value are removed by interpolation [9]--Second, place your cursor in the first paragraph. Go to the Format menu, choose Columns, choose one column Layout, and choose “apply to whole document” from the dropdown menu.

$$\bar{x} = \frac{x_1+x_2+x_3+\ldots.x_n}{n} = \frac{\sum_{i=1}^{n} x_i}{n} \quad (1)$$

$$\sigma = \sqrt{\frac{(x_1-\bar{x})^2+(x_2-\bar{x})^2+\ldots.(x_n-\bar{x})^2}{n}} = \sqrt{\frac{\sum_{i=1}^{n} v_i^2}{n}} \quad (2)$$

The principle of Laida's law is to obtain n observations after observing n times for an object. Assuming that the n-time detection data has eliminated the systematic error, there is only a random error, and the average detection value can be calculated by the formula (1) and the standard deviation can be obtained according to the formula (2). The data larger than the detected data is regarded as a large error and is eliminated [10] and interpolated.

Interpolation is a method of constructing a polynomial function to solve an approximation or a predicted value of a data-free time point through limited known data, which can complement the missing data and weaken the outlier. The "nearest" interpolation method takes the known value of the nearest neighbor of the position as its data. This method is often used to fill the valueless when the data is relatively complete, and the effect is better for evenly

spaced data. Performing such interpolation twice on the observed data can result in significantly improved data [9].

IV. REMOVING STEP DATA

Since the data length is large, the steps are only in part of the time period, in order to enhance the interpolation fitting effect, a sliding rectangular window is used for local judgment. After comprehensive consideration, the window length and step size are initially set to 180*1440 (180 days) and 1440 (1 day). This parameter can be reasonably adjusted according to the data and the actual processing effect to meet the processing requirements. At the same time, in order to ensure that the useful information is not changed, the original data is compared with the processed data, and the obtained image is judged to be successful according to the obtained result image. If it is unsuccessful, the processing parameter can be changed to achieve a better preprocessing effect. Taking the north-south s1 component of the borehole strain data from January 2008 to December 2014 in Guyu station as an example, as shown in Figure 2(a) after character substitution, the original observation data can be seen through the figure. Missing values have been replaced with zero values, and there are large kicks and steps, and effective earthquake anomalies are submerged.

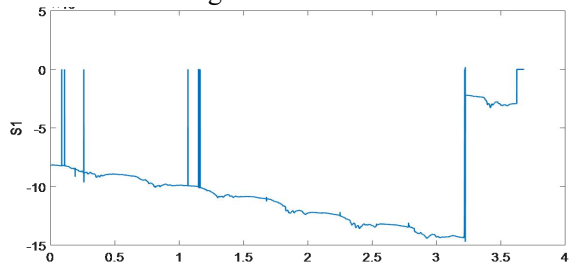

(a) Replace missing data with zero-valued raw data

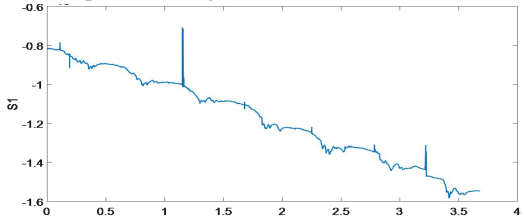

(b) Removal of jumps and steps by differential interpolation reconstruction

Fig.2 Comparison of original data and differential reconstruction of North-South S1 component of borehole strain data at Guzan station from 2008 to 2014

Fig. 2(b) is the result of screening the anomaly and interpolation by the Laida criterion, the difference of the step-by-step anomaly and the post-reconstruction result. It can be seen that the missing measurement data is removed, and the large jump and partial time periods caused by the non-seismic factors The stepping phenomenon of the overall upward shift of the data is also eliminated, and the range and trend of the data are more obvious. The abnormal changes existing after the processing are close to the seismic event period.

V. REMOVING DATA TREND

According to the measurement principle of the four-component borehole strain gauge, the general borehole component strain gauge actually directly measures the relative change of the aperture given, and cannot directly measure the reference value of the terrain change in the region, which is affected by the zero drift of the sensor and the surrounding environment of the sensor. The size of the reference value tends to change with time, and the change of the measured value data is meaningful. It reflects the change of the underground strain, so it is necessary to continue the trend processing of the processing result of the previous section. Methods for eliminating trend terms usually have a difference method and a mean filter method.

It can be seen from Fig. 2(b) that the measured data from 2008 to 2014 is non-stationary and the local variation trend is different. Considering that there may still be abnormal data, the overall mean filtering cannot be performed, in order to ensure the trend of removal and the trend error of the data itself. It is not large, and the method of improving the clipping mean filtering is improved by sliding the rectangular window. The cropping mean filter combines the mean filtering and median filtering characteristics, and has a significant effect on removing Gaussian noise and impulse noise. The use of sliding rectangular window also enables the adaptive effect [11].

The data in the set rectangular window is sorted, the maximum value of a% and the minimum value of a% are discarded, and the mean value of the remaining part is taken. The average value is subtracted from all the data to obtain the final result. Where a% is the cutting ratio, and the range is required to be $0 \leq a\% \leq 0.5$. It can be adjusted by changing the cutting ratio or changing the window length and step size to achieve better results. Compare the data before processing and the trend of removal, in order to verify the detrending effect under the parameter, if the fitting effect of the two Ok, think that the trend is good.

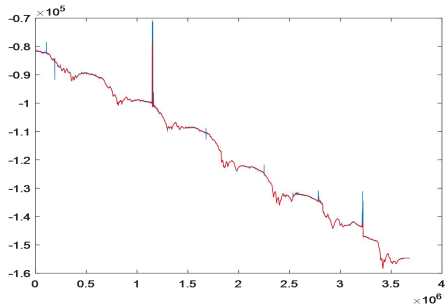

Fig.3 Comparison of the Trends before and after the North-South Components of Guzantai S1 Decline from 2008 to 2014

The blue data waveform in Figure 3 is the result of interpolation processing and differential reconstruction. The red data waveform is the trend curve when the sliding window length and the step length are both set to 1440 and the a-0.2 is removed when cutting the mean value filtering. The trend curve that goes out is fitted to the real trend of the data, and the trend item in the data is well eliminated. Figure 4 shows the results obtained by cropping the mean filtering, ie the variation of the borehole strain data, which reflects the change in the subsurface strain.

V. CONCLUSION

Taking the original borehole strain observation data of the north-south component of Guyutai Station in Sichuan Province from 2008 to 2014 as an example, the following processing methods are used to process the data step by step. The sliding rectangular window is used for data scanning, and the Layida criterion is used for judgment, and the adjacent interpolation method is used for compensation to remove the missing measurement value and the non-oscillation abnormality of the kick. After the differential processing, the same interpolation processing method is used for the result, and the differential data of the rising and falling edges of the step is removed, and then the data is restored by differential reconstruction, and the basic processing result is obtained. In order to obtain the change of the data, the sliding rectangle window is used, and the clipping average filtering method is used to remove the trend of the data, or directly perform the difference to obtain the final desired result. The original data and the processed results are displayed, and the two are compared to highlight the processing effect.

References

[1] Zhang Guomin, Yang Jun. Tidal phenomena and earthquake precursor prediction [J]. 1983（1）:3-7

[2] Simpson D W, Rechards P G. A slow earthquake sequence following the Izu-Oshima earthquake of 1978[M]. Earthquake Prediction. American Geophysical Union，2013:617-628

[3] Wang Yusheng. Li Siguang's Theory of Geomechanics and Seismology [J]，2008，26（11）:98-98

[4] Ishii H，Asai Y，Aoki H. Comparison of tidal strain changes observed at the borehole array observation system with in situ rock properties in the Tono region，Central Japan[J]. Journal of Geodynamics，2009,48（3-5）:292-298

[5] Barbour A J，Parker R L.psd：Adaptive，sine multitaper power spectral density estimation for R[J]. Computers & Geosciences，2014,63（2）:1-8

[6] Qiu Zehua. A review of important events in the development of in-situ stress-strain observation in component boreholes in China [J]. Geodesy and geodynamics，2010,30（5）:40-47

[7] Chi Shunliang. Precursory strain anomalies of strong earthquakes in Wenchuan and Lushan recorded by component borehole strain gauge [J], 2013, 31(12)

[8] Liu Qi, Zhang Jing, Yan Rui et al. Coseismic Response Analysis of Four Component Borehole Strain with High Sampling Rate [J]. China Earthquake, 2013, 29(1):57-67

[9] Li Jinwu, Qiu Zehua. Preliminary analysis of surface strain tidal factors observed by borehole strain gauge [J].Progress in Geophysics, 2014(5):2013-2018

[10] Liu Yuan. Error Theory and Data Processing [D]. Dalian University of Technology, 2009

[11] Hu Hao, Wang Mingzhao and Yang Jie. Adaptive Fuzzy Weighted Mean Filter [J]. Systems Engineering and Electronic Technology, 2002, 2: 15-17

More adjustable parameters and noise source

Li Shuqi, Li Shuxian, Wei Meng
（jilin university instrument science and engineering institute,changchun,130021）

***Abstract*—The detection of the electronic devices' anti-interference ability requires a device that can provide a standard signal with different noise. Therefore, a multi-parameter adjustable noisy signal source is designed to provide a variety of standard signals containing noise for the device under testing. The signal source is based on the STM32 series of single-chip microcomputers of the ARM core. It adopts the basic principles of direct digital frequency synthesis technology (DDS technology), digital-to-analog conversion, program-controlled amplification and switching, and generates various forms and amplitudes such as DC, sine and square waves. A standard signal with adjustable frequency and phase parameters, and a noise signal in the form of Gaussian white noise, fixed frequency noise, and band frequency, and then synthesizing the two signals to achieve standard signal noise.**

***keywords*—STM32 DDS technology digital-to-analog conversion program-controlled amplification waveform generation**

I. INTRODUCTION

THE signal source is a electronic instrument used commonly in the laboratory. It can generate several types of signals, and it is used as an incentive source for the circuit under test. It is combined with other instruments to measure the reliability and stability of the circuit.It is difficult to determine the amount of noise contained in the input signal for most measuring instruments, . At the same time, the influence of these noises on the processing results of the instrument is difficult to determine, so it is difficult to determine the anti-interference ability of the instrument system. As a signal source that can selectively add a known noise signal to the output, a known standard signal, the noise-added signal source can easily and intuitively observe the influence of the input noise on the output of the instrument,so that testing the anti-interference ability of this instrument.

II.OVERALL DESIGN AND TECHNICAL INDICATORS

A.Overall design

The signal source mainly includes a main control module, a power module, a keyboard scanning module, an LCD display module, a standard signal generation module, a noise signal generation module, a program-controlled amplification module (two channels), a two-way signal synthesis module, and a switch (two channels).

The keyboard scanning module is composed of a 4X4 button switch, selects the type of signal generated, and sets the amplitude and frequency of the signal; the LCD display module is composed of the LCD5110 display and its peripheral circuits, and displays the parameters set by the keyboard scanning module.

The standard signal generation module outputs a standard signal, and its waveform mainly includes sine, square wave, and direct three types current signals. The sinusoidal signal is generated by the DDS unit to achieve accurate and adjustable frequency; the square wave signal is generated by the sinusoidal signal output by the DDS unit through the zero-crossing comparator; the DC signal is output by the built-in DA of the main control module.

The noise signal generation module outputs noise signals, including Gaussian white noise, fixed frequency noise, and band-frequency noise signals. The fixed frequency noise is generated by the DDS unit, and the others are converted by the external digital-to-analog conversion unit, and the Gaussian white used for conversion is used. Both the noise array and the band-frequency noise array are generated by matlab software and have good randomness [1].

The program-controlled amplification module uses two-channel amplifying circuit to control the standard signal and the noise signal separately. The specific amplification factor is controlled by the voltage-type program-controlled amplification chip and the post-stage amplification circuit, and the level value of the digital-analog conversion output is used to control the program-controlled amplification chip. Magnification, the two signals are amplified; the power module provides the appropriate power supply voltage for each of the remaining modules [2][3].

The main control module uses STM32F103ZET6 chip. The main control module receives the key value sent by the keyboard scanning module through the I/O port, and sends a waveform and a frequency parameter control word to the standard signal generation module

and the noise signal generation module through the I/O port according to the key value to generate two intermediate signals. At the same time, the output level value is sent to the programmable amplification module to control the amplification of the two signals to generate the final standard and noise signals. The output two signals are respectively combined into two signal synthesis modules by the switch closure or open control to form an output signal, and realize three kinds of signal outputs of standard signal, noise signal and noise addition signal. The system plan is shown in Figure 1.

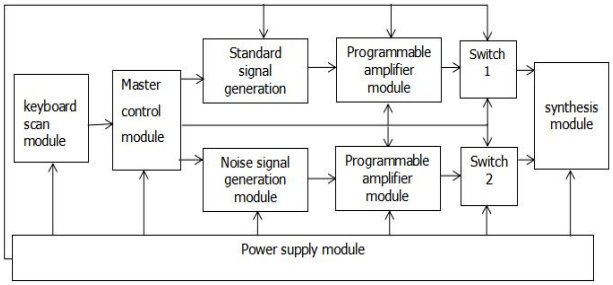

Fig.1 System solutions

B.Technical indicators of this design

The waveform of the standard signal is sinusoidal, square wave and DC. The frequency range is adjustable from one to one kilo hertz, the voltage amplitude is from negative twelve to twelve, and the error range of output voltage is ±10mV. The form of noise are Gaussian white noise, fixed frequency noise and band noise.The frequency range is adjustable from one to one kilo hertz .The voltage amplitude is from zero to five volt. The output mode is divided into a noise signal, a standard signal, and a noise added signal.

III.HARDWARE CIRCUIT DESIGN

A.DDS circuit

DDS technology is a frequency synthesis method which is different from traditional mixing and phase-locked loop methods. Its structure mainly consists of four parts: phase accumulator, waveform memory, D/A converter and low-pass filter. It has high output frequency resolution,low cost, low power consumption, fast frequency generation and switching speed, and continuous phase. The structural block diagram is shown in Figure 2.

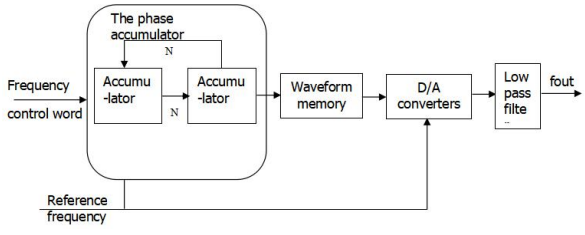

Fig.2 The circuit structure diagram of DDS

As shown in the figure 2, the phase accumulator consists of an N-bit adder and an N-bit accumulator register, which directly determines the resolution of the sinusoidal signal frequency generated by the DDS circuit, and is extremely important in the DDS circuit. The DDS circuit can operate normally with an external reference clock (mostly a crystal oscillator).Each time a clock pulse is added, the adder accumulates the frequency control word and the value of the register output, and sends the added result to the data input of the accumulation register, so that,the data generated when the last reference clock is applied is fed back to the accumulation register by feedback.The adder continuously accumulates the phase of the frequency control word driven by the next clock pulse. At this time, the data output from the accumulator is used as an address, its conversion from phase to amplitude can be completed by looking up the amplitude corresponding to the address in the waveform memory[4][5].

In the DDS module, the formula for the output frequency is

$$f_{out} = \frac{f_{clk}}{2^N} FW \tag{1}$$

The frequency resolution of the output signal is

$$\Delta f = \frac{f_{clk}}{2^N} \tag{2}$$

This design uses the AD9850 chip to generate sine waves of different frequencies and a 50MHz reference frequency. Since the sine wave generated by DDS technology contains a lot of high-frequency noise, it needs to be filtered by a low-pass filter. This design selects the active second-order low-pass filter obtains a better sine wave of the waveform, and then generates a square wave of equal frequency through the zero-crossing comparator. In order to meet the requirements of subsequent program-controlled amplification, the generated square wave is divided [6], and the specific circuit is shown in Figure 3, Figure 4.

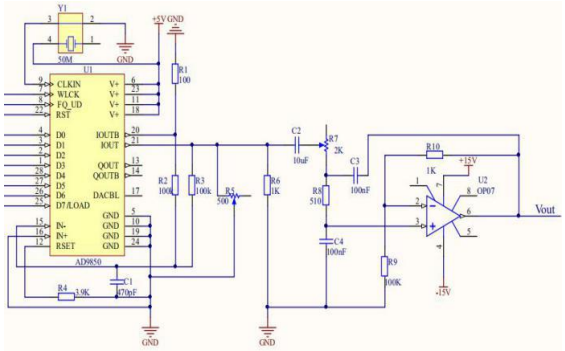

Fig.3 The peripheral circuit of AD9850

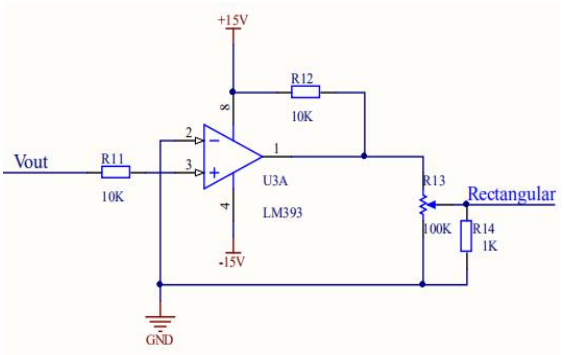

Fig.4 The square wave generating circuit

B. D / A conversion circuit

This design adopts 8-bit D/A conversion integrated chip-DAC083,which is widely used in single-chip application system,because it has the advantages of low price, simple interface and easy conversion control.Since the characteristic of stepped shape of the generated signal,it needs to be filtered by low-pass filter. As for DAC0832 chip, it outputs current,leading to an operating amplifier is needed to the later stage to convert current and voltage.And it is a negative polarity output,in order to meet the requirements of the index,the bipolar output circuit is selected, which can output voltage from - 5 to 5V [7]. The specific circuit is shown in Fig. 5.

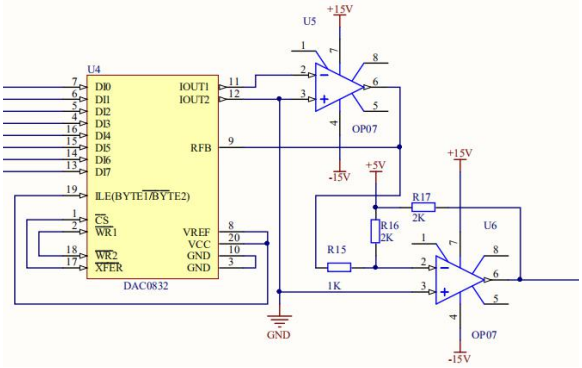

Fig.5 D/A conversion circuit

C. Program-controlled amplifier circuit

The two-way control amplifier circuit includes an AD603 front-stage programmable amplification unit, a post-stage amplification circuit unit composed of op07 chips, and a DAC0832 digital-to-analog conversion unit. The voltage value generated by the DAC0832 digital-to-analog conversion unit controls the amplification factor of the AD603 front-programmed amplification unit; the amplification factor of the post-stage amplification circuit unit is fixed, and the two control the amplification of the input standard signal and noise signal together [8][9]. The two-way control amplifier circuit is shown in Figure 6 and Figure 7.

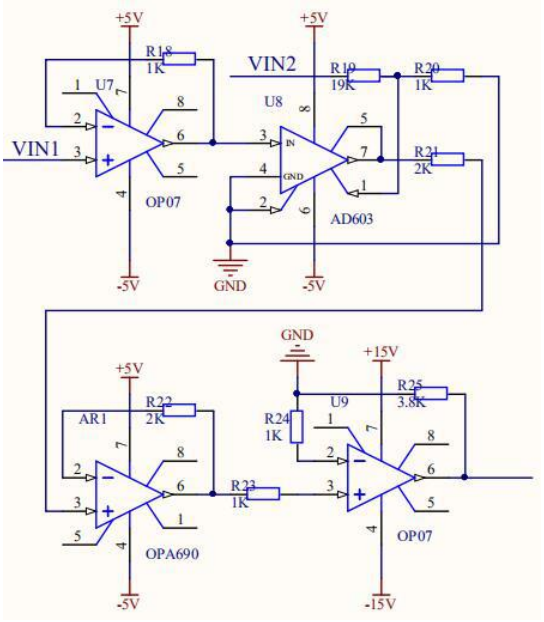

Fig.6 The circuit of Standard signal programmable amplifier

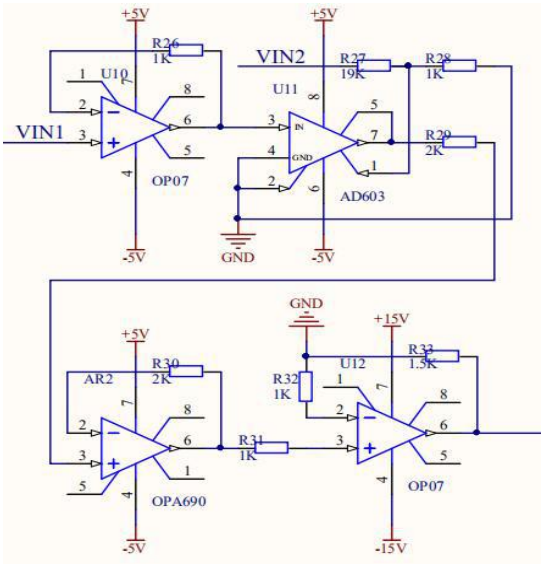

Fig.7 The circuit of noise signal programmable amplifier

D. Synthetic circuit

There are two common forms for adder circuits - in-phase adders and inverting adders. When the in-phase adder is used, the input impedance is low, while the output impedance is large, and the two signals input will interfere with each other, and the obtained signal noise is large, which affects the accuracy of the final result. Because the inverting adder has a large input impedance and a low output impedance, the two signals are more likely to flow into the adder without interfering with each other, and it has low noise and high precision. Therefore, the design uses an inverting adder.

The synthesis circuit uses a more classical inverting addition circuit in the mode, and the op amp uses a low-noise and high-precision bipolar op amp op07.

Since the signals obtained by the inverting adder are opposite in phase, an inverter is added before the adder to maintain the phase consistency. The specific circuit is shown in Figure 8.

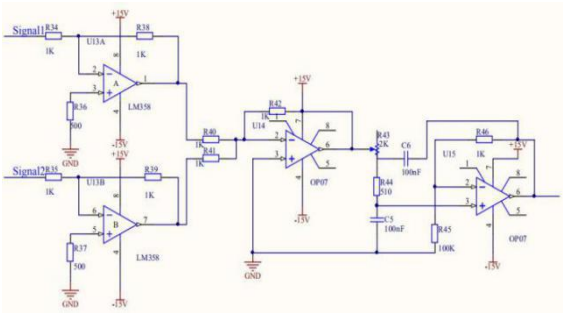

Fig.8 The synthesis circuit of signals

IV.SYSTEM SOFTWARE DESIGN

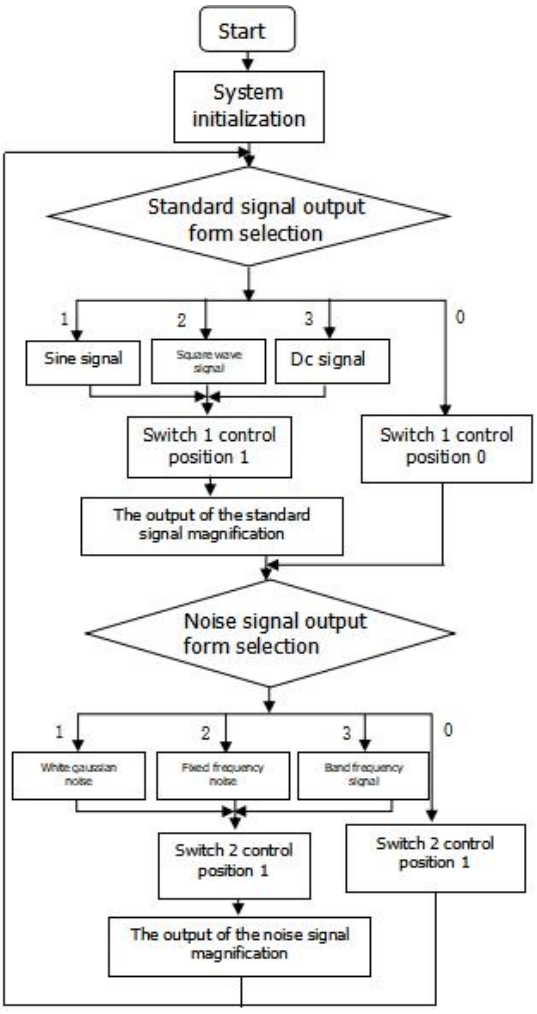

Fig.9 The Program flow chart of STM32

V.SYSTEM TEST RESULTS

TABLE I Test results of standard signals

Test result	Sine signal		Square wave signal		Dc signal	
	Ideal value /V	Real value /V	Ideal value /V	Real value/ V	Idea l valu e	Real value/ V
1	1.0	0.96	1.0	0.98	1.0	1.03
2	2.0	1.98	2.0	2.04	2.0	1.98
3	3.0	3.00	3.0	3.12	3.0	2.90
4	4.0	3.96	4.0	3.94	4.0	4.31
5	5.0	5.12	5.0	5.06	5.0	4.78
6	6.0	6.00	6.0	6.08	6.0	5.89
7	7.0	6.92	7.0	6.98	7.0	7.14
8	8.0	8.00	8.0	8.00	8.0	8.28
9	9.0	9.18	9.0	9.24	9.0	9.16
10	10.0	10.4	10.0	10.2	10.	10.3
11	11.0	*	11.0	*	11.	*
12	12.0	*	12.0	*	12.	*

Note: * is the data that cannot be measured by the actual test.

TABLE II Frequency results of standard signals

Number	wave type	Ideal value （Hz）	Real value （Hz）
1	Sine signal	50	50.002
2		200	200.000
3		500	500.000
4		700	700.000
5		800	800.000
6		1000	1000.001
7	Square wave signal	50	50.013
8		200	200.007
9		500	500.001
10		700	700.000
11		800	800.004
12		1000	1000.000

It can be seen from Table 1 that most of the measured values are close to the expected values, but there are still a few error data . Table 2 shows that the measured frequency obtained by the DDS technique is 0.1 Hz less than the technical index.

VI.CONCLUSION

This paper designs a multi-parameter adjustable noise-adding signal source, including main control module, keyboard scanning module, LCD display module, power module, standard signal generation module, noise signal generation module, two-way control amplification module, and two-way signal synthesis and switches, which are based on the

combination of software and hardware to output the three types of known standard signals, known noise signals and noise-added signals, and the signal waveform, frequency, amplitude and other parameters are adjustable to check the anti-interference ability of the precision instrument.

References

[1] Gui cai Geng,Yu bin Shao,Di Xiao.Research and Implementation of Gaussian White Noise Generation[J]. Electronic technology,2006(11):16-18+22.

[2] Yang Li,San qiang Yuan,Wei feng Yan.Design of Programmable DC Broadband Amplifier Based on AD603[J].Journal of Chongqing University of Arts and Science (Natural Science Edition),2010,29(06):28-31.

[3] Xin nan Zhao,Rong li Cai.Design of Program-controlled Gain Amplification Circuit Based on AD603[J].Journal of Shandong Agricultural University(Natural Science Edition),2018,49(01):40-43.

[4] Wan rong Lin.Design and Implementation of DDS Signal Generator System Based on AD9850[J].China Cable Television,2015(11):1286-1290.

[5] Han ping Huang,Bo Qiu.Design and implementation of DDS sine wave signal generator based on AD9850[J].Electronic world,2013(04):57-59.

[6] Jie hua Zong.Design of Practical Signal Generator Based on DDS[D].Hunan University,2012.

[7] Ye ting Tang.Implementation and research of multi-band digital Gaussian white noise based on multi-sampling rate[D].Hebei University of Science and Technology, 2015.

[8] Lin Zhang,Jun xi Zhao,Yin bing Zhang.Design of a low frequency signal source with noise based on DDS AD9832[J]. Electroacoustic Technology,2007,(05):37-39.

[9] Peng Zhang,You Hua Ding,Han Ao Xia. The Design of Dynamic Target Echo Intermediate-Frequency Signal Source of Radar[J]. Applied Mechanics and Materials,2014,3468(644).

[10] Hang Zhu,Shu ning Zhang,Hui chang Zhao. Single-channel source separation of multi-component radar signal based on EVD and ICA[J]. Digital Signal Processing,2016,57.

[11] Hang Zhu,Shu ning Zhang,Hui chang Zhao. Single channel source separation and parameter estimation of multi-component PRBCPM-SFM signal based on generalized period[J]. Digital Signal Processing,2015,40.

Neck Massage Instrument with Bluetooth Headset and Beat Capture

Zhao Hanqing, Zhou Zijian, Cheng Hao
(School of Instrument Science and Electrical Engineering, Jilin University, Changchun 130022)

***Abstract*-Electronic product technology development to date, wireless headset and neck massager is still full of promotion prospects and high consumer demand of electronic products. Because the headset is different from other headphones for long hours of work without injury, high sound quality characteristics, most people today will choose to buy wireless headphones as a necessary product for work, amateur, but because of the hairstyle, sweating and a series of reasons, many people will head headphones hanging in the neck use, But the original head-mounted design of the headset makes the way the headset is worn have a big impact on the stability of the headset, which has prompted the formation of a dedicated neck wearing headset. On the other hand, today's social population because of life and work habits, more or less there is a certain neck illness, compared to the medical institutions to treat, more people choose to buy a massage instrument for relief, it is inevitable to wear in the neck. and "Neck massage wireless Headset" is put forward in this context of the two-bit one can meet the two products, not only the simple combination of the two, but through the investigation of technology and appearance and other improvements, a combination of headphone users and massager users of the requirements and optimization, more in line with the consumer population and needs.**

Our aim is to combine the existing headphones with the neck massager organically to solve the problems arising from product design and production through research and technical processing to improve the overall performance of the product.

***Key words*—DSP technology Signal processing Voice recognition**

I.INRTODUCTION

BEAT Capture Massager is through Bluetooth will be mobile phone or computer music files (such as MP3 format files) first decoded into a PCM encoded audio signal, and then decoded as a child band encoding (SBC) data through the top layer of the Bluetooth module data transmission to the DSP chip, DSP chip docking received audio files first for window preprocessing , the Fourier transform of the signal after the window is carried out, the spectrum information of the signal is observed, then the audio rhythm is found by the difference between the current frame and the previous frame, and then the position of the beat point is found more accurately by the Statistical Time series analysis method, so as to complete the process of the beat recognition and capture[1]. Then according to the amplitude and position of different beat points, the corresponding output of different PWM waves, control the working state of the motor, driving the massage instrument to make different massage effects. To achieve the effect of adjusting the massage frequency according to different music.

II.AUDIO BEAT DETECTION

According to the requirements of the Innovation project, in order to complete the music beat to control the motor speed, it is necessary to recognize the input audio beat[2]. Figure 1 shows the flowchart for beat recognition:

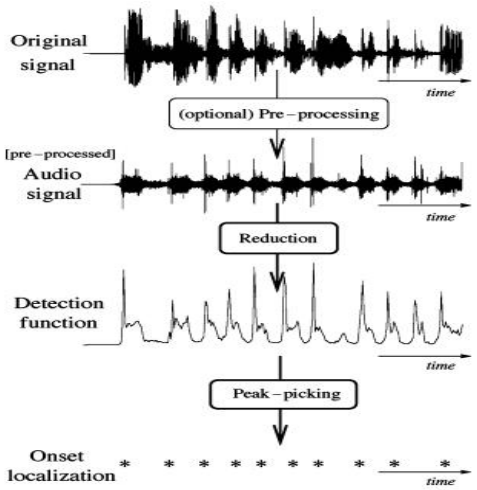

fig. 1 Flowchart of a standard onset detection algorithm.

Preprocessing of Audio Signal

For the input audio signal, the first preprocessing, that is, the audio signal to add windows and sub-frame processing [3-5]. The window size is 1024 and the number of frames is typically about 33-100 frames per second. In order to smooth the frame and frame, the sub-frame generally adopts the method of alternating segmentation. The length of the overlapping signal

segment between the previous frame and the next frame is the frame shift. Typically, the frame shift is no longer than 1/2 of the frame length. The implementation process of the sub-frame is to weighted the fixed-length removable window, that is, use the window function w (n) to multiply the original signal s (n) to form the window signal SW (n) as shown below.

Sw（n）=s(n)*w（n）

The signal after windowed and framed is shown in Figure 2.

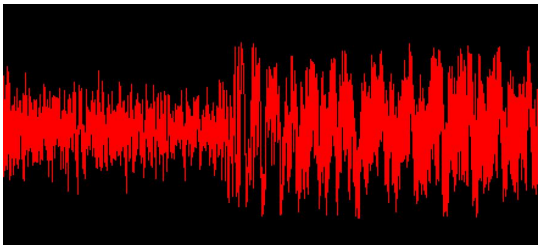

fig. 2 audio signal on frequency domain

The frequency domain analysis of the signal will produce truncation effect, cause the energy leakage of frequency, in order to maintain the short time stability of the sound signal, it is necessary to select the appropriate window function. Because the Hemming window can effectively overcome the truncation effect, its short-time spectrum is smoother. Fourier transform is performed after the window is divided into frames.

Fourier transform of audio signal

Fourier transform is performed on the signal after the window is divided into frames. The basic idea of the fast Fourier transform method is to use the periodicity and symmetry of the complex exponential function to make full use of the intermediate operation results, so that the computation workload is greatly reduced [6-7]. It is to decompose a long time series X (n) into a relatively short time series, the child time series can continue to decompose into a smaller sub-time series, recursive down until finally get a simplest sub-time series, that is, until a number; Then Fourier transform is carried out on the simplest sub-time series obtained by Fourier transform calculation formula, and then the Fourier transform results of each sub-time series are combined according to certain rules, and the Fourier transform results of the original time series are obtained finally[8].

Depending on the size of the window you took earlier, and take a general audio sample rate of 44100, the number of Windows within 1s is:

N=44100/1024=43

The frequency domain of the signal is observed in each 1s and is divided into 43 frames.

But even with the spectrum of time-domain signals for each frame[9], we don't know how to compress all the information in the spectrum into a manageable one-dimensional floating-point array, making it easy to peak detection.

It is applied here to the differential processing method.

Differential Treatment of Audio Signal

For a more accurate beat capture of the processed data, we used the method of time series data analysis [10]. Time series analysis (Timing series analysis) is a statistical method of dynamic Data processing. Based on stochastic process theory and mathematical statistics method, this method studies the statistical laws followed by stochastic data sequences to solve practical problems.

The basic steps are:

(a) The dynamic data of the time series of the observed system are obtained.

(b) According to the dynamic data, the correlation diagram is carried out, and the autocorrelation function is obtained.

(c) Identify the appropriate stochastic model and curve fitting, that is, use the general stochastic model to fit the observation data of the time series.

For the beat capture of the audio signal, the moving average is analyzed.

The time that a window is known to represent is

1000 / (44100 / 1024) = 23.21ms

Then you need to calculate the mean in 0.5s as an interval, and the number of Windows required is about 22. Take the first 10 Windows + the second 10 windows to calculate the mean.

Comparison of its mean graph with original audio as Figure 3:

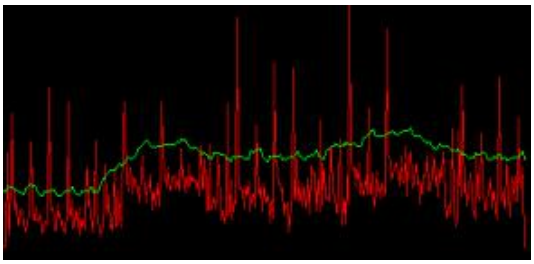

fig. 3 Moving average figure

Then take the corresponding frame in each window that is greater than the average, and you can get Figure 4.

fig. 4 Beats of audio

In this way, for an audio signal, its beat is well done to capture the work.

III. System Hardware Design and Implementation

Holistic Design of Hardware System

The whole system is designed on the basis of DSP, with TMS320F28335 as the main control chip, data transmission through Bluetooth, and the metronome is found out and the corresponding PWM wave control motor is generated to drive the massager to work by decoding audio files, windowing, Fourier transform, difference value and time series analysis, etc.

Design and Implementation of Bluetooth Audio Transmission

Bluetooth technology is an open short-distance wireless communication technology jointly launched by Ericsson (Ericsson), NOKIA (NOKIA), TOSHIBA (TOSHIBA), IBM (IBM) and INTEL (INTEL) and other companies in 1998. It combines communication technology and computer technology to realize data transmission between different devices [11].In essence, whether it is audio video or other forms of file, the transmission is essentially a byte stream transmission, but due to the different transport protocols supported by the device and the differences between the top-level file system resolution, there will be audio transmission this special category.

Bluetooth USES circuit switching and packet switching technology to support asynchronous data channel, voice channel and asynchronous data and synchronous voice transmission channel at the same time.Each voice channel has a data rate of 64KbsP, and bluetooth voice can use either pulse code modulation (PCM) or continuous variable slope delta modulation (CVSD).Bluetooth has two link types: asynchronous connectionless (ACL) links and synchronous connection-oriented (SCO) links.ACL link supports symmetric or asymmetric, packet switching and multi-point connection, which is suitable for data transmission.SOC links support symmetry, circuit switching, and point-to-point connections for voice transmission.

Bluetooth technology supports both voice and data transmission, enabling devices that support voice or data, or both, to communicate with each other[12].

In the selection of Audio transmission format, according to the code rate from low to high can be divided into SBC (sub-band coding, subband coding) ACC (Advanced Audio coding, Advanced Audio coding) APTX and LDAC.Considering the speed problem in the actual transmission process, the scheme of appropriately reducing the sound quality and improving the transmission speed is selected here, and the transmission is carried out by means of SBC coding.Therefore, the format change of data in the actual transmission process is shown in figure 5:

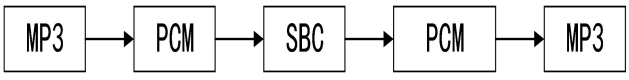

fig.5 Data formats in transmission process

As the data entry point of the overall design, the bluetooth module is paired and connected with the bluetooth of the mobile phone and computer, and the audio signal is transmitted to the DSP chip through the bluetooth module, followed by the data processing process. Therefore, the stability and accuracy of bluetooth transmission are particularly important. According to the previous investigation, the audio transmission of PCM interface is more advantageous and more extensive than that of UART interface.Therefore, the PCM interface is selected at transport time.When considering the choice of the bluetooth transmission module, the traditional HC - 05 master-slave one-piece bluetooth module can complete data transmission, but is based on the data flow in the form of the underlying transport mode, the existing technology has to integrate the audio module into a SOC, including for audio signal encoding and decoding, and the corresponding filter, power amplifier circuit [13].It is more convenient and fast to use.

The bluetooth module USES BT201 module, which has the advantage of low cost: because it is a domestic chip, it reduces the cost by relying on overseas shipments and strong market competition.There are many functions supported: AT control function of serial port, BLE transparent transmission, and SPP transparent transmission.Chip internal software support, and the interface is very rich, also worth in-depth study.The overall bluetooth data transmission is shown in figure 6:

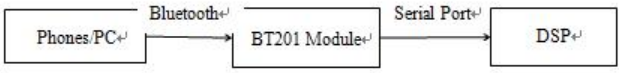

fig.6 Bluetooth Data Transmission design

Motor Modules

In the neck massage instrument, the motor is responsible for driving the massage instrument rotation, and its rotation frequency and phase should correspond to the beat in the music at all times. Therefore, the stepper motor, stepper motor is easy to control, by controlling the starting point of the motor to achieve the control of the initial position of the massage rod and so that the two synchronize the purpose. In addition, the stepper motor does not have the characteristics of accumulated error is also very suitable for the consistency of music beat, will not appear in the second half of the song more error and affect the auditory experience.

Single stepper motor requires two PWM pulses, all the way for stepper control and the other way for steering control. Using the tms320f28335 internal PWM module to produce two independent epwm1a waveforms and epwm1b waveforms, the two-way PWM signal with dead zone is directly generated from the PIN [14-15]. In the control of stepper motor, the control signal is determined

by the processing result of audio data by DSP, and the contents and methods of its control are as follows:

(a) Initial position and pedometer

From the program, the first position of the music will have a certain amount of time of the Beat Blank, and the first beat of different songs are also in different positions, in order to make the starting beat of the music and the starting position of the massage stick synchronized, need to design a pedometer. Of course, the purpose of such a pedometer is not to record the number of steps that have been turned, but to find the correct position. Therefore, the pedometer with the number of steps to turn a circle is the maximum loop count can be [16].

When Matlab calculates the audio data, it gets the following data that needs to be transferred to the DSP: first, the initial time, the time when the music starts to the music debut, and the initial position, the position of each of the strong beats in the beat of most music is the same, but the music debut is not necessarily the beginning of a beat, So the initial position is related to the nature of the music debut, and is not fixed, and the third is the music frequency, assuming that each beat of the music is two seconds (in fact, this is the conventional thing in the music), but the four-point Pat and the eight-point take-off circle cycle is not the same.

(b) Rotational Speed and Musical Frequency

The speed of stepper motor is determined by pulse frequency. There are two methods of pulse regulation. The system adopts software method to realize pulse regulation. When periodic interruption occurs, when interruption processing subroutines are processed, the corresponding bits in the comparative mode register ACTRA/B are "forced high" or "forced low" to control a certain phase-on and power-off, thus realizing commutation [17]. The speed control of stepping motor is realized by controlling the frequency of stepping pulse sent by DSP specifically, by controlling the periodic value of DSP_timer to control the frequency of stepping pulse.

The shape of the massage bar has two peaks corresponding to the strong beat and the sub-strong beat in the music beat. In music, there are seldom more than two strong beats in a whole beat (excluding two), so the highest frequency is eight minutes four strong beats corresponding to one second two laps, and the lowest four minutes one strong beat corresponding to two seconds one circle.

(c) Steering and phase change

The power-on phase Change Order of the stepper motor is strictly in accordance with the working mode of the stepper motor, in the power-up mode of the double four-beat, the power order of the motor is A-B-A^--B^-, and the reverse order is A-B^--A^--B. In the neck massage instrument, a single-directional massage is a big bogey. So we change between the song and the song, which is not transmitted by the host computer, but changes made after the beat changes in the DSP.

IX. CONCLUSION

Based on Bluetooth technology and DSP technology, the neck massage instrument can allow users to enjoy music while enjoying the comfort of massage, the existing products can not achieve two kinds of effects. This design adjusts the massage frequency to achieve the expected function by decoding the audio signal and capturing the beat point.

By testing 3 different types of music, the motor working process and the massage instrument output effect is significantly different, in the bass part of the headset output effect is good, with a high enough level. through MATLAB upper computer audio software detection found in the low frequency band of energy accounted for more than 40%.

References

[1] G. Pacini Panebianco,M.C. Bisi,A.L. Mangia,R. Stagni,S. Fantozzi. Analysis of temporal gait parameters during walking on sand using inertial wearable sensors[J]. Gait & Posture,2018,66.

[2] He Xiaoliang. Recognition of Musical Rhythm in Dance Robot [J]. Electronic Design Engineering, 2013, 21 (04): 19-21+25.

[3] Hu Jianjian, Zeng Peifeng, Tang Liping, Zang Zhuping. Music beat extraction based on Gauss lowpass filter [J]. Journal of Donghua University (Natural Science Edition), 2011, 37 (01): 72-75+80.

[4] Li Na. Research and application of real-time music beat tracking system [D]. Shandong University, 2011.

[5] Hu Jianjian. Research on music beat extraction method based on Gauss lowpass filter [D]. Donghua University, 2011.

[6] Yang Jie, Li Shuangtian. An efficient music beat detection algorithm and its implementation in DSP [J]. Signal Processing, 2010, 26 (08): 1246-1251.

[7] Yang Jie, Li Shuangtian. An efficient music beat detection algorithm and its implementation in DSP [J]. Signal Processing, 2010, 26 (08): 1246-1251.

[8] Cao Haitao. Research on Audio Signal Filtering and Recognition Technology Based on Time-Frequency

Domain Analysis [D]. Guangzhou University, 2016.

[9] Luruizi. Research on Active Speech Signal Detection Technology in Audio Monitoring System [D]. Shenyang University of Technology, 2016.

[10] Li Yu. Wavelet-based filtering and spectrum analysis of audio signals [D]. Harbin University of Engineering, 2013.

[11] Zhang Qin. Research on Voice Transmission Based on Bluetooth Technology [D]. Nanjing University of Technology, 2004

[12] Xu Ming. Principle and Implementation of Bluetooth Technology [D]. Graduate School of Computing Technology, Chinese Academy of Sciences, 2002

[13] Zhao Xiuling, Qiu Sijie, Lin Yongjun. Blind Guide Based on Bluetooth Voice Transmission [J]. Electronic World, 2013 (15): 78-78

[14] Hu Peiru, Rui Yanan. Design and implementation of a Bluetooth audio streaming transmission scheme [J]. Modern Electronic Technology, 2006, 29 (3): 31-33.

[15] Lin Biao, Chen Xinyue, Hu Xiuting, Wang Shun, Zhang Ruiyi, Wang Ye. Design of a self-powered power supply and vibration temperature rise detection sensor based on DSP28335 motor [J]. Electronic World, 2018 (24): 66 + 68.

[16] Xiong Yongkang, Li Yuezhong, Quanrich. Design of micro-displacement stepping motor control system based on TMS320F28335 [J]. Electronic technology, 2014, 43 (04): 61-63+54.

[17] Jia Jia, Liu Juan. Research on stepping motor control system based on TMS320F28335 [J]. Equipment manufacturing technology, 2015 (11): 293-294.

Portable blood flow measurement system based on photoplethysmography

Guangda Liu, Meng Wu, Yuzhu Li, Fuxiao Guo, He Hu
(College of Instrumentation and Electrical Engineering, Jilin University, Changchun, 130026, China)

***Abstract*—This system is a portable blood flow velocity measurement system based on photoelectric volume pulse wave, and collects two paths of pulse wave form. Differential threshold method was used to calculate the propagation time, and then the blood speed was calculated. The measured results are very close to the actual blood speed.**

keywords—method of photoelectric volume blood speed pulse wave differential threshold

I. INTRODUCTION

THE pressure created by systole is the source of blood flow. The blood flow rate is affected by factors such as blood clots, blood viscosity and cardiac function. It can be used as a monitoring indicator for many physiological conditions, has good physiological and pathological significance for clinical diagnosis and monitoring, and is an important detection method for medical clinical diagnosis. Measurement of blood flow can help diagnose some diseases, such as valvular heart disease caused by abnormal blood flow, poor blood flow, short-circuit flow, etc. Congenital heart malformation or diagnosis of carotid artery and extremity artery peripheral stenosis, occlusion and other lesions, and determine its severity.

In 1975, Sten reported the first use of Doppler flowmetry to monitor skin microcirculation blood flow[1]. In 1993, Lin Guoxing of China recommended measuring the blood flow rate according to the laser Doppler effect. The laser Doppler effect is an implantable measurement[2]. In 2010, Jiang Hong of China proposed a method for microwave detection of blood flow rate[3]. In 2014, Zhou Heng proposed a blood flow measurement method based on fiber optic sensing technology[4]. In 2017, Zhao Min proposed a method based on multi-electrode electromagnetic measurement of blood flow rate[5]. In 2018, Wang Xiaochun et al. proposed a method for measuring blood flow rate based on very high frequency ultrasound[6]. With the advancement of science and technology, China's medical equipment has entered an era of non-invasive or micro-trauma. Miniaturization and intelligence will be the development direction of medical instruments inthefuture[7].

Based on the above research, based on Lambert-Beer theorem and light scattering theory, this paper proposes a non-invasive blood flow rate detection method based on photoplethysmographic pulse wave, which divides the distance between two points on the arm by the conduction time of the pulse wave between two points. The conduction velocity of the pulse wave between the two points is obtained, which is approximated as the blood flow rate between the two points.

II. INVASIVE BLOOD FLOW VELOCITY MEASUREMENT METHOD

At present, most common blood flow measurement methods are invasive methods. Take the coronary angiography blood flow method as an example. Conventional coronary angiography is a catheter technique that injects an X-ray contrast agent directly into the coronary arteries to form a digital sequence image. Storage analysis. The computer technology is used to track the front end of the intracoronary contrast agent, and the distance L of the contrast agent front end moving between the two frames is measured, and the coronary blood flow velocity V=L/T can be obtained by setting the inter-frame duration time T.

The invasive blood flow rate measurement brings great discomfort to the person being tested, and the invasive blood flow rate measurement brings great discomfort to the person being tested, and is more likely to cause physical damage to some patients with blood diseases.

III. NON-INVASIVE BLOOD FLOW RATE MEASUREMENT METHOD

A .Measuring Principle

The degree of light absorption of matter can be described by the law of lamber-beer [9]: when monochromatic light of intensity I0 is incident on a homogeneous substance, part of the light energy is absorbed by the substance, and another part of the light

is absorbed from the substance. The intensity I of the emitted light is—

$$I=I_0e^{\wedge}(-\varepsilon(\lambda)cd) \quad (1)$$

—ε(λ) is the molar extinction coefficient of matter versus wavelength λ light

—c is the concentration of light absorbing material

—d is the path length of light propagating in the medium, called the optical path length

It can be seen from the above formula that when the wavelength is constant, the absorbance of the substance is proportional to its concentration. When the light of constant wavelength is irradiated onto the human tissue, the light intensity measured by absorption and reflection attenuation of the human tissue reflects to some extent. Structural features of the tissue being irradiated.

Photons are absorbed and scattered in human tissues. When light is irradiated into human tissue, a part of the photons will undergo multiple scattering to change the original transmission path and eventually exit the tissue surface; another part of the photons will be absorbed by the tissue during the propagation process, as shown in Figure 1.

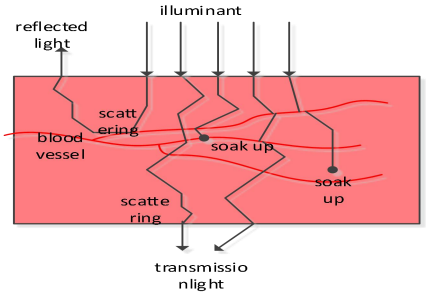

Fig.1 The diagram of the photon propagation in Human tissues

Due to the pulsation of arterial blood, the degree of absorption of photons passing through the arterial blood periodically changes with the pulsation of the arterial blood: when the heart contracts, the arterial blood is pumped into the surrounding blood vessels, and the blood at this time is absorbed. When the photon increases, the light intensity decreases; when the heart expands, the blood flows back to the heart, at which time the photons absorbed by the blood decrease and the intensity of the emitted light increases. We define this light intensity component as the AC component over time. Another portion of the photon that does not pass through the arterial blood is absorbed and scattered by non-jumping components such as soft tissue, bone, and venous blood, and the emitted light intensity is relatively stable. We define the average of the emitted light intensities as the DC component. When a photodetector is used to detect emitted light on a tissue surface, a signal is obtained that varies in intensity as a function of heartbeat. We call this signal a photoplethysmography (PPG) signal, as shown in Figure 2.

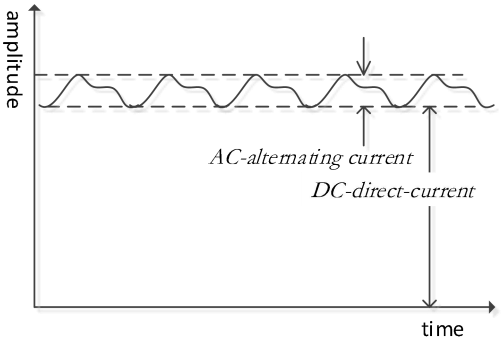

Fig.2 the PPG signals produced by the body's absorption of light

Since the absorption spectra of oxyhemoglobin (HbO2) and deoxyhemoglobin (Hb) in the blood (600~1000 nm) are unique in the red and infrared regions (600~1000 nm), the wavelength λ is 940 nm. Light is used as the light source of the system, and the light emitted from the surface of the skin is received by the receiver to obtain a photoplethysmographic pulse wave.

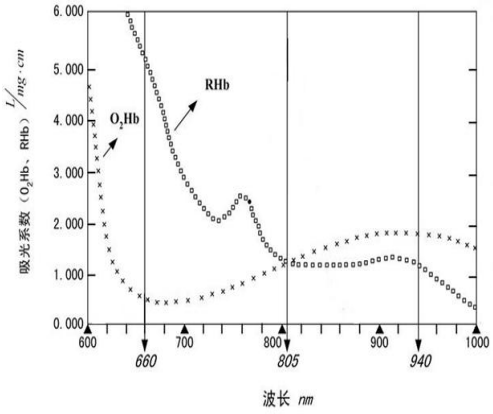

Fig.3 O_2Hb and RHb absorption spectrum

According to Lambert-Beer's law, when monochromatic light with a light intensity of I0 (wavelength λ1) is irradiated onto human tissue, the intensity of the emitted light is

$$I(t)=I_0e^{-\{\varepsilon_0(\lambda_1)c_0d_0+[\varepsilon_1(\lambda_1)c_1+\varepsilon_2(\lambda_1)c_2]d(t)\}} \quad (2)$$

In the above formula, ε0(λ1) represents the total extinction coefficient of the non-jumping component such as muscle, fat, skin, bone, and venous blood in the tissue to the light source of wavelength λ1. C0 is the total concentration of the above substances. D0 is the effective optical path length of light propagating in these non-jumping components.

E1(λ1) and ε2(λ1) are the extinction coefficients of oxygen-containing hemoglobin and reduced hemoglobin for light of wavelength λ1, respectively, and c_1 and c_2 are concentrations of oxygenated

hemoglobin and reduced hemoglobin, respectively. d(t) is the long path length of light propagating in arterial blood, which changes with pulse beat.

When the heart contracts to the highest pressure point during systole (see Figure 4), vasodilation reaches its maximum, and the optical path length d(t) also reaches the maximum value of d_max, at which point the intensity of the emitted light is the weakest:

$$I_{min} = I_0 e^{-\{\varepsilon_0(\lambda_1)C_0 d_0 + [\varepsilon_1(\lambda_1)C_1 + \varepsilon_2(\lambda_1)C_2]d_{max}\}} \quad (3)$$

When the heart is dilated, the vasoconstriction is minimized at this time, and the optical path length d(t) is reduced to the minimum value d_min, at which time the output light intensity is the strongest

$$I_{max} = I_0 e^{-\{\varepsilon_0(\lambda_1)C_0 d_0 + [\varepsilon_1(\lambda_1)C_1 + \varepsilon_2(\lambda_1)C_2]d_{max}\}} \quad (4)$$

The above two equations are divided:、

$$\frac{I_{min}}{I_{max}} = e^{-[\varepsilon_1(\lambda_1)C_1 + \varepsilon_2(\lambda_1)C_2](d_{max} - d_{min})} \quad (5)$$

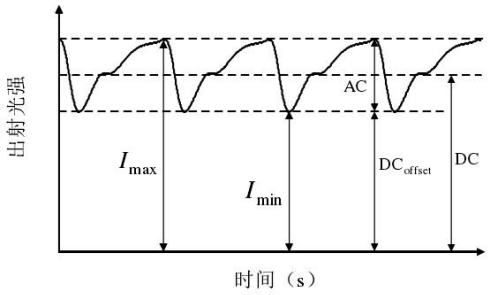

Fig.4 the change of the transmission light's intensity along with heartbeating's schematic diagram

Define $\Delta d \overset{\Delta}{=} d_{max} - d_{min}$

$$\ln\left(\frac{I_{min}}{I_{max}}\right) = -[\varepsilon_1(\lambda_1)C_1 + \varepsilon_2(\lambda_1)C_2]\Delta d \quad (6)$$

Since the transition component (AC) in the outgoing light is much smaller than the non-jumping component (DC), the above equation can be approximated as

$$\ln\left(\frac{I_{min}}{I_{max}}\right) = \ln\left(\frac{DC_{offset,\lambda_1}}{AC_{\lambda_1} + DC_{offset,\lambda_1}}\right) \approx \frac{AC_{\lambda_1}}{DC_{\lambda_1}} \quad (7)$$

As can be seen from the above, when the light of the fixed wavelength λ1 illuminates the blood vessel, the blood flow pulsation does cause a change in the absorbance, and the degree of change is defined as ΔA1.

$$\Delta A_1 = -[\varepsilon_1(\lambda_1)C_1 + \varepsilon_2(\lambda_1)C_2]\Delta d = \frac{AC_{\lambda_1}}{DC_{\lambda_1}} \quad (8)$$

In summary, based on the Lambert-Beer law and the absorption spectra of oxyhemoglobin (HbO2) and deoxygenated hemoglobin (Hb) in the blood, the photoelectric volume pulse wave sensor can obtain a signal whose intensity changes with heartbeat, that is, a photoplethysmographic pulse wave. We can use this signal to conduct the following research.

Similar to the measurement principle of invasive blood flow velocity, two photoelectric volume pulse sensors are placed at a distance from the same blood vessel, and pulse waves of two positions are acquired, and the conduction time T of two pulse waveforms is obtained according to the pulse wave waveform. On the premise of measuring the equivalent blood vessel length S, by the formula:

$$V = \frac{S}{T} \quad (9)$$

The pulse wave transit time is calculated by placing a photoelectric pulse sensor in two parts of the body's radial artery, and then using a single-chip microcomputer to perform simple amplification and filtering on the two pulse waves to obtain an ideal pulse wave. Then use A/D conversion to convert these two pulse waves into digital signals. By calculating the time difference between the main peaks of the upper and lower channel pulse waveforms, that is, the pulse wave transit time T between the two parts of the radial artery. The acquisition device channel measures the pulse wave waveform of the radial artery near the elbow joint, and the channel 2 measures the pulse wave waveform of the radial artery near the wrist. The measurement principle of time T is shown in Fig. 5.

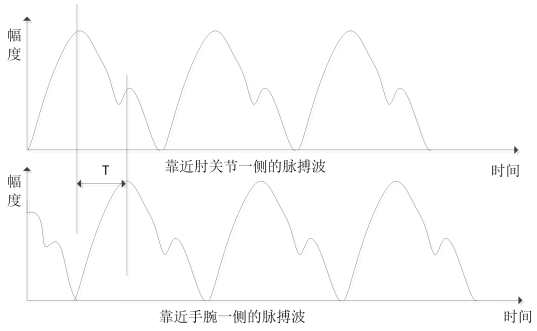

Fig.5 the measurement schematic diagram of the pulse wave's conduction time T

Among them, the main peak of the pulse wave signal is found to be the weight of the weight, and the threshold difference method can be used.

B Waveform Characteristics Of Pulse Signals

The characteristic points of the pulse signal waveform diagram are shown in Fig. 6. Among them, point A and point G are aortic open points, also called initial shooting points, which can be used as the starting point and ending point of the pulse signal; B is the main peak of the pulse signal, C is the tidal wave front of the pulse signal, and D is the pulse signal The

tidal wave (pre-pulse front wave), E is the pulse signal of the middle canyon (heavy wave wave valley), and F is the peak value of the pulse signal and then pulsation. Figure 6 Schematic diagram of pulse signal feature points

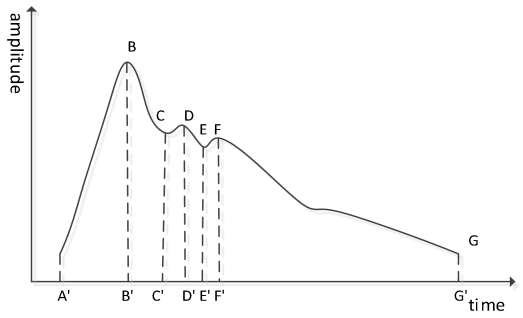

Fig.6 Schematic diagram of the pulse signal feature points

C Determination Of The Main Peak Of The Pulse Signal

Define that the pulse signal is x(t) and find the maximum value of x(t) m;

$$m = \mathrm{Max}\,[x(t)] \tag{10}$$

Subtracting a certain value a from the maximum value m and recording b = ma as the threshold value, performing threshold processing of the pulse signal, setting the value higher than b to b, otherwise setting it to 0, and recording the result as y(t) .

$$y(t)=\begin{cases}0, x(t) < b\\ b, x(t) \geq b\end{cases} \tag{11}$$

The difference is obtained for y(t), and the result is denoted as z. The rising branch of the pulse signal corresponds to the point where z is 1, and is recorded as the sequence C_0. The descending branch of the pulse signal corresponds to the point where z is -1, which is recorded as the sequence D_0, and the pulse signal is recorded. The main wave peak position is the maximum value max between each adjacent two rising branches, and the minimum value min is the position of the pulse signal starting point;

$$z = \mathrm{y(t)} - \mathrm{y(t-1)} \tag{12}$$

$$max = Max(z) \tag{13}$$

$$min = Min(z) \tag{14}$$

The maximum value is found between the maximum value max and the minimum value min, and the point close to the main wave is the point where the tidal wave peak is located. For the waveform in which the pulse signal is severely disturbed, the above method is used, and there is an error. Here, the smoothing is performed by the arithmetic mean filtering method, and then the processing of step 2) is performed.

For high-pressure pulse signals, the peak value of the tidal wave may exceed the peak value of the main wave, that is, the maximum detection value may be a tidal wave rather than a main wave. According to the characteristics of the main wave rise and the pulse signal branch generally rising rapidly and smoothly, the slope of some points before the maximum value can be calculated and then compared with the slope on the rising branch. If the phases are similar, it is considered to be the main peak. Otherwise, it is considered to be a tide. Move this point to the left to find the main peak again. Figure 7 is a flow chart of threshold difference method

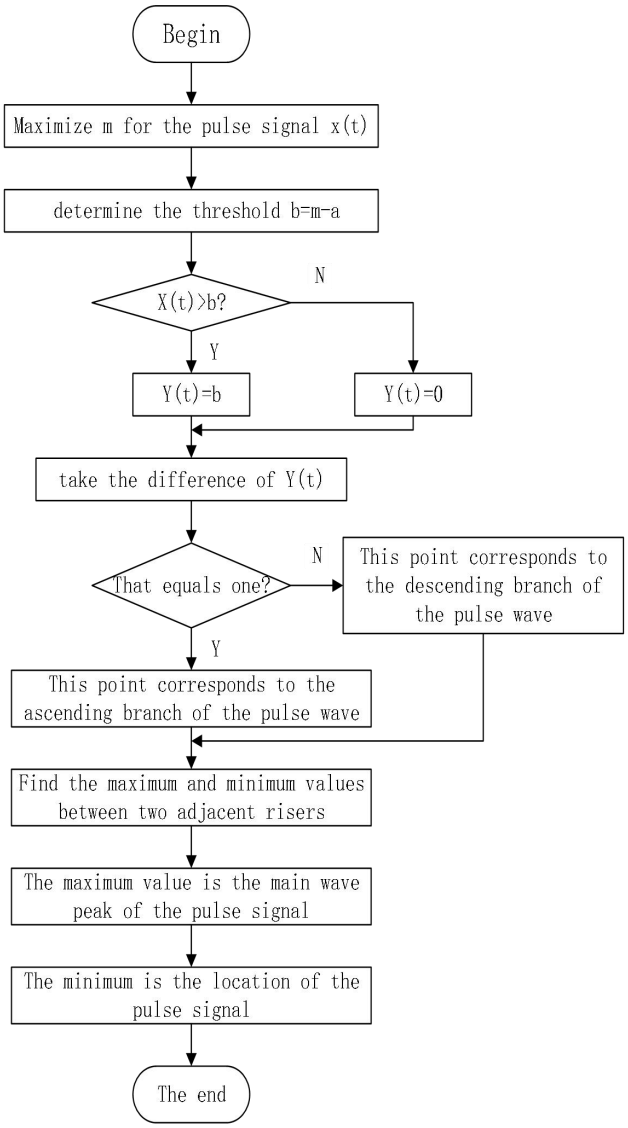

Fig.7 Differential threshold method flow chart

In this way, the peak point of each signal is recorded, and the time difference between the peak points of the two pulse signals is observed, and several groups are recorded and the average value is obtained, which is

the pulse wave transit time T. The differential threshold of the two pulse waves is shown in Figure 8.

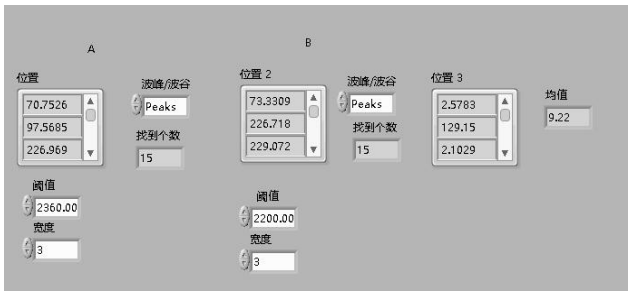

Fig.8 Two-way waveform differential threshold

IV. PORTABLE BLOOD FLOW MEASUREMENT SYSTEM

A Hardware System Composition

Figure 9 is a block diagram of the blood flow rate measurement system, which is mainly divided into an analog circuit part and a digital circuit part. The analog circuit part mainly limits, amplifies and filters the human body pulse signal collected by the pulse sensor, so that the pulse signal collected by the sensor can be applied to digital processing; the digital circuit part is mainly a small system of the microprocessor (51 single chip microcomputer). The main function of the circuit, A/D conversion circuit and display circuit is to complete the processing and display of the pulse signal. The main functional modules include photoelectric pulse sensor and its interface circuit, amplification filter circuit of sensor output signal, A/D sampling interface circuit, related operation processing (completed by MCU, part of software), display circuit and so on. Figure 9 is a system block diagram of a blood flow meter.

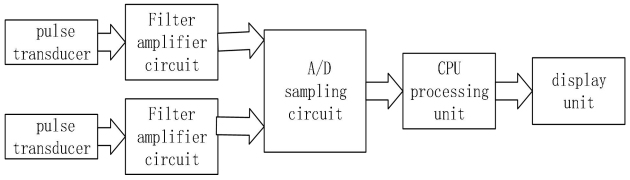

Fig.9 the system chart of the blood velocimeter

B.Photoelectric Pulse wave signal processing

After signal conditioning, the two photoelectric volume pulse wave signal waveforms output by the photoelectric pulse sensor are as shown in FIG.

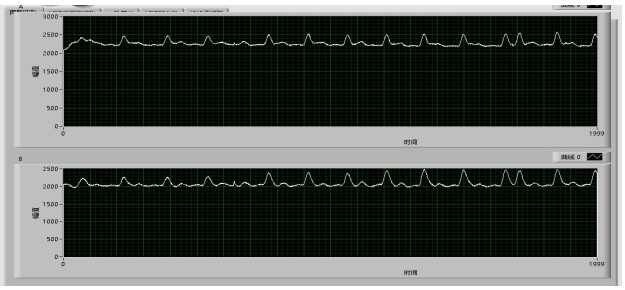

Fig.10 Pulse wave signal original waveform

In order to remove the power frequency interference in the pulse signal, we can design a 50 HZ notch filter, and the transfer function and frequency response of the 50HZ trap are:

$$H_{RS}(z) = H_{AP}(z) - H_{BP}(z) = (z^{-4l})^k - [\frac{1+z^{-4(2l+1)}}{1+z^{-4}} \cdot \frac{1}{2l+1}]^l \quad (15)$$

$$H_{RS}(e^{j\omega}) = H_{AP}(e^{j\omega}) - H_{BP}(e^{j\omega}) = [1 - [\frac{\cos(2(2l+1)\omega)}{\cos(2\omega)} \cdot \frac{1}{2l+1}]^k] e^{-j4lk\omega} \quad (16)$$

Since the notch signal is processed by the notch filter, there is still severe EMG interference in the pulse signal, and the interference of the low pass filter to the pulse signal is reduced. To this end, a simple low-pass filter is designed using a zero-pole cancellation method. The transfer function and frequency response of the filter are as follows

$$H_{LP}(z) = \frac{1-z^{-M}}{1-z^{-1}} = 1 + z^{-1} + \cdots + z^{-M} \quad (17)$$

$$H_{LP}(e^{j\omega}) = e^{\frac{-j(M-1)\omega}{2}} \cdot \frac{\sin(\frac{\omega M}{2})}{\sin(\frac{\omega}{2})} \quad (18)$$

After filtering, the two photoelectric volume pulse wave signal waveforms are shown in Figure 11.

Fig.11 Filtered pulse wave signal waveform

V. EXPERIMENT ANALYSIS

Time domain feature points are extracted from typical hypertension chord pulse signals. The result is shown in FIG. In the figure, the abscissa is the number of points of the pulse signal. The ordinate is the quantized value of the pulse pressure. As can be seen from Fig. 12, the main wave and the tidal wave of the pulse signal are accurately extracted. Figure 12 Time domain feature extraction of pulse signals

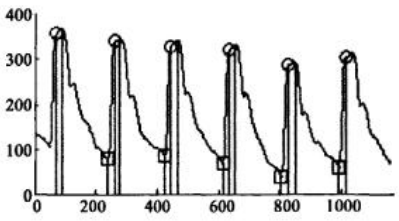

Fig. 12 The time—domain feature extraction of the pulse signal

After obtaining the peak-to-peak value of the two waveforms by the differential threshold method, the mean value of the difference is calculated to obtain the blood flow time. In the experiment, the distance between the two sensors is 5cm, and the time result is shown in Figure 13.

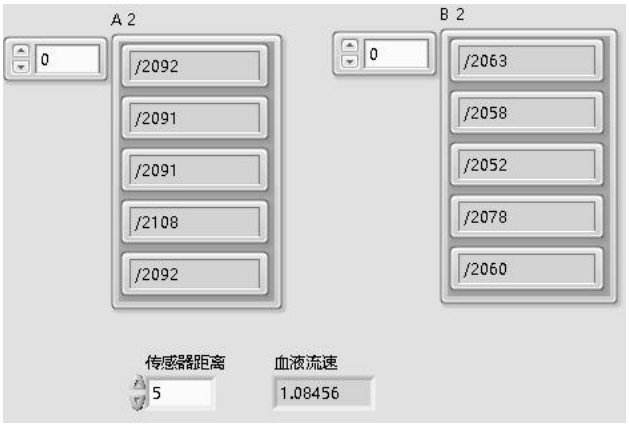

Fig. 13 Blood flow rate measurement

VI. IN CONCLUSION

Through the photoelectric volume pulse sensor, two complete pulse wave signals can be collected, and the differential threshold method can also effectively extract the peak and peak of the pulse wave. The final result of the system is very close to the actual blood flow rate, which verifies the feasibility of the method.

References

[1] Stern MD. In vivo evaluation of microcirculation by coherent light scaling. Nature, 1975, 254: 56-58

[2] Lin Guoxing. Measuring blood flow rate with fiber Doppler effect. Instrumentation Technology and Sensors, 1993, 1:34-35

[3] Jiang Hong. Development of blood flow microwave detector: [Master's thesis]. East China Normal University, 2010

[4] Zhou Heng. Research on blood flow measurement technology based on optical fiber sensing technology: [Master's thesis]. Changchun University of Science and Technology, 2014

[5] Zhao Min. Research on blood flow meter based on multi-electrode electromagnetic measurement: [Master's thesis]. Hebei University of Science and Technology, 2017

[6] Wang Xiaochun, Zhou Sheng, Yang Jun, Xing Weizhong, Wang Xiaoning, Wang Yanqun, Ji Jianjun. Experimental study of a very high frequency ultrasound blood flow measurement system. Biomedical Engineering and Clinical, 2018, 2: 138-142

[7] CIC Consultant. 2016-2020 China Medical Device Industry Investment Analysis and Forecast Report

[8] Li Jingwen, Long Cun, Zhang Baozhou. Design and application of reflective oxygen saturation monitor. Biomedical Engineering and Clinical. 2003, 7(1): 3-6.

[9] Lu Yuguang. Instrumental Analysis. China Medical Science and Technology Press, 2016

Non-destructive Testing System for Watermelon Maturity Based on MEMS Acceleration Sensor

Liu Wenyan, Gao Jiaqi, Wang Yuhang
（jilin university instrument science and engineering institute,changchun,130021）

***Abstract* —As one of the important economic crops in China, watermelon has become the best choice for farmers to increase their income. After analyzing the existing watermelon non-destructive testing technology and the research status at home and abroad, this paper proposes a non-destructive testing system for watermelon maturity based on MEMS accelerometer. Using the principle of acoustic vibration method and combining embedded technology with MEMS technology, The system has the characteristics of low cost, portable and non-invasive. In this paper, the scheme of watermelon maturity detection was firstly demonstrated, and the system software and hardware design was carried out. The test results were given to realize the function of detecting watermelon maturity without destroying watermelon.**

***Key words*— watermelon maturity; MEMS Acceleration Sensor; noninvasive**

I. INTRODUCTION

WITH the rapid development of the economy, people's lives have become more and more affluent, and the concept of consumption has been greatly improved. The requirements for the quality of fruits and vegetables are also increasing. As one of the important economic crops in China, watermelon has formed a large-scale production. At present, the sales of watermelons can be seen on the market, especially the greenhouse cultivation of facilities is good, and it is highly valued by various production areas. However, with the increasing production of watermelon, the problem of food safety becomes more and more serious. In order to promote the early maturity of watermelon, some farmers use hormone ripening in the production of watermelon, which has become an open secret. Due to the current shortage of farmyard manure, chemical fertilizers must be used in order to increase the yield of watermelons. In addition, watermelon pest control is also over-reliant on chemical control methods, which results in the maturity of watermelons entering the market is still uneven. According to statistics, in the process of watermelon transportation and sale, there are more than 30% of watermelons. Not mature enough. Most consumers can only use the common method of identification of watermelon maturity: counting, reading, listening, etc., and can not accurately judge the maturity of watermelon.

The purpose of this paper is to help farmers and consumers to measure watermelon maturity accurately, quickly and simply. After analyzing the existing non-destructive testing technology for watermelon maturity and the research status at home and abroad, a non-destructive testing system for watermelon maturity based on micro-electro-mechanical acceleration sensor is designed, which combines micro-technology with embedded technology and uses FFT transform technology to process data. That makes the system has the characteristics of portability, low cost, using the principle of acoustic vibration method overcomes the disadvantages of detecting instrument damage on watermelon[1]. This design is of great theoretical and practical significance for avoiding the entry of immature watermelon into the market and for storage, transportation and sales according to the maturity after harvesting.

II . OVERALL SCHEME DESIGN FOR DETECTING WATERMELON MATURITY

A. Design principle

Sound-vibration method is an effective non-destructive testing method for watermelon quality. The internal structure of watermelon includes the skin and pulp. The content of soluble solids in watermelon increases gradually from the skin to the center of pulp[2]. Wang Shumao et al. (1999) analyzed the elastic modulus of peel and pulp of Jingxin watermelon produced in Beijing from the mechanical point of view. The results showed that the elastic modulus of peel was about 5 times of that of pulp, and the elastic modulus of each part of pulp was different, but the difference was not obvious. The elastic modulus of pulp of watermelon with different sugar content changed more than 20%. The change of elastic modulus of watermelon pulp also affects the vibration characteristics of watermelon, which makes it possible to use the vibration characteristics to detect watermelon maturity nondestructively[3]. The study suggests that the following formulas can be used[4]:

$$E \propto f^2 m^{2/3} \quad (1)$$

As the maturity index of non-destructive testing of watermelon to judge the maturity of watermelon, the formula can be known that the Young's modulus has a certain relationship with the quality and natural frequency of the fruit. The weight of the fruit can be measured by the load cell and the fruit can be measured by the acceleration sensor. The vibration signal and the FFT transform are used to extract the natural frequency of the fruit, calculate the Young's modulus, and estimate the maturity[5].

B. System overall design block diagram

The overall block diagram of the system is shown in Figure 1:

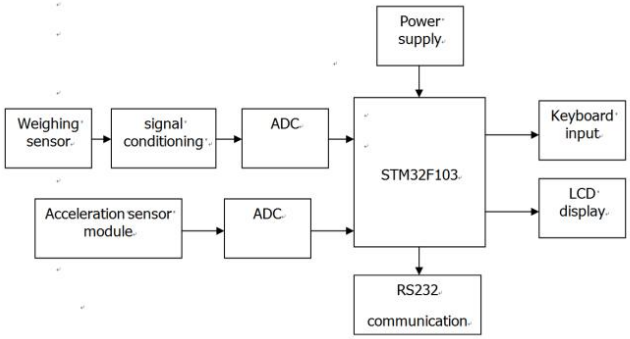

Fig. 1 General design block diagram of the system

The watermelon is placed on the load cell, and the data is transmitted to the single-chip microcomputer through the A/D acquisition to measure the quality of the watermelon. At the same time, the watermelon is struck to generate the vibration signal, and the acceleration sensor collects the acceleration signal through the A/D collection in the STM32. The acquired acceleration signal is subjected to FFT transformation to extract the first-order natural frequency. According to formula (1), the acquired frequency and the quality signal are exponentially multiplied to obtain the maturity index and corrected, and the mature is determined after comparison with the standard amount. Whether or not, the relevant parameters and maturity are displayed by the button control display.

III. THE DESIGN OF SYSTEM HARDWARE

The system data acquisition part consists of the load cell and the acceleration sensor. The signal amplification and A/D conversion are mainly realized by the special high-precision 24-bit AD conversion chip HX711 (the A/D conversion and signal amplification module are included in the acceleration sensor). The human-computer interaction interface is keyboard input and lcd5110 liquid crystal display. It mainly uses the elite keyboard and lcd5110 liquid crystal display, which can input data and intuitive display data conveniently. The main modules are introduced below.

A． Load cell module

（i）Sensor selection

Through market research, select the load cell N426 and select the 30kg range[6]. The internal schematic of the sensor is shown below.

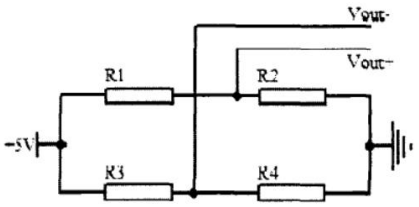

Fig.2 Internal circuit diagram of N426

（ii）Load cell A/D selection

For the load cell, the load sensor-specific analog/digital (A/D) converter chip HX711 is used.

The HX711 is a 24-bit A/D converter chip designed for high-precision load cells. Compared with other chips of the same type, the chip integrates peripheral circuits required by other types of chips including a regulated power supply and an on-chip clock oscillator, and has the advantages of high integration, fast response, and strong anti-interference. The overall machine cost of the electronic scale is reduced, and the performance and reliability of the whole machine are improved.

B. Acceleration sensor module

Due to the low frequency of the vibration signal collected in this design, the MXR9500MZ-B triaxial accelerometer with small measuring range and high sensitivity is selected, and its measuring range is ±1.5g and the sensitivity is 500mv/g[7]. The MXR9500MZ-B accelerometer has a resolution of 1mg/√HZ and can measure signals below 1mg at low frequencies.

The internal thermodynamic principle of the MXR9500MZ-B triaxial accelerometer is that a heat source placed in the center of the silicon chip creates a suspended hot air in the cavity. At the same time, a thermoelectric group consisting of polysilicon and aluminum is placed symmetrically equidistantly around the heat source[8]. When the horizontal placement or no acceleration occurs, the temperature drop steepness is completely symmetrical around the heat source, and the voltage generated by all the surrounding thermoelectric disaster groups due to the induced temperature is the same. The chip integrates gain adjustment, temperature sensor and heater, A/D, D/A, gain adjustment and low-pass filter. When the

chip detects an acceleration, the hot air mass inside the chip will deviate from the center position, so that different thermocouples in the chip will detect different temperature signals. Then, through A/D conversion and D/A conversion, a low-pass filter is finally output to the voltage signal proportional to the acceleration. The X-axis measurement of the MEMS accelerometer is actually shown in Figure 3.

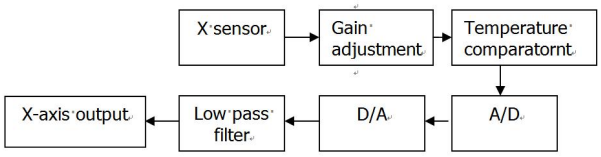

Fig.3 X-axis measurement schematic diagram of MEMS accelerometer

The Y and Z axis measurement principle is the same as the X axis. Since the acceleration sensor is placed on the opposite side of the tapping point, only the Z axis can output a more significant useful signal. Therefore, this experiment performs FFT transformation on the vibration signal by collecting the Z axis output.

C. Signal conditioning module

For load cells, the HX711 can acquire and collect data from symmetric sensors. For acceleration sensors, MEMS accelerometers integrate gain adjustment, temperature sensor and heater, A/D, D/A, gain adjustment and low pass. A filter or the like that outputs a voltage signal whose acceleration is proportional.

However, due to the high sensitivity of the acceleration sensor, the interference during the measurement process, especially the high frequency noise, will reduce the signal quality and affect the judgment of the starting point. Therefore, this experiment has designed a second-order active voltage control type. Low pass filter to filter out high frequency noise.

Design basis: Since the first-order natural frequency of watermelon vibration signal is within 100Hz to 400Hz, it is determined that a second-order voltage-controlled low-pass filter with a cutoff frequency of 500Hz and a gain of 1.5dB is designed. The circuit diagram is as follows.

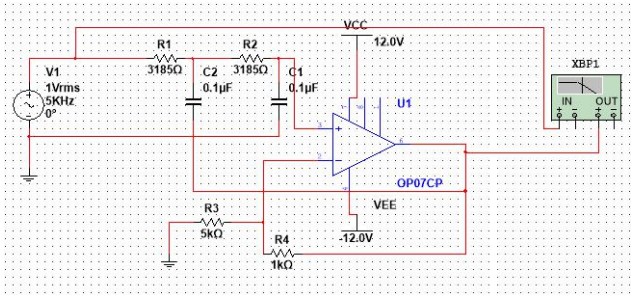

Fig.4 Schematic diagram of second-order voltage-controlled low-pass filter

IV. THE DESIGN OF SYSTEM SOFTWARE

The system software part is for programming the STM32 single-chip microcomputer. Firstly, the system is initialized. The quality signal and the vibration signal are sampled and processed by the sampling program to calculate the quality of the watermelon. After the linear correction processing of the quality, the data is stored in the memory of the single-chip microcomputer[9]. On the other hand, the vibration signal collected by the acceleration sensor is transformed, and the first-order natural frequency of watermelon is extracted by FFT transform of the vibration signal by STM32 single-chip microcomputer, and the maturity index formula is used for calculation, and the maturity index is corrected by the correction algorithm. The watermelon was graded according to the calculation results, and finally the results were displayed through the liquid crystal.

A. Weighing part

First, the initialization program is executed. The design initialization program includes display initialization, load cell A/D module initialization, serial port initialization, etc., to determine whether it is overloaded, if overloaded, alarm, if not overloaded, obtain the fur weight, and measure the weight, and finally After peeling, the final watermelon weight is obtained on the display.

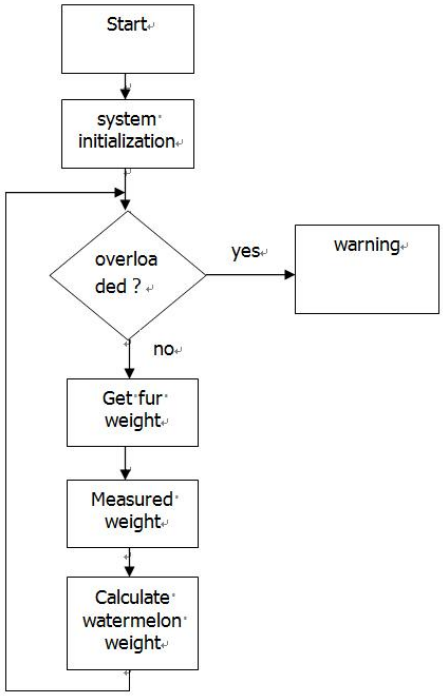

Fig.5 Software flow pattern of the weighing section

B. Acceleration sensor section

The vibration signal measured by the MEMS accelerometer is processed by A/D and then enters STM32 for processing. First, it is judged whether the starting condition is satisfied (whether the absolute

value of the difference between the collected data and the previous data is greater than 200), and the acquisition is not satisfied. After the condition is satisfied, the 2048 points after the oscillating are subjected to FFT transformation, and the first-order natural frequency of the watermelon vibration is obtained, and the Young's modulus is calculated by the formula (1), and then the maturity is calibrated and corrected, and finally the result is obtained. Displayed on the LCD5110 display.

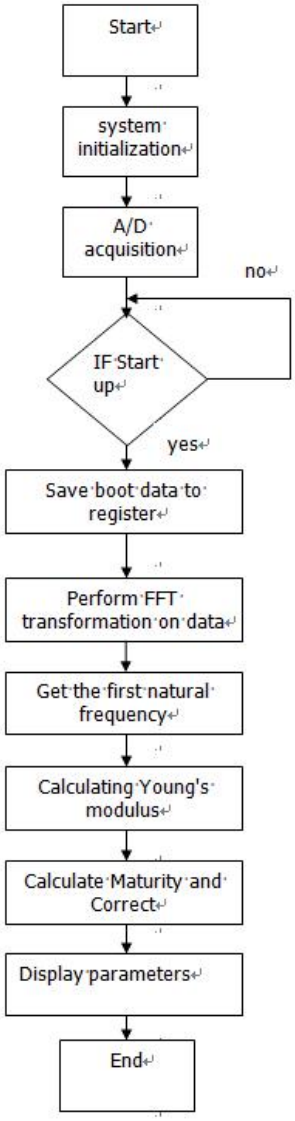

Fig.6 Software flow pattern of the acceleration part

V. EXPERIMENTAL TEST

Place the MEMS accelerometer on one end of the watermelon equator, tap the other end of the watermelon equator with a raft, and generate the vibration to meet the vibration conditions. Then collect the data with STM32 and transmit the data to the host computer. Simulate the vibration waveform with MATLAB. Perform FFT spectrum analysis and the results are shown in Figure 7:

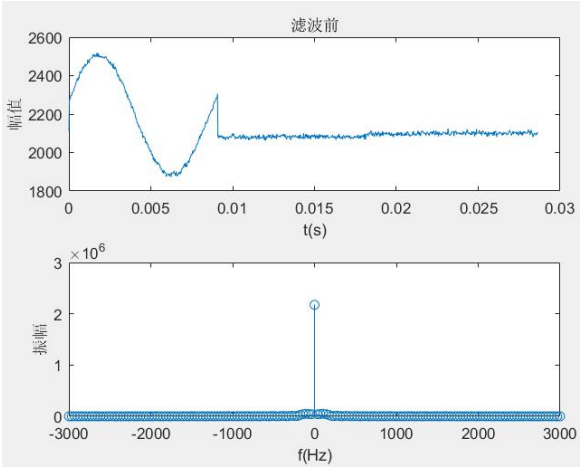

Fig.7 Time-domain and frequency-domain diagrams of data collected before filtering

A Butterworth filter is designed with MATLAB to filter the collected data. The result is shown in Figure 8.

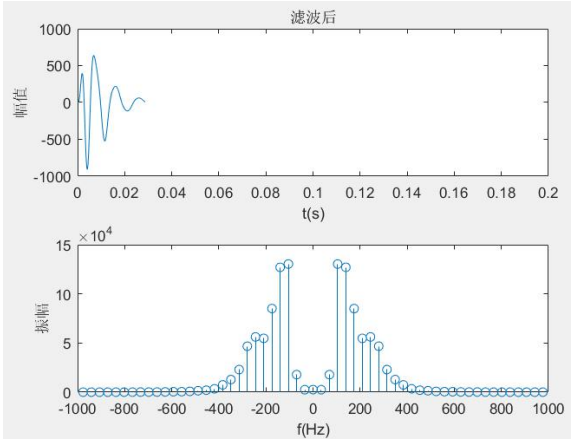

Fig.8 Time-domain and frequency-domain diagrams of filtered data

It can be seen from the figure that the natural frequency of the vibration generated by tapping watermelon is in the interval of (0 Hz, 400 Hz), and is mainly concentrated in the interval of (100 Hz, 300 Hz). With the support of theoretical data, the parameters of watermelon measured by several experiments are shown in Table 1 below.

Table 1 Parameters and sugar content of watermelon

Number of experimental watermelon	Watermelon mass（kg）	Natural frequency（Hz）	Maturity index	Sugar content（%）
1	4.75	147	61153.47	11.34
2	5.13	156	72423.94	9.90
3	5.22	153	70461.09	10.17
4	5.46	164	83377.60	8.48
5	5.69	168	90034.56	7.76
6	5.72	149	71043.20	10.08
7	5.91	138	62273.88	11.16
8	6.11	174	101121.84	6.48
9	6.20	167	94264.82	6.91
10	6.43	163	91928.74	7.33

The least squares fitting of the data was carried out,

and the relationship between the maturity index and the sugar content of the watermelon was obtained to satisfy the functional relationship 100y=-0.000137x+19.82, where x represents the maturity index and y represents the sugar content of the watermelon. The calibration sugar content is less than 5% is immature, 5%-7% is basic maturity, and more than 7% is mature. After many experiments, the error between the measured result and the expected value is within the allowable range, and the equipment meets the expected requirements.

Through the design of the software and hardware, the operation results of the entire device are shown in Figure 9.

Fig.9 Man-machine interface diagram

The first behavior device starts the logo, the second row shows the watermelon maturity detection starts, the third row shows the watermelon quality, the fourth row shows the watermelon natural frequency detected by the FFT transformation, and the fifth behavior detects the vibration interruption identifier, the sixth The line shows the ripeness of the watermelon.

The final physical map is shown in Figure 10.

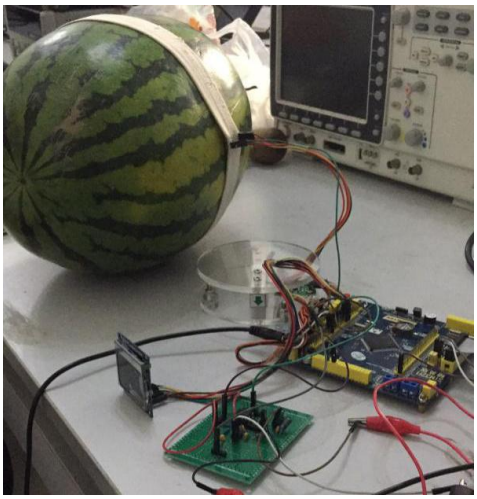

Fig.10 Practicality of non-destructive testing system for watermelon maturity

VI. Conclusion

After testing, the device can complete the non-destructive testing of watermelon maturity. It can complete the functions of displaying the weight of the measured object, and obtaining the natural frequency and maturity through FFT transformation. The design of this system is to help melon farmers and consumers to measure the maturity of watermelon accurately, quickly and easily, avoid the listing of raw watermelons, and have great theoretical and practical significance for all aspects of grading storage, transportation and sales.

References

[1] Han Yun. Overview of the development of MEMS sensors [J]. World of Electronic Products, 2019, 26 (01): 4-8.

[2] Yuan Peipei. Limit Learning Model and Application of Nondestructive Testing of Watermelon Maturity [D]. Huazhong Agricultural University, 2017.

[3] Wei Wei. Study on Vibration Characteristics of Watermelon and the Effect of Vibration on Its Quality [D]. Inner Mongolia Agricultural University, 2015.

[4] Lu Yong, Li Junfeng, Li Jing, Pu Hongjie, Xu Wanxiu. Application of Acoustic Technology in Non-destructive Testing of Watermelon Quality [J]. Fujian Agricultural Science and Technology, 2014 (10): 77-81.

[5] D.V. Bangalore, W.G. McGlynn, D.D. Scott. Effects of Fruit Maturity on Watermelon Ultrastructure and Intracellular Lycopene Distribution [J]. Journal of Food Science, 2008, 73 (5).

[6] Sun Tingyao. Suggestions on how to select weighing sensors [J]. Metrology Technology, 2001 (1): 53-54.

[7] Shock Failure Simulation Analysis and Test of Ding Limei, Li Shizhong, Duan Rongjie, Yang Le. MEMS Acceleration Switches [J].Mechatronics Engineering, 2019,36(02): 197-200.

[8] Zheng Weiwei. Design and analysis of micro-electromechanical sensor chips [J]. Science and Technology Bulletin, 2018, 34 (08): 90-94.

[9] Li Yingshun. Principle and Application of Single Chip Microcomputer [M]. Beijing: China Water Resources and Hydropower Press. 2010

Environmental Detection vehicle based on WIFI signal

Liu Yuntao, Zhang Wenxuan, Guo Hongrui

(jilin university instrument science and engineering institute,changchun,130021)

***Abstract*—Due to the rapid popularization and development of the Internet, network technology terminals are becoming more and more popular. More and more mobile terminals support WIFI. But not many of them use WIFI as an electronic control module. In wireless control, infrared Bluetooth and other wireless control module have been basically developed, because the wIFI control started relatively late and therefore can only be in the budding stage, compared with infrared and Bluetooth wireless control, the WIFI control distance is further. However, because the limited coverage of WIFI restricts the development of WIFI control, it is believed that with the development of the times, the coverage of WIFI area will be wider and the product prospect of using WIFI control will be considerable[1]. In this design, the WIFI signal is applied to the control of the car. On the basis of the control of the car, the video monitoring, temperature, humidity, oxygen content and other basic environmental parameters are measured. DC encoder motor is used to realize stable measurement.**

***keywords*—WIFI Control Video Transmission Parameter Measuremen**

I. INTRODUCTION

BECAUSE of the rapid popularization and growth of the Internet, network technology terminals are becoming more and more popular, and more mobile terminals support WIFI, but there are not many electronic control modules using WIFI. In the field of wireless control, infrared control technology, Bluetooth control technology and other wireless control modules have been basically developed. WIFI control starting late, it can only be in the emerging stage. Compared with infrared control technology and Bluetooth control technology, WIFI control technology is farther away, but because of the limited coverage of WIFI signals, the development of WIFI control technology is restricted. I believe that with the development of the times, the coverage of WIFI area
will be wider and wider. The application prospects of WIFI-controlled products will be unlimited[2].

II.DESIGN THINKING

The overall design idea of the system can be divided into hardware design and circuit design, including camera image acquisition module design, WIFI transmission and reception module design, sensor module design and other parts, as shown in Figure 1.

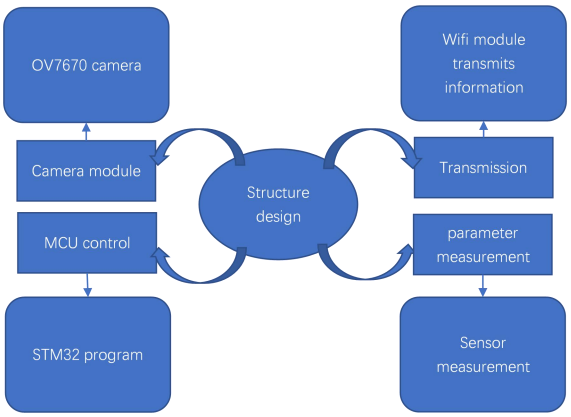

Fig.1 Structural Design Drawings

III.INTRODUCTION OF CAMERA IMAGE ACQUISITION MODULE

The OV2640 is a CMOS UXGA (1632 * 1232) image transmission sensor. The OV2640 requires lower operating voltage and smaller sensor size, providing all functions of an image processor and a single chip UXGA camera[3]. OV2640 controlled by SCCB bus can provide various resolutions such as sub-sampling, full frame and scaled output 8/10 bits of image. The UXGA image of the OV2640 can transmit as fast as 15 frames per second. Users have complete control over the data format, transmission method and quality of images[4]. SCCB interfaces are programmed to implement image processing functions such as white balance, contrast, gamma curve, and chroma. OV image sensor uses special sensor technology to reduce

and even eliminate optical (or electronic defects) such as fixed mode noise, sloshing, smearing, etc. as devices to improve image quality and obtain clear and stable color images.

A.Main function modules of OV2640 sensor Photosensitive

Camera module.

Maximum output size: UXGA (1600*1200).

10-bit A/D conversion

After the original signal passes through the amplifier, the signal enters a 10-bit A/D converter, and the A/D converter works at exactly the same frequency as the pixel frequency. The *module also* has BLC function[5].

Digital Signal Processor

This part controls the image quality and the interpolation process from the original signal to the RGB signal.

Output Format Module

The module controls all the output data of the image and its format, according to the set priority[6].

Compression engine

The compression engine consists of three parts: QZ, DCT and Entropy Encoder, which output JPEG data and compress the initial data stream.

Analog signal processing

The analog functions of analog signal processing include gain control, analog amplification, channel balance and control balance.

Microprocessor

OV2640 module comes with an 8-bit microprocessor, which has 4KB ROM, 512 bytes SRAM, fine-tuning image quality and flexible host-to-control system command interface.

SCCB interface

The operation of image sensor chip is controlled by SCCB interface.

Digital Video Interface

OV2640 has a 10-bit digital video interface (supporting 8-bit connections). The LSB and MSB of OV2640 are arranged before and after the program. The modules in the experiment are connected by 8 bits.

B.Camera Working Process and Related Parameters Configuration

The program runs, integrates camera work, and collects images. RGB565 mode was adopted. The collected pixels are sent to the upper computer software through serial port. The serial port adopts the WIFI module serial port 2 which has been successfully matched with the upper computer. Pixel points are sent to the host computer through WIFI, and the host computer receives and converts them to 16-digit display.

IV.Introduction of Control Transfer Module

A.ESP 8266 WIFI Module

ATK-ESP8266 is a highly performance UART-WIFI module launched by ALIENTEK and ESP8266 module produced by ATK-ESP8266 board AT company. This module supports the mode of serial port to AP, serial port WIFI STA and AP WIFI+WIFI STA, and then quickly establishes a serial port[7]. In WIFI transmission scheme, it is convenient to use the Internet for transmission. The ATK-ESP8266 module is connected by MCU and serial port (LVTTL) and has a built-in TCP/IP protocol stack to ensure the conversion between WIFI and serial port[8]. Traditional serial device, ATKESP8266 module, only needs simple modification of serial port configuration, and can transmit its data through WIFI. The ESP8266 module is connected to the outside through six pins[9].

B.Configuration method

```
AT+CWMODE=2
AT+RST
AT+CWSAP="ATK-ESP8266","12345678",1,4
AT+CIPMUX=1
AT+CIPSERVER=1,8086
AT+CIPSEND=0,25
```

C.Operation process

After the ESP8266 is configured by the computer client (such as the program configuration above), the LCD display screen of the car is opened by ESP8266, and the screen display is deployed to the state to be connected[10]. The network debugging assistant of the mobile terminal is configured. After the configuration is successful, the screen display is connected successfully. After the mobile phone is successfully connected with the car WIFI module, the car screen displays 1:1 after sending two 1 to the mobile phone, as shown in Figure 2.

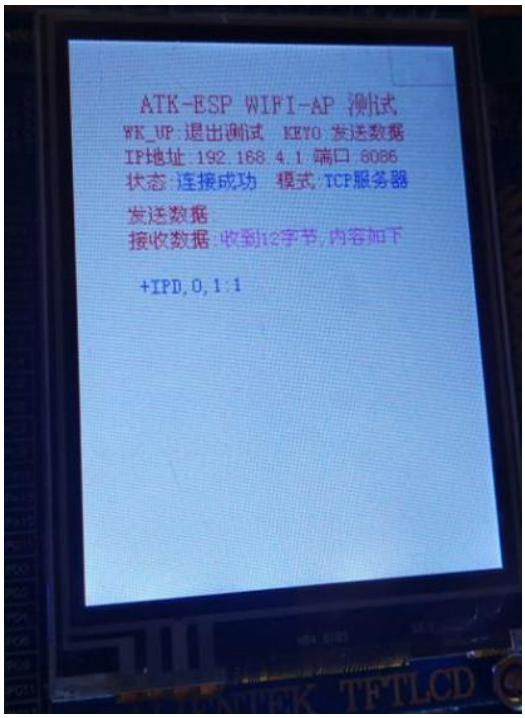

Fig.2 WIFI Configuration success

D.Working process

After opening the WIFI connection, the mobile phone sends the signal to ESP8266[11]. After receiving the signal, ESP8266 transmits the signal to the serial port 2 of STM32. The serial port 2 is programmed on STM32[12]. When receiving the integer 1, the P5 port on STM32 outputs a high level (marked as 1). The P5 port acts as the driving switch of the wheels to drive the car. Similarly, ESP8266 receives the P6 port of integer 2 on STM32 as the steering switch of the car, and more control functions follow this principle[13].

V.Introduction of Sensor Measurement Module

A.Detailed Introduction of Oxygen Sensor (O2-A2)

Oxygen sensor (O2-A2) is one of the best-selling gas sensors in Shenzhen Xinshilian Science and Technology Co., Ltd. Oxygen sensor (O2-A2) is used to measure the concentration of gas in the surrounding environment, which means oxygen only[14]. According to the difference of measuring range and working life, there are many types of oxygen sensor, such as: oxygen sensor O2-A3, long life, oxygen sensor O2-A2, oxygen sensor O2-A1 short life, oxygen sensor O2-G2 (small specification), oxygen sensor O2-C2, oxygen sensor O2-C3 and so on.

①Main Characteristics of Oxygen Sensor (O2-A2)

Measurement Range of Oxygen Sensor(%): 0-30

Working life:>24 Months when 85% of the initial signal is reached

Size(mm): Φ20.3×16.8mm

Output: 80-120mA 22°C, 20.9% O2

Response time:90(s): <15

From 20.9% to 0(Load 47 Ω)

Linearity:<0.6 Good linearity[15]

Weight:<20g

Temperature range:-30 - 55℃

Pressure range:80 - 120Kpa

Humidity range:5 - 95%RH

Storage time:6 month

(Storage temperature3 - 20℃)

Load resistance:47 - 100 Ω

②Application of Oxygen Sensor

Oxygen sensors are widely used in various applications, including coal mines, steel, petrochemical products and medical applications[16].

③Typical application of oxygen sensor (O2-A2)

Oxygen alarm, atmosphere analyzer

B.Temperature sensor LM35

The LM35 sensor is manufactured by NS Company. Its principle is shown in Fig. 3. The output voltage is proportional to the temperature scale. The output voltage is zero volt at zero time[17]. The output voltage increases by ten millivolts for every 1 C increase.

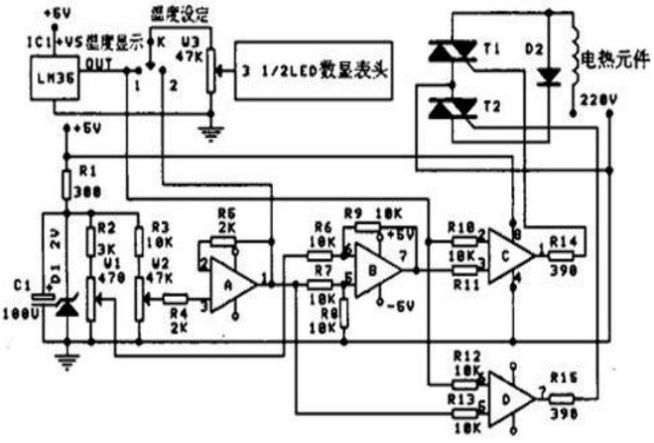

Fig.3 The circuit principle diagram

$$V_{\text{out\_}LM35}(T) = 10\text{mV}/℃ * T℃$$

The temperature sensor has a variety of packaging methods. The self-heating effect is low at constant temperature. The single power mode has a static current of about 50 mu A at 25° C. It has a wide operating voltage, and can work normally in the voltage range of 4 to 20 volts, and is very energy-saving.Its power supply mode is: single power supply, positive and negative dual power supply.As shown in Figure 4, the positive and negative dual power supply modes can provide &OUT+-, temperature measurements.

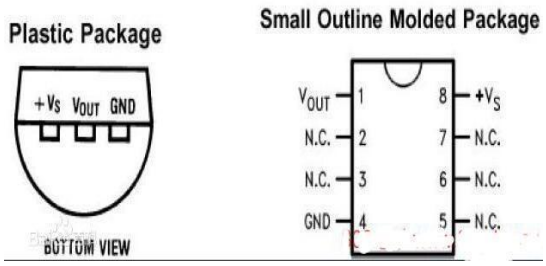

Fig.4 Power supply mode

Single power mode Positive and negative dual power mode

Power supply voltage-0.2V-35V

Output voltage-1.0V-6V

Output current10mA

Designated operating temperature range

LM35A -55℃ to +150℃

LM35C, LM35CA -40℃ to +110℃

LM35D 0℃ to +100℃

VI. Screening of experimental scheme and its application

A.Experimental scheme

Plan 1: Serial wireless AP, only need to realize the connection between mobile phone modules, meet the functional requirements.

Plan 2: STA, need to connect the wireless network to realize data transmission between serial port and other devices, need to use external network.

Plan 3: AP + STA, also need to connect to the wireless network, considering that the campus network can not be used, so the purchase of wireless routers, the process is too complex and therefore abolished.

To sum up, the analysis of the three schemes considers the most reasonable one.

B.Design of objects

The car frame is shown in Fig.5.

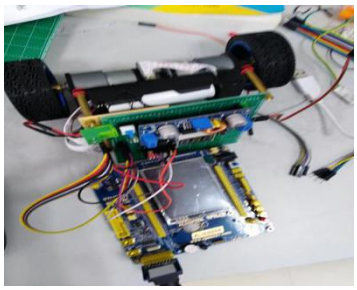

Fig.5 Car physical drawings

VII.Expectation

With the rapid development of science and technology in China, intelligent robots will be more and more used in production and life, which requires higher and higher intelligence and reliability.

Due to the limited time and level, only a part of the relatively simple functions can be achieved on the hardware of the car, so there are still many aspects to be further improved, especially in the hardware, mainly including the following two aspects:

Firstly, in the choice of controller, the upgraded industrial control board can be selected. The upgraded product can make full use of the intelligent car designer of wireless video surveillance based on STM series, and provide more internal storage space. At the same time, providing detailed technical support can greatly reduce the difficulties encountered in hardware debugging [18].

Secondly, because of the limitation of WIFI control signal, the design can not achieve the purpose of working at any time. In the next step, we will consider how to realize unrestricted real-time wireless control or expand the scope of LAN to provide better and more effective control.

VIII.Conclusion

In the era of rapid development of science and technology and information, the research contents of mobile robots include industrial control technology, sensing technology, system engineering, computer network technology and other aspects [19]. Manipulable intelligent robots are more suitable to replace people in those dangerous and complex environments because of their intelligent, compact and flexible characteristics. Whether it is video surveillance intelligent robot or mobile car is the inevitable result of the development of high-tech, its application has gradually penetrated into daily life, making life and production very convenient [20]. The above needs are the purpose of this research.

This paper focuses on WIFI-based transmission as the core, and adds some hardware around STM32 [21].

A complete environment detection vehicle system based on WIFI signal is constructed [22]. Firstly, this paper analyses the research background of some topics related to robots and intelligent cars, and then puts forward the design idea and implementation scheme of WIFI environment detection car system [23]. Then the specific operation mode and results of each hardware module and module of the system are introduced. Based on the basic functions of STM32, some peripheral hardware circuits are added. Finally, the overall design of the environmental sounding vehicle system based on WIFI signal is basically completed.

Finally, the performance of the system is tested, and the stability and usability of the system are verified from each test and the whole experiment of each

hardware module. The test results show that the system can achieve the functions of wireless control and video transmission with the car under the condition of no abnormal WIFI signal, and basically reach the original goal.

Reference

[1] Zhou Zhu. Research on Smart Car Based on STM32[J].Southwest Jiaotong University,2011 3(12): 42.45.

[2] Xu Guohua, Tan Min. Development Status and Trend of Mobile Robot. Robot Technology and Application, 20018(03):7-14.

[3] Dong Zongxiang, Shi Hongrui, Yang Jie. Design and Implementation of Embedded Intelligent Vehicle Measurement and Control System. Computer Measurement and Control,20107(02):357.359.

[4] Cai Zixing, He Hanjiao and Tao Hong. Some problems in navigation control of mobile robots in unknown environments[J].Control and decision-making,2002 1 5(04):385.390.

[5] Xinhua. Opportunity and Courage are both up to standard and the success of the US Mars Exploration Program[EB/OL].http://teeh.sina.eorn/other/2004:04:27/1 41 8355367.shtml,2004:04:27.

[6] Li Ning, Li Jie. Da Vinci Surgical Robot[J].Southeast National Defense Medicine ,2010(05):427—430.

[7] Yu Jinxia, Wang Lu, Cai Zixing. Mobile Robot Self-localization Technology in Unknown Environment[M]. Beijing: Electronic Industry Publishing House,2001:1.15.

[8] Sun Shuyun. Research and Implementation of Motion Control Algorithms for Wheeled Soccer Robots [D]. Chengdu: Chengdu University of Technology, 2009:13.35.

[9] Wang Yonghong, Xu Wei, Hao Liping.Principle and Practice of STM32 Series ARM Cortex.M3 Microcontroller [M]. Beijing: Beijing University of Aeronautics and Astronautics Press, 2008:1.300.

[10] Zhang Runjing, Zhang Limin, Wang Wei. Altium Designer schema and PCB Design [M]. Beijing: Electronic Industry Press, 2009:20.120.

[11] Li Dongsheng, Introduction and Application of Protel99SE Circuit Design Technology [M]. Beijing: Electronic Press, 2002:20-190.

[12] Joseph VI u, Song Yan. ARM Cortex-M3 Authoritative Guide [M]. Beijing: Beijing University of Aeronautics and Astronautics Press, 2009:30.259.

[13] Li Ning. Development and application of STM32 processor based on MDK [M]. Beijing: Beijing University of Aeronautics and Astronautics Press. 2008:1-260.

[14] Gao Peiqiang. Wireless LAN technology IEEE802.11. Popular standardization [J]. Computer product technology, 200312 (09): 41-43.

[15] Song Wei, Huang Jin, et al. Research on information control terminal of intelligent control system for household appliances based on WIFI Internet of Things. Information communication, 2013 10 (01): 199.200.

[16] Yan Dan. Research on Key Technologies of Rapid Inter-AP Switching for Vehicle WiFi Applications [D]. Nanjing: Central South University, 201 1:20-35.

[17] Zhou Zhou, Research and Implementation of WiFi Network Handover Technology [D]. Shanghai: Shanghai Jiaotong University, 2008:3-35.

[18] Cheng Kefei. Embedded System Design [M]. Beijing: Machinery Industry Press, 2010:27.79.

[19] ST'S terms.Using the high-density STM32F 1 0xxx FSMC peripheral to drive external memories. http://www.st.com,2009-4-7.

[20] Ma Hongbing, Gu Yuantao. Hardware and Software Architecture of Embedded System [M]. Beijing: People's Posts and Telecommunications Press, 2008:25-97.

[21] Cheng Zhijiang, Li Jianbo. Development of intelligent car control system based on fuzzy control [J]. Computer application, 2008 14(12):350-353.

[22] L298N motor drive circuit diagram. Baidu Library http//wenku.baidu.com/view/85ebflcod5bbfdoa79567335. html.

[23] M.van der Schaar, and S.Shankar. Cross-layer wireless multimediatransmission: hallenges, principles, and new paradigms. IEEE Wireless Commun, Mag, v01.12, no.4,PP.1 179-l 184,2005

Research on Model-based Method for Removing Peak Noise of Ground NMR Signals

Ji Zhihao, Li Zhe, Wang Chunlu
（jilin university instrument science and engineering institute,changchun,130021）

***Abstract*—Ground magnetic resonance detection (MRI), as the only geophysical method for direct detection of groundwater in the world, has the advantages of high resolution, high efficiency and abundant information, and can give a quantitative explanation of the depth and thickness of underground aquifer, the size of water content, the porosity of underground medium and so on. In this paper, the peak noise removal of NMR groundwater detector is studied according to the characteristics of large emission power and weak receiving signal of NMR groundwater detector. In this paper, a method based on model noise removal is proposed, which is similar to the impulse response of the band band-pass filter based on the peak of the power grid. Using the convolution of pulse function and two different second-order band-pass filters to simulate spike noise, after removing the frequency harmonic interference by using harmonic modeling, the NEO algorithm is further used to emphasize and identify the position of the spikes in the ground NMR signal for the spikes with small amplitude. Finally, based on the principle of least squares method, the signal feature parameters are extracted to realize the removal of the peak noise of Mrs Signal. Compared with the traditional denoising method, the algorithm of Mrs Signal peak noise removal proposed in this paper has the advantages of strong practicability and obvious improvement of work efficiency.**

***keywords*—Spike noise Least squares Prediction model Transfer function**

I. FOREWORD

WATER is the source of life, basic natural resources and strategic economic resources, is the controlling element of ecological environment, and plays an extremely important role in economic[1], social development and national security. With the development of science and technology, the pollution of water resources is serious, coupled with the uneven distribution of water resources in China, how to effectively monitor and evaluate the state of groundwater resource reserve is an important problem to be solved urgently in the development of national science and technology. Surface Nuclear Magnetic Resonance，as know as Magnetic Resonance Sounding, is a non-invasive, direct and quantitative geophysical method for detecting groundwater developed in recent years, the basic principle of which is to realize groundwater detection by detecting the NMR signal produced by hydrogen proton resonance transition in groundwater[2].

MRS Method in the actual detection process, because the working environment is the natural magnetic field in the wild, a large number of natural and man-made noise, will have an unnegligible impact on the measurement results, resulting in low signal-to-noise ratio of the measurement data, and then affect the accuracy of the inversion results, resulting in the aquifer or water content of the judgment error. As a kind of typical interference in human noise, peak noise is mainly caused by natural or artificial discharge[3], which has the characteristics of accidental occurrence, short duration and relatively large amplitude, and its existence will lead to large error in feature parameter extraction, which seriously affects the accuracy of inversion interpretation[4].

II. HARMONIC NOISE ELIMINATION

For the acquired NMR signal, the first step is to eliminate the frequency interference in order to reduce the type of noise, and to provide advance conditions for the identification and elimination of peak noise[5].

Firstly, the harmonic noise model Vhar is established. Vhar is the cumulative result of n harmonics with a frequency F0 (50±0.1 Hz) as the base frequency:

$$V_{har} = \sum_{n=1}^{N} A_n \cos(2\pi n f_0 t + \phi_n) \quad (1)$$

Among them, An and φn are the amplitude and phase of the nth harmonics respectively, the number of harmonics[6], according to the bandwidth of the received signal (1 KHZ ~3 KHZ), take n=100. Then, the base frequency f0 is determined by adaptive scanning method. First, the 0.03 Hz is used as the step length in the range of 49.9~50.1 Hz, and the 3 frequency points with the smallest 2-order norm are obtained by using the following formula as the range of the next scan.

$$\|V_R - V_{har}(f_1)\|_2 \rightarrow min \quad (2)$$

Among them, the VR is the measurement data namely X1 (t), Vhar (f1) is the L scan value. In group 2nd scans, the scanning range is 49.99~50.05 Hz and the scan step is 0.0075 Hz, and the minimum 3 frequency points of the

norm are obtained again. When group 3rd scans, the scan range is reduced to 50.0125~50.0275 Hz and the scan step is 0.001875 Hz. At this point, the minimum value of the 2-order norm corresponds to the frequency point of 50.018125 Hz, that is, 3 sets of scans can achieve the accuracy requirements[7].

Finally, the linear coefficients are solved. The Nth subparagraph (3) in (1) is linearized:

$$A_n \cos(2\pi n f_0 t + \phi_n) = \alpha_n \cos(2\pi n f_0 t) + \beta_n \sin(2\pi n f_0 t) \quad (3)$$

Which, $A_n = \sqrt{\alpha_n^2 + \beta_n^2}, \tan(\phi_n) = \frac{\alpha_n}{\beta_n}$. From this, it is estimated that the problems of An and φn are converted into the form of solving linear coefficients αn and βn, and formula (3) is organized into linear equations[8]:

$$\boldsymbol{Ax} = \boldsymbol{b} \quad (4)$$

$x = [\alpha_1 ... \alpha_n, \beta_1 ... \beta_n]^T, b = [v_1, v_2 ... v_p]^T$.

III.Peak positioning

First of all, the NEO algorithm is used to strengthen the peak amplitude[9].

$$\phi[x(k)] = x^2(k) - x(k-1) \bullet x(k+1) \quad (5)$$

After the neo operation, and then through the appropriate low-pass filter, it will make the spike signal prominent.

Then, set the appropriate threshold. According to the MRS Duration T set to intercept the data period time t1, generally take t1 as the peak signal duration of 1.5-twice times; According to the time interval between the sample rate and the T1 setting two interception data segment t2, the integer n times of the t2 and the sum of the t1 are equal to the duration T, that is, T=t1+n*t2, and the NEO signal after the low-pass filter is divided into T1 section by t2, n+1 two parameters, and each signal is treated as a row. Combine all the rows into a data matrix, represented by me; The median number of each row in the Me matrix is obtained by using the median function, and the data is stored in vector y as the y axis of the fitting curve, the n+1 point is taken on the transverse axis, and the T/(n+1) is deposited in vector X as the x-axis of the fitting curve, and the curve Fitting with MATLAB is used. Tool, select vector x is one of the x data, vector y is y data, type polynomial (polynomial), curve fitting, generally take 3 or 4 orders can be obtained, polynomial coefficient vector P; The trend curve of the signal is established by using coefficient vector P and order n, and its expression is

$$\text{envelop\_line} = \sum_{k=0}^{n} P(k+1) t^{n-k} \quad (6)$$

The peak noise is then positioned. Get the fitting function from the foregoing envelop_line. Then, by taking the previous threshold factor (empirical value 1) as the threshold function, for the spike signal which is still below the peak of the initial region after the NEO algorithm, it is considered that the effect of this spike on the actual measurement and the late inversion is not negligible.

IV.Spike Modeling

We have modeled the multi-channel nuclear magnetic induction receiving system as a cascade of two different second-order band-pass filters. The transfer function of the second-order band-pass filter in S domain is given by the following formula[12]:

$$G(s) = \frac{s}{s^2 + 2\zeta\omega_0 s + \omega_0^2} \quad (7)$$

Among them, Ω0 and Zeta are the central frequency and bandwidth of the filter. Any gain in the filter is included by default in peak amplitude A.

First of all, because the peak of the power grid is similar to the pulse excitation of the ground NMR instrument, the peak noise model Y1 (t) is established by using two different second-order band-pass filter cascading and unit pulse function convolution[13]:

$$Y_1(t) = sp(t) = A\delta(t - t0) * grec(t) \quad (8)$$

Where a is the amplitude of the spike noise, the t0 is the initial time of the spike signal, and the grec (t) is the filter transfer function. Then position the peak.

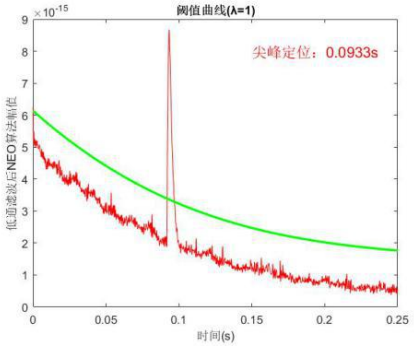

Fig.1 Threshold curve

Finally, based on the Y1 (t) of the above model and the peak data segment of location interception, the characteristic parameter A,t0 is extracted by the principle of least squares method, and the peak noise Y2 (t) is obtained, as shown in Figure 2. The truncated data is processed by the least squares method.

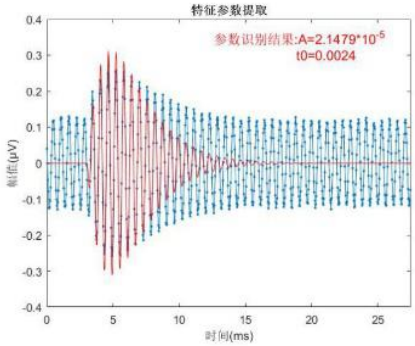

Fig.2 Parameter identification

Extract feature parameter A. A value under t0=tl can be obtained, recorded as Al and deposited in vector A.

$$A = (M^T M)^{-1} M^T H \tag{9}$$

The mean square root error (RMSE) under t0=tL is calculated and stored in vector RMSEl.

$$RMSE_l = \sqrt{\frac{1}{S}\sum_{K=1}^{S}[A_l \bullet M(k) - H(k)]^2} \tag{10}$$

The A,t0 corresponding to the minimum mean square root error are evaluated as characteristic parameters.

Finally, the spikes are removed, and the spikes-containing signals obtained in the above are subtracted from the modeled signals to realize the removal of peak noise[10].

V.CALCULATION RESULTS AND COMPARISON

In order to test the reliability and practicality of the procedure, the Romanovsky criterion compares with the Neo method parameters[11]:

Table 1 Comparison of different amplitude peak filtering effects under Romanov criterion

	Amplitude value	A_1	A_2	A_3
		0.000022	0.000020	0.000018
SNR	15.8982、7.1138、15.3561、6.4720、15.8982、15.3561、16.7991、16.2609			
SNR0	16.7330			
SNR1	15.8982、16.1068、15.3561、15.0571、15.8982、15.3561、16.7608、16.2609			
SNR10	17.9085			

	Amplitude value	A_1	A_2	A_3
		0.000025	0.000022	0.000017
SNR	15.8982、6.5108、15.3561、5.9158、15.8982、15.3561、16.7991、16.2609、			
SNR0	16.5083			
SNR1	15.8982、16.0878、15.3561、15.0647、15.8982、15.3561、16.7610、16.2609			
SNR10	17.9063			

	Amplitude value	A_1	A_2	A_3
		0.000023	0.000021	0.000016
SNR	15.8982、7.0404、15.3561、6.3971、15.8982、15.3561、16.7991、16.2609			
SNR0	166678			
SNR1	15.8982、16.1080、15.3561、15.0596、15.8982、15.3561、16.7610、16.2609			
SNR10	17.9088			

	Amplitude value	A_1	A_2	A_3
		0.000024	0.000019	0.000015
SNR	15.8982、7.2526、15.3561、6.6177、15.8982、15.3561、16.7991、16.2609、			
SNR0	16.7229			
SNR1	15.8982、16.1026、15.3561、15.0555、15.8982、15.3561、16.7608、16.2609			
SNR10	17.9080			

Table 2 Comparison of different amplitude peak filtering effects under NEO criteria

	Amplitude value	A_1	A_2	A_3
		0.000022	0.000020	0.000018
SNR	15.8982、7.1138、15.3561、6.4720、15.8982、15.3561、15.3561、16.7991、16.2609、			
SNR0	16.7030			
SNR1	15.8982、14.0222、15.3561、13.8514、15.8982、15.3561、16.7991、16.2609			
SNR10	17.8132			

	Amplitude value	A_1	A_2	A_3
		0.000025	0.000022	0.000017
SNR	15.8982、6.5108、15.3561、5.9158、15.8982、15.3561、15.3561、16.7991、16.2609、			
SNR0	16.5083			
SNR1	15.8982、14.0962、15.3561、13.8483、15.8982、15.3561、16.7991、16.2609			
SNR10	17.8181			

	Amplitude value	A_1	A_2	A_3
		0.000023	0.000021	0.000016
SNR	15.8982、7.0404、15.3561、6.3971、15.8982、15.3561、15.3561、16.7991、16.2609、			
SNR0	16.6687			
SNR1	15.8982、14.0100、15.3561、13.8280、15.8982、15.3561、16.7991、16.2609			
SNR10	17.8163			

	Amplitude value	A_1	A_2	A_3
		0.000024	0.000019	0.000015
SNR	15.8982、7.2526、15.3561、6.6177、15.8982、15.3561、15.3561、16.7991、16.2609、			
SNR0	16.7229			
SNR1	15.8982、14.0313、15.3561、13.8192、15.8982、15.3561、16.7991、16.2609			
SNR10	17.8084			

VI. CONCLUSION

Based on the characteristic that the peak noise and pulse function caused by the power grid in the ground NMR signal are very similar to the impulse response of two second-order band-pass filters, a model-based method for removing peak noise of ground NMR signals is proposed in this paper. Because the ground NMR signal is very weak, the noise of the frequency harmonic has a great influence, so the method of harmonic modeling is used to remove the harmonic interference of the working frequency first. Aiming at the spikes with small amplitude, the NEO algorithm is used to emphasize the spikes. Then the influence of random noise is eliminated by low-pass filter, and the peak value is positioned by threshold curve. The peak data segment is intercepted from the ground NMR signal according to the peak location point to reduce the workload. Based on the principle of least squares method, the peak data is fitted with the established pulse function and two second-order band-pass filter cascading models, and the amplitude and initial time two characteristic parameters are extracted, and then the spikes are subtracted and eliminated. By comparing with the traditional Neo method, it can be seen that the modeling method does not need multi-channel data superposition, which improves the efficiency, and the signal-to-noise ratio is better than the NEO algorithm. At present, there is a problem of over-fitting in the modeling method, although it has little effect on the final NMR signal inversion, but it also needs further improvement.

References

[1] W.-K. Chen, Linear Networks and Systems (Book style). Belmont, CA: Wadsworth, 1993, pp. 123–135. Marian Hertrich. Imaging of groundwater with nuclear magnetic resonance. Progress in Nuclear Magnetic Resonance Spectroscopy, 2008, 53(4): 227-248.

[2] Jakob Juul Larsen Model-based subtraction of spikes from surface

[3] Strehl,S.,Rommel,I.,Hertrich,M.,Yaramanci,U..New strategies for filtering and fitting of MRS signals. Proceedings 3rd International MRS Workshop, Madrid, Spain,2006,65-68.

[4] Strehl,S.,Development of Strategies for Improved Filtering and Fitting of SNMR-Signals. Technical University of Berlin, Institute of Applied Geosciences, Department of Applied Geophysics Diplomarbeit,2006.

[5] Wang Zhongxing, Long Liangliang, taisuki. Singular interference suppression in ground NMR water finding signal. Journal of Jilin University (Engineering edition), 2009, 39 (5): 1282-1287.

[6] wanling, Zhang Yang, Taisuki, Kakawa, Lin Tingting *. The method of sharp peak noise suppression of magnetic resonance signal based on energy operation. Journal of Geophysics, 2016,59 (6): 2290-2301.Abragam, A., The Principles of Nuclear Magnetism[M]. Oxford University. Press, 1961,648 pp.

[7] leg A. Shushakov. Groundwater NMR in conductive water[J]. Geophysics, 1996, 61(4):998-1006.

[8] Anatoly Legchenko, Jean-Michel Baltassat, Nuclear magnetic resonance as a geophysical tool for hydrogeologists[J]. Journal of Applied Geophysics, 2002, 50(1-2): 21-46.

[9] Lubczynski, M.W., Roy, J., MRS contribution to hydrogeological system parameterization[J]. Near Surface Geophysics, 2005, 3: 131–139.

[10] Kristina Keating, Rosemary Knight, A laboratory study of the effect of magnetite on NMR relaxation rates[J]. Journal of Applied Geophysics, 2008, 66(3-4): 188-196.

[11] Chen Wenxhen. Principles of MRI geophysical instruments [M]. Geological Press, 1992.

[12] Shaw aspired. Research progress and application of rock NMR [J]. Logging Technology, 1996 20 (1): 27-31.

[13] Zhang Jianzhong, Sun Cun spectrum, Magnetic resonance tutorial [M]. China University of Science and Technology Press, 1996,10.

Infusion monitoring and alarm system based on Android mobile phone

Qiao Bingrui, Lv Yang, Dong Jiandong, Wang Jiliang
(College of Instrument Science and Electrical Engineering, Jilin University, Changchun 130012, China)

***Abstract*—This design uses the infrared sensing principle of the light pipe and the Android platform technology to design an infusion monitoring and alarming system based on Android mobile phone. Through the monitoring and alarm system, the patient's infusion process can be monitored in real time and sent to the supervisor's mobile phone app via WiFi wireless transmission, realizing remote monitoring and alarming of the infusion speed and infusion, thereby reducing the workload of the medical staff. ,Improve work efficiency.**

***Key words*—Single chip microcomputer Infrared induction Android technology**

I. Introduction

In today's medical treatment, intravenous infusion is a very common method of drug intake. In the process of infusion therapy, the traditional manual infusion monitoring method requires the length of the medical staff to check the speed and infusion of the infusion. When the speed of the drop is too fast, the degree of absorption of the drug by the patient is deteriorated, and even drug poisoning may occur; when the speed of the drop is too slow, the infusion time may be prolonged without any reason. When the liquid in the infusion bottle is nearly dripped, and the medical staff does not change the medicine or pull the needle in time, it is very likely that the air enters the blood vessel and is dangerous, thus affecting life safety. The infusion monitoring system designed and manufactured by our company uses the infrared sensing principle to detect signals, and based on the Android mobile phone platform, the medical staff can receive the alarm signal in a timely and flexible manner, and can take more timely processing, thereby reducing the workload and improving the work efficiency.

II. Overall system design

The intelligent medical infusion monitoring system is mainly composed of an infrared sensing acquisition part, a data processing transmission part and an APP remote monitoring part. The infrared sensing acquisition part is installed on both sides of the infusion tube, and inputs the collected signal to the data processing circuit part composed of STM32 single chip microcomputer.The data processing transmission part sets the standard flow rate of the droplet by adjusting the pull-up resistance knob, and simultaneously amplifies the signal obtained from the acquisition part, and calculates the time obtained by the internal interrupt count, obtains the current droplet flow rate, and sends it to the 8266 WiFi module. Monitor the APP.When the absolute difference between the measured speed and the standard speed is greater than the error range, or the current infusion is about to end, the data transmission part sends an alarm signal to the monitoring APP, and the APP receives the signal to remind the medical staff to process in time, and the single-chip computer controls the corresponding circuit to emit sound and light simultaneously. Call the police. The APP platform displays the infusion speed, infusion volume and alarm reminder on different beds for real-time monitoring and treatment by medical staff.

III. Infrared sensing acquisition part

Infrared light pipe is a commonly used infrared light emitting diode, which is divided into two parts: infrared emitting tube and receiving tube. The schematic diagram of its work is shown in Figure 1.

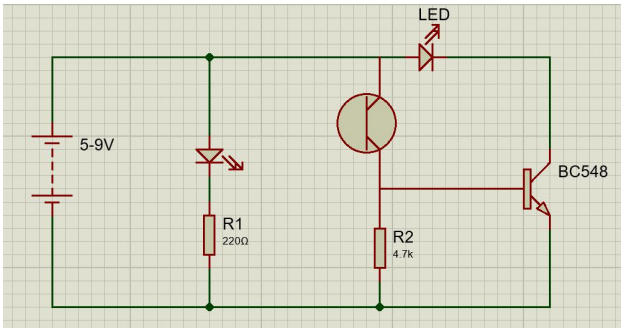

Fig.1 Infrared pair tube circuit diagram

A section of the wavelength in the range of 0.76 to 400 μm is called infrared. The wavelength of the emission center of the infrared emitter selected in this design is 940 nm. The infrared pair of the wavelength is low in cost and convenient to use. The infrared pair tube adopts a through-beam structure, and collects by

comparing the voltage signal changes when the liquid medicine passes. The infrared pair tube is used to detect the droplets in the Moffier tube. When the liquid solution is not dropped, no droplets pass between the transmitting and receiving tubes, and the receiving tube outputs a relatively low voltage signal; When passing between the two tubes, the receiving tube will output a relatively high voltage signal due to the influence of the infrared signal generated by the liquid medicine, so that a pulse signal can be generated to complete the collection of the infusion signal [1].

IV. DATA PROCESSING TRANSMISSION PART

A. Acquisition signal conditioning

Since the infrared pair tube adopts the on-beam structure to collect signals, the detected voltage variation is relatively small, and it is also affected by external factors. Therefore, a signal conditioning amplification comparison circuit is needed to shape and compare the signals. The specific circuit diagram is shown in Figure 2. Due to the measurement of the radiation structure, the voltage signals obtained from the infrared receiving tube are generally small, only a few mv or even less than 1 mv. Therefore, it must be amplified by an amplifying circuit to be recognized by the MCU. The amplifier is a four-channel operational amplifier circuit composed of the LT1014 to amplify the signal. Compared to traditional single-channel operational amplifiers, the LT1014 quad-channel op amp is smaller and less expensive, and the performance of the circuit is improved due to the multi-step channel.The calculation formula of the circuit magnification is Av=1+R3/R2=23. After the amplification process, the signal collected by the infrared photoelectric sensor can be easily processed.

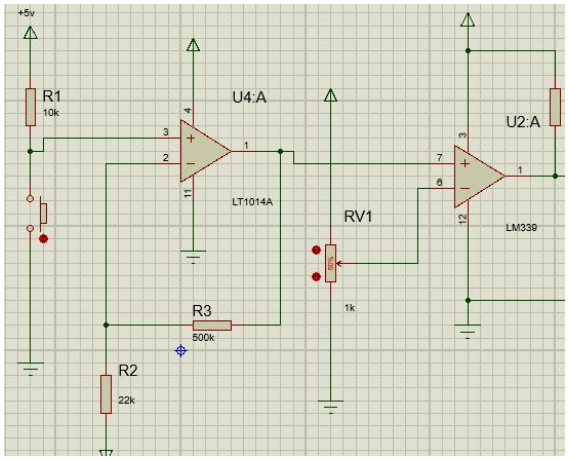

Fig.2 Amplification comparison circuit

After the amplified signal, its high and low levels are not standard values and cannot be directly recognized by the MCU. Therefore, it needs to be shaped. It is converted to a standard signal using a voltage comparison circuit. The voltage comparator compares the input voltage to the set standard voltage value. Below the standard voltage, the comparator outputs a low level; above the standard voltage, the comparator outputs a high level to achieve the conversion of the measured signal to the standard signal[2]. Here, the LM339 chip is used to form a differential comparison circuit for voltage comparison. Among them, RV1 is a potentiometer used to change the standard voltage setting. After the voltage comparison, the pulse signal that can be recognized by the single chip microcomputer can be obtained, thereby realizing the measurement of drip dripping.

B. data processing

After receiving the conditioned acquisition signal, the host computer processes and analyzes it to obtain further results. The specific work flow chart is shown in Figure 3. The infrared collection portion is mounted on the lower dropper between the Muffy dropper and the infusion needle. During the infusion, the nurse confirms the infusion rate, and the MCU receives the set speed signal and internally sets the desired control value. In the single-chip microcomputer, the droplet signal is timed by an external interrupt, and when the signal is input again, the timing is ended, and the dripping speed of the droplet in the infusion tube is obtained. At the same time, the droplets are counted using internal interrupts. Therefore, the infusion rate can be obtained by calculating the droplet dropping speed in the infusion tube and the droplet volume of the model infusion tube, and multiplying the number of droplets to obtain the infusion amount. The drip speed error taken by the device is 5 drops per minute. When the difference between the drop speed and the preset value is >5, the MCU outputs a fast signal; when the difference between the drop speed and the preset value is <5, the MCU The output is too slow to achieve speed alarm. When the infusion is over, reset the infusion monitoring system [3].

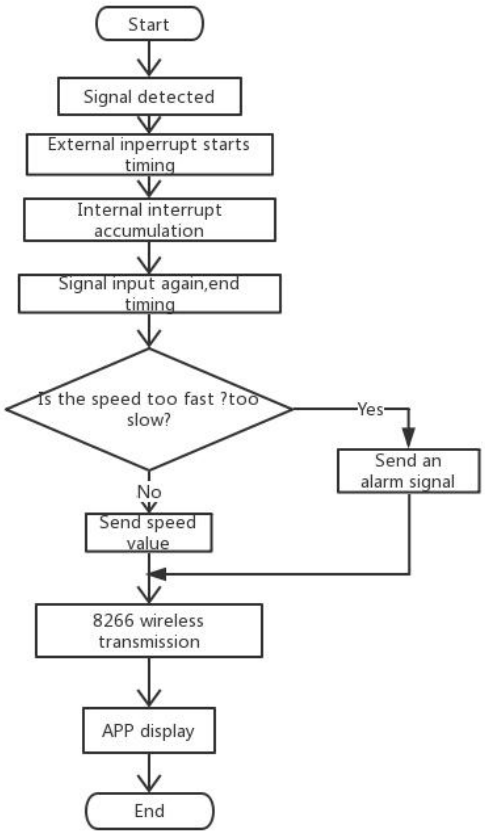

Fig.3 System work flow chart

C. Data transmission and alarm

Each infusion monitoring and alarm device is connected to the monitoring system and the mobile phone APP of the medical staff through WiFi transmission. The monitoring block diagram is shown in Figure 4. The intelligent infusion monitoring device sends the set infusion standard speed and the collected actual speed, liquid level condition, emergency alarm and other information to the upper computer app through the wireless transmission module for medical staff to observe and process in real time. The system's WiFi transmission uses the ESP8266 wireless WiFi module. The ESP8266 is a complete and self-contained WiFi network solution that can run independently or as a slave on other hosts. ESP8266 has the characteristics of small amount of data transmission, strong alarm burst, and powerful on-chip processing and storage capabilities, enabling it to integrate sensors and other application specific devices through the GPIO port, achieving the lowest pre-development and Minimize system resources during operation and realize multi-to-one communication through flexible networking to realize monitoring and management of different inpatients and multiple infusion monitoring systems.

MCU 8266 sending program

```
a[0]=js/100+'0';
a[1]=(js%100)/10+'0';
a[2]=(js%100)%10+'0';
atk_8266_wifiap_test(a);//8266 transmission program
```

Using a global variable **js**, the number of external interruptions of the droplet drop is counted and the speed is calculated, and finally converted to decimal form and sent to the APP display via 8266.

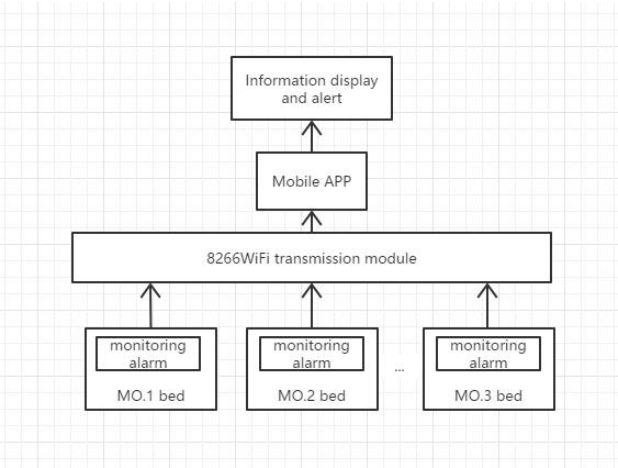

Fig.4 Data transmission monitoring block diagram

The working principle of ESP8266 has three working modes. The main one is ap mode. First, the ap mode is started by the network debugging assistant. In ap mode, 8266 is used as a relay station and connected with the single chip microcomputer. In AP mode, we can use a mobile phone to connect to it, and then we can send the ssid and psw of the connection network to the ESP8266 module. After the connection is successful, we can receive the data sent by the MCU via the 8266 network. The working diagram is shown in Figure 5.

Fig.5 Working diagram of ESP8266

The infusion alarm device of the device adopts the sound and light alarm mode. When the drug droplet speed is too fast, too slow or close to the drop, the MCU will output the corresponding signal and send it to the designed APP through WiFi transmission, waiting for the medical staff to handle it. If it is not processed within 1 minute, the buzzer will sound an alarm and the alarm light will illuminate, prompting the surrounding medical staff to handle it [4].

V. APP REMOTE MONITORING SECTION

The main function of the APP is to establish a connection with 8266 to obtain the droplet flow rate, flow rate and alarm signal transmitted by the MCU, and display the visual data on the interface: infusion speed, infusion progress and alarm signal [5].

In the specific design, the APP mainly calls the WiFi and vibration functions of the mobile phone. Firstly, the WiFi and vibration authorization of the mobile phone are obtained in the manifest, and the corresponding programming is completed to complete the WiFi signal reception and vibration activation.

Enter the APP interface to set the ip address and two edittext of the port,get the input ip address and port number to match the 8266. Set a button click event, when the mobile phone WLAN access 8266WiFi signal, click the connection to get the droplet flow rate sent by the MCU, and display it in the TextView. The disconnected button click event can disconnect the connection and stop receiving data. A picture of a light color and black and white are set. When the alarm signal of the single chip is input, it is converted into a color pattern, and the mobile phone vibration alarm is called, and the patient end of the applicator is prompted to help, and the switch button is used to stop the alarm signal. The current injection volume is manually entered by adding an edittext. The progress bar calculates the infusion progress based on the flow rate and the current amount, and visually displays it in the form of a progress bar.

Fig.6 App work interface

VI. CONCLUSION

The design is an intelligent infusion monitoring and alarming system based on Android mobile phone platform. The standard flow rate is set by the monitoring device of the lower computer and the infusion flow rate and liquid level are detected in real time. The wireless transmission module is used to transmit to the monitoring APP in real time and remotely monitored by the mobile phone APP. Real-time monitoring and management of the platform. In the actual test, 250 mL: 2.25 g saline bottle and standard No. 7 infusion tube were selected for testing, and the ratio of the volume of the droplet to the number of droplets was 1:20 under this condition. Set the standard infusion rate to 70 drops / min, set the flow rate to 0.0583mL / s, and the measured flow rate is 0.0580mL / s, the value is taken at intervals of ten minutes, The average error of the infusion flow rate calculated by multiple times was 0.023 drops/s, which satisfied the error range. The monitoring and alarming device can better realize the functions of intelligent control and real-time viewing, and is suitable for the current infusion equipment, can improve the working efficiency of the nurses, reduce the medical error rate, and improve the economic efficiency to a certain extent, and reduce the labor cost.Has a relatively broad application market.

References

[1] Kang Bing, Lin Zhiyuan, Wang Peng, et al. ZigBee-based intravenous intelligent remote monitoring system[J]. Journal of Jilin University，2016, 34 (2): 186—191.

[2] Chen Yu, Wang Wei.Design of Intelligent Infusion Monitoring System Based on Photoelectric Technology [J].Nuclear Electronics & Detection Technology, 2009, 29 (5) :1149-1154.

[3] Liu Hongqing.Design of MSP430F149 intelligent medical infusion system[D].Taiyuan: Taiyuan University of Technology，2011.

[4] Yang Guangwei.Development of a new intelligent infusion monitoring system [D].Nanjing: Nanjing University of Aeronautics and Astronautics，2012.

[5] Yan Zewen. Based on 2.4G wireless intelligent infusion monitoring system [J]. Electronic World，2017.161:171.

Research on mine detection exhaust system based on single chip microcomputer

ZHANG Chun-ling, WANG Peng-jia, WANG Qin-mian
（jilin university instrument science and engineering institute,changchun,130021）

***Abstract*—This paper designs a low-cost carbon monoxide concentration detection alarm and exhaust system. This system USES STM32F103 as the main control chip to collect the carbon monoxide concentration in the field through the ADC channel. The data are uploaded to the host computer through the WiFi module to form a concentration curve to facilitate the analysis of the concentration change trend, and can be controlled by the host computer.**

***keywords*—Single chip microcomputer Carbon monoxide detection WiFi transmission**

I. INTRODUCTION

CARBON monoxide is a kind of colorless,odorless gas that is very harmful to the human body after inhalation. It combines hemoglobin to produce carboxyhemoglobin to cause hypoxia in humans. With the development of modern industry and the acceleration of urbanization, harmful gases in the mine industry are produced in large quantities, the most common of which is carbon monoxide. Exposure to excessive carbon monoxide can severely damage the heart and central nervous system, with sequelae. Therefore, the detection of carbon monoxide concentration and the study of the discharge of carbon monoxide gas are indispensable[1][8].

Based on STM32,The carbon monoxide concentration detection system, use STM32 as the main control chip. The output signal of the carbon monoxide detection module is collected by the ADC channel. The data is sent to the host computer through the WiFi module and the data is simply filtered. Then the host computer can fit the real-time concentration curve according to the processed data. When the user needs to know the concentration of carbon monoxide in the measured area,he can use the PC to connect to the WiFi module signal to view the real-time carbon monoxide concentration, and control the parameter setting of the lower computer through the host computer[4].

II. OVERALL SYSTEM DESIGN

The detection system consists of two parts: the upper computer is developed by Labview. Its functions include data transmission, parameter control, data recording, curve fitting and so on. The lower computer is a hardware system with STM32 microprocessor as the main control chip and connected with multiple peripheral modules. In the lower computer, STM32 is the main control chip, and the output signal of the carbon monoxide detection module is collected by the ADC channel. After the signal is simply processed, it is sent to the host computer through the WiFi module, and the host computer can fit the real-time concentration change curve. When the operator needs to monitor the concentration of carbon monoxide in the measured area, the signal of the PC connected to the WiFi module can be used to check the real-time carbon monoxide concentration. When special condition is found in the measured area, the operator can control the lower position machine through the upper computer. The system structure is shown in Figure 1.

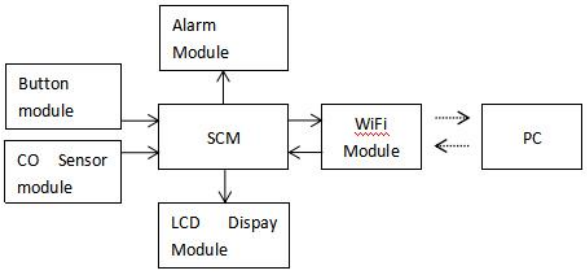

Fig. 1. The system structure.

A. WiFi Module

The connection between the host computer and the lower computer is a WiFi module. First, the module needs a stable 5V power supply, and the 5V voltage on the STM32F103 can be used as the power supply. Since the WiFi module and the MCU transfer data to each other through the serial port of the MCU, the data receiving and transmitting end of the WiFi module should be connected to the transmitting and receiving ports of the MCU,as shown in picture 2.

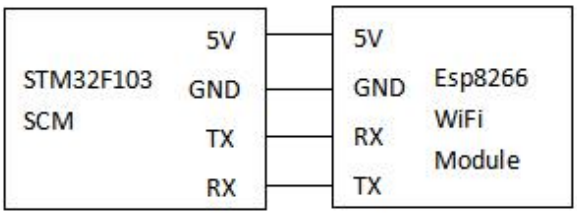

Fig. 2. SCM and WiFi module connection diagram.

B. CO Sensor Module

The MQ-7 carbon monoxide sensor module is used in this system, and the MQ-7 sensor chamber uses activated carbon filter to improve sensor selectivity. The key to the alarm and exhaust system is the detection of carbon monoxide concentration. selectivity of the carbon monoxide response of the sensor is good, and the temperature compensation is automatically performed at the same time as the signal acquisition. It has the characteristics of high sensitivity and stable performance, so it meets the demand of the device studied in this paper. The module requires a 3V stable power supply and can be powered by the 3V voltage on the STM32F103. The output of this module is connected to the A/D input pin of the microcontroller. The connection diagram between the CO sensor module and the MCU is shown in Figure 3[2-3].

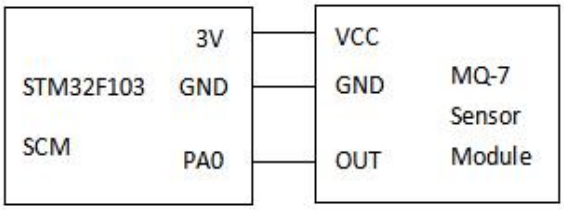

Fig. 3. SCM and CO sensor module connection diagram.

C. Display Module

The display module uses the 5110 LCD module to connected to the single-chip microcomputer, and the LCD displays the currently measured carbon monoxide concentration, the speed value of the motor rotation, the set concentration threshold, and whether the data is sent to the upper computer.

D. Input Module

The input module uses the 4*4 rectangular keyboard as the input of the single-chip microcomputer. Under the mine, the operator can input some commands through the keyboard to change the concentration threshold parameter, the motor speed, whether to send data to the upper computer, one button to enter the emergency situation, relieve the emergency situation, etc.

E. Alarm Module

The alarm module includes a buzzer and an exhaust device. The positive end of the buzzer is connected to the I/O port of the MCU, and the other port is connected to the GND of the MCU. The exhaust device refers to the motor device that discharges harmful gases under the mine.L298N The L298N driver module requires an additional 12V voltage and can be supplied with a power adapter. For proper motor operation, the GND of power supply, microcontroller and motor driver module must be connected together. The connection diagram of the motor, drive module and single chip microcomputer is shown in Figure 4.

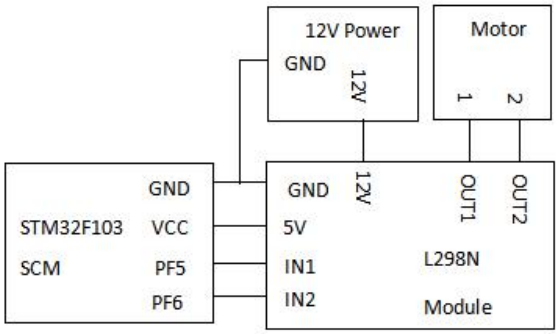

Fig. 4. SCM and motor connection diagram.

III. PC AND LOWER COMPUTER SOFTWARE DESIGN

A. Lower Computer SoftwareDesign

The development of the lower computer is based on KEIL5. After power-on, the LCD module, ADC module, serial communication module and timer are initialized first. Next, the WiFi module is configured in the server mode, and the analog voltage signal of the detection module is collected through the ADC channel, and the carbon monoxide concentration data is obtained, and the original data is simply processed and displayed on the LCD peripheral, and the data is connected through the serial port to the WiFi module, sent to the host computer. Three initial concentration alert thresholds are set:C1=5ppm, C2=15ppm, C3=24ppm. If the detected concentration value is within a certain threshold interval, the status of the LCD peripheral, motor and buzzer is as shown in Table 1. When the keyboard input control command changes the current concentration threshold. The display shows the value to be changed at this time. Press the Enter key to display all the data. The rotation of the motor is changed by the duty of the PWM wave outputted by the microcontroller. At the same time, the rotation speed of the motor can be changed by the keyboard. In the program, an emergency situation is also set. In the mine, if there is an unexpected situation, the operator presses the emergency button, the motor speed is fast, and the

buzzer alarms. When the emergency situation is solved, press the button, the alarm is released and all modules return to normal[5-6].

TABLE I The states of the external devices in different concentration ranges

Peripherals	Concentration range C(ppm)			
	0≤C＜C1	C1≤C＜C2	C2≤C＜C3	C≥C3
motor buzzer	slow no alarm	medium slow no alarm	medium fast alarm	fast alarm

B. PC Software Design

The host computer is developed based on LabVIEW. The host computer is set to the client mode.The IP address and port number are set on the host computer interface. When connected to the lower computer, the PC can receive the data. After simple filtering and data processing, the data is displayed in a curved form. The curve of concentration can be observed over time. At the same time, the upper computer is used to send the control signal to the lower computer, and the limit concentration parameter and the motor speed are set. The host computer interface is shown in Figure 5. CO concentration curve in Figure 6.

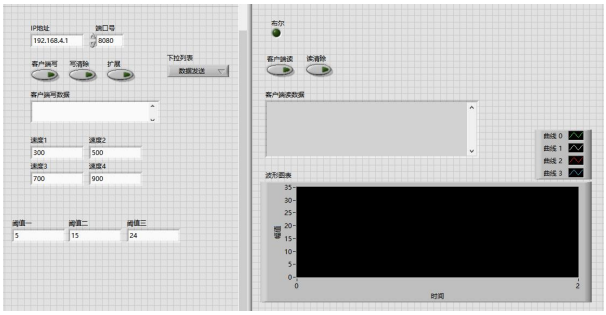

Fig. 5. Upper computer interface.

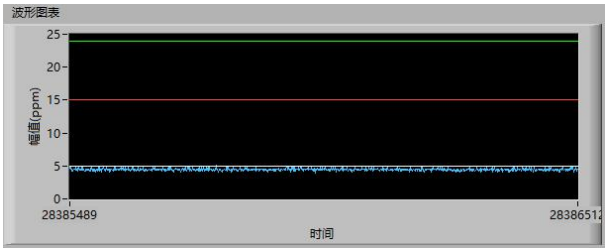

Fig. 6. CO concentration curve.

C. Communication of PC and Lower Compute

PC and lower computers transmit data through the WiFi module. First, parameters of the WiFi module are set according to the AT command, including WiFi mode, start multiple connections, WiFi name and password, setting up the server, setting the port number, etc., so that the PC can connect to the WiFi module. Secondly, the lower computer has been set to the TCP server mode, and the upper computer is set to the TCP client mode. When data are transmitted, the lower computer sends the data to the upper computer according to the AT command format, so the upper computer can receive the correct data. When the host computer sends a command to the lower computer, the command flag must be added. When the serial port receives the data sent by the host computer, it finds the command flag, and then finds the command content sent by the host computer, and controls the parameters of the lower computer according to the command content.

IV. CONCLUSION

For the large-scale development of the modern mine industry, a large amount of harmful gases are generated during the mining process, which not only leads to the loss of property resources and even the safety of personnel. Therefore, it is urgent to conduct research and testing on the concentration of carbon monoxide. We need a kind of alarm device which can provide real-time observations of the concentration of carbon monoxide under the mine. The carbon monoxide concentration detection and exhaust system studied in this paper provides an implementation plan for underground mine detection and early warning. The detection device is set up in the area where measurement is needed, the data is transmitted through the WiFi module, and the concentration can be effectively monitored by the host computer. Once the concentration exceeds the standard, the alarm is issued, with speeding up the venting in time to avoid disasters[1][7].

References

[1] ZHANG Peng-cheng, YING Bin-cheng, WANG Jin-yi, ZHU Yi-wen, CHEN Xi-ai. Carbon monoxide detection system based on STM32[J]. Science and technology information. 2018，16（15）:43+44

[2] WANG Na-lin, Gas alarm system based on mq-7 sensor[J]. Automation technology and application. 2014， 33（12）:103-105+113

[3] WANG Shui-cheng. Principle and application strategy of carbon monoxide detection alarm[J]. Forestry labor safety. 2016，29（03）:33-35+44

[4] CHEN Ke-wu, ZHAO Shang-wu, HUANG Sheng, CHEN Mei-mei. Development of automatic verification system for carbon monoxide detection alarm[J]. The southern metal. 2018，（06）:53-56

[5] JIA Huai-qing. Design of intelligent open and close window system based on single chip microcomputer control[J]. Mechanical and electronic information. 2014，（15）:149+151

[6] LI Rui-fu. Design of carbon monoxide concentration detector based on microcontroller AT89C51[J]. software. 2015，36（09）:106-108

[7] LI Yi-fei, MA Peng-fei. Design of mine carbon monoxide detection system based on single chip microcomputer[J]. Sensor world. 2013，19（09）:18-21

[8] WANG Zhong-hui, HE Yu-kai, LIU Zhong-qi. Development and research of carbon monoxide gas detection in underground coal mine[J]. Mining machinery. 2006，（05）:21-24+4

Data Processing and Display System for Three-Component Magnetic Survey on Water Surface

Jin Qiang, Sang weiye, Zhao chenyu
(College of Instrumentation & Electrical Engineering, Jilin University,Changchun 130022,China)

***Abstract*—According to the attitude correction in the magnetic measurement process, a water surface three-component magnetic measurement display system is designed by using Euler rotation method, ridge regression analysis and corrosion expansion algorithm. It can display real-time magnetic measurement distribution vector, and its human-computer interaction interface is more concise and user-friendly than before.**

***Key words*—The surface of the water Three component magnetic survey Magnetic measurement distribution vector**

0. INTRODUCTION

THE three-component magnetic measurement of water surface uses the three-component magnetic measurement system to measure the three-component magnetic field strength of the geomagnetic field [1]. Compared with the traditional total magnetic field measurement method, this method can obtain more abundant and accurate geomagnetic field information, effectively reducing the inverse The multi-solution in the performance contributes to the quantitative analysis of magnetic materials and it is widely used in many fields.The measurement of the magnetic field of lakes and lakes is a process of geomagnetic measurement on the surface of the water by a vessel carrying a magnetometer.Since the total field measurement does not require direction information, and the tow cable length is greater than 3 times the length of the ship, the influence of the ship magnet can be greatly ignored. Therefore, most of the current surface magnetic measurements are towed total field measurements.However, the geomagnetic field is a vector field [2]. The three-component measurement of the geomagnetic field (also called vector measurement) can obtain the direction information of the magnetic field, which can reflect more magnetic source structure than the total field measurement, and the water surface three-component measurement can be used as a ship. Carrying the way, the ability to break through the tow measurement is easily limited in some waters.Thus geomagnetic three component embodiment the water surface is measured geomagnetic measurement trend.With the development of ship navigation and hull positioning technology, it has become possible to carry out three-component measurement of surface geomagnetism. In fact, in industrialized countries such as Western countries and Japan, surface geomagnetic measurements have been upgraded to component and component gradient measurements [3]. In recent years, the scope of geophysical surveys in China has been expanding and the means are becoming more and more abundant.Successful implementation of water surface geomagnetic three-component measurement can greatly increase the basic geomagnetic data and it improve the geophysical survey and research level.Therefore, the three-component magnetic survey on the water surface is a very important task.

1. THREE-COMPONENT MAGNETIC MEASUREMENT SYSTEM WORKS

The three-component fluxgate measurement system is a three-component fluxgate measurement system that uses a magnetic core with a high magnetic permeability, some soft magnetic materials, and a magnetic core of the magnetic permeability of the alternating excitation signal periodically changes under the magnetization Thus, the induced electromotive force generated in the inductive coil core of the magnetic winding is a nonlinearly correlated external magnetic field, and the external magnetic field information is obtained by the detecting means.

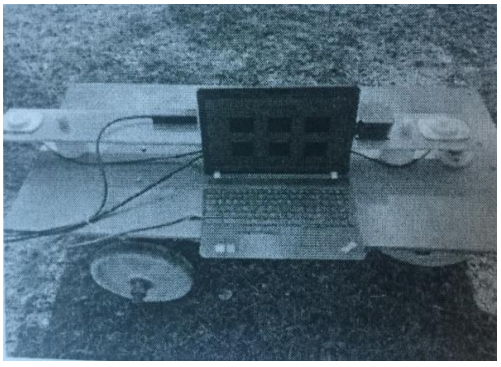

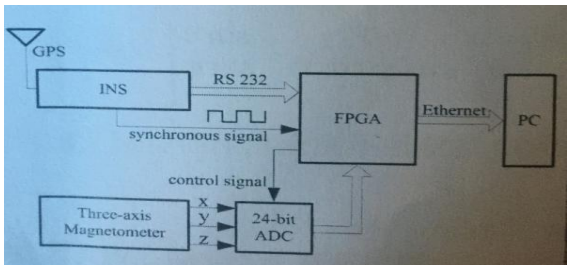

Fig. 1. Magnetometric Display System

2. Correction of three-component magnetic measurement system

According to the different mechanism of sensor error, the three-component magnetic measurement system mainly has three measurement errors [4]:Triaxial non-orthogonal error,Sensitivity error and zero offset error.

2.1 Error model of three-component magnetic measurement system

2.1.1 Three-axis non-correction error

Ideally, the three axes of the magnetic measurement system are orthogonal,However, it is difficult to guarantee orthogonality due to the limitation of processing accuracy.So build an error model,As shown below:

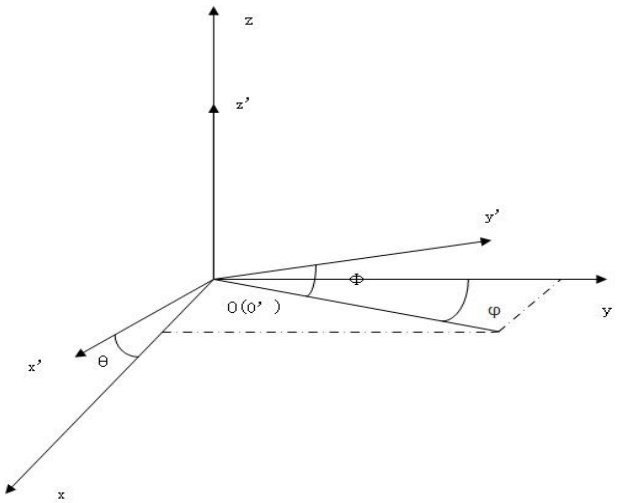

Fig.2 Triaxial error model

As shown in Fig. 2, o-xyz represents the ideal three-axis magnetic measurement system coordinate system, and o'-x'y'z' represents a non-orthogonal three-component magnetic coordinate coordinate system, assuming that the z-axis coincides with the z'-axis and the x-o-z surface Coincident with the x'-o'-z' plane, θ is the angle between the two x-axes, φ is the angle between the projection of the y' axis on the xoy plane and the y-axis, and the Φ-axis is the y 'axis and its xoy plane projection The angle between the two.This makes it possible to build a mathematical model [5]:

$$K_{nor}=\begin{pmatrix}\cos\theta & 0 & \sin\theta\\ \sin\varphi & \cos\varphi\cos\Phi & \sin\Phi\\ 0 & 0 & 1\end{pmatrix}$$

2.1.2 Sensitivity error

If the triaxial sensitivity of the three-axis amplification circuit of the magnetometer is not exactly the same, the sensitivity matrix can be expressed as: $K_{sf}=\mathrm{diag}[k_1\ k_2\ k_3]$

2.1.3 Zero offset error

In actual use, the three-axis output of the magnetometer is offset, that is,the output is not zero in an absolute zero magnetic field, and the zero offset error matrix is:

$$H_b=[H_{bx}\ H_{by}\ H_{bz}]^T$$

In summary: the measurement error model of the three-component magnetometer is:

$$Hm=KsfKnorHe+Hb\ [6]$$

3. Corrosion expansion

3.1 Corrosion

Corrosion [7] algorithm is to eliminate the boundary point of the target and shrink the boundary into the inside, which can be used to eliminate the object with small target and no actual effect.The erosion algorithm uses 3×3 structural elements to scan each pixel of the image, the AND element and its covered binary image.If both are one, the resulting image has a pixel of one, otherwise it is zero, resulting in a binary image being reduced by one revolution.The corrosion algorithm is Ba obtained by translation to the structural element B.If we include X in Ba, we record this, and all the results that satisfy the above conditions are called X-B corrosion (Erosion).Expressed as: E(X)={a| Ba X}=X B.

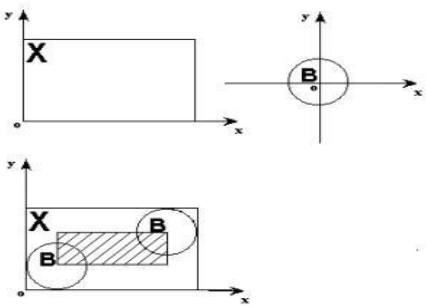

Fig.3 Schematic diagram of corrosion

X is the object being processed, and B is the structural element.It is not difficult to know that for any point a in the shaded portion, Ba is contained by X, so the result of X being etched by B is the shaded

portion.Suppose the shaded part is C. Then C is in the range of X and less than X, just as X is stripped.This is the erosion algorithm. Since the above B is symmetrical, that is, the symmetry set B of B, the result of X etched by B is the same as that of X etched by Bv.

3.2 Expansion

The expansion [8] algorithm is a process that can be used to fill a hole in the object by touching the object, combining all the background points to the object, and expanding the range to the outside.Its extension algorithm uses 3×3 structural elements to scan each pixel of the image, “or” the operation structure element and its covered binary image. If both are 0, the pixel of the obtained image is 0, otherwise 1.In result, image is expanded to binary image.Expansion can be seen as a double operation of corrosion [9], which is defined as: Ba is obtained by translating structural element B, and if Ba hits X, we record this point.All groups of points that satisfy the above conditions are referred to as the result of X being expanded by B. Expressed as:

$$D(X)=\{a \mid Ba\uparrow X\}=X\ B.$$

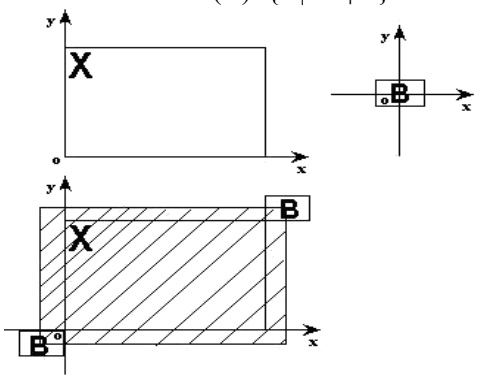

Fig.4 Expansion algorithm schematic diagram

3.3 Open operation

The open operation [10] is the process of first eroding and then expanding.

It is used to eliminate small objects, separate objects at slender points, and smooth the boundaries of large objects without significantly changing their area.The first expansion after corrosion is called on, that is: OPEN(X) = D(E(X)).

4. Ridge regression analysis

When there is a multiple collinearity between the independent variables, |XX'|0, imagine adding the normal digital matrix kI (k>0) to XX', making XX'+ kI close to the singularity, which is much smaller than XX'. The singularity takes into account the size of the variable, the data must first be normalized, and the standardized design matrix is still represented by X. Definition:

$$\hat{\beta}(k)=(X'X+kI)^{-1}X'y$$

It is called a ridge regression estimate[11] of β , where k is called the ridge parameter. Since X is assumed to be standardized, it is a related sample of the independent variables.Y can be standardized or unstandardized.If y is also standardized, the actual calculation is a normalized ridge regression estimate.In terms of stability, the estimation of β is more stable.Since the ridge parameter k is not uniquely determined, the resulting ridge regression estimate is actually an estimated family of regression parameters .In the application of ridge regression analysis, the parameter k needs to be selected and estimated. The traditional method is using the residual method, but we usually use the ridge method.Its intuitive consideration is that if the least squares estimate seems unreasonable, such as estimates and symbols are not economically meaningful, they can be determined using ridge estimates.The choice of the value of the ridge parameter is particularly important. Note the following when choosing the value:

(1) The ridge estimate of each regression coefficient is basically stable;

(2) When estimating by least squares, the regression coefficient with the sign of the ridge estimate becomes reasonable symbol is unreasonable;

(3) The regression coefficient has no absolute value which is not economically significant;

(4) The sum of squared residuals does not increase too much;

The ridge method is completely different from the traditional residual-based method. The ridge method is useful for analyzing the roles and relationships between variables.

5. Three-component magnetic measurement display system

The three-component magnetic measurement system is mainly composed of a three-axis fluxgate, an inertial navigation system, a host computer control software, a data acquisition unit, and a magnetic measurement carrier.The magnetic measurement system is used to measure the earth's magnetic field vector information.Inertial navigation system provides corresponding attitude information for three-component magnetic measurement data.The data acquisition unit uses the FPGA as the main control chip.Based on the inertial output synchronous signal, the synchronous sampling between the magnetometer and the inertial navigation is realized by controlling the analog-to-digital converter [12], and finally the measured data is sent to the PC through the Ethernet.

5.1 System block diagram of three-component

magnetic measurement system:

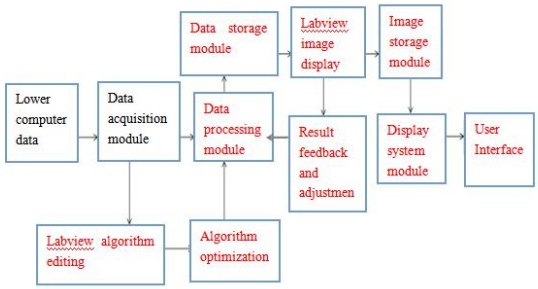

Fig.5 Three-component magnetic measurement system block diagram

After the data is collected by the computer data acquisition module, it is transmitted to the data analysis processing unit, and the data is processed and optimized according to a previously written algorithm, and then the processed data is passed through the storage module.There is a data feedback analysis module in the storage module [13] for correction. After the correction is completed, the system will send the corrected data to the HMI to display the required three-component magnetic measurement results.

5.2 HMI

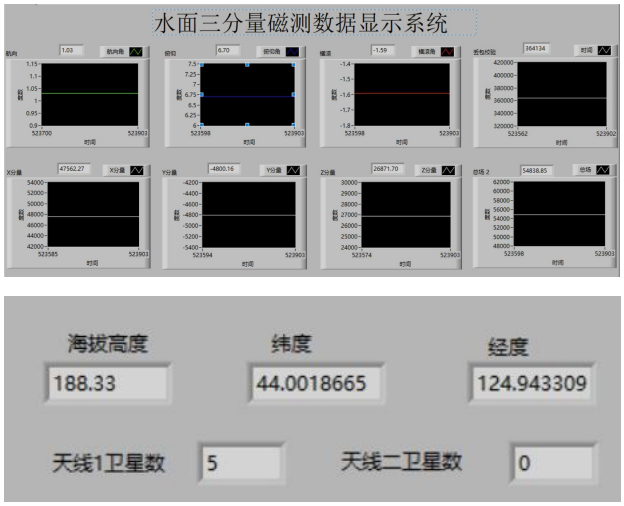

Fig.6 Human machine interface diagram

The system can display the local heading angle, pitch angle, roll angle and three-component magnetic survey total field data [14], and it can also display local altitude, latitude and longitude and other information.

5.3 Operation steps:

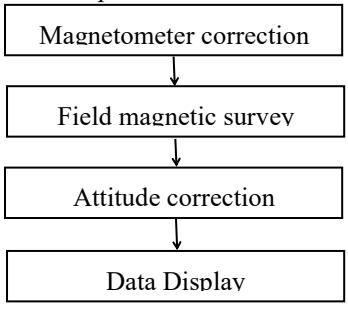

Fig.7 System Flow Chart

(a) Correct the magnetometer to eliminate the measurement error of the magnetometer itself [15];

(b) Select a line to perform a field magnetic survey;

(c) Correct the data pose [16], unifying the magnetic survey data into a coordinate system, and finally displaying the magnetic survey data uniformly;

5.4 Synthesis of magnetic measurement three-component

$$D=\begin{bmatrix}\cos\alpha\cos\gamma-\sin\alpha\sin\gamma\sin\beta & \sin\alpha\cos\gamma+\cos\alpha\sin\gamma\sin\beta & -\sin\gamma\cos\beta\\ -\sin\alpha\cos\beta & \cos\alpha\cos\beta & \sin\beta\\ \cos\alpha\sin\gamma+\sin\alpha\cos\gamma\sin\beta & \sin\alpha\sin\gamma-\cos\alpha\cos\gamma\sin\beta & \cos\gamma\cos\beta\end{bmatrix}$$

Among them, D is the transformation matrix between the geodetic coordinate system and the hull coordinate system, and the three-component magnetic field vector is synthesized by the transformation matrix [17]. The geomagnetic field measured in the water surface coordinate system can be expressed as:

$$\begin{aligned}\boldsymbol{B}_s^M &= \boldsymbol{A}\cdot\boldsymbol{D}\cdot\boldsymbol{B}_e^E+\boldsymbol{D}\cdot\boldsymbol{B}_e^E+\boldsymbol{K}_s\\ &= (\boldsymbol{A}+I)\cdot\boldsymbol{D}\cdot\boldsymbol{B}_e^E+\boldsymbol{K}_s,\end{aligned}$$

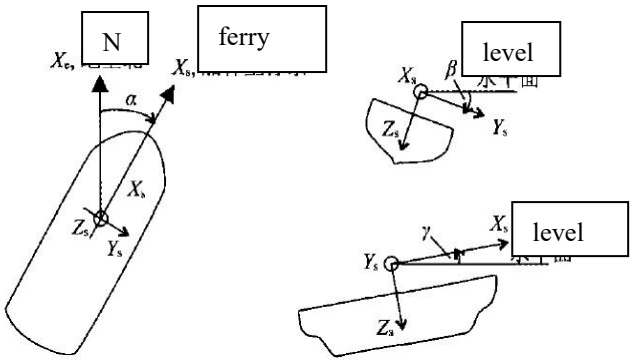

Fig.8 Definition of attitude angle of water surface

Among them, BSM is the environmental geomagnetic field [18].A is the ship magnetic induction matrix [19].Ks is the residual field.BeE is the geomagnetic field vector. I is the unit matrix.Perform a 360°rotation measurement at a known point of Be^E on the surface of the water to produce a linear equation of more than 12 observations[20].However,duringthe actual measurement of the water surface, due to the induced current generated during the movement of the water surface, it can generate an eddy current electric field opposite to the induced electric field [21].From this we can get the measured magnetic field vector is:

$$\boldsymbol{B}_s^M=\boldsymbol{A}\cdot\boldsymbol{B}_s^E+\boldsymbol{C}\cdot\frac{\partial}{\partial t}\boldsymbol{B}_s^M+\boldsymbol{B}_s^E+\boldsymbol{K}_s,$$

From this we get the total field of the magnetic field vector synthesis of the three-component magnetic survey, and the three-component magnetic field measurement [22] contains more information than the total field.

6. CONCLUSION

Based on the research on the development status of ocean geomagnetic three-component measurement at home and abroad, this paper summarizes the key technologies and development suggestions of water surface three-component measurement.And starting from the data obtained from relevant national papers, the three-component model of the instrument connected magnetic field is established, and the ridge expansion method and corrosion expansion algorithm are used to solve the data processing problem in the magnetic measurement data.From these,we get the three-component magnetic measurement data of the hull coordinate system.Corrected by the transformation matrix D of the geodetic coordinate system and the hull coordinate system,we get the magnetic field vector distribution.Finally, the local heading angle, pitch angle, roll angle and three-component total field data are displayed.From the simulation effect, the method has obvious effectiveness, and the processed data is transmitted through the data to synthesize the magnetic field vector.

However, from the results of a single data source correction, the corrected direction error is still relatively large, which indicates that the correction method has obvious sensitivity to the nature of the data source.

References

[1] Lenz J E， Rouse G F， Strandjord. A high-sensitivity magnetoresistive sensor.Solid -State Sensor and Actuator Workshop，1990，(4):114-117.

[2] TIVEY M A，JOHNSON H P． Crustal magnetization reveals subsurface structure of Juan de Fuca［J］. Gelogy，2002，30(11) : 979-982.

[3] Jorgen E E G. On the Identification of Spikes in Soundings[J]. International Hydrographic Review,1995, 72(1):33-41

[4] Herlihy D R. Filtering Erroneous Soundings from Multibeam Survey Data[J]. International Hydrog-raphic Review, 1992, 69(2):67-76

[5] Ware C. A System for Cleaning High Volume Ba-thymetry[J]. International Hydrographic Review,1992, 69(2):77-94

[6] Huang Motao,Zhai Guojun, OuyangYongzhong, etal. Robust Method for the Detection of Abnormal Data in Hydrography[J]. The International Hy-drographic Review, 1999(2):93-102

[7] Huang Motao. Marine Gravity Surveying Line Sys-tem Adjustment[J]. Journal of Geodesy, 1995(70): 158-165

[8] TIVEY M A，JOHNSON H P． Crustal magnetization re-veals subsurface structure of Juan de Fuca［J］. Gelogy,2002,30(11) : 979-982.

[9] TIVEY M A，JOHNSON H P． Crustal magnetization re-veals subsurface structure of Juan de Fuca［J］. Gelogy，2002，30(11) : 979-982.

[10] Long Dafeng，Liu Jun，Zhang Xiaoming，etal. Magnetic survey solu-tion method for flying attitude of high-speed rotating ammunition.Journal of Ballistics，2013; 25(2) : 70-75

[11] Leliak． Identification and evaluation of magnetic-field sources of mag-netic airborne detector equipped aircraft． IE Transactions on,1961;(3) : 95—105

[12] Crassidis J L， Lai K L， Harman R R.real-time attitude-independent three-axis magnetometer calibration．Measurement Science and Tech-nology，2005; 28(1) : 115—120

[13] Gebre-Egziabher D． Magnetometer auto-calibration leveraging meas-urement locus constraints． Measurement Science and Technology，2007; 23(10) : 105—115

[14] Gebre-Egziabher D， Elkaim G H， David Powell J， etal． Calibrationof strapdown magnetometers in magnetic field domain． Journal of Aer-ospace Engineering，2006; 19(2) : 87—102

[15] S Breiner． Applications manual for portable magnetomet-ers，Geometrics［M］. Inc． 1999.

[16] Mikhail Tchernychev． MAGPICK-magnetic map & profile processing User Guide ［M］． Geometrics， Inc． 2007.

[17] Geometrics， Inc． G-882 CESIUM MARINE MAGNETO-M ETE operation manual［M］. 2005.

[18] Clive A，Albert J．Passive Gravity GradiometerNavigation System ［C］． IEEE PLANS ’90: Position Location and Navigation Symposium 1990(5) : 60-66.

[19] DORVEAUX E， VISSIERE D， MARTIN A-P， etal. Iterative calibration method for inertial and magnetic sensors [C]// Pro-ceedings of the 28th Chinese Control Conference. Shanghai，China：IEEE，2009：8296-8303.

[20] NELDER J A，MEAD R. A Slmplex merhod for function mini-mi-zation [J]. Computer Journal，1965，7：308-313.

[21] Zhitian Wu, Xiaoping Hu, Meiping Wu, Hua Mu, Juliang Cao, Kaidong Zhang, Zhouhui Tuo. An Experimental Evaluation of Autonomous Underwater Vehicle Localization on Geomagnetic Map[J]. Applied Physics Letters. 2013. 103: 104102.

[22] CHEN Long-wei,ZHANG Hui,ZHENG Zhi-qiang, etal.Tech-nique of geomagnetic field continuation in underwater geomagnetic aided navigation[J]. Journal of Chinese Inertial Technology,2007,15(6):693- 697

Database of trace gas and its supporting software design for earthquake prediction

Jia Bocheng, Zhang Tao, Ye Zipeng, Chen Chen
（*College of instrumentation and electrical Engineering, Jilin University,Changchun 130012,China*）

***Abstract*—Before and during earthquakes, a variety of trace gases will escape from faults. These gases have great significance to the study of fault activities and earthquakes. In addition, by means of Microsoft. NET Framework coding model and C# language, a database query software with functions of query, addition and deletion is designed. Both of them can be used in conjunction with gas concentration data acquisition system, which can effectively improve the efficiency of earthquake researchers in studying fault gas, especially abnormal gas of earthquake precursors.**

***Key words*—Fault gases Database SQL Server .NET Framework**

I. INTRODUCTION

HOW to accurately predict earthquakes is an all-human problem. Over years, scientists all over the world have proposed various theories to try to achieve earthquake prediction. Earth deflation theory is one of them. Earth deflation theory means that before the earthquake, due to the intensification of geological tectonic activities, the rocks and the surface of the earthquake area, especially the fault area, will have slight rupture, so the trace gases such as CO2, CO, H2, CH4 are closed underground. Gases such as N2 will escape from the soil gap and escape outward, causing abnormal gas concentrations in the fault area[1].

At present, the theory of earth deflation is still in the stage of theoretical development. Researchers can monitor the trend of gas concentration change in a certain region by collecting the concentration data of the gas in the fault zone through the trace gas concentration detector or the atmospheric meteorological data detection satellite. Through this change of trend, researchers can make theoretical judgments and predictions on the future geological tectonic activities of the region. Combined with the actual geological activities, they can further develop, improve and correct the use of the Earth's gassing theory. This method of earthquake prediction.

Since earthquake precursor gas research requires a large number of gas concentration samples as data support, and most of the fault areas are in geographically remote areas with inconvenient traffic conditions, a large-scale, multi-regional study is required to establish a dedicated non-geographical location. The limited data storage system shares the collected fault gas concentration data for the first time to researchers in different regions for comprehensive analysis and comparison.

II. FUNCTIONAL DESCRIPTION

The database "Earthquake Precursor Gas Concentration Database" is established in SQL Server. Two data tables are created in the database, one primary table and one secondary table. The main table contains the main attribute information of the gas concentration data, including number, location, time, temperature, and magnitude. The sub-meter is a statistical table of gas concentration. For the time being, four gases of hydrogen, carbon monoxide, carbon dioxide and methane are used as an example. And the secondary table can only be queried with the number as the unique primary key, that is, corresponding to a number, and a single gas concentration information sub-table.

At the same time, using the .NET Framework platform and Microsoft Visual Studio software, the database's special query software is built. In addition to the basic query database function, the software also has the function of deleting corresponding entries and adding new data entries.

After the SQL Server database is linked to the network, the remote query software can access and change the data in the database directly through the network. Due to the limitations of the conditions, the function of the database is described in detail in the single-machine connection state.

III. PLATFORM INTRODUCTION

A.SQL Server database

SQL Server is a relational database management system introduced by Microsoft Corporation[2]. It has the advantages of convenient use and scalability, and high degree of integration with related software. It can run across multiple Windows operating platforms, and

can also run on different multi-processor servers. SQL Server is scalable and high-performance. The database management system designed for distributed client/server computing realizes the integration with Windows NT and provides a transaction-based enterprise information management system solution[3].

At the same time, SQL Server provides enterprise-class data management using integrated business intelligence tools[4]. The Microsoft SQL Server Database Engine provides more secure and reliable storage for relational and structured data, enabling users to build and manage highly available and high-performance data applications for the business.

In this design, we mainly use the database creation function of SQL server. The following is a brief introduction to database related knowledge:

The database, in a nutshell, can be viewed as an electronic file cabinet—where the electronic file is stored, the user can run operations such as adding, intercepting, updating, and deleting data in the file. The so-called "database" is a collection of data that is stored together in a certain way, can be shared by multiple users, has as little redundancy as possible, and is independent of the application[5].

The database engine is the core service for storing, processing, and protecting data[5]. The database engine controls access and processes transactions quickly to meet the needs of applications that are extremely demanding and need to process large amounts of data[6].

Use the database engine to create a relational database for online transaction processing or online analytical processing of data. This includes creating tables for storing data and database objects (such as indexes, views, and stored procedures) for viewing, managing, and securing data. You can use SQL Server Management Studio to manage database objects and SQL Server Profiler to capture server events.

The database management system is a DBMS (Database Management System), which is a computer software system specially designed for managing databases. It generally has basic functions such as storage, interception, security, and backup[2]. The database management system can be classified according to the database model it supports, such as relational, XML; or classified according to the type of computer supported, such as server cluster, mobile phone; or classified according to the query language used, such as SQL , XQuery; or classification based on performance impulses, such as maximum size, maximum operating speed, and so on.

B.NET Framework coding model

The .NET Framework, dubbed the Microsoft .NET Framework, is a new managed code programming model for Windows[7]. It combines powerful cross-platform capabilities with new coding technologies to build applications with a visually compelling user experience, seamless communication across technology boundaries[8], and support for a variety of business processes.

The purpose of the .NET Framework is to make the creation of Web Services and Internet applications simple. The .NET Framework includes three major parts: The first part is the Common Language Runtime (CLR, the common execution period of all .NET programming languages)[9]. Component), the second part is the shared object class library (providing all the basic objects required by the .NET programming language), and the third part is the various components[7].

The .NET Framework has two main components: the common language runtime and the .NET Framework class library. The common language runtime is the foundation of the .NET Framework. The runtime can be thought of as a proxy that manages code at execution time, providing core services such as memory management, thread management, and remoting, and enforces strict type safety and other forms of code that improve security and reliability. accuracy. In fact, the concept of code management is the basic principle of the runtime. Code that targets the runtime is called managed code, and code that does not target the runtime is called unmanaged code[10]. Another major component of the .NET Framework is the class library, a comprehensive collection of object-oriented reusable types that you can use to develop a variety of applications, including traditional command-line or graphical user interfaces (GUIs).) Applications[11], including applications based on the latest innovations available (such as Web Forms and XML Web services)[9].

The existence of a graphical user interface, coupled with the use of the C# language[12], can greatly enhance the efficiency of our programming.

IV. TECHNICAL METHOD

A.Database establishment

First, open the SQL Server software, configure the database engine in the pop-up dialog box, enter the correct login name and password, and connect to the database.

Then create a new database and create a new query in the database. Within the query we can formally enter

data and build a database. First create the main table, you need to enter the local element number, time, location, temperature, magnitude five items, of which the number is the primary key. Enter the following statement in the newly created query page:

```
Create Table BasicInformation
(
  编号 Varchar(20) Primary key,
  地点 varchar(50) Not Null,
  时间 Varchar(50) Not Null,
  温度 Varchar (60) ,Not Null,
  震级 Varchar (50),Not Null
)
GO
```

Where BasicInformation is the name of the created data table; number, location, etc. are the element items entered; Varchar(20) is the type and length of the element, Primary Key is the primary key; Not Null means the item cannot be empty. After executing the above code, the master data table is created.

Similarly, continue to create the data table AirConcentration, it is worth noting that because the sub-table and the main table are encoded by a unique link, so special statement, the code is as follows:

```
Create Table AirConcentration
(
  编号 Varchar(20)References BasicInformation(编号),
  H2_ppm numeric(16,1) Not Null,
  CO_ppm numeric(16,1) Not Null,
  CO2_ppm numeric(16,1) Not Null,
  CH4_ppm numeric(16,1) Not Null,
)
GO
```

In this way, the primary and secondary data tables are created, and then you can insert data directly into the table. The code is as follows:

```
Insert Into BasicInformation Values('0001','海原断裂带','181205','20','0')
Insert Into AirConcentration Values ('0001',60,300,890,90)
```

B.Query software function implementation

This part of the work is all done in the .NET Framework software with a graphical user interface and C# language programming. To save space, only the key parts of the .NET Framework design are presented here.

First, establish the basic framework of the system in the Solution Explorer of the .NET Framework, as shown in Figure 1.

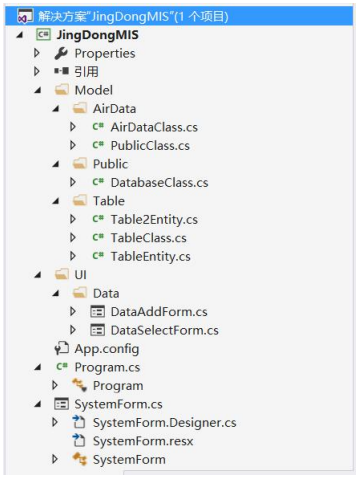

Fig.1 Basic Frame Diagram

Among them, the Model contains the basic part of the system, that is, the connection with the database, query, add and so on. The UI contains the basic human-computer interaction interface, which is the graphical interface of the software. Program.cs is the basic code for the main program. SystemForm.cs is the main page of the created system.

Then create the system main page, add the operation menu in the main page, click the "Operation" menu, the system will automatically pop up two sub-function buttons, namely "Add" and "Query". According to the functional analysis, the "Add" key is to add the new gas data along with its attributes to the existing database, and the "Query" key is to read the latest data in the database in real time.

After creating these two keys, you need to create their corresponding sub-function menus. According to the requirements analysis, in the "Add" page, we need to enter the details of the item data and enter it into the system. In the "Query" page, we need to create two display windows to display the attribute information in the data master table and the density information in the child table. In addition, the “Delete” item should be designed on this page to delete unnecessary information in the database. The encoding of the above functions can be done by using the create event function.

After the main interface is created, you need to connect the SQL Server database with the .NET Framework. Create a Public folder under the Model folder in the Solution Explorer, and create a new project in it. The project category is Class and named DataBaseClass.cs. Create a connection service in the DataBaseClass.cs file, where the key statement "string sConnect = "Server=.;database=SD;user id=sa;password=";" indicates that the connection is native, the database name is SD, the database use

The user ID is sa and the password is blank. In this way, the database tables BasicInformation and

AirConcentration we created before were successfully connected to the .NET Framework.

V. ACHIEVEMENT DISPLAY

The database establishment result established in SQL Server is shown in Figure 2 below.

结果 消息

	编号	地点	时间	温度	震级
1	0001	海原断裂带	181205	20	0
2	0002	海原断裂带	181215	22	0
3	1001	郯庐断裂带	181205	18	3
4	1005	郯庐断裂带	181215	10	5
5	1006	郯庐断裂带	181225	8	7.2
6	3033	环太平洋断裂带	190103	3	3.5

	编号	H2_ppm	CO_ppm	CO2_ppm	CH4_ppm
1	0001	60.0	300.0	890.0	90.0
2	0002	80.0	705.0	780.0	250.0
3	1001	550.0	755.0	705.0	80.0
4	1005	90.0	95.0	85.0	280.0
5	1006	905.0	250.0	2500.0	850.0
6	3033	690.0	690.0	3000.0	1500.0

Fig.2 Results of database establishment

The main interface of the query software is shown in Figure 3 below.

Fig.3 Home Interface of Query Software

The query function runs as shown in Figure 4 below.

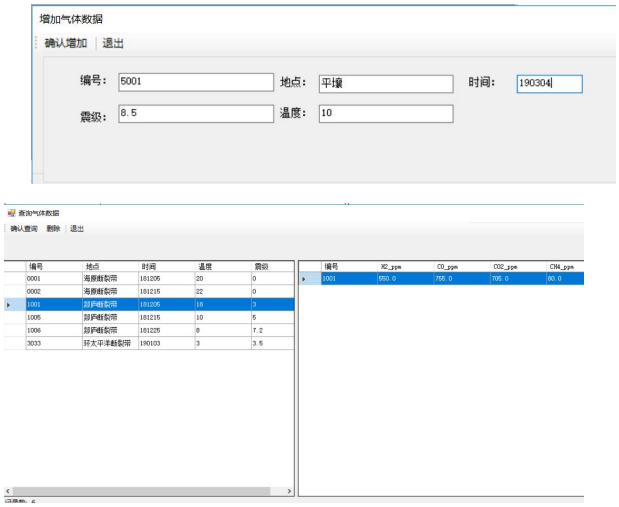

Fig.4 Query function

Add the interface as shown in Figure 5 below.

Fig.5 Interface of adding

After the addition is successful, the system will automatically pop up the following prompt window as shown in Figure 6.

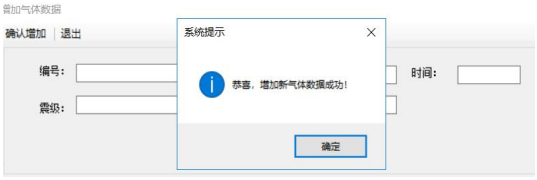

Fig.6 Bullet window of successful adding

VI. CONCLUSION AND OUTLOOK

The establishment of the earthquake precursor gas concentration database was successfully realized by using the SQL Server database software and the .NET Framework programming platform, and basic operational functions such as query, addition, and deletion were added. By networking the database, multi-user remote access and database changes will undoubtedly greatly improve the efficiency of earthquake researchers.

Due to the general ability and limited time, the current database and query software are still relatively basic. In the future, if we continue the research on this topic, there is still much room for improvement in the database content. For example, how to make the database more abundant, so that it can save more comprehensive earthquake precursor gas data. Secondly, the realization of database network preservation is also a very practical development direction. Keeping the database in the webpage allows ordinary netizens to have the right to access data and realize real data sharing.

References

[1] Qian Zuji, Kong Lingchang, Wang Yiping, Li Qiuzhen, et al. Earth deflation, thermal infrared anomalies and seismic activities [J]. Chinese Science Bulletin, 1992(24): 2259-2262.

[2] Ma Ri. Discussion on the application skills of SQL Server database [J]. Science and Technology Outlook, 2016, 26 (03): 13-14.

[3] Network Database SQL Server 2012 Tutorial [M]. People's Posts and Telecommunications Press, Ding Li, 2015

[4] Zhou Wanghong. SQL Server 2012 database T-SQL query method and instance analysis [J]. Information and Computer (theoretical version), 2018 (24): 144-145.

[5] Sun Wei.Analysis of Key Technologies of SQL Server

Database Application[J].Shandong Industrial Technology,2014(24):158.

[6] Dong Jianhua. Research on Performance Optimization Technology of SQL Server Database[J].Science and Technology Plaza,2007(05):93-94.

[7] Zhang Binwei, Zhang Gaojing, Wang Yuhui. Analysis of Software Development Model under the Net Framework[J]. Computer Products and Circulation, 2018(12): 17.

[8] Zhang Jie..NET architecture system and development research [J]. Electronic Test, 2017 (18): 52-53. Research on performance optimization of database application system based on SQL Server [J]. Wang Xuehui. Electronic Science and Technology. 2015(01)

[9] Wei Guoli,Zhang Chenggang.Design and Implementation of Online Examination Management System Based on ASP.NET Framework[J].Information and Computer (Theoretical Edition),2017(23):121-122+125.

[10] Wang Liming.Design and Implementation of Website Content Management System Based on .NET Framework[J].Computer Knowledge and Technology,2016,12(09):125-126.

[11] Wang Jie. Software development model under the net framework [J]. Electronic Technology and Software Engineering, 2017 (03): 57.

[12] Huang Zhiliang,Chen Huifen,He Dongmei.Discussion on the Teaching of SQLSERVER Database Technology Based on C#[J].Computer Knowledge and Technology,2013,9(10):2296-2297.

Design of trace gas detector for earthquake prediction

Jia Bocheng, Zhang Tao, Ye Zipeng, Chen Chen
（*College of instrumentation and electrical Engineering, Jilin University,Changchun 130012,China*）

***Abstract*—Carbon dioxide, carbon monoxide and hydrogen are taken three as measuring gases, a trace gas detector with low detection limit is designed, which can be used to detect abnormal concentration data of gas escaped from fault activities. In order to provide a new idea of high cost-effective for seismic precursor gas and fault gas acquisition, and provide powerful data support for seismic research. The trace gas detector is analyzed and introduced from three aspects: sensor, hardware design and software design.**

***Key words*—Earthquake prediction Fault gases Trace gas detection**

I. INTRODUCTION

EARTHQUAKE is a natural phenomenon in which the earth's crust releases energy quickly and causes severe vibrations and releases seismic waves. For thousands of years, the earthquake has caused immeasurable losses and damage to human civilization and wealth. How to achieve earthquake prediction and make a early warning is the final destination of many scientists' academic path around the world. This design exactly came into being under this background.

II . INTRODUCTION TO THE THEORY OF EARTH DEFLATION

Before the earthquake, a certain degree of fault geology activities are often accompanied. During the fault movement, a variety of trace gases are often escaped from the fault. This is the phenomenon of crust exhausting[1]. On the mainland, crust venting is common on fault zones, especially on active deep fault zones. This gas associated with fault activity that is emitted from the fault is called fault gas. It includes the aerosol formed from the fault to the upper soil and the spring water distributed along the fault, various escape gases in the groundwater, dissolved gas and so on[2]. As an important means of capturing earthquake precursors, fault gas monitoring can play an important role in short-term earthquake prediction. The theoretical basis behind it is the theory of earth deflation.

The theory was first proposed by former Soviet scholars[2]. By analyzing the anomalous distribution of satellite infrared gas before the earthquake, they found that due to the intensified tectonic activity before the earthquake, the rupture of the rock and surface in the area was opened[3], making the underground closed gas Gases such as H2, CO, CO2, CH4, Rn, N2, O3[3] escape the ground along the fracture channel. In the fault zone, there are many micro-cracks, which are the best channels for gas to diffuse from the depths of the earth to the surface, and are also the places where deep source gases are enriched[4]. Before the earthquake, due to the huge energy accumulates in the rock, new fissure channels are created in the fault area, so that the gas deep in the fissure and the gas originally enrichs in the fissure quickly spread to the surface, and their flow rate and mixing ratio changes a lot[5]. Before most of the strong earthquakes, the concentrations of H2, He, CH4, N2, Ar, CO2, Rn, CO, O3 and other gases have changed significantly (as shown in Table 1[3]), and their concentrations are abnormal. It usually lasts for a few days. This phenomenon is known as the theory of earth deflation. In 1998, the results of the fault gas exploration conducted by Ciotoli in the Fusina Basin, Italy, showed that the anomaly peaks of He, CH4 and CO2 were synchronously displayed in the fault zone with a magnitude 7.0 earthquake in 1915[6]. In 1976, before the Tangshan M7.8 earthquake, an abnormal increase in the total amount of carbon dioxide was observed in the Tianjin Mian No.4 well. After the earthquake, CO2 and H2 were detected on the seismogenic fault, and the line was laid in Zhengjia, south of Tangshan City. Both Zhuanghe and Lishangzhuang crossed the earthquake rupture zone. The results show that both CO2 and H2 show high-value anomalies in the cross-fault sections of the survey line[2].

After extensive data review, in order to ensure the wide application of this design, we choose carbon monoxide, carbon dioxide and hydrogen as the three measured gases.

TABLE 1 Range and average values of soil gas in Haiyuan Fault

Component (unit)	Xiao Kou		Ba Zhiyao		Cai Xiangbao		Xiao Nanchuan	
	range	mean	range	mean	range	mean	range	mean
He(ppm)	- ~ 65.3	-	~17	-	- ~ 49.8	-	- ~21.7	-
H_2(ppm)	- ~ 77.3	-	~99.1	-	- ~369.7	-	- ~35	-
CH_4(ppm)	- ~ 537.7	-	-	-	-	-	-	-
N_2/O_2(v/v)	3.8~16.1	5.5	3.8 ~ 4.6	4.0	3.9 ~ 7.7	4.4	3.3 ~ 4.3	3.9
Hg(ng/m^3)	4 ~ 28	19.4	3 ~ 107	32.7	5 ~ 215	87.1	3 ~ 245	60.5
Rn(kBq/m^3)	2.5~30.3	10.6	1 ~ 12.9	3.7	1.3~38.3	5.6	2.2~12.9	5.9

Note "-"means below the test line

III SENSOR DESIGN

In the sensor design part, our main job is to select the corresponding sensor with good measurement performance and high cost performance according to the characteristics of the gas we measured, and familiar with the principle, laying a good foundation for the design of the whole system.

By studying the historical fault gas data, it is found that the fault escape gas has a very low concentration, and the abnormal concentration is mostly in the range of several tens of ppm (parts per million) to several hundred ppm. Therefore, the sensors used in this design must have a low detection limit. Under these conditions, after considering the cost of design and the stability and achievability, we chose electrolyte hydrogen and carbon monoxide sensors and infrared carbon dioxide sensors.

The final choice in this design is the T6615 infrared carbon dioxide sensor from GE. It uses infrared method to measure the carbon dioxide content in the air. It has good selectivity, high sensitivity, strong anti-interference ability, and can obtain relatively reliable gas concentration data in a chaotic gas environment[7]. And compared to other gas sensors, infrared gas sensors have the unique advantage of long working life.

Carbon dioxide and hydrogen We have chosen electrolyte sensors, the H2-4G hydrogen sensor from Golden Science and the CO Sensor Micro+/3 carbon monoxide sensor from Solidense. The electrolyte sensor uses a chemical reaction between the measured gas and the internal components of the sensor to achieve measurement, and the final output value is proportional to the measured gas concentration. The electrolyte type sensor also has high selectivity and stability, and it also has a very high cost performance, which is very suitable for our experimental research.

IV HARDWARE DESIGN

The main hardware structure of the gas detector is shown in Figure 1. It consists of five parts: sensor, conditioning circuit, single-chip microcomputer, displaying, and data transmission. Here, the three-electrode sensor driving circuit and the sensor output amplifying circuit are mainly described in detail.

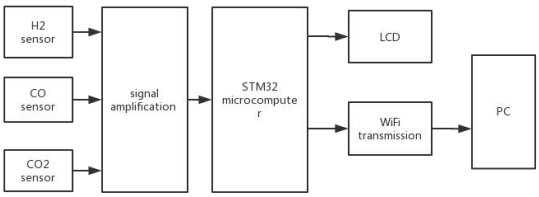

Fig.1 Overall framework sketch

A. Three-electrode sensor drive circuit

Since the electrolyte sensors we have chosen are all three-electrode sensors, there is one point that needs special attention when using them. That is the design of the potentiostat drive circuit.

The three electrodes of the three-electrode sensor are a electrode, a working electrode and a reference electrode[8], as shown in Figure 2 below. Among the three sensor electrodes of the three-electrode sensor, only a chemical reaction occurs between the working electrode and the counter electrode. When the gas concentration is continuously increased, the corresponding induced current will cause a change in the electromotive force on the counter electrode,and this is polarization. When the gas concentration increases continuously, the working electrode electromotive force will exceed its linear allowable range, and the output signal and the gas concentration become nonlinear, which leads to inaccurate measurement data of high concentration gas and loss of reference significance of the data. Therefore, in the measurement process, a new stable voltage needs to be connected outside the circuit to stabilize the electromotive force between the working electrode and the reference electrode, and to ensure that the reference electrode does not have a current flowing, and also ensures the stability of the reference electrode voltage, thus The accuracy of the working electrode data test can be guaranteed[9]. At the same time, the addition of the reference voltage can also provide a bias voltage for the sensor, which can increase the activity of a part of the inactive reactive gas, which greatly promotes the redox reaction and provides a wider measurement range for the sensor[10].

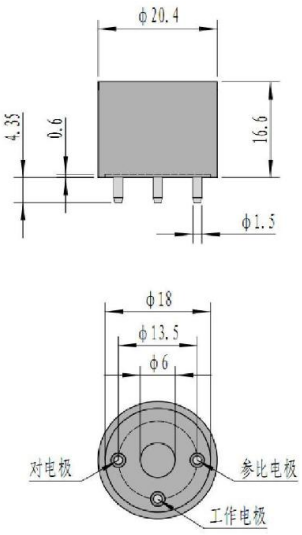

Fig.2 Schematic diagram of three-electrode sensor

To stabilize the electromotive force between the reference electrode and the working electrode as well as making no current flow through the reference electrode, the simplest method is to use a potentiostat consisting of an operational amplifier, as shown in Figure 3. The working electrode is grounded in the figure to prevent interference from spurious signals, thereby improving the stability and accuracy of current and voltage in the circuit. Thus, the constant potential becomes a constant value for ensuring that no current flows through the reference electrode. The reference potential is applied to the inverting terminal of the control amplifier, and the control voltage is applied as a reference voltage at the non-inverting input terminal, and the output terminal of the control amplifier is connected to the reference electrode to form a negative feedback regulation system.

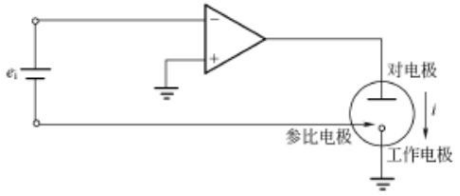

Fig.3 Schematic diagram of Potentiostat

B.Amplifying circuit

Since the measured abnormal gas concentration is on the order of a very small ppm scale, correspondingly, the output signal produced by the gas sensor is also a very weak electrical signal. Therefore, it is necessary to design a suitable amplifying circuit to amplify it.

Most of the errors in the amplifying circuit are introduced by the first-stage amplifying circuit. Therefore, if the amplifying circuit is to be reliable and stable, and the smaller error is required, the most important one is the design of the first-stage amplifying circuit. This design uses the precision operational amplifier ICL7650 to achieve the higher requirements of the first-stage amplifier circuit for error control.

The ICL7650 is a chopper-stabilized high-precision op amp made by Intersil using dynamic zero calibration technology and CMOS technology. It has low input bias current, small offset, high gain, strong common-mode rejection, fast response, and low drift. Stable performance and low price.

Secondly, the single-stage amplifying circuit is almost impossible to complete the high-magnification amplification requirement. Therefore, in order to ensure the accuracy of the circuit and reduce the distortion, the design uses a two-stage amplifying circuit to amplify the sensor electrical signal. Taking the hydrogen sensor amplifying circuit as an example, the first-stage reverse amplification is set to 2000 times, and the second-stage reverse amplification is set to 1.5 times.

The final amplifier circuit circuit diagram is shown in Figure 4 below.

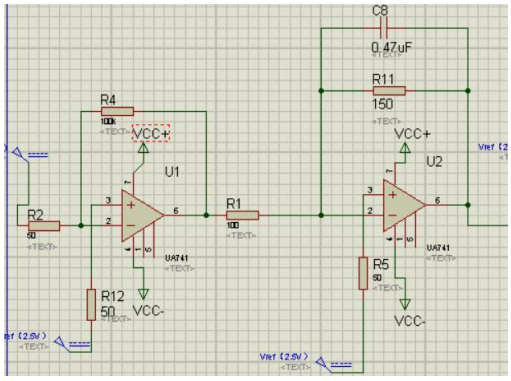

Fig.4 Schematic diagram of amplifier circuit

V SOFTWARE DESIGN

The STM32f103 family of microcontrollers has three ADCs with 12 bits of precision and up to 16 external channels per ADC[11]. Among them, ADC1 and ADC2 have 16 external channels. ADC3 has different channels according to different CPU pins. Generally, there are 8 external channels. The ADC has many modes and powerful functions, which is suitable for the multi-channel acquisition requirements of this solution. The system software is designed using a modular programming method, and the system software is written in C language. The software program includes: a system initialization module, a signal acquisition processing module, a human-computer interaction module, and a wireless transmission module. As shown in Figure 5 below.

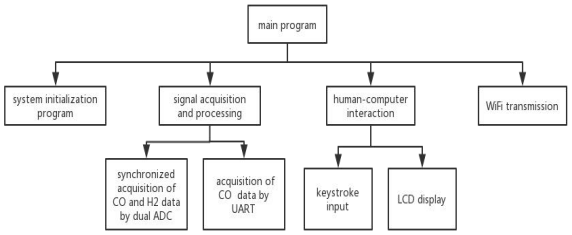

Fig.5 Software overall architecture diagram

A.ADC conversion

According to the requirements of the project, it is necessary to collect three analog signal data. Therefore, the STM32f103 independent mode multi-channel acquisition method can be used. It should be noted that the I/O ports used for ADC input cannot be multiplexed, otherwise the collected signals will be inaccurate[12].

Independent mode multi-channel acquisition programming points: (1) Initialize the GPIO of the ADC; (2) Initialize the ADC operating parameters; (3) Configure the DMA operating parameters; (4) Read the data collected by the ADC. Part of the procedure is shown in Figure 6.

```
void ADC_VAL(void)
{

      ADC_ConvertedValueLocal[0] =(float) After_filter[0]/4096*3.3;
      ADC_ConvertedValueLocal[1] =(float) After_filter[1]/4096*3.3;
      ADC_ConvertedValueLocal[2] =(float) After_filter[2]/4096*3.3;


      printf("\r\n CH0 value = %7.5f V \r\n",ADC_ConvertedValueLocal[0]);
      printf("\r\n CH1 value = %7.5f V \r\n",ADC_ConvertedValueLocal[1]);
      printf("\r\n CH2 value = %7.5f V \r\n",ADC_ConvertedValueLocal[2]);

      printf("\r\n\r\n");

}
/**
  * @brief  ADC初始化
  * @param  无
  * @retval 无
  */
void ADCx_Init(void)
{
  ADCx_GPIO_Config();
  ADCx_Mode_Config();
  DMA_NVIC_Configuration();
}
```

Fig.6 ADC Conversion Program

B.Digital filtering

The STM32 contains a 12-bit ADC internally, which takes up to 1 microsecond to detect one AD at a time. In order to prevent the peripheral circuit from occasionally disturbing the AD sampling, it is necessary to filter the collected data[13]. There are many kinds of software filtering algorithms, such as: limiting filtering method, median average filtering method, weighted recursive average filtering method, and so on. Considering that the collected data changes slowly in a short time, the median average filtering method is finally selected. A maximum value and a minimum value are removed from the collected N data, and then the remaining data is averaged. Part of the procedure is shown in Figure 7.

```
#include "filter.h"

uint16_t After_filter[3] = {0,0,0};

void filter(void)
{
   uint16_t max,min = 0;
   uint32_t sum = 0;
   u8 count,i;

   for(i=0;i<3;i++)
    {
      for ( count=0;count<N;count++)
      {
          min=max= ADC_ConvertedValue[0][i];
          sum += ADC_ConvertedValue[count][i];
              if(ADC_ConvertedValue[count][i]>max)
                  {
                    max = ADC_ConvertedValue[count][i];//一个循环之后max就是最大的值
                  }
              if(ADC_ConvertedValue[count][i]<min)
                  {
                    min = ADC_ConvertedValue[count][i];//一个循环之后min就是最小的值
                  }
      }
      After_filter[i]=(sum-max-min)/(N-2);
      sum=0;
    }
```

Fig.7 Filter program

C.Wi-Fi transmission

The ESP8266 Wi-Fi module is required to wirelessly transfer data to the computer. The main functions that the ESP8266 module can implement include: serial port transparent transmission, PWM regulation, and GPIO control. The ESP8266 module supports three working modes: STA/AP/STA+AP. According to the requirements of the project, you can configure the ESP8266 for STA mode and access the LAN and computer for data communication. The transparent transmission mode can be adopted in the case of point-to-point transmission. Part of the procedure is shown in Figure 8.

```
#include "filter.h"

uint16_t After_filter[3] = {0,0,0};

void filter(void)
{
   uint16_t max,min = 0;
   uint32_t sum = 0;
   u8 count,i;

   for(i=0;i<3;i++)
    {
      for ( count=0;count<N;count++)
      {
          min=max= ADC_ConvertedValue[0][i];
          sum += ADC_ConvertedValue[count][i];
              if(ADC_ConvertedValue[count][i]>max)
                  {
                    max = ADC_ConvertedValue[count][i];//一个循环之后max就是最大的值
                  }
              if(ADC_ConvertedValue[count][i]<min)
                  {
                    min = ADC_ConvertedValue[count][i];//一个循环之后min就是最小的值
                  }
      }
      After_filter[i]=(sum-max-min)/(N-2);
      sum=0;
    }
```

Fig.8 Wi-Fi program

D.Virtual instrument design

The gas concentration data detected by the trace gas detector will eventually be transmitted to the host computer. Therefore, we need to design a human-computer interaction virtual interface on the host computer. We chose to use LabVIEW software to achieve this function.

LabVIEW (Laboratory Virtual Instrument Engineering Workbench) is a program development environment developed by National Instruments (NI), similar to the C and BASIC development environment. LabVIEW uses a graphical editing language G to write programs. The resulting program is in the form of a block diagram. It is a graphical programming language for creating applications using icons instead of text lines. LabVIEW provides a number of controls that look like traditional instruments (such as oscilloscopes, multimeters) and can be used to easily create user

interfaces.

The final design of the LabVIEW front panel is shown in Figure 9. The gas concentration waveform can be displayed in real time, the gas concentration data is recorded, and the measurement and sampling parameters are set.

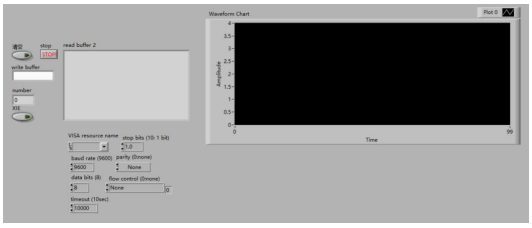

Fig.9 PC interface

V CONCLUSION

This design uses hydrogen, carbon monoxide two electrolyte gas sensors and carbon dioxide infrared gas sensor, using potentiostat technology, with suitable sensor drive circuit, combined with signal conditioning circuit, Wi-Fi transmission technology and LabVIEW virtual instrument interface design, Comprehensive trace gas detection provides a new design idea. The system can provide reference for the study of earthquake precursors and fault activities, and can also be applied to households, greenhouse gas detection and other fields. The final actual measurement results are shown in Figure 10 below.

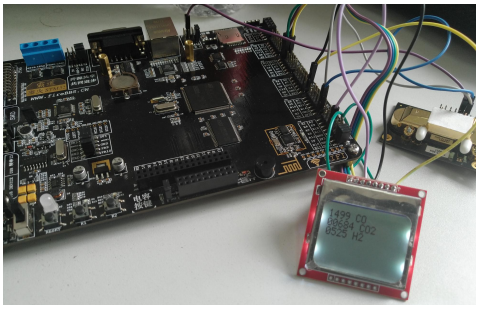

Fig.10 Measurement results

References

[1] Qian Zuji, Kong Lingchang, Wang Yiping, Li Qiuzhen, et al. Earth deflation, thermal infrared anomalies and seismic activities [J]. Chinese Science Bulletin, 1992(24): 2259-2262.

[2] Zhu Xu,Wang Yingying,Zhang Yu.Infrared sensor for fault gas measurement[J].Journal of Geodesy and Geodynamics,2011,31(05):156-159.

[3] Zhou Xiaocheng, Wang Chuanyuan, et al.Soil gas geochemical characteristics of the southeastern segment of the Haiyuan fault zone[J].Seismology and Geology,2011,33(01):123-132 .

[4] Cui Yueju, Du Jianguo, Li Ying, Guo Qiu Na. Detection of atmospheric CH_4 and CO anomalies associated with 2008 Wenchuan M_S8.0 and 2013 Lushan M_S7.0 earthquakes[J]. Bulletin of Mineralogy, Geochemistry, 2016, 35(05): 1022-1027.

[5] Zhou Xiaoling.Ozone released by rock fracture can be used for earthquake prediction[J].Recent Developments in World Seismology,2012(01):7.

[6] Fan Xuefang,Li Zihong,Zhang Lei.Characteristics of trace hydrogen in soil before earthquake[J].Recent Developments in World Seismology,2015(09):147.

[7] Liu Junfeng,Chen Yusong,Wang Aimin,Gu Haoshuang,Liu Huarong.Research Progress of Hydrogen Sensors[J].Transducer and Microsystem,2009,28(08):8-11.

[8] Wang Shuzhen, Shan Wei, Song Lingling. Principle and Application of AD620 Instrument Amplifier[J].Microprocessor,2008(04):38-40.

[9] Zheng Longjiang, Li Peng, Qin Ruifeng, Yang Junming. Research Status and Development Trend of Gas Concentration Detection Optical Technology[J].Laser & Optoelectronics Progress,2008(08):24-32.

[10] Wang Cuicui,Zhou Zhen,Qin Yong,Zhang Hongyu.Study on the Potentiostat Circuit of Current Electrochemical Sensor[J].Transducer World,2009,15(02):36-39.

[11] Wang Dalei, He Kang, Wang Nan, Wang Long, Jiang Liyong.Design of Intelligent Gas Detection and Early Warning System Based on STM32 and GSM[J].Journal of Zaozhuang University,2018,35(05):47-52.

[12] Zhou Yanju. Design and research of portable multi-gas detector for cold storage [D]. Shandong Agricultural University, 2017.

[13] Cai Liyuan. Design of gas analyzer based on STM32 single chip microcomputer [D]. Xi'an University of Technology, 2016.

THE DESIGN OF VIRTUAL AND PHYSICAL ANALOG CIRCUIT LAB PLATFORM BASED ON LABVIEW AND ARM

Zhou Zhijian, Yan Peirong, Feng Xue, Liu Zhengkai
(College of instrumentation and Electrical Engineering , Jilin University ,Changchun 130000,China)

Abstract—In this study, LabVIEW and Multisim are combined to simulate and communicate with the slave computer to adjust experimental parameters. The result of the experiment shown together meet requirements of the design.The experimental platform includes two parts: virtual computer simulation and physical experiment platform. The test results show that the platform can run stably in real time anywhere, shorten the experimental time effectively, improve the experimental efficiency. The experiment is no longer confined to physical conditions such as laboratory requirements, and has a strong teaching significance.

Key words—Analog electronic technology;Virtual and actual combination;LabVIEW

0. INTRODUCTION

AT present, the experimental mode of analog electronic circuits in colleges and universities is based on hardware experiments and virtual software experiments[1].The hardware experiment based on the actual hardware circuit has the advantages of intuitive experimental results. However, the experimental results between different hardware circuits used in the same experiment often have large gaps, so it is difficult to draw experimental conclusions[2].The virtual simulation experiment mode has the advantage of avoiding repeated experiments by students and reducing the experimental overhead [3-5], but the simulation experiment has poor real-time performance.Students can't understand the difference between the basic theory and the practice of electronic technology[6].

In order to provide a more convenient and flexible experimental environment for students and teachers, this paper designed an analog circuit experiment platform based on LabVIEW, which combines the virtual simulation and the physical circuit.Users can reach the meaning of experimental teaching.

1. OVERALL DESIGN

The experimental platform is mainly based on six analog circuit experiments: single stage amplifier, multistage amplifier, negative feedback amplifier, differential amplifier, power amplifier and RC sinusoidal oscillator. LabVIEW and Multisim are combined to simulate and communicate with the slave computer to adjust experimental parameters. When using this experimental platform, firstly, the experimental circuit diagram drawn by Multisim is called by LabVIEW, and the virtual circuit simulation experiment can be performed. Then, the actual physical circuit experiment is completed by operating the actual hardware experiment circuit on the software host computer control platform. The results of the actual hardware experiment and the virtual simulation display together in the LabVIEW, so that the user can compare the experimental results of the two experimental modes.

2. HARDWARE DESIGN

According to the design idea,the experiment box not only need to provide the same experimental content as the experiment in Multisim but also meets the requirements that the user can change the key parameters,circuit structures through the PC.

In summary, the hardware of the entire experimental box is divided into two parts: 1 six analog circuit boards; 2 controllers. In addition, the experimental box itself is designed with its own adjustable signal source and power interface.

2.1 Modular experiment circuit design

There are two main functions that need to be completed in the experimental circuit board in this design:the adjustment of the key parameter and the change of the partial circuit structure.

The main idea of the adjustment is replacing the key resistances in the original circuit with a digital potentiometer to change the key parameters of the circuit.Take the design of a single stage amplifier as an example: only a suitable static working point can be set to ensure that the signal is not distorted.

As shown in Figure 1, U1 is designed as an adjustable digital potentiometer in the circuit. By adjusting the base

resistance, the bias voltage of the amplifier circuit is changed to change the static operating point of the circuit.

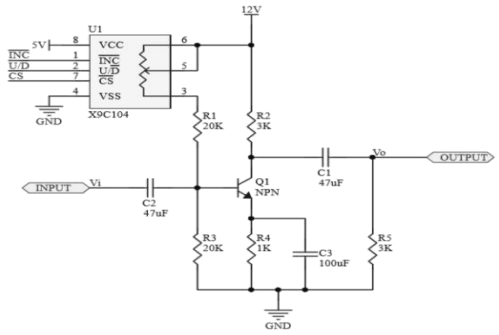

Figure 1 single stage amplifier (U1 is a digital potentiometer)

The change in circuit structure is mainly achieved by relays. Taking the design of the negative feedback amplifier as an example,in this design we add a feedback loop composed of R13 and C6 in Figure 2. The feedback loop is passed or not through the relay RELAY1.

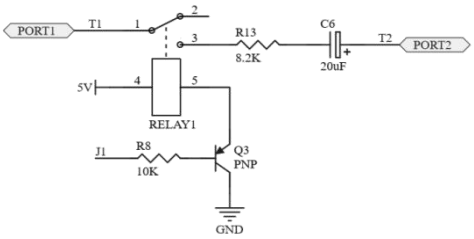

Figure 2 The principle of the relay

2.2 The design of the modular test box

In this design, the bottom plate of the experiment box mainly includes:①STM32 controller;②circuit's interfaces; ③power supply. ARM ,its peripheral circuits, adjustable signal source and power interface are designed on the same circuit board as the bottom plate of the experiment box. The interface is pulled out on the backplane. It is the interface required by the controller to perform the function and is connected to the board. One-to-one correspondence with the interfaces on the six independent test boards.The power interface is provided on the bottom of the box. To simplify the design of the experimental box, the +12V, +5V power supply required for this design is directly provided by the switching power supply.

3.THE DESIGN OF SOFTWARE

The software of the system mainly includes the design of the upper computer based on LabVIEW and Multisim and the design of the lower computer based on STM32.

3.1 Serial communication

The communication between the controller and the upper computer is master-slave.The upper computer is the main, and the controller is slave. The upper computer sends an instructions that command the controller to perform corresponding operations. The format of the instruction is as follows: “SxxxE” is the instruction name. S is the start bit, E is the end bit, and the middle is the current instruction. For example, “SdianluE”indicates that the upper computer will send three bytes of data to indicate the circuit mode, potentiometer value, and relay switch state that you want to use. The first byte represents the mode, and the circuits from 1 to 6 represent the experiments: single amplifier, multistage amplifier, negative feedback amplifier, differential amplifier, power amplifier circuit, RC sine wave oscillator . In addition, depending on the content of the instructions, the transmission of experimental data of a specific length between the host computer and the micro controller is realized. For example, the “Scome_onE” instruction means that the host computer need the micro controller to send waveform data of length 400 bytes for waveform.The transfer instructions is shown in Table 1.

Table 1 The format of instruction

Byte	1	2	3
SdianluE	the model of the circuit	potentiometer resistance	relay’s state
Scome_onE	the length of the date		
ScaiyangE	frequency		

3.2 The design of the host computer

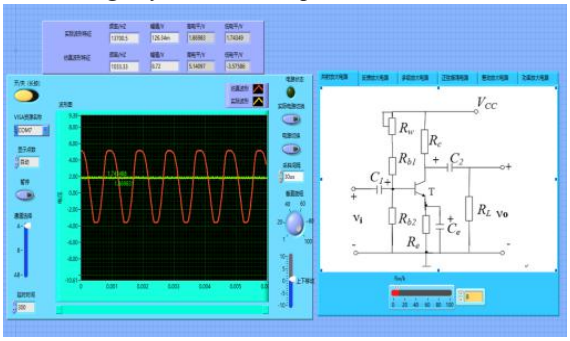

Figure 3 the host computer's interface

The host computer is realized by LabVIEW and Multisim co-simulation technology[7]. The host computer interface is shown in Figure 3. Taking the single stage amplifier circuit module as an example, the LabVIEW interactive interface HB/SC is added to the circuit in Multisim, and the data is sent and received by the LabVIEW simulation engine to realize the simulation.

In Figure 4, the resistor R1 is the voltage-controlled resistor, and the resistance value can be adjusted by adjusting the corresponding input voltage; the HB/SC interface IO1 is the voltage input terminal of the voltage-controlled resistor.It is connected to the numerical input in LabVIEW[8-9]. IO2 is the interface of output signal.

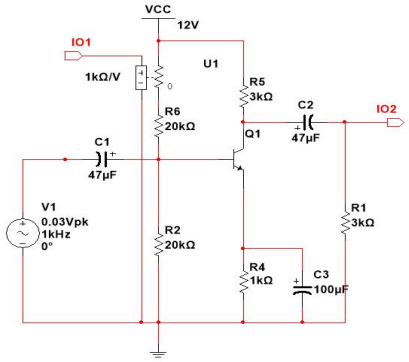

Figure 4 Multisim simulation's diagram

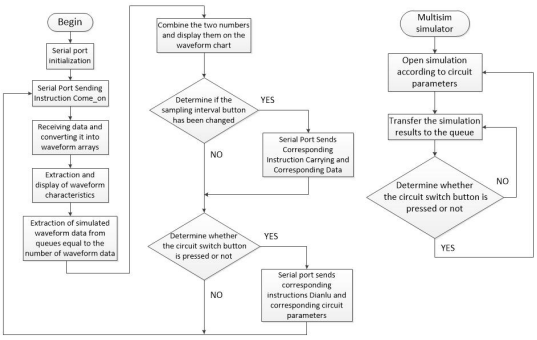

(a) (b)

Figure 5 The flow chart for the host compute

The flow chart is shown in Figure 5, and Figure (a) is the LabVIEW overall flow chart. Figure (b) is a flow chart for obtaining a simulation waveform from the Multisim simulator, in which the sample interval button and the circuit switching button determine the content of the command sent to the STM32 lower computer. During the experiment, the resistance value of the resistor R1 in the simulation circuit is adjusted.The command which inludes parameter's value and the corresponding circuit module selection is transmitted to the base controller through the serial port.In the meantime,it can control the change of the parameters and the circuit in the experimental platform.In addition, the waveform data obtained by the physical circuit simulation is obtained through the serial port. And the simulation waveform data which has the same length is called from Multisim.

3.3 The design of the lower controller

The design of the lower controller is based on STM32. According to the protocol,the upper computer will switch the circuit's parameters, change the sampling frequency and collect the waveform's data. The flow chart is shown in Figure 6. Figure (a) is the overall flow chart of the system, and Figure (b) is the corresponding operation performed after the serial port receives the interrupt.

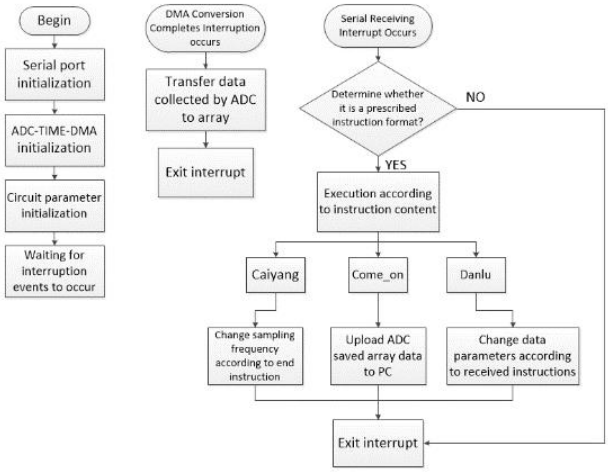

(a) (b)

Figure 6 The flow chart for the lower controller

4. TEST AND ANALYSIS

During the test, after the system is powered on, the different circuits are connected to the bottom plate of the experiment box, and the corresponding parameters are adjusted according to the instructions.

The results of the simulation in LabVIEW shown is in Figure 7. At this time, the resistance of the potentiometer R1 is 16KΩ, and the waveform is the cutoff distortion. The waveform results obtained by the experimental circuit after adjusting the potentiometer parameters are shown in Figure 8. The waveform has no distortion.

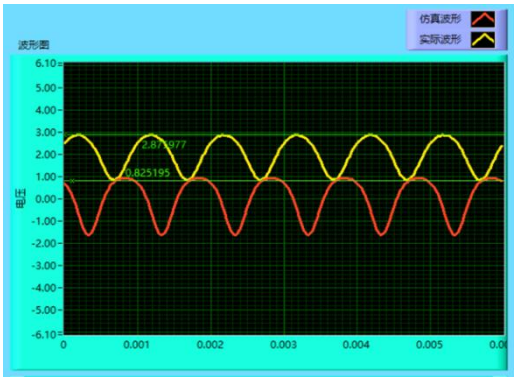

Figure 7 R1 = 16KΩ, the results of the single stage amplifier

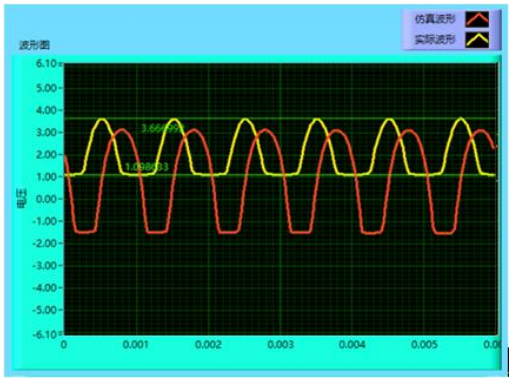

Figure 8 R1 = 72KΩ, the results of the single stage amplifier

5. CONCLUSION

This paper designs a virtual and physical analog circuit lab platform based on LabVIEW and ARM. It can combine virtual simulation and physical circuit. The results are displayed together. It make users to carry out analog circuit experiment efficiently and have great teaching significance.

References

[1] Yang-Mei L , Bo C . Electronic Circuit Virtual Laboratory Based on LabVIEW and Multisim[C]// International Conference on Intelligent Computation Technology & Automation. IEEE, 2015.

[2] He Z , Shen Z , Zhu S . Design and implementation of an internet-based electrical engineering laboratory[J]. ISA Transactions, 2014, 53(5):1377-1382.

[3] Bao Y, Jiang x. Application of virtual instrumentation which based on labview in electronic measurement technology course[C]//Electronics and Optoelectronics (ICEOE), 2011 InternationalConference on. IEEE, 2011:215-218.

[4] Odeh S. A Web-Based Remote Lab Platform with Reusability for Electronic Experiments in Engineering Education[J]. International Journal of Online Engineering, 2014, 10(4):40-45.

[5] Balamuralithara B, Woods P C. Virtual laboratories in engineering education: The simulation lab and remote lab[J]. Computer Applications in Engineering Education, 2009, 17(1):108-118.

[6] Grimaldi D, Rapuano S. Hardware and software to design virtual laboratory for education in instrumentation and measurement[J], Measurement, 2009, 42(4):485-493.

[7] Hardison J L, DeLong K, Bailey P H, et al. Deploying Interactive Remote Labs Using the iLab Shared Architecture[C]. 38th ASEE/IEEE Frontiers in Education Conference, 2008:S2A-l-S2A-6.

[8] El-Medany W M. FPGA Remote Laboratory for Hardware E-Learning Course[J], Computational Technologies in Electrical and Electronics Engineering, 2008, 8:106-109.

[9] Tawfik M, Sancristobal E, Matin S, et al. Virtual Instrument Systems in Reality (VISIR) for Remote Wiring and Measurement of Electronic Circuits on Breadboard[J. IEEE Transactions on LearningTechnologies, 2013, 6(1):60-72.

[10] Popovic B, Popovic N, Mijjic D, et al. Remote control of laboratory equipment for basic electronics courses: A LabVIEW-based implementation[J]. Computer Applications in Engineering Education,2011, 21(S1):E110-E120.

[11] Bayhan S. LabVIEW-based Remote Laboratory Experiments for a Multi-mode Single-leg Converter[J]. Joumal of Power Electronics, 2014, 14(5):1069-1078.

[12] Sun Qiuli, Internet-based distributed collaborative environment for engineering educationand design [J], Ph. D., The University of Oklahoma, 2001

[13] Chi Chung Ko, Ben M. Chen, Shaoyan Hu, Vikram Ram akrishnan, A Web-Based virtualLaboratory on a Frequency Modulation Experiment[J].IEEE,2001.

Waste Separation and Metal Based on STM32 MCU

Li Liye, Zhao Zejian, Shan Wanying
（*College of Instrument Science and Electrical Engineering, Jilin University,changchun,130021*）

***Abstract*—Based on STM32 MCU, a kind of garbage bin for garbage sorting and metal sorting has been designed. This project uses radiation photoelectric switch to detect objects, inductive proximity switch to classify objects, stepper motor to drive sorting board, and STM32 MCU to control. It can classify metal and non-metal into garbage bin, and classify strong and weak magnetic metals in metals. Classification can effectively reduce the classification time and improve the efficiency of recovering useful metals such as iron.**

***keywords*—STM32MCU,Metal Classification,Optoelectronic Switch,Inductive Proximity Switch**

I. INTRODUCTION

IN daily life, it is inevitable that new and old substitution phenomena will appear in the process of using metal products. Due to the decay, damage and natural elimination of metal products, a large number of scrap metals are produced every year. If these scrap metals are discarded casually, it will cause environmental pollution and waste limited metal resources. In daily life, with the improvement of living standards, the amount of garbage generated will also increase. There are many scrap metals, if these metals are not properly treated, it will cause a lot of waste of resources. This design aims to recycle the metal in the garbage, achieve the classification and recycling of the waste metal, improve the reuse rate of the waste resources, and reduce environmental pollution.

II. PROCEDURE FOR PAPER SUBMISSION

A.Background introduction

With the development of China's economy, the demand for non-ferrous metals is increasing year by year. China's non-ferrous metal production ranks among the top in the world for several years, and has become a country with huge production and consumption. There are many scrap metals every year. If these scrap metals are discarded at will, the environment will be polluted and the limited precious metal resources will be wasted. Waste metal is also recycled by people, but with the vigorous development of waste metal recycling, many questions arise. Many people think that waste metal products are harmful garbage, more harmful substances, not suitable for use, should not be recycled.

But if these scrap metals are discarded at will, it will not only pollute the environment, but also waste the limited metal resources. It has been estimated that recycling an abandoned aluminium cans can save 20% of the money and about 90% to 97% of the energy compared with manufacturing a new cans. Recovering 1 ton of scrap steel can produce 0.9t of good steel, which can save 47% of the cost compared with smelting with ore. At the same time, it can also reduce air pollution, water pollution and solid waste. It can be seen that establishing the concept of sustainable development, strengthening the classification and treatment of garbage, recycling and recycling of waste metals have great economic and social benefits.

Our project aims to improve the manual waste recycling part, provide front-end sorting means, more accurate classification of metal waste and other waste, while saving more human resources, and prepare for the later classification and secondary utilization of metal species.

B.System design

STM32 is used to control the whole system [1]. The high and low level of the motor is output through the signal received by the sensor, so as to realize the positive and reversal of the motor. When the motor does not work when receiving the non-object signal and receives the input signal of the object, the motor works. Then the high and low level of the signal output by the close switch feedback can make the motor rotate forward or reverse, so as to realize the discrimination of metal and non-metal. The system flow chart is shown as follows:

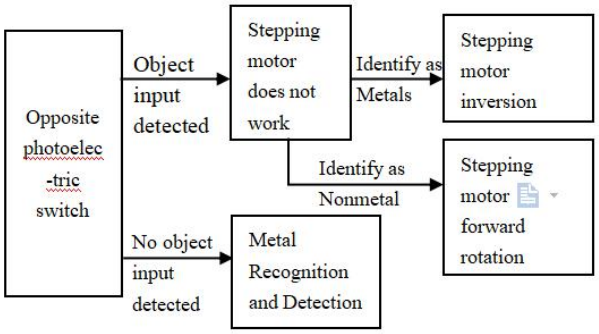

Fig.1. Implementation plan

C.Sensor Principle

a. Principle of opposite photoelectric switch

Photoelectric switch is the abbreviation of photoelectric proximity switch [2]. It is connected by synchronous circuit. It uses the occlusion or reflection of the detected object to detect the presence or absence of the object. Objects are not limited to metals, and all objects that reflect (or block) light can be detected. The photoelectric switch converts the input current into light signal in the transmitter, and the receiver detects whether there is a target or not according to the received light intensity.

b. Principle of inductance proximity switch

Linear proximity sensor [3] is a kind of linear device which belongs to metal induction. When the power supply is switched on, the induction surface of the sensor will produce an alternating magnetic field. When the metal object approaches the induction surface, eddy current will be generated in the metal, and the energy of the oscillator will be absorbed, so that the output amplitude of the oscillator will be linearly attenuated. The proximity sensor has no sliding contacts and is not affected by non-metallic factors. It has low power consumption and long life. It can be used in various harsh conditions. Inductive proximity switch [4] consists of three parts: oscillator, switching circuit and amplifier output circuit. The oscillator can produce an alternating magnetic field. When the metal target approaches the magnetic field and reaches the induction distance, the eddy current will be generated in the metal target, which will lead to the attenuation of the oscillation and even stop the oscillation. The change of oscillator oscillation and stop oscillation is processed and converted into switching signal by the later amplifier circuit, triggering the driving control device, so as to achieve the purpose of non-contact detection.

D.Hardware and Mechanical Design

a.Detection module

To detect whether the object is put into operation or not, the photoelectric switch is selected as the detection device. It needs external 24V power supply with short response time, high precision, and long effective detection distance can reach 3M, which fully meets the design requirements [5]. Two pairs of photoelectric switch are selected, and the light emitted forms a cross covering the top of the barrel to ensure that there is no mistake.

b. Metal classification module

The inductive proximity switch is used for metal and non-metal classification. Its installation circuit is complex, high precision and long detection distance. It needs 24V power supply to implement this project. In the external mechanical design, the problem of too short detection distance can be effectively solved by installing it on the rotating plate.

c. Driving module

The garbage is classified by driving partition board. The stepper motor is 57 (2-phase 4-wire) stepper motor with torque of 1.2N/M and step angle of 1.8 degrees. The orange-yellow-pink-blue four wires of the stepper motor are connected with OUT1, OUT2, OUT3 and OUT4 of the stepper motor driver chip in turn, and the external power supply must be in common with the single chip computer [6].

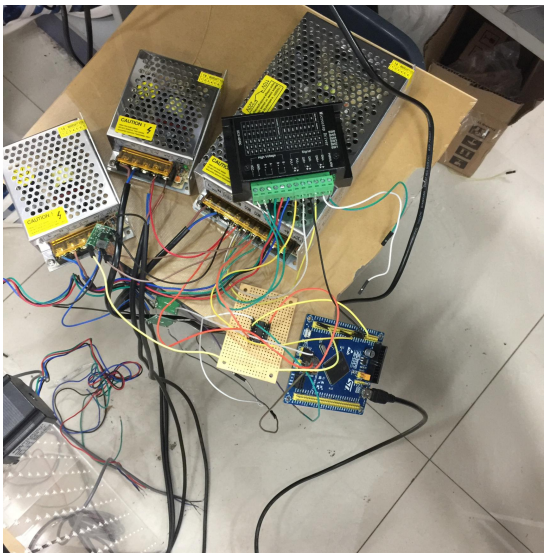

Fig.2. Hardware Connection Diagram

E.Software Design

Under the compiling environment of C language [7], Keils software is used to compile programs to collect signals from two kinds of sensors and convert the collected signals into electrical signals for transmission to stepping motors, so that the stepping motors can achieve the desired functions, and then realize the classification and recovery of metals and non-metals. The main function part code is as follows:

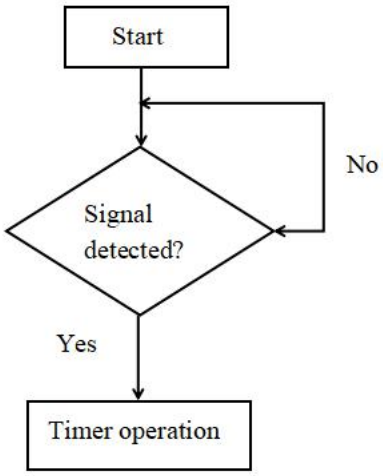

Fig.3 Program flow chart

The main function code is as follows:

```
delay_init();
NVIC_PriorityGroupConfig(NVIC_PriorityGroup_2);
uart_init(115200);
LED_Init();
TIM3_Int_Init(49,7199);
 KEY_Init();
EXTIX_Init();
  while(1)
{
  delay_ms(200);
}
```

Fig.4. Program Code Diagram

F.Test Result

This project uses metal and non-metal cans such as plastic bottles to carry out many experiments. When the cans are put in, the motor rotates to one side of the metal, and when the plastic bottles are put in, the motor rotates to make the plastic bottles turn to the other side. When nothing is put in, the motor does not turn. After many tests, the accuracy rate is over 95%, which meets the technical specifications and meets the requirements.

III. CONCLUSION

Through this project, we successfully designed a box which can classify metal and non-metal, basically achieved the expected goal, classified metal and non-metal, and classified strong magnetic and weak magnetic metals. However, there are many problems in accuracy and design. The accuracy of classification of strong and weak magnetic fields of metals is still the direction of future efforts.

References

[1] Zhang Yigang et al., Application Design of MCS32 Single Chip Microcomputer, Harbin University of Technology

[2] Fan Shangchun, Sensor Technology and Applications, Beijing University of Aeronautics and Astronautics Press

[3] Wang Xuewen, Principle and Application of Sensors. Beijing [M]: Beijing Aerospace Press, 2004

[4] Zhang Hongrun, Sensor Technology Complete, Beijing University of Aeronautics and Astronautics Press

[5] Research on the Universal Control Module of MCS-51 Series MCU, Cao Weifang, Shandong University of Science and Technology, 2005

[6] Tian Jie, Yang Xin. Foundation of Intelligent Design [M], Beijing: Electronic Industry Press, 2005

[7] Zhang Xin He Limin, Selected Technology of Single Chip Microcomputer Application [M]. Beijing University of Aeronautics and Astronautics Press, 2003, Principle and Application of Single Chip Microcomputer, Electronic Industry Press

An Internet of things based bike anti-theft tracking system

Qiu Chunling, Li Mengshi, Dong Haitao, Ren Jian, Mi Liang
（*College of Instrumentation & Electrical Engineering, Jilin University,Changchun 130026,China*）

***Abstract*—This paper puts forward a new solution to the problem of bicycle theft, which is a kind of bicycle theft proof tracking system based on the technology of Internet of things, which has the advantages of perceived anti-theft, real-time positioning and so on. As the front-end perception of the system, intelligent security lock can determine the safety status of the bicycle intelligently, and send control instructions to the main controller. The main controller controls the GPS positioning and sends the position information to the user. The user can learn the position of the bicycle in time through the mobile map APP.**

***Key words*—Internet of things technology Intelliget anti-theft lock GPS Mobile map APP**

I. INTRODUCTION

BICYCLE theft on college campuses has become more and more serious in recent years. In order to solve this problem, many companies or teams are carrying out research and development of bicycle anti-theft tracking system. In China, the rfid-based bicycle anti-theft system developed by Beijing tianyi zhonghe technology co., ltd. mainly applies radio frequency identification technology for anti-theft, which has strong practicability. However, its disadvantage is that it does not adopt GPS technology for positioning tracking, resulting in range error of tracking locations[1]. There are currently a variety of commonly used anti-theft trackers, the use of GPS technology tracking, but its anti-theft system is not complete enough to establish a timely information exchange with the owner. In addition, the more popular intelligent anti-theft lock, its function is through the voice alarm to achieve the anti-theft effect, its disadvantage is once the distance is too far, can not make the owner of the vehicle in time to obtain effective information. Abroad, smart bikes developed by Amsterdam bicycle company VanMoof are equipped with GSM and bluetooth tracking systems. However, its disadvantage is that the anti-theft lock designed for the anti-theft system is only applicable to the bike, not universal. The bicycle anti-theft tracking system designed and developed by a research and development team composed of D Godfrey and MH Song [8] USES GPS tracking. However, since vibration sensors are used for anti-theft perception, if there is a slight vibration, it may cause false alarm, and the anti-theft effect is not good. The bicycle anti-theft tracking system based on the Internet of things technology designed for the above problems has a good ability of anti-theft and positioning tracking, which can establish information exchange between the bicycle and the user and effectively prevent the frequent occurrence of bicycle theft.

II. HARDWARE STRUCTURE OF THE SYSTEM

A. Overall Structure and Function

"Bicycle anti-theft tracking system based on Internet of things technology" is mainly applied to the intelligent anti-theft tracking of private bicycles, and the application of Internet of things technology enables users to master the current state of bicycles in real time [2]. The whole system is divided into working mode and sleep mode. When a user USES a bicycle, the system is in sleep mode, and the rest of the time the whole system is in working mode for real-time anti-theft. In the working mode, the system can provide intelligent determination function of bicycle theft, location information acquisition function, data storage and transmission function, and can provide users with bicycle location information, bicycle tracking track information, alarm record, etc. [3]. This system is mainly divided into three parts: intelligent anti-theft lock, main controller and mobile APP. The system structure is shown in figure I:

Figure I System Structure Block Diagram

Intelligent anti-theft lock has the function of intelligent perception, which can determine whether the bike is stolen by fingerprint identification and whether the chain is broken and send instructions to the main controller; The main controller receives instructions to switch modes, conduct GPS positioning, and send warning information and current position information of the bicycle to the user; After receiving the information, the user can read the location information through the mobile phone map APP and display the current location of the bike on the mobile phone map in real time.

B. Structure and Function of Intelligent Anti-theft Lock

The structural block diagram of the intelligent anti-theft lock is shown in figure II: the intelligent anti-theft lock is integrated and designed by STM32 single chip microcomputer, hc-05 wireless bluetooth module, AS608 fingerprint recognition module, small electromagnet and convenient power supply, with certain intelligent judgment ability. The overall structure of the chain lock, the chain has a wire through the inside, the lock is connected by the patch magnet, the lock is a small electromagnet, the lock for the fingerprint module, including SCM, bluetooth and power supply. When the fingerprint identification is correct, the electromagnet is energized, the lock is opened normally, and the unlock signal is sent; Identify again, electromagnet power off, lock lock, send lock signal. When the fingerprint identification is wrong and the anti-theft lock is opened abnormally or is damaged artificially (the chain and internal wire are broken), the bicycle can be judged to have been stolen by itself, and the warning signal is sent to the main controller through bluetooth.

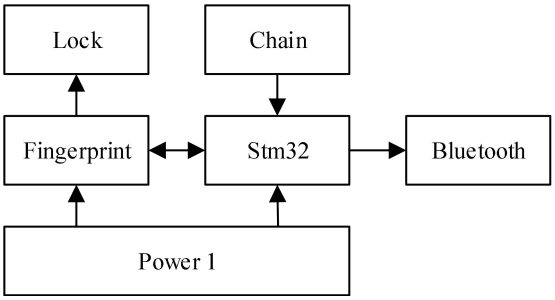

Figure II Structure Block Diagram of Intelligent Anti-theft Lock

C. Structure and Function of The Main Controller

The structure block diagram of the main controller is shown in figure III: the main controller consists of STM32 MCU, bluetooth module, sim808 module and power supply, which are integrated and installed on the bicycle. The main controller has three functions, which are controlled by the single chip microcomputer: receiving and processing the information sent by the intelligent anti-theft lock; Receive and store the location information of the bicycle, and make intelligent judgment to decide whether to send an alert to the user; Control the working state switch of the position acquisition module. The bluetooth module is used to receive signals from the smart anti-theft lock. Sim808 module mainly USES GPS positioning technology [4]. By calculating the distance between the module and the known satellites, and then synthesizing the data of multiple satellites, it receives and decodes the accurate position information and sends the position information to the single-chip microcomputer. Power supply is composed of multiple batteries can be charged and discharged battery pack. In the anti-theft mode, the system saves the location information every 10 minutes. If the second location is beyond the range of the electronic fence or the alarm signal from the bluetooth lock is received, the system will give an alarm and start real-time positioning to send the location information to the mobile phone.

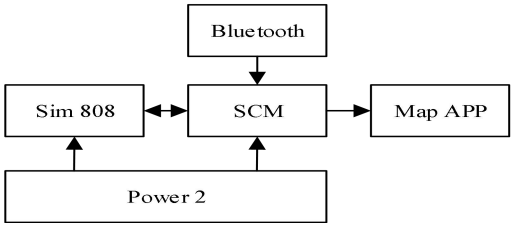

Figure III Block Diagram of Main Controller

III. SYSTEM SOFTWARE FLOW DESIGN

A. Intelligent Anti-theft Lock Program Flow Design

The program flow chart of the intelligent anti-theft lock is shown in figure IV: after the fingerprint recognition of the intelligent anti-theft lock is locked, the lock signal is sent to the main controller and the intelligent judgment is started to judge whether the chain is broken and whether the fingerprint recognition is correct again. If the chain is broken or the fingerprint identification is wrong, the alarm signal will be sent to the main controller, and if the fingerprint identification is correct, the unlock signal will be sent to the main controller.

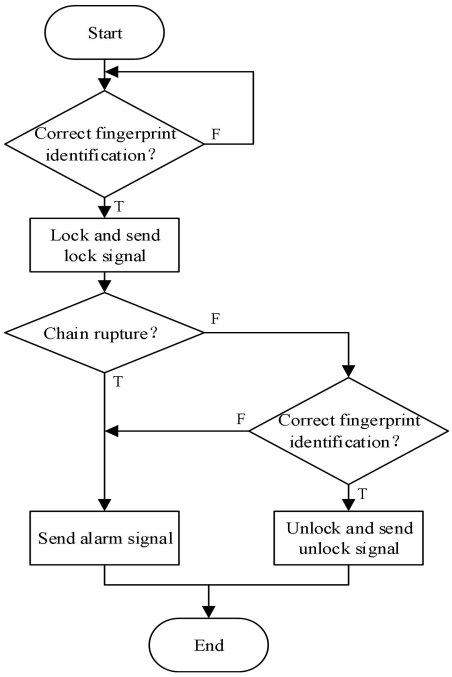

Figure IV Flowchart of Intelligent Anti-theft Lock Program

B. Main Controller Program Flow Design

The program flow chart of the main controller is shown in figure V: after receiving the lock signal sent by the intelligent anti-theft lock, the main controller enters the working mode and opens the anti-theft detection and fence alarm functions. If the control signal is received or the range of electronic fence is exceeded, real-time positioning is enabled and location information is sent to

the user.

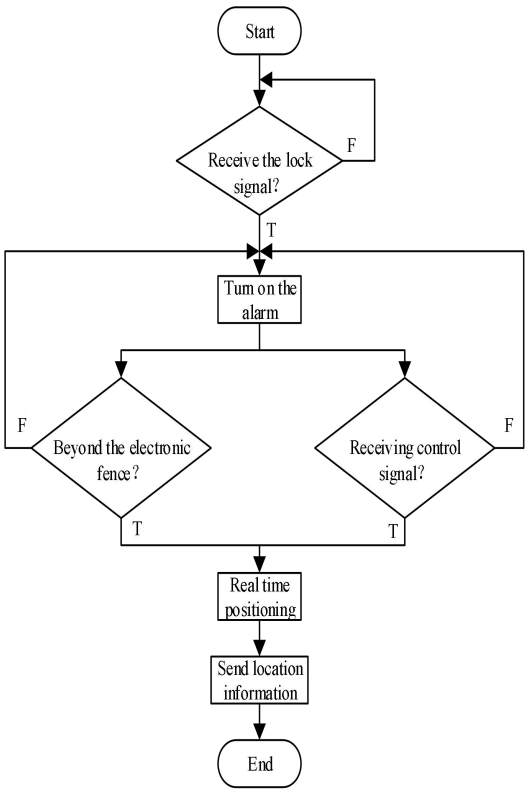

Figure V Main Controller Program Flow Chart

C. Mobile APP Design and Functions

The mobile phone map APP supports the Android system. By reading the longitude and latitude information in the alarm message received by the user, the location of the bike can be displayed on the map in real time to achieve the function of location tracking [5]. Functions of mobile map APP include:

(1) Map control: it can rotate, enlarge and reduce the map;

(2) Real-time location: the location information in SMS can be acquired and displayed on the map, and the location information can be acquired in real time;

According to the above map function, use baidu map API to develop android map application. First, we need to define a base class. As the parent class, all the application development classes inherit this class, which makes the code utilization high and the program simple. The design process is shown in figure VI:

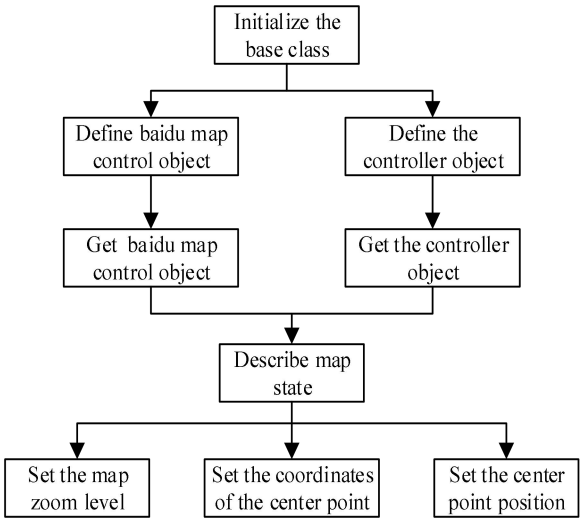

Figure VI Defines The Base Class

First initialize the base class, then define two objects, namely baidu Map control object and controller object, get the contents of the two objects, then use the Map Status Update Factory class to describe the state of the Map, such as setting the Map zoom level, coordinates and center point.

After the map is displayed, real-time positioning is required according to the location information in the SMS. The design process is shown in figure VII:

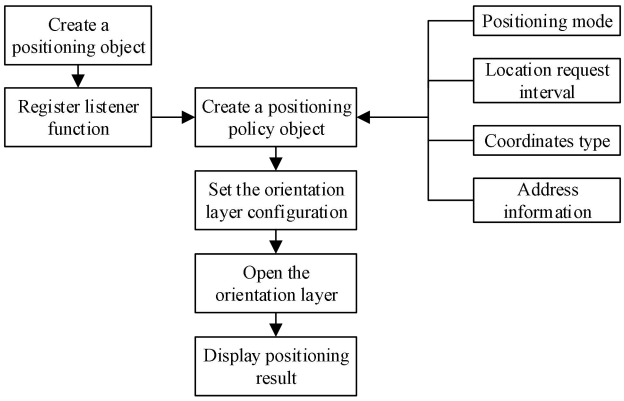

Figure VII Positioning Flow Chart

Use the Location Client class to create the Location object, and then use the Location Listener class to register the Listener function for real-time Location. Use the Location Client Option class to create the Location policy object and set the configuration parameters of the Location, such as setting the coordinate type, Location mode, address information, etc. Then configure the relevant parameters of the positioning layer, such as the display direction, and finally open the positioning layer to display the positioning results.

IV. TEST RESULTS

After the user parks the bike and locks it, the anti-theft system is started. If the bike is moved or the lock is damaged or opened abnormally, the user will receive a Warning. Your bike is moving! After that, the user will

receive a positioning information "GPS data: XXXXXXXXXX" every 10s. When opening the mobile APP, the user can see the current position of the bike [6]. The test results are shown in figure VIII:

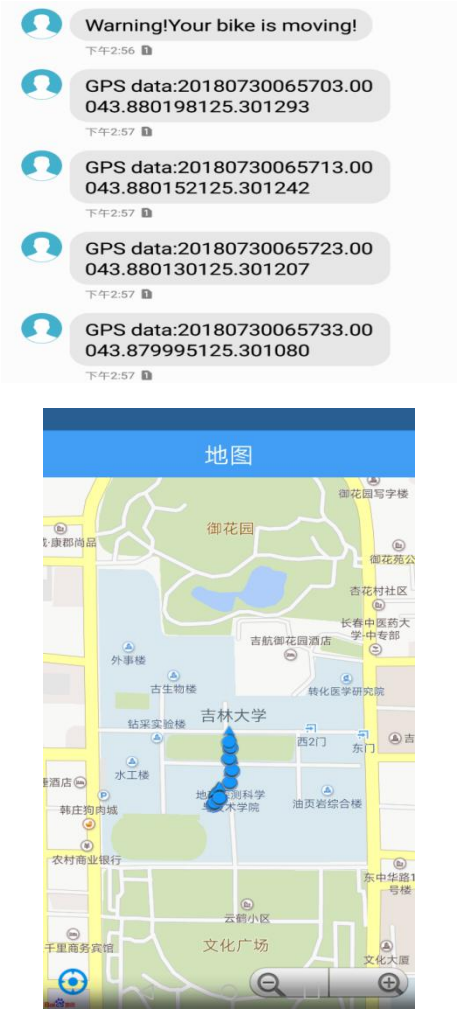

Figure VIII Test Result Diagram

The theoretical positioning accuracy of GPS module is 2.5m, and 10 groups of positioning data measured continuously every 10s after the actual stable positioning are as follows:

Table I Test Location Data Table

Test times	latitude/degree	longitude/degree
1	43.880455	125.301213
2	43.880455	125.301208
3	43.880455	125.301200
4	43.880453	125.301193
5	43.880453	125.301185
6	43.880455	125.301178
7	43.880460	125.301173
8	43.880467	125.301165
9	43.880472	125.301167
10	43.880475	125.301168

Calculate the average latitude $\bar{X}_A$ =43.880460 degrees, the average longitude $\bar{X}_B$ =125.301185 degrees, using the Bessel formula to calculate the uncertainty U_A =0.000008 degrees, U_B =0.000018 degrees. Since the difference in latitude is about ΔX_A=111 km, and the difference in longitude is about ΔX_B =111*COS(X_A) km, and the difference in latitude is the seventh place after the decimal point, which is far less than U_B, it is ignored, replace $\bar{X}_A$ with the average latitude X_A and substitute it in to get A difference of longitude $\Delta X_B = 111 * COS(\bar{X}_A) = 80\ km$. The total positioning accuracy

$\delta=\sqrt{(U_A * \Delta X_A)^2 + (U_B * \Delta X_B)^2} = 1.7\times10^{-3} km = 1.7m < 10m$.

The alarm range of the fence is calculated by the latitude and longitude through the plane coordinates, which is greater than 30m.

Since then, all the system functions have been realized. It takes about 55s from the start of GPS positioning to obtain accurate positioning, and the positioning accuracy is about 1.7m. The real-time positioning occurs once every 10s, and the electronic fence has a range of 15m, which meets the technical requirements of system positioning accuracy less than 10m, start-up time less than 2min, and electronic fence range 30m.

V. CONCLUSION

At present, with the advocacy of green and low carbon life, bicycle has gradually become one of the mainstream ways of travel, but with the increase of bicycle loss and theft. This system USES the combination of lock anti-theft, GPS positioning and mobile phone map APP to track and locate the bicycle anti-theft in real time, so as to effectively prevent the frequent occurrence of bicycle theft. In addition, this set of anti-theft tracking system can also be implanted in other application fields, the application of real-time anti-theft items, easy for people to monitor and manage.

References

[1] Yuhang Jiang . Design and implementation of anti-theft bicycle system based on RFID [D]. Jilin university, 2015.

[2] Jianlin Shen . Resident e-bike security solution based on Internet of things [C]. Wireless and mobile communications committee of China communications

association，2014 Proceedings of the national conference on wireless and mobile communications.Beijing：Posts and Telecom Press，2014:282-287.

[3] Yun Xu . Low-cost electric bicycle anti-theft tracking and monitoring module design [D]. University of electronic science and technology，2015.

[4] Hongchao Guo , Meiqun Luo , Yaocheng Yu . Design of vehicle positioning and tracking system based on GPS and GSM [J]. Science & Technology Information， 2009，（16）：67.

[5] Zheng Liu， Qiang Chen . Research and development of GPS application based on Android [J]. Western China science and technology，2010，（32）：15-16.

[6] Zhuo Chen . Research on tracking system based on GPS and GPRS [D]. Harbin Institute of Technology，2009.

[7] Fei Li. Portable equipment power management and low power consumption design and implementation [D]. Hunan university of science and technology，2015.

[8] D Godfrey， MH SONG.Safe Bike:Secure your Bicycle with this smart Arduino based GPS device[J].The International Journal of Advanced Smart Convergence，2016,5(3):16-26.

[9] PA Shinde,YB Mane,PH Tarange.Real Time Vehicle Monitoring and Tracking System based on Embedded Linux Board and Android Application[J].International Conference on Circuit,2015:1-7.

[10] VJE Jimenez,F Salmhofer,R Frosch,H Zeiner,W Haas.Safe Bicycle Parking Platform Based on RFID Technology[J].Springer International Publishing,2015.

Research on Three-primary Color Stimulated EEG Signal Recognition System Based on SSVEP

Dong Zequn, Wang Ziang, Song Hongzhen
(College of Instrumentation & Electrical Engineering, Jilin University)

***Abstract*-Steady-state visual evoked potential is one of the important directions of brain-computer interface research. Our project team used the three primary colors RGB as the stimulus source for the steady-state visual evoked EEG signals, applied stable visual stimuli, collected the EEG signals through the OpenBCI platform, and performed various band preprocessing on the collected EEG data. Separate the eigenvalues, principal component analysis quarter difference, positive skewness, kurtosis, power spectrum entropy and other eigenvalues, combined with support vector machine, decision tree, integration algorithm, etc. Classification and evaluation, comparing the statistical data of the evaluation, and obtaining a higher recognition rate and corresponding prediction model, and statistical analysis and principle conjecture of the obtained evaluation data.**

***Keywords*-Brain-computer interface; steady-state visual; evoked potential feature; classification prediction**

I. INTRODUCTION

THE brain-computer interface is a direct information exchange and control channel established between the human brain and external devices without relying on the limbs. By collecting EEG signals and identifying features, the communication or control of external things is realized. Brain-computer interface involves computer science, signal processing, clinical medicine, mathematics, control principles and other fields; usually requires 4 modules: data acquisition system; signal processing (preprocessing, feature extraction, classification algorithm) system; pattern recognition Forecasting systems, as well as external control equipment systems. The BCI system is mainly used in the field of medical rehabilitation, and it can also provide people with a way to control external equipment under special circumstances [1].

At present, BCI's research mainly focuses on the following aspects: the Wadsworth Research Center in the United States is inferior to the motion perception rhythm (the BCI study [2]; the Berlin BCI team in Germany designed a P300 paradigm based on rapid sequence visual presentation; Austria Graz BCI mainly studies BCI systems based on event-related desynchronization (ERD) and synchronization (ERS) directions [3]; the domestic Tsinghua University group is led by Prof. Gao Shangkai, mainly engaged in steady-state visual evoked potentials (SSVEP). The study [4] SSVEP refers to the external frequency scintillation stimulus applied to the subject with a stable frequency, the subject's EEG signal will produce the same frequency response as the stimulus source or harmonics [5]. Extracting the characteristic values of the steady-state visual evoked potential EEG signals, and distinguishing them, the types of the stimulus sources can be obtained, and the prediction model can be established to predict and judge the EEG signals stimulated by the three primary colors.

II. TEST EQUIPMENT AND DATA DESCRIPTION

The BCI system of this paper is based on OpenBCI's open source experimental platform. It uses three primary colors (red, green and blue) as the stimulus source. The test environment is dark and closed, no noise. Divided into EEG induction module, EEG acquisition module, communication module. The EEG evoked module uses a three-primary LED dot matrix as a stimulator to generate a stimulus signal of about 10 Hz [6]. The EEG signal acquisition module uses the OpenBCI open source experimental platform and the four-channel EEG acquisition device based on the Σ-Δ ADS1299 chip. The four-way EEG data includes two places in the frontal lobe and two in the occipital lobe. The reference electrode is set as the left and right ear papilla (ie, M1 and M2); the communication module uses Bluetooth wireless communication, and the processing uploaded to the PC is saved as a txt file. Post-processing preparation. In addition to using Processing to receive data, the software part also uses MATLAB to perform data preprocessing, feature extraction, classification and prediction model output, so that LabVIEW and MATLAB can be linked to realize human-computer interaction interface, leaving ports for future research. Perform connection control of external devices.

We tried various methods of collecting EEG signals, and finally selected elastic bands, ECG electrodes, conductive paste, DuPont line, openbci open source and experimental platform and Bluetooth transmission signals

for experiments. The Openbci open source experimental platform is shown in Figure 1.

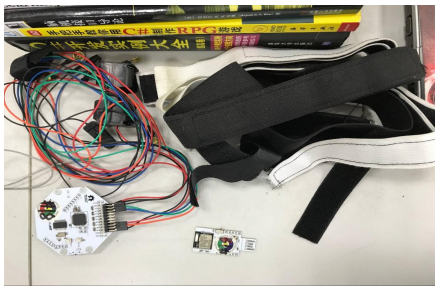

Fig.1 OPENBCI open source experiment platform

We use openbci open source experimental platform as EEG acquisition device. The circuit schematic diagram of openbci open source experimental platform is shown in Figure 2.

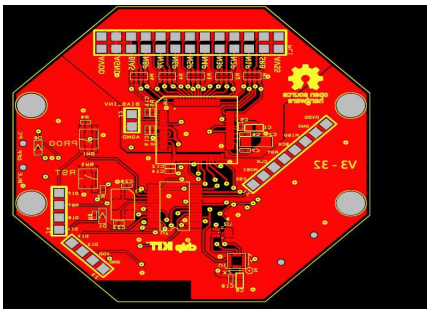

Fig.2 Principle of Openbci Open Source Experimental Platform

The test data sampling rate is 256 Hz, and each sampling time is about 1 minute; including four categories, in addition to the three primary color stimulation signals, the silent signal is also tested, that is, in the same environment, no external stimulation is applied to perform data acquisition. At the same time, the four types of signals subjected to the same filtering process are analyzed, and the spectrum analysis of the four types of signals is performed with the silent signal as a reference; whether the frequency response peak of the three primary colors is determined to determine whether the data of the group is a valid signal, and the pre-determination is completed. Processing facilitates the selection and output of the next feature classification prediction model. The interface of our measurement signal is shown in Figure 3.

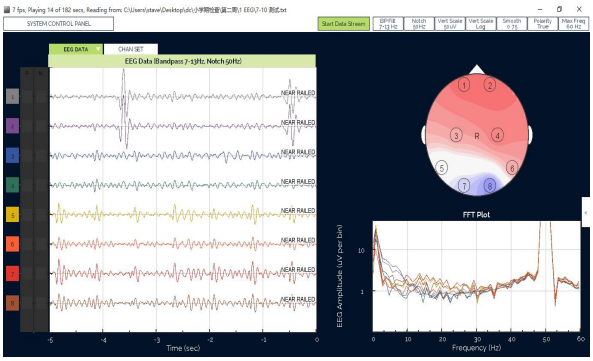

Fig.3 Collected EEG signals

At the same time, the JAVA code of OPENBCI that collects EEG signals is shown in Figure 4.

Fig.4 OPENBCI interface JAVA code

The evoked potential signal detected on the surface of the scalp belongs to low signal-to-noise ratio and is submerged in background noise, including power frequency interference, high-frequency white noise, etc. Therefore, in the preprocessing stage, we mainly use wavelet transform to obtain its time-frequency domain. The information [7] is filtered by different frequency bands respectively. The filtered data is obtained. The bandwidth ranges are as follows: 6-14Hz, 0-20Hz, 0-30Hz, 0-40Hz. We use the morse wavelet for filtering. The filtered time domain data and the time-frequency domain data are obtained [8]; as shown in Fig.5, the spectral contrast between the blue stimulus and the silence time after filtering is performed, and after the blue stimulus induces the steady-state potential, it appears obviously at around 10 Hz. The peaks, the energy of the silent signal is mainly concentrated before 10Hz, of which 1, 2 channels represent two places in the frontal lobe, and 3, 4 represent two places in the occipital lobe. It can be seen from the comparison that the blue stimuli EEG signal is available. The frequency response in the steady-state EEG signal is similar to the frequency of the stimulus source signal or similar to its harmonic frequency. Therefore, it is a multiple of 10Hz. We divide the original EEG signal with a sampling rate of 256Hz into 600 points, about two seconds. The signal is a sample, and one sample contains four channels. For signals with less than 600 points at the end, 600 points are automatically forwarded to ensure the continuous characteristics of the signal.

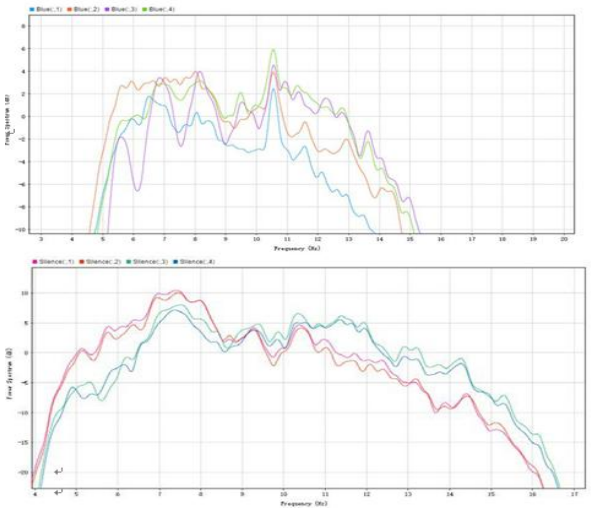

Fig.5 Filtered blue stimulated EEG signal spectrum and silent EEG signal spectrum

III. EVOKED POTENTIAL FEATURE EXTRACTION AND CLASSIFICATION EVALUATION

The signal after pre-processing needs to be extracted. The extraction method can be divided into time domain, frequency domain or time-frequency domain according to the mode [9]. In the time domain, we directly averaged, median, standard deviation, Euclidean distance, principal component analysis, quarter difference, positive skewness, kurtosis, mean absolute dispersion, quantile, singular value, Shannon entropy and other 13 eigenvalues.

In the frequency domain, we first use FFT to calculate the power spectrum of the signal, find the maximum frequency point and the energy value of the point; obtain the peak energy by the highest frequency fmax±△ range, and then calculate the spectral entropy to obtain 4 kinds. Frequency domain feature parameters, a total of 17 eigenvalues, through four decision tree classification algorithms, three discriminant analysis classification algorithms, three support vector machine classification algorithms, a variety of neighbor sampling classification algorithms, and five integrated algorithms, a total of 22 categories The algorithm, each feature value is directly evaluated with 22 classifiers, and four sets of evaluation data are obtained according to the four frequency bands. Each group of data indicates that the feature value corresponds to the classifier with the best classification effect, and the accuracy rate.

In Table 1, the results of the accuracy rate greater than 60%, in fact, due to the random selection of points as the training group and the test group, the accuracy obtained will have a fluctuation of about ± 3%. Classification of features extracted in time domain and frequency domain Random sampling points are used as test samples, and the resolution accuracy is generally not higher than 80%. Therefore, we use feature extraction from time-frequency domain.

Because EEG signals are time-varying non-stationary signals, including large-scale low-frequency events and small-scale high-frequency events, the use of wavelets can solve the time-frequency characteristics well [10,11]. The decomposition coefficient of the wavelet transform or wavelet packet transform or the mean value of the intra-subband coefficients is usually used as the characteristic value of the EEG signal [12]. We obtain the Shannon entropy of the 4th-order maximum overlapping discrete wavelet packet transform (MODPWT), and extract the multi-scale wavelet variance estimate on each sample; we use the db wavelet with the vanishing moment of 4 to estimate the variance, in addition we add 4 The coefficients of the order autoregressive model are tested as features. Comparing the frequency bands of multiple bands, the unbiased estimation of the multi-scale wavelet variance of the single term in the 0-40 Hz interval achieves better resolution accuracy.

Table 1 Time domain, frequency domain test result table

Precondition	Feature Type	Classifier Type	Accuracy
6-14Hz filtered，600points	Interquartile Range	Quadratic SVM	62.00%
	SVD	Quadratic SVM	62.40%
	All Features	Ensemble Bagged Trees	69.90%
0-20Hz filtered 600points	Interquartile Range	Weighted KNN	64.50%
	Mean Absolute Deviation	Fine Gaussian SVM	65.40%
	Mean	Fine Gaussian SVM	64.30%
	Quantile25	Weighted KNN	65.40%
	Shannon Entropy	Fine Gaussian SVM	63.10%
	Standard Deviation	Ensemble Bagged Trees	64.10%
	All Features	Quadratic SVM	67.90%
0-30Hz filtered 600points	Interquartile Range	Weighted KNN	64.50%
	Mean Absolute Deviation	Fine Gaussian SVM	65.40%
	Mean	Fine Gaussian SVM	64.30%
	Median	Quadratic SVM	64.10%
	Quantile25	Weighted KNN	65.20%
	Quantile75	Quadratic SVM	63.10%
	Shannon Entropy	Fine Gaussian SVM	63.10%
	Standard Deviation	Quadratic SVM	63.70%
	All Features	Cubic SVM	66.90%
0-40Hz filtereds 600point	Interquartile Range	Ensemble Bagged Trees	77.10%
	Mean Absolute Deviation	Medium Tree	76.20%
	Mean	Fine Gaussian SVM	64.30%
	Median	Quadratic SVM	63.70%
	Quantile25 Quantile75	Quadratic SVM Quadratic SVM	64.50% 62.20%
	Shannon Entropy	Fine Gaussian SVM	63.70%
	Standard Deviation	Ensemble Bagged Trees	70.70%
	SVD	Medium Gaussian SVM	63.30%
	All Features	Ensemble Bagged Trees	79.80%

IV. ANALYSIS AND DISCUSSION

In the calculation of time domain and frequency domain signal characteristics, although the selected feature algorithm, for example, mean, median, standard deviation, etc., there is strong correlation, and the single species as the feature value classification and multiple associations as the feature value classification effect Not very obvious [13,14]. Through the extraction of time-frequency domain features, we can get the detailed feature information of EEG signals due to the scalable translation characteristics of wavelets, and we can estimate the small signal types that the steady-state visual evoked potentials are more biased towards higher frequencies. The resonance of the harmonics can be inferred from the frequency band comparison.

From the above experiments, for the commonly used feature extraction and classification algorithms, the combination of Interquartile Range and Ensemble Bagged Trees has higher recognition accuracy and stability than other operators; the accuracy of identifying colors is more accurate than other algorithms. The degree is 10% higher, and the extended work can be applied to embedded systems to achieve faster color classification.

References

[1] Gao Nan, Fu Junying, Zhao Yunhua. Research Characteristics and Progress of Human-Computer Integration[J]. High Technology Letters, 2015.2(25): 205-218

[2] Wolpaw JR, Mcfarland DJ. The Wadsworth center

brain-computer interface (BCI) research and development program [J]. IEEE Transaction on Neural Systems Engineering, 2003, 11(2): 204-207

[3] Pfurtscheller G, Allison BZ, Brunner C, Bauernfeind G, Solis-Escalante T, Scherer R, Zander TO, Mueller-Putz G, Neuper C and Birbaumer N. The hybrid BCI [J].

[4] H. Frequency detection with stability coefficient for steady-state visiual evoked potential-based BCIs[J].Journal of Neural Engineering,2008,5(1):36-43

[5] Li Penghai, Xu Minpeng, Wan Baikun, Qi Shijiu, Ming Dong. Progress in the experimental paradigm of brain-computer interface for visual evoked potentials[J]. Journal of Scientific Instrument. 201610(37): 2340-2347

[6] Wu Zhenghua, Zhai Dezhong. Comparison of steady-state visual evoked potentials produced by monochromatic light of different colors[J]. Biomedical Engineering Journal. 2008.5(25):1021-1024

[7] Wang Fei, Zhang Yuzhong, Ning Tinghui, Wen Shiguang. Research progress of brain-computer interface[J]. Journal of Intelligent Systems. 2011.3(6):189-199

[8] He Qinghua, Peng Chenglin, Wu Baoming, Zhu Lingyun. Application of Wavelet Transform in the Extraction of Visual Evoked Potential Signals[J]. Journal of Chongqing University.2003.6(26):78-80

[9] Jonathan M Lilly and Sofia C Olhede. Generalized Morse Wavelets as a Superfamily of Analytic Wavelets [J]. IEEE Transactions on Signal Processing. 2012.11(60):6036-6041

[10] Hua Xiaomei. Application of wavelet transform to analyze visual evoked potentials in brain-computer interface technology [D]. Huazhong University of Science and Technology.2004.5

[11] En-Bing Lin, Xiaoping Shen. Wavelet Analysis of EEG signals [C]. Proceedings of the 2011 IEEE National Aerospace and Electronics Conference (NAECON): 105-110

[12] Yang Banghua, Li Wei, Yang Lei, Ma Shiwei. Pattern Recognition Technology and Its Application [M]. Beijing: Science Press, 2016:133-144

[13] Zhang Xuegong. Pattern Recognition (Third Edition) [M]. Beijing. Tsinghua University Press, 2010: 145-157

[14] Sergios Theodoridis, Konstantinos Koutroum bas. Pattern Recognition (Fourth Edition) [M]. Elsevier: 163-193

Design of GPS Positioning System for Seismograph Based on Android

Chen Liang, Sun Wentao, Liu Yutao
（*College of Instrumentation & Electrical Engineering, Jilin University,Changchun 130012*）

***Abstract*—The GPS positioning service of mobile communication equipment based on Android platform with smart phones as media is widely used in people's lives because of its excellent system performance. Based on the above advantages, the importance of improving seismograph positioning is particularly important in the comprehensive competitiveness of modern high-tech products. Firstly, the framework structure of Android is studied, and the method of GPS positioning based on Android smartphone platform is put forward. The GPS positioning and navigation system based on Android platform is realized by using LBS function programming, and a variety of array methods based on Android platform are expanded. Finally, the design of GPS positioning system for seismograph based on Android platform is completed and the accuracy of the final result is verified.**

***keywords*—GPS Location Android Array mode**

0. INTRODUCTION

AT present, the application of GPS in seismic instruments has been unprecedented development, and GPS related services have become an indispensable and important part of seismic instruments. Most instrument manufacturers have introduced seismic instruments to support GPS timing, and GPS timing function is the main feature of these products, and even the most characteristic of many products is GPS timing function.

In the process of array arrangement of seismic instruments, the existing one-dimensional positioning can not meet the requirements of experiments. In order to deploy array seismic instruments more intuitively and conveniently, two-dimensional and even three-dimensional GPS positioning technology needs further development. In the process of seismic data acquisition, the requirement of monitoring the actual vibration point position of vibroseis construction has a fundamental impetus to the application of GPS positioning in seismic instruments. Compared with borehole gun, the actual vibration point position of seismic source can not be located accurately according to the measured pile number as the actual drilling position in borehole gun construction. In borehole gun construction, the drilling position is completely drilled according to the measured pile number when there is no special topographic restriction. However, due to the combination of vibroseis and the operation of vehicle drivers, the difference between the actual vibration point and the measured point is often caused. Due to the limitation of terrain, the source vehicle often appears in the situation that the original measuring point can not stop and the vibration point needs to be selected separately according to the terrain. Such vibration point is difficult to be measured by the surveyor. Therefore, real-time location of the vibration point of the vibroseis is an urgent requirement for the quality control of the vibroseis construction, which obviously needs to be controlled by the exploration system. . With the domestic 4G entering the formal application stage, more and more smart terminals using Android system, their portability and interconnection are maintained to the greatest extent. Driven by the support of GPS positioning service in Android system and Bluetooth wireless network, it is feasible to implement navigation service with Google Map [1].

I. SYSTEM ARCHITECTURE OF ANDOIRD

A.System Architecture Of Android

Android system is an open source operating system based on Linux. In October 2003, Android et al. set up a team for Android development and founded the company. The original Android system was an intelligent operating system developed only for digital cameras. In August 2005, Google acquired Android company, and the original team continued to be responsible for the follow-up development of Android system. Android operating system is mainly applicable to smart mobile devices, such as smart phones and wearable devices. Equipment, and is the first fully open mobile software platform, with good executability, can be tailored and customized according to needs, high flexibility. In November 2007, Google released the source code of Android under the license of the second edition of Apache license; in the first quarter of 2011, Android surpassed Symbian in global market share for

the first time, ranking first in the world; in the fourth quarter of 2013, the number of devices using the system worldwide reached 1 billion[2].

Table 1 System Architecture of Android

Application Layer	Android application				
	Local Application	Third-party applications	Application development		
Frame Layer	Application framework				
	Positioning services	Content provider	Windows Manager	Activity management	Information management
	Dialing	P2P/1M	Notice	View	Resource

The chart above is a sketch of the internal architecture of Android system. The architecture of Android system is divided into three layers: Application, Operating System and Middledware. The first layer of application is mainly composed of application framework. It provides a management platform for Android services and is an important part of Android system.The core of the second operating system is mainly Linux. The basic functions provide the basic system architecture; the third layer is mainly composed of function libraries and Android runtime; the image, media, open source browser engine and other functions serve the runtime together with Android runtime; the fourth layer is Android application layer, mainly providing the required services for Android applications [3-5].

II. GPS POSITIONING BASED ON ANDROID PLATFORM

A.GPS positioning technology

The first task of positioning using GPS is to establish network connection. GPS mobile terminal first connects to GPRS or WIFI, then SOCKET module establishes connection with the system background server, receives message information from satellite through GPS navigation module built in mobile terminal, and uses GPS analysis module to calculate positioning data (longitude, latitude, time, speed, direction) and status. Data (alarm information) and so on. After uploading the analyzed information and data to the background monitoring server in a specified format for processing, besides uploading GPS positioning information, the mobile terminal can also upload the XML file to the server for processing by means of GPRS channel. The server can parse the channel protocol, and the GPRS channel can transmit the control information and service information to the mobile terminal. Ultimately, it realizes the positioning and monitoring of users'mobile phones and other services with high accuracy, timeliness and convenience.

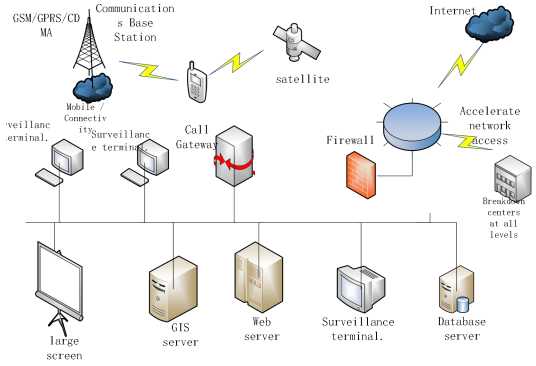

Fig.1 Map of GPS positioning

B.Application Framework Layer of GPS

The application framework of Android OS provides API packages related to GPS. These API packages are collectively referred to as the application framework layer of GPS. Under the frameworks / folders in the Android source directory, this application framework layer provides a large number of API interfaces for the upper GPS application software, mainly providing the required functions, such as Location, Location Manager, Location Provider, Location Listener and Critieria. The following table shows the important interfaces and classes in the framework layer of GPS application in Android operating system [6-7].

Table 2 Important Interfaces and Classes in GPS Application Framework Layer

Type	Name	Function
Interface	GPS Status Listener	receive notifications when GPS status changes
	Location Listener	Notification issued by Location Manager when the receiving location changes
Classes	Adress	Address Information Class
	Criteria	Select provider
	Geocoder	Geographically coded information
	GPS Status	Obtaining GPS status
	Location	Geographic Location Information
	Location Manager	Acquisition and operation of GPS system services
	Location Provider	abstract class

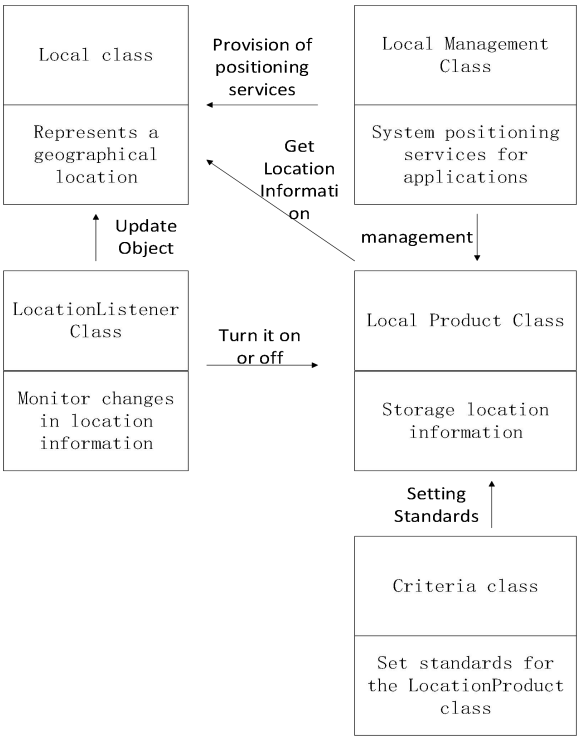

Fig.2 Classes in GPS Application Framework Layer

III. Realization of Seismometer Location with Different Array Patterns

A.Realization of GPS Single Point Positioning

The Android application framework provides the Location Manager class for the functions of GPS. All GPS related services and objects are generated by the object. The development of GPS application layer software can be completed through the Location Manager class and several other auxiliary classes.

In the programming of GPS positioning application layer software, the first step is to obtain the Location Manager object. As long as the application layer software obtains the Location Manager, it can obtain the relevant services and objects of GPS positioning by calling his method. After obtaining the Location Manager object, we can set its parameters, set the accuracy through Criteria object, whether it needs altitude, whether it needs orientation, whether it allows operators to charge, whether it is low energy consumption, etc. Then the location information is obtained by specifying its Location Provider, which is represented by the Location object. Then the longitude and latitude data source and update frequency are set by requested Location Updates () function. Location Manager allows two ways to acquire location information, one is through GPS hardware module to acquire location information, and the other is through mobile network to acquire current location information from base station[8] .

The flow chart of GPS single point positioning is shown in the following figure.

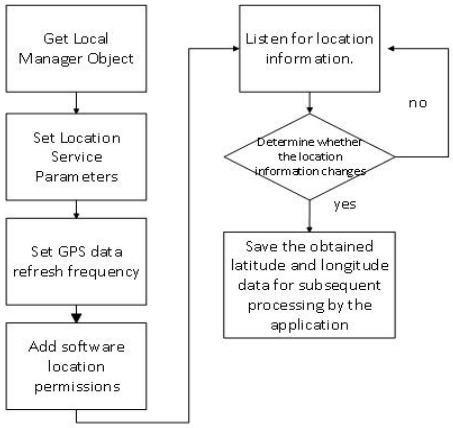

Fig.3 Map of Location flow chart

B.Realization of Multiple Array Array Patterns

In the process of array arrangement of seismic instruments, the existing one-dimensional positioning can not meet the requirements of experiments. In order to more intuitive and convenient array arrangement of seismic instruments, more and more intelligent terminals using Android system are adopted, and their portability and interconnection are maintained to the greatest extent. More importantly, it serves the sensor arrangement of seismograph, so that individuals can use it more accurately and conveniently. The following three types are listed: "L" type, straight line type and triangle type[9-10] .

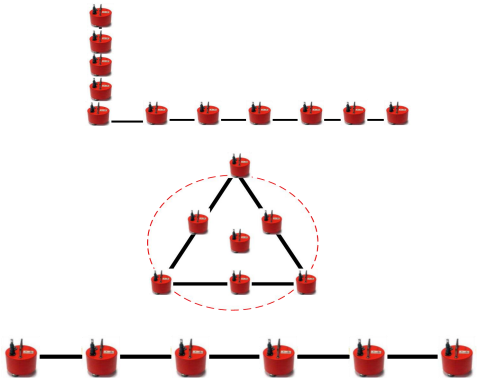

Fig.4 Map of Multiple Array Pattern

Because of the limited space, only "L" type is illustrated. After determining its longitude and latitude and inputting the interval distance, the Calculator Tool function and the interval distance can be used to calculate the precise coordinates of the corresponding interval points in longitude or latitude. The code for implementation is as follows [11-13]:

```
LatLng point = CalculatorTool.
computerThatLonLat(Lon,lat,0,distance*1.0/num*i);
aMap.addMarker(new
```

MarkerOption(point).title("L1-"+i).snippet(point(point.latitude+","+point.longtude)

IV. Testing and Result Analysis

In order to verify the reliability and practicability of the program, field measurements are carried out with software in the field[14-15].

Table 3 test result

Coordinate code	Distance/M	longitude	latitude
L1-1	500	43.8847801802	125.3082432725
L1-2	500	43.8862801951	125.3082432725
L1-3	500	43.8862801951	125.3082432725
L2-1	500	43.8834639811	125.3104599225
L2-2	500	43.8834639811	125.3125365423
L2-3	500	43.8834639811	125.3146077674

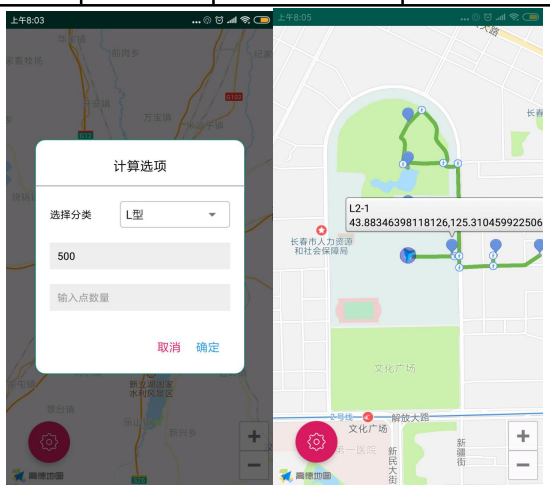

Fig.5 Software operation effect and output result diagram

According to the real data obtained from experiments and the particularity of "L" structural structure, the latitude of "L1" series points is the same, and the longitude of "L2" series points is the same. Therefore, the GPS seismograph positioning system designed in this paper can achieve the desired effect and the experimental data are accurate.

V. Conclusion

This paper analyses the architecture of Android development platform and its advantages, as well as its convenience in smartphone development. This paper discusses the design and implementation of GPS navigation and positioning machine-related applications on Android smart phone platform by using object-oriented programming technology.

References

[1] Tian Yang. Design of wireless GPS positioning system based on Android[D].Southeast University,2016.

[2] An Hengliang. Research and Design of GPS Navigation System in Vehicle Terminal Based on Vehicle Networking[D].Chang'an University,2016.

[3] Zhang Wenfei,Qian Shuguang,Zhu Kejia,Xu Huan,Qian Jin.Application of Android in Embedded Vehicle Navigation System [J].Electronic Testing,2015(07):83-86.

[4] Yuan Si, Liu Xiaodong. GPS Transplantation Based on Android[J].Electronic Design Engineering, 2015, 23(07):86-89.

[5] Zhang Sheng. Research and Development of GPS Application System Based on Android [J].Information Communication,2015(01):116.

[6] Wang Ting. Design and Implementation of Location Service Application Based on Android Intelligent Terminal [D]. Xi'an University of Electronic Science and Technology,2014.

[7] Cao Dongxing. Design of mobile monitoring and measurement system based on GPS [D]. Xi'an University of Electronic Science and Technology,2014.

[8] Li Xinze. Design and Implementation of GPS Module Based on Android [D]. Zhengzhou University,2013.

[9] Liu Shengqian, Chen Liding, Ren Zhigang. Research on Android Mobile Platform and GPS Application Service [J].Information Technology,2012,36(01):82-85.

[10] Wang Hao. Programming of GPS Positioning Based on Windows CE Simulator [J].Journal of Jianghan University (Natural Science Edition),2011,39(01):54-56.

[11] Qin Chao, Jiang Liangjun, Cai Yongxiang. Design and development of mobile terminal GPS measurement system based on Android [J],2011(01):64-67.

[12] Zhou Yuan, Zhang Qingquan, Lin Fuming. Design and research of positioning terminal software based on GPS mobile phone [J].Surveying, mapping and spatial geographic information,2010,33(05):106-111.

[13] Anita Zhang. Application Design of Android Mobile Web Map Service [D]. Nanchang University,2010.

[14] Shu Xianhua. Design of Mobile Web Map Service Based on Android Platform [D]. Dalian Maritime University,2009.

[15] Gonglei. Development of GPS Surveying System Based on Android [D]. Nanchang University,2008.

Airborne Geophysical Data Acquisition System Based on GPS Trigger

Li Jian, Liu Wei, Zhou Hao, Teng Fei
(College of Instrument Science and Electrical Engineering ,Jilin University ,Changchun 130021,China)

***Abstract*—This paper designs an aeronautical geophysical data acquisition system based on GPS second pulse trigger technology. It uses STM32 and FPGA as the control core to drive 24-bit high-speed AD module, FIFO memory module, SD memory module, three-axis gyroscope module and GPS timing module. A single-channel geophysical data acquisition system based on GPS triggering is implemented. After testing, the system has high synchronization precision and can continuously record and save valid data continuously. It provides a certain technical basis for expanding the multi-channel data acquisition system in the future.**

***Key words*—data acquisition gyroscope GPS FIFO SD wireless transmission**

I.INTRODUCTION

GROUND-SPACE cooperative time-frequency geodesy system is an important research achievement of Professor Lin Jun's team in our college. It has reached the international leading level. At present, the signal receiving terminal of the system equipment adopts the scheme of industrial computer driving acquisition card, as shown in Fig.1 [1][2]. The advantages of this scheme are stable performance, convenient upgrade of functions later, but the disadvantages are large volume and weight, high power consumption, short duration, high cost and complex operation. Therefore, this paper designs a time-frequency integrated signal acquisition system based on GPS second pulse triggering technology, which realizes the miniaturization and portability of ground-to-air electromagnetic receiver. In the future, single channel can be expanded to multi-channel by upgrading the system for higher data acquisition rate.

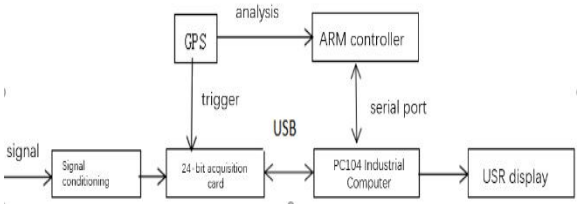

Fig 1 Block diagram of the ground-to-air detection system

II. DESIGN SCHEME

A. System Design

The block diagram of ground-space electromagnetic time-frequency integrated signal acquisition system based on GPS second pulse triggering technology is shown in Fig. 2.

Firstly, the system receives the GPS second pulse signal through the GPS receiving device as the reference signal of the synchronization chip, and triggers the AD acquisition signal data by using the digital phase-locked loop inside the chip and outputting the reference signal in phase with the second pulse. GPS information is analyzed, gyroscope data is received, and time, latitude, longitude and attitude information are combined with effective signal data into FIFO cache. STM32 microcontroller continuously reads the buffered data in FIFO and sets up TXT file according to the acquisition time to store the data in SD card.

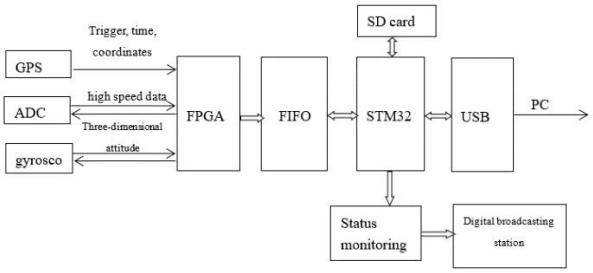

Fig.2 Overall block diagram of the data acquisition system

III. DESIGN OF SYSTEM HARDWARE

A. GPS signal acquisition

The LEA-6t GPS module produced by U-blox company is used in this system. The module has small size and high sensitivity. It can provide users with time, longitude and latitude, and the number of satellites used[3]. This module supports the complete NMEA protocol, and the system mainly parses the commonly used "GPGGA" format information.

a.Analysis of GPS Protocol

The GPS signal received by the system port is serial data, and the program is written to store the data bit by bit in the corresponding array. Different kinds of information in GPGGA format signal are separated by commas. The system determines the meaning of comma data between

two commas by judging the order of commas in the data string whose header is GPGGA. According to the need, information such as time, latitude, northern and southern hemispheres, accuracy, Eastern and Western hemispheres, and the number of analysis satellites are stored in the corresponding array to realize the accurate transmission of GPS data. The parsed valid information is shown in Figure 4.

Because the GPS module needs to receive satellite signals, it is necessary to carry out experiments in an open field, otherwise the correct GPS data can not be received. At the same time, because the collected GPS time is UTC time, in order to facilitate observation, it is necessary to set up a program to convert the collected time information into local Beijing time. The results of GPS signal acquisition are shown in Fig. 5.

b.Secondary Pulse Triggering Technology

Because the ground-to-air electromagnetic transceiver system requires very high synchronization accuracy, this design adopts the GPS second pulse triggering scheme, sets the output frequency of the GPS module pulse to 1Hz, and triggers AD by the rising edge of the output signal for data acquisition [4] –[7].

```
07:51:03  $GPGGA,075103.00,4352.85384,N,12518.07725,E,1,07,1.86,237.6,M,10.5,M,,*5A
07:51:04  $GPGGA,075104.00,4352.85386,N,12518.07727,E,1,07,1.86,237.6,M,10.5,M,,*5D
07:51:05  $GPGGA,075105.00,4352.85391,N,12518.07731,E,1,07,1.86,237.7,M,10.5,M,,*5C
07:51:06  $GPGGA,075106.00,4352.85398,N,12518.07736,E,1,07,1.86,237.7,M,10.5,M,,*51
07:51:07  $GPGGA,075107.00,4352.85402,N,12518.07738,E,1,07,1.86,237.8,M,10.5,M,,*55
07:51:08  $GPGGA,075108.00,4352.85404,N,12518.07740,E,1,07,1.86,237.9,M,10.5,M,,*52
07:51:09  $GPGGA,075109.00,4352.85401,N,12518.07740,E,1,07,1.86,237.9,M,10.5,M,,*56
07:51:10  $GPGGA,075110.00,4352.85406,N,12518.07742,E,1,07,1.86,238.0,M,10.5,M,,*5D
07:51:11  $GPGGA,075111.00,4352.85407,N,12518.07741,E,1,07,1.86,238.1,M,10.5,M,,*5F
07:51:12  $GPGGA,075112.00,4352.85408,N,12518.07742,E,1,07,1.86,238.2,M,10.5,M,,*53
07:51:13  $GPGGA,075113.00,4352.85410,N,12518.07744,E,1,07,1.86,238.3,M,10.5,M,,*5C
07:51:14  $GPGGA,075114.00,4352.85413,N,12518.07745,E,1,07,1.86,238.4,M,10.5,M,,*5E
07:51:15  $GPGGA,075115.00,4352.85416,N,12518.07747,E,1,07,1.86,238.5,M,10.5,M,,*59
07:51:16  $GPGGA,075116.00,4352.85427,N,12518.07752,E,1,07,1.86,238.5,M,10.5,M,,*5C
```

Fig.4 Valid data after GPS signal analysis

Fig. 5 The results of GPS signal acquisition (display latitude, accuracy, number of analytic satellites, time by row)

B.AD converter

a．AD7765

The system uses AD7765 analog-to-digital converter, which is a high-performance 24-bitΣ-ΔADC. The dynamic range is 115 dB at 78 kHz output data rate, 112 dB at 156 kHz output data rate and 156 kHz maximum complete filter output word rate. The over-sampling ratio of the analog-to-digital converter is 128×/256×. The over-sampling has low power consumption mode and SPI serial bus, and the on-chip differential amplifier. It has high sampling accuracy and fast speed, and is suitable for data acquisition system [8][9].

b. AD Data Acquisition

The system uses FPGA to control enable, read and clock signal lines of the chip. Firstly, the system defines the port allocation of input and output, sets various working modes of AD7765, and compiles declarations of signal frame and address bus. Then the event state of ADC and its control instructions are compiled. The trigger acquisition [10] is completed by detecting the rising edge of second pulse waveform, and the signal receiving module is set up to transmit the collected effective signal. After testing, the content of AD sampling is basically realized. The schematic diagram of AD7765 module is shown in Figure 6. The physical diagram of the module is shown in Figure 7.

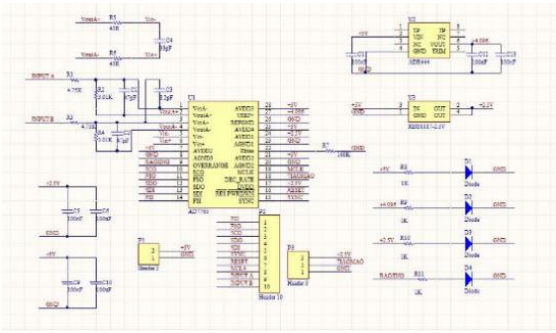

Fig.6 AD7765 module circuit schematic

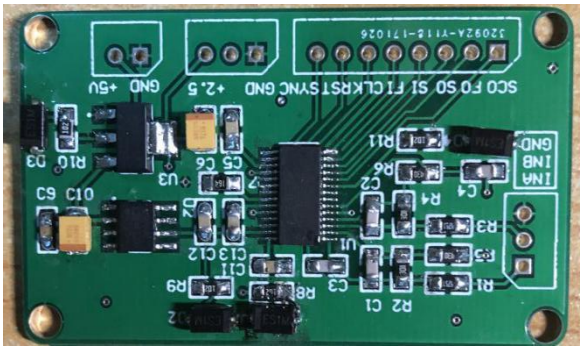

Fig.7 Module physical map

C.FIFO Data Caching

Because of the fast acquisition speed and the large amount of data collected by the system, and the high-speed data collected by the FPGA need to be transmitted to STM32, the data processing speed of STM32 can not keep up with the data output speed of the front-end FPGA, so the signal transmission across the clock domain is needed. In order to prevent data loss and facilitate storage, the collected data must be pre-stored before transmission. FIFO's full English name is First In First Out, that is, first in first out. FIFO used in FPGA is a first-in-first-out buffer for data storage. It is often used for data caching or high-speed asynchronous data interaction, or so-called cross-clock domain signal transmission.

a.FIFO Selection

According to the clock domain of FIFO, FIFO is divided into synchronous FIFO and asynchronous FIFO. Synchronized FIFO refers to the reading clock and writing clock being the same clock. Read and write operations occur at the same time as the clock arrives. Asynchronous FIFO refers to the inconsistency of read-write clocks, which are independent of each other. Synchronized FIFO is often used for data caching of synchronous clocks. Asynchronous FIFO is often used for data signal transmission across the clock domain. Asynchronous FIFO can synchronize data in different clock domains to the required clock domain, so asynchronous FIFO is adopted.

Asynchronous FIFO is a first-in-first-out memory. First-in-first data is read out. Read and write clocks are independent of each other. Asynchronous FIFO has two sets of data lines. It can read and operate at one end while writing at the other, and complete data caching at the same time of data sequential transmission.

b.Asynchronous FIFO Architecture

Asynchronous FIFO includes write clock domain and read clock domain. The core of asynchronous FIFO is a memory unit composed of two-port RAM. Accessing FIFO requires no address line, only data line and read-write control signal line. In the Write Clock Domain, the Write Port corresponds to the Write Data Signal and the Write Control Signal, and the Written Data is stored in the dual-port RAM. In the Read Clock Domain, the Read Port corresponds to the read data signal and the control signal, and the data is read out from the dual-port RAM and sent to the next level.

The most important control signals of asynchronous FIFO, Full, Empty, Almost Full, and Almost Empty, are generated by comparing write addresses with read addresses. The internal structure of the asynchronous FIFO memory is shown in Figure 8. To distinguish the empty/full state of asynchronous FIFO, binary read pointer and write pointer should be compared. The read and write pointer values in FIFO accumulate continuously with the continuation of the read and write operation, and return to the loop again when the counter is full.

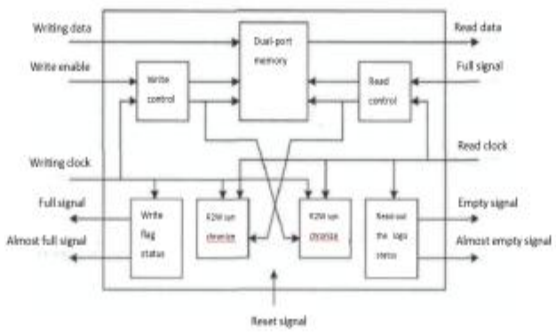

Fig. 8 Asynchronous FIFO memory internal structure

c.Implementation of Asynchronous FIFO

In order to simplify the system structure, the internal storage resources of the FPGA can be configured according to the need. In this design, the asynchronous FIFO is realized by internal RAM of the FPGA. The width of the data is 24 bits, and the depth is 1024. The effective data collected by the system is written to the asynchronous FIFO by 50MHz clock control. After the data is cached by the asynchronous FIFO, STM32 reads out the data from the asynchronous FIFO and completes the buffering function of FIFO for the collected data.

D. Data Storage

SD cards are non-volatile, small in size, simple in protocol, low in power consumption, and low in cost. Since the amount of data collected is large and the data collected by the system needs to be saved, a large-capacity memory SD card is used as a storage medium for data. In this system, the role of the SD card is to collect data records, data playback, for off-line analysis of data and fault diagnosis of the system.

a. SD card storage method

From the physical layer, the data is stored on the SD card sector. If there is no file system support, the PC desktop system needs software to identify the data, and the binary raw data is obtained. The data needs to be compared with the ASCII code table. Pre-processing, so in order to facilitate data exchange, the FAT file system is built on the SD card, so that the data can be accessed under the PC desktop system. This system uses FatFs file system, which is an open source file system in foreign countries. It is specially developed for embedded systems. The code size is small, small data buffer processing and direct reading and writing of big data make it have excellent read and write speed. And with good portability and stability, it is especially suitable for this system.

b.SD card workflow

This system uses the SD card as a storage module, and the creation, writing and reading of files are implemented using the FatFs system. In order to conveniently view the stored data, the design names the folder name and file name in units of time, and collects the time data, latitude and longitude, number of parsed satellites, and posture data to create a txt file according to the collection time and store it. The SDIO bus and the faster transfer of multiple blocks of read and write operations greatly increase the file storage and read speed, thus achieving high-speed storage of collected data.

E. Attitude information collection

Because the system needs to be mounted on the drone platform, and the tilt of the aircraft during flight causes errors in signal acquisition, the attitude of the receiver needs to be detected and recorded.In the data processing, by combining the collected signals with the aircraft

attitude data, the compensation of the received signal is realized, thereby reducing the error of the system collecting data.The attitude information acquisition module uses MPU-6050, which is a low-cost three-axis gyroscope module. The working voltage is 3-5v, the power consumption is small, the volume is small, and the accuracy meets the system requirements. The working principle is that the gyroscope and the acceleration sensor are subjected to a data fusion algorithm, and finally the direct angle data is obtained. This gyroscope module uses standard IIC serial bus communication. The three-dimensional data of the gyroscope is received by the FPGA, and the data is combined with the external information collected by the AD and transmitted.

F. Wireless Detection System

Since the system is mounted on the aircraft, the experimenter needs to observe the running status in real time [15], and send the aircraft's power, parsing the satellite number, and attitude data to the tUse XBEE PRO 900HP S3B digital radio, module frequency range 902~928MHz, default maximum transmit power 250Mw/24dBm.

According to official data, the module we use has a maximum transmission distance of 6.5KM in motion and is used with a dedicated base, either on the airborne or on the ground.There are 20 pins on the module to connect the ports. Each port has different functions. According to the purpose, we need to complete the one-way data transmission. The power supply VCC terminal, GND ground terminal, TX transmitter terminal and RX on the module are performed. The receiving end is similar to the GPS module.errestrial receiver for monitoring in real time through the digital radio.

IV . EXPERIMENTAL TEST

The sinusoidal signal generated by the function signal generator is used as the signal source, and the rising edge of the second pulse triggers the AD acquisition signal. According to the AD characteristics, in order to make the collected data amount rich enough, the display is intuitive and easy to debug, the sampling rate is configured to be 156kSPS, and the valid signal data received by it is received and stored and sent to the upper computer end. The host computer uses the virtual instrument to establish a display window to realize the basic display of the signal, and the test result is basically consistent with the input signal.

The AD acquisition signal diagram is shown in Figure 9. The experimental results show that the system achieves the expected goal, and finally realizes GPS signal analysis, second pulse trigger AD acquisition, transmission and storage of each valid data, wireless detection and other functions.

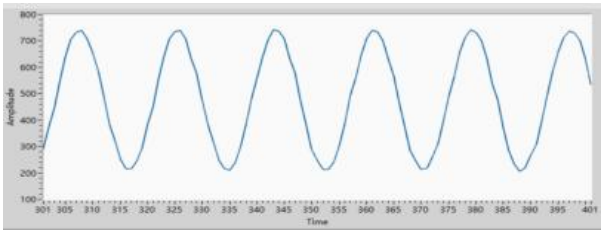

Fig.9 acquisition signal graph of AD7765

V. CONCLUSION

The system uses the GPS second pulse as the AD trigger source, combines the time signal, the attitude data and the effective signal to achieve the synchronization of the data transmission; the collected data is stored in the SD card through the FIFO buffer; the device status is wirelessly transmitted using the digital transmission station. Quantity, remote monitoring of receiving work status. Compared with the old ground-air detection system, the system is small in size, light in weight, cost-effective and easy to operate. It realizes the original system simplification of this expected goal and provides technical support for the development and improvement of the data detection system.

References

[1] Liu Lichao. Research on key technologies of networked controllable source audio magnetotelluric receiving system [D]. Changchun. Jilin University. 2014.

[2] Qi Lin. Key technologies and experiments of time domain aeronautical electromagnetic transmitter [D]. Jilin University, 2012.

[3] AA Basheer, AI Taha, A. El-Kotb, FA Abdalla, SO Elkhateeb. Relevance AEM and TEM to Detect the Groundwater Aquifer at Faiyum Oasis Area, Faiyum, Egypt[J]. International Journal of Geosciences, 2014, 05 (06).

[4] Yin Changchun, Zhang Bo, Liu Yunhe, Ren Xiuyan, Qi Yanfu, et al. Development status and prospects of aviation electromagnetic survey technology[J]. Chinese Journal of Geophysics, 2015, 58 (08)): 2637-2653.

[5] Lei Dong, Hu Xiangyun, Zhang Sufang. The Development Status of Aviation Electromagnetic Method[J]. Prospecting Research, 2006(01): 40-44+53.

[6] Wu Chengping. Thoughts on Promoting the Development of Aviation Electromagnetic Law in China [A]. Youth

Work Committee of China Geological Society. Proceedings of the First National Youth Geology Conference [C]. Youth Work Committee of China Geological Society: 2013: 2.

[7] Li Nan. Research on time domain aviation electromagnetic data preprocessing technology [D]. Jilin University, 2010.

[8] Song Guoyang. Application of Transient Electromagnetic Method in Geological Exploration[J]. Coal Technology, 2009, 28(11): 136-137.

[9] Cui Zhiqiang, Zhai Zhili, Li Junfeng, Li Fei, Gao Weidong. Current status and prospects of R&D and application of unmanned aerial vehicle geophysical exploration technology[J]. Geophysical and Geochemical Exploration and Calculation Technology, 2016, 38(06): 740-745.

[10] Bernhard Siemon, Annika Steuer, Angelika Ullmann, Margarete Vasterling, Wolfgang Voß. Application of frequency-domain helicopter-borne electromagnetics for groundwater exploration in urban areas[J]. Physics and Chemistry of the Earth, 2011, 36(16) .

[11] Liu Wei. Application prospect of aviation electromagnetic method in railway exploration [A]. Engineering Geological and Subgrade Committee of Railway Engineering Branch of China Railway Society. 25th Annual Meeting of Engineering Geology and Subgrade Professional Committee of Railway Engineering Branch of China Railway Society Proceedings of the Academic Exchange Conference [C]. China Railway Society Railway Engineering Branch Engineering Geology and Subgrade Professional Committee: 2016: 4.

[12] Wang Weiping. Development and application of frequency domain aviation electromagnetic method [C]. China Geophysical, 2011: 1.

[13] H. Leväniemi, D. Beamish, H. Hautaniemi, M. Kurimo, I. Suppala, J. Vironmäki, RJ Cuss, M. Lahti, E. Tartaras. The JAC airborne EM system: AEM-05 [J] Journal of Applied Geophysics, 2007, 67(3).

[14] David Beamish. An assessment of inversion methods for AEM data applied to environmental studies [J]. Journal of Applied Geophysics, 2002, 51(2).

[15] Wan Jianhua, Xiong Shengqing, Fan Zhengguo, He Wei. Analysis of the status quo and future work of national aviation geophysical exploration work [J]. China Mining, 2011, 20 (S1): 151-154+166.

Rock Stress Measurement System Based on Resistance Strain Gage

Dai Kaifang, Zhang Zehua, Lu Mei
（jilin university instrument science and engineering institute,changchun,130021）

***Abstract*—This design uses a resistive strain gage to measure stress and centrally analyze the acquired data in the form of wireless transmission. Analyzing the characteristics of various short-range wireless communication technologies, it is considered that short-range wireless communication based on Zigbee technology is an effective way to collect terminal information transmission in wireless bridge detection system. As a result, Zigbee wireless transceiver module based on CC2530 chip is selected to realize effective wireless transmission of information. The experimental results show that the sensitivity of the rock stress measurement system meets the design requirements.**

***Keywords*—Static stress Resistance strain gage Zigbee technology CC2530**

I. INTRODUCTION

STRESS is the internal force that interacts between parts of an object when the object deformed due to external factors (force, humidity, temperature field changes, etc.).To resist the external cause and try to make the position restored to the position before the deformation, and the internal force per unit area at a certain point of the section to be examined becomes the stress.

Strain is the amount of mechanics used to describe the degree of deformation at a point, expressed as ε.

The stress measurement of rock mainly measures the static and dynamic stress of the rock. The static stress and dynamic stress are classified according to the strain rate, that is, the unit time dependent variable. The static stress is mainly in the range of strain rate less than 10-1 εs-1[1].The static stress and static mechanical parameters of rock are important physical quantities in rock mechanics and petrophysics and are the basis of many analyses. Therefore, it is necessary to measure the static stress of the rock to obtain static parameters.

Electrical measurement is a relatively common method of stress measurement. Measurement with strain gauges is also an effective measure of stress and strain in medium and low frequency. The traditional stress detection system collects data by wire. The wiring work is cumbersome and inconvenient to operate. There are certain limitations in practical applications.

In this paper, the design of a rock stress measurement system based on resistive strain gauges can effectively solve the problems of complicated wiring and inconvenient operation of traditional stress detection systems, and can be used for static stress detection.

II. SYSTEM DESIGN

A.Principle Analysis

This project mainly measures the static stress and strain of rock, and obtains static Poisson's ratio and static Young's modulus of static mechanical parameters.

The Poisson's ratio refers to the ratio of the transverse positive strain to the absolute value of the axial positive strain when the rock is subjected to uniaxial tension or compression. It is also called the transverse deformation coefficient, which is the elastic constant reflecting the lateral deformation of the material. The static Poisson's ratio is passed by the formula μ = Δε1 / Δε2.Δε1 is the axial strain increment of the rock sample, and Δε2 is the lateral strain increment of the rock sample.

Young's modulus is a physical quantity that describes the ability of a solid material to resist deformation and is defined as the ratio between uniaxial stress and uniaxial deformation within the range applicable to Hooke's law. The static Young's modulus e is calculated by the formula, f/s is the force per unit area of the rock sample, δl is the shape variable in the direction of the force of the rock sample, and l is the original length of the rock sample.

This design uses common electrical measurement methods for measurement. The electrical measurement method is easy to perform amplification, filtering and other operations, facilitating high-precision dynamic measurement and even transient measurement. Young's modulus and Poisson's ratio are obtained by analyzing the corresponding ratio of stress and strain. Therefore, the Wheatstone bridge formed by the strain gauge in the sensor part is used as a conversion circuit to convert the stress in the corresponding direction into a voltage

signal for collection and processing.

B.Overall Design

The whole system consists of two parts: upper computer and lower computer. The system block diagram is shown in Fig. 1.

The host computer uses a laptop or desktop computer as the terminal processing module to complete the command delivery and data processing for all data collection nodes. The lower computer includes three modules: a front-end module, a wireless communication module and an embedded system. The embedded system receives the command to complete the wireless signal transmission and reception control of the wireless communication module, and can perform necessary conversion and pre-processing on the tested data signal. The front-end acquisition module can be set up multiple times, and the number can be controlled by itself to realize networked multi-node measurement to meet the measurement requirements.

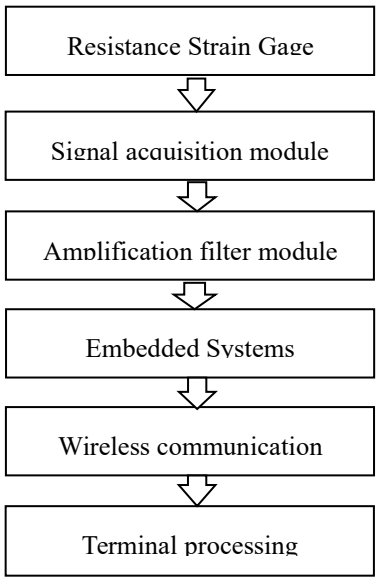

Fig.1 System block diagram

III. HARDWARE DESIGN

A.front acquisition module

The hardware circuit of the front-end acquisition module is shown in Fig.2. It consists of a resistive strain gauge, a signal acquisition module and an amplification filter module . The sensitive component in the circuit is a resistive strain gauge. The strain gauge with a high precision resistance and a sensitivity coefficient of 2.0 is used to form a Wheatstone single-arm bridge circuit. y1 is a resistance strain gauge, r4=r5=r13, the initial resistance of each bridge arm is equal, and the error does not exceed 1‰.

The derivation process of the output voltage is as follows:

$$U_0 = \mathrm{E}\frac{R_1R_4 - R_2R_3}{(R_1 + R_2)(R_3 + R_4)} \tag{1}$$

When U0=0, the bridge is in equilibrium, with R1R4=R2R3

For a single-arm bridge, if R1 is the working strain gauge, R2,R3, R4 are fixed resistors, and E is the bridge power supply. When r1 has an increment ΔR1, the bridge output is:

$$\mathrm{Uo} = \mathrm{E}\frac{(R_1 + \Delta R_1)R_4 - R_2R_3}{(R_1 + \Delta R_1 + R_2)(R_3 + R_4)} \tag{2}$$

After finishing, you can get:

$$\mathrm{Uo} = \frac{n}{(1+n)^2}\frac{\Delta R_1}{R_1}E \tag{3}$$

Where n is the bridge arm ratio n=R2/R1, n=1 in this design, and the following relationship exists for resistive strain gauges:

$$\frac{\Delta R}{R} = K\varepsilon \tag{4}$$

Where k is the resistive strain gauge, the sensitivity factor is a known amount, and the strain value can be calculated by combining the above formula:

$$\varepsilon = \frac{1}{K}\frac{(1+n)^2}{n}\frac{Uo}{E} \tag{5}$$

The Young's modulus is based on the isotropic linear elasticity theory, assuming that a uniform distribution is applied, then$\sigma_{11}=\sigma_{al}$, where σ_{al} The stress on the axial direction of the standard aluminum sample. The Young's modulus and Poisson's ratio of the rock sample are:

$$\sigma_{11} = E_{rx}\varepsilon_{11}^{rx} = \sigma_{al} = E_{al}\varepsilon_{11}^{al} \tag{6}$$

$$\mathrm{E}_{rx} = E_{al}\frac{\varepsilon_{11}^{al}}{\varepsilon_{11}^{rx}} \tag{7}$$

$$\mu = -\frac{\varepsilon_{22}^{rx}}{\varepsilon_{11}^{rx}} \tag{8}$$

σal, the stress on the axial direction of the standard aluminum sample, rx representing rock, ε11 represents axial strain, ε22 represents aluminum sample is a known constant of 69 GPa.

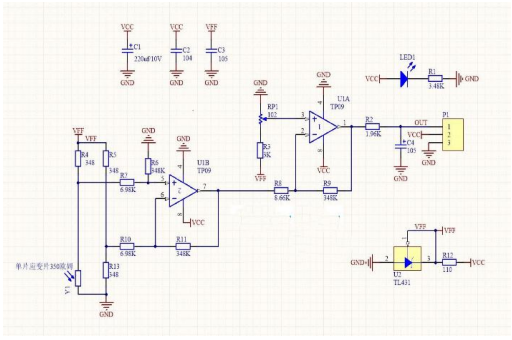

Fig2 Acquisition Hardware Circuit

The voltage outputted by the single-arm circuit bridge is further processed by the filter amplifier circuit, and the amplified data is collected by the MSP430 microprocessor, and the collected multiple signals are sent to the STM32F103 microprocessor for aggregation by the Zigbee wireless communication module. Then the data is transmitted to the host computer through the serial communication for saving and processing

B.Wireless transmission module

The CC2530 is a true system-on-a-chip (SoC) solution for 2.4-GHz IEEE 802.15.4, ZigBee and RF4CE applications. It is capable of building powerful network nodes at very low total material costs[2].

ZigBee technology has powerful networking capabilities, which can form star, tree and mesh networks. You can select the appropriate network structure according to the actual project needs. The topology structure is shown in Fig 3:

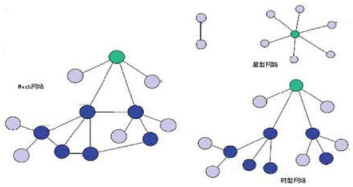

Fig3 Topology diagram

The star topology is the simplest form of topology. It consists of a Co-ordinator node and a series of End Device nodes.Each End Device node can only communicate with the Co-ordinator node. If you need to communicate between two End Device nodes, you must forward the information through the Co-ordinator node[3-4].

In this design, because there are fewer nodes and the functions are not very complicated, the star topology is selected to meet the design requirements.

IV. HOST COMPUTER SYSTEM

This design uses a notebook computer as the host computer, using LabVIEW2017 Chinese version programming, LabVIEW serial communication can use VISA (Virtual Instrument Software Architecture) node configuration to achieve communication with the lower computer. VISA is a general term for standard I/O function libraries for instrument programming and related specifications. This I/O function library is generally called VISA library. The VISA library is placed in the computer system and is a software layer connection between the computer and the instrument for realizing the manipulation of the instrument. VISA is an industry standard for the development of instrument drivers that can communicate with instruments using the same operations for different interfaces. Because the instrument driver in LabVIEW is mainly used for writing, you need to install the VISA driver before programming the serial port driver. Otherwise, serial communication cannot be realized[5-7].

Visa can realize the uploading of the data of the lower computer, and can also set the stress collection channel of the lower computer through the upper computer; real-time display of data, history display, data analysis and management[8]. After the communication between the upper and lower machines is successfully established, real-time monitoring and command control of the lower computer can be realized by the upper computer, and the data collected by the lower computer in real time should also be uploaded to the upper computer[9].

V. UPPER COMPUTER COMMUNICATES WITH LOWER COMPUTER

A.Communication interface

The computer and the single-chip microcomputer should perform data communication. In the case of close-range data communication[10], the RS232 serial communication standard is commonly used.RS232 is a serial physical interface standard developed by the Electronic Industry Association (EIA).RS is an abbreviation of English "Recommended Standard" and 232 is an identification number. The RS232 bus standard has 25 signal lines, including a main channel and an auxiliary channel. In most cases, the main channel is mainly used. For general duplex communication, only a few signal lines are needed, such as one transmission line, one reception line, and one ground line. Because of the ease and universality of RS232, the serial communication standard used in this design is RS232, which meets the serial communication requirements required by the design.

B.PC software design

As shown in the figure, the serial port is configured through the visa configure serial port. The visa write is sent by the host computer to the microcontroller

through the serial port, and the visa read reads the data sent from the microcontroller. As a virtual instrument, you should have a friendly and convenient user interface. In order to facilitate the processing and preservation of the data, as well as the reflection of the initial data collection, the program designed real-time waveform display, data storage, channel selection and other functions.

VI. Test and Result Analysis

The hardware test of the distributed stress measurement system is mainly to test and analyze the sensitivity of the stress measurement[14]. The front-end acquisition system and the A/D converter in the ZigBee module are both 12-bit, the reference voltage is 3.3V, and the output voltage resolution is LSB= $\frac{Reference\ voltage}{2^N} = \frac{3.3}{2^{12}} = 0.81mV$. At this time, k=2, and E is 3.3v. The system uses one-arm measurement, and the bridge output ΔU= $\frac{EK}{4}\varepsilon_1$For the 1μV bridge output is 1.65μV, the total amplification factor is 1000, the output voltage is 1.65mV, and the corresponding resolution is 0.81/1.65=0.49με, so the design sensitivity can reach the requirement of 1με.

In the experimental measurement, the system outputs different voltage values under different stresses. The system real-time measurement of the upper computer interface is shown in Fig.4:

Fig4 PC interface

In this measurement, the system output voltage is calibrated by applying known different stress values. The system stress values and output voltage values are measured as shown in Table 5 below:

Table 1 Stress Value and Output Voltmeter

Voltage（mV）	Stress value (N/cm^2)
880	0
1125	2.5
1320	5.0
1582	7.5
1750	10.0
1990	12.5
2210	15.0
2370	17.5
2475	20.0
2522	22.5

The data is analyzed by Matlab (using three-time fitting) to obtain the relationship between the stress value and the output voltage value as shown in Fig. 5:

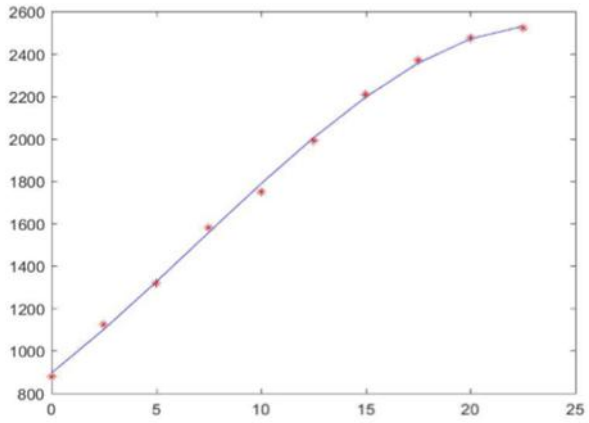

Fig5 Stress Value and output voltage curve

It can be seen from the relationship between the stress value and the voltage value that the stress value shows a good linear relationship with the output voltage value in the range of 0~15.0n. The stress value exceeds 15.0n and the output voltage value The linear relationship is weakened.

VII. Conclusion

This paper presents a resistive strain gauge system based on resistive strain gauge .The transmission path based on ZigBee wireless network, the data processing platform is based on Labview's rock stress measurement data acquisition system. The measurement principle, hardware design, upper and lower machine communication, and host computer program design are all described in detail. Through practical experiment debugging, the system has been successfully applied to rock stress measurement, meeting design requirements and achieving good results.

References

[1] Luo Nan, Sun Yunqiang, Lin Lirong, Wang Wen, Song Wei. Software Design of Distributed Strain Test System [j]. Science and Technology Information, 2011 (18): 255-256.

[2] María Viqueira Villarejo, Amaia Méndez Zorrilla, Begoña García Zapirain. A Stress Sensor Based on Galvanic Skin Response (GSR) Controlled by ZigBee. 2012, 12(5):6075-6101.

[3] Li Jianping,Li Juxia.Strain Measurement and Static Experiment Based on LabVIEW[J].Mechanical Engineering & Automation,2013(03):113-114+117.

[4] Jiasong Mu. A minimum physical distance delivery

protocol based on ZigBee in smart grid. 2014, 2014(1):1-10.

[5] Fu Liangrui, Zhu Baoliang, Hu Xiangchao, Fan Chengzhou, Li Yanxia. A multi-channel wireless static strain measuring device [j]. Instrumentation Technology and Sensors, 2017(11): 45-50+55.

[6] Ma Zhiyan.Design and Application of Strain Measurement System Based on LabVIEW[J].Machinery & Electronics,2014(05):62-65.

[7] Shengbo Sang, Xiao Fan, Xiaoliang Tang, et al. Portable surface stress biosensor test system based on ZigBee technology for health care. 2015, 29(4):798-804.

[8] Ke Zhipeng. Discussion on Resistance Strain Measurement [j]. Technology Wind, 2012 (11): 218.

[9] SU Liancheng,MA Lei,ZHAO Yun.Design of strain measurement and alarm system based on LabVIEW[J].四川兵工学报,2010,31(05):77-80.

[10] Seong Hoon Kim, Poh Kit Chong, Taehong Kim. Performance Study of Routing Protocols in ZigBee Wireless Mesh Networks. 2017, 95(2):1829-1853.

[11] Zhu Wenliang,Huang Xiuling,Fang Yu.Design of Stress and Strain Test System for Bogie Based on LabVIEW[J].Electric Locomotive & Urban Rail Vehicle,2012,35(01):68-70.

[12] Wang Pengliang,Ding Jinhua,Lei Xiaojing,Fu Qing.Design of multi-channel stress measurement system based on ZigBee[J].Journal of Dalian Polytechnic University,2011,30(04):281-284.

[13] Wu Rui. Research and design of wireless bridge stress sensor based on ZigBee[D]. Xi'an University of Science and Technology, 2011.

[14] Huang Qiao, Li Zhonglong, Sha Xuejun, Xu Yubin.Experiment of Bridge Wireless Test System Based on Strain Sensor[J].Journal of Tongji University(Natural Science), 2007(10):1322-1325.

Water quality evaluation and prediction algorithm based on T-S fuzzy neural network

Shanshan Li, Hanjia Zhang, Bosen Zhang
（Jilin university instrument science and engineering institute,changchun,130021）

***Abstract*—In order to make a reasonable quantitative evaluation of water quality, the T-S fuzzy neural network model is used to realize water quality evaluation, and the network model training is carried out with reference to surface water environmental quality standard GB3838-2002. Three water quality evaluation parameters of pH value, dissolved oxygen amount and conductivity of water were selected as model input, and water quality grade was used as model output. Use MATLAB to train and predict neural networks to achieve water quality rating of water bodies.**

***keywords*—T-S model; fuzzy neural network; water quality evaluation**

I. INTRODUCTION

So far, the water quality evaluation methods used by people have single factor evaluation method [1-2], fuzzy comprehensive evaluation method [3], artificial neural network method [4] and so on. The single factor evaluation method is simple to operate, but the one-way evaluation method of the one-factor evaluation method is often unable to comprehensively reflect the specific situation of the water body. There is not a quantitative evaluation of the water body status, and there is no strong difference between different water bodies. Comparability, in the fuzzy comprehensive evaluation method, the linear weighted average calculation is used to obtain the evaluation results, which are prone to distortion and jump. Artificial neural network is a novel mathematical modeling method with nonlinear mapping, parallelism, self-adaptation, self-learning and fault tolerance. It can solve the water quality evaluation problem that belongs to the mode design [5-6]. However, due to the ambiguity of water quality types and grading standards, artificial neural networks do not have the ability to recognize ambiguities, so sometimes the recognition results are incorrect. Therefore, some scholars have proposed using T-S fuzzy neural network model to study water quality [7-8]. The neural network and the fuzzy system are combined to construct a fuzzy neural network (FNN) [9]. The constructed FNN can directly encode the events described by the experts in language, and can use the language description to collect knowledge and introduce inspiration easily. Sexual knowledge can also track the reasoning process and make the weights in the network have obvious meaning. On the other hand, like other neural networks, it has a learning function, which can improve the accuracy of coding through learning.

In this paper, three indexes of pH value, dissolved oxygen content and conductivity of water are selected as the main parameters of water quality evaluation. Referring to the surface water environmental quality standard GB3838-2002, the T-S fuzzy neural network model was used for water quality evaluation under the MATLAB platform. The relative membership degree and neural network in the fuzzy theory are organically combined, taking into account the randomness and ambiguity of the water environment system, and can achieve a reasonable evaluation of the water quality level. Experiments show that the water quality of relevant waters is scientifically grasped, providing a theoretical basis for rational and effective monitoring and management of water resources.

II. T-S FUZZY NEURAL NETWORK MODEL [10-12]

A.Introduction To Fuzzy Mathematics

The most basic concepts of fuzzy mathematics are membership degree and fuzzy membership function. Among them, the membership degree is the degree of membership of the element u belonging to the fuzzy subset f, expressed by μf(u), which is a number between [0, 1]. The closer μf(u) is to 0, the smaller the degree to which u belongs to the fuzzy subset f; the closer to 1, the greater the degree to which u belongs to f.

B.T-S Fuzzy Neural Network Model

The T-S fuzzy neural network model was proposed by Takagi and Sugen in 1985[13]. The T-S fuzzy system is a fuzzy system with strong adaptive ability. The model can not only update automatically, but also continuously modify the membership function of the fuzzy subset. The T-S fuzzy neural network is divided into four layers: input layer, fuzzy layer, fuzzy rule calculation layer and output layer. Let x=[x1,x2,•••,xk] be the model input vector, which means that k in the

water environment is used as the parameter for water quality evaluation, and y is the model output result, indicating the water quality level. The constructed T-S fuzzy neural network structure is shown in Fig.1.

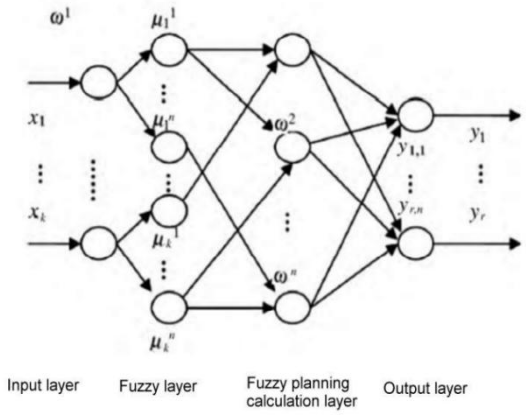

Fig.1. T-S fuzzy neural network structure

The T-S fuzzy system is defined by the following "if-then" rule form. In the case where the rule is Ri, the fuzzy reasoning is as follows:

$$R^{i}: If \ \text{x1 is } A_1^i, \text{x2 is } A_2^i, \bullet\bullet\bullet, \text{xk is } A_k^i \ \text{then}$$

$$y_i = p_0^i + p_1^i x_1 + \cdots + p_k^i x_k \tag{1}$$

A_j^i is the fuzzy set of the fuzzy system; p_j^i (j=1,2,•••,k) is the fuzzy system parameter; yi is the output obtained according to the fuzzy rule, the input part (ie the if part) is fuzzy, the output part(That is, the then part)is determined, and the fuzzy reasoning indicates that the output is a linear combination of inputs.

Assume that for the input quantity x=[x1,x2,•••,xk], the Gaussian function is selected as the membership function in the fuzzification layer, and the membership degree of each input variable xi is calculated according to the fuzzy rule:

$$\mu_{A_j^i} = \exp(-(x_j - c_j^i)^2 / b_j^i) \tag{2}$$

Where c_j^i, b_j^i are the center and width of the membership function, respectively; k is the input parameter; n is the number of fuzzy subsets.

The fuzzy degree is calculated for each membership degree in the rule layer, and the fuzzy operator is used as the multiplication operator to obtain the applicability ωi of each rule, which indicates the applicability of the input vector to the rule:

$$\omega^i = \mu_{A_j^1}(x_1) * \mu_{A_j^2}(x_2) * \cdots * \mu_{A_j^k}(x_k) \tag{3}$$

Calculate the output value yi of the fuzzy model based on the fuzzy calculation result:

$$y_i = \sum_{i=1}^{n} \omega^j (p_0^j + p_1^j x_1 + \cdots + p_k^j x_k) / \sum_{i=1}^{n} \omega^j \tag{4}$$

The input layer is connected to the input vector xi, and the number of nodes is the same as the dimension of the input vector. The fuzzification layer uses the membership function "(2)" to blur the input value to obtain the fuzzy membership value μ. The fuzzy rule calculation layer uses the fuzzy multiplication formula" (3)" to calculate ω. The output layer uses the formula" (4)" to calculate the output of the fuzzy neural network.

C.T-S Fuzzy Neural Network Learning Algorithm

The learning algorithm of fuzzy neural network is as follows:

Error Calculation:

$$e = \frac{1}{2}(y_d - y_c)^2 \tag{5}$$

Where y_d is the expected output of the network; y_c is the actual output of the network; e is the error of the desired output and the actual output.

Coefficient Correction:

$$p_j^i(k) = p_j^i(k-1) - \alpha \frac{\partial e}{\partial p_j^i} \tag{6}$$

$$\frac{\partial e}{\partial p_j^i} = (y_d - y_c)\omega^i / \sum_{i=1}^{m} \omega^i \cdot x_j \tag{7}$$

Where P_j^i is the neural network coefficient; α is the network learning rate; xj is the network input parameter; and ω^i is the product of the input parameter membership.

Parameter Correction：

$$c_j^i(k) = c_j^i(k-1) - \beta \frac{\partial e}{\partial c_j^i} \tag{8}$$

$$b_j^i(k) = b_j^i(k-1) - \beta \frac{\partial e}{\partial b_j^i} \tag{9}$$

Where c_j^i, b_j^i are the center and width of the membership function, respectively, and β is the membership function adjustment factor.

III. Model Building And Training

A.Model Establishment

The flow chart of the fuzzy neural network water quality evaluation algorithm based on T-S is shown in Fig.2.The fuzzy neural network determines the number of input and output nodes of the network according to the input and output dimensions of the training sample. Since the input dimension is 3 and the output data dimension is 1, the number of input nodes of the network is determined to be 3, and the output node is 1, according to the number of network input and output nodes, the number of membership functions is determined by multiple experiments to be 6, so the network structure constructed is 3-6-1, random initialization fuzzy membership function c, width b and coefficient P0-P3.

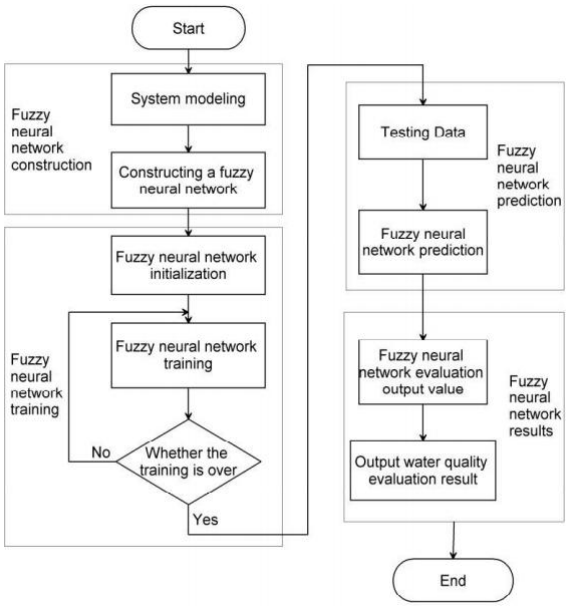

Fig.2. Fuzzy neural network water quality evaluation algorithm flow

The fuzzy neural network training uses the training data to train the fuzzy neural network, and generates 400 sets of training samples by randomly inserting the water quality index standard data to generate samples by the equal distribution method recommended by the literature [14], and randomly selects 350 sets of data as training samples. The remaining 50 sets of data were used as test data for the performance stability of the model. The standard data of water quality indicators used are from Table I, and the network is trained repeatedly for 150 times.

TABLE I Surface Water Environmental Quality Standards

Serial number	Indicator name	I	II	III	IV	V
1	PH	6.5-8.5				9
2	Dissolved oxygen≥	7.5	6	5	3	2
3	Conductivity (S/m)	0.005	0.05	1	5	>5

B.Training Data Prediction

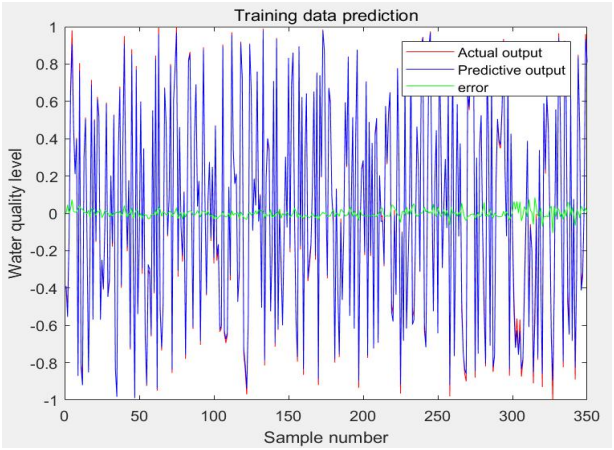

Fig.3.T-S fuzzy neural network training data prediction results

Using the generated 350 sets of data as training samples, the training data prediction graph shown in Fig. 3 is obtained. It can be seen from the figure that the model training error is small and the training effect is good.

C.Test Data Prediction

The performance of the trained T-S fuzzy neural network model is verified by using 50 randomly selected data, and the performance stability of the model is tested by the absolute value of the error.

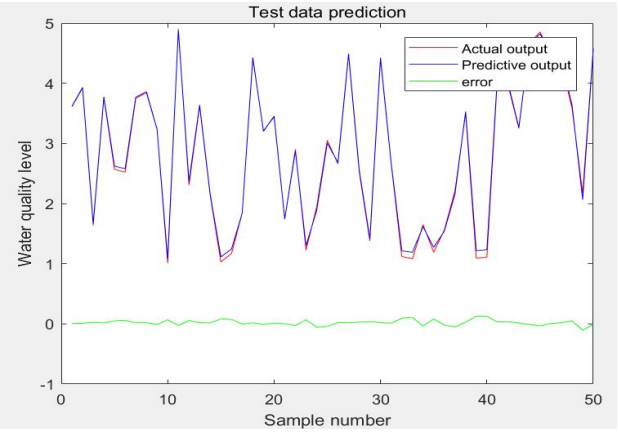

Fig.4.T-S fuzzy neural network test data prediction

It can be seen from the actual output and predicted output of Fig.4 that the predicted value of the T-S fuzzy neural network is better fitted to the actual value, and the absolute error curve fluctuates with a small

amplitude near the zero value, meeting the requirements of comprehensive evaluation of water quality.

IV. CONCLUSION

Although the fuzzy neural network is also a local approximation network, it is established according to the fuzzy system model. Each node and all parameters in the network have obvious physical meanings. Therefore, the initial values of these parameters can be determined based on the fuzzy or qualitative knowledge of the system, and then use the above learning algorithm can quickly converge to the required input and output relationship, which is the advantage of fuzzy neural network. At the same time, because it has the structure of a neural network, the learning and adjustment of parameters is relatively easy. In this paper, the T-S fuzzy neural network model is applied to water quality evaluation, which makes the advantages of both fuzzy system and artificial neural network, and solves the problem of randomness and ambiguity of water environment system. Since the network model has obtained training results with less error, it can make a reasonable evaluation of water quality.

References

[1] Wang Wenjing, Gao Pengcheng, Li Jie, et al. Water quality evaluation and trend analysis of typical inflow tributaries of Danjiangkou Reservoir[J]. Water Resources Protection,2016,32(3):127-130.

[2] Luo Fang, Wu Guorong, Wang Chong, et al.Application of Nemero Pollution Index Method and Single Factor Evaluation Method in Water Quality Evaluation[J]. Environment and Sustainable Development, 2016, 41(5): 87-89.

[3] Wei Wenjie, Zhang Xinhua, Luo Jizhong, et al. Application analysis of fuzzy comprehensive method in water quality evaluation[J]. Water Saving Irrigation,2014(9):46-49.

[4] Bian Jianmin, Hu Yuxin, Li Yusong, et al. Water Quality Evaluation of Liaohe Source Area Based on BP Neural Network[J]. Research of Soil and Water Conservation,2014,21(1):147-151.

[5] Lou Wengao, an artificial neural network model for seawater quality assessment [J]. Journal of Environmental Science [J]. 2001, 20(4): 49-53.

[6] Yang Hong, Li Risong. Establishment of artificial neural network model for water quality in the Yangtze River estuary and evaluation of its current status[J]. Journal of Shanghai Fisheries University, 2002, 11(1): 31-36.

[7] Gao Kai, Jia Wei. Evaluation of water quality in Hanzhong section of Hanjiang River based on T-S fuzzy neural network[J]. Microcomputer Applications, 2016, 32(2): 51-53.

[8] Zhang Wen, Wang Li. Analysis of Temporal and Spatial Variation Characteristics of Water Quality of Yinghe River Based on T-S Fuzzy Neural Network[J]. Environmental Science and Technology,2015,38(12):254-261.

[9] Sun Zengqi. Fuzzy neural network based on T-S model[J]. Journal of Tsinghua University (Natural Science Edition), 1997(3): 76-80.

[10] Qi Xin, Liu Jiafu. Evaluation of water quality of rainwater collection in western villages and towns based on T-S fuzzy neural network model [J]. Water saving irrigation, 2015 (3): 28-30.

[11] Hu Hua, Wang Dongqing. Application of T-S Fuzzy Neural Network in Water Quality Evaluation[J]. Journal of Inner Mongolia Agricultural University(Natural Science Edition), 2015(4): 128-132.

[12] Wang Xinbo, Su Xiaoling. Comprehensive evaluation of groundwater quality in Minqin based on T-S fuzzy neural network[J]. Agricultural Research in Arid Areas, 2013, 31(1): 188-192.

[13] LEEHK, OHKD, PARKDH, et al. Fuzzy expert system to deter-mine stream water quality classification from ecological information[J]. Water Science and Technology,1997,36(12):199-206.

[14] Shi Feng, Wang Xiaochuan, Yu Lei, et al. 30 Case Analysis of MATLAB Neural Network [M]. Beijing: Beijing University of Aeronautics and Astronautics Press, 2010.

Design of garbage sorting robot based on machine vision

Qian Chenghui, Hou Tianyuan, Xiao Ruolan, Zhang Xiaojian
(jilin university instrument science and engineering institute,changchun,130021)

***Abstract*—A machine vision-based garbage sorting robot that uses a gyroscope and an encoder to coordinate with GPS for path planning, a camera with an ultrasonic module for object detection, and a robot arm for garbage capture. In order to acc urately identify the type of garbage, the SIFT image matching algorithm is used to solve the trajectory of the robot arm by in verse kinematics. After testing, the robot can correctly identify most of the trademarked garbage without the influence of ligh t and other factors, and can complete the pair. The grasping of certain shaped objects has initially achieved the goal of garba ge sorting.**

***Keywords*—Machine vision; garbage sorting; robotic arm; path planning**

I. INTRODUCTION

GARBAGE sorting is an important part of the garbage disposal process, and its implementation process mainly includes positioning, identification, grabbing and placement. The existing garbage is mostly sorted by sanitation workers manually, with high work intensity, low efficiency and serious harm to the health of sanitation workers [1]. Foreign FRANKE designed the LD series and FWD series household waste disposers. The Magpie waste treatment system invented in the UK enables fast and automatic waste sorting [2]. Domestic research on automatic garbage sorting is short. However, the current garbage sorting device is large in size and fixed in position, and cannot solve the garbage classification problem alone without the participation of workers.

This paper proposes to design a smart garbage sorting robot. The mechanical structure, hardware circuit and system software design of the robot were carried out. Combining multiple sensors enables the purpose of traveling, planning, identifying, and picking up trash on a planned path. The garbage sorting robot has the characteristics of small volume, strong terrain adaptability and strong anti-interference ability.

II. SYSTEM HARDWARE DESIGN

A. System Hardware Circuit Design

The system hardware circuit includes a controller, a binocular camera, a gyroscope, an infrared sensor, a GPS module, an ultrasonic module, a motor drive, a servo drive, a 4G router, and a power module. Intel's UP2Board microcomputer is selected as the main controller. It is equipped with Intel Pentium N4200 processor. It has 4GB LPDDR memory and 64GB eMMC hard disk. It is used to collect image data, identify the object type and process the sensor data provided by the lower computer. The controller uses STMicroelectronics' STM32F103C8T6, which uses the Cortex-M3 core and has a wide range of peripheral interfaces, such as USART, IIC, and timers, to enable multi-sensor data acquisition. The camera adopts the blue enchantress 70P camera. The camera supports 1080P high-definition images.

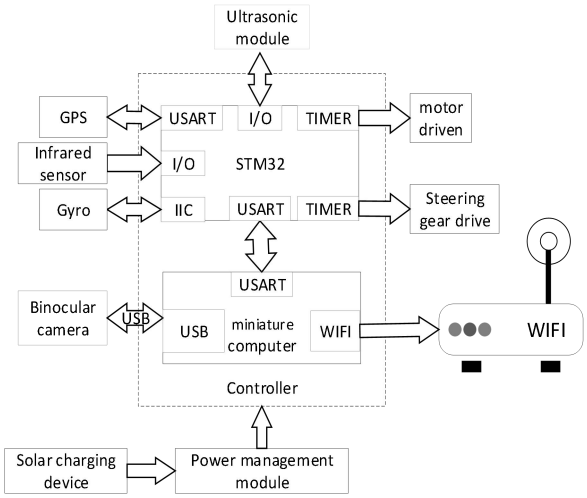

Fig.1. system hardware block diagram

The video capture rate is higher than 30FPS, and the image information can be transmitted by USB cable. The ultrasonic module uses HC-SR04, and its measuring range is HC-SR04 with an accuracy of 3mm.

B. System mechanical structure design

The overall block diagram and physical map of the designed garbage sorting robot are shown in Fig.2. The overall mechanical structure is mainly divided into four parts. The first part is the tracked vehicle chassis, which is driven by two symmetrical DC motors, which can carry up to 10KG and is responsible for the movement of the garbage sorting robot. The second part is a 50cm*50cm*9mm acrylic platform mounted on the top of the crawler chassis. Three 15*15*20cm storage boxes, hardware circuits, solar panels and symmetric distribution

on both sides are installed on the platform. Steering gear head. The third part is a 6-degree-of-freedom manipulator mounted on the two servo heads. Each of the robot arms is responsible for grabbing garbage in an area with an angle of 180° and a radius of 40 cm with the respective heads as the origin. The fourth part is the image acquisition device shown in Fig.2. The device consists of an ultrasonic and camera device mounted above the servo head, which can look at objects in the range of 180° and determine the distance of the object by ultrasound.

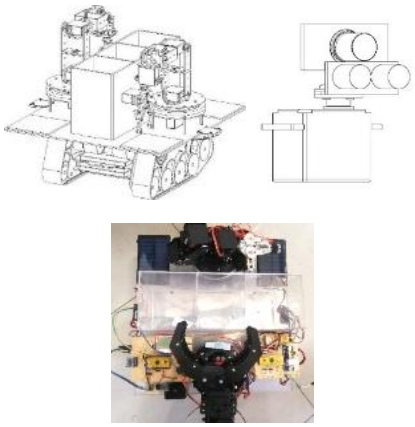

(a)Overall mechanical structure (b) Object detecting device (c) Physical map

Fig.2. Mechanical structure

III. ALGORITHM DESIGN

A. Image recognition algorithm

The primary task of the garbage sorting robot is to complete the detection and type identification of the object. The visual system not only needs to quickly identify the type of object, but also avoids misjudgment caused by illumination, image scale, rotation and deformation [3]. Therefore, the system uses the SIFT feature extraction algorithm [4-6], and the SIFT algorithm flow is as follows:

First establish the scale space and perform extreme point detection: the scale space is usually represented by Gaussian scale space:

$$L(x,y,\sigma) = G(x,y,\sigma) \times I(x,y) \tag{1}$$

Where σ is the scale space factor G(x, y, σ) is a Gaussian kernel function, and I(x, y) is an image subjected to grayscale processing. The detection extreme points are performed in a differential Gaussian space, and the differential Gaussian space is as follows:

$$\begin{aligned} D(x,y,\sigma) &= [G(x,y,k\sigma) - G(x,y,\sigma)] \times I(x,y) \\ &= L(x,y,k\sigma) - L(x,y,\sigma) \end{aligned} \tag{2}$$

Where k is the scale factor of the adjacent two-level scale space. Each pixel point is compared with the same scale space and adjacent points of the scale space, and the condition that the point can be used as an extreme value is that it is smaller or larger than the remaining pixel points.

The precise position determination of the key points is then performed: the above-mentioned difference space D(x) is a discrete function, which is converted into a continuous function for obtaining the exact pole position, so Taylor expansion is performed:

$$D(x) = D + \frac{\partial D^T}{\partial x}\Delta x + \frac{1}{2}\Delta x^T \frac{\partial^2 D}{\partial^2 x}\Delta x \tag{3}$$

The exact position of the extreme point is solved as x = (x, y, σ) ^ T.

Obtaining the feature point direction: After finding the key after the second step, the scale space factor σ is determined, and each point L(x, y) in the region with the radius of 3*1.5σ as the center is calculated. The amplitude m (x, y) and the angle θ (x, y). Use the histogram to count the main direction of the key points.

$$m(x,y) = \tag{4}$$

$$\sqrt{[L(x+1,y) - L(x-1,y)]^2 + [L(x,y+1) - L(x,y-1)]^2}$$

$$\theta(x,y) = \arctan\frac{L(x,y+1) - L(x,y-1)}{L(x+1,y) - L(x-1,y)} \tag{5}$$

Finally, a description of the key points is made to obtain a descriptor.

B. Robot arm path planning algorithm design

In this system, the garbage sorting robot needs to use the inverse kinematics algorithm to obtain the angle of each mechanical arm joint according to the position of the target object [7]. Given the position and orientation of the end of the mechanical arm, the robot arm is modeled by DH method. The coordinate system is established in each joint, the pose transformation between the coordinate systems is described by homogeneous transformation [8], and finally the inverse solution is obtained to obtain the angle of each mechanical arm joint [9-10]. As shown in Fig. 3, the gimbal is placed at the center of the base coordinate system (x0, y0, z0), and the rotation angle is determined by the x, y value of the end position to The (X, Y) coordinate system in Fig. 3 is a two-dimensional plane coordinate system.

The end pose is (x,y,β),Then there is $\beta = \beta_2 + \beta_1 + \beta_0$, Hypothesis $a_6 = a_4 + a_5$, $k = a_6 * \cos\beta - x$, $z = a_6 * \sin\beta - y$. then:

$$a_3 = (a_2 \times cos\beta_0 + k)^2 + (a_2 \times sin\beta_0 + z)^2 \tag{6}$$

Finally get

$$\beta_0 = asin\left(-n \pm \frac{\sqrt{n^2 - 4mc}}{2m}\right) \tag{7}$$

among them $b = \frac{(a_3{}^2 - a_2{}^2 - k^2 - z^2)}{2a_2}$, $m = k^2 + z^2$, $n = -2zb$,

$c = b^2 - k^2$.

The same method can be obtained β_1, Finally, the joint angle values of the arm are obtained.

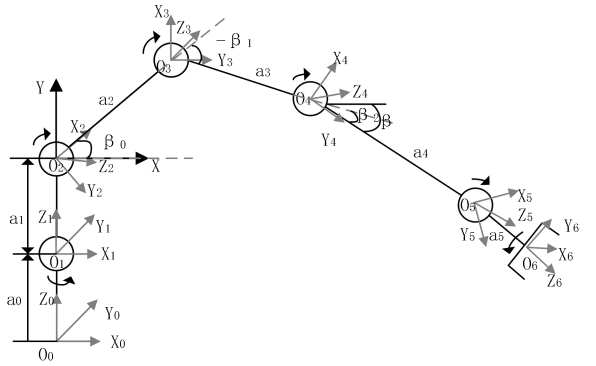

Fig.3. Robotic arm model diagram

C. Design of track vehicle path planning algorithm

Set the coordinates of the current position of the crawler car as (0,0),The coordinates of the end point are (x_F,y_F), Wheel diameter is d. The coordinates of the crawler at time t are (x_t,y_t), Gyro heading angle is θ_t,The number of encoder pulses isn_t.among them:

$$x_t = x_{t-1} + l \times \sin\theta_t \quad (8)$$

$$y_t = y_{t-1} + l \times \cos\theta_t \quad (9)$$

$$l = \pi \times d \times n_t \quad (10)$$

In the formula, $t \geq 1$, and (x_t, y_t) is gradually approached (x_F, y_F) to reach the specified end point.

IV. System Software Design

The overall workflow of the garbage sorting robot is shown in Fig.4. After the robot starts normally, it will patrol according to the pre-planned path. At the same time, the camera on both sides of the robot body continuously collects images, and the main controller performs image processing. If a target is detected, the type of the target is identified. After determining the target type, the robot stops moving, and then the ultrasonic module installed on the servo head is started in the range of 0-180°. The inner scan determines the distance of the object to the ultrasonic module, and then calculates the coordinates of the object according to the angle rotated by the servo head. After that, the master sends the coordinate information and the object type information to the corresponding robot arm controller. After receiving the data, the robot arm controller controls the arm grab to move to the target point and grabs, and then the grabbed object is prevented from being corresponding to the corresponding type. In the object storage box, after completing this process, the robot continues to patrol according to the prescribed path, and the camera collects data.

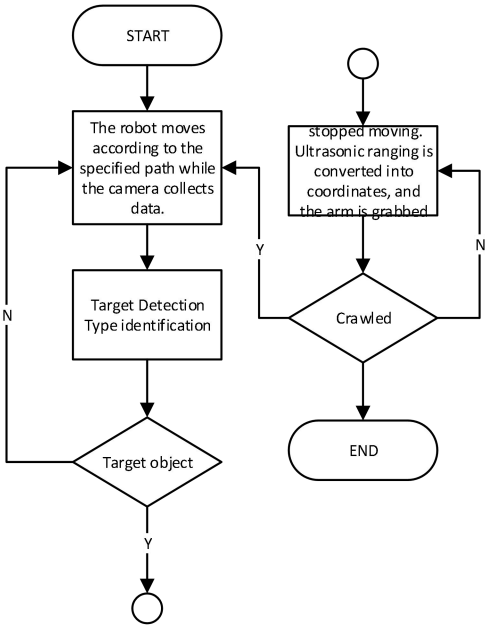

Fig.4. software flow chart

V. Results Analysis

A. Analysis of object detection results

As shown in Fig.5, when performing image recognition of the cans, a total of 259 feature points are extracted, wherein the number of feature points matching the image of the canned sample image in the database is 166, and the image is recognized when the image of the milk box is imaged. Out of 263 feature points, the number of matching feature points with the image of the milk box sample in the database is 177, and the result is very satisfactory.

Fig.5. SIFT algorithm image matching results

Object detection includes the determination of the object class and the determination of the object position. The test method is as follows: the target object is placed in the field of view of the camera, and the return value of the serial port print is checked. If the return object represents the same type of object as the actual object to be placed, the position in the return value is the same as the actual position, and this is proved. The test was successful. The

experimental results are shown in Table 1. Since the object type is judged based on the corner, edge and spot features of the object image [6-7], the identification of cans, milk cartons and mineral water bottles with trademark pattern information is correct. The rate is higher [8], and the recognition rate for paper balls is very low. The object position determination test results indicate that the detection accuracy of the hard material is high.

TABLE 1 Test results

	Type recognition result				Position determination result			
Measured object	A	B	C	D	A	B	C	D
Testing number of times	50	50	50	50	50	50	50	50
Correct number of times	46	47	44	6	49	46	48	5

Note: A-cans; B-milk box; C mineral water bottle; D-paper group

B. Analysis of the results of mechanical arm grabbing

The method of testing the robot arm is as follows: the category information and the position information of the target object are transmitted to the robot arm through the serial port.

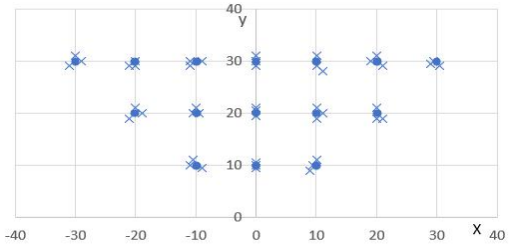

Fig.6. Robot arm gripping point analysis

Observe whether the robot arm can accurately grasp the target object and place the object in the garbage bin to which it belongs. The actual number of tests was 50, and the number of successful completions of the grab was 41. Fig.6. '·' for the specified position of the robot arm, 'x' for the actual position of the robot arm, the arm of the arm cannot reach the specified position accurately every time. The analysis of this result is mainly due to the error in the position of the object detected by the ultrasonic wave, and the structure of the robot arm has a large defect.

VI. Conclusion

This paper designs a machine vision-based garbage sorting robot, on which the gyroscope and encoder can be installed to travel on the planned path, the garbage type can be identified by the camera, the ultrasonic module determines the garbage position, and the robot picks up the garbage placed. The robot designed in this paper is not affected by light and has strong terrain adaptability. It has initially realized the miniaturization and automation of garbage picking, and provides a basis for garbage picking robots.

References

[1] Liao Ruzhen, Huang Jianzhong, Yang Danrong. Current Status and Countermeasures of Urban Domestic Waste Sorting in China[J]. Occupational Health and Diseases, 2012, 27(1): 30-34.

[2] Liu H C, Wu J, Li P. Assessment of health-care waste disposal methods using a VIKOR-based fuzzy multi-criteria decision making method.[J]. Waste Management, 2013, 33(12):2744-2751.

[3] Wang Jinlong, Zhou Zhifeng. Research on Feature Extraction and FLANN Matching Algorithm Based on SIFT Image[J]. Computer Measurement & Control, 2018.Tan X. Image Retrieval via CURE Clustering and SIFT Algorithms[J]. Applied Mechanics & Materials, 2013, 303-306:1573-1576.

[4] Bing-Jie Q I, Liu J G, Zhang B Y, et al. Research on matching performance of SIFT and SURF algorithms for high resolution remote sensing image[J]. Chinese Optics, 2017, 10(3):331-339.

[5] Anonymous. Image feature point extraction and matching based on SIFT algorithm[J]. Journal of Nanjing Medical University(Natural Science), 2013(2): 286-290.

[6] Li Shengqian, Xie Xiaopeng. Inverse kinematics solution analysis of 6-DOF robot based on spin theory and Sylvester knot method[J]. Transactions of the Chinese Society of Agricultural Engineering, 2015,31(20):48-54.

[7] Koker.A genetic algorithm approach to aneural-network-based nverse; kinematics solution of robotic manipulators based on error minimization[J].Information Sciences, 2013, 222(3):528-543.

[8] Xiao Junming,Han Wei,Wang Wei et al. Kinematics analysis and simulation of a six-degree-of-freedom manipulator[J].Journal of Zhongyuan Institute of Technology,2018,29(04):77-83.

[9] Jiang Q, Kumar V. The Inverse Kinematics of Cooperative Transport With Multiple Aerial Robots[J]. IEEE Transactions on Robotics, 2013, 29(1):136-145.

Intelligent Anti-theft Device Based on WIFI Communication System

Shixuan Xie, Kai Qin, Zongliang Ma
（jilin university instrument science and engineering institute,changchun,130021）

***Abstract*—Using many sensor technologies in the Internet of Things and WIFI communication, an intelligent anti-theft device is designed, which can monitor indoor environment in practical application and react to mobile app in real time through WIFI communication.**

***keywords*—Internet of Things, Sensors, WIFI Communications, Anti-theft Devices**

I. INTRODUCTION

WITH the rapid development of science and technology in today's society, new technologies are constantly emerging and applied to people's production and life, bringing convenience to people. Especially in recent years, the concept of the Internet of Things is different from the previous Internet. The Internet of Things extends and extends its client to any object and goods for information exchange and communication. This new concept provides us with a new way of life.

With the popularity of WIFI devices and smart phones, we design an intelligent anti-theft device which can connect with mobile app through WIFI communication. This anti-theft device uses a variety of sensors, including infrared, vibration, temperature and humidity, smoke, etc. It realizes real-time monitoring of indoor environment and reflects it on mobile app through WIFI.

A,System Overall Design

The system uses STM32 chip as the core, and monitors the environment through vibration sensor, infrared sensor, temperature and humidity sensor, smoke sensor, ultrasonic ranging sensor and so on. Real-time data is transmitted to the mobile phone through WIFI for display.

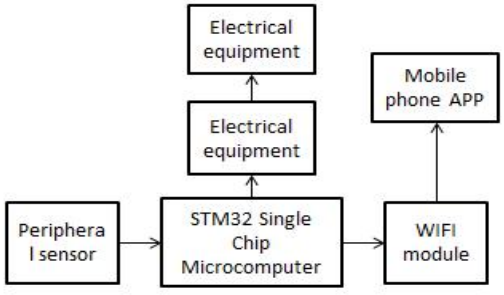

Fig. 1. System Overall Structure Diagram.

B,System Hardware Circuit Design

The hardware circuit of the system is composed of MCU control circuit, WiFi communication circuit, infrared induction circuit, vibration induction circuit, temperature and humidity induction circuit, smoke sensor circuit, ultrasonic ranging circuit and so on[1].

After the analysis of the target of the system in the early stage, the STM32 single chip computer is selected as the core of the system. It can use general I/O port to receive the digital signal of sensor, and communicate with WIFI module through serial port, which is in line with our expectation.

ESP8266 module can realize data communication between serial devices and wireless networks. The module can connect serial devices only by connecting common WIFI or hot spots. It has stable performance and better security than other WIFI modules[2].

Infrared induction module is mainly composed of infrared pyroelectric sensor, Fresnel lens and BISS0001. It can detect the change of infrared energy radiated by human body in a non-contact form and convert it into voltage signal output. It is used to monitor whether people enter or leave the room under the condition of monitoring.

Vibration sensor circuit consists of vibration switch and peripheral circuit. Vibration switch is open-circuit OFF state when it is still. When it is touched by external force and reaches corresponding vibration force, or when the moving speed is appropriately deviated from the centrifugal force, the conductive pin will generate instantaneous on-off state; when the external force disappears, the switch will restore to open-circuit OFF state. Used to monitor the movement of items.

DHT11 temperature and humidity sensor has an output with data correction signal, and has advanced sensing and acquisition technology which other modules do not have[3]. This module is stable and cost-effective. It is the best choice for the system to collect temperature and humidity.

C.System Software Design

The flow chart of the system software is shown in the figure. Firstly, the serial port of WIFI communication module is initialized, and then the WIFI communication sub-function is called[4]. When the WIFI module receives the data, the MCU interrupts and adds a judgment function to judge whether the communication APP is in the open state, so as to prevent the communication failure caused by the failure of the link between the WIFI module and the APP.

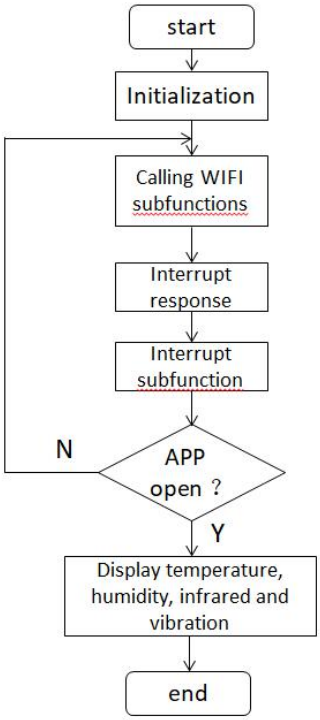

Fig. 2. System Flow Chart

The communication of WIFI module involves serial communication, so it is necessary to configure and initialize the serial port first. Fig. 3 is the communication flow of WIFI module.

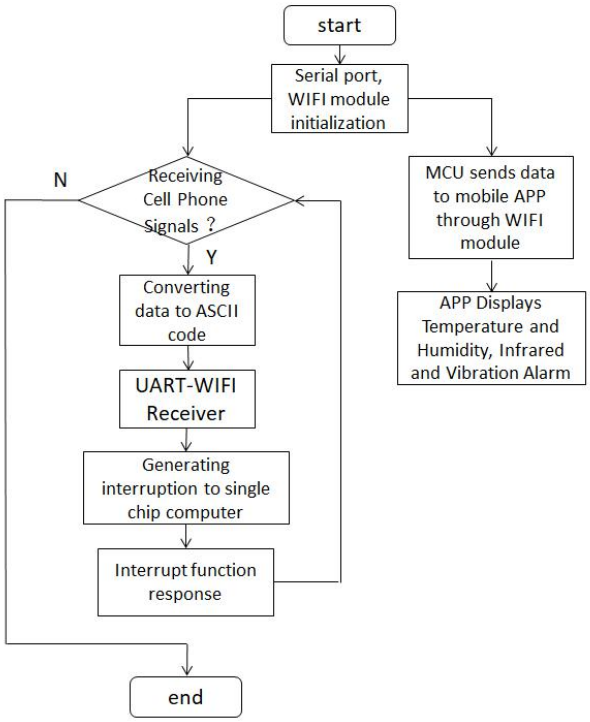

Fig. 3. Communication flow chart of WIFI module

D.System Function Display

As shown in the following figure, the APP interface is mainly composed of user login interface, setup interface and display interface.

Real-time display of current ambient temperature and humidity on APP, ambient air monitoring, and monitoring the movement of valuables, indoor access and so on. All can be displayed intuitively on APP.

Fig. 4 App Page Display

After the completion of the system, the system has been tested many times in different environment scenarios, all of which can work steadily, and the results meet the expected technical indicators.

E.Conclusion

With the development of science and technology,

more and more new technologies will be put into the field of life, bringing us a new way of life. On the basis of such an anti-theft device, it can also be expanded into a complete, more functional Internet of Things platform, so that our lives become more intelligent and technological.

References

[1] Chen Lixian, You Mingxian, Lin Zixuan, Fu Bin. Design of greenhouse intelligent control system based on WIFI communication [J]. Fujian Computer, 2018, 34 (09): 130-131.W.-K. Chen, Linear Networks and Systems (Book style).Belmont, CA: Wadsworth, 1993, pp. 123–135.

[2] Wang Chaohua, Chen Deyan, Huang Guohong, Tonghuai. Research and Implementation of Intelligent Home System Based on Android [J]. Computer Technology and Development, 2012, 22 (06): 225-228+233.

[3] Sun Haowen. Design of greenhouse temperature and humidity acquisition system based on single chip computer [J]. Automation and instrumentation, 2017 (03): 198-200.

[4] Liao Yingsheng. Design of WiFi-based remote control system for flower watering [J].Woodworking Machine Tool, 2018 (04): 8-9+13.

Motion platform SLAM system based on millimeter wave radar

Wei Li, Tongning Li, Tianduo Dong
(School of Instrument Science and Electrical Engineering, Jilin University,Changchun 130012,China)

***Abstract*—In order to realize the environment perception, location, obstacle avoidance and path planning of mobile platform, we propose a simultaneous positioning and mapping (SLAM) system based on millimeter wave radar. The system includes a millimeter wave radar sensor module, a difference frequency signal conditioning circuit module, a DDS module, a host computer, and a motion platform. The signal conditioning module[1] is composed of a high pass filter, a variable gain amplifier, and a low pass filter. The AD8671[1] operational amplifier is used to implement the fourth-order Butterworth filter and the fourth-order Butterworth low-pass filter. The AD603[2] operational amplifier and potentiometer are designed to implement a variable gain amplifier. The system control and data processing module is implemented by the STM32F103RCT6 microprocessor. The system can achieve ranging within 10 meters.**

***keywords*—Millimeter wave radar SLAM (simultaneous localization and mapping)**

I. INTRODUCTION

WITH the rapid development of social economy and the continuous improvement of people's material living standards, cars play an increasingly important role in people's daily life, but traffic accidents have brought serious economic losses and casualties to the development of society. [3,4,5]At the same time, the driverless car is one of the forms of future car development, using the sensing system instead of the driver to perceive the traffic environment [5,6,7], through different sensors to detect the environmental information of the vehicle and its surroundings, for the whole The smart car driving strategy and path planning provide the basis. In view of the increasing complexity of the domestic traffic environment, people's requirements for car safety performance continue to increase, coupled with the huge differences in the field of millimeter wave radar technology at home and abroad, this topic is based on the above considerations, research on millimeter wave radar technology System-level analysis and research from the perspective of vehicle-mounted millimeter-wave radar systems, development of a simultaneous positioning and mapping (SLAM) system based on millimeter-wave radar (24G~70GHz), and plans to apply it to unmanned vehicles and drones. Environmental awareness, location, obstacle avoidance and path planning for mobile platforms. [11,12] hope that this research work will help the development of the domestic intelligent transportation system. Based on the K-LC2 millimeter wave radar sensor produced by Rfbeam, this paper develops a radar ranging SLAM system for motion platform.

1.Principle Of Ranging

An emission signal is emitted by the oscillator oscillation, One of them is transmitted through the transmitting antenna. One way and then split into two channels into the mixer of the channel I and Q, The signal of the Q channel needs to be phase shifted by 90° before mixing. The signal of the Q channel needs to be phase shifted by 90° before mixing; the echo signal received by the receiving antenna is first processed by low noise amplification, and then separately subjected to two signals of the mixer and the real-time shunt. mixing. The signal obtained after mixing is amplified by the intermediate frequency filter, and finally the two intermediate frequency signals of I and Q are obtained. Both the I and Q intermediate frequency output signals carry the speed information of the detection target.

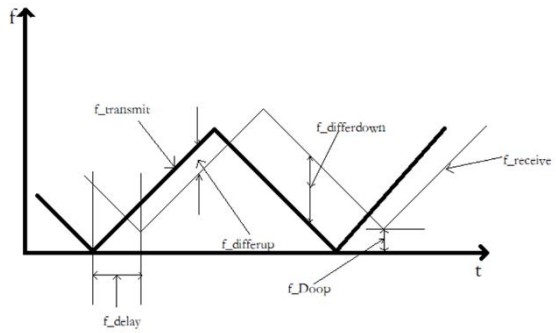

Fig.1 Relationship between time and frequency of FMCW radar transmit waveform and received waveform during target relative radar motion

When the relative velocity of the object and the radar exists, the time-frequency relationship between the radar transmitting signal and the radar receiving signal is as shown in Fig. 1. Where f_transmit is the radar transmit signal, f_receive is the radar receive signal, f_delay is the frequency difference caused by the time

delay effect, and f_Doop is the frequency shift caused by the Doppler effect. During the ascent phase, the time delay effect and the Doppler effect cancel each other out; in the downhill phase, the two effects overlap. Therefore, the sensor output signal *f*_differup during the ascending phase of the triangular modulation signal and the output signal *f*_differdown during the downgrade phase can be calculated;

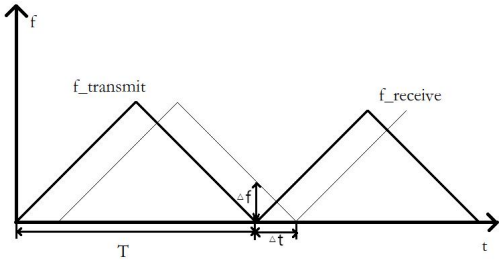

Fig. 2 Relationship between time and frequency of FMCW radar transmit waveform and received waveform when target versus radar is stationary

When the object is relatively stationary with the radar, the time-frequency relationship between the radar transmit signal and the radar received signal is as shown in Figure 2, which becomes more concise. The system only needs to achieve the distance measurement of the target, and does not need to realize the speed measurement function. Therefore, the situation of the target and the radar is relatively static, and only one of the I and Q signals needs to be processed. In the figure, T is the modulation period of the frequency-modulated triangular wave, Δt is the time difference between the transmitted signal and the received signal, and Δf is the frequency difference between the transmitted signal and the received signal at the same time. [8]

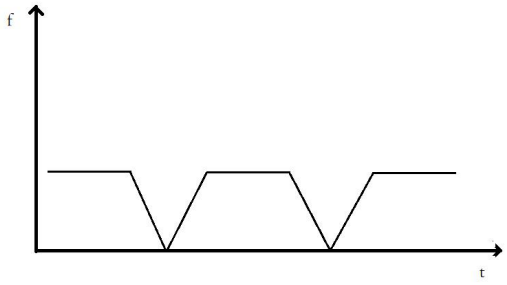

Fig. 3 Time-frequency diagram of the difference frequency signal between the transmitted signal and the received signal

According to the radar ranging formula: fI=4BR/CT, where fI is the frequency of the difference frequency signal output by the sensor, ie Δf, B is the modulation bandwidth of the frequency-modulated triangular wave VCO, R is the measured target distance, C is the speed of light, T It is the period of the frequency modulation triangle wave.When B, C, and T are set, the value of fI is only related to R. Therefore, the frequency range of the difference frequency signal fI can be calculated according to the range of distances to be measured; otherwise, according to the frequency of the sensor output signal, it can be solved. The distance from the target object to the radar sensor.

II. RANGING RADAR SYSTEM DESIGN

2.1 Overall System Design

The overall design of the ranging radar system is shown in Figure 4. The system consists of five modules, namely a direct digital frequency synthesizer (DDS) module, a radar sensor module, a difference frequency signal processing circuit module, a digital signal processing module and a radar base. Seat servo module. Among them, the digital signal processing module is composed of a single chip and a host computer. The DDS module is used to generate the FM triangular wave signal transmitted by the radar sensor module; the radar sensor module is used for transmitting and receiving the radar RF signal; the difference frequency signal processing module is used for amplifying and filtering the difference frequency signal output by the radar sensor; The sampling and analysis of the difference frequency signal and the implementation of the related algorithms in the upper computer simultaneously complete the control of the relevant modules in the system; the radar base servo module is used to realize the scanning of the surrounding environment by the radar sensor.

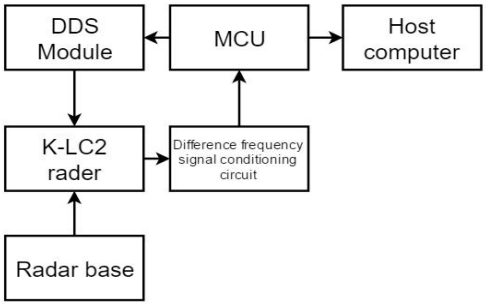

Fig. 4 system overall structure block diagram

2.2 DDS Module

The DDS module is composed of AD9834 and its peripheral circuits. The chip can output up to 37.5MHz triangular wave or sine wave, which can meet the frequency modulation triangle wave required by the VCO input of the latter radar sensor. The FSY, SCK, SDA, DDS-RST, FS and PS of the AD9834 are given by the STM32 microprocessor. The frequency of the output FM triangle can be changed by pressing the button.

2.3 K-LC2 Radar Sensor Module

The K-LC2 radar sensor module is a 24GHz low-cost radar sensor with a 140MHz modulation input and a 50MHz bandwidth double balanced mixer. The sensor consists of two channels, I and Q, as well as a mixer and a voltage controlled oscillator (VCO). The output signal of the VCO is provided by the DDS module controlled by the single chip microcomputer. In this paper, the FM triangle generated by the DDS is connected to the VCO input by the radar sensor and transmitted through the transmitting antenna array. The transmitted signal is reflected by the detected target object, and the reflected signal is received by the receiving antenna, and then mixed with the current time VCO signal. The device is mixed to obtain a difference frequency signal, and the difference frequency signal is connected to a subsequent difference frequency signal processing circuit for

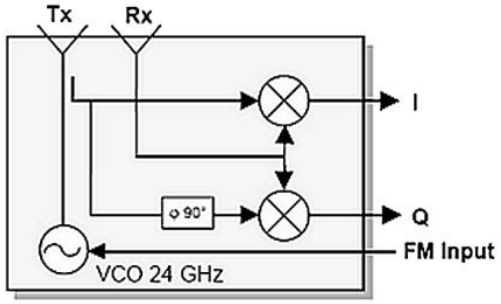

correlation amplification filtering and the like.

Fig. 5 K-LC2 radar sensor structure

2.4 Difference Frequency Signal Processing Module

The circuit structure of the difference frequency signal processing module is shown in Figure 6 [1]. The module consists of four main components: preamplifier, high pass filter, variable gain amplifier and low pass filter. First, the amplitude of the signal output from the sensor is amplified by 10 times through a preamplifier consisting of a high-performance OPA211 for subsequent processing. Since the input VCO of the sensor cannot be completely isolated from the two signals of output I and Q, the FM triangular wave signal with leakage [3] exists in the differential frequency output signals of I and Q, so it is necessary to use a high-pass filter to make the difference. The triangular wave leaking in the frequency signal is filtered out. The high-pass filter uses two AD8671 operational amplifiers to form a fourth-order Butterworth high-pass filter circuit. The low-frequency 3dB cutoff frequency of the filter circuit is 2000Hz. The variable gain amplifier circuit [2] is mainly realized by using the AD603 operational amplifier and potentiometer. The amplitude of the signal is amplified or reduced by adjusting the potentiometer. The gain is -11dB~31dB, which enables it to be sampled by the STM32 microcontroller. Within the range of amplitudes. The main function of the low-pass filter is to filter out the high-frequency noise carried by the sensor output signal and the high-frequency noise generated by the difference-frequency signal processing circuit module, in preparation for the ADC sampling of the latter stage. The low-pass filter is also implemented by using two AD8671 operational amplifiers to form a fourth-order Butterworth low-pass filter. The 3dB cutoff frequency of the filter circuit is 395KHZ.

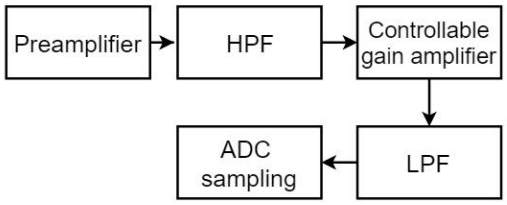

Fig. 6 Circuit diagram of the difference frequency signal processing module

2.5 Digital Signal Processing Module

The digital signal processing module [9, 10] mainly completes the extraction of digital signal feature information and the overall control of the circuit system, and its structure is shown in the figure.

The digital signal processing module is mainly composed of the STM32F103RCT6 microprocessor and its related peripheral circuits and the host computer on the PC side. In this paper, the microprocessor sends a control word to the DDS module through its own I/O port to generate the required frequency-modulated triangle wave as the modulation signal into the VCO of the radar sensor; the microprocessor pair of the microprocessor is processed by the difference frequency signal. The signal output from the circuit is sampled and transmitted to the PC via its peripheral usb port. In this paper, the PC side performs digital filtering on the received data through matlab, and then performs Fourier transform to calculate the frequency information of the signal, and calculates the distance of the measured object from the radar sensor through the radar ranging formula; The function of map drawing and distance display is realized by the related algorithm in the GUI of the host computer.

2.6 Radar Base Servo Module

The radar base servo module is mainly composed of a 9g motor and a 3D printed base ring gear. The motor is controlled by a 2.4GHz programmable remote control system, enabling the radar sensor to scan from -180° to 180°, thus 360° around. The environment is measured by distance.

2.7 Host Computer

The data communication between the hardware circuit and the host computer is completed by the serial port. Therefore, it is necessary to complete the serial communication setting in the host computer software. The software part is written by Matlab to complete the GUI display part and realize the display function. The functions of the host computer include serial port open and close, data receiving and display, synchronous motor operation, drawing and storing data and map. The host computer finally completes the reception, analysis, display of real-time maps and stores data and maps. Figure 7 shows the host computer interface.

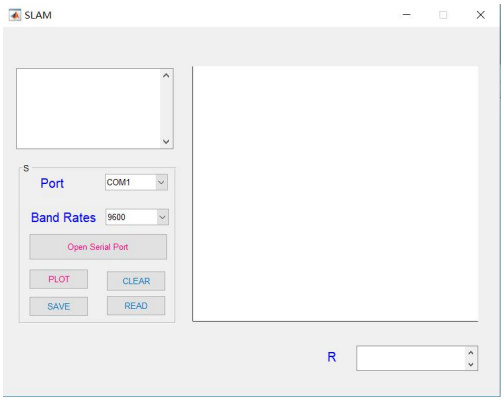

Fig. 7 host computer interface

2.7.1 Serial Communication

Serial port parameter setting.

First initialize the serial port and related parameters.

```
handles.displayT = 0;%表征串口是否打开
handles.hasData = 1;%表征串口是否接收到数据
handles.isShow = 1;%表征是否正在进行数据显示，即是否正在执行函数dataDisp
handles.strRec = '';
handles.baud_rate = 9600;
handles.com = 'COM1';
handles.verifiedBits = 'NONE';
handles.dataBits = 8;
handles.stopBit = 1;
handles.flowControl = 'NONE';
```

Fig. 8 initialization parameters

Open and close the serial port

```
    fopen(handles.serial);
else
    fclose(handles.serial);
```

Fig. 9 Serial port opening and closing operation

```
com = get(hObject,'string');
handles.com = com{get(hObject,'Value')};
guidata(hObject, handles);
```

Fig. 10 parameter configuration

Use Figure 10 to configure the parameters for the serial port, including COM port, baud rate, data bits, parity, flow control, and stop bits.

Serial port. Use the set(handles.edit1, 'string', strRec); statement to display the serial port data into editable text. Use if (strcmp (handles.serial.status, 'closed')) statement to determine whether the serial port is open and give a prompt statement.

Serial program interface.

The completed serial port program interface is shown in Figure 11. The ability to change serial port configuration parameters includes selecting ports, setting baud rates, data bits, parity bits, stop bits, and flow control. However, in this design, it is not necessary to repeatedly set some serial port parameters, so only the port selection and baud rate settings are included in the final system interface, and other parameters are set in the code interface. Use the button switch to open or close the serial port. The clear button clears the text box data, and the data received by the serial port is displayed in the text box.

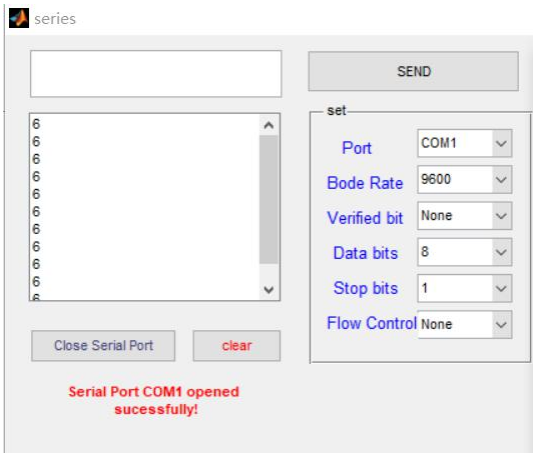

Fig. 11 serial interface

2.7.2 Filtering And Peak Determination

A low-pass filter was designed using Matlab's FDAtool toolbox. The design interface is shown in Figure 12.

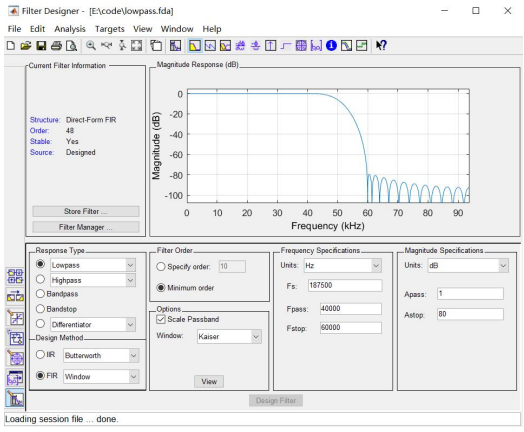

Fig.12 FDAtool design low pass filter

The filter designed in this paper is a low-pass filter with a maximum passband frequency of 40KHZ and a corresponding stopband minimum frequency of 60KHZ. In order to minimize the end of the results, select the Kaiser window as a window function. The attenuation inside the stop band is 80dB. The design results are shown in Figure 12. The order of the filter is

48 steps, and the amplitude-frequency characteristics are as shown in the upper right corner. There is no attenuation in 40KHZ, and attenuation starts after 40KHZ, and is attenuated to 80dB at 60KHZ. [4]

The signal is discrete according to this sampling rate, and two sinusoidal signals are set, one low frequency and one high frequency. The filter parameters are designed by fdatool in matlab, and then the generated .m file is used for filtering. The code to call the filter is as follows:

```
Hd=mylowpass;
H=filter(Hd,y3);
plot(H);
```

The final simulation is very good and can be used to set the filter function. Figure 13 is a filter effect diagram.

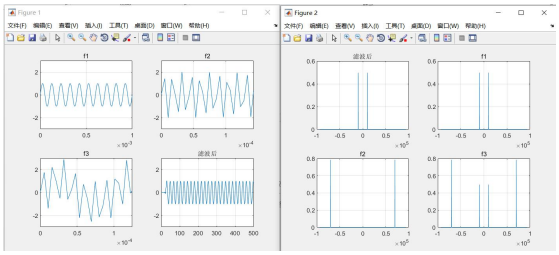

Fig. 13 Filtering

The peak matching is to analyze the frequency of the received signal by an algorithm, and take out the frequency value to calculate the corresponding distance. This process is very easy to implement for a single frequency signal. The process is to first perform FFT processing on the signal, and then take out the amplitude-frequency characteristic data. The frequency corresponding to the point with the largest amplitude in the amplitude-frequency characteristic data table is the dominant frequency of the received signal, and then the frequency value is added to the position algorithm. The distance corresponding to this frequency value can be found.

The advantage of this algorithm is that if the received signal contains low frequency noise that cannot be filtered by the filter, the correct signal dominant frequency can still be found, thereby realizing a part of the filtering function and effectively improving the accuracy. [13]The effect of peak matching after adding Gaussian white noise is shown in Fig. 14.

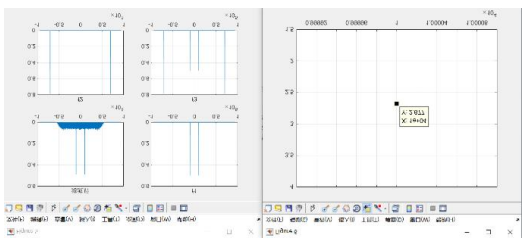

Fig. 14 Peak Matching

2.7.3 Ranging And Displaying Real-time Maps

After the distance corresponding to the relevant frequency can be calculated by simulation, the next step is to determine the position parameter of the measured point by distance and other parameters, and write the function of turning on the radar base servo system on the host computer to set the speed of the servo system. And synchronized with the host computer, you can get the phase information of the radar signal.After obtaining a set of frequency information and phase information, the corresponding polar coordinates can be established, and the position of each set of signal points in the real-time map is located. [7,14,15] In the map display, it is necessary to convert the polar coordinates into rectangular coordinates to facilitate the construction and display of the map. The conversion code of the polar-straight coordinates is as follows: X=(sin(i))*R; Y=(cos(i))*R; Where i is the angle and R is the distance of the corresponding point. From this equation, the corresponding coordinate position can be determined and displayed on the map in real time.

III. SYSTEM FUNCTION TEST

In the upper computer, the surrounding 360° environment map is drawn by the relevant algorithm, and the obtained test result is shown in FIG. 15. A laboratory signal generator is used to generate a fixed frequency signal and input to the system for testing. The effect of the test can be seen from the graphic display interface of the host computer. It can be seen that the system can decode most of the frequency signals and convert them into distance information, and complete the rendering of the real-time map.

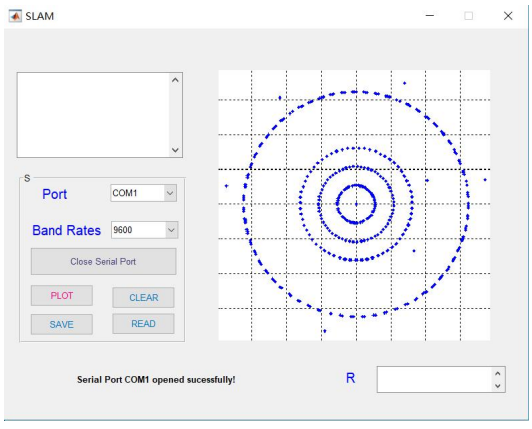

Fig. 15 Real-time map drawing

IV. CONCLUSION

This paper introduces the design of a millimeter wave radar motion platform SLAM system. The

system is simple in structure, small in size and low in cost. It can meet the basic requirements for the verification of the new SLAM scheme of the millimeter wave radar SLAM system, which can be further deepened in the future. Research lays the foundation and serves as a reference.

References

[1] Chen Tianqi, Yang Hao, Dai Zhiwei. 24 GHz FMCW vehicle ranging radar system design [J]. Embedded technology，2016，42（22）,37-40.

[2] Li Jian. Research on signal processing technology of 24GHz frequency modulated continuous wave radar [D]. Nanjing: Nanjing University of Science and Technology，2016.

[3] Yue Wenbao. Research and implementation of FMCW radar ranging system [D]. Taiyuan: North University，2013.

[4] Hey, Jie Guangjun, Zhang Jian. FMCW radar system and its front data acquisition module design [J]. Electronic technology，2012（05）：44-46.

[5] Wang Hong, Zhang Jie, Zhang Dazhao. Frequency modulated continuous wave (FMCW) radar signal conditioning circuit [J]. Instrument technology and sensors，2012（01）：105-107.

[6] Zou Bowei.Perception of Vehicle Local Traffic Environment Based on Multi-sensor[D].2013.6. Changchun: Master's Thesis of Automobile Dynamic Simulation and Control, Jilin University.

[7] Pang Cheng. Forward Vehicle Detection System Based on Fusion of Ranging Radar and Machine Vision Data [D].2015.5. Nanjing: Master of Science in Instrument Science and Technology, Southeast University.

[8] Yan Hongjun.Study on the analysis of the millimeter wave radar system and the key technology of the frequency source in the 24GHz vehicle [D].2015.6. Harbin: Master's thesis of electromagnetic field and microwave technology of Harbin Institute of Technology.

[9] Ren Xingbo. Design and implementation of intelligent car millimeter wave radar signal processing system [D]. Harbin Institute of Technology, 2017.

[10] Chen Haining. Design of Vehicle Anti-collision Radar System Based on DSP[D].Jiangsu University,2009.

[11] Yu Wei. Improvement of indoor positioning and mapping (SLAM) algorithm for LiDAR/INS combination [D]. Wuhan University, 2017.

[12] Pang Cheng. Forward Vehicle Detection System Based on Fusion of Ranging Radar and Machine Vision Data [D]. Southeast University, 2015.

[13] Zheng Xinglin. Research on Key Technologies of Signal Processing for Millimeter Wave Vehicle Collision Avoidance Radar[D]. National University of Defense Technology, 2007.

[14] Qu Feiyuan,Cao Ning.An Effective Method for Accurate Detection of Multiple Targets by Vehicle FMCW Radar[J].Science and Technology and Engineering,2012,12(06):1263-1267.

[15] Zhu Weili,Zeng Bi,Cao Jun.Parallel Optimization and Implementation of SLAM Algorithm Based on Particle Filter[J].Journal of Guangdong University of Technology,2017,34(02):92-96.

Design of Children's Anti-forgetting System Based on GPRS Communication Module

Yi Li, Jichen Liu, Ning Liu
(College of Instrumentation & Electrical Engineering,Jilin University,Changchun 130012,China)

***Abstract*—To avoid the potential safety hazards caused by parents'personal negligence of leaving children in the car for too long, this system is designed to improve the safety seat for children. The oxygen sensor ZE03-O2 is used to detect the oxygen content in the car, the temperature sensor DS18B20 is used to detect the temperature in the car, and the pressure sensor HX711 is used to detect the personnel distribution in the car. The data is processed by the single chip STM32. When the children in the car are alone and the temperature and oxygen value reach the threshold, the GPRS communication module is activated to inform parents by short message. If the parents do not arrive in time, the GPS is activated. The positioning module sends the alarm of the current vehicle location information to ensure the safety of children.**

***Keywords*—automatic control technology monitoring and alarm system experiment GPRS communication**

I.INTRODUCTION

ORDINARY safety seats can only reduce the impact on children, limit the movement of children's body to reduce the damage to them, and ensure the safety of children. Children who are alone in the car for a long time may pose a safety hazard, and ordinary safety seats cannot solve this problem[1]. The system monitors the oxygen value and temperature value in the vehicle through the oxygen sensor and the temperature sensor. When the child is detected to be in the vehicle for a long time, when the detected oxygen value and the temperature value reach the set first warning value, the system sends the GPRS communication module. The short message is sent to the preset recipient; if the oxygen value and the temperature value reach the set second warning value, when the child is still in the vehicle, the short message is sent to the preset multiple recipients through the GPRS communication module. If the oxygen value and temperature value reach the set third warning value, when the child is still in the car, the GPS positioning system is used to determine the current location of the car, and then the GPRS communication module sends a text message to the alarm and sends a text message to the preset. The intended recipient. The system improves the safety seat based on the GPRS communication module to improve the performance of the safety seat.

II. OVERALL SYSTEM DESIGN

The system is mainly composed of GPRS communication module, gravity sensor, oxygen content sensor, temperature sensor and GPS positioning module. The overall structure is shown in Figure 1.

Firstly, when the pressure sensor HX711 judges that the child is alone in the vehicle, the temperature sensor and the oxygen sensor detect the current oxygen value and the temperature value in the vehicle, and then the GPRS communication module sends a short message to inform the parents, if the parents do not arrive in time, start the GPS. The positioning module sends an alarm of the current car address information.

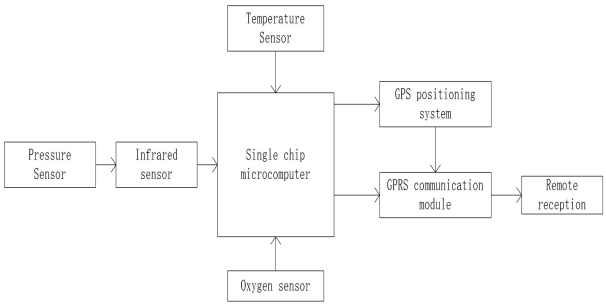

Fig.1 system overall structure design

III.HARDWARE DESIGN

A. Pressure Sensor, Infrared Sensor Module

The pressure sensor consists of simple digital control and serial communication. All control is input by the pin. The on-chip voltage regulator circuit can directly supply power to the external sensor and the on-chip A/D converter. The on-chip registers do not need to be programmed[2].

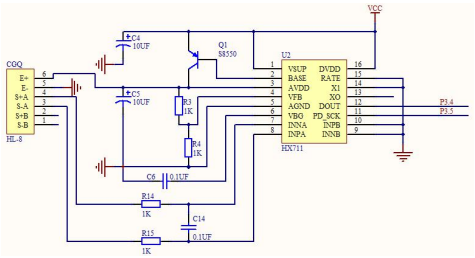

Fig.2 Schematic diagram of the internal structure of the HX711 pressure sensor

After the infrared sensor senses the output high level, if the human body is active in its sensing range during the delay time period, its output will remain high until the person leaves, and then the high level is changed to low level.

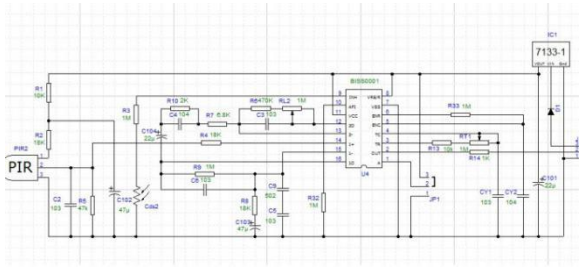

Fig.3 Schematic diagram of the internal structure of the HC-SR501 infrared sensor

B．Temperature Sensor, Oxygen Sensor Module

The temperature sensor selects the DS18B20, which has the characteristics of small size, low hardware overhead, strong anti-interference ability and high precision. DS18B20 temperature range -55 °C ~ 125 °C, accuracy is ± 0.5 ° C, working power 3.3V ~ 5.5V / DC (data line parasitic power supply), wiring is single-port wiring, only one I / O line, single bus The two-way communication of data is realized, which greatly improves the anti-interference of the system, and does not require any peripheral originals in use[3].

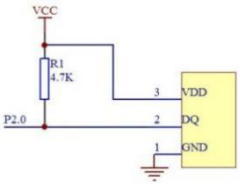

Fig.4 Schematic diagram of the internal structure of the DS18B20 temperature sensor

The oxygen sensor selects the electrochemical module ZE03-O2; the ZE03-O2 is a high-performance, general-purpose electrochemical series module that uses a three-electrode electrochemical gas sensor and a high-performance microprocessor that can be measured with different gas sensors. Corresponding gas. The built-in temperature sensor is used for temperature compensation, which can accurately measure the gas concentration in the environment. It also has digital output and analog voltage output, which is convenient for users to use and debug, which greatly shortens the user's design and development cycle[4].

C． GPS Positioning System, GPRS Communication Module

GPS positioning technology provides users with accurate location information services anytime, anywhere. Its basic principle is that the signal received by the GPS receiver is processed by error processing to obtain the position information, and then the position information is transmitted to the connected device, and the connected device performs certain calculation and transformation on the information (such as map projection transformation). , the transformation of the coordinate system, etc.) is passed to the mobile terminal. With high sensitivity, low power consumption, miniaturization, and its extremely high tracking sensitivity, it greatly expands its positioning coverage. In places where ordinary GPS receiver modules cannot be located, such as narrow urban sky and dense jungle environment, UBLOX 6M can be high. Precision positioning, very suitable for car[5].

GPRS technology provides medium speed data transfer by utilizing unused TDMA channels in the GSM network. GPRS breaks through the GSM network can only provide circuit switching thinking mode, only by adding corresponding functional entities and partial transformation of the existing base station system to achieve packet switching, the investment of this transformation is relatively small, but get The user data rate is quite impressive. Moreover, because the mediation converters required by current wireless applications are no longer needed, connectivity and transmission are more convenient and easy[6].

The GPRS communication module is divided into four application modes, a network transparent transmission mode, an HTTPD mode, a short message transparent transmission mode, and an AT command mode. In the network transparent transmission mode, the user's serial device can send data to the specified server on the network through this module. The module can also receive data from the server and forward the information to the serial device. SIM900A, dual frequency band: 900/1800Mhz, can realize voice, SMS (SMS), data and fax information transmission with low power consumption. The ATK-SIM900A module supports RS232 serial port and LVTTL serial port, with hardware flow control, and supports an ultra-wide working range of 5V-24V, making this module very convenient to connect with products, providing voice, SMS and GPRS data to the product. Transfer and other functions[7][8].

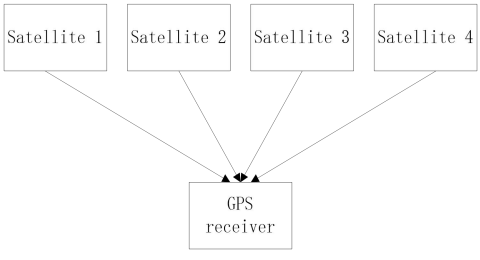

Fig.5 Schematic diagram of GPS positioning module

IV.SOFTWARE DESIGN

A．Infrared Sensor, Pressure Sensor Programming

The pressure sensor and the infrared sensor detect the

passengers in the vehicle, determine the number of passengers in the vehicle through the pressure sensor, and ensure that only the safety seat has pressure on the vehicle; the infrared sensor can detect the infrared signal emitted by the human body, and can be used to exclude the safety seat. In the case of placing items, ensure that children are using safety seats. When both are satisfied, it can be determined that there is only one child in the car, and the next stage of detection can be started.

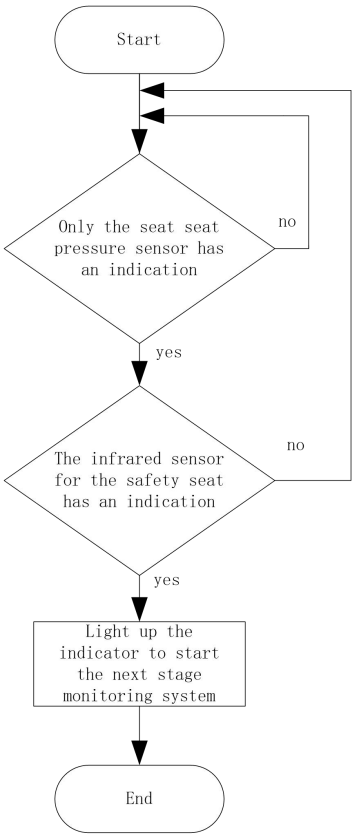

Fig.6 Infrared , pressure sensor program flow design

B. Temperature Sensor, Oxygen Sensor Programming

The oxygen sensor and the temperature sensor detect the temperature and the oxygen concentration in the vehicle, and when the temperature or the oxygen concentration reaches the first warning value, the child is reminded that the child is in the vehicle through the short message; when the temperature and the oxygen concentration value in the vehicle reach the second warning value By SMS again, remind the parents that the child is alone in the car, and the temperature inside the car is too high or the oxygen concentration is too low, the child's body may have been uncomfortable; when the temperature or oxygen concentration in the car reaches the third warning value, the car The internal environment has endangered children's lives, and the location information is sent to parents and the police through SMS.

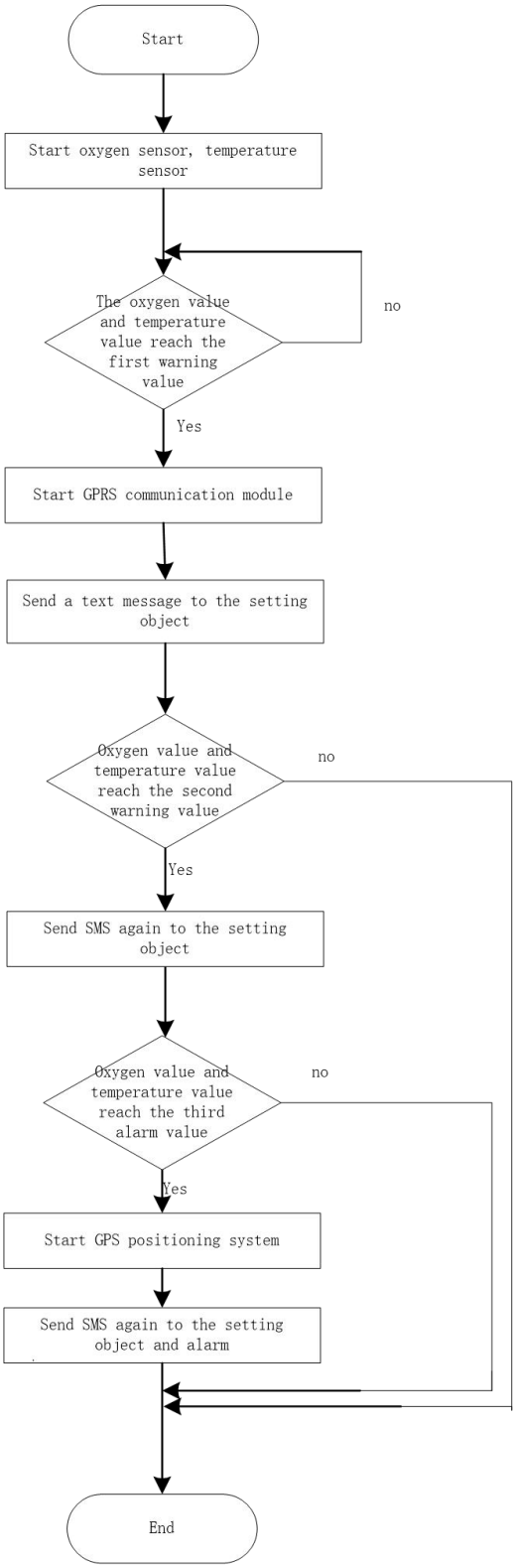

Fig.7 temperature, oxygen sensor program flow design

C. GPS Positioning, GPRS Communication Module Programming

The GPS positioning module determines the specific location of the current vehicle where the child is located. When the temperature and oxygen collected by the sensor reach the threshold, the location information is sent to the parent or the police through the GPRS communication

module, so that the child can get help as soon as possible to avoid adverse situations.

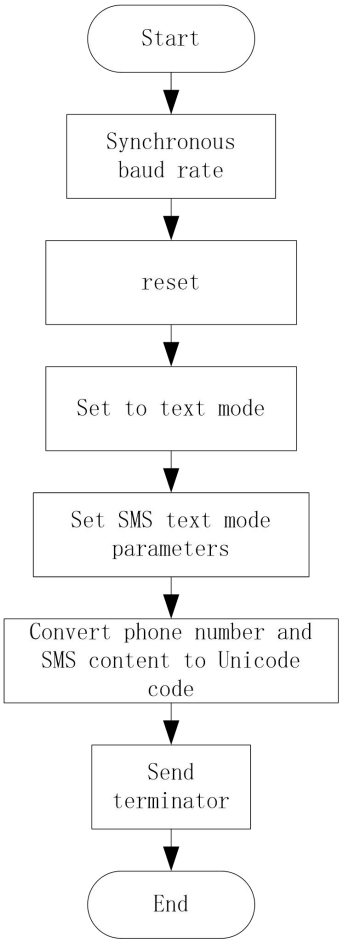

Fig.8 GPS positioning, GPRS communication module program flow design

V.TEST RESULTS

The design and function of the ordinary safety seat have been optimized and improved. It has been proved by practice that the child riding anti-forgetting system based on the GPRS communication module improves the safety index of children riding.

The system is based on the GPRS communication module, which can correctly collect temperature and oxygen concentration data and perform data processing. When triggering different warning values, the GPS positioning module and the GPRS communication module can be used to notify the parents and the police by SMS.

The basic component modules used have low process costs and are of positive significance for ensuring children's safety by car, which can be promoted on a large scale.

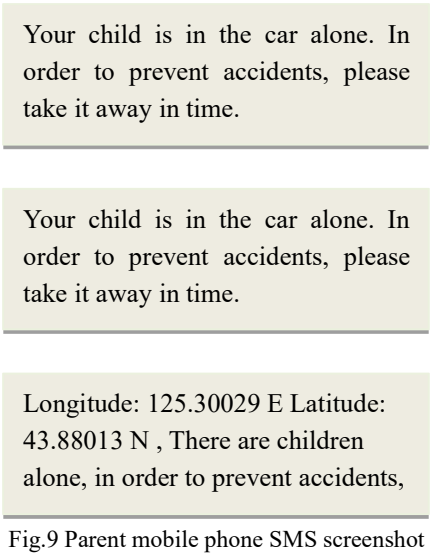

Fig.9 Parent mobile phone SMS screenshot

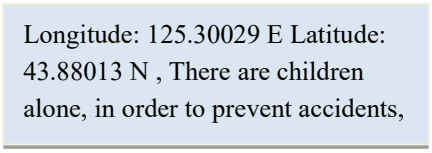

Fig.10 Police SMS screenshot (simulation)

References

[1] Pan Leren, Xue Jun and Hu Ying. Investigation and analysis of the use of child seat in China [J]. Automobile Industry Research, 2017 (01): 22-25.

[2] Deng Xiao, Jinye, Duan Leilei, Qi Qi, Jiang Yu, Zhou Haibin, Liu Shengyuan, Wang Linhong. Use and cognitive status of 9484 children's seat in 3 cities of China [J]. China Maternal and Child Health Research, 2016, 27 (05): 551-555.

[3] Ren Jie, Zhang Junhui, Xie Liuhong. Discussion on Several Issues Concerning the Use of Child Safety Seats [J]. Highway and Motor Transportation, 2011 (02): 23-27.

[4] Shang Ting, Tang Boming, Liu Tangzhi. Current situation and Countermeasures of child seat use in China [J]. Traffic Information and Safety, 2010, 28 (05): 69-72.

[5] Cao Libo, Ren Xijuan, Chen Zen. Structural characteristics and development trend of automobile child seat [J]. Automotive parts, 2010 (03): 53-57+60.

[6] Ren Xijuan, Cao Libo, Ouyang Zhigao. Design and Simulation of integrated car child seat [J]. Automotive Engineering, 2009, 31 (12): 1133-1136.

[7] Yang Yi. Performance analysis and engineering application of GPRS-based wireless data transmission system [D]. Xi'an University of Electronic Science and Technology, 2013.

[8] Liu Guozhong. Design of wireless data acquisition and transmission system based on GPRS [D]. Shandong University of Science and Technology, 2011.

[9] Ma Hongwei, Sheng Yizhi. Application of GPRS technology in wireless data transmission [J].Microcomputer Development, 2005 (03): 101-103.

Orithm Design of Magnetic Resonance Sounding Signal Based on Independent Component Analysis under Complex Noise

Li Shuo, Zhao Ouyang, Dong Ran
(College of Instrument science and Electrical Engineering, Jilin University,Changchun 130026,China)

***Abstract*—In actual use, the signal detected by the magnetic resonance magnetic resonance sounding (MRS) water detector is very weak and is highly susceptible to various noises in the environment[1-3]. The main forms of these noises are power frequency, pulse and white noise. In order to accurately extract the characteristic parameters and reduce the probability of subsequent inversion interpretation errors, it is crucial to study how to reduce or even eliminate these noises[4]. In view of the complex diversity of environmental noise, this paper proposes a fast fixed-point algorithm based on independent component analysis that can effectively and satisfactorily meet the acquisition requirements for signal-to-noise separation. When the digital orthogonal method is used to solve the blind source separation problem, the original signal amplitude recovery is realized by the spectrum correction method. By further comparison and demonstration, the algorithm is found to perform well on the signal-to-noise separation. The simulation results show that the algorithm can effectively The signal-to-noise separation of the full-wave MRS signal is achieved[5], and the relative error between the initial amplitude and the relaxation time after data fitting is less than ±5.00%.**

***Key words*—NMR sounding; signal to noise separation; complex signal; independent component analysis**

INTRODUCTION

Water resources are one of the most important natural resources for human survival and an irreplaceable strategic resource in the development of the national economy[6]. With the rapid development of industry and agriculture and the continuous improvement of people's living standards, the demand for water is increasing, and the contradiction between water supply and demand is becoming more and more serious. Therefore, in the 2006-2020 National Medium- and Long-Term Science and Technology Development Plan, the “Optimization of Water Resources Allocation and Comprehensive Development and Utilization” will be included in the key areas and its priority themes. Groundwater is an important part of water resources[7]. At the same time, the unreasonable development and utilization of groundwater may cause some geological disasters such as landslides, dam leakage, mine/tunnel water inrush, resulting in major losses in the national economy，and threaten the safety of people's lives and property[7-10]. Therefore, the high-efficiency and high-precision exploration of groundwater has become a major problem that needs to be solved urgently in social and economic development[11].

The Independent Component Analysis (ICA) method is an effective blind source separation method[11-14]. The basic idea is to separate the source from a set of mixed observation signals when the source signal, noise and mixing mechanism are unknown[15]. An analytical process of signals. In view of the complexity of the noise contained in the MRS signal and the uncertainty characteristics of the hybrid mechanism[16], this project conducts research on the magnetic resonance sounding signal detection technology based on the independent component analysis theory. The implementation of the project can improve the anti-interference ability of the magnetic resonance detector[17-18]. Expanding the application range of instruments, providing strong support for solving groundwater detection and evaluation under complex noise background, has important social significance and broad application prospects[19-20].

1 OVERALL STRUCTURAL DESIGN

In order to detect the magnetic resonance signal effectively in complex noise environment, it is necessary to understand the source, distribution and intensity of the noise of the magnetic resonance signal[21]. The time-frequency characteristics of noise are obtained by analyzing several typical noises, such as power frequency harmonics, spike noise and random noise, in the complex environment measured in the field[22-26]. At the same time, according to the different water content, porosity of water reservoir and *electrical conductivity of underground media, the*

magnetic resonance signal is simulated, and according to different mixing mechanism, the data model of noisy magnetic resonance signal is constructed, which lays a foundation for the follow-up research of magnetic resonance signal detection based on independent component analysis[27].Independent Component Analysis (ICA) algorithm requires that the observed signal M is composed of independent source signal N through some unknown linear combination (m < n), and at most one of the source signals is Gauss distribution. The basic idea of ICA model solving method is to use some objective function and optimization algorithm to measure the independence of separated random variables[28].According to the central limit theorem, the measurement of dependence degree between random signals can be accomplished by non-Gaussian measurement. At present, negative entropy and kurtosis are mainly used to measure the non-Gaussian property of random variables. In view of the better stability of negative entropy, FastICA algorithm[29-31] with negative entropy as the objective function is chosen to achieve the separation of MRS signals with noise.Therefore, the algorithm design of magnetic resonance conjecture measurement signal based on independent component analysis under complex noise should have the following functions:Firstly, the characteristics of each noise and signal are analyzed, then the signal and noise are superimposed by MATLAB to simulate the NMR signal with power frequency noise, white noise and impulse noise. Then, the signal-noise separation of the NMR signal with power frequency noise, white noise and impulse noise is carried out by independent component analysis algorithm.Secondly, the amplitude of the obtained NMR signal is restored[32].

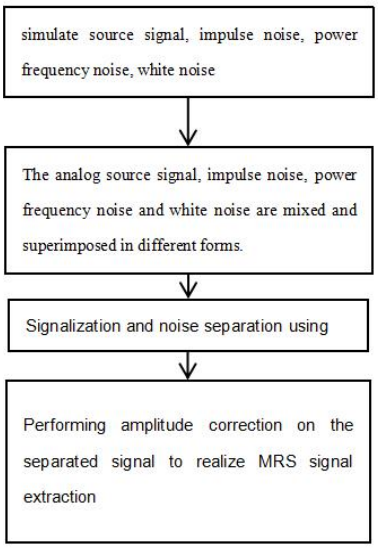

Fig.1 block diagram of the whole structure

2 Each part of the function and implementation process

2.1 Analog various signals

Firstly, the NMR source signal, pulse signal, power frequency noise and white noise are simulated by matlab, and the amplitude and phase frequencies of each signal are analyzed respectively.

2.2 Superposition and Mixing of Various Signals

In order to achieve effective separation of mixed signals, the maximum negative entropy of FastICA algorithm is taken as the goal. In order to obtain the maximum negative entropy, the selection of non-linear functions becomes very important in the implementation of the algorithm[33]. Because different non-linear functions are suitable for processing different types of signals (Gauss, sub-Gauss, Super-Gauss), the selection of non-linear functions in FastICA algorithm for MRS signal is realized by analyzing the Gauss property of MRS signal itself and its typical noise[34-35].Therefore, it is required that the observed signal M is composed of independent source signal N through some unknown linear combination (m n), and at most one of the source signals is Gauss distribution.The algorithm simulates four-channel signal acquisition. Four non-linear combinations of NMR source signal, pulse signal,power-frequency noise and white noise are combined to generate power-frequency noise, white noise and impulse noise with different sizes to simulate NMR signals collected in complex environments[36].

2.3 Signal-Noise Separation

Independent component analysis (ICA)[23] is used to separate the simulated four NMR signals with different sizes of power frequency noise, white noise and impulse noise.

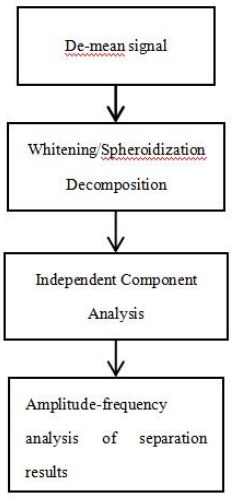

Fig.2 Signal and noise separation overall steps

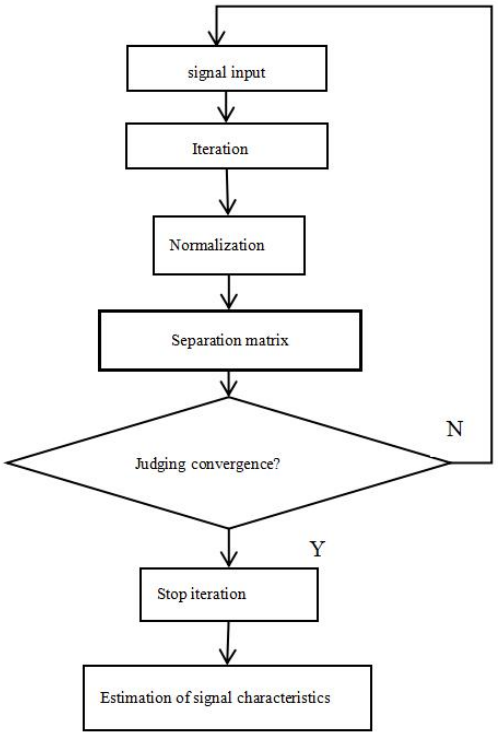

Fig.3 Independent component analysis block diagram

2.4 Nuclear magnetic signal amplitude recovery

When the ICA algorithm is applied, the separated signal may have an inconsistent amplitude and inconsistent order compared with the source signal. The order inconsistency problem can be determined by the MRS signal and the spectral prior information of the noise. However, for the amplitude uncertainty problem, the initial amplitude of the MRS signal determines the amount of groundwater[37], which will lead to the wrong estimation of the water content, which will affect the data interpretation results. Therefore, the recovery of the effective MRS signal amplitude becomes the key factor affecting the performance of the algorithm. . Since the MRS signal is a cosine signal with an E-index attenuation centered on the Larmor frequency of the measured region, its spectrum has obvious characteristics. In view of this, a method based on the frequency domain characteristics of the signal is proposed to carry out the amplitude recovery of the effective MRS signal.

After the ICA separation, the amplitude of the MRS signal is far removed from the initial amplitude of the known ideal MRS signal[38-39]. Therefore, the spectral correction method is needed to separate the amplitude recovery of the MRS signal.

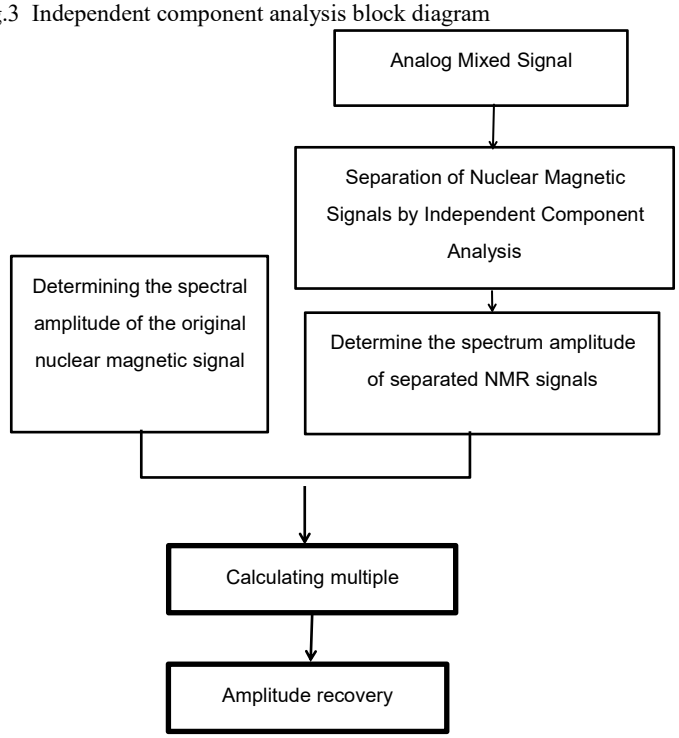

Fig.4 Amplitude recovery block diagram

3 ALGORITHM SIMULATION

3.1 Simulate four source signals

The Ramohr frequency of the simulated site is 2325 Hz, and the NMR signal is generally satisfied:

$$E(t,q) = E_0(q)\exp(-t/T_2^*)\cos(2\pi f_L t + \varphi_0)$$

Here $E_0 = 150, T_2^* = 180, \varphi_0 = \frac{\pi}{4}$

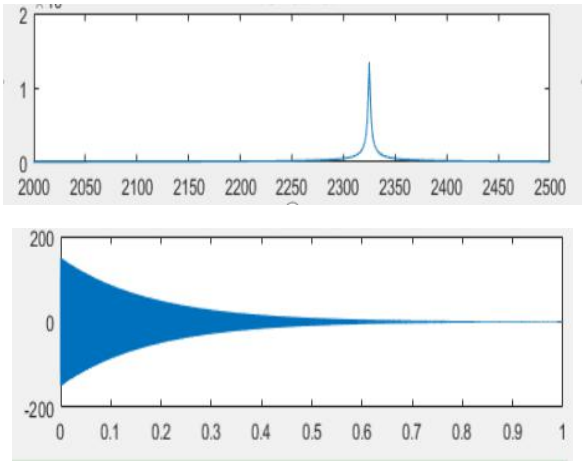

Fig.5 Source signal time domain (a), frequency domain (b) curve

Simulated pulse signal, power frequency noise of 2300Hz, white noise:

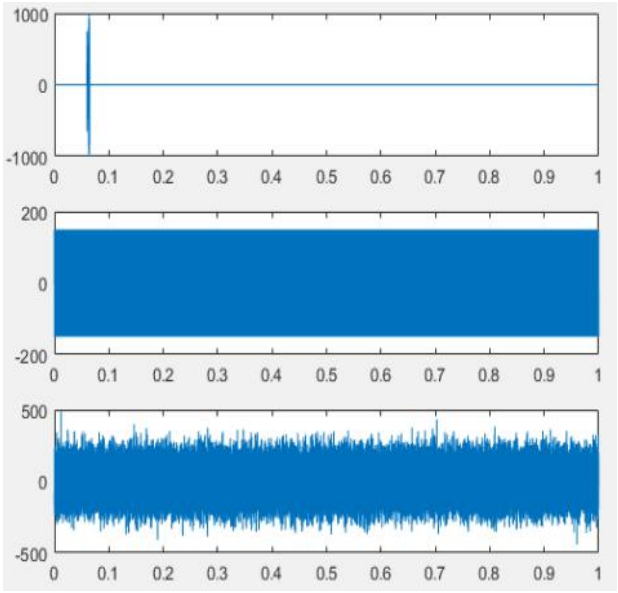

Fig.6 Pulse, power frequency, white noise time domain curve

3.2 Linear superposition of four source signals

The four source signals are linearly combined as follows:

$$\begin{pmatrix} x_1(t) \\ x_2(t) \\ x_3(t) \\ x_4(t) \end{pmatrix} = \begin{pmatrix} 1 & 0.1 & 0.1 & 0.1 \\ 1 & 0.7 & 1.6 & 1.9 \\ 1 & 2.1 & 0.85 & 2.0 \\ 1 & 1.0 & 2.0 & 1.5 \end{pmatrix} \times \begin{pmatrix} E(t,q) \\ f_m(t) \\ f_g(t) \\ f_b(t) \end{pmatrix}$$

Among them, $x_1(t), x_2(t), x_3(t),$ and $x_4(t)$ are analog four-way NMR signals with different degrees of pulse signal $f_m(t)$, power frequency $f_g(t)$, 2300 Hz powe r frequency noise $f_b(t)$, white noise.

The simulation and signals are as follows:

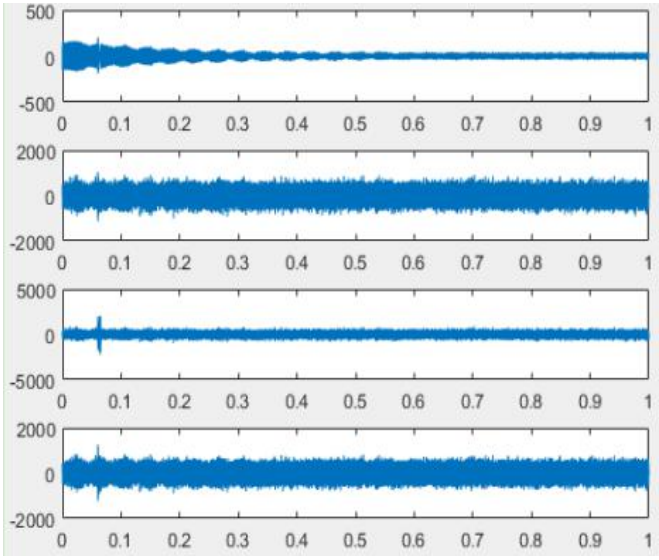

Fig.7 Time domain curve after pulse, power frequency, white noise and nuclear magnetic signal superposition

3.3 Independent Component Analysis to Separate Unmixing Signals

Independent component analysis of the above four combined signals yields the following four de-mixing signals:

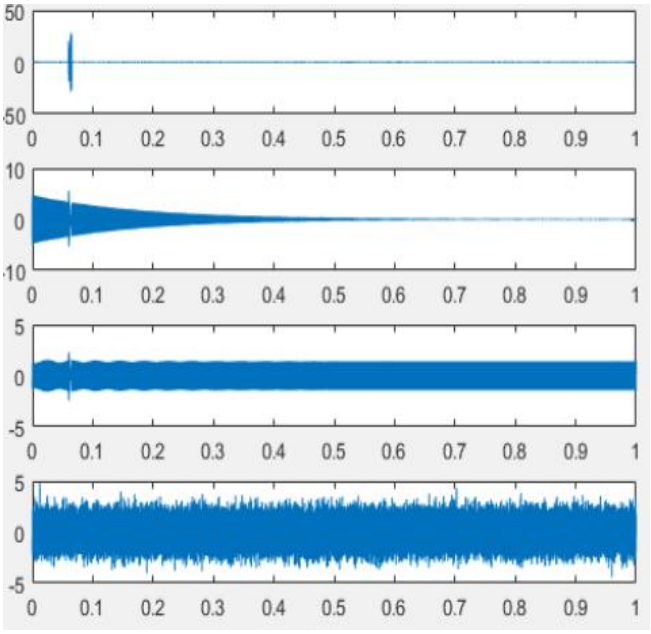

Fig.8 Independent component analysis, time domain curve after unmixing

3.4 Spectrum Correction Method for Amplitude Recovery of Separated MRS Signals

It can be seen from Fig. 9 that the demixed signal obtained by the independent component analysis method is substantially identical in form but different in order from the original signal.

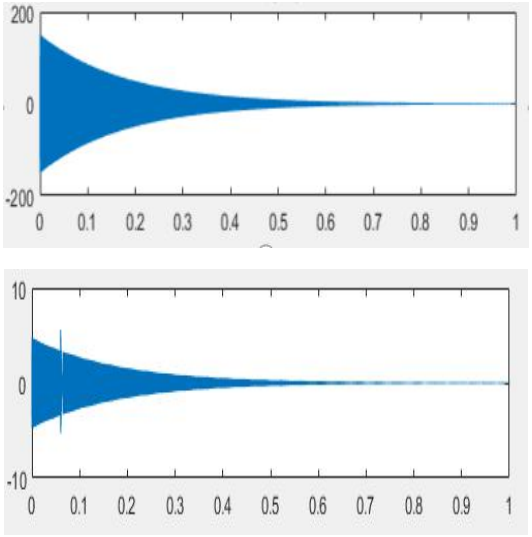

Fig.9 Source signal and unmixed signal comparison chart

It is not difficult to find that the amplitude difference between the decomposed signal of original NMR and that of independent component analysis (ICA) is about 32 times that of the decomposed signal.The amplitude of separated MRS signal is recovered by spectrum correction method.

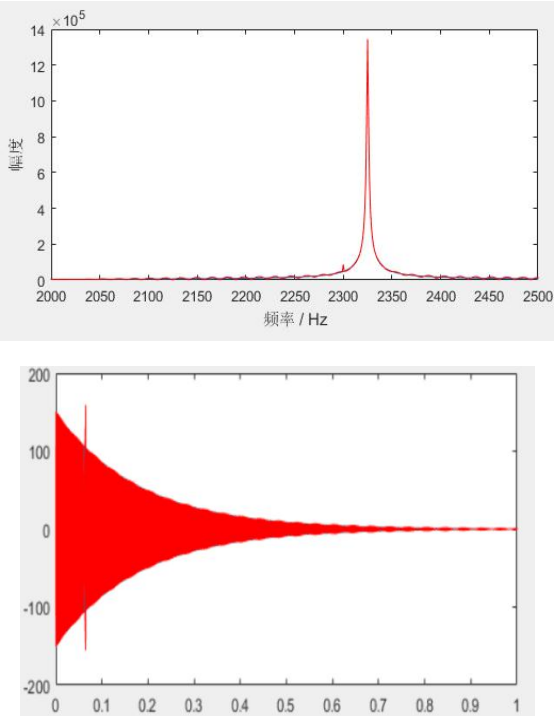

Fig.10 Time domain (a), frequency domain (b) curve comparison diagram of source signal and unmixed signa

It is found that the amplitude of the NMR signal obtained by independent component analysis is basically the same as that of the source NMR signal, and the relative error is small.

4 CONCLUSION

By using the independent component analysis (ICA) algorithm to decompose the mixed signal with noise, the signal obtained by the spectrum correction method is basically the same as the original NMR signal[40], thus the separation and restoration of the mixed signal are basically realized. In the process of researching the denoising method of NMR signal, the four mixed signals obtained from actual acquisition are simulated by MATLAB software, and the non-linear function suitable for the characteristics of NMR signal and noise is selected through the application of independent component analysis algorithm. Because the amplitude of the separated de-mixing signal can not be determined, but it is similar to the original signal in form, the original signal itself and its solution are obtained by spectrum correction method. The amplitude relation of mixed signal is used to recover the amplitude of separated signal. Through matlab simulation and algorithm processing, as well as the analysis of frequency domain, It is proved that the independent component analysis algorithm and the spectrum correction algorithm can effectively remove the power frequency interference[41], impulse noise and white noise in the nuclear magnetic signal while retaining the time domain of the source nuclear magnetic signal. The frequency domain characteristics show its effectiveness and practicability.

Reference

[1] Zhou Yuanyuan. Research on Denoising Method of Full Wave MRS Signal Based on ICA[D].Jilin University, 2016.

[2] Tian Baofeng, Zhou Yuanyuan, Wang Yue, Li Zhenyu, Yi Xiaofeng.Study on noise filtering method of full-wave NMR signal based on independent component analysis[J].Acta Physica Sinica,2015,64(22):446-457.

[3] Chen Junlin, Peng Runmin, Yan Yan, Zhao Weiguang. Extraction of Cognac Water System Based on Independent Component Analysis and Morphological Characteristics[J]. Remote Sensing for Land and Resources, 2018, 30(04): 163-170.

[4] Wang Haiyu, Wang Yinglong, Yan Jianliang, Hu Jianfeng.Fatigue EEG Analysis Based on Independent Component Analysis Noise Reduction and Integrated Classifier[J].Science Technology and Engineering, 2018, 18(32):200-205.

[5] Xie Xueduo, Xiao Li, Qu Wenzhong. Independent component analysis method for bolt loosening detection

under temperature changing conditions [J]. Vibration. Test and Diagnosis, 2018, 38(05): 922-928+1078.

[6] Gao Yijin, Tong Jixin, Dai Jie. Oil price prediction based on wavelet neural network based on independent source analysis[J].Statistics & Decision,2018,34(19):95-99.

[7] Wu Jie, Zhou Chunyu, Yang Ye, Fu Ling.Study on the activation area of brain by emotional stimulation based on group independent component analysis method[J].Progress in Biomedical Engineering,2018,39(03):125-129 .

[8] Wang Ziming, Zhao Wenjie. Analysis of the method of band selection for hyperspectral imagery using independent component analysis [J]. Science and Technology Economics Guide, 2018, 26 (27): 157+159.

[9] Fu Ling,Wu Jie.Application of Independent Component Analysis in Visual Motion Nuclear Magnetic Resonance Data Processing[J].Chinese Journal of Medical Physics,2017,34(07):676-680.

[10] WANG Peiliang, YE Xiaofeng, YANG Zeyu.Adaptive fault monitoring method for independent component correlation analysis[J].Control Theory & Applications, 2018, 35(09):1331-1338.

[11] Gao Yusheng,Zhao Yingjun.Study on high-resolution satellite image change detection method[J].Uranium Geology,2018,34(04):245-251.

[12] Wang Jing,Jin Andi.Dimension Reduction and Segmentation of Hyperspectral Image Based on Independent Component Analysis[J].Surveying and Spatial Geography Information,2018,41(06):86-90.

[13] Liu Ning,Yang Jian.Application of Generating Confrontation Network in Classification of Depression[J].Computer Applications and Software, 2018, 35(06):163-168+233.

[14] Liu Gang,Wang Hang,Mu Wenjun.A Method for Identifying Bit Vibration Signal Based on Independent Component Analysis[J].Science Technology and Engineering,2018,18(16):33-37.

[15] Zhao Junxia. Resting state brain network based on independent component analysis[D].Hunan Normal University, 2018.

[16] E Jianwei. Analysis and forecast of international gold price based on independent component analysis [D]. Shaanxi Normal University, 2018.

[17] Sun Jingyang,Yu Chunyu,Dong Shijia.Research on Noise Reduction of Independent Component Analysis for Nonlocal Mean Noise Prediction[J].Optics and Precision Engineering,2018,26(02):511-516.

[18] Quan Haiyan, Gao Lue. Independent Component Analysis of Gravity Solid Tide Signal Based on a Simplex Neighborhood and Multi-role Evolution Strategy Algorithm[J].Progress in Geophysics, 2018, 33(04): 1403-1409.

[19] Gao Likun. Real-time ECG signal extraction algorithm and ASIC design based on FastICA[D].Zhejiang University, 2018.

[20] Dong Zhe,Liu Wenjuan.Fault Monitoring Based on Improved Dynamic Kernel Independent Component Analysis[J].Industrial control computer, 2017, 30(10): 24-26.

[21] Dai Wei, Shang Zhenhong, Xu Yonghua, Liu Hui, Yang Yaguang, Qiang Zhenping. Method for Eliminating Radio Frequency Interference Signals Based on Independent Component Analysis [J/OL]. Astronomical Research and Technology: 1-11[2019-01-03].672 -7673.20181219.001.

[22] Comment on ‘Differential evolution technique-based short-term economic generation scheduling of hydrothermal systems’ by K.K. Mandal, N. Chakraborty Electric Power Systems Research 78 (2008) 1972–1979[J]. Mohammad Reza Ahmadi,Abdollah Ahmadi, Mohammadreza Janghorbani, Foad H. Gandoman. Electric Power Systems Research.

[23] Connectionist model predicts the porosity and permeability of petroleum reservoirs by means of petro-physical logs: Application of artificial intelligence[J]. Mohammad-Ali Ahmadi,Mohammad Reza Ahmadi,Seyed Moein Hosseini,Mohammad Ebadi. Journal of Petroleum Science and Engineering.

[24] Is Complexity Reachable through Planning Conditions in Written Task Performance?[J]. Reza Khorasani,Seyyed Hossein Kashef,Mohammad Reza Ahmadi. Procedia - Social and Behavioral Sciences.

[25] Influence of the time to egg stripping on eyeing and hatching rates in rainbow trout Oncorhynchus mykiss under cold temperatures[J]. Azin Mohagheghi Samarin,Mohammad Reza Ahmadi,Teruo Azuma,Gholam

Reza Rafiee,Bagher Mojazi Amiri,Mohammad Reza Naghavi. Aquaculture. 2008(1)

[26] Comment on “Multi-objective optimization for combined heat and power economic dispatch with power transmission loss and emission reduction” Shi B, Yan LX, Wu W [Energy 2013; 56: 226–34][J]. Abdollah Ahmadi, Mohammad Reza Ahmadi. Energy.

[27] Assessment of parameters for precipitation simulation of heat treatable aluminum alloys using differential scanning calorimetry[J]. Ahmad FALAHATI,Jun WU,Peter LANG ,Mohammad Reza AHMADI,Erwin POVODEN-KARADENIZ, Ernst KOZESCHNIK. Transactions of Nonferrous Metals Society of China. 2014(7)

[28] Microstructural investigation of thermally aged nickel-based superalloy 718Plus[J]. Lawrence Whitmore,Mohammad Reza Ahmadi,Martin Stockinger, Erwin Povoden-Karadeniz, Ernst Kozeschnik,Harald Leitner. Materials Science & Engineering A.

[29] Comment on “Hybrid DE–SQP algorithm for non-convex short term hydrothermal scheduling problem” by S. Sivasubramani and K. Shanti Swarup [Energy Convers. Manage. 52 (2011) 757–761][J]. Mohammad Reza Ahmadi. Energy Conversion and Management.

[30] A note on short-term hydro-thermal scheduling[J]. Ali Esmaeily,Fatima Raeisi,Abdollah Ahmadi,Mohammad Reza Ahmadi. Energy Conversion and Management.

[31] The microstructure of heat-treated nickel-based superalloy 718Plus[J]. Lawrence Whitmore,Mohammad Reza Ahmadi,Laure Guetaz, Harald Leitner,Erwin Povoden-Karadeniz, Martin Stockinger, Ernst Kozeschnik. Materials Science & Engineering A.

[32] Evaluating the effectiveness of mixed-integer linear programming for day-ahead hydro-thermal self-scheduling considering price uncertainty and forced outage rate[J]. Ali Esmaeily,Abdollah Ahmadi,Fatima Raeisi,Mohammad Reza Ahmadi,Ali Esmaeel Nezhad,Mohammadreza Janghorbani. Energy.

[33] Cutoff grade optimization based on maximizing net present value using a computer model[J]. Mohammad Reza Ahmadi. Journal of Sustainable Mining. 2018(2)

[34] Cutoff grade optimization in open pit mines using genetic algorithm[J]. Mohammad Reza Ahmadi,Reza Shakoor Shahabi. Resources Policy.

[35] Comment on “Hybrid DE–SQP algorithm for non-convex short term hydrothermal scheduling problem” by S. Sivasubramani and K. Shanti Swarup [Energy Convers. Manage. 52 (2011) 757–761][J]. Mohammad Reza Ahmadi. Energy Conversion and Management.

[36] Cutoff grades optimization in open pit mines using meta-heuristic algorithms[J]. Mohammad Reza Ahmadi,Abbas Aghajani Bazzazi. Resources Policy.

[37] Comparative efficacy of two anesthetic agents in the Sobaity sea bream, Sparidentex hasta (Valenciennes 1830)[J]. Majid Afkhami,Mohammad Reza Ahmadi, Alireza Salarzadeh,Maryam Ehsanpour. Comparative Clinical Pathology. 2014(4)

[38] Plasma biochemistry values in wild female hawksbill turtles (Eretmochelys imbricata), during nesting and foraging seasons in Qeshm Island, Persian Gulf[J]. Maryam Ehsanpour,Mohammad Reza Ahmadi,Amir Houshang Bahri,Majid Afkhami,Kimberly J. Reich. Comparative Clinical Pathology. 2015(3)

[39] New computer program to calculate the symmetry of molecules[J]. Ali Reza Ashrafi,Mohammad Reza Ahmadi. Central European Journal of Chemistry. 2005(4)

[40] RETRACTED ARTICLE: Evolving artificial neural network and imperialist competitive algorithm for prediction permeability of the reservoir[J]. Mohammad Ali Ahmadi,Mohammad Reza Ahmadi,Seyed Reza Shadizadeh. Neural Computing and Applications. 2013(2)

[41] The effect of levamisole hydrochloride on survival of Persian sturgeon (Acipenser persicus) fry[J]. Shahabeddin Safi,Habib Vahabzadeh Roodsari,Mohammad Reza Ahmadi. Journal of Applied Ichthyology.

Design and development of anti-collision porcelain system based on STM32

Mao Ruimin, Tang Yanghui, Min Jie
(College of Instrumentation & Electrical Engineering, Jilin University)

***Abstract*—This system is designed to solve the problem of collision between porcelain when driving a car. Ultrasonic sensors and pressure sensors are used to measure the distance between pedestrians and vehicles. When a certain safety distance is exceeded or pedestrians move to the vehicle at a certain speed. The car alarm system issues a warning to inform pedestrians. At the same time, for normal pedestrians, the driver may be prompted that there may be dangers at present, so as to reduce the incidence of traffic accidents; the pressure sensors used in the system can actually detect pedestrians and vehicles. When colliding, the magnitude of the collision force between the pedestrian and the car can be used as auxiliary evidence for the traffic police to judge the responsibility of the accident.**

***Keywords*— anti-collision porcelain, automotive, ultrasonic sensor, pressure sensor**

0 FORWORD

WITH the improvement of the national economic level and comprehensive national strength, cars have gradually become the main means of transportation, and each household has its own private car. There is a strange phenomenon that has spread along with it, that is, it touches porcelain. And almost every day of the news has reports on bumping porcelain. The cost of illegally hitting porcelain is small, and the responsibility for on-site responsibility is difficult. This is also the reason why it is impossible to contain the porcelain. Even if it is not possible to touch the porcelain, you can continue to touch the car and let the owner prevent it[1].

The emergence of the driving recorder solved the problem of difficulty in identifying the site responsibility, effectively curbed the occurrence of the collision of porcelain, but there are still some people who touch the porcelain and hold the luck, continue to try to touch the porcelain, some owners clearly have a driving recorder, but also not sure Their own responsibilities, but because of the rush, they were forced to compromise, and condone the behavior of the porcelain. Some people who touch porcelain, technical performance is relatively high, even if you watch the driving recorder, you can not be held responsible.

From the perspective of the porcelain player, the porcelain is also a piece of Very dangerous things, there are many cases in China and abroad that are killed by the collision of porcelain. Due to the blind spot of the driver's vision or the lack of reaction, it is likely to cause casualties of the porcelain touchers, causing great losses to both parties. The present invention intends to provide an anti-collision porcelain device during driving of a car, which can turn on the camera when the car is moving, and reminds the owner and pedestrian when the porcelain is found to be in contact with the porcelain, effectively preventing the collision of the porcelain and improving the driving safety.

1 OVERALL SYSTEM DESIGN

The system design uses the single-chip model STM32F103ZET6 as the core processor, with two ultrasonic modules HC-SR04 for distance measurement, in order to accurately measure the distance between pedestrians and vehicles and pedestrian speed; with the pressure sensor HX711 to measure when the pedestrians collide with the car Time force; use the camera OV7670 and LCD display for real-time image display.

2 HARDWEAR DESIGN PART

2.1 Overall system design

The emergence of the driving recorder solved the problem of difficulty in identifying the site responsibility, effectively curbed the occurrence of the collision of porcelain, but there are still some people who touch the porcelain and hold the luck, continue to try to touch the porcelain, some owners clearly have a driving recorder, but also not sure Their own responsibilities, but because of the rush, they were forced to compromise, and condone the behavior of the porcelain. Some people who touch porcelain, technical performance is relatively high, even if you watch the driving recorder, you can not be held responsible.

From the perspective of the porcelain player, the porcelain is also a piece of Very dangerous things, there are many cases in China and abroad that are

killed by the collision of porcelain. Due to the blind spot of the driver's vision or the lack of reaction, it is

likely to cause casualties of the porcelain touchers, causing great losses to both parties. The present invention intends to provide an anti-collision porcelain device during driving of a car, which can turn on the camera when the car is moving, and reminds the owner and pedestrian when the porcelain is found to be in contact with the porcelain, effectively preventing the collision of the porcelain and improving the driving safety.

The system design uses the single-chip model STM32F103ZET6 as the core processor, with two ultrasonic modules HC-SR04 for distance measurement, in order to accurately measure the distance between pedestrians and vehicles and pedestrian speed; with the pressure sensor HX711 to measure when the pedestrians collide with the car Time force; use the camera OV7670 and LCD display for real-time image display.

The system adopts integrated development board and standard modular circuit design. The overall block diagram structure of the system is shown in Figure 1.

2.1.1 Ultrasonic module

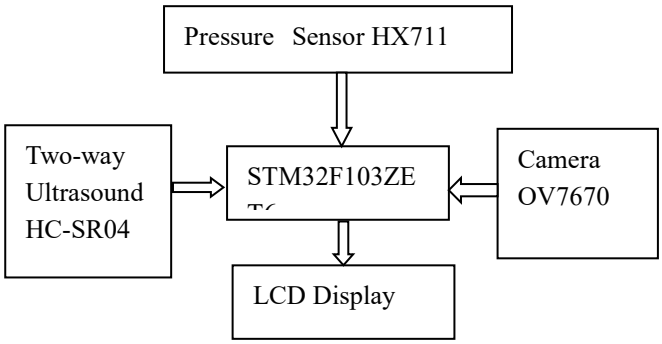

Fig.1 System block diagram

The system's distance measurement module uses SC-SR04Ultrasonic distance measuring sensor, which has high measurement performance and strong stability, and has almost no gap with foreign ultrasonic sensors such as SRF05 and SRF02.[2][3] The module's measurement dead zone is minimal, only 2cm, and can be used for stable measurement. Most of it is used for non-contact measurement. How the module works:

(1) Trigger I/O ranging, giving a high level signal of at least 10 microseconds;

(2) The module clock circuit can automatically transmit 8 square wave signals with a frequency of 40khz and automatically detect the state of the return signal.

(3) When a return signal is detected, the I/O port is used to output a high-level clock signal, and the time during which the rising edge of the high-level signal continues is the time from the transmission to the return;

(4) Distance = (signal rising edge duration * speed of sound) / 2. Sound speed default: 340m / s.

The ultrasonic operation timing chart is shown in Figure 2.

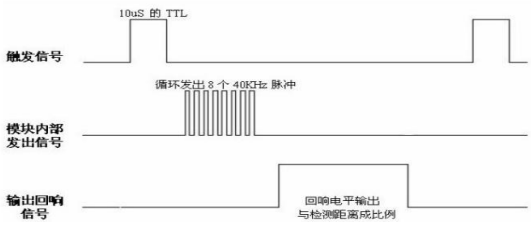

Fig.2 Ultrasonic working sequence diagram

This design uses a two-way ultrasonic module, which increases the data acquisition range of distance measurement, and reduces the blind area measurement range, improving the overall measurement accuracy of the system. Figure 3 is a schematic diagram of the ultrasonic working circuit:

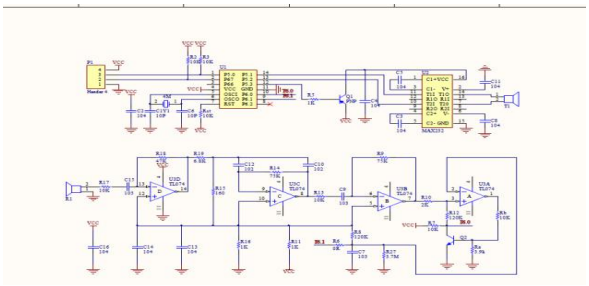

Fig.3 Ultrasonic module circuit diagram

2.1.2 Pressure sensor HX711

The pressure measurement module selected for this design is the HX711 called heavy duty sensor. The HX711 AD converter is a high precision AD conversion chip with up to 24 bits of conversion. Compared with others AD of the same type, the chip has more integrated circuit modules, including power supply voltage regulator circuit, on-chip clock frequency oscillator, etc., as well as peripheral circuits required by the same type of chip, so that it has high integration. The response speed is faster and the anti-interference is enhanced when measuring. The overall manufacturing cost of the pressure sensor is reduced, and the performance and reliability of the module are improved [4]. The main reason for choosing this sensor in this design is that it is cheap, easy to use, and flexible to operate.[5] [6]

Principle of the measurement procedure of the pressure sensor: Assume that the gravity is M Kg, (x < 5Kg), and the measured AD value is y， The sensor output, the voltage sent to the AD module is M Kg * 4.3mV / 20Kg = 0.215 mV, the gain is 128 times after the amplification is 128 * 0.215A = 27.52 AmV is converted to 24 bit The digital signal is 27.52 mV * 2^24 / 4.3 V = 107374.182, so y = 107374.182A, so that M = y / 107374.182;

Measuring procedure Weight_Shiwu=(unsigned long)((float)Weight_Shiwu/107.4);

The HX711 range used in this design is 20kg, and the schematic diagram of the module circuit is shown in Figure 4:

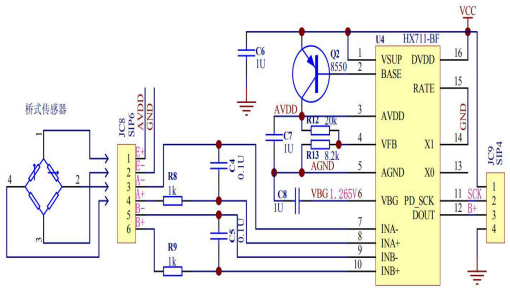

Fig.4 Pressure sensor module circuit schematic

The internal AD of the gravity sensor module converts the analog quantity into a digital quantity, and internally contains a strain resistor. The two-range 1K strain resistance of the bridge affects the input voltage, and the output voltage is converted into a 24-byte digital signal by 128-fold gain. The weight of 0-5kg is passed through the strain resistance corresponding to a digital signal. Since the value of the dependent variable y varies little with the independent variable, it can be regarded as a linear relationship, and the internal program of the chip module also regards it as a linear relationship. Our gravity sensor converts the 0-5kg range to the 0-50N range and corresponds to the digital one-to-one. The gravity sensor is changed to a pressure sensor to output the collision pressure value. Matlab draws the independent bridge resistance x (ohm) and the dependent variable output voltage V (mv) as shown below.

```
x=0:0.1:1000;
y=1.65-3300./(1000+x);
plot(x,y);
xlabel('应变电阻阻值Ω');
ylabel('输出电压压值mV');
grid on
```

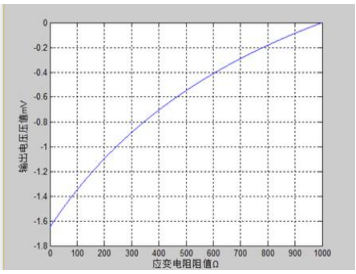

Fig.5 Matlab draws bridge input and output diagram

2.1.3 Camera and LCD display module

OV7670 CAMERACHIPTM image sensor with low power consumption and relatively small size. It also provides all the functions of VGA image transmission and image processor·The OV7670 has a pixel size of 656x488, of which 640x480 effective pixels (ie 307200). Controlled by the SCCB bus protocol [9]. The product's VGA image transfer rate can be up to 30 frames per second. Can meet the image acquisition functions required for the design. In fact, the object is shown in Figure 6

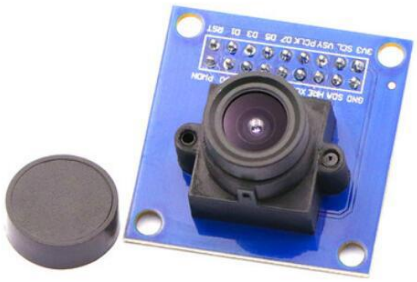

Fig.6 Camera physical cable diagram

The screen used in this system is a TFTLCD screen with a resolution of 800*480. It is driven by the NT35510 chip, so no additional drivers are required, and STM32 or other types of microcontrollers can be easily used. The frame rate is calculated as fps*(640+144)*(510+x)*2 = 12M(Pclk) [10] [11]. Figure 7 shows the OV7670 working sequence diagram:

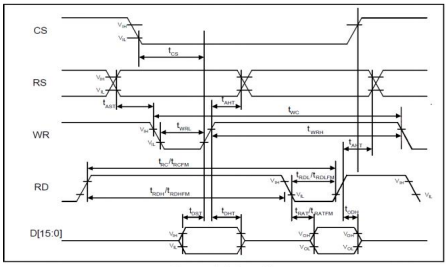

Fig.7 OV7670 working sequence diagram

OV7670 onboard backlight, only need 3.3V & 5V supply voltage to work, no additional voltage, built-in FIFO memory, its processing speed can reach 78.9 frames / S [12] [13]. Figure 8 shows the schematic diagram of the OV7670 circuit design:

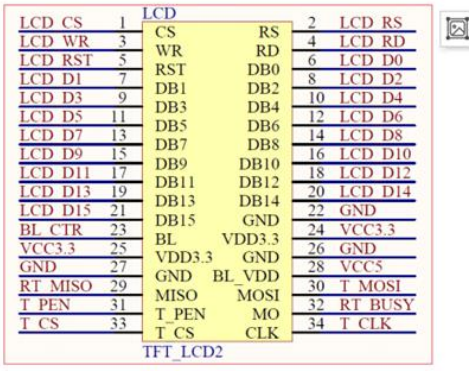

Fig.8 OV7670 pin circuit diagram

3 STM32ZET6 SYSYEM PROGRAMMING

In addition to real-time measurement of collision stress with HX711, ultrasonic HC-SR04 performs real-time distance detection. When the distance is less than the safety distance, the alarm circuit is activated and the LED flashes at the same time. The pedestrian and road conditions are monitored in real time through the camera OV7670. When the ultrasonic sensor measures that the

distance between the vehicle and the vehicle is less than the safety distance, the OV7670 camera is started to take the image, and one frame of data is sent to the host computer, and the image is displayed by the host computer software, and the image before the collision is saved and saved. [14] · The system flow chart is shown in Figure 9. The OV7670 camera captures images in real time as shown in Figure 10. The host computer receives signals as shown in Figure 11.

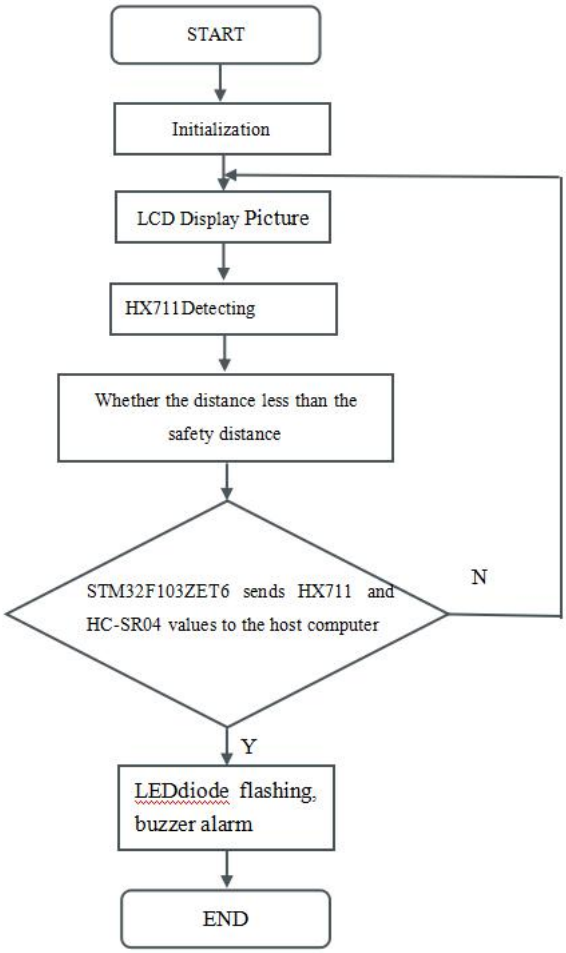

Fig.9 System flow chart

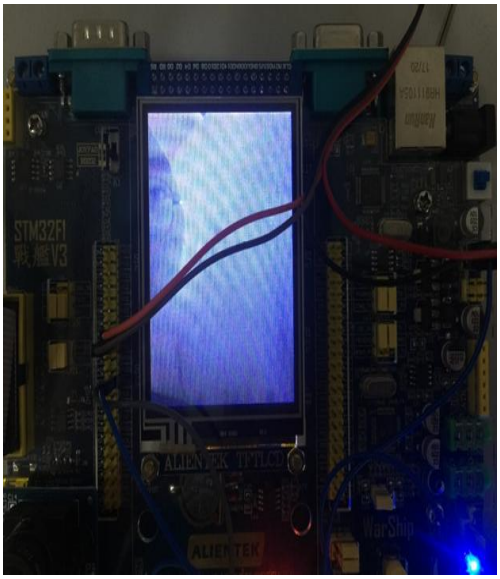

Fig.10 OV7670 camera captures images in real time

Fig.11 The host computer receives the signal

4 TEST RESULTS

TABLE1 System-to-Pedestrian Distance Test Value

Measuring distance/cm	Actual distance / cm	Relative error	Measuring distance/cm	Actual distance / cm	Relative error
50	49.57	0.86%	50	50.33	0.66%
100	100.15	0.15%	100	100.97	0.97%
150	151.92	1.28%	150	152.35	1.57%
200	203.56	1.78%	200	205.02	2.51%
250	255.75	2.3%	250	257.34	2.94%

The HC-SR04 partial values of pedestrian distance measurement results are shown in the above figure. It is easy to see from the table that the accuracy of HC-SR04 is high, which satisfies the system's requirement for pedestrian distance detection, but the clothing of different materials will have measurement results. influences. This should be improved.

5 IN CONCLUSION

The project successfully completed the design and development of the STM32 anti-collision porcelain system. By constructing pressure sensors, cameras and two-way ultrasonic modules, it is possible to complete the measurement of the expected distance between the vehicle and the pedestrian and the vehicle close to the vehicle.The measurement of collision stress and the data acquisition function such as image can complete the real-time transmission and analysis, and use the upper computer software to judge whether there is a collision. With the onboard resources of the STM32 development board, the system optimizes the system structure and saves time spent on the project.

References

[1] Investigation on the accident prevention effect of automobile driving recorder Pang Changle, 2006 Beijing University of Technology

[2] Design of Synchronous Exciter Monitoring and Switching Device Based on Single Chip Microwave Broadcasting System "Journal of Anhui Electronic Information Vocational and Technical College", 2008 Gu Yaoyu, etc.

[3] Research on ultrasonic water level measurement system based on CPLD Zhang Zhuomin, 2010 Wuhan University of Technology

[4] Research on steel wall climbing robots Ding Peng, 2012 Taiyuan University of Technology

[5] Research and design of marine multi-functional integrated navigation device based on OMAP3530 "Industrial Control Computer", 2011 Zhou Hui et al

[6] Research and application of wireless home security system for security control Shi Jianzhen, 2006 Southeast University

[7] Gold,K.Brown,A.Architecture and performance testing of a software GPS receiver for space-based applications. IEEE,2005:56-78

[8] Wright,M.Stallings,D.Dunn,D.The effectiveness of global positioning system electronic navigation. Southeast-Con,2003:2-7

[9] Bachir,Benslimane.Towards supporting GPS-unequipped vehicles in inter-vehicle geocast.IEEE,2003:23-26

[10] Design and Implementation of GPS Module Based on Windows Mobile Operating System Mobile Phone Tian Hao, 2008 Xiamen University

[11] Development of an experimental system for rough signal processing of AC power smart sensors Cheng Zhi, 2012 Xihua University

[12] Xu Jin, Zhou Ning. Single-chip communication interface of GPS receiver. Department of Astronomy, Nanjing University. Nanjing

[13] Microcontroller principle and interface technology He Hong et al Research and Implementation of GPS Locator Based on Single Chip Microcomputer Hu Chenglong, 2006 Huazhong University of Science and Technology

[14] Lai Yuwen. The thorough application of 51 single-chip C language. Science and Technology Press C language programming Tan Haoqiang.

High dynamic image synthesis based on different exposures of the same scene

Fang Tianyu, Tian Jiaxin, Yu Hang
(School of Instrument Science and Electrical Engineering, Jilin University, Changchun 130022, China)

***Abstract*—Aiming at the problem that the partial area of the image in the scene of large light is too bright or too dark, a method of combining high-dynamic range images with different exposure images of the scene is proposed. Firstly, different exposures are obtained by changing the aperture size of the camera and the length of exposure time. The images of different exposures are used to determine the camera response function, and then the high dynamic range image is synthesized according to the response curve. The experiment proves that the method can effectively improve the method. The dynamic range of the image has a good effect.**

***Keywords*—high dynamic range image image synthetic illumination**

0. PREFACE

THE dynamic range of natural scenes that can be perceived by the human eye can reach 10,000:1. Due to the technical level of ingestion and display, the video system in the consumer electronics field has been constructed in a ratio of 100:1 - 300:1. In some scenes with large light ratios, especially when shooting backlit, the images obtained are far less than the human eye[1,2].High-Dynamic Range (HDR) images can solve this problem better.Compared with ordinary images, high dynamic range images can provide more dynamic range and image details. According to the images taken at different exposure times, the final hdr image can be synthesized by using the ldr image corresponding to the best detail for each exposure time. Better reflect the visual effects in the real environment[3].It can better record and express the optical characteristics of bright and dark areas in the scene and increase its detailed features.

Many scholars have studied the synthesis methods for acquiring high dynamic range images[3].Tocci MD et al.[4] used spectroscopic techniques to acquire circuitry for different exposure images in the study.This method is to obtain an HDR image directly from a hardware device.This method generates an HDR video by changing the hardware design of the imaging system, dividing the light into different rays, and obtaining images of different exposures by fitting the light response function.This method uses a neutral filter in the design, the light utilization rate is low, and there are high requirements in hardware.Zhou Jiquan et al. gave an HDR acquisition algorithm based on camera display. In order to adapt to dynamic illumination, this method sets different exposure parameters for different digital cameras. At the same time, different images are corrected to obtain high dynamics. Range image.This method is more complicated and has a higher amount of calculation.

In this paper, the camera response curves[5] of the color image rgb channel are restored by using multiple images of different exposures in the same scene, and the mapping relationship between the pixel values of the illuminance images of each channel is obtained, and then the hdr image is synthesized.Color images create a camera response curve for the rgb channel, which causes the generated high dynamic range image to produce color cast, so color correction is required for the fused high dynamic range image.

I. BASIC PRINCIPLES

The hdr image can obtain the illumination information of the real scene, so that the picture is closer to the scene seen by the human eye.In this paper, the synthesis of high dynamic range images is performed using different photos of exposure.The algorithm flow is shown in Figure 1:

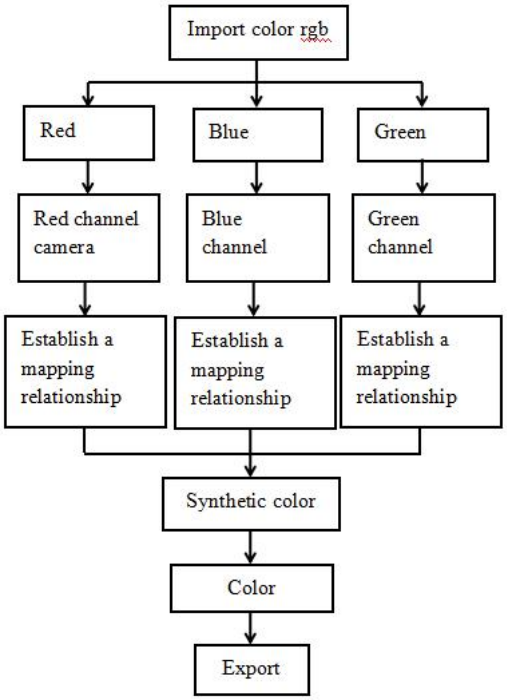

Fig.1 HDR synthesis proces

The imaging process of the camera is as follows: the light reflected by the scene is transmitted to the ccd through the lens of the camera, and the ccd performs color filtering and sensitization (photoelectric conversion), and the object is "decomposed" into a pixel by a certain arrangement. The pixel is transferred to the "analog-to-digital converter" in the form of an analog image signal[6], converted into a digital signal, transmitted to the image processor, processed into a real image, and then compressed and stored in a storage medium.The camera's imaging process is a mapping between the scene's illumination intensity and the image, the camera response curve.

A. Calculate the response curve of each channel

The rgb image is obtained by varying the three color channels of red (r), green (g), and blue (b) and superimposing them on each other.Therefore, it is necessary to calculate the response curve[7] for each of the three channels of rgb.

The images used in the algorithm are shot by the camera at a fixed point and captured under the premise of ignoring the illumination change, so the illumination intensity value Eai of the pixel i at the same position in each picture is constant.

The relationship between the pixel value Xij and the illumination intensity Eai and the exposure time Δtj is as follows:

$$X_{ij} = f(Ea_i \Delta t_j) \tag{1}$$

Where j is the jth frame image corresponding to the exposure time Δtj in each picture.

Invert the function of equation (1) and take the logarithm.

$$g(X_{ij}) = \ln Ea_i + \ln \Delta t_j \tag{2}$$

Introduce the constraint in (2), assuming that the corresponding unit exposure in the middle of the gray value in the picture is obtained, ie

$$g(X_{mid}) = 0, X_{mid} = \frac{1}{2}(X_{max} + X_{min}) \tag{3}$$

When the number of taken pictures is N, the number of sampling points of each picture is P. In order to calculate the corresponding mapping relationship, it is necessary to solve 256 g(Xmid) and P lnEai[8] in the formula (2).The number of pictures N and the number of sampling points P must satisfy the formula (4):

$$N \times P + 1 \geq 256 + N \tag{4}$$

Bringing the gray value of the sample point and the exposure time into equation (2) yields an equation, but this equation cannot find a unique solution.Solving by the least squares method, satisfying the formula (5)

$$Q = \sum_{i=1}^{N} \sum_{j=1}^{P} [g(X_{ij}) - \ln Ea_i - \ln \Delta t_j]^2 \tag{5}$$

In order to reduce the influence of nonlinear factors at both ends of the curve, the weight ω(v) can be introduced.

$$\omega(v) = \begin{cases} x - X_{min}, x \leq 1/2(X_{min} + X_{max}) \\ X_{max} - x, x > 1/2(X_{min} + X_{max}) \end{cases} \tag{6}$$

Bringing ω(v) into equation (5) gives:

$$Q = \sum_{i=1}^{N} \sum_{j=1}^{P} \{[\omega(X_{ij})[g(X_{ij}) - \ln Ea_i - \ln \Delta t_j]\}^2 \tag{7}$$

Equation (7) is the camera response curve.The color rgb image requires a separate response curve for the three channels.

B. Establish the mapping relationship between illumination and pixels of each channel

The mapping relationship between the pixel value and the illumination intensity value of each channel can be obtained by the response curve of each channel[8].

According to formula (2):

$$\ln Ea_i = g(X_{ij}) - ln\Delta t_j \tag{8}$$

Substituting ω(v) into equation (8) gives:

$$\ln Ea_i = \frac{\sum_{j=1}^{P} \omega(x_{ij})(g(x_{ij}) - \ln \Delta t_j)}{\sum_{j=1}^{P} \omega(x_{ij})} \tag{9}$$

Equation (9) is the mapping relationship between the

illumination intensity and the pixel value.

C. Synthesis of high dynamic range images

According to formula (9), the illumination intensity of each pixel can be obtained. In order to reduce the influence of error and noise, the illuminance value Eai of each pixel can be calculated by weighted averaging method using all N original images. High dynamic range image[10].

D.color correction

The response curves are calculated for the three channels of the rgb of the color image, and the synthesized high dynamic range image will produce color shift.Therefore, it is necessary to perform color correction on the synthesized image.The method adopted is to perform white balance processing[11] on the synthesized picture.Common white balance processing methods include gray world method, perfect reflection algorithm, and the like.The gray world method has a poor effect on the processing of a single color image, and color correction cannot be performed well when the color of the photograph is relatively simple[12].The perfect reflection algorithm corrects the brightest points in the image as white points for high dynamic range image color correction.The perfect reflection algorithm assumes that the brightest point on the image is the white point, and the white point is used as the reference to automatically white balance the image. The brightest point is defined as the maximum value of r+g+b[13].Specific steps are as follows:

（1） Calculate the sum of r\g\b of each pixel and save it to a temporary memory block.

（2） The threshold T[14] of the white reference point of the first 10% or other Ratio is calculated according to the size of the R+G+B value.

（3） By traversing each point in the image, the average of the cumulative sum of the r\g\b components of all points where r + g + b is greater than t is calculated.

（4） Pixels are quantized to [0, 255] for each point.

II. EXAMPLES

Using the method of this paper, the experiment of hdr picture synthesis was carried out. Fig. 2 and Fig. 3 are two pictures with different exposures in the same scene, and Fig. 4 is the hdr picture after generation.Figures 4-6 are the luminance histograms of Figures 2-4, respectively

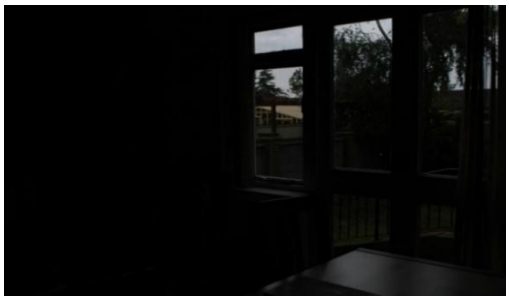

Fig.2 Low-exposure photos

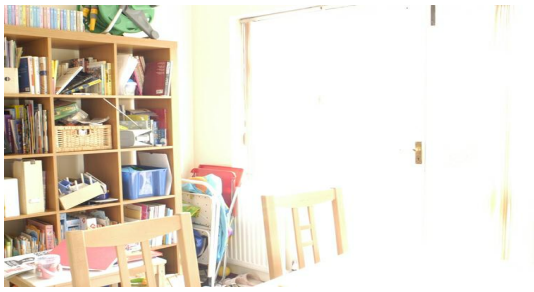

Fig.3 Excessive-exposure photos

Fig.4 Synthetic HDR Pictures

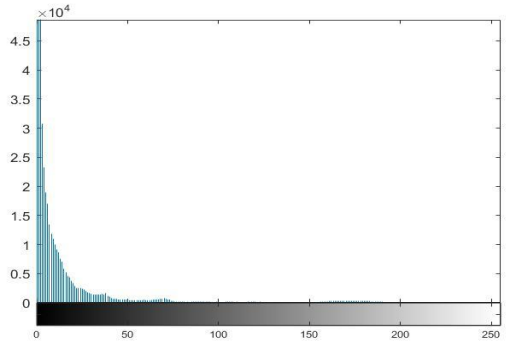

Fig.5 Low exposure picture histogram

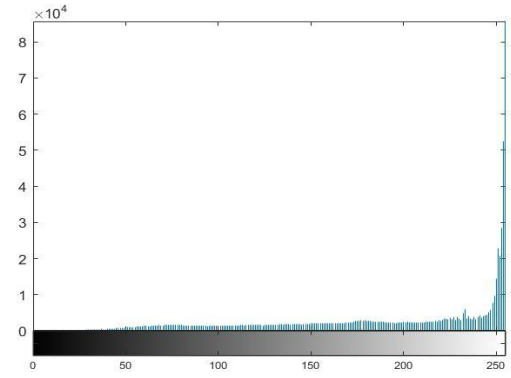

Fig.6 High exposure picture histogram

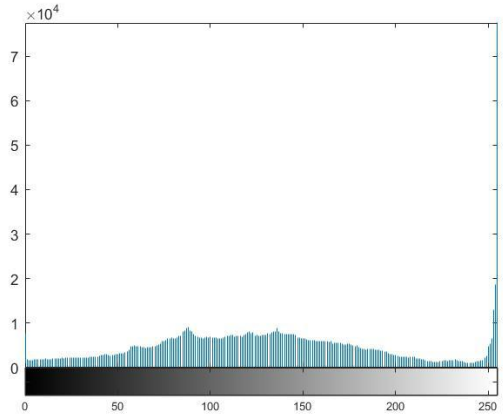

Fig.7 Synthetic high dynamic range image histogram

III. SUMMARY

In order to obtain high dynamic images and synthesize the process of ordinary cameras, this paper proposes to obtain multiple images with different exposure values of the same scene by fixed-point shooting, calculate the camera response curves for the three channels of rgb, and establish the pixel values of each channel. The mapping relationship between scene illuminances, in turn, the synthesis of high dynamic range images.White balance processing is performed on the synthesized image to eliminate the influence of color shift.As can be seen from the histogram above, in underexposed photos, the pixels are mostly concentrated in the darker portions.In an overexposed photo, the pixels are concentrated on the maximum side of the brightness.Although the synthesized photos still have some pixels stacked in the bright part, the overall distribution is normal, and the detail reduction of the photos is the best.Due to the slight jitter that may occur during the shooting process, errors occur in the fitting of the response curve and the image synthesis process, so the image needs to be registered. This problem has not been considered in this paper.

References

[1] Xie Zhifeng, Ye Guanhua, Yan Shuzhen, He Shaorong, Ding Youdong. Hdr image style migration technology based on generating confrontation network [j]. Journal of Shanghai University (Natural Science Edition), 2018, 24 (04): 524-534.

[2] Yan Suqi. Research on high dynamic range image synthesis technology based on sCMOS [D]. University of Chinese Academy of Sciences (Institute of Optoelectronic Technology, Chinese Academy of Sciences), 2018.

[3] Guo Cambridge. Research on multi-exposure fusion algorithm and hdr image synthesis and tone mapping algorithm design [d]. University of Science and Technology of China, 2016

[4] Yao Hongtao,Li Xinyan.Hdr Image Synthesis and Color Adjustment Algorithm in rgb Space[J].Journal of Changchun University of Science and Technology(Natural Science Edition),2015,38(05):145-149.

[5] Jiao Shuyun. Research on high dynamic range image acquisition algorithm based on synthesis [d]. Xi'an University of Posts and Telecommunications, 2015.

[6] Chen Jun, Hu Fuqiao.Color image hdr synthesis algorithm in yuv space[j].Computer Engineering, 2012, 38(09): 214-216+233.

[7] Chen Jun. Research on hdr image synthesis algorithm based on DaVinci platform [d]. Shanghai Jiaotong University, 2012.

[8] Ge Cheng. Research on high dynamic range image synthesis and registration technology [d]. Shanghai Jiaotong University, 2010.

[9] Zhang Jun, Dai Xia, Sun Dequan, et al. Direct fusion method for images with different exposure values[J].Journal of Software,2011, 22(4):813-825.

[10] Tocci M D,Kiser C,Tocci N,et al.A versatile HDR video production system[J]908.ACM Transactions on Graphics,2011,30(4):41-89

[11] Ilija Popadić,Branislav M. Todorović,Irini Reljin. Method for HDR-like imaging using industrial digital cameras[J]. Multimedia Tools and Applications,2017,76(10).

[12] Kang-Hyun Jo,Andrey Vavilin. HDR Image Generation based on Intensity Clustering and Local Feature Analysis[J]. Computers in Human Behavior,2010,27(5).

[13] Akasaka, H.,Yanagisawa, M.,Togawa, N.. Energy-efficient high-level synthesis for HDR architectures with clock gating[P]. SoC Design Conference (ISOCC), 2012 International,2012.

[14] Wu, J.C.-H.,Guo-Shiang Lin,Hsiao-Ting Hsu,You-Peng Liao,Kai-Che Liu,Wen-Nung Lie. Quality enhancement based on retinex and pseudo-HDR synthesis algorithms for endoscopic images[P]. ,2017.

Design and Implementation of Magnetically Coupled Wireless Charging Circuit for Cardiac Pacemaker

Di Yunpeng, Zhang Yang, Zhang Jiawei
（jilin university instrument science and engineering institute,changchun,130021）

***Abstract*--This paper firstly proposes an inductive charging design scheme for the shortcomings of the battery life of implantable cardiac pacemakers. And introduced the development status of wireless charging technology at home and abroad, the current main theories, technical means and so on. Then use the principle of coil coupling and high frequency switching technology to build a power transmission system, and simulate the system from the perspective of equivalent circuit. The system analyzes the transmission efficiency and transmission power, and the transmission distance, the frequency of the coil current, and the load size. The relationship between. Finally, the radio energy transmitting module and the radio energy receiving module are designed, and the rectification, filtering, voltage regulation and battery charging management circuits are added after receiving the power module. Experiments were carried out under the premise of working frequency of 4MHZ. It has solved the problem that the battery of the pacemaker can only be used once.**

***Keywords*--Wireless charging Magnetic coupling resonance Class E power amplifier Energy transfer efficiency Charge management**

I.INTRODUCTION

IMPLANTABLE medical devices are medical devices that are buried inside the human body. With the rapid development of modern medical technology, the variety of implantable medical devices is becoming more and more abundant, but the attendant question is: How to give long-term power to implantable medical devices?

The traditional method is generally to use disposable battery power, in the case of pacemakers, this disposable battery can generally last for 3-4 years. Once the battery runs out, you have to operate to replace the battery[1]. However, the patient does not know the battery charge surplus. Even patients may have missed the battery replacement time for some reason, causing the pacemaker to lose power. In this way, the patient has to bear the high cost of surgery, on the other hand to bear the risk of surgery. In order to solve the problem that the pacemaker needs to change the battery frequently, the radio transmission technology is applied to the charging of the pacemaker. In this paper, a high frequency low power radio transmission scheme based on magnetic coupling is proposed, the electromagnetic coupling structure is equivalent to a loosely coupled transformer without iron core, the alternating current with high frequency flows through primary coil, and according to Faraday's law of electromagnetic induction, the inductive high frequency AC voltage can be generated at both ends of the transformer secondary coil, By using rectifier Bridge to turn alternating current into direct current and voltage regulator, it can provide energy for the load and realize the transfer of electric energy from primary coil to secondary coil.

As early as the 1990s, Europe, America, Japan and other countries have begun to study radio transmission technology, and has made a major technological breakthrough[2]. Since 2007, Professor Marin Soljacic of MIT has proposed a magnetic coupling resonant wireless charging theory, that is, when two coils resonate at the same frequency, a powerful magnetic field is generated on the axis of the coil, at which point the flux of the receiving coil changes and the voltage is sensed at both ends of the coil. and successfully used this principle to light a 60W bulb two meters away[3]. Then there was a upsurge in the research of radio energy transmission technology. Han Wenjuan The transmission of wireless percutaneous power, Class E power amplifier is systematically analyzed, and a wireless percutaneous inductive charging circuit is designed. For the design of the circuit but only for the transmission efficiency of mathematical modeling, and did not carry out simulation analysis, and the charging system is an open-loop system. At present, we have a new idea and idea for the wireless charging of pacemaker, and have carried on the improvement and the design.

II.CIRCUIT MODEL AND ANALYSIS

Because it is the wireless charging technology of the pacemaker, it needs to be divided into the outer part and the implant part of the body, and its design circuit is

shown in Figure 1-1. The in vitro part is a wireless charging transmitter, which is a high frequency signal generator and a power amplifier circuit respectively. The implanted part of the body is a device for charging the pacemaker, including a rectifier filter circuit, a voltage regulator circuit and a charging circuit. It should be noted that in vitro part in the experimental process needs to be tied on the animal surface, and primary coil should be as far as possible with the implant secondary coil corresponding. At the same time, the wireless percutaneous energy transmission belongs to the loose coupling system, the transmission performance is generally poor, in order to improve the transmission capacity of the system, it is necessary to drive the original edge ring with high frequency signal[4].

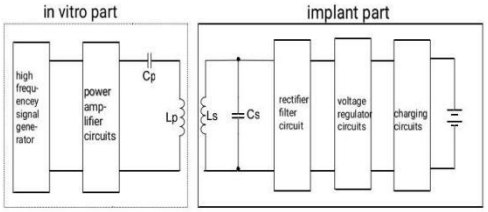

Fig.1-1 Overall circuit design

III.CIRCUIT DESIGN AND ANALYSIS

3.1 Power amplifier Analysis and design

The main types used in high frequency power amplifiers are Class C, class D and class E. For class C power amplifiers, the transistor works in the active state, the dissipation power of the leakage pole is relatively large, the efficiency of the amplifier is low, in the actual use can only reach about 60%. For class D and class E power amplifiers, transistors work in the switching state, the leakage pole voltage and current do not appear at the same time, thus greatly improving the efficiency, in the actual circuit can reach up to 90%. They are also the main types of amplifiers used in high-frequency wireless power transmission systems.

Class D Power amplifiers consist of two transistors, two tubes take turns to guide the work, but in the moment of switch conversion, two transistors may be on or off at the same time, which will reduce efficiency and may cause two of breakdown resulting in damage to the transistor. Class E power amplifier is composed of a single transistor, which makes up for the defects of class D to a certain extent, and further improves the working frequency and efficiency, but it also has its shortcomings. Class E not only requires the transistor to have a higher tolerance voltage, but also works under different load conditions, which can lead to unpredictable peak value leakage poles voltage or current, resulting in damage to the transistor. Combining the characteristics of two types of amplifiers, this product decides to select Class E[5], the typical structure of which is shown in Figure 3.1-1.

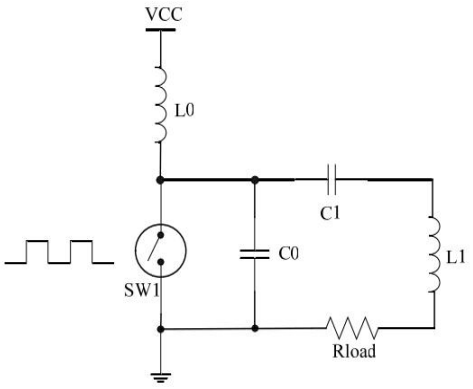

Fig.3.1-1 Typical structure of class E amplifier

Among them, L0 is a high-frequency choke coil, its role is to make the flow of the current as DC as possible, so when choosing should make the value of L0 large enough.

Capacitance C1 and inductance L2 form a series resonant circuit (primary winding impedance is mainly perceptual, the power factor of the system is very low. Capacitors need to be placed in the circuit to compensate for primary winding inductors. If the primary inductance and the compensating capacitor reach the resonant at the operating frequency of the system, the reactive power required by the system is provided entirely by the compensating capacitor, and the high frequency power supply only needs to provide the active power required by the system.）

Rload is the equivalent load impedance reflected from the secondary circuit to the transmitting circuit.

In the actual circuit, the switch SW1 is implemented by transistors (BJT or MOSFET), all of which use the gate source voltage to control the switch tube through the break.

3.2 Drive coil Carrier frequency selection

For implanted medical electronic products, the electromagnetic structure parameters are subject to strict application restrictions. The coil volume and quality of the percutaneous transformer should be as small as possible in order to reduce the discomfort of the human body or animals, and it has been proved by experiments that increasing the frequency of alternating electricity on the primary coil can achieve the same effect as increasing the number of coil turns. Therefore, the operating frequency of the wireless energy transmission system should be in the high frequency band. However, when the frequency of the current through the wire, the "skin effect" is more significant, it can be thought that the current only in the wire surface of a very thin layer of flow, which is equivalent to the wire cross-sectional area reduction, resistance increased. If the carrier frequency is low, the coupling coefficient will be lowered, resulting in

reduced energy transmission efficiency[6].

After consulting the relevant data, it was decided to select the carrier 4MHz.

3.3 In vitro energy emission circuits

The in vitro energy emitting circuit is shown in Figure 3.3-1.

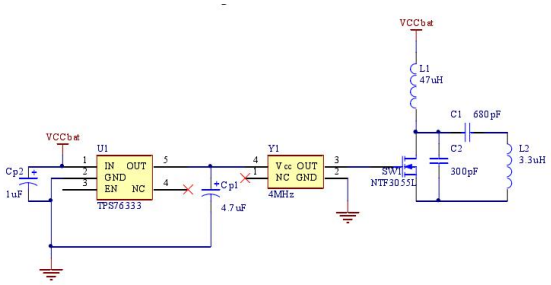

Fig.3.3-1 External energy emission circuit

The switch tube of Class E power amplifier selects the field effect tube produced by on Semiconductor company in the United States, and the model is ntf30551108. Due to its good high speed switching performance, it is ideal for use on this product. The Y1 is a 4MHz active crystal, with a square wave output frequency of 4MHz on the Out pin, which acts as a switching signal for MOSFET in class E amplifiers. The U1 is a TPS76333 of the 3.3V low voltage differential linear regulator, whose function is to transform the DC power supply voltage of +5v into 3.3V DC voltage to power the active crystal Y1[7].

3.4 Voltage doubler rectifier circuit

The voltage received by coupling is a high frequency AC voltage at the same frequency as the transmitter carrier, which needs to be rectified and filtered before it can be used by subsequent circuits. So the design circuit is shown in Figure 3.4-1[8].

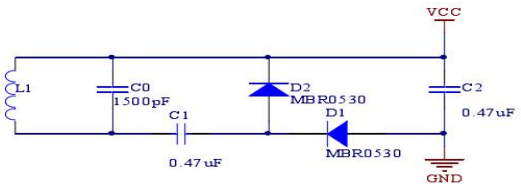

Fig.3.4-1 Voltage doubler rectifier circuit

Transformer secondary coil output voltage is high-frequency alternating power, diode in the guide will have a large amount of power consumption, is not conducive to the body energy receiving circuit power consumption reduction. Compared with the bridge rectifier circuit, it can be seen that the former only uses two diodes, which reduces the loss of energy on the diode and reduces the power consumption of the circuit in the body. And the capacitance in the double pressure rectifier circuit has a filtering effect, so the subsequent circuit no longer need to add filter capacitance, so that the circuit will be simpler.

3.5 Voltage Regulator Circuit

In order to provide a stable charging voltage for the subsequent charging circuit, the voltage fluctuation caused by the change of the position of the two coils will not affect the voltage input of the charging circuit, and the voltage of the rectifier will need to be stabilized.

The choice of voltage stabilizer chip should also follow the principle that the chip has low power consumption, small volume and simple peripheral circuit. By comparing our selection of NCV4264 voltage stabilizer chip developed by on company, the chip has a low static current and a small footprint. The connection circuit is shown in Figure 3.5-1[9].

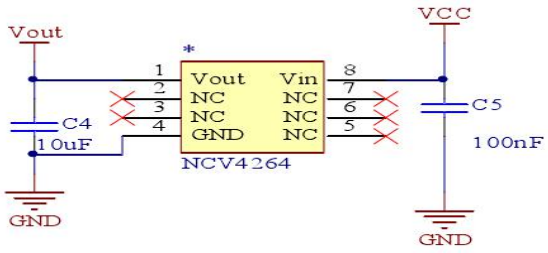

Fig.3.5-1 Regulator circuit

3.6 Internal charging management circuit

First choose lithium battery as rechargeable battery. The traditional constant voltage charging mode, in the charging process, as the battery voltage rises, the charging current decreases gradually, when the charging current drops to the set value, the battery can be considered to reach full charge, end charging. As the charging current decreases, the charging rate of the battery decreases, resulting in a lower average charging rate of the battery and longer charging time. And when the battery discharge depth is too deep, in the early stage of charging, if the charging current over the assembly caused serious damage to the battery. The use of constant current/constant voltage stage charging mode can provide fast charging, overcome the shortcomings of a single way constant pressure charging mode. This design chooses to use LTC4054L special single-section lithium-ion charging and discharging management chip. The design is shown in Figure 3.6-1[10].

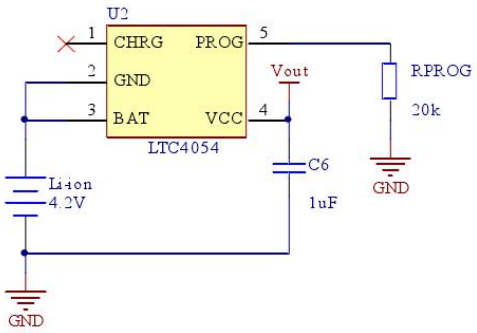

Fig.3.6-1 In vivo charge management circuit

THE BAT pin is the charging current output, which provides the charging current for the lithium-ion battery and controls the 4.2V charging termination voltage with

an accuracy of ±1%. VCC is the power supply side.

V.TEST RESULTS AND COMPARISON

After the design is completed, the charging data test is carried out, and the test results are obtained: the charging efficiency is about 6%~7% and the charging current is 8mA.

The voltage and current changes in the charging process are shown in Figure 4-1.

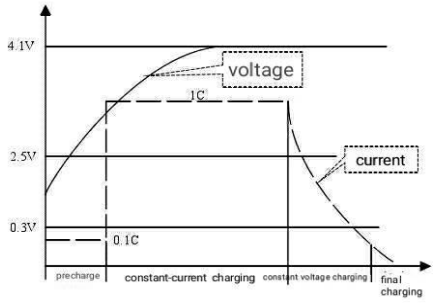

Fig.4-1 Battery charging process curve

The final prototype of the finished product is shown in Figure 4-2. A prototype of a wireless percutaneous charging system made from a universal board, including an in vitro energy emission module and an in-vivo energy receiving and battery charging module. Both the transmitting and receiving inductance coils are planar hollow helical rings made of Leeds wires, and in the course of the experiment, a certain distance is maintained between the two coils.

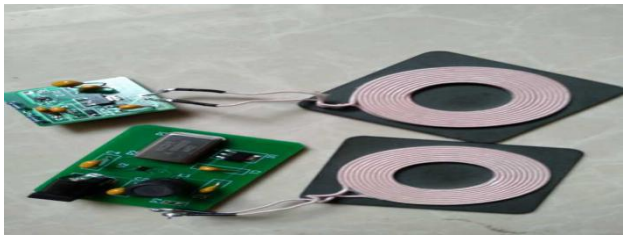

Fig.4-2 Prototype

IV.CONCLUSION

This design achieves the purpose of long-term power supply to implantable medical devices, by applying wireless charging technology to implantable pacemakers, it is possible to carry out wireless charging in vitro and replenish electricity in the case of low power consumption, thus prolonging its service life, reducing the frequency of patient replacement, surgical pain and risk. It also provides an experimental basis for wireless charging technology to be more widely used in more areas of daily life.

REFERENCES

[1] Alex L,De Rooij M A.Performance Enhancement–Mode GaN Transistors in Class-D and Class-E Wireless Power Transfer Systems[J]. Bodo's Power Systems, 2014, 1(5):66-7

[2] Jian Li Zhao,Quan Xin Bai,Peng Zhang. Application of Wireless Transmission Technology in the Detection of Capacitive Charged Device[J]. Advanced Materials Research,2014,3593(1049).

[3] Design of tunable optimal load circuit for maximum wireless power transfer efficiency[J] . Youn-Kwon Jung,Bomson Lee.Microw. Opt. Technol. Lett.2014 (11).

[4] Fundamental Evaluation of Power Supply and Rectifiers for Wireless Power Transfer Using Magnetic Resonant Coupling[J] . Keisuke Kusaka,Jun-ichi Itoh.Electr Eng Jpn . 2015 (3).

[5] Xiaojing. Research on wireless charging system based on RFID technology [D]. Posts and telecommunications, 2008.

[6] Sun Geoji. Development of wireless charging technology [J]. Semiconductor information, 2010, (06): 18-19.

[7] Sun Jun. Research on a new portable contactless charging system [D]. University. 2012.

[8] Guan Fei. Research on wireless charging technology [J]. Information Technology and Informatization, 2015, (02): 59-62.

[9] Zhou Xiaoming. Research and design of wireless charging system [D]. Tianjin University of Technology. 2015.

[10] Chu Hong. Application status and development prospect of wireless charging technology [J]. Science and technology innovation and application, 2016, (15): 75.

State Criterion of Chaos Detection System Based on Frequency Spectrum Amplitude Method

Jianxin Shi, Juntao Luo, Weizhe Sun

(College of Instrumentation & Electrical Engineering,Jilin University,Chuangchun 130012,China)

***Abstract*—Spectrum analysis is used on research on state criterion of chaos detection system to put forward frequency spectrum amplitude method.The basic idea of frequency spectrum amplitude method appears and the fulture is outlooked.The simulation test attain a result conforms to the features of chaos detection system,which admits the qualification of frequency spectrum amplitude method.**

***Key words*—Chaos detection State criterion Frequency spectrum**

I. INTRODUCTION

WITH the rapid development of science and technology，traditional technology is challenged every moment，which is prominent in field of signal detection.Detection of some tiny physical quantities ,such as micro-sound、micro-light and micro-displacement, plays an important role in production and living,which can not be completed through traditional detection technology.As a result,scientist invented weak signal detection technology to extract the weak signal from complex noise.

At present there are two main research direction of weak signal detection:one is development of device used exclusively in weak signal detection,such as phase-locked amplifier;the other is the research of weak signal detection method,which developed adequately.There are lots of methods about weak signal detection now,some of them are used commonly:correlate detection,wavelet transform, adaptive filtering. These methods damaged the signal to be measured during the process of noise suppression,which cannot meet the needs of development. New technologies are urgently needed to be discovered.

Chaos detection technology is a new technology.As a nonlinear system,chaos detection system is not only immune to noise,but also sensitive to measured signal,which conforms to needs of the time.The development of chaos detection technology is prosperous today,new progress turns up constantly. Method for detecting weak signal with unknown frequency[1-3] and coupled chaotic oscillator[4-5] are frontier science of chaos detection technology.

II. DUFFING CHAOS DETECTION SYSTEM

Duffing detection system is commonly used at present,the whole system is built through a typical Duffing equation as:

$$\ddot{x}(t)+k\dot{x}(t)-ax(t)+bx^3(t)=\gamma\cos\omega t \qquad (1)$$

In the equation,parameter k is damping coefficient, parameter a and parameter b are nonlinear impact factors, parameter γ is the amplitude of driving force,and parameter ω is the frequency of driving force.One feature of chaos detection system is that system will show a cyclical-chaotic-cyclical change following the increase of γ when other parameters remain unchanged.This feature makes Duffing detection system capable for weak signal detection.If a weak signal have the same frequency with a system,it will change the status of system, especially a critical system.

Solving the Duffing equation through fourth order Runge-Kutta differential equation solution,we get the time-domain figure and phase track diagram of the system.A chaotic system is shown as figure 1:

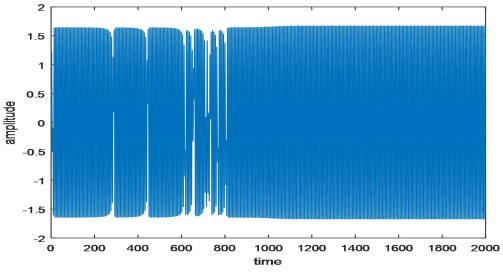

（a）Time wave

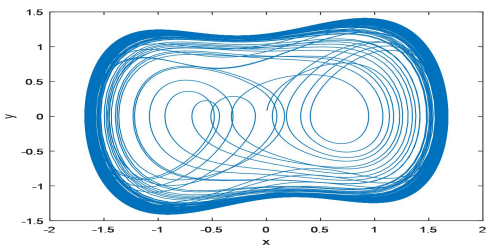

（b）Phase distribution

Fig1.Time wave and phase distribution of chaotic system

Increasing the amplitude of driving to 0.8265,system turns to large scale cyclical state.The system is shown as figure 2:

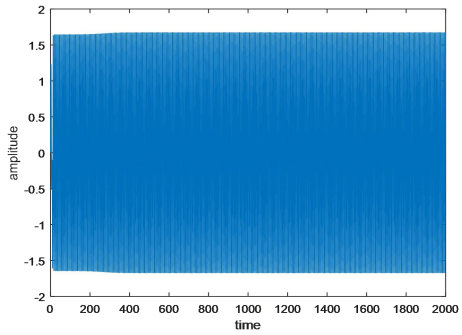

（a）Time wave

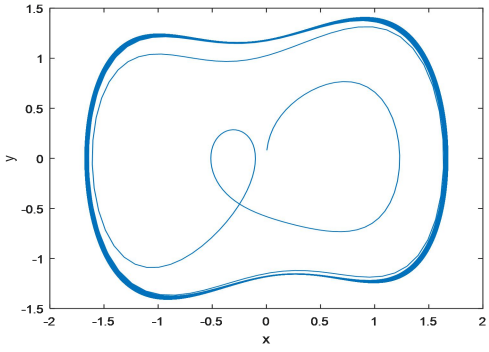

（b）Phase distribution

Fig2.Time wave and phase distribution of cyclical system

The system will show a partial turbulence on account of instability.It will turn to large scale cyclical state earlier and turn back quickly.The turbulence will make weak signal detection wrong.

III.The Criterion of The Chaos System

Estimate of system is important in chaos detection technology,which will influence the result of detection.Scientists have worked out many criterions to judge system state. There are two types of criterions:parameter calculation and image recognition.

Parameter calculation methods judge system state by calculating a complex parameter.Typical parameter calculation methods include Lyapunov exponent algorithm、Melnikov method and Kolmogorov entropy method.The type is high precision and stable with a complex calculation process and a long time consumption.Image recognition methods make use of time-domain figure、frequency spectrum and phase track diagram of the system. Typical image recognition methods include polar radius invariant moment method、grid partition method and Poincare section method.Calculation of the type is easy but accuracy and stability are slightly poor.Then two typical criterions and their principle will be introduced.

Lyapunov exponent algorithm is a commonly used criterion in chaos detection system.The key parameter of Lyapunov exponent algorithm is Lyapunov exponent.On the one hand,chaos detection system will be judged as a chaotic system if at least one Lyapunov exponent is positive;on the other hands, chaos detection system will be judged as a cyclical system if both Lyapunov exponents are negative.There are lots of methods to calculate Lyapunov exponent now,such as definition method、Jacobian method and Wolf method.Calculating through a Jacobi matrix is easy with a known and simple system equation. Comparing with another commonly used parameter calculation method----Melnikov method, Lyapunov exponent algorithm is accurate and intuitive,but complex and time-consuming.

Grid partition method is a new kind of image recognition method.It parts the phase track diagram of the system and gives a value to every part.The value will be “1” if the phase track traverses the part,and the value will be “0” if not.The final parameter is the sum of all values.Obviously,the final parameter of a cyclical system is far less then the final parameter of a chaotic system,which gives the method qualification to judge the system.As a image recognition method,grid partition method not only perform intuitively and have a high efficiency,but also connect to intelligent and automation ideologically.However,result of the detection is influenced by the mode and the degree of the partition,which need a advanced consideration.

IV. Spectrum Amplitude Method

The article puts forward a criterion of chaos detection system named frequency spectrum amplitude method.The method not only continues the advantages of image recognition method,but also improve the accuracy and stability.The principle of the method is solving the Duffing equation through fourth order Runge-Kutta differential equation solution and carrying on fourier transfer to get the frequency spectrum,just like figure 3:

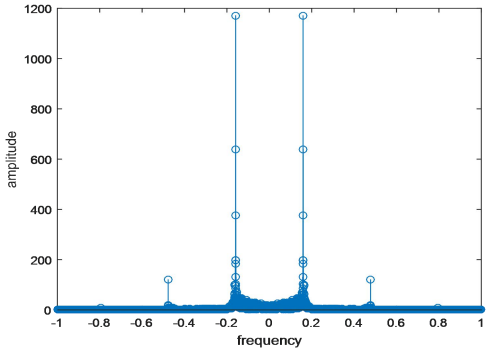

（a）Frequency spectrum of chaotic system

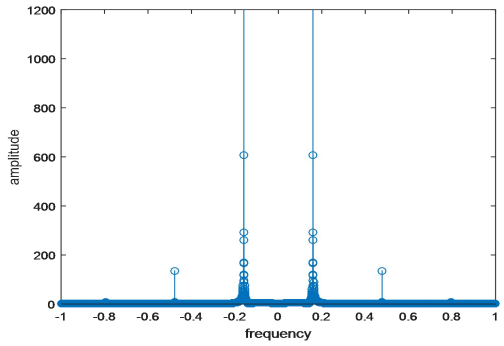

（b）Frequency spectrum of cyclical system

Fig3. Frequency spectrum of cyclical system and chaotic system

As shown, frequency spectrum of a large scale cyclical system is concentrated. On the contrary, frequency spectrum of a chaotic system is sporadic. Taking advantage of that,we can select a part of frequency point and calculate the mean of their amplitude.The mean is used as a criterion.

There are two notable points in the working process of the criterion.One is the selection of frequency points,which needs a certain standard.The standard used now is that amplitudes of the selected frequency points change obviously during the turn of the system states.The standard is not specific which needs an implementation of digital details.The other is the algorithm to deal with selected amplitudes.The algorithm need to be easy and expressive,which is immature.

V. Simulation Results

The curve of driving force amplitude changed with the characteristic value(the mean) without noise is shown as figure 4:

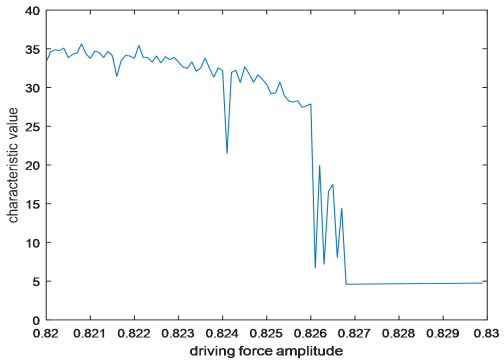

Fig4. Characteristic value-driving force change curve

As shown， the characteristic value waves in small increments with a high mean before the threshold value of the driving force amplitude. The characteristic value locates in a transition stage when the amplitude increases to the nearby area of the threshold.As the amplitude is greater then the threshold,the characteristic value becomes small and stable.The result explains that the characteristic value is available as a criterion.

The curve of threshold value of the driving force amplitude changed with the noise intensity is shown as figure 5:

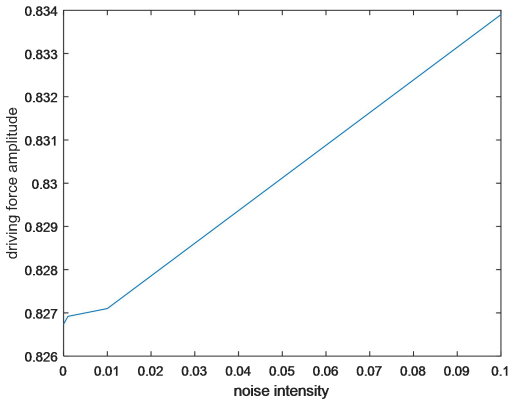

Fig5. Threshold value of driving force-noise intensity change curve

As shown, the threshold value increases with the noise intensity as a whole,which is consistent with the basic feature of the chaos detection system.

VI.Conclusion

This article puts forward a criterion of chaos detection system named frequency spectrum amplitude method,which judges the system state through the characteristic value of frequency spectrum.The result explains that the criterion can distinguish two states of chaos detection system.Furthermore,the method has the qualification to be a criterion.The next mission is adding working parameters to the method to make the method practical.

References

[1] Lan-Lan X , Chun-Lan L I , Cheng-Bin W , et al. Summary of the Research on Weak Signal Detection Based on Duffing Chaotic System[J]. Modern Computer, 2016.

[2] Yanhua W U , Qingli M A . Blind detection method of weak signals with Duffing oscillator[J]. Systems Engineering and Electronics, 2017.

[3] Li G, Zhang B. Novel method for detecting weak signal with unknown frequency based on duffing oscillator[J]. Chinese Journal of Scientific Instrument, 2017.

[4] Ma S S , Lu M , Ding J F , et al. Weak signal detection method based on Duffing oscillator with adjustable frequency[J]. Science China Information Sciences, 2015, 58(10):1-9.

[5] Si-Ming W , Yun L I , Kang L I , et al. The Weak Signal Frequency Detection Based on Hybrid Chaotic Oscillator[J]. Control Engineering of China, 2018.

[6] Peng H H , Xu X M , Yang B C , et al. Implication of Two-Coupled Differential Van der Pol Duffing Oscillator in Weak Signal Detection[J]. Journal of the Physical Society of Japan, 2016, 85(4):044005.

Research on Virtual Design Experiment Technology of Controlled Source Electromagnetic Instrument

Li Mingnan, Liu Jiacheng, Liu Haixin
(College of Instrument Science and Electrical Engineering, Jilin University, 130022,China)

***Abstract*—Firstly, aiming at the complex and expensive design of controllable source electromagnetic instrument and the current situation that virtual laboratory is popular in universities at home and abroad, a virtual design experiment platform based on LabVIEW is proposed. This paper introduces the components of the platform, makes a detailed analysis of each component, and gives the schematic design. According to the principle design diagram, a virtual design experimental technology research platform for controllable source electromagnetic instrument is built. In the field virtual practice part, the test results are given to verify its performance and accuracy.**

***Key words*—LabVIEW CASMT Transmitter Receiver Apparent resistivity of horizontal layered media**

I. INTRODUCTION

MOST electromagnetic instruments are complex in design and expensive. For example, the value of controlled source electromagnetic detection equipment is more than one million yuan, and most of them are imported products. The field construction cost is high, and the general teaching unit does not have this kind of equipment, or it cannot be easily disassembled and tested, thus becoming the black box.In addition, the technical difficulty of instrument development, development cycle is long, is not conducive to the system design of this kind of experimental teaching.

Virtual laboratory is developed by American and used in medicine. In many foreign universities, virtual laboratory has been set up to provide students with better teaching methods and intuitive feelings.In order to keep up with the pace of social progress, China has gradually established a virtual laboratory in many universities. Virtual laboratory is to build an intuitive virtual environment that does not exist in the computer based on the collected image data [1].The laboratory teaching is the important guarantee of the theory teaching, at present the application computer virtual technology teaching gradually becomes the experimental teaching development direction.

In order to uncover the instrument system black box [2], let students understand the overall structure and working principle of the instrument system.Combined with the idea of virtual laboratory, LabVIEW is used to develop the experimental software of virtual design for instrument of controlled source electromagnetic method.The software allows students to intuitively understand the structure of the instrument system at a low cost, and deeply understand its working principle, providing a fast, economical and intuitive experimental approach for college students taking advanced courses.

II. STRUCTURE AND ANALYSIS OF THE

The purpose of this platform is to enable students to understand and study the working principle and field experiment process of the instrument from the perspective of function and practice.It not only requires the platform to run stably and prompt students for improper operation, but also allows users to systematically learn the instrument of controllable source electromagnetic method.

The platform should be able to accurately reflect the inclusion relationship of each part:In this paper, two main parts of controllable source electromagnetic instrument are reconstructed modularly with structure function as unit--Transmitter and Receiver,allows users to carefully observe how each module works and the resulting system response differences.

Based on the geographical layout of real field experiments, the necessary one-dimensional forward calculation of CASMT is added to enable users to experience the basic process of field experiments by adjusting the parameters of each part and observing the response caused by it.

The function module component library strives to be universal and representative. In order to enable users to make more effective use of the function module component library, several demonstration cases based on the modules in the library are provided.

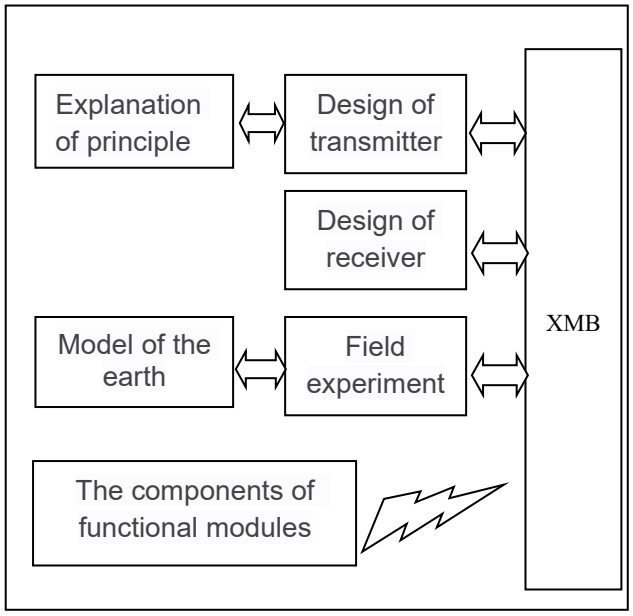

Fig.1. Overall architecture design

III. ANALYSIS AND DESIGN OF MODULES

A.Analysis and design of transmitter

Divide the internal structure of the transmitter by function [3], and obtain a series of functional modules as described below： 1) An alternator providing high power electrical energy.2)The power frequency rectification module converts the current from the alternator into direct current..3)Inverter module that converts direct current back to alternating current..4) A variable voltage module that changes the amplitude of alternating current and voltage.5)The alternating current coming out of the transformer is rectified again into the high-frequency rectification module of the direct current.6) Adjust the dc voltage and current of the steady current (chopper) module.7)The output bridge module takes the steady current electrical signal as the required waveform output of the power supply.

The modular design of the transmitter [4] is a cascade of modules 1) 2) 3) 4) 5) 6) 7. The specific principle design drawing is shown in figure 2.

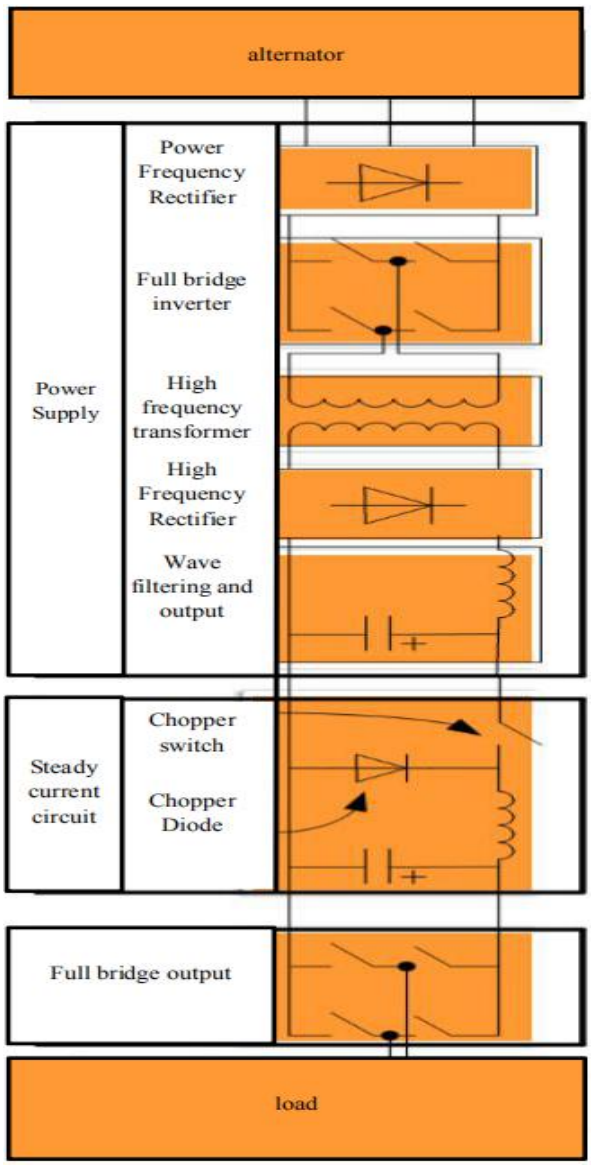

Fig.2. Principle design of Transmitter

The above design is implemented in LabVIEW environment,The obtained core design block diagram is shown in figure 3.The terminal output waveform is the output of resistive load.

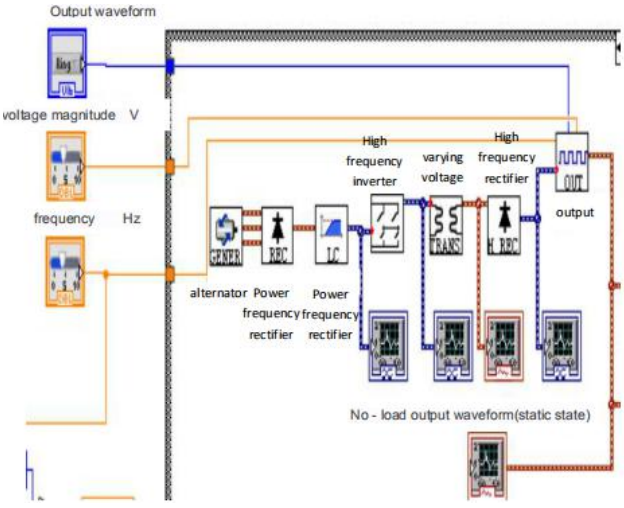

Fig.3. Partial design block diagram

B.Analysis and design of receiver

Similarly, the internal structure of the receiver is divided according to functions [5], and a series of functional modules are obtained as follows： 1)An induction device module for receiving electromagnetic signals.2) An amplifier module for amplifying weak signals.3)Pre-low pass filter module and adjustable filter module.4)A power frequency notch module used to remove noise from a generator.5)A program-controlled amplifier module that amplifies specific components of a signal.6)ADC module that converts analog signal into digital signal.

The specific principle design drawing is shown in figure 4.

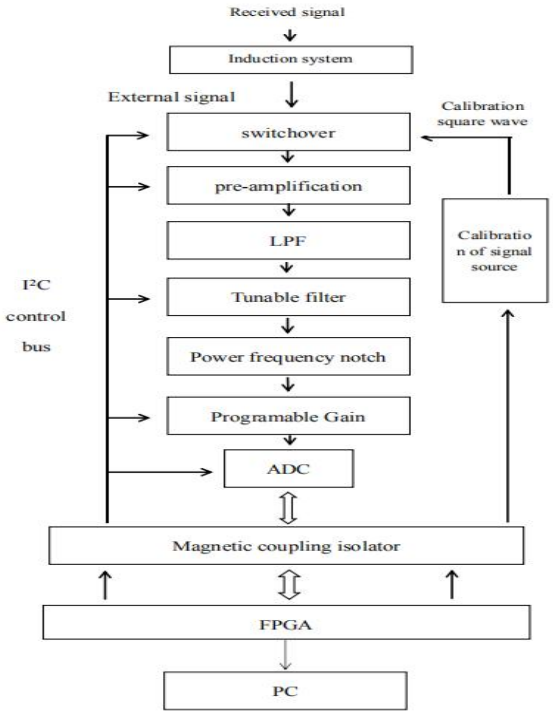

Fig.4. Principle design of Receiver

Because this principle design diagram contains many hardware components, it is an unnecessary part in the virtual experiment design.According to the practical use of virtual experiment software design, the principle design drawing is redesigned, and the design drawing is shown in figure 5.

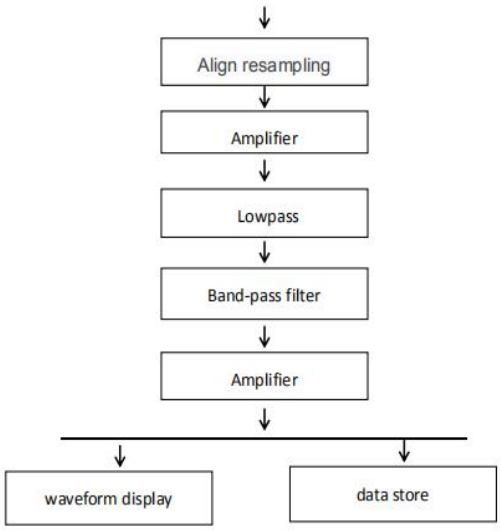

Fig.5. Actual design of Receiver

Among them, resampling replaces the whole process of ADC converting analog signal into digital signal and transmitting it to PC.The following part is used to realize the signal processing function of the actual receiver.

The difference is that the actual receiver first processes the signal, then converts it into digital signal and transmits it to PC, while in this design, the signal is processed digitally after transmission.Although the latter loses real-time performance, its overall effect is not much different from that of the actual receiver, which can meet the requirements of virtual experiment.

C.Earth response model

In this design, the meaning of the earth response model is the process of computing the user-set earth model according to a predetermined algorithm to obtain the apparent resistivity curve [6].

In the design, the horizontal three-layer earth model with small computational complexity but without loss of representativeness is selected.Relevant algorithms can be referred to references [7], which are not detailed here.

Although the computational complexity of this model is low, it still requires high CPU utilization and memory consumption for real-time computing, and LabVIEW is not good at complex mathematical operations, which may eventually lead to large response delay, or even the result that the computer is stuck.

Therefore, it is not simple to calculate the corresponding apparent resistivity at each frequency by taking uniform points.In order to solve the value problem, the method of mapping and interpolation is adopted in the design.For example, the obtained apparent resistivity curve can be applied to frequency from 0.001 to 1000Hz by performing exponential operation with base 2 on -10~10 and interpolating the

obtained result by 10 or 100 times. The more the interpolation, the higher the precision will be. However, the occupied resources will also increase exponentially and the inherent systematic errors cannot be eliminated.

It has been proved that the apparent resistivity curve obtained by this method can basically meet the requirements of demonstration teaching although its accuracy is not high.

D.Field virtual practice

In this design, field virtual practice refers to the process of adjusting parameters of transmitter, receiver and model device, and then obtaining a series of system responses [8].

In addition to the parameters of transmitter and receiver, this part also needs the real apparent resistivity curve and model parameters such as emitter distance, receiver distance and transceiver distance calculated from the earth model [9].

The design of this part also needs to reduce the occupation of computer resources:1 The transmitting frequency of the transmitter is read, and the value of transmitting frequency is indexed according to the set rules to reflect the number of arrays in the real apparent resistivity curve, and then the apparent resistivity of the characteristic parameter that should be used by the system at this time is obtained.2 According to the predetermined algorithm, in order to reduce the occupation of computer resources by calculation, the characteristic parameters of electric field and magnetic field due to the one-dimensional forward modeling system can be calculated by taking only the modulus and calculating only the electric field (Ex) in the x direction and the magnetic field (Hy) along the y direction. The detailed calculation formula can be referred to the references for details.3 Taking Ex and Hy as amplitudes and frequency as transmitter frequency, the sine wave waveform was constructed, and then noise was added to send the data stream to the receiver.4 Adjust the parameters of the electric field or magnetic field receiver to signal process the data flow described in 3), and then output it to the designated area [10][11][12].

It is worth noting that if the transmitter is not transmitting a sinusoidal signal, it needs to calculate the spectrum components separately, and then stack the results according to the superposition principle.

The flow chart is shown in figure 6.

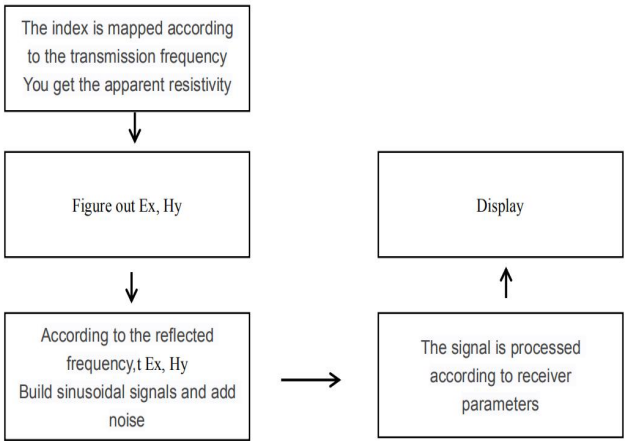

Fig.6. Flow chart

In addition, the actual field practice requires repeated measurements of different frequencies at different locations to obtain a series of amplitude-frequency characteristic curves and draw geological sections according to the above amplitude-frequency characteristic curves.

Limited by the undeveloped computational performance of LabVIEW environment, only the function of one-key drawing amplitude-frequency characteristic curve is designed. Repeated measurements of different frequencies were made at the same location and the results were plotted as curves.The principle is similar to the above ideas, but there is no need to build a signal for display.

IV. TEST RESULT

As the functions of transmitter and receiver are embodied in the field practice, this part only tests and displays the results of the field virtual practice part.

Set the resistivity of corresponding model parameters of the earth.ρ_1=10，ρ_2=30，ρ_3=20，T_1=1，T_2=10， The apparent resistivity curve is shown in figure7.

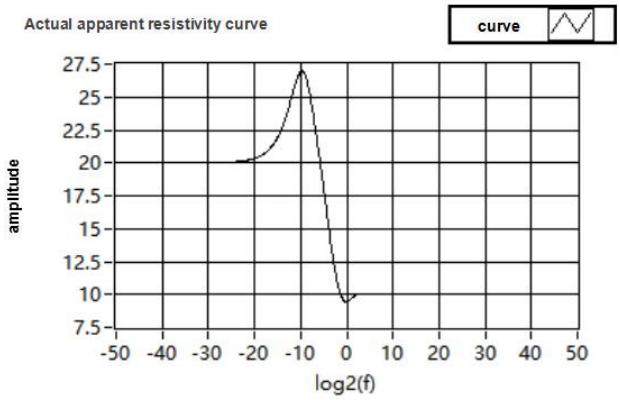

Fig.7. Apparent resistivity curve

Set the generator parameter 20A， 10Hz.Receiving pole distance=Emission pole distance=100, Transceiver distance=1000, Set the receiver parameter

50Hz,9~11Hz,1bei,2000fps.Then, the waveforms obtained by lighting the elliptical buttons of the electric field collection station and the magnetic field collection station are shown in figure 8 and figure 9 respectively.

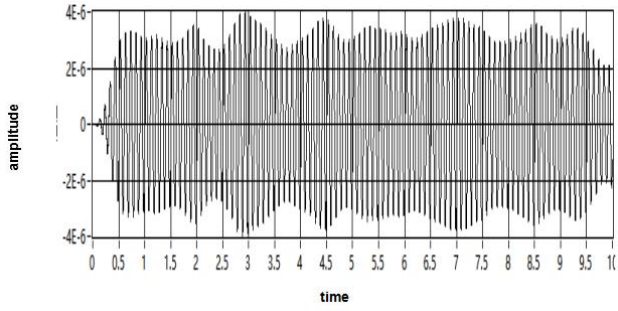

Fig.8. Waveform of Electric field

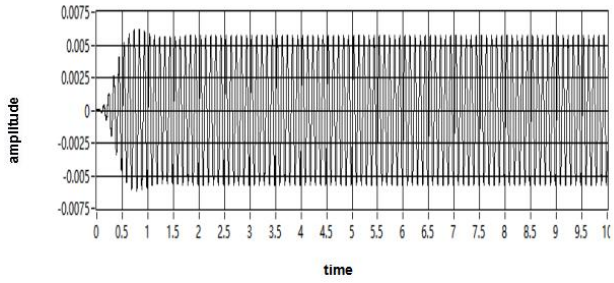

Fig.9. Waveform of Magnetic field

The amplitude-value spectrums are shown in figure 10 and figure 11 respectively.

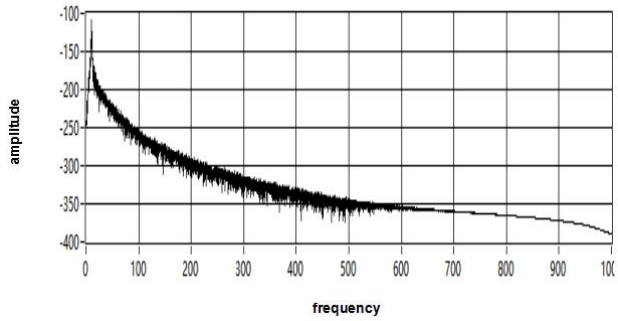

Fig.10. Frequency spectrum of Electric field

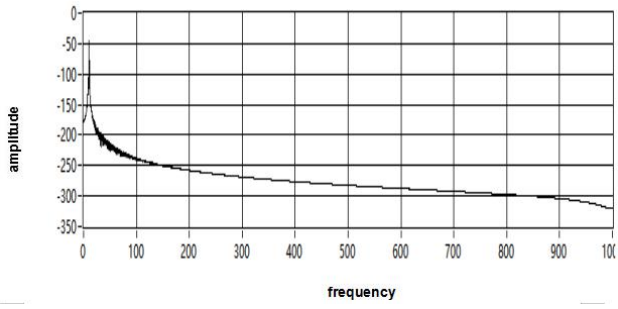

Fig.11. Frequency spectrum of Magnetic field

Due to the influence of noise, seemingly random waveforms in the time domain can be observed in the frequency domain with a frequency of 10Hz.

The amplitude-frequency characteristic curve of Ex and Hy can be obtained by using the function of drawing amplitude-frequency characteristic curve with one key, as shown in figure12 and13.

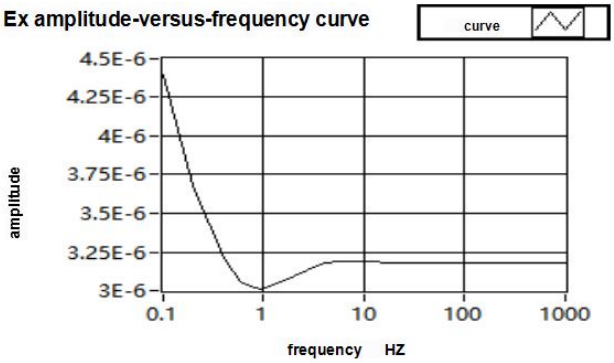

Fig.12. Amplitude-frequency Curve of E_x

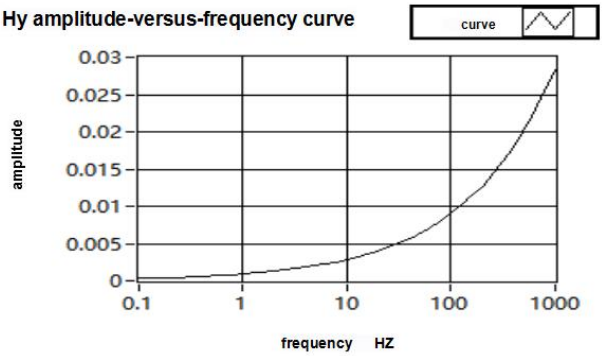

Fig.13. Amplitude-frequency Curve of H_y

Compared with the actual apparent resistivity curve as shown in figure 3-1, it is found that the calculated amplitude-frequency characteristic curve can reflect the actual apparent resistivity.

V. CONCLUSION

Research on the experimental technology of virtual design of instrument with controllable source electromagnetic method for the purpose of teaching has good teaching performance and can reflect the relationship between system response and input parameters to a certain extent.It provides a fast, economical and intuitive experimental approach for college students studying relevant courses.The accuracy of the calculated values and the accuracy of the drawn figures need to be further improved by the algorithm and design.

References

[1] S.K. Singla,R.K. Yadav.Optical Character Recognition Based Speech Synthesis System Using LabVIEW[J].Journal of Applied Research and Technology,2014,12(5):.

[2] Y. Wahab,N.A. Bakar,M.Z. Zainol,A.F.M. Anuar,H. Fazmir,M. Mazalan. Labview-based Gait Analysis System

for Rehabilitation Monitoring[J]. Procedia Computer Science,2014,42.

[3] Zihao Cui,Zhaoshuo Tian,Yanchao Zhang,Zongjie Bi,Shiyou Fu. Study on real time 3D imaging of streak tube lidar based on LabVIEW[J]. Optik,2018,157.

[4] BELHADJ Hamdi,UESUGI Kaoru,MORISHIMA Keisuke. Image Processing based Closed Loop Automated Control System for Cell Bio-Manipulation using LabVIEW and FPGA[J]. The Proceedings of JSME annual Conference on Robotics and Mechatronics (Robomec),2017,2017(0).

[5] Abdullah Beyaz. Harvest glove and LabView based mechanical damage determination on apples[J]. Scientia Horticulturae,2018,228.

[6] Ayşe Nur AY,Mustafa Zahid YILDIZ,Barış BORU. Real-time feature extraction of ECG signals using NI LabVIEW[J]. Sakarya University Journal of Science,2017,21(4).

[7] Ayşe Nur AY,Mustafa Zahid YILDIZ,Barış BORU. Real-time feature extraction of ECG signals using NI LabVIEW[J]. Sakarya University Journal of Science,2017,21(4).

[8] Qingyun Di,Zhiguo An,Changmin Fu,Zhongxing Wang. Imaging underground electric structure over a potential HLRW disposal site[J]. Journal of Applied Geophysics,2018,155.

[9] Qingyun Di,Zhiguo An,Changmin Fu,Zhongxing Wang. Imaging underground electric structure over a potential HLRW disposal site[J]. Journal of Applied Geophysics,2018,155.

[10] Qingyun Di,Zhiguo An,Changmin Fu,Zhongxing Wang. Imaging underground electric structure over a potential HLRW disposal site[J]. Journal of Applied Geophysics,2018,155.

[11] Controlled-source audio-magnetotellurics in geothermal exploration. Sandberg S K,Hohmann G W. Geophysics . 1982

[12] Study on multifunction electromagnetic transmitter. Li J Q. . 2009

Design of wireless temperature and humidity detection system based on ZigBee

SHAN Junna, HUI Zhenhua, JING Guoan
（*College of Instrument Science and Electrical Engineering, Jilin University,changchun,130021*）

***Abstract*—This paper designs a temperature and humidity detection system based on ZigBee wireless transmission technology. The system includes a ZigBee module, a temperature and humidity detection module, a temperature control device, and a host computer software. The device can work in a greenhouse to realize the detection and processing of temperature and humidity, and has the advantages of quick layout, unattended, low power consumption and low cost.**

***keywords*—Temperature and humidity sensor; ZigBee; Wireless; LabVIEW**

I. INTRODUCTION

MOST of the temperature and humidity detection systems used in traditional greenhouse use wired connections. When the number of monitoring nodes is relatively large, it would lead to many problems such as cumbersome wiring, difficult installation, and inconvenient maintenance. The wireless temperature and humidity detection system built with ZigBee technology can solve the above problems. The system has the advantages of quick layout, unattended, low power consumption and low cost[1].

II. THE PRINCIPLE OF THE SYSTEM

The design is based on ZigBee wireless transmission technology, temperature and humidity detection system, which main function is detecting the temperature and humidity in the greenhouse, then send the collected signal wirelessly to the upper computer.The upper computer displays the collection on each sensor group. If the humidity or temperature exceeds the threshold set by the system, the processor 8051 would send an alarm signal and takes relative measures, such as driving the fan when the temperature is high.

ZigBee is a low-power LAN protocol based on the IEEE802.15.4 standard. The networking topologies of the three device types can be divided into a star topology, a tree topology, and a mesh topology[2]. In order to improve the communication efficiency, regardless of the topology used in the ZigBee networking, the network will select the best routing path as the data transmission channel according to the ZigBee protocol algorithm. This system adopts the network topology design[3].

The wireless temperature and humidity detection system designed in this paper is shown in the Figure 1.

The ZigBee network supports Star, Tree, and Mesh topologies, in which we use the mesh topology of the ZigBee network[4]. The mesh topology is a single-hop network that includes a sink node and multiple monitoring nodes. All ZigBee monitoring nodes can only communicate with ZigBee aggregation nodes. If a ZigBee monitoring node is to communicate with another ZigBee monitoring node, it needs to send the data to the ZigBee aggregation node, and then the ZigBee aggregation node sends the data to the destination ZigBee monitoring node[5].

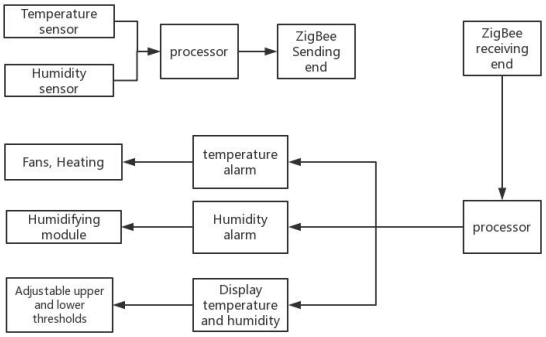

Fig. 1 System block diagram

III. THE DESIGN OF THE HARDWARE

The monitoring system is mainly composed of a router node and a terminal node. The terminal node module includes two parts: data acquisition and peripheral control. precision humidity +-5%RH, temperature +-2 °C, range humidity 20-90% RH, temperature 0~50 °C. The sensor transmits the measured temperature data to the ZigBee module CC2530. After the CC2530 processes the data, it sends control information to control the lower device to adjust the temperature or the humidity inside the greenhouse[6].

The ZigBee network of this design adopts a three-node star structure, in which the circuit diagram of the transmitter is shown in Figure 2, and the circuit diagram of the receiver is as follows Figure 3 shows.

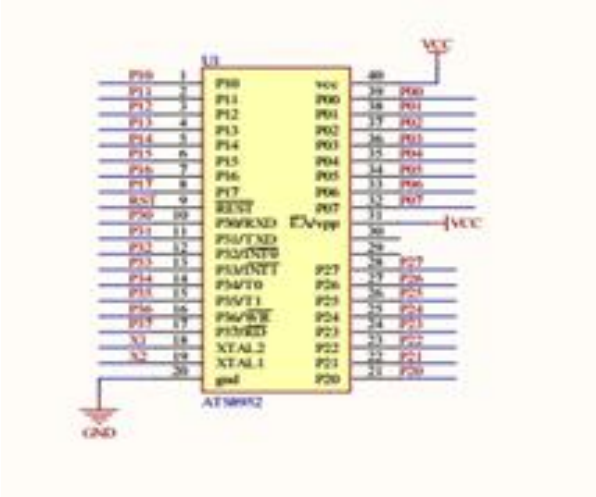

Fig. 2 Transmitter circuit diagram

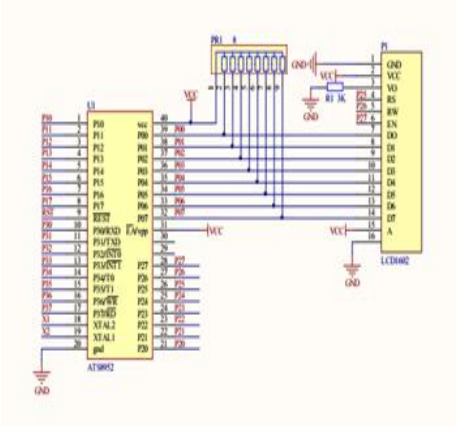

Fig. 3 Receiver circuit diagram

IV. SOFTWARE PART DESIGN

The ZigBee wireless module of this system uses the idea of the operating system to construct the software system protocol stack, which is processed by the adaptive polling algorithm. After the system is initialized, it enters the sleep state. The role of the router node is to select routes and forward data. ZigBee devices have a 64-bit MAC address and a 16-bit network address[7]. The network address is assigned by the coordinator or router after the device is connected to the network, and is unique in the network. ZigBee's scheme for assigning network addresses uses distributed addressing[8]. The network flow chart of ZigBee node and routing node is shown in Figure 4.

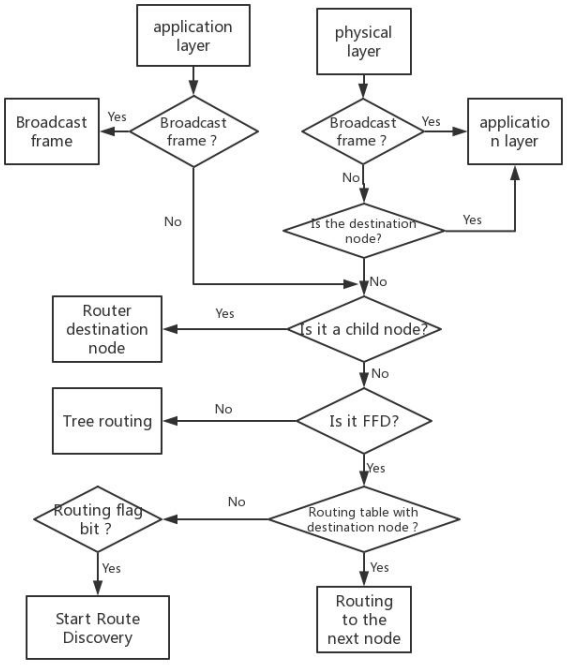

Fig. 4 ZigBee node and routing node network flow chart

The terminal node is used to collect the indoor temperature data. On the one hand, it establishes a certain relationship with the coordinator to send the temperature data to the coordinator. On the other hand, receives the control command sent by the coordinator, and controls the lower device air conditioner to perform corresponding operations[9][10] . Once the relationship is established, the data can be sent without knowing the explicit destination address. The terminal node data delivery process is shown in Figure 5.

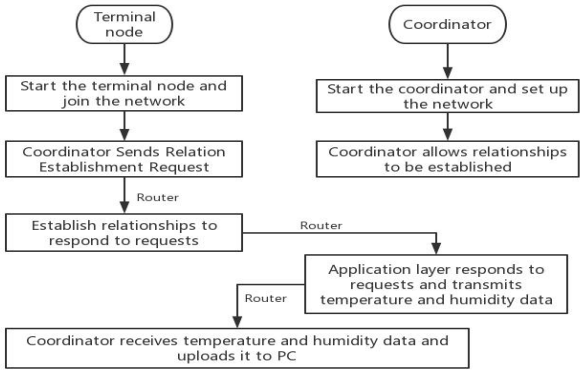

Fig. 5 End node data transfer flow chart

V. PC SOFTWARE DESIGN

The PC software of the device is implemented by LabVIEW programming.

The LabVIEW host computer interface is shown in Figure 6.

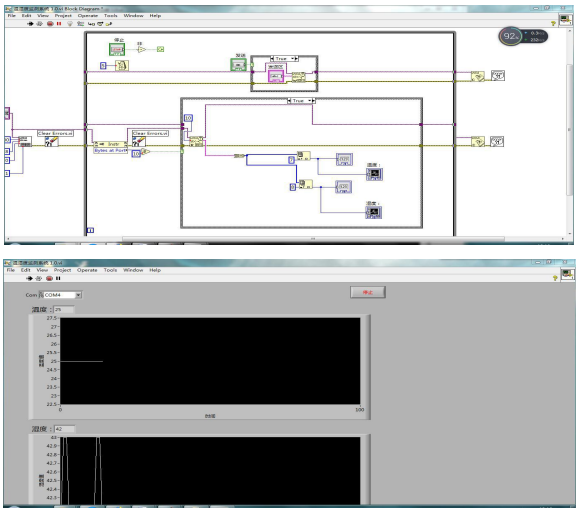

Fig.6 LabVIEW Control Interface

VI. Experimental Result

After continuous debugging and improvement, the system finally achieved the expected goals. Complete a ZigBee-based wireless detection technology, design the temperature and humidity detection system, its main function is to detect the temperature and humidity in the greenhouse, and then transmit the collected signal wirelessly to the integrated 8051 core of the chip, the internal microprocessor makes Corresponding judgment and processing, the processed signal is transmitted to the upper computer by the wireless transmitting module. Besides, the upper computer displays the information collected on each sensor group. If the temperature exceeds the threshold set by the system by 25 degrees Celsius, the integrated 8051 core of the chip will drive the sound and light alarm controller, send out an alarm signal and drive the fan. When the humidity is lower than 35%, the system would start the humidifier. The physical diagram is shown in Figure 7.

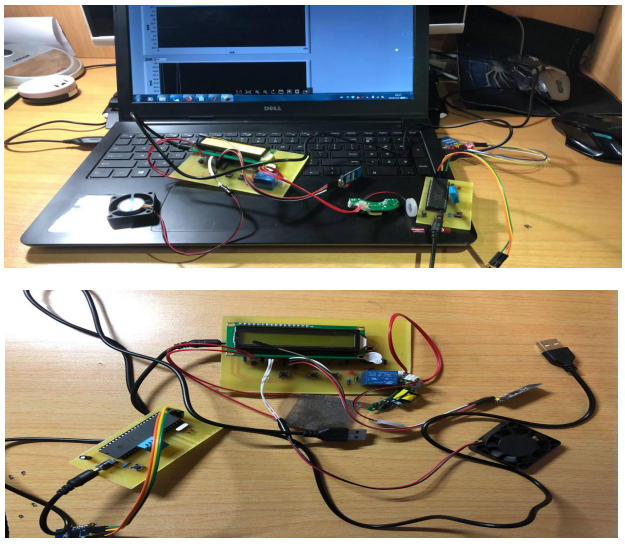

Fig.7 Physical map

VII. Conclusion

Compared with the traditional temperature and humidity detection equipment, we designed a wireless temperature and humidity detection system based on ZigBee technology. The system has low power consumption, strong real-time performance, convenient use[11]. Besides, it can reduce unnecessary manpower input. It has certain advantages for agricultural production realistic meaning. However, there are still some improvements in the detection system. Firstly, the function of the system is relatively single: the function of the network can only monitor the information of the environment, and can not control the direction of the network. Secondly, the upper computer interface is relatively simple: the upper computer interface only presents the serial data to users in a curve way. In the next step, a more intuitive way and a database can be used to replace the simple storage of data, which is more convenient for users to operate the upper computer interface

References

[1] Majid Karami,Gabrielle Viola McMorrow,Liping Wang. Continuous monitoring of indoor environmental quality using an Arduino-based data acquisition system[J]. Journal of Building Engineering,2018,19.

[2] Samet Tonyali,Ruben Munoz,Kemal Akkaya,Utku Ozgur. A realistic performance evaluation of privacy-preserving protocols for smart grid AMI networks[J]. Journal of Network and Computer Applications,2018.

[3] Raghavendra Rao Kanchi,Naveen Kumar Uttarkar. Design and development of a semiconductor bandgap measurement system using Microcontroller: MSP430G2553 and ZigBee: CC2500[J]. Materials Today: Proceedings,2018,5(1).

[4] Răzvan Andrei Gheorghiu,Valentin Iordache,Marius Minea. Messaging capabilities of V2I networks[J]. Procedia Manufacturing,2018,22.

[5] Aashay Gondalia,Dhruv Dixit,Shubham Parashar, Vijayanand Raghava,Animesh Sengupta,Vergin Raja Sarobin. IoT-based Healthcare Monitoring System for War Soldiers using Machine Learning[J]. Procedia Computer Science,2018,133.

[6] Vishal Kumar Arora,Vishal Sharma,Monika Sachdeva. On

QoS evaluation for ZigBee incorporated Wireless Sensor Network (IEEE 802.15.4) using mobile sensor nodes[J]. Journal of King Saud University - Computer and Information Sciences,2018.

[7] Hang Guo,Huixia Li,Jian Xiong,Min Yu. Indoor Positioning System Based on Particle Swarm Optimization Algorithm[J]. Measurement,2018.

[8] Anthony S. Deese,Julian Daum. Application of ZigBee-Based Internet of Things Technology to Demand Response in Smart Grids[J]. IFAC PapersOnLine,2018,51(28).

[9] Peijie Huo,Fang Yang,Hongbo Luo,Mingkuan Zhou,Yanlin Zhang. Distributed monitoring system for precision management of household biogas appliances[J]. Computers and Electronics in Agriculture,2019,157.

[10] Zechariah Balan,Harikrishnan Ramiah,Jagadheswaran Rajendran, Nandini Vitee,Pravinah Nair Shasidharan,Jun Yin,Pui-In Mak,Rui P. Martins. A coin-battery-powered LDO-Free 2.4-GHz Bluetooth Low Energy/ZigBee receiver consuming 2 mA[J]. Integration,2019.

[11] Yan,Jianwei. Monitoring and fault diagnosis system of wind–solar hybrid power station based on ZigBee and BP neural network[J]. Australian Journal of Mechanical Engineering,2018,16(sup1).

Structured - light 3D Surface Imaging Technology

Xiaoyu Zhang, Dong Zhang, Qiming Gao
(jilin university instrument science and engineering institute,changchun,130021

***Abstract*—In this paper we provide a review of recent advances In 3D surface imaging technologies and focus particularly on con-tact 3D surface imaging techniques based on structure illumination.Performance indexes of 3D imaging system are discussed, and vari-ous 3D surface imaging schemes are categorized, illustrated, and rich. Calibration techniques are also discussed, since they playcritical roles in achieving the required precision.**

***Keywords*—3D reconstruction Structural illumination Camera and projector system**

I. INTRODUCTION

3D imaging technology has a broad application background. With the appearance of high definition and high speed image sensor and the improvement of computer operation ability, 3d imaging technology has been greatly developed in the past decades. According to the reconstruction results, it can be divided into surface reconstruction and body weight reconstruction (mainly referring to CT and MR in medicine).The 3d imaging technology mentioned in this paper mainly refers to the surface reconstruction technology. Surface 3d imaging technology can be divided into two categories: passive 3d imaging and active 3d imaging. The images obtained in passive 3d imaging technology are completely derived from the reflection of the object surface to the ambient light, while active 3d imaging refers to the need to radiate energy to the measured surface during the reconstruction process, and reconstruct its 3d shape by collecting the reflected energy. Several commonly used 3d reconstruction techniques include laser scanning, binocular vision, structured light, and TOF(time of flight).Laser scanning method can obtain good accuracy, but it has high cost, slow measurement speed, is not suitable for dynamic scene measurement and is easy to cause damage to human or animal eyes. The current TOF sensor is not widely used because of its low resolution, low precision and high cost. The binocular vision system USES a pair of cameras to form a binocular camera. The images captured by the two cameras are matched and searched. Finally, the depth of matching points is calculated by triangulation method.The polar line constraint reduces the matching search scope to a one-dimensional search along the line direction. However, the computation of binocular image matching is still very large and time-consuming. At the same time, some scenes with less obvious texture features, such as white walls, are often not satisfactory. These problems limit the practical application of binocular vision. Since the projector and camera have the equivalent optical model, the 3d reconstruction system of structural light formed by replacing one camera in binocular vision with the projector and the binocular vision have the equivalent optical structure. However, due to the introduction of the projector, the matching problem can be made very simple by projecting different patterns. In the 3d reconstruction system of structural light, by encoding the projection pattern of the projector, we can analyze and decode the projection pattern captured by the camera, so as to establish the corresponding relationship between the pixels of the projector and the camera image.If the calibration data of the 3d imaging system of structured light is known, the 3d information can be calculated by the same method as in binocular vision.

The three-dimensional reconstruction technology of structural light has the characteristics of stable imaging results, high precision, dense point cloud and so on. Therefore, it is widely used in many fields, such as: reverse engineering, product quality testing, plastic surgery and so on.The content of this paper will be expanded as follows. The second section mainly introduces the calibration method and imaging principle of structured light 3d imaging system, and the third section classifies and compares different structured light codes.The fourth section introduces the performance evaluation of the camera projector system. Finally, the thesis is summarized in the fifth section.

II. CALIBRATION AND BASIC PRINCIPLE OF 3D IMAGING SYSTEM OF STRUCTURAL LIGHT

A.Optical model of camera and projector

In the field of computer vision, the camera is usually described by a simplified model called the eyelet model [1]. Camera models are usually represented by a matrix

called the camera matrix. Since there is no difference between the optical model of the projector and the optical model of the camera except that the projection direction is different, this matrix is also applicable to the projector. The camera matrix is used to describe points in three dimensions $M = [X,Y,Z,1]^T$ And its corresponding point on the camera imaging sensor $M = [X,Y,1]^T$ Location:

$$m \sim KR[i|-t]M$$

Among them: $K = \begin{bmatrix} f_x & s & u_x \\ 0 & f_y & u_y \\ 0 & 0 & 1 \end{bmatrix}$

Among them K is the internal parameter matrix, f_x , f_x The focal lengths of x and y squared, $u_x u_y$ For the coordinate of the main point, the main point of the camera is usually in the center of the image, while for the projector, the main point of the image is usually in the middle of the bottom of the image. s Is the distortion between the X-axis and Y-axis. R Is the rotation of the camera coordinate system and the world coordinate system, t Is the coordinates of the origin of the camera coordinate system in the world coordinate system.

B.Calibration of camera projector system

The camera parameter matrix mentioned in the previous section can be determined by calibrating the camera projector. The result of calibration directly determines the reconstruction accuracy of 3d system. The camera calibration is to establish the correspondence between the points on the sensor and the lines passing through the light center in space. This relationship also needs to take into account the effect of lens distortion. The current camera calibration technology in the field of computer vision has been relatively mature, there are many camera calibration module can be used directly. Firstly, a common calibration algorithm is introduced [2]. And then introduce the calibration method of the projector.

1.camera calibration algorithm

Suppose the position of the plane calibration template is in the plane of Z=0 in the world coordinate system, so that the second coordinate of every point on the plane becomes $M = [X,Y,Z,1]^T$ Therefore, the position relation between any point on the calibration board and its corresponding point in the image can be described by a homography matrix H:

$$m \sim K[r_1,r_2,r_3][I|-Rt][X,Y,0,1]^T$$

$$m \sim K[r_1,r_2,-Rt][X,Y,1]^T$$

$$m \sim H[X,Y,1]^T$$

Among them $H = [h_1,h_2,h_3] = K[r_1,r_2,-Rt]$. It's called the homography matrix r_1,r_2,r_3 Are the three column vectors of the rotation matrix. For the rotation matrix, its three column vectors are orthogonal to each other, so the following equation is true:

$$h_1^T (KK^T)^{-1} h_1^T = 0$$

$$h_1^T (KK^T)^{-1} h_1^T = h_2^T (KK^T)^{-1} h_2^T$$

Each homography matrix can give a set of above equations and two constraints on the internal parameters. In the top equation $(KK^T)^{-1}$ It's a symmetric matrix, so it only has six degrees of freedom, so the above equation can also be written as a six dimensional vector.

$$A = K^{-T}K^{-1} = \begin{bmatrix} A_1 & A_2 & A_4 \\ A_2 & A_3 & A_5 \\ A_4 & A_5 & A_6 \end{bmatrix}$$

$$\alpha = [A_1,A_2,A_3,A_4,A_5,A_6]$$

The homography matrix H The first i Vector writing $h_i = [h_{i1},h_{i2},h_{i3}]$Then we can get:

$$h_i^T (KK^T)^{-1} h_i^T = V_{ij}\alpha$$

Among them

$$V_{ij} = [h_{i1}h_{j1}, h_{i1}h_{j2} + h_{i2}h_{j1}, h_{i2}h_{j2}, h_{i1}h_{j3} + h_{i3}h_{j1}, h_{i2}h_{j3} + h_{i3}h_{j2}, h_{i3}h_{j3}]^T$$

The above equations can be reformulated as homogeneous equations.In order to solve for the unknown internal parameter vector α, we need to get at least 3 different views of the board image.However, in practical use, more than three pictures are usually used for calibration due to noise. For the overdetermined equation, SVD decomposition is used to obtain a least squares solution.Finally, the following energy function is optimized to reduce the back projection error.

2. Brightness calibration of the projector

In practice, in order to get a better display effect, the actual brightness of the projected image and the brightness value of the pixel in the projected image do not meet the linear relationship. In some 3d imaging systems,

the brightness value will be used to restore the coordinates of the point in the imaging plane of the projector. Therefore, it is necessary to calibrate the brightness of the projector, so that the actual brightness of the projected image and the brightness value of the projected image meet the linear relationship. To calibrate the brightness of the projector, it is often necessary to capture several different patterns projected by the projector, which usually include a set of grayscale and black and white patterns. By the collected images can get projector projection images of the actual brightness and projection design the brightness values of relation curve, then using high order polynomial function fitting for this again to get the fitting function of inverse function, finally using the inverse function of 3 d imaging used in pattern projection transformation, which can restore brightness projector and projection design to the pixels in the linear relationship (figure 1).

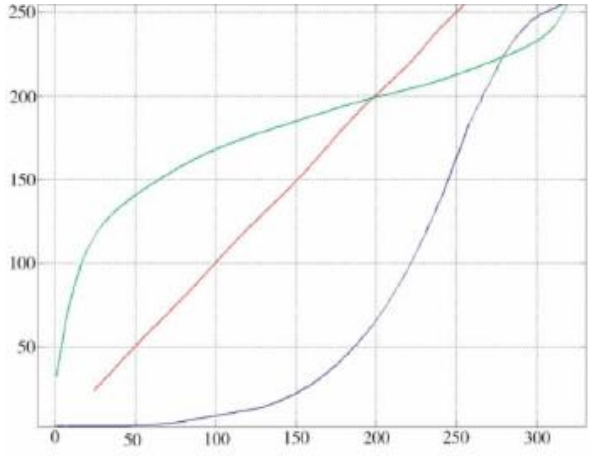

Fig. 1. brightness calibration of the projector.
(blue is the original brightness curve, green is the inverse function fitted, and red is the corrected brightness curve)

3. Geometric calibration of the projector

The projector has the same optical model as the camera, so it has something in common with the camera calibration. Camera calibration algorithm is now more mature, so the projector calibration can also learn from the camera calibration algorithm. However, due to the different directions of projection, it is difficult to establish the correspondence between points in the world coordinate system and points in the projector pattern. Different projector calibration algorithms use different methods to determine the correspondence between spatial points and planar pixels of the projector. Usually the projector is calibrated using a calibrated camera and a calibrated template. Firstly, the 3d plane of the calibration template is calculated by using the calibrated camera. Then the projector is used to project a calibrated pattern, such as a checkerboard pattern[3,4]. The checkerboard pattern was collected with the camera. Since the plane where the template was located was known, the coordinates of the detected corner points in the space could be obtained, while the position of corner points in the projector calibration pattern was known. In this way, the corresponding relationship between the plane and spatial points in the projector was established.The principle of this method is simple and easy to implement, but the accuracy of calibration often depends on the camera precision of pre-calibration to a large extent. Some calibration methods use projection structured light or binary coding method to determine the position of calibration template in the plane of the projector by decoding the collected images. This method does not need to calibrate the camera in advance, so cumulative error will not be introduced. However, this method is often affected by factors such as light exposure. The different colors in the checkerboard pattern cause the brightness of the corner points to change, which affects the final positioning accuracy. Therefore, some methods use the red and blue checkerboard to avoid the error caused by this situation.

C.Basic principles of 3d imaging of structural light

The basic principle of stereoscopic (binocular) vision is to triangulate parallax to calculate the depth of an object.The optical model of the projector is basically the same as that of the camera, except that there are differences in the projection direction. Therefore, the optical model of binocular vision and structural light 3d imaging system is equivalent, and the imaging principle is basically the same.Because of the introduction of projectors, the problem of binocular matching can be solved by encoding and decoding the projected images in the structured light 3d imaging system. As shown in figure 2, for the 3d imaging system of calibrated structured light, if we have found a pair of matching points on the projection pattern of the projector and the image acquired by the camera, the position of the point in the 3d space can be easily calculated:

$$R = \frac{B\,sin(\theta)}{sin(\alpha = \theta)}$$

Among them θ, α and B It can be determined by the position of calibration parameters and corresponding points in the image. The actual system may not use this formula to calculate the depth, but the basic principle is to use the triangulation method.

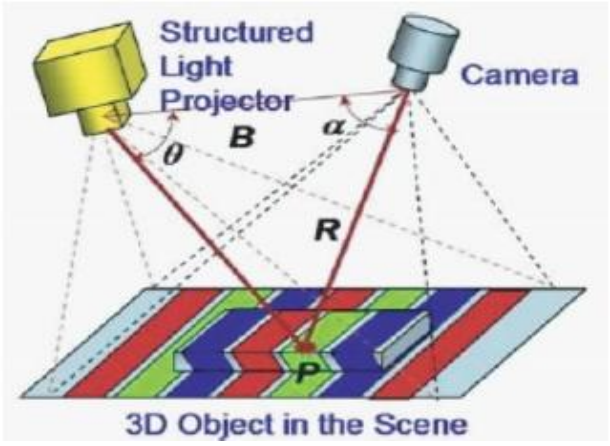

Fig.2. Basic principles of 3d imaging of structural light

III. STRUCTURAL LIGHT 3D IMAGING TECHNOLOGY

Structural light 3d imaging is an important method in 3d reconstruction. It USES a projector to project structural light or patterns on the measured surface, and then USES a camera to capture these patterns and calculate the shape of the surface through the distortion of the patterns. The design criteria for this projection pattern are usually to minimize the number of patterns, to maximize the accuracy and to provide a simple and efficient decoding process. 3d reconstruction of structural light is often referred to as "strong" 3d reconstruction system, because compared with other methods, 3d imaging results of structural light have better performance in terms of accuracy, reliability and so on, and are not limited by the characteristics of the object surface.For example, a structured light 3d imaging system can perform 3d imaging of white walls without any features. Currently, there are many different structural light 3d imaging methods. According to the projection pattern type and decoding principle, we divide them into four categories: (1) spatio-temporal coding projection;(2) single color space coding projection; (3) fringe index coding; (4) grid index coding, there are some subclass methods in each category, figure 3 shows a general classification framework. We focus on the most representative clustering methods in each category including binary sequential coding, phase shift, rainbow, color coding and other complex coding patterns.

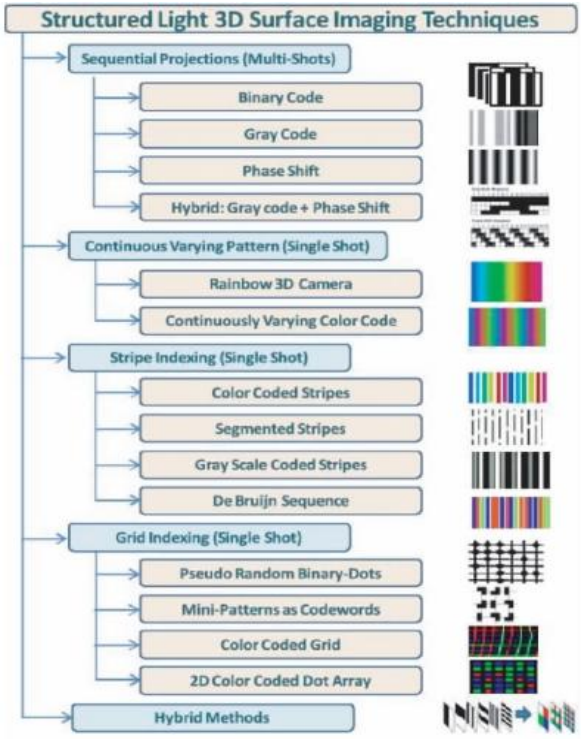

Fig. 3. Classification network of structural light 3d imaging technology

We use the phase shift method, which is a kind of space-time coding.

Phase shift method is a commonly used 3d imaging method for structural light [5,6]. It USES a set of sine wave patterns, where each pattern is separated by a fixed phase. The advantage of the phase-shifting algorithm is that the number of projected patterns is relatively small, which can obtain high-resolution results with good precision. We use the three-step phase shift method as an example to describe the concept of the phase shift method. The pattern obtained in the image sensor can be represented by the following equation.

$$I_{pn}=I'_p + I''_p\cos\left[\Phi_p - 2n\pi/3\right]$$

Among them I_{pn}Represents the vector prime value of the captured image, I'_p Represents ambient light intensity, I''_p Is the sine wave modulation intensity, Φ_pRepresents the phase shift value. When n is equal to 3, we can solve this equation up here Φ_p:

$$\Phi_p = \arctan\left(\sqrt{3}\frac{I_{p1}-I_{p3}}{2I_{p2}-I_{p1}-I_{p3}}\right)$$

And since the inverse trigonometric function is periodic, this is what you get here Φ_p between($-\pi/2$, $\pi/2$), a process known as phase

unwrapping. The commonly used phase unwrapping algorithms include branch cut, path integral, quality graph-based phase unwrapping and so on. After the absolute phase shift value is obtained after the phase expansion, the depth of the point can be calculated based on the position of the pixel and the phase value of the pixel [7]. If the surface has a discontinuous region greater than or equal to 2 times the phase, the phase spread algorithm will most likely return the wrong result.It is difficult to develop a reliable phase unwrapping algorithm because it is difficult to avoid errors or discontinuities on the measured surface.In practical use, the phase shift method often has some other defects. For example, when there is a texture with obvious changes on a smooth surface, due to the interference of texture color, some phases will not be recovered accurately, resulting in some errors similar to the relief texture on the final measured surface. Daniel Lau proposed a dual frequency phase multiplexing (DFPM) method.[15,16]. In this method, two codes of different frequencies are superimposed together, usually one code of high frequency plus one code of unit frequency. The brightness of the projected image can be written as:

$$I_{pn}=A_p + B_{p1}\cos\left(2\pi f_h y_p - \frac{2\pi}{n}\right) + B_{p2}\cos\left(2\pi f_u y_p - \frac{4\pi}{n}\right)$$

Among them I_{pn} Is the brightness value of the image, A_p Is the ambient brightness, f_h , f_u and B_{p1}, B_{p1}Are the frequency and modulation intensity of two different sine waves. Y_p Is the abscissa of the corresponding pixel point, that is, the phase shift value of the final solution required by the phase shift method. This method not only reduces the number of projected patterns, but also makes the phase unwrapping easier. After decoding, the high frequency component of the phase-shift diagram can give a better detailed performance, and the low frequency component as a base value for the phase expansion.

IV. Performance evaluation of 3D surface imaging system

THE performance of 3d surface imaging systems can be evaluated from many different angles. From the perspective of application, the performance of 3d imaging system is usually compared by four main factors:

A. measurement accuracy.

The measurement precision reflects the maximum deviation between the data collected by the 3d surface imaging system and the actual size data of the measured object. Usually, the accuracy of 3d imaging system varies in different directions due to the system design structure or principle. At the same time, different manufacturers use different ways to express the accuracy, such as: average error, mean square error, and statistical error. When comparing different systems, it is necessary to have an accurate understanding of these parameters and convert them to the same framework for comparison.

B. image resolution.

In two-dimensional images, resolution is mainly used to indicate the resolution of optical system imaging results to different points or lines. Similarly, in a 3d imaging system, the 3d resolution refers to the smallest structure that can be resolved in a 3d imaging system. However, in the field of 3d imaging, the number of point clouds collected separately is often referred to as resolution. For example, a 640-by-480 3d sensor can collect 307,200 or 307,200 data points at one time. At the same time, there are resolutions in different directions in the 3d imaging system, such as field Angle, imaging distance, imaging space depth, etc., which can be converted to each other.

C. image acquisition speed.

The acquisition speed is inversely proportional to the single acquisition time, which can be divided into two parts: image acquisition time and processing time. Image acquisition time is very important for detecting moving objects.For the spatio-temporal coding 3d imaging system or laser scanning system, when the object under test moves, due to the relatively long acquisition time of such system, the object may have a large movement during the acquisition time, so the final result may be inaccurate. For some systems, the acquisition time may be very short, but the post-processing time is relatively long, such a system can be used to shoot moving objects, but often can not be applied to the system with high real-time requirements.

The three most important performance indicators mentioned above can be used to compare different 3d imaging systems.In the actual application, in addition to the three indicators, cost performance is also an important factor to be considered in the actual application.Field Angle, baseline distance and measurement distance are also commonly used to describe the characteristics of 3d imaging systems of structural light. Due to the limitation of projection light ability, the measurement distance is often limited in 3d systems of structural light. In contrast, tof-based systems may measure distances of several kilometers.Actual application should be based on the application needs of the overall evaluation of system performance.

V. CONCLUSION

THIS paper introduces the main methods and some new methods of 3d reconstruction of structured light and classifies these different active 3d imaging methods. The representative methods are described in detail and the actual projection patterns make them easier to understand. At the same time, the main indexes of performance evaluation of 3d imaging system are discussed. Each different approach has its own advantages and disadvantages, so there is no single approach that can be applied in all situations. For the needs of specific occasions, different methods must be comprehensively compared from different perspectives such as resolution, accuracy, speed cost and reliability to select the most suitable method. 3d reconstruction of structural light is a technology in many fields, such as integrated optical design, modulating light technology, image sensor technology, structural design and software algorithm.Previous studies on 3d imaging technology often come from different disciplines, so they often have different emphases. The trend in recent years has been to bring different disciplines together, called computational imaging, and to consider different aspects of optical design, sensor characteristics, and software algorithms. This new research trend will ensure that future 3d imaging systems will continue to develop towards high performance and high cost performance. Compared with the two-dimensional imaging technology which has been studied for decades and invested millions of dollars in, the field of three-dimensional imaging is still a relatively young direction. It is hoped that more and more new 3d imaging systems and applications will attract more talented researchers to promote the development of 3d imaging.

Reference

[1] Hartley, R.I.Zisserman, A.Multiple View Geometry in Computer Vision.Secondedn.Cambridge University Press, ISBN:0521540518 (2004).

[2] 2 Zhang, Z.: A exible new technique for cameralibration. IEEE Transactions on Pattern Analysis and Machine Intelligence 22(2000): 1330-1334

[3] Projector and Camera Calibration Toolbox.HTTP: / / code.Google.Com/p/procamcalib /.

[4] Hu, Q.Huang, P.S.Fu Q., Chiang, F.P. Calibration of a 3-d shape measurement system Opt.Eng 42 (2003) 487-493

[5] Huang, P.S., Zhang, S.: A fast three-step phase shifting algorithm. The Apply.Opt for 45 (2006) : 5086-5091

[6] Zhang, S., Yau, S.T. · High resolution, real-time 3d absolute coordinate measurement based on a phase-shifting method. Opt. Express 14 (2006) : 2644-2649

[7] Sagan, H.: Space Filling Curves.Springer(1994) structured light for rapid active ranging.IEEE Trans.The Pattern Anal.The Mach.Intell.9 (1987) : 14-28

[8] Liu，K.，Wang，Y．C.，Lau，D．L.，Hao，Q.，Hassebrook，L．G．: Dual－frequency pattern scheme for high－speed3－dshape measurement．Opt．Express 18 (2010) : 5229

[9] Wang．Y.，Liu，K.，D．L．Lau，Q．H.，Hassebrook，L．G．: Maximum snr pattern strategy for phase shifting methods in struc-tured light illumination．Journal of the Optical Society of America A 27 (2010) : 1962

Research on Optical Fiber Refractive Index Sensor

Tianfeng Wu, Song Hu, Tuo Xu
（*College of Instrument Science and Electrical Engineering Jilin University ,Changchun 130022,China*）

***Abstract*— This paper proposes and studies the Mach-Zehnder mode interference refractive index sensor, which is based on the splice point core offset SMF-MMF-SMF (SMF, single mode fiber; MMF, multimode fiber) structure. The single-mode fiber is a sensing arm fiber, and the multimode fiber excites a fundamental mode in the transmission fiber to excite a high-order mode. When the light enters the single-mode fiber, the core diameter of the multimode fiber is smaller than the core diameter of the single-mode fiber. Large, so the high-order mode excited in the multimode fiber will be transmitted in the cladding of the single-mode fiber, and finally the cladding mode and the core mode will be intervened at the fusion point of the sensing single-mode fiber and the multimode fiber. Coupling output. The relationship between the sensitivity of refractive index measurement and the length of multimode fiber and the misalignment distance between the two ends is studied by numerical simulation and experiment. Simulation and experimental results show that the sensitivity increases with the decrease of multimode length and the increase of core offset distance in the refractive range of 1.3333-1.3737. Studies have shown that the sensing structure has good linearity and repeatability.**

***keywords*—ptical fiber sensor Refractive index measurement Mach-Zehnder interference High sensitivity Multimode optical fiber Core offset dislocation structure**

I. INTRODUCTION

REFRACTIVE index measurement has become one of the hot issues in the research of optical fiber sensing technology [1] [2].There are two main methods for measuring liquid refractive index based on optical methods: optical path measurement method and optical fiber measurement method [3]. Optical path measurement is a common method, but the optical path structure is complex, the optical path is unstable. Optical fiber is the main method of refractive index measurement because of its simple structure. The advantages of mach-Zehnder interferometer are easy to manufacture and measure, and it is a common method for the study of fiber optic interferometric sensors[4]. The mach-zehnder interferometric sensor is achieved through the fabrication methods of dislocation fusion [5][6], fusion [7][8] of different optical fibers, pull cone fusion [9][10] and sensitive material coating [11][12].

In this paper, a mach-zehnder mode interferometric refractive index sensor was proposed and studied, which was composed of a core offset mach-zehnder interferometer (MZI).Core migration MZI is achieved by splicing two single-mode optical fibers (SMF) with a small lateral offset. As a result of this intentional drift, there is interference between the core pattern and the claplayer pattern. The field of the cladding mode extends beyond the cladding of the main optical fiber and changes in the refractive index of the surrounding liquid can then be detected. When the RI of the environmental material changes, the spectral pattern of the device will change accordingly. The cladding mode is easy to be excited at the location of dislocation fusion [13][14]. The core diameter of the multi-mode fiber is large, and more optical signals can be received for mode coupling. Because the part of the fusion joint of the optical fiber is in the liquid, and part of the light is transmitted to the external environment at the fusion joint, and then enters the optical fiber after the transmission in the external environment, the refractive index of the external can be perceived.

II. THEORY

Figure 1 shows the mach-zehnder interferometer of smf-mmf-smf structure proposed in this paper.Figure 1 (a) is an outline interferometer directly integrated with the smf-mmf-smf structure mach-zehnder, and figure 1 (b) is a schematic diagram of the smf-pcf-smf structure mach-zehnder interferometer with offset and dislocation of the fiber core. In traditional SMF, the RI of the cladding layer is higher than that of the cladding layer. Thus, light is confined to the main fiber and absorbed there in the cladding mode, which prevents MZI from forming with the coating.To solve this problem, we offset the two SMF cores by a few microns, as shown in figure 1 (b).The light from the transmitting fiber is divided into two paths, some of which remain in the core of the receiver fiber, while the rest is transferred to the cladding and then propagated as the cladding mode. After that, the light in the cladding passes through MMF and enters another core

offset. The light in the cladding can be coupled back to the core. Due to the phase difference between the cladding and the core mode, the two kinds of beams form coherent interference at a certain wavelength. The cumulative phase difference between the core mode and the cladding mode is $\frac{2\pi\Delta n_{eff} L}{\lambda}$, where Δn_{eff} is the effective refractive index difference between the core and the cladding, L is the offset length, and λ is the working wavelength. When RI changes, the optical path difference between the two spectra will change.

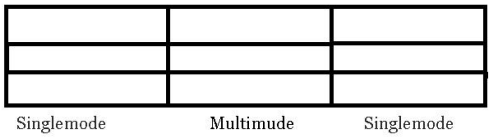

Figure 1 (a) Direct fusion SMF-MMF-SMF structure

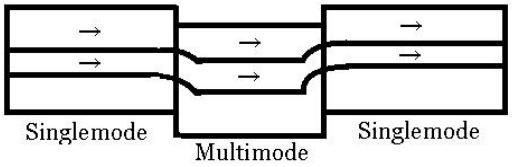

Figure 1 (b) conical SMF-MMF-SMF structure with connection points

$$I = I_1 + I_2 + 2\sqrt{I_1 I_2}\cos\varphi \qquad (1)$$

Where I_1 and I_2 are the light intensity in the fiber core and fiber cladding respectively, and φ is the phase difference.

$$\varphi = \frac{2\pi\Delta n_{eff} L}{\lambda} \qquad (2)$$

In the formula, L is the interferometer with the length of optical path, that is, the length between two conical joints; λ is the wavelength of light; Δn_{eff} is the difference between the effective refractive index of the fiber core and the cladding.

$$\Delta n_{eff} = n_{eff}^{core} - n_{eff}^{cladding} \qquad (3)$$

When the difference between the cladding mode and the core mode is equal to $(2m+1)\pi$, the interference between the fiber core and the light in the cladding will lead to destructive interference, that is, the interference trough will be generated. The wavelength of the m-order interference valley will change with the surrounding refractive index [15], as shown in equation (4) :

$$\Delta\lambda_m = \frac{2\left(\Delta n_{eff} + \Delta n\right)L}{2m+1} - \frac{2\Delta n_{eff} L}{2m+1} = \frac{2\Delta nL}{2m+1} \qquad (4)$$

The effective refractive index of the multimode fiber cladding is a function of the surrounding refractive index, and the effective refractive index of the multimode fiber core has nothing to do with the surrounding refraction [16]. Δn Is the change of effective refractive index of multimode fiber cladding with the change of surrounding refractive index.

Mach-zehnder interferometer is formed by the migration between the multi-mode fiber core and the single-mode fiber. Compared with the smf-mmf-smf mach-zehnder interferometer directly spliced, more high-order cladding modes can be excited in the smf-mmf-smf mach-zehnder interferometer at the offset, and the high-order mode of the MMF cladding is more sensitive to the change of external refractive index. Therefore, the smf-mmf-smf core offset mach-zehnder interferometer will achieve higher sensitivity.

III. SIMULATION

In order to explore the propagation law of light in optical fiber, the simulation of electric field distribution is shown in figure 2, where the vertical axis and the horizontal axis represent the length and diameter of fiber respectively.

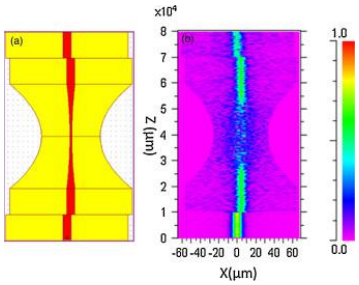

Figure 2 (a) simulation model diagram of core migration structure, (b) simulation results

Figure 2 (a) is the simulation model diagram, in which the core is red and the cladding is yellow.FIG. 2 (b) shows the corresponding electric field distribution, indicating that there is an obvious light field distribution in the cladding.It is easy to imagine that the interference spectrum can be observed and that it is affected by the environmental RI.

IV. EXPERIMENTS AND DISCUSSIONS

In the experiment, the concentration of NaCl solution was 0%, 2%, 4.76%, 9.91%, 15.25% and 20% respectively, and the refractive index was measured. The relationship between concentration and refractive index is shown in table 1.As can be seen from table 1, NaCl solution concentration ranges from 0% to 20%, covering the refractive index range of ordinary liquids.

Table 1: Relationship between NaCl solution concentration and refractive index

Naclconcentration (%)	0	2	4.76	9.91	15.25	20
The refractive index	1.3333	1.3411	1.3493	1.3574	1.3656	1.3737

The experimental system is shown in figure 5.The experimental light source is a broadband source of amplified spontaneous emission (ASE) with a wavelength range of 1520-1570 nm. The spectrum analyzer (OSA, AQ6370) is produced by yokogawa motor. The single mode fiber is smf-28.The multimode fiber is om3-150.Figure 3 is a schematic experimental system of the multi-mode fiber mach-zehnder interferometer. In this paper, we first used the system to study the influence of the length of the smf-mmf-smf mach-zehnder interferometer on the sensitivity of liquid measurement. The length of the multimode crystal fiber is 1.5 cm, 2 cm and 3 cm. Then, we studied the interference maps with different core offsets (10mm and 20mm, respectively) to measure the sensitivity of the liquid through the system. The optical fiber sensor head is fixed in the liquid tank under test and connected to the broadband ASE light source and the spectrum analyzer (OSA) respectively through two single-mode optical fiber jumper wires.ASE light source is used to provide input light in the wavelength range of 1520-1570nm, and spectrum analyzer is used to display and analyze the output interference spectrum. The optical fiber is stably fixed by the fiber foot in the liquid pool under test, and the sensing head of smf-mmf-smf mach-zehnder interferometer is kept straight and suspended in the liquid pool, so as to ensure that the optical fiber sensing head can prevent small external force interference and fully contact with the liquid under test.

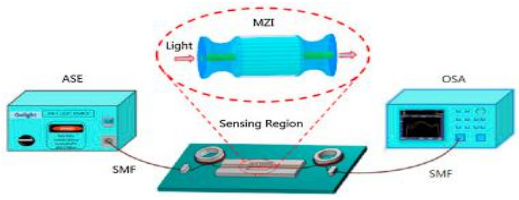

Fig.3 Experimental system setup

The photos of the experimental system Settings are shown in FIG. 4 The specific experimental operations are as follows :(1) connect the light source-fiber sensor head-spectrum analyzer;(2) measure the spectrum of the optical fiber sensor head in the air and save it as the reference spectrum;(3) inject distilled water into the liquid tank with a syringe, and then measure and save the spectrum;(4) the liquid is discharged from the liquid tank through the outlet. The distilled water and alcohol washing liquid tank are used alternately and repeatedly. The liquid tank is dried with compressed air until the spectrum is the same as the reference spectrum in the air. The interference spectra of NaCl solutions with different refractive indexes were measured through the above steps. The average of three repeated measurements is performed to reduce the measurement error.

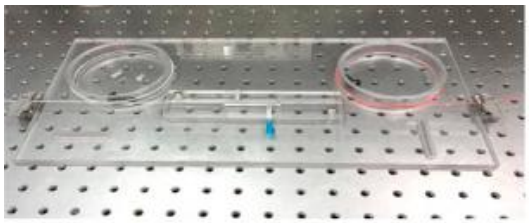

Fig.4 Physical map

Figure 5 (a) - (b) is the change of the output interference spectrum at different concentrations when L=2cm is used.

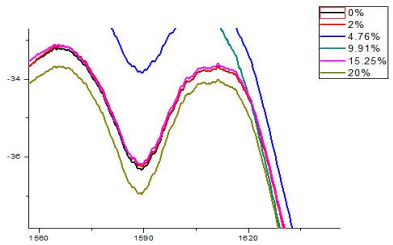

Figure 5 (a) Interference spectra with core offset of 10μm

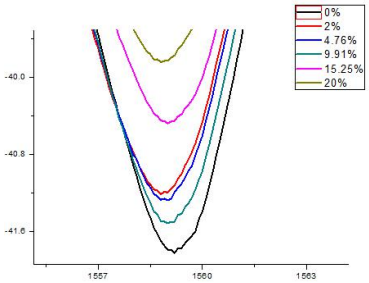

Figure 5 (b) Interference spectra with core offset of 20 μm

Figure 5 (c) - (d) is the change of the output interference spectrum at different concentrations when L=3cm is used

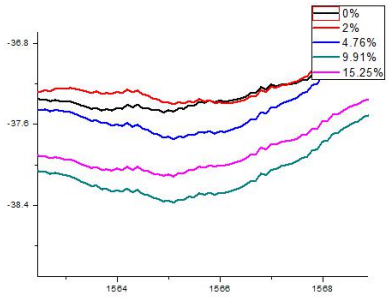

Figure 5 (c) Interference spectra with core offset of 10 μm

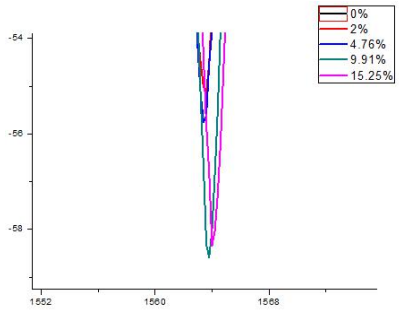

Figure 5 (d) Interference spectra with core offset of 20 μm

According to figure 5 (a) - (d), with the increase of Nacl solution concentration, the length of the interference wave shifted to the right, that is, the length of the interference wave became larger and larger. With the increase of the core offset, the interference wavelength changes more and more obviously with the concentration, that is, the refractive index. However, this value should be subject to upper limit and conditions, which are not discussed in this paper. At the same time, with the decrease of MMF length, the measurement sensitivity becomes higher and higher. See figure 6.

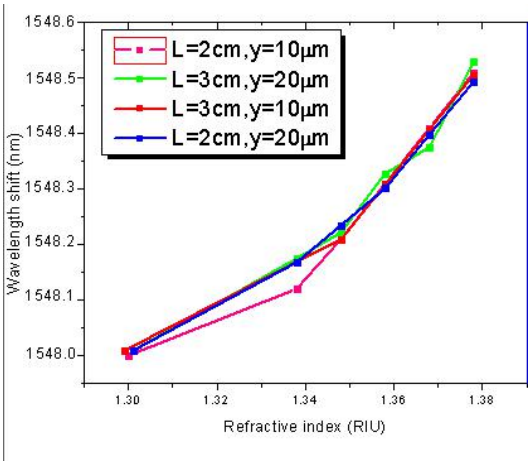

Figure 6: The relationship between wavelength drift and surrounding refractive index

Figure 6 shows the relationship between the wavelength offset of the splice point offset smf-mmf-smf mach-zehnder interferometer and the surrounding refractive index. The parameters of the interferometer used are multi-mode fiber length of 2cm, and the core offset of 20μm.If you want to measure the refractive index of the unknown solution, just use the spectrometer to measure the drift of the interference wavelength. It can be seen from figure 6 of the experimental results that the length and core offset of the multi-mode fiber can improve the refractive index measurement sensitivity of the smf-mmf-smf mach-zehnder interferometer. The reason is that at the offset splice junction, the input light from the first line SMF is spit out into two paths. One path is coupled to the core mode of the sensing SMF, and the other is transferred to the cladding mode. Core migration will stimulate more high-order modes, which will penetrate into the external environment, and the contact area between cladding modes will gradually disappear and the external refractive index will increase, so the change of surrounding refractive index will affect the transmission characteristics of the cladding mode. According to the definition of refractive index, the effective refractive index of cladding mode can be reduced because the surrounding refractive index is smaller than that of cladding, while the effective refractive index of core mode will remain unchanged.

V Conclusion

In this paper, a Mach-Zehnder mode interferometric refractive index sensor was proposed and studied.In this paper, multimode optical fiber (MMF) was spliced between two single-mode optical fibers to make the sensor. In the two spliced point areas, two core excursions coupled the light in different optical paths together to form coherent interference, and the output interference spectrum was formed by spectrometer. The relationship between the sensitivity of refractive index measurement and multi-mode length and core offset is studied by numerical simulation and experiment. Simulation and experimental results show that the sensitivity increases with the decrease of multi-mode fiber length and the increase of core offset. The experimental results show that the center wavelength of the interference spectrum is offset with the increase of the surrounding refractive index.

References

[1] G. Rajan, S. Mathews, G. Farrell, et al.A liquid crystal coated tapered photonic crystal fiber interferometer J. Opt., 13 (1) (2011), pp. 40-47

[2] P.R. Cooper Refractive-index measurements of liquids used in conjunction with optical fibersAppl. Opt., 22 (19) (1983), pp. 3070-3072

[3] S. SinghDiffraction method measures refractive indices of liquids Phys. Educ., 39 (3) (2004), p. 235

[4] H.Y. Choi, M.J. Kim, B.H. LeeAll-fiber Mach-Zehnder type interferometers formed in photonic crystal fiber Opt. Exp., 15 (9) (2007), pp. 1-3

[5] Dong B，Zhou D P，Wei L，et al．Temperature- and phase-independent lateral forcesensor based on a core-offset multi-modefiber interferometer［J］. Optics Express，2008，16(23):19291-19296.

[6] Fan J，Zhang J，Lu P，et al．A single-mode fiber sensor based on core-offset inter-modal interferometer［J］. OpticsCommunications，2014，320(1) : 33-37.

[7] Kumar A，Varshney R K，Sharma P．Transmission characteristics of SMS fiber optic sensor structures［J］. Optics Communications，2003，219(1) : 215-219.

[8] Liu Y，Wei L．Low-cost high-sensitivity strain and temperature sensing using graded-index multimode fibers［J］. Applied Optics，2007，46(13) : 2516-2519.

[9] Wang P F，Brambilla，Ding M，et al．A High-sensitivity，evanescent field refractometric sensor based on a tapered，multimode fiber interference［J］. Optics Letters，2011，36(12) : 2233-2235.

[10] Shao M，Qiao X G，Fu H W，et al．High sensitivity refractive index sensing of Mach-Zehnder interferometer based on multimode fiber core sandwiched between two waist-enlarged fiber tapers［J］. Optics Communications，2013，311(15) : 359-363.

[11] An J L，Zhao Y，Jin Y X，et al．Relative humidity sensor based on SMS fiber structure with polyvinyl alcohol coating［J］. Optik，2013，124(23) : 6178-6181.

[12] Wang H，Pu S，Wang N，et al. Magnetic field sensing based on singlemode-multimode-singlemode fiber structures using magnetic fluids as cladding［J］. Optics Letters，2013，38(19) : 3765-3768.

[13] Wu Q，Semenova Y，Wang P F，et al．. High sensitivity SMS fiber structure based refractometer-analysis and experiment[J]. Optics Express，2011，19(9) : 7937-7944.

[14] Guo S P，Albin S．Transmission property and evanescent wave absorption of cladded multimode fiber tapers［J］. Optics Express，2003，11(3) : 215-223.

[15] H.C. Nguyen, B.T. Kuhlmey, E.C. Magi, et al.Tapered photonic crystal fibers: properties, characterization and applications Appl. Phys. B, 81 (18) (2005), pp. 377-387

[16] R. Jha, J. Villatoro, G. Badenes, V. PruneriRefractometry based on a photonic crystal fiber interferometer Opt. Lett., 34 (5) (2009), pp. 617-619

[17] Y.Y. Jiang, Y.I. LiqingWEI YongTao amp. The finite element analysis of square-lattice multi-core photonic crystal fiber Scientia Sinica, 41 (3) (2011), pp. 319-324

[18] R.E. Campos, C.J. Soares, P.S. Quagliatto, et al.In vitro study of fracture load and fracture pattern of ceramic crowns: a finite element and fractography analysis J. Prosthodontics Off. J. Am. College Prosthodontists, 20 (6) (2011), pp. 447-455

Design of environmental monitoring system based on rod-climbing robot

Hu Jinming, Wang Junsheng, Gao Yuan

(College of materials Science and Engineering, Jilin University,Changchun,China,130021)

***Abstract*—Aiming at the problem of high-altitude environment detection, an environmental monitoring system for air temperature, humidity and dust concentration at different altitudes was designed by using rod-climbing robot as carrier and carrying various sensors. Data terminal collects data and uploads environmental data to monitoring host through wireless transmission device. LabVIEW is a visual interface for realizing the display of environmental parameters and the motion state control of the rod-climbing robot, which can be used for real-time remote monitoring.**

***Keywords*—Rod-climbing robot STM32 Environmental monitoring LabVIEW**

I. INTRODUCTION

WITH the development of modern society, people have a lot of work to be done in high altitude environment. Therefore, rod-climbing robots are widely used in the fields of tree pruning, street lamp replacement and aerial reconnaissance. In recent years, they have gradually become one of the research hotspots in the field of robotics at home and abroad. With the continuous expansion of the application of robots, as a new field, high altitude operation has many problems, such as high danger, high labor intensity and low efficiency. Typical high-altitude operations include pruning fruit trees, picking fruit, cleaning glass curtain walls, inspecting wall defects of large boilers, building trusses, inspecting and replacing street lights, and inspecting cable-stayed bridges. The existing rod-climbing robots are mainly used in these fields, but not in reconnaissance and detection[1].

With the rapid development of computer technology, data acquisition and processing system is widely used in industrial production and life. Data acquisition and processing technology is an important part of information science. It covers acquisition, storage, data processing and system control. It is a comprehensive technology based on sensor signal and micro-computer measurement and processing. Its task is to collect all kinds of parameter data on the spot, then send it to the computer, and according to different needs, calculate and process the data accordingly, and get the desired results. At the same time, the computer output results are displayed or printed as needed to monitor the real-time changes of some physical quantities[2].

In view of the above background, this paper introduces a rod-climbing robot with multiple sensors, which enables the rod-climbing robot to detect temperature, humidity, air quality and other information in high altitude or complex geographical environment. Then through wireless communication technology, the data is transmitted to the computer, and the collected data is analyzed and displayed by LabVIEW. This can replace human beings in dangerous reconnaissance and detection activities.

II. SYSTEM OVERALL SCHEME DESIGN

A. System Requirement Analysis

According to the actual needs: This paper designs an environmental monitoring system based on rod-climbing robot, STM32 controller and wireless communication control. The technical indicators of the system are as follows:

1) Set up STM32 control system, and WIFI wireless communication technology is combined to realize the control of the upper computer to the rod-climbing robot;

2) The system collects the data of the surrounding environment in real time and transmits the terminal data to the host computer through ZigBee module;

3) The system needs to use LabVIEW software to design the interface to display the real-time data collected by the slave computer.

B. Overall design of system scheme

The overall structure of the environmental monitoring system based on the rod-climbing robot is shown in Figure 1. The overall structure of the design consists of seven modules: (1) STM32 controller, (2) motor drive, (3) power supply, (4) sensor, (5) ZigBee, (6) WIFI, (7) computer. Each sensor of the lower machine of the rod-climbing robot collects the surrounding environment data and sends it to the computer through ZigBee for display and processing. The computer sends instructions to control the motor drive module through the WIFI module and STM32 controller to change the operation

status of the motor.

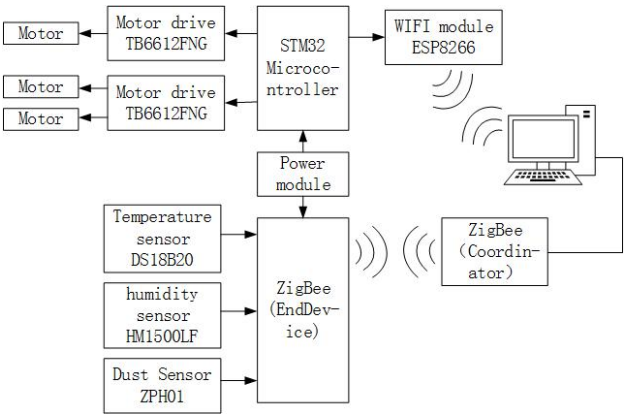

Fig.1 System Block Diagram

III. System Hardware Circuit Design

A. Structural Design of Rod-climbing Robot

At present, there are four kinds of rod-climbing robots studied at home and abroad [3-5]: (1) Robots have two grippers, which realize the rod-climbing action in a clamping and relaxing way. (2) Relying on the wheel movement on the pole to achieve the climbing pole action. (3) Bionic rod-climbing robot with creeping or creeping motion. (4) The robot has many fixed ends, and the climbing action of the rod is complex.

In this paper, the second one mentioned above will be used as the basic type of this design. In this design, the three wheels are 120 degrees each other, and the motor drives the wheels to rotate to complete the climbing rod motion of the robot. The planar structure and object of the rod-climbing robot are shown in figs. 2 and 3.

B. Motor Drive Module

The motor driver chip used in this design is TB6612FNG with MOSFET-H bridge structure. The output of the circuit is two channels, so two motors can be driven at the same time. The module circuit is shown in Figure 4.

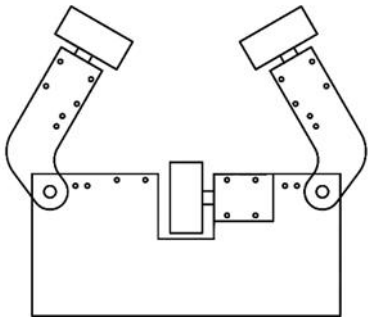

Fig.2 Plane Structure Diagram of Rod-climbing Robot

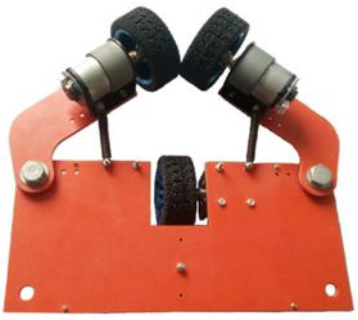

Fig.3 Structure Physical Chart of Rod-climbing Robot

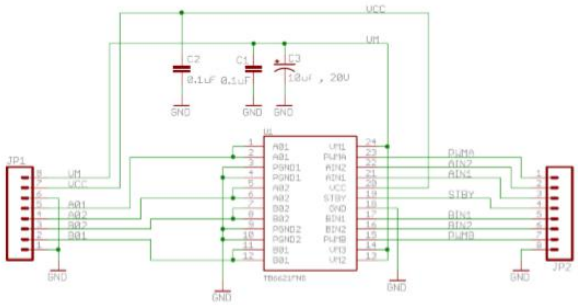

Fig.4 Schematic diagram of motor drive module

C. Sensor module

This module uses DS18B20, HM1500LF and ZPH01 to monitor the temperature, humidity and PM2.5 of the environment around the rod-climbing robot. The circuit schematic diagram of DS18B20 is shown in Fig. 5. The working voltage of the temperature sensor is 3.0~5.5V/DC, the resolution is 0.0625 ℃, and the range of temperature measurement is -55~+125℃. The physical diagram of the humidity sensor is shown in Fig. 6. Its characteristics are small size, wide measurement range and being able to cope with harsh environment. The working voltage of the sensor is 3.0-7.0V, and the output is 1-4V analog signal (corresponding to 0-100% humidity information), with an accuracy of ±2%. The circuit schematic diagram of the dust sensor is shown in Fig.7. Its characteristics are high sensitivity and stability. The sensor operates at a voltage of 5V and outputs a PWM pulse width modulation signal. The smallest particle with a diameter of 1μm can be detected.

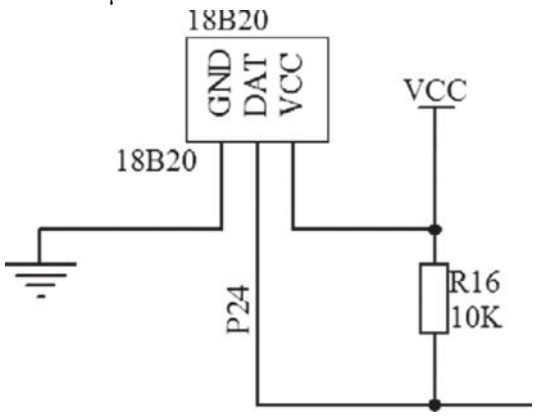

Fig.5 Circuit schematic diagram of DS18B20

Fig.6 HM1500LF physical picture

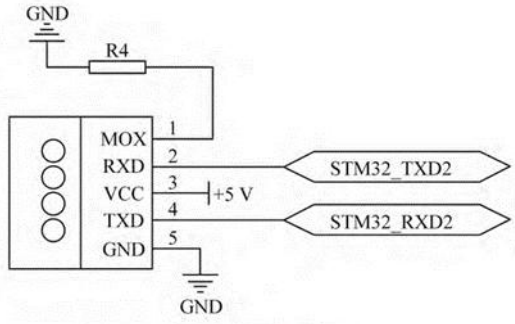

Fig.7 Circuit schematic diagram of dust sensor

D. Wireless communication module

This module uses WIFI and ZigBee technology. WIFI uses LEXIN ESP8266 module, which has processing chips supporting RTOS. Through SPI/SDIO interface or I2C/UART interface communication mode, it can be used as an external device to connect to the external MCU. It can also be used as a single MCU to develop its internal chip.

The WIFI module designed in this paper is used to control the motion of the rod-climbing robot, so that the rod-climbing robot can go up and down at different speeds. In this design, ESP8266 is set as serial transmission mode, that is, if STM32 sends data to ESP8266 chip, the chip sends data directly to the host computer through WIFI, and if ESP8266 receives wireless data from the host computer, it also sends data directly to STM32. In this way, the communication between the rod-climbing robot and the host computer is realized.

ZigBee, as a low-speed and short-distance wireless communication technology, is widely used in the Internet of Things industry[7,8]. Unlike other wireless communication technologies, ZigBee can be networked. Each ZigBee network can be regarded as a node, and each node can communicate with each other; the distance between each node can be extended from 10 to 100 meters, to several hundred meters, or even several kilometers. Zigbee also has the characteristics of low power consumption, low cost, low delay, high reliability and confidentiality.

In this module, Zigbee is used to send the data collected by the sensor to the host computer. ZigBee module is divided into terminal and coordinator. The terminal is loaded on the lower computer, and the data collected by the sensor is transmitted to the coordinator. The coordinator connects with the computer, receives data and transmits it to the computer through the serial port.

IV. System Programming and Software Design

A.Design of Control Program for Rod-climbing Robot

In this program, STM32 controller receives the instructions sent by the host computer through WIFI, and commands TB6612FNG to drive the motor to run, so as to control the motion state of the rod-climbing robot. The procedure flow is shown in Figure 8.

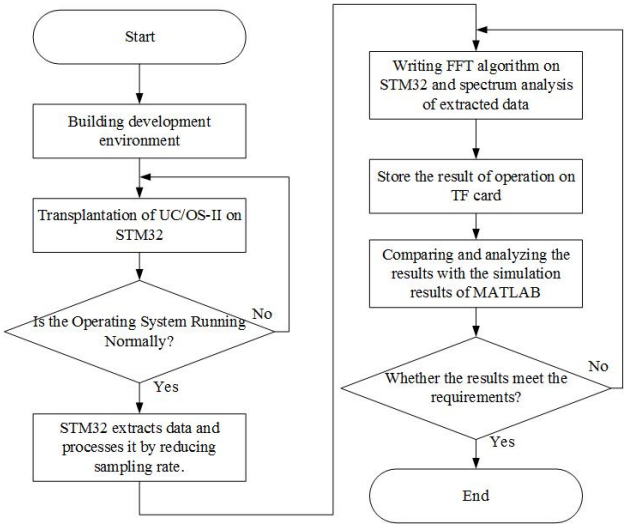

Fig.8 Flow chart of control program for rod-climbing robot

B. Design of Data Acquisition and Processing Program

The functions of this program include data acquisition, transmission and reception. The data collected by the sensor is transmitted to the coordinator through the terminal of the ZigBee module and sent to the upper computer through the serial port. The specific procedure flow is shown in Figure 9.

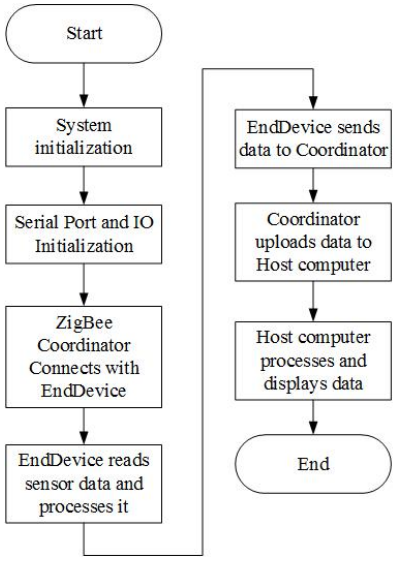

Fig.9 Flow chart of data acquisition and processing program

C. Design of Human-Computer Interactive Interface

The man-machine interface of the system is designed by LabVIEW [9]. The main tasks can be divided into:

(1) The computer connects with the robot through WIFI

to control the movement of the robot.

(2) The computer reads the data collected by ZigBee coordinator through serial port.

(3) Display temperature, humidity and PM2.5 information on computer software.

D. Front panel design

The front panel design mainly includes the data acquisition part and the motion state part of the rod-climbing robot. Data acquisition includes temperature, humidity and dust concentration. The motion state of the rod-climbing robot includes up, down and speed. The specific design is shown in Figure 10.

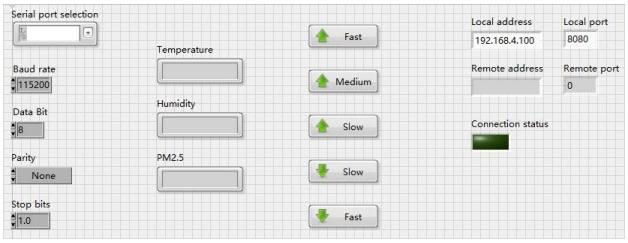

Fig.10 Front panel design diagram of system software

E. Program block diagram design

The program block diagram is mainly divided into two parts:

(1) WIFI motion control part, as shown in Figure 11. This part is mainly used to connect the computer and the robot through WIFI, so as to control the movement of the robot.

(2) Serial port receiving and displaying part, as shown in Figure 12. This part is mainly used to receive and display temperature, humidity and PM2.5 data received by ZigBee.

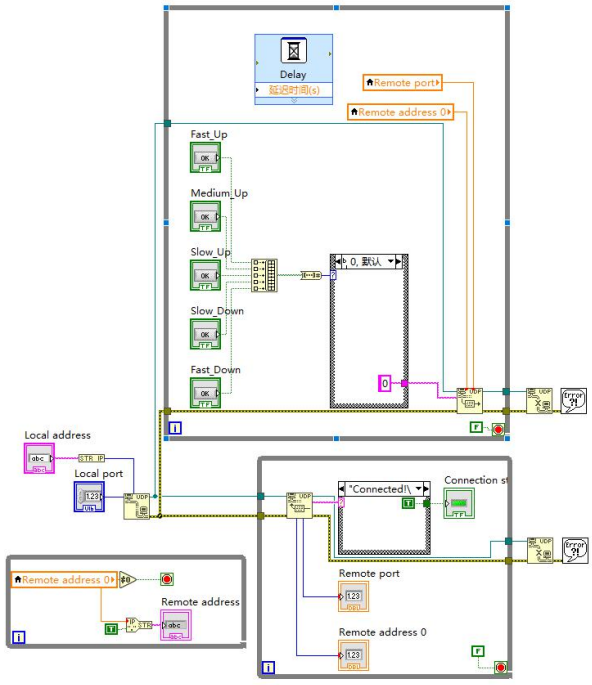

Fig.11 Program block diagram of WIFI motion control part

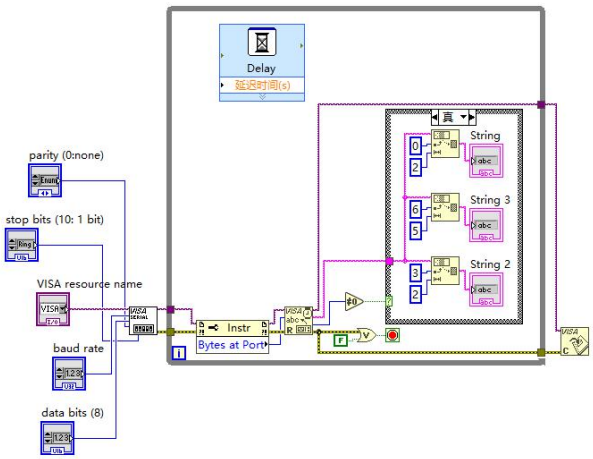

Fig.12 Program block diagram of serial port receiving and displaying part

V. System debugging and test results

After continuous debugging, the upper computer can control the motion state of the rod-climbing robot through WIFI, can go up and down at different speeds, and can display the data collected by the sensor through LabVIEW to complete the real-time monitoring of the air environment.

The prototype of the system is shown in Figure 13.

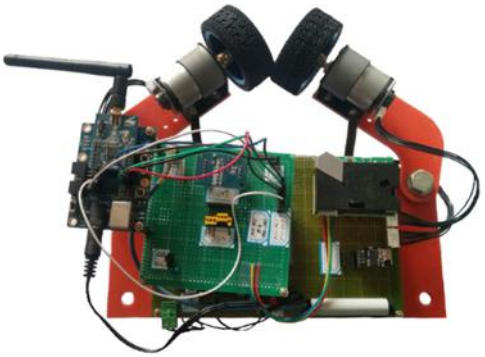

Fig.13 System prototype physical drawing

The specific data are shown in the table 1.

Table 1 Test results of the system at different locations

Parameter / Place	Temperature (℃)		Humidity (%)	PM2.5 (μg/m³)	Average error
Indoor	Actual value	15.9	20.6	21	0.27
	Measured value	16	23	17	
Corridor	Actual value	15.2	24.3	62	2.33
	Measured value	15	27	55	
Water room	Actual value	15.5	30.1	48	5.33
	Measured value	15	32	43	

VI. CONCLUSION

This paper completes the research and design of all parts of the whole system, such as rod-climbing robot, motor drive module, sensor module, etc. The prototype has been made and debugged, and its function meets all the requirements of the design system.

References

[1] Chen Mingsen. Research on kinematics and dynamics of rod-climbing robot [D]. Wuhan: Wuhan University of Technology, 2009.

[2] Ding Zongling. Research on data acquisition card control and temperature acquisition method based on LabVlEW [J]. University Physics Experiments, 2013, 26 (1): 81-84.

[3] M. P. Murphy, C. Kute, Y. Menguc, et al. Waalbotii: Adhesion Recovery and Improved Performance of a Climbing Robot Using Fibrillar Adhesives[J]. The International Journal of Robotics Research, 2011, 30(1):118–133.

[4] O. Unver, A. Uneri, A. Aydemir, et al. Geckobot: A Gecko Inspired Climbing Robot Using Elastomer Adhesives[C]. IEEE International Conference on Robotics and Automation. Orlando, FL, USA, 2006:2329–2335.

[5] Jiang Li, Guan Yisheng, Zhou Xuefeng, et al. Clamping performance analysis of Two-claw rod-climbing robot [J]. Journal of Mechanical Engineering, 2016 (03): 34-40.

[6] Xu Wen. Design of smart home monitoring system based on WiFi and Android [D]. Chengdu: Southwest Jiaotong University, 2017.

[7] Wang Xiong, Yang Ruifeng, Guo Chenxia, etc. Design of ZigBee-based wireless environmental monitoring network system [J]. Science and Technology Bulletin, 2017 (04): 144-147+1.

[8] Luan Luxiang. Design of Smart Home System Based on Zigbee Technology [J]. Information and Computer (Theoretical Edition), 2014 (09): 126-127.

[9] Wang Haibao, Wu Tingting, Wu Guangjie. Environmental Air Quality Monitoring System Based on LabVIEW [J]. Computer Measurement and Control, 2011, 19 (3): 525-527.

Design of centralized seismograph acquisition station based on STM32

Zeng sencai, Li wei, Yu xiaoyang, Bao jie
(College of Instrumentation & Electrical Engineering, Jilin University,Changchun 130022,China)

***Abstract*—Aiming at the characteristics of high dynamic range of seismic wave, a centralized seismograph acquisition station based on STM32 is designed. The signal conditioning circuit is used to complete the signal amplification and filtering process for the detected signal. The ADS1256 is used to process the processed analog signal. Corresponding conversion, the GPS module receives the location information and the clock information, and the A/D converted data and the GPS obtained information are transmitted to the TF card by the STM32 and stored in the tf card. The collection station has a built-in GPS receiver and does not require cables. It can record and store large amounts of data autonomously.**

***Key words*—STM32 centralized ADS1256 GPS**

I. PREFACE

AFTER the earthquake exploration in the last century, most of the exploration techniques used cable-connected geophones and central recording systems. However, such a system itself is heavy and unfavorable for handling. In addition, the cost of the system is high. After a certain period of use, the related equipment must be replaced even if it is not damaged by external forces, because the cable has been used. Aging will occur after a long time, and this problem will affect the quality of the data [1,14]. Therefore, a centralized seismograph acquisition station with low cost and low power consumption can effectively overcome the shortcomings of the original instruments, and can reduce the cost and promote the development of large-scale seismograph collection stations. The digital seismograph collection station has a built-in GPS receiver and does not require cables. It can record and store large amounts of data autonomously. Compared with the cable-collecting system, the centralized cableless acquisition system has the advantage of relatively flexible operation and can adapt to the rapid development of exploration technologies such as wide azimuth and high density in the future [2, 11]. The centralized acquisition system makes data processing more convenient and flexible, which also enriches seismic data processing methods.

II. ACQUISITION SYSTEM COMPOSITION

As shown in Figure 1, the seismograph acquisition station consists of STM32 main control module, signal conditioning circuit, 24-bit A/D conversion module, GPS clock timing positioning module, TF card storage module and system power supply module. The signal conditioning circuit amplifies and filters the detected signal, and the chip of the A/D conversion module is ADS1256, performs analog-to-digital conversion on the processed analog signal, obtains position information and clock information by using the GPS module, and passes through the A/D. The converted data and the GPS obtained information are transmitted to the TF card through the STM32 and stored in the TF card.

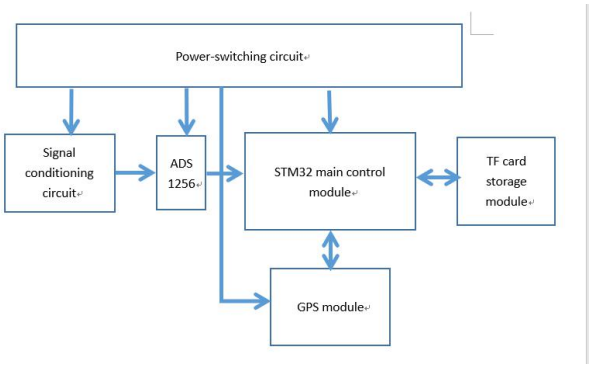

Fig.1 Overall block diagram

III. HARDWARE DESIGN

A Power section

As shown in Figure 2, the chip LM2676 and LM1117 are used to design 12V to 5V and 5V to 3.3V circuits to provide a clean input power supply.

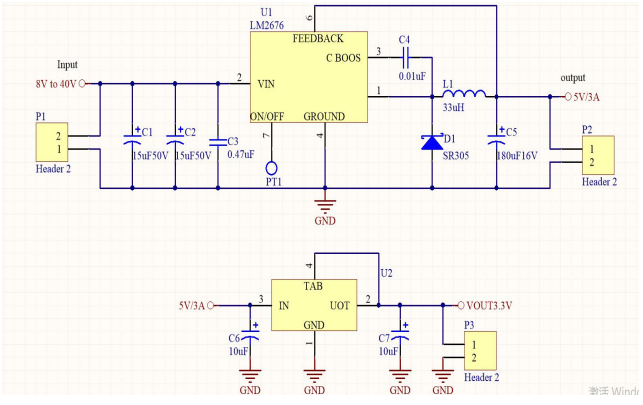

Fig.2 Power-switching circuit

B A/D conversion module

As shown in FIG. 3, the chip used by the A/D conversion module is ADS1256. The ADS1256 is a low noise, high resolution 24-bite Sigma-Delta (Δ-Σ) analog-to-digital converter (ADC). Compared with the traditional successive approximation and integral ADCs, the delta-sigma ADC has the advantages of low conversion error and low cost. The ADS1256 is suitable for systems that acquire analog data with a maximum frequency of only a few kilohertz. The data output rate can be up to 30K sample points per second (SPS), with a complete self-calibration and system correction system, SPI serial data transmission interface[3,6].

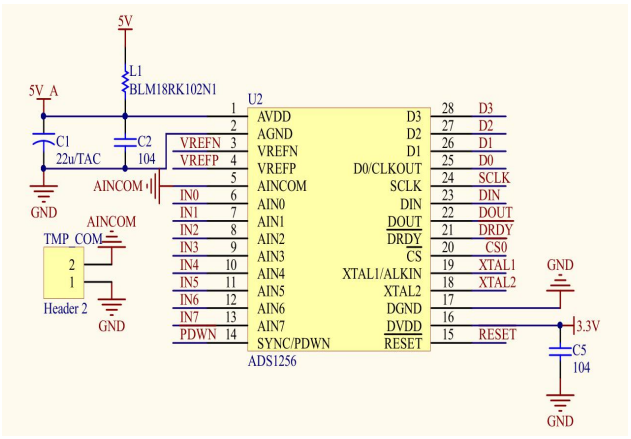

Fig.3 ADS1256 switching circuit

C Signal Conditioning Circuit

The signal conditioning circuit is shown in Figure 4. It has low power consumption and low noise. The amplifier chip used in the signal conditioning circuit is the AD8422. The chip is a low-power, high-precision, low-noise rail-to-rail instrumentation amplifier with ultra-low distortion performance that facilitates signal reduction and the load is unaffected throughout the output range. The voltage output function is

Vout= G*(VIN+-VIN-)+VREF

(1) wherein the magnification G is: G=1+19.8kΩ/Rg

(2) The magnification of the circuit is changed by adjusting the potentiometer R4. Low-pass RC filter circuit for signal input and output to remove high frequency noise [4,10,13].

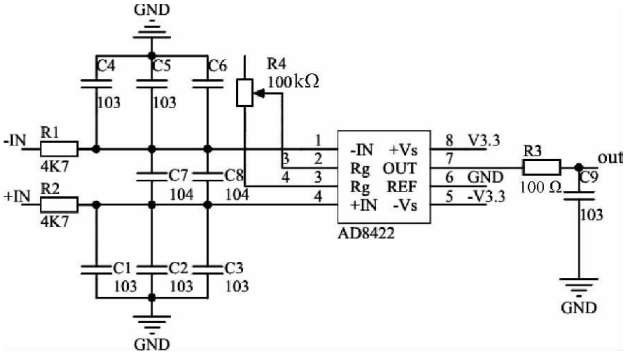

Fig.4 Signal conditioning circuit

D GPS module

As shown in Figure 5, the GPS module uses the U-BLOX NEO-6M module, which is compact in structure and can be set with various parameters through the serial port, and the parameters can be saved in the EEPROM. It can connect a variety of active antennas, adaptability.

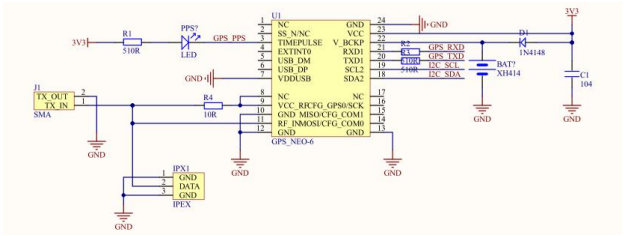

Fig.5 GPS module

IV.EXPERIMENTAL METHODS AND RESULTS SIMULATION

A Experimental methods

The data output rate of ADS1256 is (fCLKIN/256)*(1/Num_Ave). When fCLKIN is 7.68MHZ, Num_Ave takes 1 to get the highest data rate of 30KSPS, and Num_Ave takes 120000 to get the lowest data rate of 2.5SPS. When fCLKIN takes different values. The corresponding various Data Rates vary linearly according to the value of the 7.68 MHz clock frequency. For example, fCLDIN is reduced by half and the highest data rate is changed from 30KSPS to 15KSPS.

ADS1256 internal digital filter overall frequency response function H(f) is given by：

$$|H(f)| = \left|\frac{\sin\left(\frac{256\pi \times f}{fCLKIN}\right)}{64 \times \sin\left(\frac{4\pi \times f}{fCLKIN}\right)}\right|^5 \cdot \left|\frac{\sin\left(\frac{256\pi \times Num\_Ave \times f}{fCLKIN}\right)}{Num\_Ave \times \sin\left(\frac{256\pi \times f}{fCLKIN}\right)}\right|$$

The digital filter attenuates the output noise of the analog modulator. From the above equation, we can see that the H(f) and Num_Ave parameters are also related. In fact, changing the Num_Ave changes the output bandwidth of the digital filter. The larger the Num_Ave value, the smaller the filter bandwidth, and the more noise is subtracted. . The first zero point of the low-pass filter is at a frequency point where the value is equal to the Data Rate, and the other zero points are located at a frequency point that is an integer multiple of the Data Rate [5, 8, 12].

The output of ADS1256 is the bipolar output represented by 24bite, the lower 23 bits represent the effective value of the converted data, the highest bit represents the sign bit, the sign bit is 0 means the input is positive, and the sign bit is 1 means the input is negative. Its positive full-scale output is 7fffffh and the negative full-scale output is 800000h. The relationship between the measured input voltage value and the converted data over the range is:

When the output data is positive, the measured value = (2Vref / PGA (223-1)) output data

When the output data is negative, the measured value = (2Vref / PGA (223-1)) [7fffffh - (output data - 800000h) +1] output data [7,9].

B Results Simulation

Hammering source experiment Figure 6 is an experimental record of a location on a line with a track spacing of 0.5 m, a sampling interval of 0.5 ms, and a sampling time of 0.3 seconds.

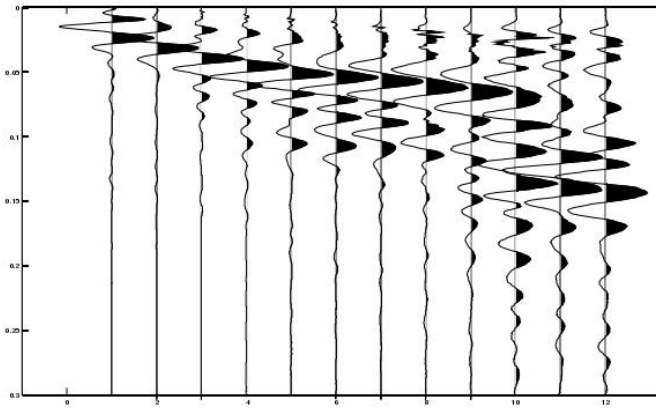

Fig.6 Single data acquisition chart of hammer source

V. CONCLUSION

Cable-based seismic exploration systems have long dominated seismic exploration technology. Cable-based seismic survey systems work by connecting large conductors, so exploration costs have long been high. In order to reduce exploration costs, cableless seismic exploration systems have become a new approach to low-cost exploration systems [1-3]. Future seismic exploration proposes large-scale, avenue-number exploration requirements, and the use of cable-free storage seismometers is a viable solution. The cable-free storage seismograph uses distributed acquisition and centralized recovery to simplify the field work flow and system composition, which can greatly save exploration costs.

In this paper, STM32 is used as the main control chip to study the system composition of the centralized seismic acquisition station. The seismograph is designed and implemented in the form of single station. Achieve the miniaturization and low cost of the instrument, easy to carry, and conducive to field work.

References

[1] Wang Sujing. Development of a low-cost cableless seismograph acquisition station [A]. Institute of Geology and Geophysics, Chinese Academy of Sciences. Institute of Geology and Geophysics, Chinese Academy of Sciences, 2015 (15th) Academic Papers - — Oil and Gas Resources Research Office [C]. Institute of Geology and Geophysics, Chinese Academy of Sciences:, 2016: 9.

[2] WANG Sujing, LU Chuan, YOU Qingyu, ZHANG Wei.Development of a low-cost cableless seismograph acquisition station[J].Chinese Journal of Geophysics,2015,58(04):1425-1433.

[3] Wu Haichao, Lin Jun, Li Zhe, Zhang Huaizhu, Yang Yuyuan, Chen Zubin, Zheng Fan. Wireless Network Monitoring Technology for Cableless Seismic Seismograph[J].Journal of Jilin University:Engineering Science,2012,42(05):1296 -1301.

[4] Zhang Huaqi. Research and software implementation of telemetry seismograph data transmission technology [D]. Jilin University, 2010.

[5] GUO Jian, LIU Guangding. Current Status and Prospects of Cableless Storage Digital Seismographs[J]. Progress in Geophysics, 2009, 24(05): 1540-1549.

[6] Liu Chunyan. Design of 12 centralized seismographs [D]. Jilin University, 2012.

[7] YANG Yiyuan, HAN Liguo, CHEN Zubin, LIN Jun. Low-power design of cable-free telemetry seismograph acquisition station[J].Electrical Measurement & Instrumentation,2009,46(01):49-53+63.

[8] Chen Lianqing, Jia Yanfang, Gu Xinli. GPS timing (network) seismograph [J]. Geophysical Equipment, 2006 (S1): 1-7.

[9] Burdick S, Li C, Martynov V, et al. 2008, Upper mantle heterogeneity beneath NorthAmerica from travel time tomography with global and USArray transportable array data, Seismological Research Letters, 79(3), 384–392

[10] Burdick S, van der Hilst R D, Vernon F L, et al. 2009. Model update December 2008: Upper mantle heterogeneity beneath North America from P-wave travel time tomography with global and USArray transportable array data, Seismological Research Letters, 80(4), 638-645.

[11] Buehler J S., Shearer P M. 2010. Pn tomography of the western United States using USArray, Journal of Geophysical research, 115, B09315.

[12] Carr G R, Andrew A S, Denton G J, et al. 1999. The “Glass Earth”-Geochemical frontiers in exploration through cover. Aust Inst Geosci Bull, 28: 33–40.

[13] Tang D L, Li Z S, Yang H S. 2000. Seismic Data Acquisition Technology for Complicated Mountainous Area[J]. Potroleum Explorationist, 2000, 5(2): 25-30.[16]Gao J Z. 2016. Electronic Noise and Low Noise Design [M]. Beijing:Tsinghua University Press.

[14] Dai Y S. 1984. Electronic System Noise and Low Noise Design Method [M].Changchun：Jilin People's Press.

Design of an intelligent segmented linear constant current LED driver

Zhang Jiawei, Wang Zixu, Jin Junxian
（*College of insitrumentation &electrical engineering, Jilin University,Changchun 130022,China*）

***Abstract*—There are electrolytic capacitors with large value and high frequency transformers in traditional switch-mode LED drivers. They will result in large size and short life of a LED driver. A novel segmented linear constant current LED driver which avoids using electrolytic capacitors and high frequency transformers was proposed. It adapts to automatically control LED working with constant current in stages that high voltage pulsating DC voltage after rectification. The LED driver circuit with smaller volume and longer service life can be integrated in a monolithic chip except the rectifier bridge and the sampling resistor. In addition, this driver will achieve intelligent control through an extended pin. The circuit of this LED driver was designed and simulated based on HG 0.5 μm 700 V BCD process. Simulated results show that the driver circuit works in four stages under the condition of high pulse input voltage of 0～311 V cycle, the maximum constant output current is 97.17 mA and the current transient precision error is only about 0.031%. These simulated results indicate that all parameters of this high-voltage regulator are validated.**

***keywords*—LED driver；segmented control；linear constant current；intelligentize.**

I. INTRODUCTION

LED（Light emitting diode）Lighting is a new lighting technology and a typical green lighting source. In the LED lighting technology, the performance of the driving power supply is very important, which involves the electrical performance and reliability of the whole LED lamp. LED driver power is generally developed into switching power supply and linear power supply [2]. The switching power supply has the advantages of high efficiency and low power consumption, but it has serious electromagnetic interference problems. The problem of linear power supply is smaller, the ripple of output current and voltage is smaller, but the efficiency is lower than that of switching power supply [3]. In LED lighting, it is required that the service life of driving power supply is longer than that of LED light source, so as to ensure the service life of the whole LED lamp. However, due to the use of electrolytic capacitors in the circuit, it is vulnerable to the influence of working temperature,electrolyte volatilization, capacitance capacity decline and other issues, the service life of the driving power supply is greatly reduced, thereby reducing the service life of the whole LED lamp [4-6].

II. DESIGN OF DRIVING POWER CIRCUIT

Traditional switching LED power supply usually contains large electrolytic capacitor and high frequency transformer, which results in large size and short service life of LED power supply. Figure 1 shows the system block diagram of the traditional switching LED driving power supply for municipal power supply. The main purpose of the filter circuit in the figure is to transform the rectified voltage waveform into a smooth DC current. The output rectifier can filter the voltageand maintain the consistency of the output current. Thecircuit needs energy storage elements such as electrolytic capacitor and inductance. The transformer works in flyback mode, and the transformer can realize the eme conversion by repeatedly switching on and off. It can be seen that the traditional switch-type LED driving power supply uses a large volume of transformers, electrolytic capacitors, inductors and so on in the circuit structure, and the circuit has the problems of huge volume and short service life [8]. The piecewise linear constant current LED driver can effectively solve the above problems

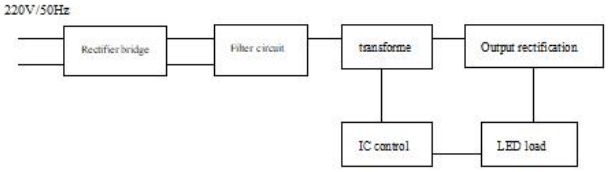

Figure 1 System block diagram of a traditional switched LED driver

Figure 2 shows the system block diagram of the intelligent segmented constant current linear LED driver power supply designed by our group. With the drive circuit, we can not use large electrolytic capacitors and high-frequency transformers, and can adaptively control the linear constant-current operation of LED strings according to the specific changes of the voltage after rectification. In the figure, the rectifier bridge of the module 1 can perform full-wave rectification of the sinusoidal voltage waveform. In the figure, the LED string N1 to the LED string N4 adopts

a series connection of N LE D bulbs, and Rsen uses an external precision resistor. The input voltage is output to VDD through a voltage-lowering high-voltage circuit. This voltage is used as the operating voltage of the chip. The multi-value output provides reference voltage for each of the four constant-current linear circuits. Four sets of linear constant-current control LEDs The string operates in a linear constant current mode; the level conversion function module can convert the externally sensed signal level into a level that the chip can recognize, and can also control the multi-valued output reference circuit and control the multi-value. The output of each parameter of the output reference circuit; the internal protection circuit of various functions can prevent extreme conditions such as excessive heating of the driving chip or excessive voltage or excessive current, so that the circuit can be operated normally.

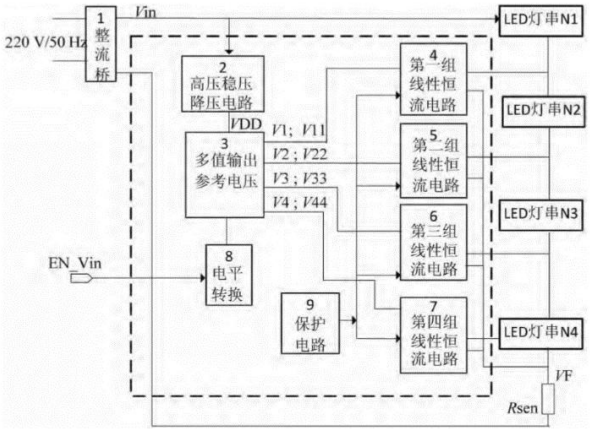

Figure 2 Block diagram of the LED driver power supply

The following is the basic working principle analysis of the circuit: after the input 220V/50Hz AC power is rectified by the rectifier bridge, the pulsed DC high voltage can be obtained at the two output ends of the rectifier bridge. The peak value of the pulse DC high voltage is 311V. The voltage of a sinusoidal half-wave pulse with a period of 10 ms. This voltage provides the operating voltage of the high voltage regulated buck circuit and the input voltage Vin of the LED driving power supply. The high voltage regulated step-down circuit can stably output the working voltage of the chip before the first string of LEDs is turned on to ensure that the chip can work normally. The circuit output of the reference voltage of the multi-value output is V1 < V2 < V3 < V4, and the voltages of the four channels can be regarded as the reference voltages of the four sets of constant current linear circuits, respectively. In the gradual increase phase of the input voltage, when the input voltage is increased to a voltage that is turned on in the positive direction of N1, the LDMOS1 in the constant current linear circuit of the first group is in an on state, and the LED string N1 is lit. The current is controlled by the first set of constant current linear circuits. When the input voltage becomes the respective passable voltage of the LED string N1 and the LED string N2, the current of the branch will increase significantly, and the feedback voltage will be significantly improved, resulting in the output of the first group of constant current linear circuits. The voltage is low voltage, so the first group of LDMOS1 can be turned off. The LED string N1, the LED string N2 and the LDMOS2 can form a branch circuit, and the current is controlled by the second group of constant current linear circuits. The current is V2/. Rsen. According to the above working principle, the LED string N3 and the LED string N4 are lit, and similar results can be obtained. During the falling phase of the input voltage, the order in which the four sets of constant current linear circuits operate is opposite to the rising phase of the input voltage. The sensing signal from the outside can be controlled by a high-low level switching circuit to output a reference voltage circuit to achieve the purpose of changing the output current. The segmented linear constant current LED driver circuit can operate in two modes, as shown in Table 1. The LED is lit one by one in four stages. In the table, V11/V1=V22/V2=V33/V3=V44/V4=2, and Rsen is an external sampling resistor.

Table 1 Two current operating modes of LED driving

Output current	The first stage	The second stage	The third stage	The fourth stage
EN off	V_1/R_{sen}	V_2/R_{sen}	V_3/R_{sen}	V_4/R_{sen}
EN on	V_{11}/R_{sen}	V_{22}/R_{sen}	V_{33}/R_{sen}	V_{44}/R_{sen}

III CIRCUIT DESIGN

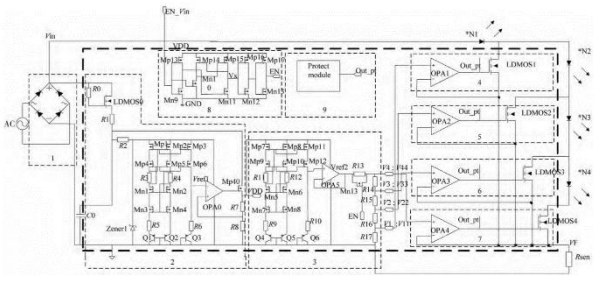

Figure 3 shows the structure of an intelligent segmented linear constant current LED driver

For rectifier bridge 1 in the circuit, we need to select a full-wave rectifier bridge. The reverse voltage of the diode on each leg of the figure is above 700 V, and the maximum forward current is above 330 mA. As for the buck circuit 2, the branch circuit of the CR charging.Function consisting of LDMOS0 and capacitor C0 is then used for Zener diode Zener1 with a regulated voltage of 5.8V to achieve the regulation purpose, thus the pre-reference voltage source and

linear regulator. The device works fine. The pre-reference voltage source generates Vref1, which is used as the reference voltage value and is also linearly regulated.OPA0 adjusts the gate voltage of Mp40 according to the voltage drop change of resistor R8 in the feedback feedback network, so that the output voltage VDD is stable, and VDD can be calculatedby the following formula:

$$VDD = \frac{R_7 + R_8}{R_8} \times V_{ref1} \quad (1)$$

Where Vref1 = 1.2V and R7/R8 = 3.2, VDD =5V is obtained. The power tube Mp40 is obtained according to the saturation threshold

$$ID=12\mu pCoxW/LV2od \quad (2)$$

(2) where μpCox is the process-related parameter value of the power tube, Vod is the overdrive voltage, and W/L is the ratio of width to length. The rated load current value can be set to 10mA, and the width-to-length ratio of Mp40 can be taken as 4000/2=2000, so that VDD has a certain load capacity, making it the operating voltage of the low-level module of the chip. . The multi-valued output reference voltage circuit 3 is composed of a reference voltage source, a buffer device and a resistor divider network. The reference voltage source is a weight that uses voltages of mutually opposite temperature coefficients, and is added in an appropriate ratio, whereby a reference voltage having a zero temperature coefficient [9] can be obtained. The output of the operational amplifier OPA5 is connected to its opposite end to form a buffer device. After the reference voltage passes through the buffer device, Vref2 can be obtained, and a plurality of reference voltages can be obtained by proportionally dividing the voltage by a specific resistor. The buffer device ensures that the reference voltage and the reference voltage have almost the same characteristics. By adding a switch Mn13 to the resistor divider network, the turn-on and turn-off of Mn13 can be controlled according to EN, thereby changing the ratio of the resistor divider network, resulting in a significant change in the output reference voltage value. In the circuit, R13=40kΩ, Vref2=1.2V, R15=6.4kΩ, R14=7kΩ, R16=6.8kΩ, R17=21 kΩ. If EN is invalid, the output of the reference circuit V1=0.3V, V2=0.4V, V3= 0.5V, V4=0.6V; when EN acts, the circuit output V11=0.6 V, V22=0.8V, V33=1 V, V44=1.2 V. If the circuit is controlled by EN, the circuit will output two different reference voltages. The linear constant current circuit 4 is mainly composed of an operational amplifier OPA1, a high voltage LDMOS1, and a sampling resistor Rsen. When the input is increased to the positive voltage drop of the first string of LED lamps N1, the drain-source current of the LDMOS1 begins to increase, and the voltage drop across the sampling resistor is gradually increased and can befeedback to the inverting terminal of the operational amplifier, and the OPA1 passes through the input terminal. The terminal voltage is changed, and the LDMOS1 is adjusted so that the output current gradually becomes constant [10], so that the LED string N1 operates at a constant current, and the output current can be calculated by the equation (3):

$$I_1 = \frac{V_1}{R_{sen}} \quad (3)$$

I1 is the constant current output by the LED controlled by the first constant current linear circuit, V1 is the reference voltage of the multi-valued reference output circuit, and Rsen is the external sampling resistor. The constant current linear circuits 4, 5, 6 and 7 operate on the same principle. The level switching circuit 8 can pass the signal EN through the level shifting circuit to adjust the signal EN to match the operating voltage of the chip to obtain the enable EN of the output. The EN controls the multi-valued output reference circuit to enable the multi-valued output reference circuit to output two different reference voltages, and also to convert the LEDs into two completely different operating states. The protection circuit 9 is composed of an over temperature prevention circuit, an overvoltage prevention circuit, and an overcurrent prevention circuit.

IV Simulation and results analysis

Based on the workflow of Hua Hong 0.5μm 700VBCD, the spectre simulator under Cadence platform is used to simulate the circuit. During verification, the LED string in the circuit is tested in series with resistors in series with various other diodes. Figure 4 shows the results of a simulation of the LED output constant current as a function of input voltage over time.

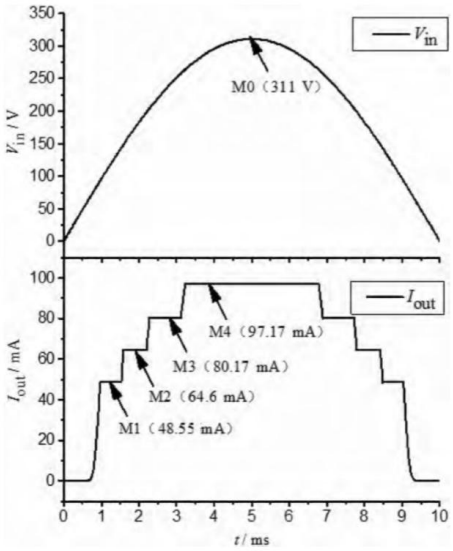

Figure 4 LED input voltage and output current

From the simulation results, it can be seen that when the voltage is input, when EN is connected to VDD, as the input voltage increases, the output constant current value of the LED is gradually increased in four stages, and all four stages are in a constant state; In the case of a low level, the LED output current is also reduced in four stages, and the circuit implements a piecewise constant current operation function. Figure 5 shows the simulation results of transient current changes when the LED output current is operating in a fourth stage power tube. It can be clearly seen from the simulation results that in the constant current output stage, the maximum constant output current is 97.17 mA, the minimum value is 97.14 mA, the current fluctuation range is only 0.03 mA, and the transient accuracy error of the current is only 0.031%.

Figure 6 shows the simulation results for the multi-valued output reference circuit. The circuit enable signal EN is activated at 5 ms. It can be clearly seen from the simulation results that the multi-valued output reference voltage is changed from V1:V2:V3:V4 to V11:V22:V33:V44, which realizes the manipulation of multi-valued reference output voltage.

Figure 7 shows the simulation results of the LED output current and input voltage after the EN signal is turned on. The circuit enable signal EN is activated at 5 ms. It can be clearly seen from the simulation results that in the first 0~5ms phase, the output current is controlled by V1:V2:V3:V4. In the last 5~10ms phase, the output constant current is controlled by V11:V22:V33:V44, and the output current of each constant current stage is doubled, and the circuit can achieve intelligent control.

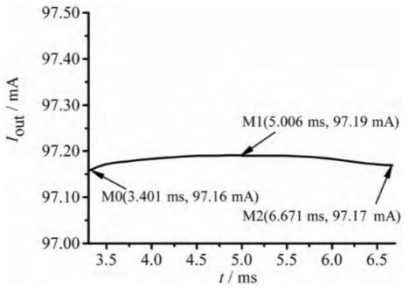

Figure 5 LED transient current change in the fourth constant current phase

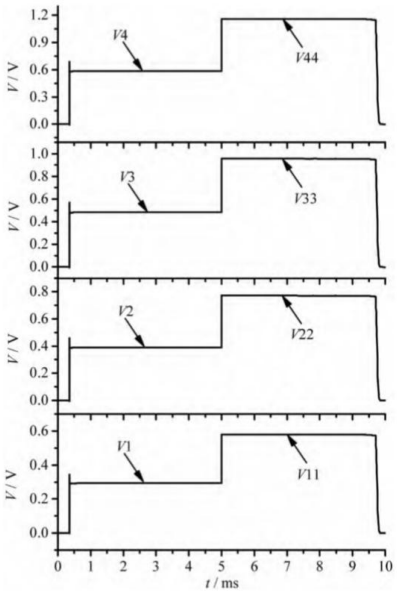

Figure 6 Multi-value output reference voltage simulation value

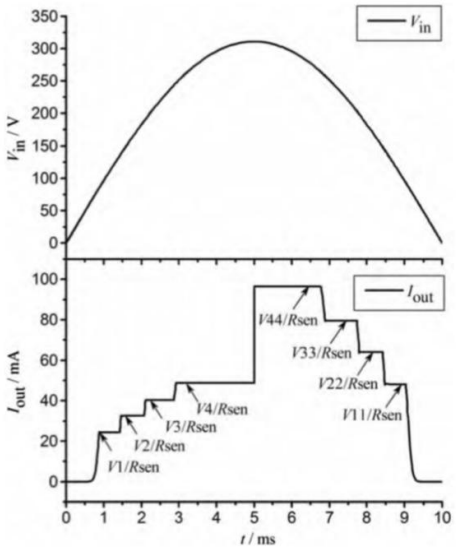

Figure 7 Two output current states after the smart extension is enabled

V CONCLUSION

Among the LED lighting technologies, the power source used for driving is very important. To promote the development of LED lighting technology, it is

absolutely necessary to improve the performance of the driving power supply. Our intelligent segmented linear constant current LED driver chip, which does not require large electrolytic capacitors and high frequency transformers, significantly improves the operating life of the drive power supply and greatly reduces the size. Due to the frequent changes of the input voltage, the chip can work in a constant current at multiple stages, and the inside of the chip also constitutes a perfect circuit for protection, ensuring the stability and reliability of the circuit. The circuit that has a driving effect on the chip is also designed to expand the intelligent functions, so that the LED can be intelligently expanded to control the lighting. It can be seen from the simulation results that under the high-level input condition of 0-311V periodic pulse, the output of the chip can be divided into four stages to keep the current constant, and the highest constant current can reach 97.85mA, in constant current. At the stage, the accuracy error of each transient of the current is only 0.031%. The circuit also accepts a sensed signal from the outside world, causing the control circuit to be two completely different current output states. The driver chip has the advantages of small size and convenient assembly, and can implement the advantages of intelligent control, and is beneficial to improving various functions of the LED driving power supply.

REFERENCES

[1] Chen DAhua. Green lighting LED technology [M].BeiJing：Chemical Industry Press，2009：12-15.

[2] Wang Jincheng，Li Youzhen，Chen Jingbo，etc. Research on AC LED Driver Circuit [J]. Journal of Lighting Engineering，2006，17(4)：16-18.

[3] WANG B，RUAN X B，YAO K，et al.A method of reducing the peak-to-average ratio of LED current for electrolytic capacitor-less AC-DC drivers[J].Trans.on Power Electronics， 2010，25(3)：592-601.

[4] LI Y，GUO W，ZHU Z M.A high efficiency and factor，segmented linear constant current LED driver[J].Journal of Semiconductors，2015，36(4)：1-7.

[5] Ai Yan，Wen Hao. Segmented high voltage linear constant current source LED driving technology [J]. Digital technology and application，2015(1)：89-90.

[6] WU H， TU W C.Controllable and dimmable AC LED driver based on FPGA to achieve high PF and low THD[J].2013 (9)：1330-1332.

[7] Chen Yue. Design and Implementation of High Efficiency Step-Down DC_DC Power Management IC XD1129 [D].XiAn： Xian University of Electronic Technology， 2012.

[8] WU C，HUI S Y .Elimination of an electrolytic capacitor in AC/DC light-emitting diode(LED) driver with high input power factor and constant output current[J].IEEE Trans Power Electron.2012，27(3)：1598-1602.

[9] Zhang Long，Feng Quanyuan，Wang Dan. A High Precision Bandgap Reference Source Design with Curvature Compensation [J]. Microelectronics，2015，45(2)：222-224.

[10] Ye Wenfeng， Yang Zhihao， Chen Kai， etc. Design of Piecewise Linear Constant Current Drive Power Supply for LED Lighting [J]. Chinese Lighting Appliance，2015(2)：16-18.

Time-frequency Analysis of Seismic Data Based on Synchrosqueezing Wavelet Transform and Research on Noise Suppression

Ma Jiliang, Luo Yuwei, Chen Heng, Chen Cong

(College of Instrument Science and Electrical Engineering,Jilin University,Changchun130012,China)

***Abstract*—Although continuous wavelet transform is widely used as a time/frequency analysis method in the field of geophysics because of its multiresolution,the resolution of time/frequency is negatively affected by the Heisenberg uncertainty principle.The synchrosqueezing wavelet transform(SWT) is to squeeze and reconstruct complex coefficient spectra in scale orientation.It enhances the resolution of wavelet transform and preserve its mathematic reversibility.When analyzing seismic data, introducing the time-frequency analysis method of spectral rearrangement can accurately analyze complex seismic signals, and at the same time, it is more convenient to denoise the data and improve the quality of exploration.This article aims at designing a software based on synchrosqueezing wavelet transform the time-frequency analysis method of weak seismic signals and noise suppression,using synthetic data and practical examples validate the treatment effect of this method.**

***Keywords*—Synchrosqueezing wavelet transform Reassigned spectrum Time-frequency analysis Suppression of noise Matlab GUI**

I. INTRODUCTION

IN recent years, with the continuous development of society, the continuous progress of science and technology, and the increasing means of seismic exploration, more and more advanced technologies have been widely used in the field of seismic exploration. Seismic exploration technology is tending to be multi-parameter, multi-dimension and high resolution. With the deepening of seismic exploration depth and the increasingly complex exploration environment, more and more noise, it is necessary to use more convenient and effective methods to analyze and process, so as to meet the requirements of high-precision seismic exploration. Since Fourier transform was proposed in 1980s, Fourier transform has been an important tool for digital signal processing[1].

In 1946, Gabor proposed a windowed Fourier transform (called Short Time Fourier Transform or Gabor Transform). It can analyze signals by taking a certain width of time window function. It has a certain localization function and plays a certain role in studying the local characteristics of signals. Although the time window of Gabor transform can vary with the parameters, and the size and shape of the window are independent of time and frequency, once the time window is selected, its length can not be changed. It is obvious that the time window with the same width in the whole time domain is inconsistent with the requirement of actual signal analysis[2].Wavelet transform can use short time window to analyze the high frequency component and large time window to analyze the low frequency component, which accords with the law of reality and can better analyze the non-stationary and non-linear signal[1,3].

In the past two decades, wavelet analysis has become an important tool for seismic data processing. The idea of wavelet transform originates from people's demand for non-stationary and non-linear signal analysis, but its excellent characteristics in one-dimensional can not be simply extended to two-dimensional or higher-dimensional. In order to overcome the limitations of wavelet transform and develop in two-dimensional data or other high dimensional spatial data, multi-scale geometric analysis has developed rapidly. Boashash and Mesbach[6]) proposed a Time-Frequency Peak Filtering Algorithm to reduce random noise based on time-frequency analysis theory. Its basic principle is to transform the signal submerged in noise into the instantaneous frequency of a constant amplitude FM signal by frequency modulation, and estimate the instantaneous frequency by the peak value of Wigner-Ville[4] distribution, so as to realize signal enhancement. Wavelet transform is the use of continuous wavelet transform to suppress noise. The signal and noise can show different properties. Based on this, the low signal-to-noise ratio can be determined, and the corresponding orthogonal wavelet components can be removed. After inverse transformation, the

purpose of suppressing noise can be achieved[3].

Short-time Fourier transform and wavelet analysis are the two earliest and most original methods of time-frequency analysis. The difference is that the former is "time-frequency" and the latter is "time-scale". Later, all video transformation methods are based on the upgraded version of the two methods. The compressed wave transform used in this project is no exception. It is a method to extract the instantaneous frequency characteristics of signals. Methods Daubechies[1] and others used it to characterize the instantaneous frequency of speech signals; Shan[2] and others used it to analyze the time-frequency characteristics of seismic signals to verify the applicability of the compressed wavelet transform method to seismic signals; Herrera[3] used it to analyze River identification. The rapid development of wavelet theory began in the 1980s. In domestic research, wavelet transform was first applied to seismic data compression. Later, it has achieved results that traditional methods can not achieve in image processing and fault diagnosis. Domestic development lags behind that of foreign countries. However, there is no lack of predecessors who have made achievements in this field in China. I believe that the future generations are in this field. Talents in this field will also emerge in large numbers.

II.SYNCHROSQUEEZING WAVELET

For signal $x(t)$, its Fourier transform can be expressed as:

$$X(\xi)=\int x(t)e^{-i\xi t}dt \qquad (1.1)$$

In the formula, zeta represents the angular frequency. The inverse transformation of $x(t)$ is:

$$x(t)=\int X(\xi)e^{i\xi t}d\xi \qquad (1.2)$$

For signal $x(t)$, it can be expressed as the sum of a series of harmonics with different frequencies. Most signals in nature satisfy this hypothesis. We describe this phenomenon in the following way: for signal s (t), it is:

$$s(t)=\sum_{k=1}^{K}m_k(t)+e(t) \qquad (1.3)$$

In the formula: $m_k(t) = A_k(t)\cos[\varphi_k(t)]$, representing a single time-varying harmonic component, $A_k(t)$ representing the instantaneous amplitude, $\varphi_k(t)$ representing the instantaneous phase of the k component, and $e(t)$ representing noise or interference.

The instantaneous frequency $f_k(t)$can be obtained from the derivative of the phase[3]:

$$f_k(t)=\frac{1}{2\pi}\frac{d}{dt}\varphi_k(t) \qquad (1.4)$$

The wavelet transform is written in the form of frequency domain:

$$W_s(a,b)=\frac{1}{2\pi}\int a^{-\frac{1}{s}}\hat{s}(\xi)\hat{\psi}^{*}(a\xi)e^{ib\xi}d\xi \qquad (1.5)$$

In the formula:a is the scale factor;b is the time translation factor;ξ is the angular frequency;ψ(ξ) is the Fourier transform of the mother wavelet.

Then for a single harmonic signals$(t)=A\cos(\omega t)$,its wavelet transform is:

$$\begin{aligned}W_s(a,b)&=\frac{a}{2}\int a^{-\frac{1}{s}}[\delta(\xi-\omega)+\delta(\xi+\omega)]\bullet\\&\quad\hat{\psi}^{*}(a\xi)e^{ib\xi}d\xi \qquad (1.6)\\&=\frac{A}{2\sqrt{a}}\hat{\psi}^{*}(a\omega)e^{ib\omega}\end{aligned}$$

If the dominant frequency of mother wavelet is $\xi=\omega_0$,the wavelet coefficient spectrum should concentrate on the scale $a=\omega_0/\omega$ in theory.However, the actual spectrum of wavelet coefficients often diffuses in the scale direction and can not be well focused, which makes the time-frequency image blurred[3,4].

Although the wavelet coefficients diffuse in the scale direction, their phase remains unchanged. Therefore, for the wavelet coefficients $W_s(a,b)$,the instantaneous frequencies are calculated:

$$\omega_s(a,b)=\frac{1}{2\pi}\frac{\partial}{\partial b}\arg[W_s(a,b)] \qquad (1.7)$$

In the formula:arg( ) denotes the phase of complex wavelet coefficients.

By calculating the instantaneous frequency, the wavelet coefficients can be projected from (b,a) to $(b,\omega_s(a,b))$,This is the basic idea of compressed wavelet transform. For discrete cases, both scale coordinates and frequency coordinates are discrete values $(\Delta a_k=a_k-a_{k-1},\Delta\omega=\omega_l-\omega_{l-1})$,so the formula of compressed wavelet transform can be expressed as follows[6]:

$$T_s(\omega_l,b)=\Delta\omega^{-1}\sum_{|\omega(a_k,b)-\omega_l|\le\Delta\omega/2}[W_s(a_k,t)a_k^{-3/2}\Delta a_k] \qquad (1.8)$$

Because the compressed wavelet transform rearranges the complex wavelet coefficients in the frequency direction, it is reversible and its inverse transformation can be expressed as:

$$\begin{aligned} s(t) &= \mathrm{Re}\{C_\varphi^{-1}\int_0^\infty W_s(a,b)a^{-3/2}da\} \\ &= \mathrm{Re}\{C_\varphi^{-1}\sum_k [W_s(a_k,b)a^{-3/2}\Delta a_k]\} \\ &= \mathrm{Re}\{C_\varphi^{-1}\sum_l [T_s(\omega_l,b)\Delta\omega]\} \end{aligned} \quad (1.9)$$

Inside, $C_\varphi = \int_0^\infty \hat{\psi}^*(\xi)d\xi$.

III. Time-frequency Analysis Method

A. Fourier Transform

Fourier transform is often used in general frequency response analysis, but only through frequency domain analysis can not fully describe the characteristics of seismic signals, it must be combined with time domain common analysis.Ordinary Fourier transform can not meet the requirements. An improved Fourier transform method is proposed. On the basis of the original method, the whole input signal is divided into local and segmented signals by adding windows. Each signal is transformed separately by Fourier transform. We call this transformation method short-time window Fourier transform, STFT for short[4].

The significance of STFT method lies in its local characteristics, such as formula 2.1

$$F(t,\omega) = \int x(\tau)h(\tau - t)e^{-j\omega t}d\tau \quad (2.1)$$

In formula: $x(\tau)$ is the input signal to be transformed,$h(\tau)$ is the sampling window related to time.

As time goes on to the right, the sampling window moves to the right. Fourier transform is applied to the signals in the sampling window corresponding to each time, and the frequency response obtained has local characteristics. In the frequency domain, the frequency response of the whole input signal can be obtained, and the original input signal can be reconstructed by Fourier inverse transformation of the spectrum, such as formula 2.2:

$$x(\tau) = \iint F(t,\omega)h(\tau - t)e^{j\omega t}d\omega dt \quad (2.2)$$

The time and frequency resolution of STFT varies with the width of the sampling window. The narrower the window, the higher the former and the lower the latter; on the contrary, the wider the window, the lower the former, while the higher the latter, the impact on both is relative.

B. Gabor Transform[1]

In STFT, since the influence of the width of the sampling window on time and frequency resolution is relative, one of them is large, and the other one is inevitably small, so it is impossible to take any small size at the same time. At the same time, due to the principle of uncertainty, two The product of the resolution cannot be less than a constant C.However, a minimum value can be found $\Delta t \times \Delta\omega = 1/2$,which is true when the sampling window is a gauss window. A transformation that satisfies the above conditions is a special case of STFT, which is called a Gabor transform.

The Gauss window is like the formula 2.3:

$$h(\tau) = \frac{1}{2\sqrt{\pi a}}e^{\frac{\tau^2}{4a}} \quad (2.3)$$

Where: the size of a is related to the width and width of the Gauss window, directly affecting the two resolutions of the Gabor transform.

C. Wavelet Transform[4]

Wavelet transform is a new transformation method generated in the background of solving the problem of seismic signal processing, which makes up for the shortcomings of STFT. In the STFT, once the sampling window is determined, both the frequency resolution and the time resolution are determined and cannot be changed throughout the conversion process. In the wavelet transform, the resolution is variable. According to the needs, the low frequency area pays attention to the frequency, and the high frequency area pays attention to the time, and the corresponding setting can be higher.

Continuous wavelet transform for $x(\tau)$, referred to as CWT for short, gives the formula 2.4:

$$W(b,a) = \frac{1}{\sqrt{a}}\int x(\tau)\psi^*(\frac{\tau - b}{a})d\tau, a > 0 \quad (2.4)$$

Where: $W(b,a)$ is the CWT spectrum, $\psi(\tau)$ is the mother wavelet, $\psi^*(\tau)$ and $\psi(\tau)$ are conjugated.

If you scale, translate, normalize $\psi(\tau)$,you can get a set of $\psi_{a,b}(\tau)$, as in formula 2.5:

$$\psi_{a,b}(\tau) = \frac{1}{\sqrt{a}}\psi((\tau - b)/a) \quad (2.5)$$

Where: a is the scale parameter and b is the translation parameter[4,5].

IV. Denoising Principle

In the process of seismic signal collection and sampling, there are often random noises to interfere with the seismic signal recording process, causing its pollution. One of the special methods in these methods is to use an iterative threshold or a time-frequency domain threshold. However, what is not clearly distinguishable is their energy level, ie the level of

signal and noise energy. Because the time spectrum is obtained by analysis of traditional time-frequency analysis methods, it is generally smooth, not focused.By suppressing random noise at the time-domain spectral threshold, it is impossible to guarantee that the effective seismic signal is not damaged. Under the above conditions, the advantages of the rearranged spectrum time-frequency analysis method are outstanding. In this way, in the domain after the rearrangement spectrum, the seismic data energy is focused to a higher degree, and at the same time, the energy of the random noise can be more dispersed, so that the signal level can be clearly distinguished and The level of noise. Therefore, random noise can be suppressed by using the method of rearranging the spectral domain threshold[6,7].

A fast iterative soft threshold algorithm, the FISTA algorithm[6]. In the FISTA algorithm, increasing the convergence speed is achieved by transforming m_k in the formula. It is necessary to declare a variable y_k,and define the following relationship with m_k and m_{k-1},

$$y_k = m_k + (\frac{\beta_{k-1}}{\beta_{k+1}})m_k - m_{k-1} \qquad (3.1)$$

In the formula, a parameter β_k is defined, and β_k changes with the number of iterations, which is determined by the following formula:

$$\beta_{k+1} = \frac{1+\sqrt{1+4\beta_k^2}}{2} \qquad (3.2)$$

In order to calculate the updated expression of the FISTA model, you can use m_k in the y_k substitution formula to calculate m_{k+1}, as follows:

$$m_{k+1} = soft(y_k + \frac{1}{\alpha}D^H b - Dy_k, \frac{\lambda}{2\alpha}) \qquad (3.3)$$

The implementation steps of FISTA can be summarized:

(1) First assigned to the initial value:$y_1=m_0$;

(2) Then perform the k step calculation to complete the iteration;

(3) Then calculate m_k according to the above formula;

(4) Using formula $\beta_{k+1} = \frac{1+\sqrt{1+4\beta_k^2}}{2}$ count the number of iterations;

(5) Final calculation

$$y_k = m_k + (\frac{\beta_{k-1}}{\beta_{k+1}})m_k - m_{k-1}$$

In summary, the fast iterative soft threshold algorithm compares the ISTA algorithm with its incomparable advantages. Not only can the convergence speed be improved, but also it can be implemented as easily as the iterative soft threshold algorithm. It seems that it is more suitable for processing complex numbers, so this algorithm works better when spectral decomposition[7].

V.Experimental Results and Analysis

The Matlab GUI is used to make time-frequency analysis software for seismic data. Because the development method of Matlab GUI is simple and easy to understand, it is object-oriented like other interface writing platforms. It needs to set the properties and callback functions of each object. The interface design can be implemented through the underlying code or by programming in the “guide”. The steps to write the primary interface are also very simple. Take the “guide” writing method as an example: first enter “guide” in the command window, select the new blank GUI in the interface that appears; the layout window appears, and the left side of the window is the commonly used control. List, the right side is the layout area;Select Edit Text, Static Text, Axes, Push Button and other controls, drag and drop them to the layout area for layout; double-click each control to change its properties[7]; the most critical step is to set the control's callback function, especially Push Button's callback function, right click on the button, select View Callbacks, you can program the callback function of each button. By following the above steps, you can draw a simple GUI interface, as shown in Figure 4.1.

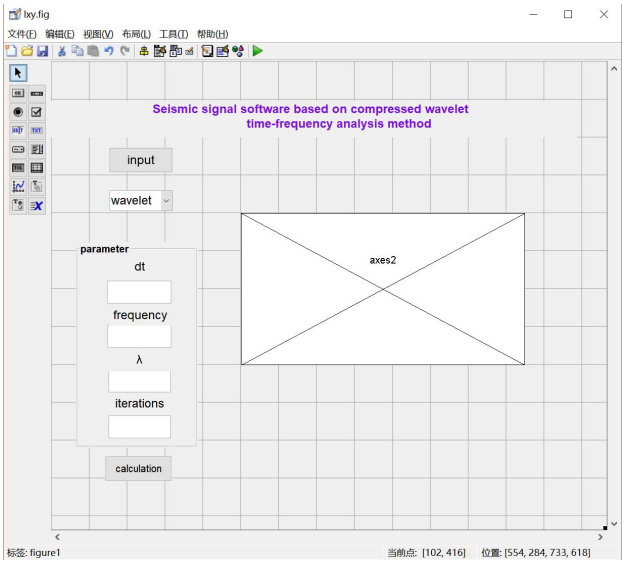

Fig4.1 Matlab GUI development of interface

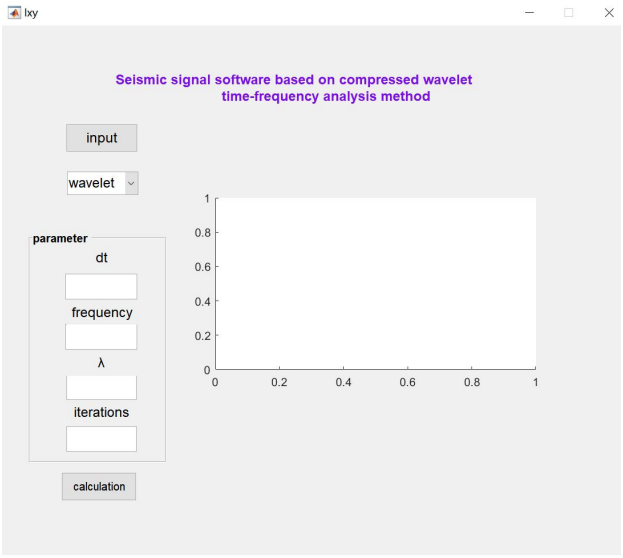

Fig4.2 Initialization Interface for Time-Frequency Analysis

The time-frequency analysis interface is initialized as shown in Figure 4.2. Click the "Input" button and select the "data.mat" seismic data file to be analyzed in the window that appears. After loading the data, load the seismic signal to be analyzed in the main interface. The test run results are shown in Figure 4.3.

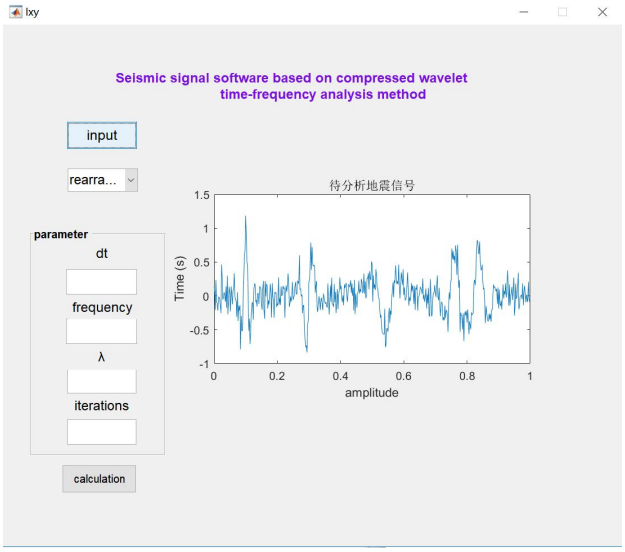

Fig4.3 Seismic signals to be analyzed

After inputting the parameters according to Figure 4.4, click the "Calculate" button to get the results of the rearrangement spectrum analysis as shown in Figure 4.5. The results obtained by wavelet analysis are shown in Figure 4.6.

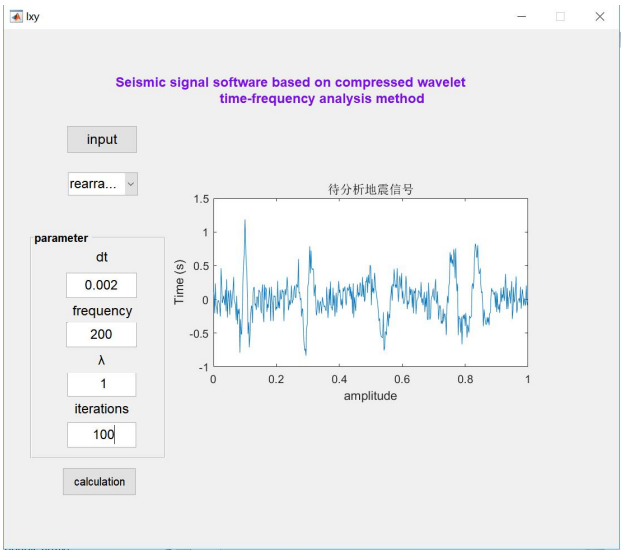

Fig4.4 Parameter setting

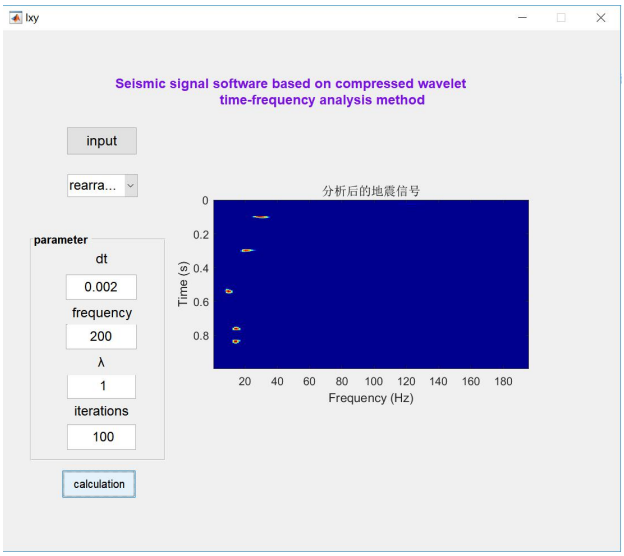

Fig4.5 Time-frequency analysis results of rearrangement spectrum

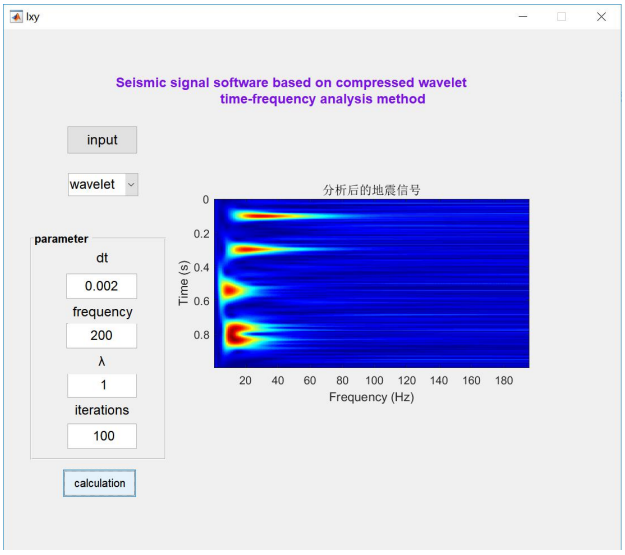

Fig4.6 Time-Frequency Analysis of Wavelet Transform

By comparing the spectrum obtained by the rearrangement spectrum and wavelet transform analysis in Figure 4.5 and Figure 4.6, it can be seen that the spectrum obtained by the rearrangement spectrum

analysis has high degree of focus and can clearly distinguish between signal and noise. It can be seen that the effect of the rearrangement spectrum analysis method is obviously better than the wavelet time-frequency analysis method.

VI.CONCLUSION

In this paper, by reviewing relevant domestic and foreign literatures, the time-frequency analysis of spectral re-arrangement and wavelet transform is performed on complex seismic data. The time-frequency analysis software is developed by Matlab GUI, which makes the analysis of seismic data more convenient and can be applied to various kinds. Different seismic data, by comparing the time-frequency analysis results of spectral rearrangement and wavelet transform, it can be seen that the results of spectral rearrangement analysis are clearer and more convenient for the next stage of data denoising, but there are certain deficiencies. The accuracy of time-frequency analysis can be further strengthened, and the expected target can be achieved, and a convenient time-frequency analysis and denoising software for seismic data can be made.

REFERENCES

[1] Daubechies I, Lu J, Wu H T. Synchrosqueezed wavelet transforms: an empirical mode decomposition - like tool[J]. Applied and Computational Harmonic Analysis, 2011, 30(2):243-261.

[2] Shang S, Han L G, Hu W. Seismic data analysis using synchrosqueezing wavelet transform [J]. Expanded Abstracts of 83rd Annual Internat SEG Mtg, 2013, 4330-4334.

[3] Herrera R H, Han J J, van der Baan M. Application of the synchrosqueezing transform in seismic time-frequency analysis [J]. Geophysics, 2014, 79(3):V55-V64.

[4] Shang Shuai, Han Liguo, Hu Wei. Application research on seismic spectrum decomposition method of compressed wavelet transform[J]. Petroleum geophysical exploration, 2015,54(1):51-55.

[5] Han Li.Research on high resolution full spectrum decomposition method[D]. Jilin University, 2013.

[6] Boashash B,Mesbah M. Signal enhancement by time-frequency peak Filtering[J]. IEEE Trans. Signal Processing,2004,52(4):

[7] Xia Hongrui, Zhu Yong, Zhou Kaiming. Wavelet Transform and Its Application in Denoising[J]. Petroleum geophysical exploration,1994(03):274-285+398.

Fault Stress Monitoring Anchor Stress Meter

Lv Peitong, Hou Yuqing, Yang Yunrui
（jilin university instrument science and electrical engineering institute, changchun,130021）

***Abstract*—This paper presents an anchor stress meter for stress monitoring. Stress monitoring is an important indicator for studying fault activity. The anchor stress meter proposed in this paper is equipped with five FBGs, including four strain FBGs and one temperature compensation FBG. Four strain FBGs are fixed on the same section of the anchor to monitor stress changes and determine the direction of force. The experimental results show that the anchor stress gauge designed in this paper has a variable range of -2500 με~2500 με. The anchor can judge the force in the horizontal and vertical directions. The force received by the anchor has a good linear relationship with the grating wavelength. It reached 0.998, and the fault sliding distance and the wavelength of the anchor grating also changed linearly, and the linearity was 0.97.**

***Keywords*— Fault Stress monitoring FBG Anchor**

I.INTRODUCTION

FULLY aware of the fault stress field is essential for hazard assessment of crustal motion[1]. It is because of the stress is the main driving force of the geological movement. For geological tectonic movement monitoring, by monitoring the crustal movement and the stress accumulation and release of the new fault zone, the risk of the fault zone can be assessed in time[2].

Despite the strong indication of the fault stress-strain monitoring and its importance on seismic surveillance, few studies of this issue have carried on. Currently stress-strain monitoring is mainly measured by resistance strain gauges and stress gauges. Although these conventional electromagnetic sensors have been widely used, their disadvantages are also obvious, such as difficulty in long-term stable operation in underground complex environments, and are susceptible to electromagnetic interference. Moreover, due to the influence of on-site construction conditions, the survival rate of the instrument is generally low, and it is difficult to remotely monitor and entirely survey the monitoring object, which can't fully meet the needs of stress monitoring.

With the rapid development of the fiber Bragg grating (FBG) sensing technology in recent years,FBG sensors have been widely used for sensing and monitoring in geological exploration, aerospace, railway construction and other industries[3-6]. Compared with traditional electrical sensors, FBG sensors have the advantages of immunity to electromagnetic interference, low loss, small size, light weight, possibility of remote sensing, low energy consumption, wide bandwidth, good corrosion resistance, and high sensitivity[3-12].

In order to alleviate the problem of lack of monitoring methods for stress changes at the fault plane, In this paper, we have proposed a small-sized anchor stress gauge for stress monitoring. The anchor strain gauge is equipped with four strain FBGs and a temperature compensated FBG. The grating is fixed in four grooves 90° of each other on the surface of the anchor, wherein the four strain FBGs are fixed on the same section of the anchor. The anchor stress gauge designed in this paper has a variable range of -2500~2500 microstrain. The anchor can judge the force in the horizontal and vertical directions. The linear force of the bolt and the grating wavelength has a linear relationship of 0.998. The fault sliding distance and the wavelength of the anchor grating also vary linearly with a linearity of 0.97.

II.EXPERIMENTAL SECTION

A.Sensor Constructive Description

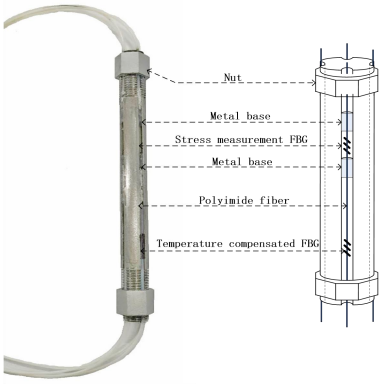

a b

Figure 1. (a) Photography of the prototype with one sensing element; (b) Scheme of the FBG sensing element.

Four axial sections are formed into 90° grooves on

the surface of 8mm diameter 11cm long thin anchor rod. A fiber grating is placed in the groove, and the grating is fixed on a special metal base. In order to enable the fiber grating to measure both the change in the tension of the fiber and the stress change in the shrinkage of the fiber, a certain amount of pre-stress is applied to the fiber when the grating is fixed using a metal base, which gives the grating a proper offset of the wavelength, and the grating can retain this change after the fixing. From Figure 1, we can see that there are 5 gratings on the sensor, FBG1, FBG2, FBG3, FBG4 are used to measure strain, and FBG5 is used for temperature compensation. FBG1, FBG2, FBG3, FBG4 are fixed on the same section of the anchor. The strain-measured grating is fixed by two metal pedestals and retains the pre-stress, while the temperature-compensated grating is unconstrained. The nut on both sides of the sensor has two functions: 1.When the sensor is not in use, loosen the nut to protect the grating for easy storage and transportation; 2. When the sensor is used, an additional pre-stress is applied to the anchor by tightening the nuts on both sides of the bolt to provide a sensitization and anchoring effect.

B.Experiment

The calibration of the experiment was done on the platform of simulated surface fault, named triaxial testing machine. As shown in Fig.2, two aluminum blocks with a 15 degree of Angle were used to simulate the fault in order to imitate the movement of fault and monitor the stress of fault. Three columns and two rows of through-holes，8.5 mm in diameter and 25 mm pitch， are designed in the aluminum block for the anchor stress gauge. The anchor rod is installed in the experimental block so that the grating has a pair in the horizontal direction and the vertical direction, and 1-6 anchor rods can be installed as needed. Tighten the fixing parts on both sides to anchor the anchor. The two aluminum blocks will slide along the diagonal section under external forces.

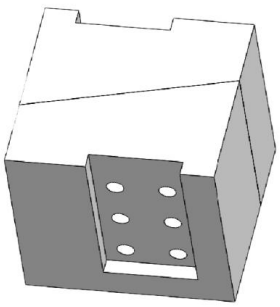

Fig.2. Aluminum block model simulating faults

Twelve strain gauges are placed at corresponding positions on the surface of the aluminum block to monitor the change of surface strain, as shown in Fig.3.a, used for data comparison and analysis. The strain gauge has two columns of 6 in each column, including two groups of axial measuring strain gauge and two groups of strain rosette. The strain rosette contains three strain gauges, which are horizontally, perpendicularly and at an angle of 45° to the anchor respectively, for monitoring the strain in different directions. The platform is equipped with hydraulic propulsion devices in the front, rear and left and right directions. Each propulsion device is equipped with a pressure sensor and a displacement sensor for real-time monitoring of the fault loading force and fault sliding displacement.

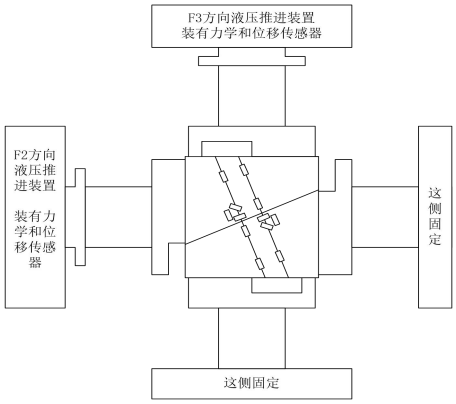

a

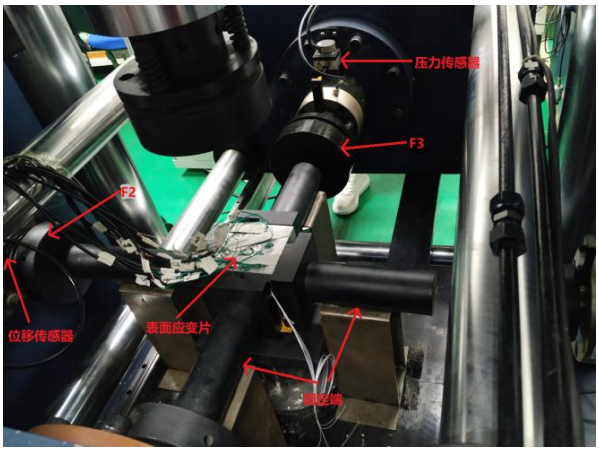

b

Fig.3. Strain gauge position and test machine structure

Before the experiment, place the test block with the anchor on the test bench. Push the test bench into the experimental position and lock the bottom of the test bench to prevent sliding during the experiment, affecting the experimental results. Connect the strain gauge and the anchor stress pre-test equipment. Contact and lock the front and right sides of the test block to the test bench then start the equipment. Then the computer controls the hydraulic propulsion device in the direction of F2 and F3, and advances to the steel block in the direction of F2 and F3 with the placed

experimental block. Next, the force is gradually increased from 0 to 10KN in the left and rear of the experimental block, which is used to constrain the experimental block, and the data is recorded at the moment.

In the F2 direction, the hydraulic device maintains a force of 10KN, and the hydraulic device in the F3 direction gradually increases to 50KN. The test block will slip due to the difference in force between F2 and F3. Record the data of fiber grating wavelength and strain gauge micro-strain during this process, record 5 times per second, named strain 1, fiber 1, fiber 2, fiber 3 and fiber 4 respectively.

Keep the stability for a while, then the hydraulic device in the F3 direction continues to maintain the force of 50KN, and the hydraulic device in the F2 direction gradually applies displacement until 1 mm, simulating the fault movement.

Record the data of fiber grating wavelength and strain gauge micro-strain during this process as well, record 5 times per second, named strain 2, fiber 5, fiber 6, fiber 7 and fiber 8 respectively. Fig.3.b shows actual situation at the time of the experiment.

III. Data analysis

A.Comparison of 10-50KN applied force part

Fig.4 compares the strain data of anchor grating and the strain data of strain gauge. Data shown in Fig.5 includes the strain gauge and fiber strain data corresponding to the force in the F3 direction from 10KN to 50KN. The part of the figure where the data remains unchanged is to maintain the steady state for a period of time during the experiment, in order to facilitate the recording of data. As can be seen from the figure, the micro strain of the strain gauge changes from 0 to 250. At the same time, the micro-strain of the four gratings changed from 0 to 600, 700, 800 and 1000, respectively.

Fig.4 shows that in the process of applying pressure, the strain data of the fiber and the strain data of the strain gauge change in the same trend, and the amplitude is larger. It can be inferred that the FBG sensor can reflect the change of the force of the fault layer and the performance is better than the traditional strain gauge.

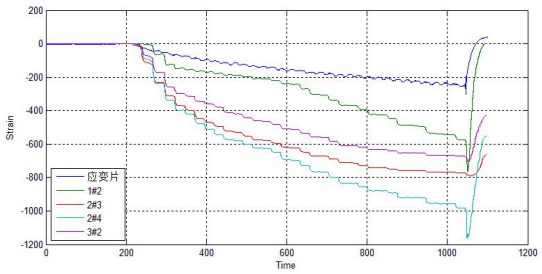

Fig.4. Strain versus force change diagram

B.Comparison of applied displacement parts

Fig.5 compares the strain data of anchor grating and the strain data of strain gauge. Data shown in Fig.6 includes the strain gauge and fiber strain data corresponding to the displacement in the F2 direction from 0 to 1mm. The part of the figure where the data remains unchanged is to maintain the steady state for a period of time during the experiment, in order to facilitate the recording of data as well. As can be seen from the figure, the micro strain of the strain gauge changes from 0 to 300. At the same time, the micro-strain of the three gratings changed from 0 to 700, 1000 and 1050, respectively.

Fig.5 shows that in the process of applying displacement, the strain data of the fiber and the strain data of the strain gauge change in the same trend, and the amplitude is larger. It can be considered that the fiber Bragg grating sensor can well reflect the change of the force of the fault plane when simulating the fault movement and the performance is better than the traditional strain gauge.

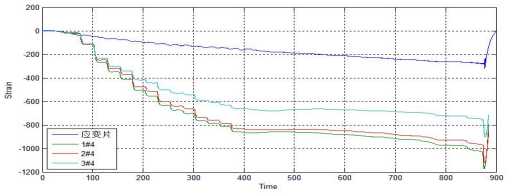

Fig.5. Strain versus displacement change diagram

IV.Conclusion

In this paper, a small anchor stress gauge for fault stress measurement is proposed, and the experiment is completed on a triaxial test machine. The stress gauge can monitor the fault stress change in real time and judge the direction of the force of the rod. Experiments show that the force received by the anchor in the fault is linear with the change of the grating wavelength, and the linearity reaches 0.998. The sliding distance of the fault and the wavelength of the grating are also linear, and the linearity is 0.97.

References

[1] David,P.;Sri,W;Masyhur,I. Stress heterogeneity and its impact on seismicity pattern along the equatorial bifurcation zone of the Great Sumatran Fault, Indonesia[J]. Journal of Asian Earth Sciences,2018,164.

[2] ZHANG Chongyuan,WU Manlu,CHEN Qunce,LIAO Chunting.Piezomagnetic In—situ Stress Monitoring and its Application in the Longmenshan Fault Zone.ACTA GEOLOGICA SINICA(English Edition)Vo1．88 No．5 PP．1592—1602

[3] YulongLi,ChangjinWen,YujieSun,YanFeng,HuaZhang.Capillary encapsulatingof fiber Bragggratingandtheassociated sensing model.Optics Communications333(2014)92–98.

[4] Wen-Ping Chen, Fu-Hung Shih, Po-Jun Tseng, Chih-Hsien Shao, and Chia-Chin Chiang.Application of a Packaged Fiber Bragg Grating Sensor to Outdoor Optical Fiber Cabinets for Environmental Monitoring.IEEE SENSORS JOURNAL, VOL. 15, NO. 2, FEBRUARY 2015

[5] Changyu Shen, Chuan Zhong .Novel temperature-insensitive fiber Bragg grating sensor for displacement measurement.Sensors and Actuators A 170 (2011) 51– 54

[6] Ji-an Chen, Di Huang,* Hai-tao Zhao, Quan-bao Wang, Ye Qiu, and Deng-ping Duan.Fiber Bragg grating-based plane strain monitoring of aerostat envelope structures.APPLIED OPTICS,Vol. 52, No. 19,July 2013

[7] Rajini Kumar Ramalingam, Rainer Nast, and Holger Neumann.Fiber Bragg Grating Sensors for Distributed Torsional Strain Measurements in a (RE) BCO Tape.IEEE SENSORS JOURNAL, VOL. 15, NO. 4, APRIL 2015

[8] Parne Saidi Reddy;R. L. N. Sai Prasad;Dipankar Sengupta;Putha Kishore;M. Sai Shankar;K. S. Narayana;U. K. Tiwari.Method for Enhancing and Controlling Temperature Sensitivity of Fiber Bragg Grating Sensor Based on Two Bimetallic Strips.IEEE Photonics Journal,Vol 4,No 5,June 2012

[9] Yutang Dai, Minghong Yang, Gang Xu, Yinquan Yuan.Magnetic field sensor based on fiber Bragg grating with a spiral microgroove ablated by femtosecond laser.OPTICS EXPRESS,Vol. 21, No. 14,July 2013

[10] N. Basumallick, I. Chatterjee, P. Biswas, K. Dasgupta, S. Bandyopadhyay. Fiber Bragg grating accelerometer with enhanced sensitivity. Sensors and Actuators A 173 (2012) 108–115

Family Fall Alarm System for Elderly People Living Alone based on Video Surveillance

Yang Yang, Zhangheng Chen, Shuo Zhang, Jin Zhang, Hong-liang Cui.
（jilin university instrument science and engineering institute,changchun,130021）

***Abstract*—Falling is an important hidden danger threatening the safety of the elderly living alone. In view of the increasing number of elderly living alone and the problem that falling at home can not be treated in time, this paper designs a fall detection and alarm system for the elderly living alone based on video surveillance, which uses the speed of falling head to judge whether the fall occurs. Firstly, the system uses face detection based on skin color features and particle filter tracking algorithm based on multi-feature Camshift optimization to locate the face, then judges whether the elderly falls or not according to the speed of head descent. Finally, the fall information is sent to the elderly's family in time through GSM module, so that the fallen elderly can be treated in time. In order to verify the feasibility and accuracy of the system, experiments are carried out under various complex conditions, such as different scenes, different illumination and different falls. The experimental results show that, overall, the correct rate of fall alarm can reach 75.0%, and the Non-falling action of false alarm rate is as low as 0%.**

***keywords*—Old people living alone; Face detection; Face tracking; Fall detection; GSM module.**

0. INTRODUCTION

IN today's society, with the rapid development of economy, the problem of aging becomes more and more serious. According to the results of the Sixth National Population Census [1], the population over 60 years old in China has approached 178 million, accounting for 13.26% of the total population, and the population over 65 years old has approached 119 million, accounting for 8.87% of the total population. However, due to the implementation of family planning in China for more than 30 years, most families are in the "421" family model, that is, four elderly people, a couple and a child. Many families have children who leave the elderly at home alone because of work and other reasons. However, as the elderly get older and move inconveniently, the possibility of accidents increases. Among them, the fall of the elderly living alone at home has become the number one killer of the elderly. In 2013, 83.5% of the elderly in Shanghai were hospitalized because of falls. In the United States, falling has become the sixth leading cause of death for people over 70. Therefore, it is necessary to study the fall detection of the elderly. It is particularly important to find out in time that the elderly who live alone fall at home and call for help for the elderly.

At present, researchers at home and abroad have done a lot of research on the detection of elderly falls. The research directions are mainly divided into three categories: (1) detection of elderly falls based on wearable equipment [3,4]. Most of these systems use sensors such as triaxial acceleration and gyroscope to collect data of the elderly when they fall, and then analyze them to determine whether the elderly fall or not. However, such wearable devices may have a certain impact on the normal behavior of the elderly, while some elderly people are unwilling to wear such devices. (2) Detecting the falls of the elderly based on sound signals [5,6]. This kind of system can judge whether an old man falls by collecting the volume and frequency of the sound produced when he falls. This kind of system is easy to be disturbed by other external sounds and produce misjudgement, and it is not suitable for the popularization of the system to install sound acquisition equipment in the home. (3) Fall detection system based on video surveillance [7,8]. This kind of system usually collects image information by camera, calculates the aspect ratio of the old people in the image, and considers the old people fall when the aspect ratio exceeds the threshold. This method can not distinguish the normal and fallen movements such as squatting and lying down by using aspect ratio information only. It has some limitations.

Based on the above analysis, this paper proposes a new video surveillance-based home fall detection and alarm system for the elderly living alone, which uses the speed of the head drop of the elderly to judge whether the fall occurs. This system effectively combines face detection based on skin color feature [9,10] and particle filter algorithm based on color and motion feature combination [11,12], which improves the accuracy of face location. At the same time, according to the speed of head descent between adjacent frames, it can effectively judge whether the

elderly fall or not. This system uses the speed of head drop as the method of fall judgment. It can distinguish many kinds of disturbing actions such as squatting and lying down from falling. It can correctly detect whether the elderly fall or not. At the same time, it makes up for the shortcomings of wearable equipment and sound detection equipment.

I. System Design

The system is divided into four modules: monitoring data acquisition, face location, fall detection and fall alarm. The monitoring data acquisition module takes pictures through the camera, and then transmits them to the computer through the data line. This system uses the camera of Haikangwei Video. Its focal length is 4mm and the horizontal field of view angle can reach 86 degrees. It can basically obtain all indoor scenes with a resolution of 1280px * 720px. Facial location module includes two parts: face detection in the initial frame and face tracking in the subsequent frame. Fall detection module uses the descending speed of the head of the elderly to judge whether a fall occurs or not. These two parts will be discussed in detail in the following chapters of this paper. The fall alarm module transmits alarm information to the mobile phones of the elderly and children through the GSM (Global System for Mobile Communications) module to realize the alarm function [13,14]. This module is composed of SIM800c (four-frequency GSM module) and USB (Universal Serial BUS) to TTL (Transistor-Transistor Logic, double transistor logic level). It can work in 850/900/1800/1900MHZ four bands. It can realize voice, DTMF (Dual Tone Multi-Frequency), TTS (Text to Speech, from text to voice), TTS (Text to Speech). Short message and data transmission of GPRS (General Packet Radio Service). The schematic diagram of the system is shown in Figure 1.

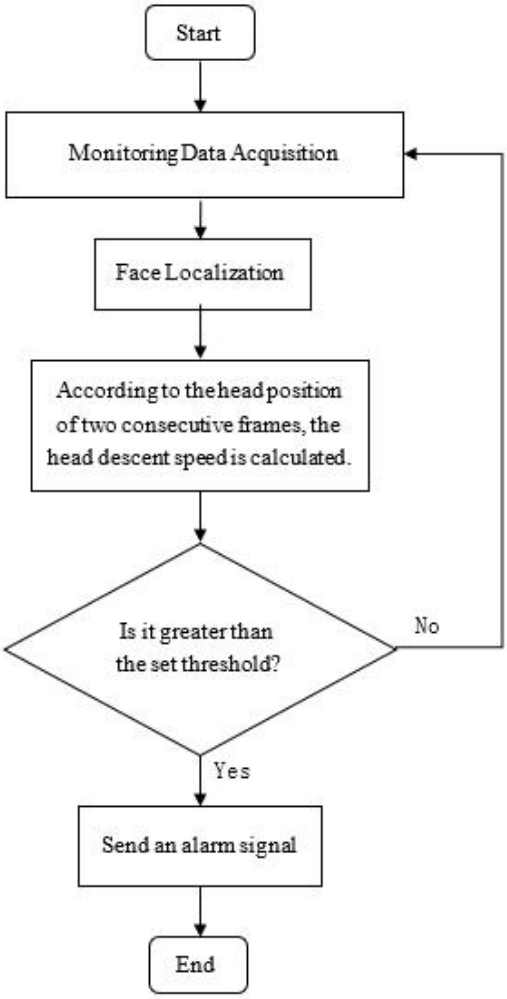

Fig. 1 Schematic diagram of system principle

II. Face Location

For the initial frame, a face detection method based on skin color features is used to locate the initial position of the head of the elderly. The main principle of face detection method based on skin color features is that skin color has better clustering characteristics in YCbCr color space and is mainly affected by brightness information. When the brightness component is used, it can be directly judged as non-skin color pixels. When the brightness component is used, the skin color information is mainly concentrated in and interval. In addition, in order to avoid the influence of other indoor objects with similar skin color on face detection, this paper adds background difference method to face detection based on skin color features. By choosing unmanned scenes as background, background image and current frame image are subtracted to extract human motion region, which avoids the interference of similar skin color objects in the background. At the same time, because of the influence of illumination, high-light areas may appear on human clothes, which may affect the

judgment of human face skin color areas. In this paper, the method of eliminating high-light areas proposed by Chen Yaosheng et al. [15] is adopted. For an image with high light characteristics, we first find the pixels with high light characteristics (Y > 0.8*Ymax, Y is the brightness component of YCbCr color space, Ymax is the maximum value of the brightness component in the image), and then remove these pixels. As shown in Fig. 2, assuming that the pixel P5 has high light characteristics, the pixels whose brightness components belong to the interval of [Ymax*0.7, Ymax*0.8] are found in P5's trusted neighborhoods P1, P2 and P 3 by top-down processing. Then the average value of the brightness components of these pixels is calculated as the credible value of the brightness components of the pixel P5, if P1, P2 and P 3 are three pixels. The brightness component of a point does not belong to the range of [Ymax*0.7, Ymax*0.8]. Then 0.75 of the brightness component of P5 is taken as the confidence value of the brightness information of P5 pixels, so as to achieve the effect of removing high-light region.

P1	P2	P3
P4	P5	P6
P7	P8	P9

Fig. 2 Neighborhood information

After locating the head position of the elderly in the initial frame, the particle filter tracking algorithm based on color and motion features is used to locate the face in the subsequent frame [12]. In terms of color features, this paper uses HSV color space to describe the color, and statistics the H component of the face location. In terms of motion features, background subtraction is used to subtract the current frame from the background frame to obtain the motion region after the subtraction. In addition, CamShift is used to optimize the particle filter, so that each particle in the particle filter moves to its local maximum, and each particle converges as close as possible to the target, which greatly enhances the effectiveness of the particle, makes it possible to achieve stable tracking with fewer particles and reduces the computational cost.

III. Fall Detection

Considering that human beings are non-rigid objects, there are many ways of movement. If the aspect ratio is used to judge whether an old person falls, it will lead to misjudgement of the system. For example, the aspect ratio of an old person's normal lying down is very similar to that of a fall, which is often misjudged as a fall in actual detection. Because the old people usually move slowly, generally there is no large range of movement, the head movement will not be too large. In normal activities, the speed of the old man's head downward will not be too big, relatively stable, far less than the speed of the old man's head downward when he falls. Therefore, it can make up for the deficiency of aspect ratio to judge whether a fall occurs by using the speed of head descent of the elderly.

The system uses face location module to get the position of the old man's face in each frame, and regards the position of the old man's head as the position of the old man's head. Then according to the position of the old man's head in two consecutive frames, the speed of the old man's head descending (the direction of the head descending is the positive direction of the speed) is calculated, and a reasonable speed threshold is set. When the speed of the old man's head desc When the threshold value is set, the old man falls down. On the contrary, the old man is considered to be in normal activity.

This system is a fall detection and alarm system for the elderly family, but because of the special reasons of the elderly body, it is not suitable for the elderly to simulate the fall action to verify the correctness of the system. Therefore, we invite the laboratory students to simulate the various movements of the elderly, such as sitting, squatting, lying down and falling, in order to collect data. Fig. 3 (a), (b), (c) and (d) are the data collected by simulating the activities of the elderly under laboratory conditions.

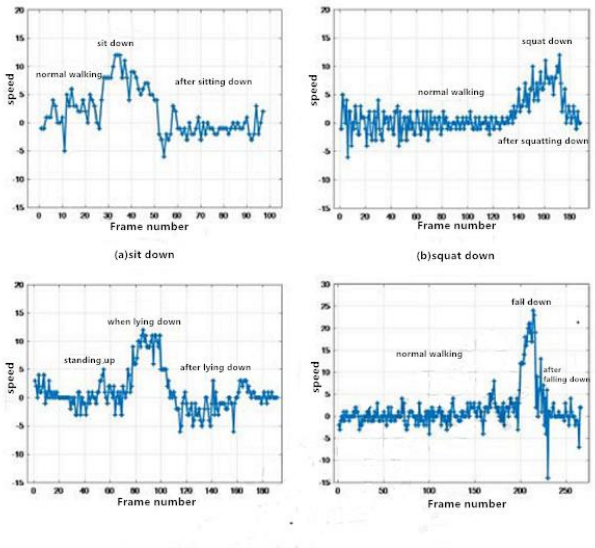

Fig. 3 The speed at which the old man's head falls when different movements occur :(a) sit down,(b) squat down, (c) lie down (d) fall down

From the four curves in Figure 3, it can be seen that

the head dropping speed when falling is obviously different from that of other movements such as sitting, squatting and lying down. Because of the contingency of a single experiment, we repeated 40 experiments for each action, then selected the maximum speed of head descent for each action, and drew it in Figure 4. By comparing the head drop speed of different movements in Figure 4, we can see that there is a big difference between the head drop speed of fall and that of other movements. Therefore, this paper chooses a reasonable median value as the threshold to judge whether the elderly fall or not.

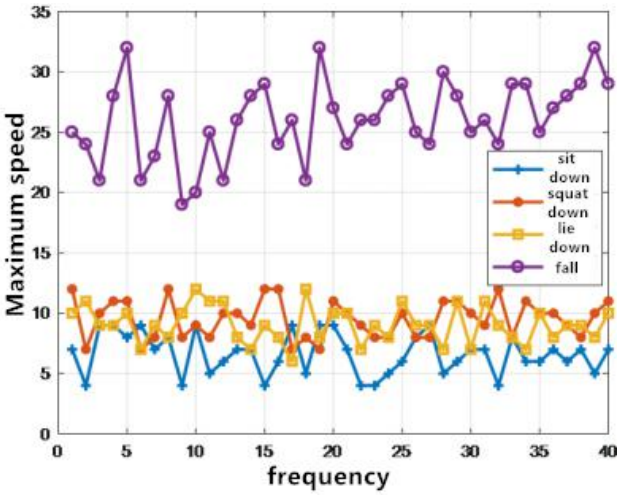

Fig. 4 Comparison of the maximum descending speed of the old man's head in two consecutive frames of different actions

IV. EXPERIMENT

In order to verify the reliability of the system, this paper will illustrate the feasibility and reliability of the system from the following four aspects. Because of the resolution of the camera selected in the experiment, the image shown in the following experiment may be a little unclear after shrinking.

(I) Improvement of Face Detection Accuracy in Initial Frame

The accuracy of face detection in the initial frame is the premise of the system's correct detection of falls. Therefore, this paper carries out the following experiments to verify the selected face detection method. The carton color in Fig. 5 is very close to the skin color of the face. When the background difference method is not used in the face detection process, the system mistakes the carton as a face, and the face detection fails. After using background subtraction, the system can locate face correctly. In Figure 6, high-light areas appear on human clothes, which will interfere with the selection of face areas. By eliminating high-light areas, the wrong selection of face areas can be avoided. Therefore, on the basis of face detection based on skin color features, background subtraction and high-light region elimination methods are added to effectively improve the accuracy of face detection, which provides a guarantee for the follow-up detection of the system.

Fig. 5 Influence of background difference method on face detection:(a) background difference method was not adopted (b) background difference method was adopted

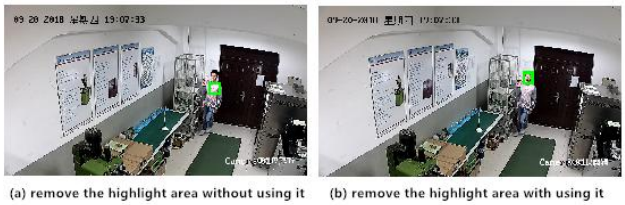

Fig. 6 The influence of whether to use highlight region removal on the correct detection of face:(a) remove the highlight area without using it; (b) remove the highlight area with using it

(II) Effects of Different Scenes on Fall Detection and Alarm

Because the ultimate goal of this system is to be applied in different families, it should be able to track and detect falls correctly in different scenarios. Therefore, this paper chooses several scenarios for experiments to verify the reliability of the system in different scenarios. Fig. 7 (a) and (b) are validated in laboratory and outdoor corridors respectively. As can be seen from Fig.7, when the experimental environment changes, the stability of the system is not affected, and the alarm can still be tracked correctly.

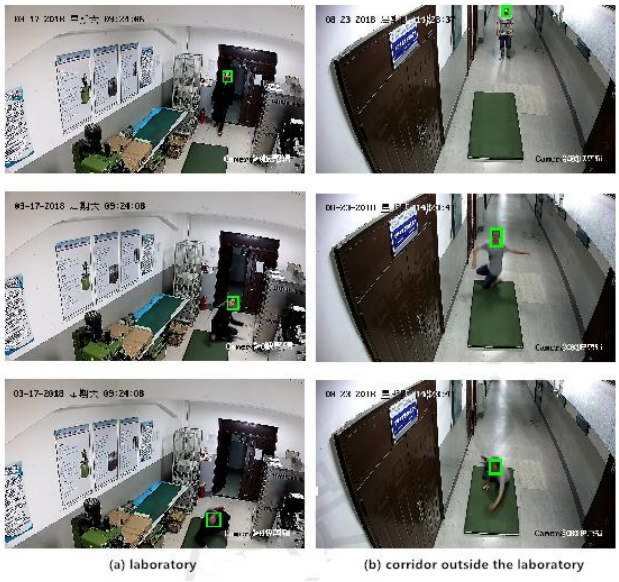

Fig. 7 Correct face tracking under different scenes : (a) laboratory, (b) corridor outside the laboratory

(III) Effect of Different Illumination Conditions on Fall Alarm

When the system is applied in the family, the illumination conditions will change. Therefore, the system should not only be able to alarm correctly under normal illumination conditions, but also have certain anti-interference ability under strong and weak light conditions, so as to promote its use. In strong light simulation, this paper uses desk lamp illumination method. In weak light simulation, this paper forms weak light condition by closing part of the lamp in the laboratory. Fig. 8 (a) and (b) are experimental verification under simulated strong and weak light conditions respectively. From Figure 8, we can see that the system still meets the requirements of tracking and alarming correctly when the illumination changes.

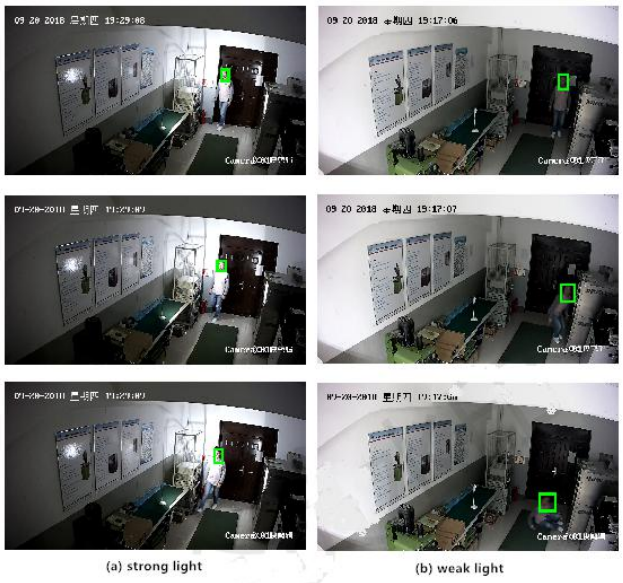

Fig.8 Correct face tracking under different illumination conditions :(a) strong light (b) weak light

(IV) The Effect of Different Persons and Actions on Fall Alarm

When the system is applied to different elderly people and the elderly perform other normal activities without falling, the system should have correct tracking and judgment. Fig. 9 (a) and (b) show the experiments of different people in different actions respectively. The system can still track correctly without causing fall alarm.

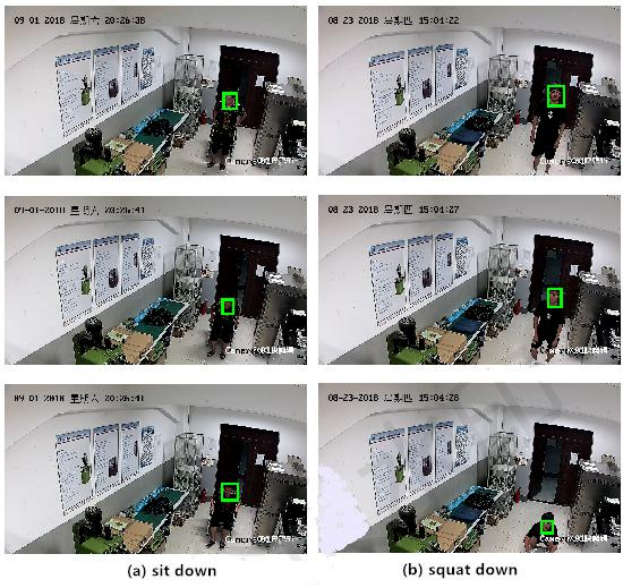

Fig.9 The face tracking of different people in different movements is correct :(a) sit down, (b) squat down

(V) Statistics of experimental data

In this paper, under different illumination conditions, several people were selected to simulate the different movements of the elderly, such as forward fall, backward fall and side fall, as shown in Table 1. From Table 1, it can be seen that under the same illumination conditions and different fall modes, the correct rate of backward fall alarm is the highest, and the correct rate of backward fall detection under normal light conditions can reach 87.5%. This is because in the process of face location, when backward fall, the skin color area of the face is larger, and the color features play a larger role, which is conducive to face location. When side falls and forward falls, the area of facial skin color gradually decreases in the process of falling, which is not conducive to face location, resulting in a decrease in the accuracy of fall alarm. Under the condition of the same fall mode and different illumination conditions, the correct rate of normal light fall alarm is the highest. This is because under normal illumination, the skin color area of human face is easier to be recognized, while under abnormal illumination, especially under weak illumination, the light is weak, the brightness of the camera image is low, and the skin color area may be considered as the non-skin color area by the system, so that the skin color area can be recognized as the non-skin color area. The effect of skin color features is reduced, resulting in a lower accuracy rate of fall alarm, but the minimum can also reach 62.5%. All the experiments show that the correct rate of fall alarm can reach 75.0% on average.

Tab. 1 Fall test under different light conditions

Illumination condition	Fall situation	Number of experiments	Correct identification and alarm times	accuracy rate
Strong light	fall over	40	27	67.5%
	Fall backward	40	32	80.0%
	Fall sideways	40	29	72.5%
Normal light	fall over	40	32	80.0%
	Fall backward	40	35	87.5%
	Fall sideways	40	33	82.5%
Weak light	fall over	40	25	62.5%
	Fall backward	40	30	75.0%
	Fall sideways	40	27	67.5%
Total		360	270	75.0%

In order to verify the impact of other normal activities of the elderly on the correct alarm of the system, this paper selects a large number of people to simulate other non-fall actions, and observes whether the system can separate them from the fall actions without causing false alarm, as shown in Table 2. Table 2 shows that when simulated squatting, sitting and lying down non-fall movements, the system will not give false alarm, and the false alarm rate is as low as 0%. This is due to the fact that the head drops at a much slower rate than the head drops at the time of a fall in the non-fall movements of squatting, sitting and lying down, so there will be no false alarm. This experiment shows that the system has strong anti-jamming ability to non-fall action, verifies the reliability of the system, and also shows that the fall detection scheme designed by the system has strong feasibility.

Tab. 2 Influence of non-fall action on fall alarm

Daily action	Number of experiments	Number of Error Recognition and Recognition	False positive rate
Squat down	50	0	0%
Sit down	50	0	0%
Lie down	50	0	0%

V. EPILOGUE

This paper designs a fall detection and alarm system based on video surveillance for the elderly living alone. The falling speed of the head of the elderly is used to judge whether the fall occurs or not. The system locates the face by face detection based on skin color features and particle filter based on Canshift optimization combined with color and motion features. Then, according to the position of the old man's head in two consecutive frames, it calculates the falling speed of the old man's head, and judges whether the old man falls or not according to the falling speed of the old man's head. Finally, it sends the falling information in time through GSM module. To the family of the elderly, let the fallen elderly get timely treatment. The experimental data show that the system has a higher correct rate of fall alarm and strong anti-jamming ability for non-fall action. Therefore, the system has good reliability and is suitable for the detection and alarm of falls in families of the elderly living alone.

References

[1] International Statistical Bureau of the People's Republic of China. Main Data Bulletin of the Sixth National Population Census 2010 (No. 1) [R]. Beijing: Chinese Journal of Family Planning,2011, 19(8):511-512.

[2] Runge M. Diagnosis of the risk of accidental falls in the elderly [J]. The Umsch,2002, 59:351-381.

[3] AK Bourke , PVD Ven , M Gamble , R O'Connor , K Murphy . Evaluation of waist-mounted tri-axial accelerometer based fall-detection algorithms during

scripted and continuous unscripted activities [J]. Journal of Biomechanics, 2010, 43 (15) :3051.

[4] YS Delahoz , MA Labrador. Survey on fall detection and fall prevention using wearable and external sensors [J]. Sensors, 2014, 14 (10) :19806.

[5] Y Li , KC Ho , M Popescu. A Microphone Array System for Automatic Fall Detection [J]. IEEE Transactions on Biomedical Engineering, 2012, 59 (5) :1291-1301.

[6] Y Zigel, D Litvak , I Gannot. A Method for Automatic Fall Detection of Elderly People Using Floor Vibrations and Sound—Proof of Concept on Human Mimicking Doll Falls [J]. IEEE Transactions on Biomedical Engineering, 2010, 2010 (10) :2242-2245.

[7] B Mirmahboub , S Samavi , N Karimi , S Shirani. Automatic monocular system for human fall detection based on variations in silhouette area [J]. IEEE Transactions on Biomedical Engineering, 2013, 60 (2) :427-436

[8] M Yu , SM Naqvi , A Rhuma , J Chambers. One Class Boundary Method Classifiers for Application in a Video-Based Fall Detection System [J]. Iet Computer Vision, 2012, 6 (2) :90-100.

[9] Y Ban , SK Kim , S Kim , KA Toh , S Lee. Face detection based on skin color likelihood [J]. Pattern Recognition, 2014, 47 (4) :1573-1585.

[10] A Amjad , A Griffiths , MN Patwary. Multiple face detection algorithm using color skin modeling [J]. Iet Image Processing, 2012, 6 :1093-1101.

[11] C Li , Q Wei , Z Xiong. Color spatial feature-based approach for multiple-vehicle tracking [J]. Applied Optics, 2010, 49 (31) :6043-6056.

[12] Hongguang Sun, Jin Zhang, Yantao Liu, qian Bu, Yannan Xie. Particle filter tracking based on multi-feature CamShift optimization [J].Photoelectric Engineering,2010,37(02):16-31

[13] CY Yu , SC Lu ,YH Chen , LC Cho , CHE Sun. A SAW-Less GSM/GPRS/EDGE Receiver Embedded in 65-nm SoC [J]. IEEE Journal of Solid-State Circuits, 2011, 46 (12) :3047-3060

[14] A Mirzaei , H Darabi , A Yazdi , Z Zhou , E Chang . A 65 nm CMOS Quad-Band SAW-Less Receiver SoC for GSM/GPRS/EDGE [J]. IEEE Journal of Solid-State Circuits, 2011, 46 (4) :950-964

[15] Yaosheng Chen,Zhengkai Liu. Automatic Detection and Correction of Highlighted Face Areas in Color Images [J].Journal of Software,2003(11):1900-1906

Research on short-range radio tracking and navigation technology

Liu Xinran, Xue Yanan, Zhao Wanting
（jilin university instrument science and engineering institute,changchun,130012）

***Abstract*—In modern life, GPS positioning is widely used, but in some spaces with more obstacles or more closed space, GPS positioning error is very large or even impossible to locate, and electromagnetic wave stability is high, even if the signal is weak, GPS is difficult to cover. More precise positioning can be achieved in the region. Therefore, in this study, dwm1000 is used as the radio transmitting base station and mobile carrier. The carrier module obtains the RSSI value of the base station and transmits it to the 32 single-chip microcomputer. The 32 single-chip microcomputer calculates the distance between the carrier module and the base station to locate the carrier. The location of the module and the coordinates of the mobile carrier and the location relative to the base station are displayed in the mobile phone interface.**

***Keywords*— radio navigation location display RSSI algorithm research**

I. INTRODUCTION

SINCE the advent of the GPS global positioning system, the demand for positioning and navigation services has increased, and the development of "wireless cities" has led to various indoor environments, such as airport halls, warehouses, supermarkets, libraries, large shopping malls and underground. Locations such as parking lots are becoming more and more demanding. However, GPS positioning terminals need to receive satellite signals in relatively open places to implement positioning. When GPS terminals are in high-rise buildings or complex indoor environments, due to wireless signals. It is disturbed by environmental noise, which causes the received signal strength to be attenuated, which makes the positioning accuracy low or not enough to complete the positioning. In contrast, the electromagnetic wave has high stability, and even in the region where the signal is weak and the GPS is difficult to cover, it can achieve more accurate positioning. Therefore, the use of radio for positioning has become a hot trend in the development of positioning technology.

In 2009, Han Gang of Harbin Institute of Technology conducted a study on the response time of indoor positioning technology based on radio and ultrasound [1]. The research and design of a typical system for wireless sensor network indoor positioning technology based on radio and ultrasound - Cricket An improvement in the response time of the system. The improved positioning method has an accuracy of about 10 cm, which reduces the system response time and increases the system response stability. The use of UMB as the positioning medium mentioned in the study provides a theoretical basis for our UMB-based positioning method. However, this improvement scheme also has its limitations. For example, adding a central control node increases the cost, and at the same time, it also damages the stability and scalability of the overall system to some extent.

In 2011, Yao Jinjie of North University of China conducted research on the design of target location systems including radio beacons, terrestrial base stations, long-distance data forwarding and central processing platforms [2], and from signal propagation, base station measurements, positioning parameter estimation and positioning. The system error source analysis is carried out in the aspects of algorithm, etc. It is pointed out that the base station layout, time difference measurement and positioning algorithm are important factors affecting the positioning accuracy. The new positioning algorithm proposed in the research has higher positioning accuracy; compared with various improved particle swarm optimization algorithms, it has a faster convergence speed. Moreover, the practical method of base station distribution proposed in the study has played a guiding role in the distribution of base stations determined in our research, so our base station distribution is in the form of 2*3.The innovation of this research is that it can realize the high precision positioning by using the radio module, the positioning accuracy is about 10cm, and the positioning information can be transmitted to the upper computer, and the position of the mobile carrier can be displayed in the upper computer.

II. POSITIONING SYSTEM DESIGN

In the scheme, the data acquisition of the RSSI algorithm, the execution of the positioning algorithm, and the display of the positioning result are all

performed by the client. The client requires a certain level of data processing and can load the positioning software. The design and implementation of the client-based positioning algorithm is relatively easy, and the algorithm complexity is relatively low. In particular, the popularity of mobile phones and PDAs on the Android platform now makes software development easier.

At present, the Android device-based terminal device can easily obtain the RSSI from the UWB positioning module [3], and can develop an Android positioning application software based on this. However, the terminal machines produced by different manufacturers have different quantization standards for RSSI measurements. Different UWBs have different A values due to transmit power and antenna gain. It is necessary to do some testing work on the operating parameters of different wireless positioning modules in advance.

In this positioning system, the terminal machine must acquire a map of the positioning area in advance, and simultaneously acquire information such as the position coordinates of the beacon node within the range of the positioning area. When performing the positioning algorithm, the terminal receives information from the beacon node within the communication range, and automatically selects the reference node and acquires the RSSI for positioning calculation. The positioning diagram and the location area map are shown in Figure 1; the map simulation diagram is shown in Figure 2.

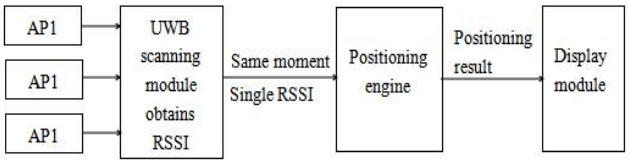

Fig.1 Client positioning diagram

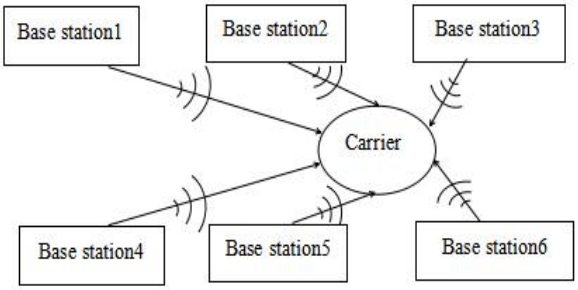

Fig.2 Specified map simulation

III. Hardware Design

a. Radio Module

The DWM1000 is a DW1000 chip developed on the basis of DecaWave. It is an ultra-wideband wireless transceiver chip that is compatible with the IEEE802.15.4-2011 protocol. It is used for positioning objects in real-time positioning systems with an accuracy of up to 10 cm and a data transfer rate of up to 6.8 Mb/s. The communication distance is about 300 meters, which has stronger anti-interference ability for multipath weakening and reliable and effective communication in high attenuation environment. Moreover, its physical size is very small, it is very convenient to integrate into Real Time Location System (RTLS) and Wireless Sensor Network (WSN). The DWM100O pin diagram is shown in Figure 3.

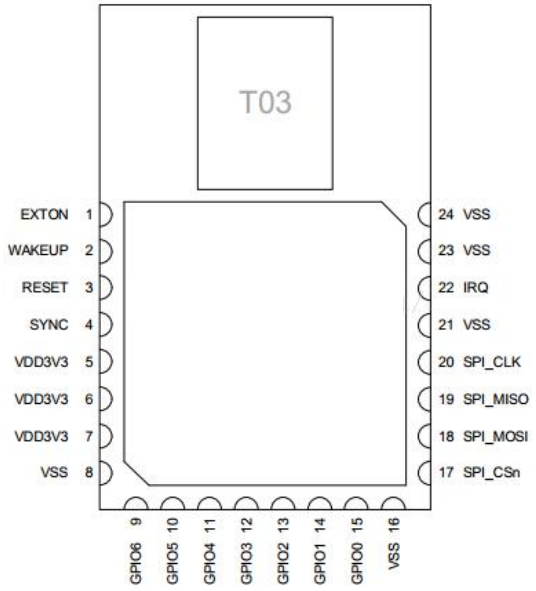

Fig.3 DWM1000 model block diagram

The DWM1000 ultra-wideband ranging uses the TOF (time of fly) method, which is to calculate the wireless electromagnetic wave transmission time, which is converted into distance by the transmission time. By using the DWM1000 as a base station and a mobile carrier, it is possible to achieve a wide range of positioning and to ensure high accuracy.

b. Information Processing Module

STM32 microcontroller [4], compared with the traditional 51, has greatly improved in terms of speed, function and resources. STM32 MCU interconnect series In terms of architecture, in addition to the newly expanded functions can enhance the peripheral interface, it also provides the same standard interface as other STM32 microcontrollers. This peripheral hardware device sharing enhances the application of the entire product line. Flexibility allows developers to reuse the same software across multiple designs, reducing the cost of developing software and increasing chip flexibility. In this design, the 32-chip microcomputer is used for the firing of the program and the processing of the position information, so that the

specific position of the carrier module can be calculated and further input into the upper computer interface, thereby realizing the visualization of the positioning. In this study, the STM32F103C8T6 model MCU will be used.

c. Algorithm Design

RSSI positioning algorithm [5-9]: RSSI is the received signal strength indication, optional part of the wireless transmission layer, used to determine the link quality, and whether to increase the broadcast transmission strength. It varies with the distance of the communication, usually the farther the distance between the nodes, the lower the RSSI value. In general, using RSSI to estimate the distance between several nodes requires the use of methods that know the transmit power of these transmit nodes and measure the received power at the receiving node. From this, the loss of the radio wave propagation is calculated, and finally the propagation loss calculation is converted into the distance in the theoretical radio propagation model.Commonly used radio propagation models are:

$$P_{r,dB}(d) = P_{r,dB}(d_0) - \eta 10\lg\left(\frac{d}{d_0}\right) + X_{\delta,dB}$$

Where Pr,dB(d) is the received power of the signal at d0 reference points; η is the path attenuation coefficient; $X_{\delta,\ dB}$ is a normal distribution with a variance of σ2, in order to explain the influence of the obstacle. In theory, if the environmental conditions are known, the path attenuation coefficient is constant, and the received signal strength can be applied to the distance estimation. However, the inconsistent attenuation relationship affects the quality of the distance estimation, so the RSSI positioning algorithm sometimes has a large error, so In some specific environments, the error caused by RSSI can be properly compensated, so that the RSSI-based ranging technology can achieve better accuracy.

IV.System Software Design

This paper mainly introduces the implementation of UWB-based positioning system. The UWB-based positioning system mainly has the following workflow:

(a) The user side turns on the Bluetooth function, and the user requests the location service information from the server through the client software. The server verifies the user terminal, and the verification passes, and the server starts the communication module to monitor.

(b) The positioning module in the UWB receives the signal of the terminal, and executes the positioning algorithm through the positioning engine to calculate the coordinate position of the terminal.

(c) The positioning server feeds back the positioning result to the end user.

(d) The terminal user transmits information through the Bluetooth module, and displays coordinate information and relative position on the software client.

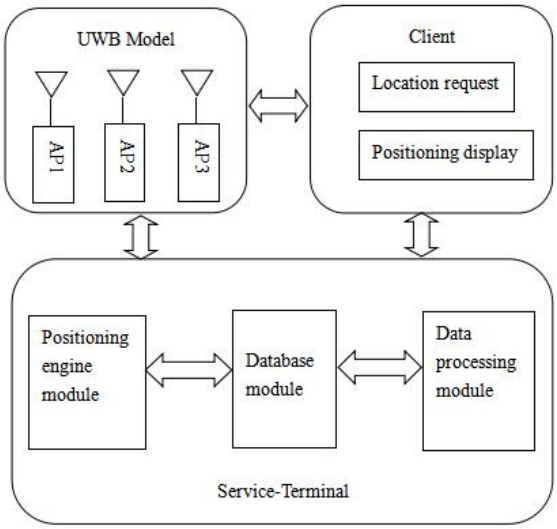

Fig.4 Positioning system module

As shown in the positioning system module diagram shown in Figure 4, the software design structure of the system adopts the typical C/S structure [10], which is divided into two parts: client and server. The client and the server communicate through the Bluetooth module, and the server reads the positioning data sent by the UWB positioning module through the module, and stores the positioning information in a database in a table structure. The original data is processed by the data processing module in advance, and then the processed result is stored in the database as a table structure, and the positioning engine module calls the execution positioning algorithm. The positioning result is stored in the form of a log, and the positioning display module requests the log information to display the position and motion trace of the terminal to be located.

V. Function Test

The whole process from requirements analysis to client development is actually a continuous analysis and testing process. The main test done in this test is to test the client interface and function (logical aspects). Due to the special nature of Android development, we used the Android virtual machine, and the physical

machine used the existing member's mobile phone model such as vivo to test. As for the test system version, we used the version of Android 5.0 in the virtual machine. In the real machine test, due to the condition, we only tested the positioning test environment on the real machine for the system above 4.2, when entering the designated area. The position information of the carrier can be seen later.

(a) UWB positioning information push

In the UWB algorithm positioning detection, when the carrier developed by the STM32 microcontroller enters the positioning area, the developed software can receive the information of the location of the carrier in time.

(b) UI design

For the UI test, we designed the software and software interface in a simple and reasonable way according to the usual usage habits, mainly in the following aspects:

a) The operation interface is simple and the function modules are distributed reasonably;

b) Beautiful interaction;The entire design is clear and easy to use.

(c) Functional logic

For the functional test of radio tracking and positioning in this paper, it can be seen that the functions have met the requirements in the requirements analysis. During the running process, the client runs more smoothly, and the functional logic is prominent in the following aspects:

a) Full-featured, fit design needs;

b) Functional design provides a relative logical measure for the modification of the software while catering to the usage habits;

c) The function module runs normally and is dynamically updated with the database connection in real time.

(d) Accuracy test

After displaying the position coordinates and relative position on the mobile phone and measuring it in kind, the error is about 1 decimeter. Meet the specified technical indicators.

VI. CONCLUSION

In this paper, based on the research of short-range radio tracking and navigation technology, a tracking and positioning method based on UWB positioning module is proposed [11-16]. UWB positioning technology can solve the problem of more accurate real-time positioning of indoors, underground passages, underground powerhouses, etc., and solve the problem that GPS can not work indoors or in complex environments. In this study, the base station transmits and receives the signal of the positioning module, then completes the positioning and tracking of the target according to the RSSI positioning algorithm, and feedbacks and processes the result, which is displayed in the designed APP client, which is an efficient and feasible technology. Program. With the rapid development of positioning and navigation technology in various countries, the tracking and positioning of radio signals will become more and more indispensable. At present, although the system that has been put into operation can meet the needs of monitoring work, it also has the problem of more false convergence results and further improvement of positioning accuracy, which requires continuous learning and improvement.

References

[1] Han Gang. Response time of indoor positioning technology based on radio and ultrasonicResearch [D]. Harbin Institute of Technology, 2009.

[2] Yao Jinjie. Research on target location technology based on ground base station [D]. North University of China, 2011.

[3] Huang Haihui, Li Longlian. An improved RSSI-based mobile node location algorithm in WSN[J].Application of Electronic Technique, 2015, 41(1): 86-89.

[4] . Zhang Chenchen, Mao Yongyi, Zhang Xiaojia, et al. A Data Fusion Wireless Location Algorithm Based on AHP[J].Microcomputer & Application, 2015, 34(12): 51-53, 60

[5] Wang Wei, Chen Wei, Zhou Yong. RSSI localization algorithm based on ranging correction and position correction[J]. Computer Engineering and Design, 2011, 32(002): 409-412.

[6] Zhang Jianwu, Zhang Wei, Ying Wei, et al. Research on RSSI Ranging Based on ZigBee[J]. Journal of Transduction Technology, 2009, 22(2): 285-288.

[7] Chen Weike, Li Wenfeng, Shouyi, et al. Weighted centroid localization algorithm for wireless sensor networks based on RSSI[J]. Journal of Wuhan University of Technology: Transportation Science and Engineering, 2006, 30(2): 265-268.

[8] Zhang Jieying, Sun Wei, Wang Xia. Dynamic Distance Estimation Algorithm Based on RSSI and LQI[J]. Electronic Measurement Technology, 2007, 30(2): 142-145.

[9] Zhu Jian, Zhao Hai, Sun Peigang, et al. Equilateral triangle positioning algorithm based on RSSI mean[J]. Journal of Northeastern University: Natural Science Edition, 2007, 28(8): 1-094.

[10] Wang Lei, Li Hongming, Du Xiaotong. Research on WSN Multilateral Location Algorithm Based on Tikhonov Regularization[J]. Journal of Transduction Technology, 2009, 22(6): 852-856.

[11] Liu Jiangting. Research on Digital Precision Ranging Technology [J]. Modern Electronic Technology, 2012,35(07):161-163.

[12] Whitehouse K, Karlof C, Culler D. A practical evalua tion of radio signal strength for ranging-based localizat ion[J] ACM SIGMOBILE Mobile Computing and Co mmunicationReview, 2007, 11(1): 41-52.

[13] Bruno R, Conti M, Gregori E. Mesh networks: comm odity multihop ad hoc networks[J].Communications Ma gazine, IEEE, 2005, 43(3): 123-131.

[14] Figuera C, Rojo-Álvarez J L, Mora-Jiménez I, et al. Time-space sampling and mobile device calibration for WiFi indoor location systems[J].Mobile Computing, I EEE Transactions on, 2011, 10(7): 913-926.

[15] Fang Z, Zhao Z, Geng D, et al. RSSI variability char acterization and calibration method in wireless sensor network[C].Information and Automation (ICIA), 2010 IEEE International Conference on. IEEE, 2010: 1532-153 7.

[16] Kuo S P, Tseng Y C. A scrambling method for finge rprint positioning based on temporal diversity and spati al dependency[J].Knowledge and Data Engineering, IEEE Transactions on, 2008, 20(5): 678-684.

Design of ground three-component magnetic daily variable measuring device

Jia Daipeng
（jilin university College of Instrument Science and Electrical Engineering,changchun,130021）

***Abstract*—The design solves the initial alignment problem by mechanical device, accurately completes the orientation of the three-axis direction of the sensor, makes the magnetic measurement data processing calculation small, and can quickly solve the magnetic measurement data, and has high real-time performance. Through in-depth analysis of the existing geomagnetic daily change station observation system, a complete portable solution is proposed, which aims to significantly reduce the power consumption, volume and weight of the whole system, realize the integration and portability of the system, and facilitate the magnetic daily change. Station measurement implementation meets maneuvering measurement requirements.**

***keywords*—Magnetic orientation Magnetic daily measurement Portable solution**

I. INTRODUCTION

THE geomagnetic field is one of the inherent physical fields of the Earth. People mainly use geomagnetic observation data to understand the physical properties of the geomagnetic field[1-4]. Geomagnetic observation data has important research significance for basic geophysics, space physics, space weather science, seismology and other basic disciplines; and is directly or indirectly applied to geological exploration, environmental monitoring, aircraft navigation, radio communication, natural disasters Forecasting and other social fields are closely related to human life, national economy and national defense construction; especially in the process of earthquake monitoring and forecasting research, has attracted the attention of scientists in recent years[5]. The basic task of geomagnetic observation is to obtain continuous, accurate and reliable observations of geomagnetic field changes. In order to obtain more accurate and rich geomagnetic observation data, a large number of reliable geomagnetic observation devices are urgently needed [6-8].

This instrument is mainly used as a daily variation of the three components of the geomagnetic field. In the field survey work, it is possible to provide daily correction values, and if necessary, other geomagnetic elements of the geomagnetic field can be recorded at the same time[9].

II. COMPOSITION OF THE MEASUREMENT SYSTEM

The ground three-component magnetic directional exploration device, Refer to FIG. 1 , includes a controller module, a clock control module for synchronization, and a power module for power supply, the sensor module includes a positioning module, a fluxgate sensor, and a fluxgate The X axis of the sensor is in the same line as the optical axis of the non-magnetic theodolite; the controller module is an MCU controller module, and the positioning module is bidirectionally connected to the MCU controller module through a USART serial port, and the three axes of the fluxgate sensor Each of them is connected to a 24-bit A/D conversion module through a set of signal conditioning modules. The 24-bit A/D conversion module is bidirectionally connected to the MCU controller module through the SPI serial port, and the liquid crystal display module is bidirectionally connected to the MCU controller module through the USART serial port, SD The card storage module is bidirectionally connected to the MCU controller module through the SPI bus, and the clock control module and the power module are connected to the MCU controller module; the SPI bus adopts an 8-bit data transmission width, and the frequency is 500 MHz.

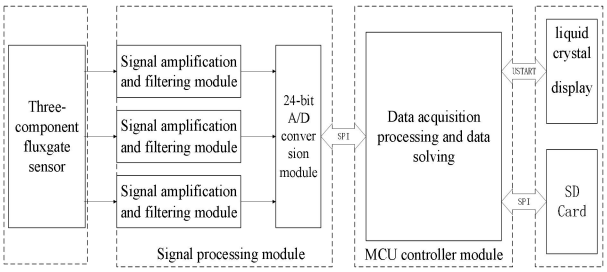

Fig.1 Schematic diagram of the fluxgate measurement system module

III. DESIGN OF HARDWARE

A.Power section

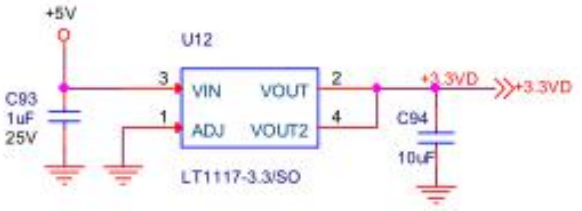

Fig.2 3.3V generation circuit

Refer to Figure 2, the circuit is a 3.3V generating circuit, using the AMS1117 control chip, J1 is the +5V input terminal, please provide a clean input power supply here.

B.Acquisition input section

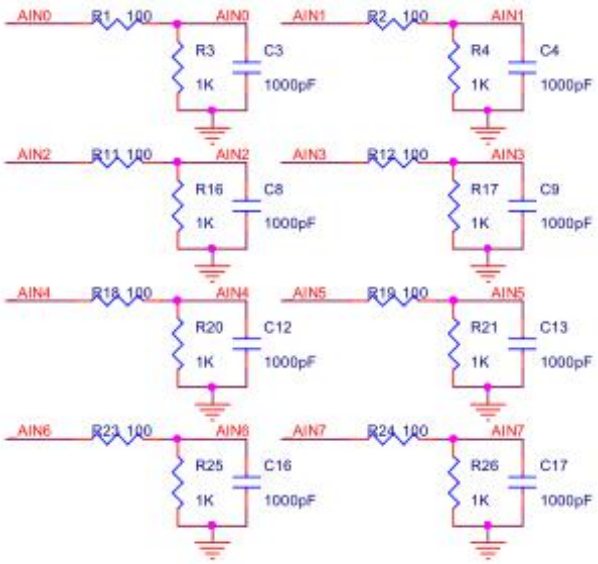

Fig.3 Acquisition input circuit

Refer to Figure 3, J2-J9 is the acquisition input point, and the tested voltage enters the ADC chip through this point. Even resistor R0 R2 R4 R6 R8 R10 R12 R14 is the input resistor. It is composed of an RC filter circuit with the latter capacitor, and an odd-number resistor R1 R3 R5 R7 R9 R11 R13 R15 constitutes an input attenuation circuit that attenuates the input signal greater than 5V.

C.Acquisition input section

Refer to Figure 4, ACOM can be flexibly configured. Can be grounded, or can be connected to an external model, as a reference, JP10 jumper cap connection, ACOM grounding; JP10 jumper cap disconnected, ACOM suspended. D0 D1 D2 D3 is exported to J11 for debugging and reading data.

IV. EXPERIMENTAL METHOD AND TEST RESULTS

A. Experimental method

The device is composed of a GPS base station, a GPS mobile station, a fluxgate detection system and a non-magnetic theodolite. The fluxgate detection system is composed of a fluxgate sensor, an electronic circuit, a display system and a power supply part. The fluxgate sensor is fixed to the top of the telescope without the magnetic theodolite by a mechanical fixing structure, and is adjusted in both horizontal and vertical directions by the mechanical fixing structure, so that the magnetic axis of the fluxgate sensor is parallel to the optical axis.

The base station calibration uses a differential method to form a control network through multiple points.

The rover correction uses the base station - the rover correction mode: the base station is set up at a known point, the known coordinates are input, the rover is set up at another known point, and the coordinates are input for rover correction.

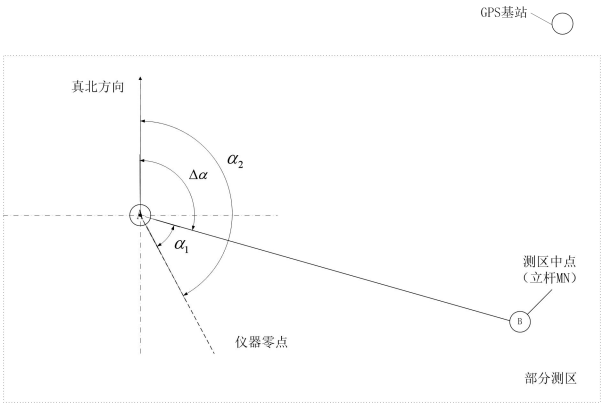

Fig.5 Magnetic orientation diagram of ground mobile three-component magnetic measurement system

Refer to Fig. 5, a vertical MN perpendicular to the local horizontal plane is placed at the center B of the survey area and the coordinates of the M point (R_b, λ_b, L_b) are measured by differential GPS, where the distance, longitude and latitude from point A to the center of the earth, respectively. Place a measuring device (composed of a non-magnetic theodolite and a fluxgate magnetometer) at point A to be measured, and use the aiming aid to align the crosshair of the eyepiece of the non-magnetic theodolite to the vertical MN, and record the azimuth at this time. Then, using differential GPS to measure the coordinates of point A of the point to be measured (R_a, λ_a, L_a), which is the distance, longitude and latitude of point A to the center of the earth, respectively, the plane ABC and point A are coincident, and intersect with MN at point B, and The Earth's rotation axis intersects at point C, and the plane ABC is parallel to the equatorial plane.

Then the angle $\Delta\alpha$ between the straight line AM and the true north can be requested,

$$\cos\Delta\alpha = \frac{\overrightarrow{n_{AB}} \bullet \overrightarrow{n_{AC}}}{\left|\overrightarrow{n_{AB}}\right| \bullet \left|\overrightarrow{n_{AC}}\right|} \tag{1}$$

The Cartesian coordinates of point A are:

$(X_a, Y_a, Z_a) =$

$(R_a \cos L_a \cos\lambda_a,\ R_a \cos L_a \sin\lambda_a,\ R_a \sin L_a)$

The Cartesian coordinates of point B are:

$(X_b, Y_b, Z_b) =$

$(R_b \cos L_b \cos\lambda_b,\ R_b \cos L_b \sin\lambda_b,\ R_b \sin L_b)$

The Cartesian coordinates of point C are ;

$(X_c, Y_c, Z_c) = (0,0,\ R_a / \sin L_a)$

$$\overrightarrow{n_{AB}} \bullet \overrightarrow{n_{AC}} = (X_B - X_A)(X_C - X_A) + (Y_B - Y_A)(Y_C - Y_A) + (Z_B - Z_A)(Z_C - Z_A) \tag{2}$$

$$\left|\overrightarrow{n_{AB}}\right| = \sqrt{(X_B - X_A)^2 + (Y_B - Y_A)^2 + (Z_B - Z_A)^2} \tag{3}$$

$$\left|\overrightarrow{n_{AC}}\right| = \sqrt{(X_C - X_A)^2 + (Y_C - Y_A)^2 + (Z_C - Z_A)^2} \tag{4}$$

Turning the non-magnetic theodolite to α_2 ($\alpha_2 = \alpha_1 + \Delta\alpha$), the alignment direction of the theodolite optical axis (flux gate X-axis) is the true north direction, and the Y- and Z-axis alignment directions of the fluxgate are the Y and Z component directions. Measurement, the measured value at this time is the three components of geomagnetism B_X, B_Y, B_Z.

According to the definition of the magnetic declination, its expression can be written as

$$D = \arctan(B_Y / B_Z) \tag{5}$$

According to the definition of the magnetic dip, its calculation expression can be written as

$$I = \arctan(B_Z / \sqrt{B_X{}^2 + B_Y{}^2}) \tag{6}$$

B. Test results

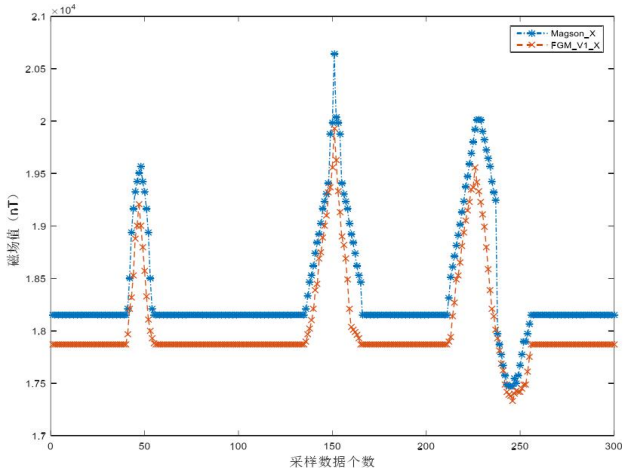

Fig.6 Magnetic measurement system and Magson magnetometer X-axis change trend

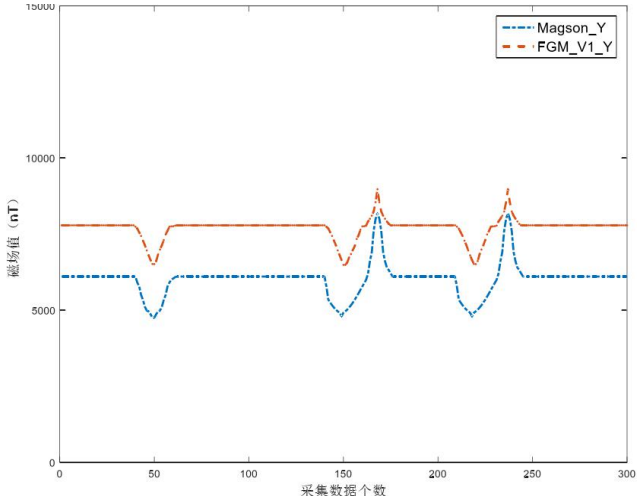

Fig.7 Magnetic measurement system and Magson magnetometer Y-axis change trend

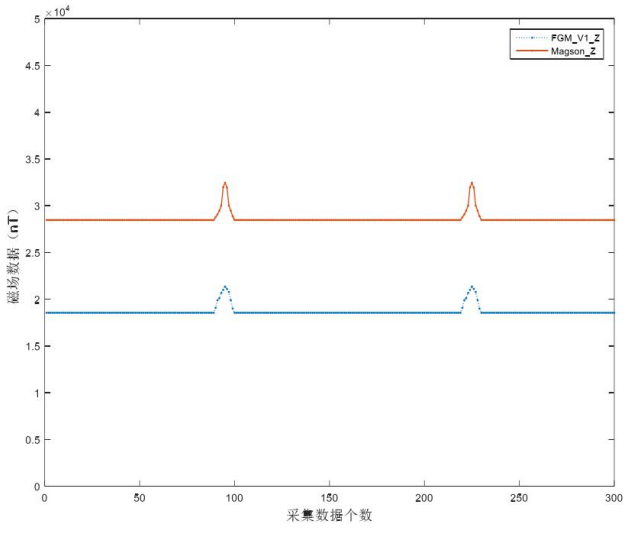

Fig.8 Magnetic measurement system and Magson magnetometer Z-axis change trend

The fluxgate detection system and the non-magnetic theodolite were tested. Figure 6, Figure 7, and Figure 8 are the contrast curves of the X, Y, and Z triaxial magnetic field trends plotted by matlab. The test results

are as follows: the noise of the fluxgate detection system is less than 0. 1 nT, the resolution is 0. 1 nT, the zero field offset is less than ± 1nT, and the zero field offset temperature coefficient is better than 0. 1 nT / C, The measurement range reaches ±100000nT, and the conversion range is not required; the horizontal and vertical accuracy of the non-magnetic theodolite reaches 6". When the whole machine and all components are 1cm away from the fluxgate sensor, the material magnetic is less than 1nT; the whole machine test is tested. The latitude is the magnetic declination D. The baseline accuracy is 0.045', and the magnetic dip angle I has a baseline accuracy of 0.017'.

The test results show that the technical indicators fully meet the design requirements, and the individual indicators are much better than the design requirements. The test results of the whole machine reach or exceed the domestic similar products. Compared with the imported high-precision fluxgate magnetometer, some indicators reach their level. However, compared with the accuracy of the non-magnetic theodolite, it needs to be further improved.

IV. CONCLUSION

The design solves the initial alignment problem by mechanical device, accurately completes the orientation of the three-axis direction of the sensor, makes the magnetic measurement data processing calculation small, and can quickly solve the magnetic measurement data, and has high real-time performance.

Through in-depth analysis of the existing geomagnetic daily change station observation system, a complete portable solution is proposed, which aims to significantly reduce the power consumption, volume and weight of the whole system, realize the integration and portability of the system, and facilitate the magnetic daily change. Station measurement implementation meets maneuvering measurement requirements.

References

[1] Geometry structure optimization of hexagonal pyramidal full tensor mag-netic gradient probe. SHEN M D,CHENG D F,AN ZH F,et al. IEEE Transactions on Magnetics . 2016

[2] MRS noise investigations with focus on optimizing the measurement setup in the field. Costabel S,Müller-Petke M. 5th International meeting on Magnetic Resonance . 2012

[3] Magnetic gradiometer on an AUV for buriedobject detection. Pei Y H,Yeo H G,Kang X Y, et al. OCEANS 2010 . 2010

[4] Searchlights for gravity and magnetics. Dransfield M. Geophysics . 2015

[5] nitial design and testing of a full—tensor air-borne SQUID magnetometer for detection of unexploded ordnance. T Jeffrey Gamey,,Tatiana Starr,William E Doll,et al. SEG Technical Program Expanded Abstracts . 2004

[6] Equatorial Pacific magneticanomalies identified from vector aeromagnetic data. Homer-Johnson B C,Gordon R G. Geophysical Journal . 2003

[7] An empirical relation to correct storm-time thermospheric mass density modeled by NRLMSISE-00 with CHAMP satellite air drag data[J] . Y.L. Zhou,S.Y. Ma,H. Lühr,C. Xiong,C. Reigber. Advances in Space Research . 2008 (5)

[8] Rifting to Spreading Process along the Northern Continental Margin of the South China Sea[J] . Yukari Kido,Kiyoshi Suyehiro,Hajimu Kinoshita. Marine Geophysical Researches . 2001 (1)

[9] A high- T c</SUB> flip-chip SQUID gradiometer for mobile underwater magnetic sensing[J] . S T Keenan,J A Young,C P Foley,J Du. Superconductor Science and Technology . 2010 (2)

Design of Data Acquisition and Storage Module for Three-Component Magnetic Measurement System

Tao yi
（ College of Instrument Science and Electrical Engineering, Jilin University, Changchun130022）

Abstract—**Compared with the traditional total field measurement, the three-component magnetometer can obtain more abundant geomagnetic field information, effectively reduce the multi-solution in inversion, help to quantitatively interpret the magnetic body, and then to identify geological structure, look for mineral resources and solve hydrology problems. Problems of engineering geology and environmental monitoring.**

Keywords—**three component geomagnetic exploration STM32 AD**

0 Preface

Overseas, Canada and Russia have developed borehole magnetometers, but their common disadvantage is that they are bulky and can only measure the total field value of the downhole magnetic field, but can not measure its horizontal and vertical components, which is very disadvantageous to locate the abnormal magnetic field position accurately [1-2] .

With the development of three-component magnetometer in China, the gap between the three-component magnetometer in some aspects and the international level has increased in the past ten years. China's three-component magnetic measurement technology was once in the leading position in the world in the 1970s and 1980s, but the development of the instrument remained at the low precision level for a long time more than twenty or thirty years ago, while high-precision products have been produced abroad. At present, the vertical component observation accuracy of the three-component magnetometer produced in China is only 100 nT to 150 nT, and the horizontal component is lower, so it can only be used to detect strong magnetic anomalies.

For example, the JCX-3 three-component magnetometer developed by Chongqing Geological Instrument Factory in China has been improved on the basis of JCX-1 and JCX-2 vertical systems with two degrees of freedom. It overcomes some weaknesses of JCX-1 and JCX-2 instruments and adopts three-component measurement, but it still has some fatal weaknesses, such as high failure rate and low sensitivity of the system. Standards such as steering difference of X, Y magnetic sensor < 400nT, steering difference of Z magnetic sensor < 300nT, range and accuracy of measuring inclination and azimuth angle are far from meeting the needs of actual survey [2].

1 Design Contents and Requirements

(1). The data display program based on STM32 is designed, including three-component, magnetic dip and magnetic declination display.

(2). The data acquisition program based on STM32 is designed. The serial data acquisition of AD module is completed by SPI communication.

(3). The data storage program based on STM32 is designed. Stm32 stores the collected data into the SD card.

(4). Complete the integration of program modules and debug them to make them compatible with each other.

2 Overall design scheme

STM32F407ZGT6 MCU is an enhanced processor based on Cortex-M4 core. Its working frequency can reach 168MHz. It has three 12-bit ADC channels. Each ADC shares up to 21 external channel interfaces, which can realize single or continuous external data sampling. [3-7]. SD card is currently the most commonly used large-capacity data storage medium, supporting two modes of operation: SDIO mode and SPI mode. SPI mode can usually adopt SPI interface of MCU or simulate SPI communication with common I/O port. STM32 has a SPI interface. The hardware part of SD card fast data reading and writing system mainly consists of ADC sampling and conditioning circuit and SD card hardware connection circuit. In order to improve the accuracy of data, it is necessary to provide an external voltage reference source for STM32. In addition, the input voltage of the external sensor may be different from that of the ADC sampling range,

which often can not be directly input to the AD sampling pin of the MCU. It is necessary to adjust the signal so that the combination of the sensor and ADC can achieve the best accuracy. Combining the above two considerations, use external reference voltage [8-12].

3 Implementation process

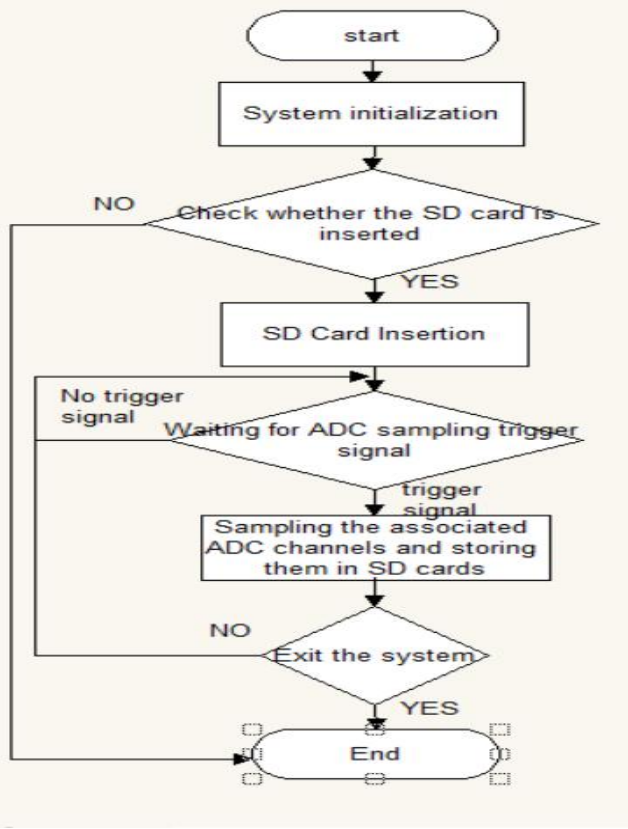

To create files and store information in FAT32 file system format, SD card format must be converted into FAT32 file system format, which is the initialization of SD card. After confirming that the communication of SD card is normal, the initialization begins. The process includes reading the original FAT table, searching the space cluster and determining the starting cluster number, writing the new FAT table back to SD card, reading the catalog item information, assigning the file information to the file information structure, writing the new catalog back to SD card, and reading and writing the SD card after initialization is completed.

```
  while(SD_Init())
    {
      LCD_ShowString(30,150,200,16,16,"SD Card Error!");
      delay_ms(500);
  LCD_ShowString(30,150,200,16,16,"Please Check! ");
      delay_ms(500);
    }
    exfuns_init();
    f_mount(fs[0],"0:",1);
    res=f_mount(fs[1],"1:",1);
    if(res==0X0D)
    {
      LCD_ShowString(30,150,200,16,16,"Flash Disk Formatting...");
      res=f_mkfs("1:",1,4096);
      if(res==0)
      {
        f_setlabel((const TCHAR *)"1:ALIENTEK");
        LCD_ShowString(30,150,200,16,16,"Flash Disk Format Finish");
      }else LCD_ShowString(30,150,200,16,16,"Flash Disk Format Error "); delay_ms(1000);
    }
  LCD_Fill(30,150,240,150+16,WHITE);
    while(exf_getfree("0",&total,&free))
    {
      LCD_ShowString(30,150,200,16,16,"SD Card Fatfs Error!");
      delay_ms(200);
      LCD_Fill(30,150,240,150+16,WHITE);
      delay_ms(200);
    }
```

The AD sampling signal triggers the writing command to SD card after starting. The command contains the writing address. The writing address must correspond to the physical address of SD card. The SD card receives data and verifies the address. CRC checks and sends out the response command. After initialization of SD card, a text format file named after channel is created. The file is associated with the structure pointer fnew. The operation of the file again is accomplished through the structure pointer. The specific method is to convert the current date to a string type and add ". text" at the end of the string, then use the f_open() function to create, write the title information (channel name) in the first line of the file. Then close the text format file, complete the initialization of the system, and wait for the arrival of ADC sampling time.

```
  res=f_open(&fil1,"0:/CHR1.txt",FA_CREATE_ALWAYS|FA_WRITE);
      f_close(&fil1);
    res=f_open(&fil2,"0:/CHR2.txt",FA_CREATE_ALWAYS|FA_WRITE);
      f_close(&fil2);
    res=f_open(&fil3,"0:/CHR3.txt",FA_CREATE_ALWAYS|FA_WRITE);
```

```
            f_close(&fil3);
    delay_ms(20);
```

The above information is recorded when the AD trigger signal arrives. Sampling channel records the input pin name of ADC. Sampling name is the corresponding data form of the sampling channel, such as pressure, temperature, etc. Sampling data is a single precision type, which is converted into a string type and reserved five decimal points and assigned to the corresponding pointer. Triggering mode indicates the form of sampling data acquisition, including timing trigger, external key trigger and so on. In order to make the data in the text format orderly and normative, the string pointed to by each pointer of the structure is stored in the text File Buffer [] string array according to the specified width by using sprintf function.

```
  sprintf(dataTemp, "%.3f \r\n",ADC_Vol);
  sprintf(dataTemp2, "%.3f \r\n",ADC_Vol2);
  sprintf(dataTemp3, "%.3f \r\n",ADC_Vol3);
  res = f_open(&fil1,"0:/CHR1.txt", FA_WRITE | FA_OPEN_ALWAYS);
  res = f_open(&fil2,"0:/CHR2.txt", FA_WRITE | FA_OPEN_ALWAYS);
  res = f_open(&fil3,"0:/CHR3.txt", FA_WRITE | FA_OPEN_ALWAYS);
   if ( res == FR_OK )
   {
      f_lseek(&fil1, f_size(&fil1));
        res = f_write(&fil1, &dataTemp, sizeof(dataTemp), &bww1);
      printf( "\r\n ?????? \n" );
      f_close(&fil1);

   f_lseek(&fil2, f_size(&fil2));
        res = f_write(&fil2, &dataTemp2, sizeof(dataTemp2), &bww2);
      printf( "\r\n ?????? \n" );
      f_close(&fil2);

  f_lseek(&fil3, f_size(&fil3));
        res = f_write(&fil3, &dataTemp3, sizeof(dataTemp3), &bww3);
      printf( "\r\n ?????? \n" );
      f_close(&fil3);
   }
```

After each SD card is written, the file needs to be closed and reopened the next time it is written. The newly written data should be immediately followed by another line at the end of the last file. Using the f_lseek (& fnew, f_size (& fnew)) function, we can know the size of the current file and obtain the pointer offset value, so that the re-written string follows the end of the file without calculating the total number of bytes written accumulatively.

```
  res = f_open(&fnew, sample_date, FA_OPEN_ALWAYS |FA_WRITE);
  if(res!=FR_OK)
  while(1);
  else
  {
  res = f_lseek(&fnew, f_size(&fnew));
  if(res!=FR_OK)
  while(1);
  else
  {
  res = f_write(&fnew,text File Buffer,
  sizeof(text File Buffer), &bw);
  if(res!=FR_OK)
  while(1);
  }
  }
  f_close(&fnew);
```

4 Test analysis and conclusion

Figure 1 the whole system

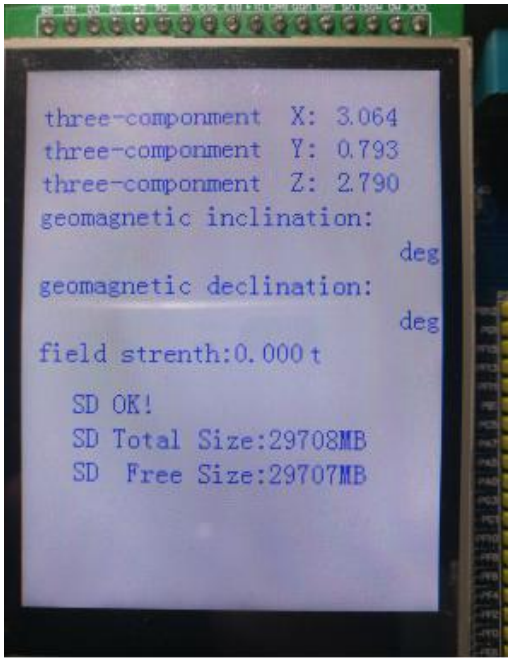

Figure 2 LCD screen display case

Fig. 2 shows that the system can complete the real-time display of ADC voltage data acquisition, including three channels, SD card can be displayed, including the design requirements of all class capacities.

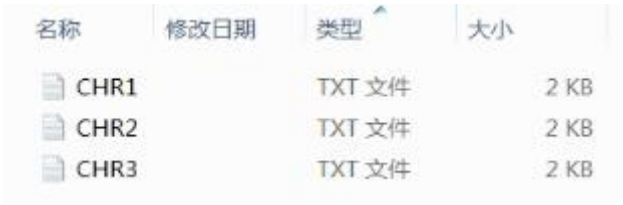

Figure 3 TXT folder creation

After the collection is completed, the SD card is inserted into the computer. As can be seen from Figure 3, the system has successfully created three TXT folders.

Figure 4 three channel data storage conditions

Open three channels corresponding to the TXT folder, you can see that the corresponding data is the voltage collected by the three channels.

5 Summary and Prospect

SD card, as a large capacity data storage device, is more and more widely used in embedded systems. In this paper, STM32 is used to realize the communication between SPI and ADC, data transmission between SDIO interface and SD card, text format is created, and data management mode is proposed to facilitate data management, which has high practical value. However, the accuracy of ADC sampling is not high enough. This is mainly because the input voltage of the external sensor may not be equal to the voltage span of the ADC sampling range. It often can not be directly input to the AD sampling pin of MCU. It is necessary to adjust the signal so that the combination of the sensor and ADC can achieve the best accuracy. Considering the above considerations, special chips such as TI's REF2030 can be used to provide reference voltage for ADC sampling and operation conditioning circuits.

Reference

[1] AD Conversion Procedure and Application of Lyon STM32 (I) [N]. E-Newspaper, 2017-10-01 (009).

[2] Yang Fuxing. Data acquisition and correction of fluxgate sensor based on PIC single chip computer [D]. Wuhan University, 2017.

[3] Huo Liangsheng, Li Yuefeng, Zhao Xiong, Liu Hui. Development of an automatic sampler based on STM32 [J]. Analytical Instrument, 2017 (02): 7-13.

[4] Du Jialiang, Ding Yadong, Zhao Junjie. AD acquisition and SD card data storage based on STM32 [J]. Computer knowledge and technology, 2016, 12 (12): 235-237.

[5] Wang Chenhui, Wu Yue, Yang Kai. Design of multi-channel data acquisition system based on STM32 [J]. Application of electronic technology, 2016,42(01): 51-53+57.

[6] Yang Lisheng, Zhang Anwei, Wang Lei, Wei Lan. Research and Implementation of External Spi Flash Word Library Based on STM32 [J]. LCD and Display, 2015, 30 (02): 290-295.

[7] Liu Zhiyong, Chen Pengfei, Sulei, Liao Guanglan. Research on file transfer technology of U disk/SD card

based on STM32 chip [J]. Modern electronic technology, 2014, 37 (18): 107-109.

[8] Shao Qing. LCD Display Design Scheme Based on STM32F4x9 [J]. Application of Single Chip Microcomputer and Embedded System, 2014, 14 (06): 82-83.

[9] Meng Qiang. Design of data acquisition system based on STM32 [D]. Nanjing Forestry University, 2014.

[10] Tao Navy, Zhang Yiming, Zeng Zhihui. Design of multi-channel data acquisition system based on AD7606 [J]. Industrial and mining automation, 2013, 39 (12): 110-113.

[11] Hao Wen, Shen Jinxin, Mei Cheng. Design of Storage Data Acquisition System Based on STM32 Single Chip Microcomputer [J]. Electronic Design Engineering, 2013, 21 (17): 80-82.

[12] Song Jingwei, Fu Guangchun, Ma Xianguo. Multi-channel voltage acquisition based on STM32 [J]. Electronic World, 2013 (12): 55-56.

Research on Distributed Optical Fiber Sensing System with Mobile Phone Push Function

Tian Chen, Boan Zeng, Xianwen Wang
(College of Instrumentation and Electrical Engineering, Jilin University, Changchun 130012, China)

***Abstract*—Based on the original distributed optical fiber temperature measurement system, in order to further improve the observability and convenience of temperature measurement, the project team combined with Internet technology to store the local temperature information in the cloud by setting up a cloud platform.And based on the application written by the Android operating system, the temperature data stored in the cloud platform is displayed in real time. The experimental results show that the temperature data can be displayed well on the mobile phone.**

***Keywords*—distributed optical fiber temperature measurement system cloud platform Android**

I. PREFACE

WITH the development of science and technology, pipelines and cables are widely used in various fields of industrial production, but in pipelines or cable systems, such as oil, natural gas pipelines, power line tunnels, underground or submarine cables, elevated cables[1], which are widely distributed and in urgent need of comprehensive monitoring, traditional point sensors can not solve the problem of system monitoring very well and economically. Therefore, in order to solve this problem, distributed optical fiber temperature measurement system has been designed and widely used in related fields in recent years.

Distributed Fiber Temperature Measurement System (DTS) is a temperature measurement system based on the relationship between scattered light intensity and temperature in sensing optical fibers[2-3]. At present, the technology of temperature measurement using distributed optical fibers is mainly based on the principle of Raman scattering, collecting and sensing temperature information[4].It can be divided into the following two technologies:

a) Distributed optical fiber sensing technology based on Raman optical time domain reflection principle;

b) Distributed optical fiber sensing technology based on Raman optical frequency domain analysis principle.

Distributed optical fiber temperature sensor system overcomes the shortcomings of traditional temperature measurement methods, and has its unique advantages, such as anti-electromagnetic interference, good insulation performance, small occupation area, low weight and suitable for long-distance distributed temperature measurement, etc. It has a wide range of applications [5-6].

Based on the mature distributed optical fiber temperature measurement system, this project adds Internet technology, which makes the real-time temperature data that can only be displayed in a fixed location can be monitored at any time and anywhere, and further improves the practicability and convenience of the design.

II. SYSTEM FUNCTION AND DESIGN SCHEME

A. System Functions

The distributed optical fiber system of this project consists of three parts: distributed optical fiber temperature measurement host part, cloud platform database part and APP for Android system. Distributed optical fiber temperature measurement host mainly consists of optical fiber, acquisition card and processor; cloud platform completes real-time data upload and download; APP displays data information and system working status. These three parts connect with each other through the Internet, so that the three parts of the system can obtain the required temperature data in turn. This process is also the core and main research content of this project.

B. Design Scheme

The process can be roughly divided into data acquisition, data preliminary processing, data upload, data further processing and storage, data acquisition and display, etc.

(1)Design Principle of Distributed Optical Fiber Sensor

Distributed optical fiber sensing technology is a new type of sensing technology, which can monitor multiple locations in real time. This kind of technology includes optical fiber Raman sensing technology, optical fiber Brillouin sensing technology, interferometric disturbance distributed sensing, coherent optical time domain reflectometer (Φ-OTDR) sensing technology, optical frequency domain reflectometer (OFDR) sensing technology[7].

Distributed optical fiber sensing technology takes advantage of the special optical characteristics of Rayleigh reflection, Raman reflection and Brillouin reflection of light, and because the optical characteristics will change when the optical fiber receives the change of external stress or temperature, the optical signal returned from the monitoring point will change accordingly, so the monitoring can be obtained by recording the time of optical signal propagation. Distance information of points. Based on the above principles, we can get distributed detection information.

At present, optical fiber temperature sensors are generally based on Rayleigh scattering, Raman scattering and Brillouin scattering[8]. Compared with Rayleigh scattering, Raman scattering and Brillouin scattering are more convenient to fabricate and use sensors, and the measurement range is wider, so the former is gradually replaced by the latter. However, Brillouin scattering also has some problems. Although it has high accuracy, its frequency shift is only 10-20 GHz and its linewidth is only about 50 MHz. This poses a great challenge to the performance of lasers [9]. Therefore, Brillouin scattering can not be put into practical production at present. Therefore, distributed optical fiber temperature measurement system based on Raman scattering[10] has become a hot topic in academic research, and this design also uses this method.

Raman discovered spontaneous Raman scattering in 1928. In the experiment, he observed that in addition to the original input light frequency ω0, there were other frequencies of light ωs and ωa in the scattering spectrum. Among them, ωs<ω0 is Stokes light and ωa<ω0 is anti-Stokes light [11], as is shown in Figure 1.

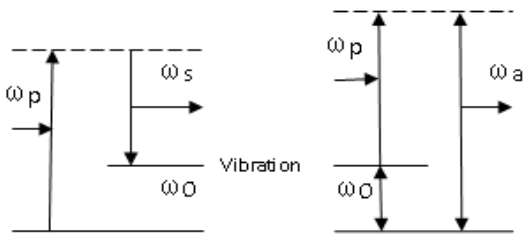

Fig.1 Stokes and anti-Stokes Raman scattering diagram

As is shown in the figure above, there are two kinds of collisions between the fiber molecules—elastic and inelastic, and the interaction of the excited photons. Raman scattering is an inelastic collision that produces Stokes light and anti-Stokes light, respectively. The former is generated from the photon transition of the ground state molecular absorption frequency ωp to the virtual energy level (the actual non-existent energy level due to the quantum uncertainty principle), and then transitions from the virtual energy level to the vibrational energy level (first excited state). In the process, the latter is generated in the process in which the fiber molecule at the vibration level absorbs the photon of the frequency ωp and transitions to another virtual level, and then the level is relaxed to the ground state. Because in the thermal equilibrium state, the number of molecules in the ground state is much larger than the number of molecules in the vibrational level, so the number of Stokes photons is much more than the number of anti-Stokes photons, and the Stokes scattered light is far stronger than the inverse Stokes scatters light, which indicates that the population number at the molecular level is related to temperature [12].

(2)PCIADD12 series high speed data acquisition card design

PCIADD12 is a high-speed weak signal data acquisition card. PCIADD12 uses the hardware real-time accumulation averaging technology designed by transient technology to realize weak signal enhanced acquisition and extract relevant signals that are submerged by noise. With on-board synchronization technology, the signal-to-noise ratio of the signal can be increased by nearly 180 times after the required original signal is accumulated by no more than 32,768 times.

The PCIADD12 onboard two 12-bit high-speed A/D converters are available in three sample rate versions of 100MSPS, 125MSPS, and 150MSPS. PCIADD12 features a unique parallel sync signal acquisition and accumulation technique that allows acquisition and accumulation to be synchronized. For the original signal with a length of 10000 points, 32,768 acquisitions and accumulations are performed, and the computer obtains the final result in only 4 seconds (100M version 4 seconds, 150M version 3 seconds).

In addition, PCIADD12 has two trigger modes: external trigger and internal trigger. The user can arbitrarily select the device to trigger the capture card mode or the capture card to trigger the device mode. After the integrity processing, the trigger pulse given by the device is within 5% to ensure that the device is not triggered by mistake.The PCIADD12 capture card connection is shown in Figure 2.

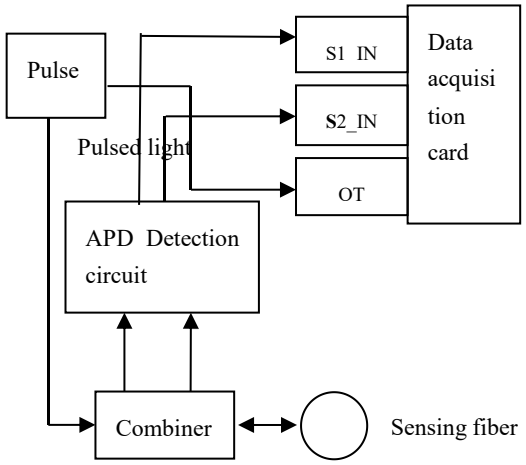

Fig.2 Capture card connection

The PCIADD12 accurately recovers, detects, and measures the characteristics of submerged weak signals, making it ideal for distributed fiber optic sensing systems.

(3) Data collectionIn

The first part of the system, the main device is the fiber optic temperature measurement collector. First, the optical signal is emitted by the collector, and the optical signal collects the reflected optical signal while traveling along the optical fiber and records the time difference, and the time difference can be converted into the distance data, and at the same time, because of the backward Stanley scattered light The relationship between the light intensity difference between the X-ray and the Stokes light is proportional to the temperature, and the temperature information is obtained, and the original distance temperature data can be obtained by combining the two. The main hardware of this part is provided by the instructor's original project, and can be coordinated with the current project through debugging. The programming process is as follows:

The first step is to initialize the capture card.

Routine:

```
if(daq_open_card())
   AfxMessageBox("Open capture card error！ ");
```

The second step is to start sampling.

Routine:

```
daq_reset();/Restart the capture card
Sleep(10);
daq_SetRange(0,0,0,0,0);// Internal configuration function
daq_SetController(0,16000,10000);
daq_SetTrigger(0,200,2);/ Sleep(10);
daq_StartSample();//Start collecting
```

The third step is to query the acquisition status and read the data.

Routine:

```
double datan[2][20000];
int now_add_times=daq_ReadStatus();
if (now_add_times ==32768)
{
daq_stop();
   int flag=daq_ReadData(datan[0],datan[1]);
   daq_reset();/Restart the capture card
   daq_ReadStatus(); if(flag==500)
   AfxMessageBox(Sampling accumulated successfully！ ")
 }
```

(4)Preliminary data processing.

It is completed in the first part of the system. Although the first part has acquired the original data, it contains all kinds of noise because it has not been processed by noise reduction. If the noise reduction is not carried out, the subsequent operation will not be able to proceed. After acquiring the denoised data, it is necessary to choose the storage format of the data. This project stores the temperature data of all points at each time in TXT format in the local computer, which is convenient to access at any time and does not occupy too much local storage space. At the same time, the interface is programmed by C++ and the UI is designed reasonably to realize convenient and efficient monitoring and adjustment at the base station.

(5) Data upload.

In this part, the temperature information collected by the front-end and the alarm information generated are transmitted to the cloud platform database through the Internet, so that the data can be queried and subsequently processed.

(6) Further processing and storage of data.

The received data are stored as real-time data and historical data in a reasonable way, which further increases the readability and operability of the data. These two steps constitute the second part of the whole system. In order to complete the function of this part, the first thing is to choose a reasonable cloud platform. At present, the major domestic Internet companies have launched their own cloud platform services, we integrated functional and economic considerations and finally chose Aliyun, which can meet the requirements through experiments.

Real-time data and historical data can be easily accessed by client and displayed by browser by giving appropriate IP address and designing appropriate UI.

(7) Data acquisition and display.

This is also the third part of the system to complete the content. In order to meet the most extensive needs, the writing of APP is accomplished through Android platform. In this project, APP needs to complete data reception, data display and UI design. The program is written through Android Studio, which is an official

Android program. It is easy to operate and powerful. This part is the core content of this project, so the design and implementation of this part will be introduced in detail next.

III. APP COMPILATION & FUNCTIONS REALIZATION

The compilation and function realization of APP is the key content of this project. The main functions of this part are downloading data from cloud platform, storing data and displaying data. The coordinated work of the three parts can achieve the required functions of the project.

Data download is realized through the network, and data download in Android is Get mode. Get mode needs to use HTTP communication class. Android provides two types of communication: HTTP URL connection and HTTP client, which Google has always recommended users to use, but which has more advantages than OKHTTP. OKHTTP not only has high request efficiency, but also saves broadband. It also provides many solutions to network problems [13]. So this project uses OKHTTP, the main code is as follows:

```
OkHttpClient okHttpClient = new OkHttpClient();
Request.Builder builder = new Request.Builder();
Request request =
builder.get().url("http://173.82.168.157/json").build
();
Call call = okHttpClient.newCall(request);
```

173.82.168.157/json is the IP address that stores real-time data for this project.

Because this project contains a lot of data, although it has been stored on the cloud platform, in order to make the final result closer to the product-level APP, we also store some data locally on the mobile phone, so that sometimes we can see the data when there is no network, although it is not necessary at this stage of the project. In Android, data storage includes sharedpreferences, SQLite database and file storage. SQLite database is used in this project, because of its lightweight, high portability, open source [14] and other characteristics, it is suitable for this project.

The last part is the display data, because the temperature data need to be displayed, so the polyline chart is used for display. In the process of Android development, due to the characteristics of open source, chart display is often done by using open source icon library. The widely used icon libraries include MPAndroid Chart, hellocharts and Android-Charts. But these icon libraries are powerful, but not light enough. So this project uses hellocharts, which is small in size and can also achieve the required functions. The main procedures are as follows:

```
private LineChartView lineChart;
private List<PointValue> mPointValues = new
ArrayList<PointValue>();
private List<AxisValue> mAxisXValues = new
ArrayList<AxisValue>();
private float minY = 0f;
private float maxY = 100f;
protected void onCreate (Bundle
savedInstanceState){
super.onCreate(savedInstanceState);
setContentView(R.layout.activity_actualtime);
lineChart = (LineChartView)
findViewById(R.id.chart);
getAxisXLables();
getAxisPoints();
initLineChart();
}
```

IV. TEST RESULTS & CONCLUSIONS

After the system is basically implemented, the temperature can be displayed locally and the error is within the allowable range. Data can be displayed in the cloud. At the same time, APP can download and display data normally. But at present, the system is not complete, it can only display real-time data, and other parts are still in the process of improvement.

References

[1] Chen Lijun, Li Haibo, Wu Qian, Shi Mei. Research status and development trend of distributed optical fiber temperature measurement technology [J]. Chemical automation and instrumentation.2010 , 37 (12) :1-4

[2] Zhiqiang Wang， Jiajia Ye.Design of large -mode-area single-mode optical fiber with lowingbending loss for Raman distributed temperature sensor [J].Optical Fiber Technology 19（2013）：671-675.

[3] Manoj Kumar Saxena， S.D.V.S.J. Raju. Raman optical fiber distributed temperature sensor using wavelettransform based simplified signal processing of Ramanback scattered signals [J].Optics & Laser Technology，65（2015）：14.

[4] Gabriele Bolognini， Arthur hartog. raman-based fiber sensors ： Trends and applications [J].Optical Fiber Technology，7 Septem－ber，2013：678-681.

[5] Li Xiuqi. Research and design of distributed optical fiber temperature measurement system based on raman

scattering [D]. North China Electric Power University，2008.

[6] Zhou Qi, Le Jianhao, Liu Jiasheng. Development status of distributed optical fiber temperature measurement technology and its application in power field [J]. Science Association Forum,2012 (11) :20-22

[7] Fei Qin. Design and optimization of distributed optical fiber temperature measurement system based on raman scattering [D]. University of Science and Technology of China，2016.

[8] Chen Jianpei，Research progress in distributed Raman fiber optic temperature measurement system [J]. Journal of Guangdong University of Technology，2015，32（3）：104-105.

[9] Zhang Chunyang. Application of distributed optical fiber temperature measurement system in power cable online monitoring [J]. Jiangsu Electrical Engineering ，2014(04):56-58

[10] David Krohn.Fiber Optic Sensors： Fundamentals and Applications [R].2015：31.

[11] R.M. Butler，SAGD comes of AGE! [J].Can. Pet. Technol. 37（7）（1998）：9-12.

[12] Song Wensheng. Design and implementation of distributed optical fiber temperature measurement system [D]. Dalian University of Technology，2007.

[13] An Hui.Android App Development from entry to mastery [M].: Tsinghua University Press.

[14] Dong Hui. Design of Industrial Monitoring System Based on Android Intelligent Terminal [D]. North University,2017 G. O. Young, “Synthetic structure of industrial plastics (Book style with paper title and editor),” in Plastics, 2nd ed. vol. 3, J. Peters, Ed. New York: McGraw-Hill, 1964, pp. 15–64.

Design of Shift-type AGV Intelligent Sorting Device Based on Magnetic Navigation

Li Sanmingzhu, Wu Chenyue, Wang Yingying
（jilin university instrumentation & electrical engineering,changchun,130012）

***Abstract*—On the basis of further research of relevant information of AGV and logistics automation, this paper introduces the basic principles, the developments and the research actuality of the AGV technology. At the same time, this paper points out that it is necessary to develop the AGV technology according to actual domestic demand. Due to the disadvantage that magnetic guided AGV cannot get station messages from guide path, this paper takes radio frequency identification technology as site identification technology innovatively, experiments show it can completely replace the traditional mode which uses magnetic marker and magnetic marker sensor.**

***Keywords*—automated guided vehicle magnetic navigation radio frequency identification load transfer**

I. INTRODUCTION

WITH the rapid development of logistics systems such as automated warehousing system, flexible manufacturing system, flexible handling system and flexible assembly system, modern factories require higher and higher production efficiency and production automation. In this environment, AGV (Automated Guided Vehicle) emerges as the times require[1]. AGV is a kind of automatic intelligent handling equipment which uses storage battery as power supply and uses some guidance mode to control its operation route[2].

The magnetic navigation intelligent vehicle is an autonomous line-finding car based on electromagnetic induction technology. It uses magnetic strips laid on the road to locate and navigate, so as to realize the direction control of motion. Literature [5] provides a positioning detection method based on three sensors [5]. Literature [6] studies the layout of positioning detection sensors[6]. Literature [7] analyses the detection characteristics of sensors. Some literatures put forward the design scheme[8] of intelligent vehicle and discuss the specific implementation methods[9] of steering gear control and motor control. A series of research results have been achieved[10.11]. In this paper, the basic principle of magnetic navigation technology is sorted out, the overall technical scheme of the reload magnetic navigation AGV is put forward, and the key technology of magnetic navigation AGV applied to logistics sorting transportation line is completed.

II. SYSTEM SCHEME DESIGN

A.General introduction

The overall design of this paper is divided into eight modules, in which the main control unit is responsible for controlling and balancing the coordinated operation of sensors and modules; Tracking unit is mainly realized by sensors, so that the car can travel along the laid track accurately; steering unit mainly refers to steering gear control; Driving unit is the control of motor; site identification refers to the input of different destination information and cargo information; the main difficulty of loading unit is the design of mechanical structure; safety auxiliary unit needs to realize the function of emergency stop when there is obstacle in front of the car.

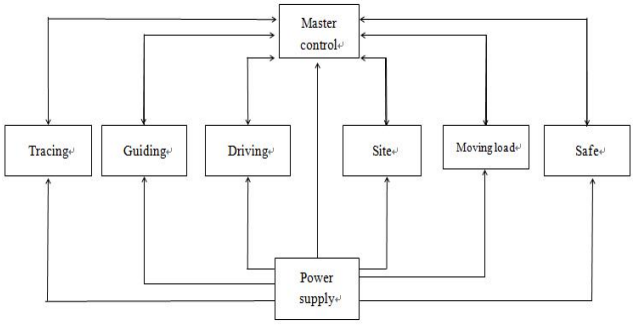

Fig.1 AGV functional block diagram

B.Comparison and determination of guidance modes

Navigation system is the core component of AGV. There are many kinds of guidance modes for AGV. Different guidance modes should be selected according to different application environments. The commonly used guidance modes are electromagnetic induction guidance, optical emission guidance, inertial guidance, visual guidance, laser guidance and magnetic guidance.

Magnetic navigation mainly measures the magnetic field signal on the path to obtain the position deviation between the vehicle itself and the target tracking path, so as to achieve vehicle control and navigation.

TABLE 1 Performance comparison of various sensors in AGV guidance applications

	Electro-magnetic induction	Optical emission	Inertia	Vision	Laser	Magnetism
Range	****	***	*****	****	*****	****
Accuracy	±3mm	±10cm	±1mm	±10mm	±1mm	±3mm
Flexibility	*	**	*****	*****	**	****
Reliability	*****	*	****	**	**	****
Controllability	*****	****	****	**	***	***
Cost	****	*****	*****	*****	***	**

Magnetic navigation has high measurement accuracy and good repeatability. Compared with optical navigation system, magnetic navigation is not susceptible to the influence of light changes. In the course of operation, magnetic sensing system has high reliability and robustness. Once the magnetic strip is laid, the maintenance cost is very low, the service life is long, and it is easy to add and change the path.

Considering the actual cost of production and use, as well as the precision and flexibility of route laying required by the specific sorting environment, the comparison of Table 1 shows that the magnetic guidance method is more suitable for the sorting system of the logistics industry in China at present.

III. Structure and Hardware Design

A.Control object

The structure of AGV in this paper is shown in Figure 2. The AGV body is composed of left and right differential driving wheels and universal wheels. The navigation sensor is installed at the bottom of the front end of the vehicle to detect the offset between the AGV center and the tape track. The command sensor is fixed at the right back side of the vehicle to detect the special command trigger signal. Navigation track is composed of continuous tape, and special command trigger unit is composed of discrete tape segments.

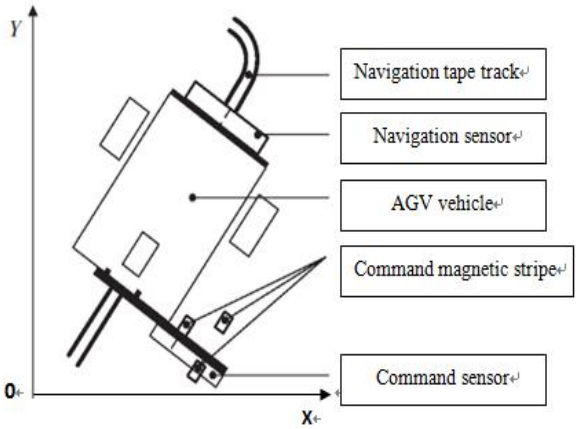

Fig.2 Sketch of AGV

B.Steering gear and motor control

This paper uses Arduino UNO R3 chip to control the steering gear and motor. The core of UNO processor is ATmega328, which has 14 digital input/output ports (6 of which can be used as PWM output), 6 analog inputs, a 16MHz crystal oscillator, a USB port, a power socket, an ICSP header and a reset button.

Arduino development environment has a large number of operation functions, and it is very convenient to program AGV motion control. The control of actuator usually needs a 20ms time-base pulse. The high-level part of the pulse is generally the angle control pulse part in the range of 0.5ms to 2.5ms. The steering gear used in this paper is 180 degree angle steering gear, and its corresponding control relations are: 0.5ms-0 degree; 1.0ms-45 degree; 1.5ms-90 degree; 2.0ms-135 degree; 2.5ms-180 degree. The angle is absolute. The steering gear is installed to keep the front steering wheel of the car at a straight angle of 90. The front steering wheel of the car turns left at 45. The front steering wheel of the car turns right at 135. In order to overcome the errors caused by the mechanical

structure and correct the angle of the steering gear when turning left and right, if turning left to correct, the steering gear will turn to 100 degrees (right).

The motor control module is drawn from the corresponding expansion board of UNO R3. The PWM port on the expansion board controls the speed and the DIR port controls the direction of the motor: high-level motor forward, low-level motor reverse, so as to control the speed. The motor drive function is defined. The module controls the car forward, backward and emergency stop by command.

C.Radio Frequency Identification Devices, RFID

The basic measuring principle of Hall sensor is as follows:

$$U_H = k\frac{IB}{d} \quad (1)$$

Formula: D is the thickness of the sheet, K is the Hall coefficient, I is the control current at both ends of the semiconductor sheet, B is the uniform magnetic field applied in the vertical direction of the sheet, and UH is the potential difference generated in the direction perpendicular to the current and magnetic field.

For the magnetic tracking module, there are switching type and linear Hall sensor. Because the switching Hall ES3144 can't measure the magnetic field accurately, the S49E linear magnetic Hall sensor is chosen in the measurement. After integration, it can output both analog and digital quantities. The digital quantities are similar to the switching Hall, and only distinguish between high and low. When the magnetic field intensity is greater than Bop, the D0 output becomes low level, the indicator light is on, and the analog output port can use Arduino. The serial display in the development environment can see the different voltage values of the specific output (dividing 5V into 1024 parts of the output voltage, and then calculating the magnetic field by converting the output voltage).

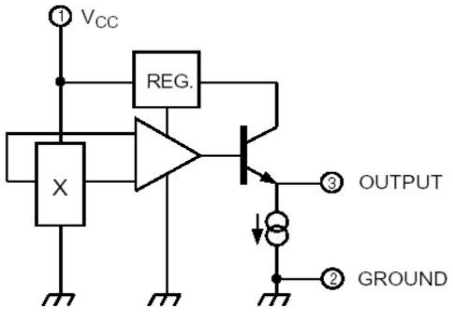

Fig.3 Linear hall sensor schematic

For the RFID module, because the complete equipment of UHF UHF radio frequency identification can only connect the computer to adjust the parameters and then control the reading and writing, RC522 radio frequency identification module and its supporting reading and writing card are used. The device fully integrates all types of passive non-contact communication modes and protocols at 13.56MHz. The internal transmitter can drive the reader antenna to communicate with ISO 14443A/MIFARE card and transponder without any other circuit. The receiver part provides a demodulation and decoding circuit for processing ISO14443A compatible transponder signals. The flow chart of the read-write process after connecting the Arduino main chip is shown in Figure 4 below.

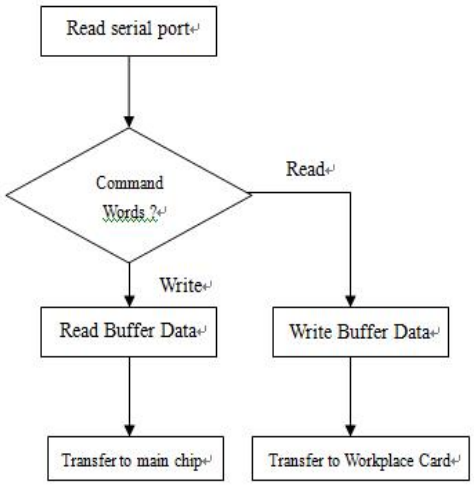

Fig.4 RFID reading and writing flowchart

D.Construction of Loading Platform

AGV cargo dumping side is on the left side. In order to prevent the car from overturning on the left side of the whole center caused by cargo dumping to the left during the process of cargo dumping, the chip, power supply and other loads are placed on the right side of the car, and the left fixed point of the transfer platform is fixed on the left side of the car, so as to prevent the car from overturning.

In this paper, the push rod motor is used to dump the cargo. There are only two positive and negative outlets of the push rod motor. When the voltage is - 12V, the expansion rod extends, that is, to push the cargo loading platform; when the voltage is + 12V, the expansion rod retracts, that is, to drop the cargo loading platform. Different dumping angles correspond to different push rod travel, which is controlled by power supply time. For the error accumulation of incomplete correction that may occur each time when the initial position is returned, the "over-correction" is controlled by retraction time, that is, if the extension delay is 5 seconds and 3 cm, the retraction time is set to 7 seconds, and there is a travel limit switch at both ends of the push rod. After the retraction rod runs to the end or reaches the top, it will stop automatically, thus eliminating the error caused by incomplete correction

IV. Test analysis and conclusion

In order to test the feasibility and stability of the designed AGV control system, the actual field simulation test of AGV is carried out in this paper. In addition to the guide tape, there are also radio frequency identification cards for steering, cargo classification and unloading instructions. The AGV on-board and tape tracks tested in this paper are shown in Figure. 5.

Fig.5 Testing AGV and its magnetic tape track

A.Steering Engine Testing

In the field test of AGV, the steering function is realized by adjusting the steering gear to control the universal wheel. In this paper, the steering accuracy of AGV under different steering angles is tested. Finally, the steering angle with minimum error is determined as shown in Table 2.

Table 2 Steering gear parameter setting

Before / Angle / Now	Turn	Right	Advance / Retreat
Turn	35	35	35
Right	140	140	140
Advance / Retreat	100	80	90

In order to overcome the errors caused by the mechanical structure and correct the angle of the steering gear when turning left and right, if turning left to correct, the steering gear will turn to 100 degrees (right).

B.Magnetic navigation test

Since the magnetic navigation module needs to control the AGV according to the magnitude of the magnetic induction and the output voltage it detects in the subsequent use, the magnetic field in the whole path area is measured, and the data are read and recorded by the serial port monitor in the development environment. Some of the magnetic map data obtained from the measurement are shown in Fig. 6 below. Then, according to the linearity of the sensor and other conditions, the distribution of the magnetic map is plotted in matlab. The magnetic map of the bifurcation path is shown in Figure 7 below.

-4	-3	-2	-1	0	1	2	3
523	524	563	539	538	548	526	525
526	523	551	537	536	558	525	526
549	553	565	554	553	564	557	553
523	524	564	539	538	542	526	525
523	524	541	539	538	550	526	525
549	553	564	554	553	563	557	553
523	524	559	539	538	545	526	525
523	524	561	539	538	552	526	525
525	525	545	533	535	562	525	526
526	524	543	533	537	559	526	525
524	524	565	535	537	562	525	526
525	525	561	537	534	549	526	525
524	523	546	534	535	548	525	526

Fig.6 Partial magnetic map data

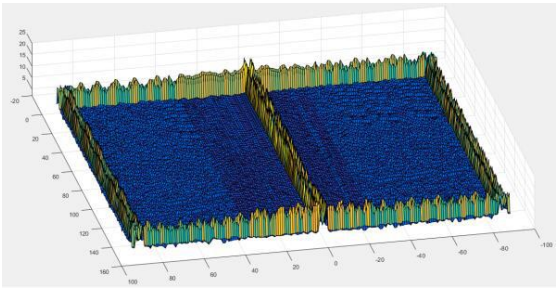

Fig.7 Branch track magnetic map

C.Safety Assisted Unit Testing

Infrared obstacle avoidance sensor has a pair of infrared emitting and receiving tubes. The transmitting tube emits a certain frequency of infrared rays. When the detection direction encounters obstacles (reflecting surface), the infrared rays are reflected back and received by the receiving tube. At this time, the indicator lights are on. After the circuit processing, the signal output interface outputs digital signals. The detection distance can be adjusted by the potentiometer knob, and the effective distance is 2-2. 40cm, working voltage is 3.3V~5V, which can work stably under the condition of large fluctuation of power supply voltage.

Table 3 Distance test of infrared obstacle avoidance

Infrared Barrier Avoidance	Data line	Tissue paper	Board	Person
Sun (cm)	3	15	15	5
Dark (cm)	5	20	20	7

After actual testing and consulting data, it is found that different objects have different detection distances. For small objects and human bodies, the test distances will be reduced. After comprehensive testing, the requirements are basically met.

V. Structure and Hardware Design

In this paper, the traditional AGV guidance, site identification and reloading methods are analyzed, and the overall technical scheme of reloaded magnetic navigation AGV is proposed. The key technologies of magnetic navigation AGV applied to logistics sorting transportation line are studied, including the theoretical analysis and implementation scheme of magnetic navigation technology, the site identification technology based on RFID, and the guidance drive one. The integration unit design and development, loading platform design and development.etc.

The AGV system in this paper has flexible structure, fast action, high efficiency, high controllability and good security. It can fully reflect the flexibility and automation in the automated logistics system, and realize efficient, economical and flexible production. Therefore, the research of this technology has important practical value and broad application prospects.

References

[1] .Beeley P R. Cast steels for tools and dies: a review[J].The Brithish Foundryman，1986, 24(11):441-445.

[2] Naiqi Wu， MengChu Zhou． AGV muting for conflict resolution in AGV systems[A].Proceedings of IEEE International Conferenceon Robotics and AutomationC1.2003：1428—1433．

[3] Seo，Yoonho，Egbelu，Pius Wang Integrated manufacturing planning for an AOV-based FMS．International Journal of Production Economics Volume：60-61，Aprii 20，1999：473·478.

[4] Wang Fuli, Liu Keru. Research and application of precision casting dies [J]. Special casting and non-ferrous alloys. 1996, 20 (3): 24-26

[5] Sun Shuyong. Research on Track Detection Method of Electromagnetic Track Intelligent Vehicle [J]. Journal of Xi'an University of Posts and Telecommunications, 2011, 16 (6): 39-41.

[6] Li Shibo, Ma Xu, Zhuo Qing. Research on Sensor Layout of Tracking Car Based on Magnetic Field Detection [J]. Electronic Products World, 2009, (12): 41-44.

[7] Yin Jiwu. Analysis of Horizontal Detection Coil Characteristics in Magnetically Navigated Intelligent Vehicle [J]. Journal of Shaanxi Institute of Technology: Natural Science Edition, 2010, 26 (4): 18-21. (8)

[8] Zhang Xi, Yang Xuhai, Xue Lingyang. Design of Intelligent Vehicle Control System Based on Electromagnetic Sensors [J]. Application of Electronic Components, 2012, 14 (12): 12-16.

[9] Zhang Limin, Zhang Lele, Liu Yingtao. Research on intelligent vehicle control algorithm based on electromagnetic sensor [J]. Industrial control computer, 2012, 25 (2): 59-60.

[10] Tang Yawei, Qin Yuping. Summary of classification algorithms based on data mining [J]. Journal of Bohai University: Natural Science Edition, 2011, 32 (4): 372-375.

[11] Qin Yuping, Wang Lijun, Liu Wei. Calculating method of average search length of search algorithm [J]. Journal of Bohai University: Natural Science Edition, 2011, 32 (4): 353-357.

Design of intelligent control system of six degrees of freedom manipulator

Meng Xianfeng, Tan Jixin, Long Dajiang, Zhang Dening
(College of instrument Science and electrical Engineering, Jilin University, Changchun 130012, China)

***Abstract*—In order to solve the problem of the multi-degree-of-freedom manipulator function of the factory, the project team proposed a design scheme for simulating a six-axis industrial robot for fast, real-time and accurate control of the mechanical arm to complete the setting action. The program uses STM32 MCU and 24 servo servo controller to design and complete the six-degree-of-freedom manipulator control system. Using Qt Widgets as the development framework, a six-degree-of-freedom robotic arm simulation platform was created using the Open GL interface. In order to facilitate the practical application, a mobile phone app written in Java language and suitable for the Android operating system is designed, and software and hardware communication is performed through Bluetooth. The final experimental results show that the system is stable and can flexibly capture objects within a certain range.**

***Key words*—STM 32; 24 servo steering machine controller; Six degrees of freedom robotic arm; Bluetooth**

I. INTRODUCTION

WITH the advancement of industrial production automation and intelligence, there has been a trend of robots replacing labor on various production lines in China. This has also contributed to the development of the robot industry to a considerable extent, especially the development and use of six-degree-of-freedom robotic arms. Today, robotic arms are used in a wide range of applications in the steel industry, the automotive industry, cargo handling and road traffic. In order to reduce production costs, developed countries and some developing countries around the world are vigorously developing robotic arms. The traditional industrial robotic arm has a single action route and is not flexible enough. To this end, research and development are required in conjunction with six degrees of freedom robotic arms and associated sensors. In this paper, the intelligent movement of the robot arm is realized by designing and developing the small six-degree-of-freedom manipulator controlled by STM32.

II. PLATFORM FUNCTION AND DESIGN IDEAS

A. Overall layout design

The main part of this design hardware is STM 32 MCU and 24 servo servo controller. At the same time, the app written in Java language is used as the control platform. The system working block diagram is shown in Figure 1.

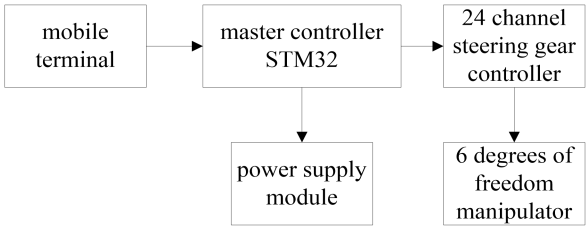

Fig. 1. System work block diagram

B. Mechanical arm mechanical structure

The six-degree-of-freedom robotic arm has six steering gears to control its joints. The steering gear, which belongs to the servo motor, is a position servo drive. It receives the control signal and outputs a certain angle of rotation. The steering gear consists of small DC motor, variable speed gear set, adjustable potentiometer, control board and other components. It is a closed-loop control system suitable for control systems that require controlled angle change and can be maintained in the joints of robots and robots. There are extremely wide applications. The steering gear that controls six degrees of freedom is shown in Figure 2. The steering gear No. 1-3 can be used to determine the spatial position of the robot arm; the fourth is to control the up and down movement of the mechanical wrist, and the fifth is to control the left and right movement of the mechanical wrist, No. 6 The opening and closing of the mechanical claws are controlled, and the three servos determine the posture of the mechanical arm. This kind of distribution is the optimal way of assigning degrees of freedom. Many industrial robots use this form [1].

The design uses 24 servo servo controllers to control the coordinated operation of 24 servos. It can not only realize position and speed control, but also has functions such as delay, send command and breakpoint [2].This control system is mainly composed of the

servo drive controller and the host computer software. By operating the PC software and sending control commands to the controller, individual control or coordinated control of the servo servo can be realized.

Fig. 2. 3-D model of 6-DOF robot

III. Structure and Function Design

A. PWM steering machine working principle

The servo control signal is a PWM signal with a period of 20ms. The steering angle of the servo is linearly changed with the pulse width. The relationship is shown in Figure 3. Each time a pulse of a certain width (0.5-2.5ms) is supplied, its output shaft will rotate to the corresponding angle (0-180 degrees). Only if it is given a pulse signal of other width, it will output another corner and change the angular position of the servo. The steering gear also contains a reference circuit that produces a reference signal. There is also a comparator inside, which compares the input signal with the reference signal to determine the magnitude and direction of the output signal to generate a motor rotation signal [2-3].

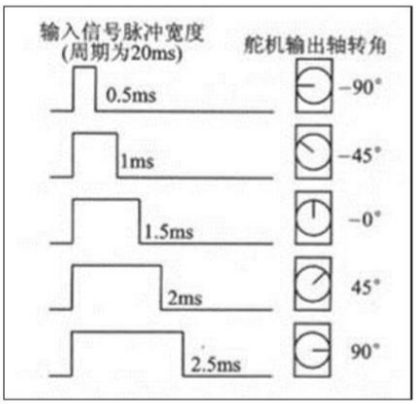

Fig. 3. Rudder output angle and pulse relationship

B. STM32 microcontroller

The STM32 microcontroller is a 32-bit microcontroller from STMicroelectronics, which is also based on the ARM architecture. As a versatile microprocessor with high performance, it has greatly improved speed and resources compared with the commonly used 8-bit 51 single-chip microcomputer. The STM32 has two more timers than the 51 MCU, and there are more external interrupt I/O ports, so the interrupt program processed is more efficient and meets the needs of this design. And 32 MCU has a large FLASH program memory, this memory can be instantaneously erased and rewritten by electricity, and it supports serial program programming.

C. Multi-way servo controller

The servo controller is based on the microprocessor (MPU). In this design, we use the STM32 series chip, which uses multi-channel PWM to realize the signal output to the multi-channel servo controller, and also realizes the communication control with the host computer. [4]. This also applies to systems requiring multiple servos such as robots and other multi-channel PWM systems. The servo control system is mainly composed of a host computer and a lower computer. The user who uses the servo controller does not need to know the internal program. As long as the software of the PC host computer is operated, the robot motion can be debugged and controlled. The user only needs to use the PC host computer to download the robot arm and set related parameters, and communicate with the servo controller through other CPU serial ports to achieve secondary development. You can use the servo controller, which is the implementation of the lower computer source code. Figure 4 shows the communication diagram between the host computer and the servo controller.

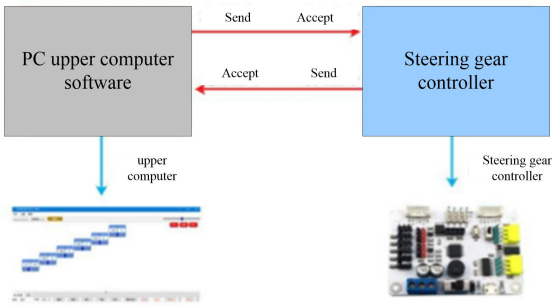

Fig. 4. Communication diagram between host computer and servo controller

IV. Programming and Motion Control

A. Control process

After processing the information collected by the sensor, the STM32 MCU sends and calls the action command in the servo controller through the serial port communication, and the servo controller controls the six-degree-of-freedom mechanical arm to complete the grabbing action. The program flow chart is shown in Figure 5.

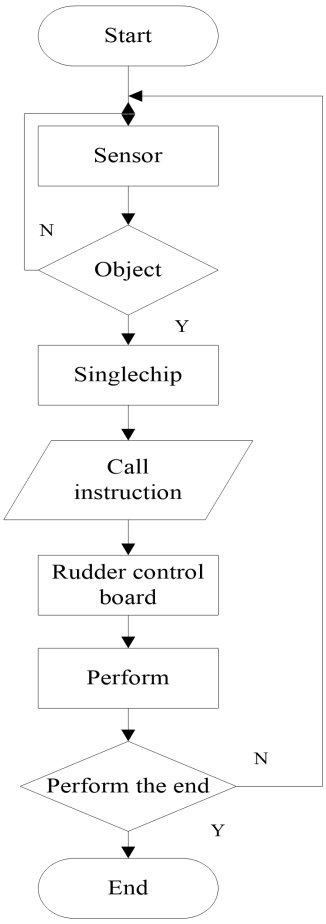

Fig. 5. Control flow chart

B. Trajectory planning

The trajectory planning includes Cartesian space trajectories and general space trajectory planning. Cartesian trajectory planning can express the velocity and acceleration of the manipulator through an analytic function, and then inverse kinematics can be used to solve the information of each joint; the spatial trajectory planning of the joint is planned according to the initial pose and the target pose of the joint. Path to meet the set kinematic constraints and dynamic constraints. In comparison, the Cartesian trajectory is planned to decompose kinematics for each position on the trajectory. Especially for the inverse motion of the redundant manipulator, there may be many situations in the joint angle. This requires a certain rule to select the optimal joint angle. The calculation is very complicated; and the joint space trajectory planning is relatively calculated. The amount is small because there is no need to calculate inverse kinematics. This makes it more real-time, and it is not easy to produce structural singularity problems, so its application is more extensive [6]. The spatial trajectory planning of joints is mainly based on the combination of parabola, polynomial, spline curve and different curves. In practical applications, a cubic polynomial or a fifth-order polynomial is usually used. Obviously, if the trajectory of the joint is planned using multiple polynomials, the higher the number of polynomials, the higher the motion and control accuracy of the orbital planning, but the calculation will be more complicated, so it is not recommended to use too many times. Polynomial.

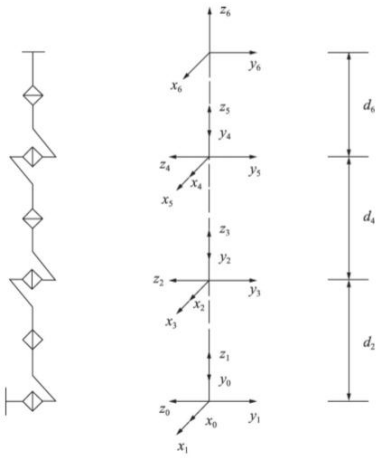

Fig. 6. Arm configuration joint coordinate system

C. Host computer interface design

The host computer of the experimental platform used in this design is developed by Qt Widgets, including communication (serial port), offline simulation, joint space control and other modules and the instantaneous coordinates of the back end of the arm (As shown in Figure 7). This design allows off-line simulation and motion control of the robot arm in different modes. At the same time, the platform's simple and clear interface makes it have good human-computer interaction.

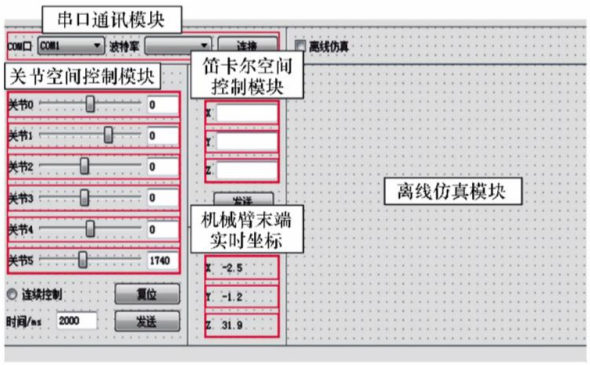

Fig. 7. Qt Host computer interface

Open GL is relatively easy to achieve high-definition real-time 3D simulation, and is gradually being widely used in robot design and motion simulation. It uses modular technology to create 3D models that are more flexible and easier to extend [5-7].Using this graphical development language, build the basic components of the robot and then assemble them together on the platform to implement a three-dimensional model of the robotic arm (As shown in Figure 8). The model of this design can also receive signals from other modules, and the view can be continuously refreshed by a timer, which can achieve dynamic simulation effects. This design model can show the pose of the end effector of the arm and simulate the robot arm to perform the corresponding target such as

grabbing [7].

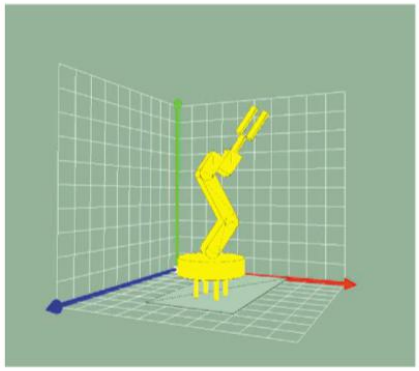

Fig. 8. Robotic arm simulation interface

V. Offline Simulation

The six-degree-of-freedom robot arm has its various joints formed of different shapes, each of which is composed of a plurality of faces. When drawing a 3D model, the faces are drawn first, then the different faces are used to form the corresponding shapes, then the joints are formed by different shapes, and finally the six related joints form the complete mechanical arm.

The spatial position of each joint of the robot varies with the rotation of the joint of the previous stage. In order to achieve the effect of joint linkage, the local coordinate system of the latter joint must be consistent with the previous joint. Call the Open GL library function glPushMatrix() when calling the Draw() interface of the joint, so that the local coordinate system of the previous joint is the current coordinate system.

If this joint happens to be the last joint, you must call glPushMatrix() to release the current coordinate system when the drawing is complete. The final experimental results show that the interface of the Open GL simulation of the robot arm can perform off-line simulation of the robot arm more efficiently. The effect of simulation versus actual operation is shown in Figure 9.

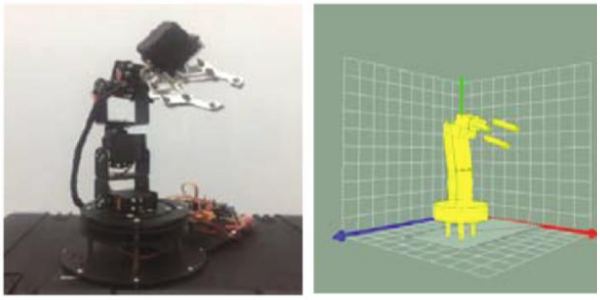

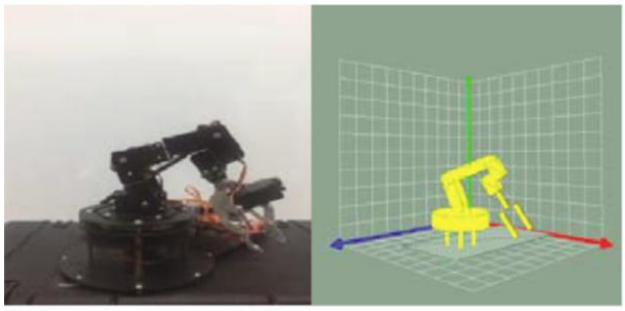

Fig. 9. Mechanical arm 3D model simulation effect comparison chart

VI. Mobile Phone Interface

The mobile phone-side App based on the Java language adopts a graphical interface. After connecting with the robot arm through Bluetooth, the horizontal direction of the joint is dragged to operate the steering direction of the steering gear, which is more convenient than the general human-machine interface. As shown in Figure 11.

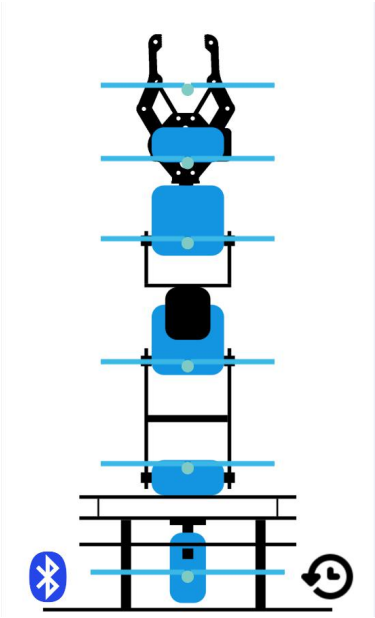

Fig. 10. App interface display

VII. Conclusion

Through the collaborative design of the six-degree-of-freedom manipulator hardware and intelligent control software and hardware, the free movement of the robot arm and the grasping function of the object are realized. This design uses the STM 32 MCU as the main control board to control each joint movement through the 24-way servo controller. The experimental platform PC is developed based on the Qt Widgets framework and has a 3D offline simulation function of the robot arm. Based on the Java language, a mobile app is applied to the Android operating system, so that the operation of the robot arm can be performed on the mobile

end, which is more convenient to use and also provides possibilities for the expansion of the use field.

References

[1] Yuan Yuan. Kinematics and singularity simulation analysis of a six-degree-of-freedom manipulator [J/OL]. Mechanical and Electrical Engineering, 2018(12): 1329-1333.

[2] Deng Xiaoyan, Lin Canguang, Shi Xiangyu, Wu Zerong, Chen Haobin.Construction of 3D Modeling and Simulation Experiment Platform for Five-DOF Manipulators[J].Experimental Technology and Management,2018,35(03):118-122.

[3] Liu Hao, Li Zebin, Wang Benyou. Design of Intelligent Control System for Six Degrees of Freedom Manipulators [J]. Electronic Technology, 2018, 47(10): 70-72.

[4] Li Xianhua, Fan Kaijie, Shu Yang, Zhang Jun. Trajectory planning and simulation of a six-degree-of-freedom modular manipulator [J]. Manufacturing Technology and Machine Tools, 2018(09): 73-77.

[5] 5. Xiao Junming, Han Wei, Wang Wei, Li Jipeng, Liang Wang.Analysis and Simulation of Six-DOF Manipulator Motion[J].Journal of Zhongyuan Institute of Technology,2018,29(04):77-83.

[6] Yun Yang,Song Hua,Xu Bingji.Study on Kinematics Simulation of Six Degrees of Freedom Industrial Manipulators[J].Mechanical Science and Technology,2018,37(08):1167-1176.

[7] Wang Shiyu,Zhai Xianfeng.Development of Five-axis Mechanical Arm Electronic Control System for Double Furnace Reactivity Tester[J].Coal Quality Technology,2017(S1):52-55.

Design of FET Characteristic Tester Based on Virtual Instrument

Chenglong Wang, Hepeng Li, Jiaying Peng
（Jilin university Instrument science and Electrical engineering institute,changchun,130021）

***Abstract*—With the development of electronic technology, semiconductor devices are playing a more and more important role. However, although the traditional measurement method can accurately measure the characteristic curve of FET, the measurement process is very complicated. Moreover, the equipment required for testing is generally very large and can only be placed in the laboratory, which is inconvenient to carry and cannot meet the testing flexibility. Up to now, there is no instrument that can achieve these points. If the virtual instrument measurement can be realized, it can fill the gap in this aspect. The combination of virtual instrument and computer to replace physical testing equipment will greatly promote the development of testing field. It can not only meet the requirements of testing accuracy, but also is a very convenient means to analyze and process data by testing personnel.**

***Key word*—Virtual instrument Field effect tube Characteristic test**

I. FOREWORD

THE invention of transistors is a milestone in the field of technology. Before the advent of transistors, electronic devices used vacuum tubes. Compared with vacuum tubes, transistors have smaller size, lower power consumption and larger magnification. The switch frequency is higher, the reliability is higher, the integration is easy, and the work can be performed without preheating. Due to the advantages of transistors, it has replaced the vacuum tubes that are technically close to the bottleneck. Nowadays, transistors have been widely used in various fields of production and life, and become one of the most important components in the electronics and electrical sciences. A transistor is a semiconductor device that functions primarily for amplification, switching, voltage regulation, rectification, and detection. In a broad sense, a transistor includes all electrical and electronic components based on semiconductor materials, including diodes, transistors, and Silicon control, etc., but usually referred to as transistors are more commonly referred to as triodes. Transistors mainly consist of two major categories: bipolar transistors and field effect transistors. The field effect transistor is abbreviated as a field effect transistor, and is divided into a junction field effect transistor and a metal-oxide semiconductor field effect transistor (Metallic Oxide Semiconductor Field Effect Transistor, MOSFET for short)[1-4]. MOSFETs are divided into N-channel MOSFETs and P-channel MOSFETs, each of which has an enhancement type and a depletion type. JFETs also have N-channel and P-channel divisions, but only depletion type. A field effect transistor is a voltage-type control device that controls a small drain current with a small gate-to-source voltage[5].

Virtual Instrument technology utilizes highly integrated modular hardware circuits and devices, combined with efficient and flexible software to implement the functions of various traditional instrumentation[6]. The concept of virtual instrument was first proposed by National Instruments (NI), which led to a major revolution in traditional instrumentation measurement technology, which made computer technology enter the field of measurement instruments in an unstoppable situation. In the field of electronic measurement, 'software is the first of its kind[7-8]. There are three main components of virtual instrument: computer as the basic carrier; software as the core of the whole instrument; high-performance A / D acquisition and signal conditioning circuit as a key link. Virtual instruments mainly have several advantages: high performance, small size, high integration, flexible organization, strong scalability, and short development cycle of new products[9].

II. DESIGN METHOD

Since the MOSFET is a voltage-controlled device, its base current is very small in any case, and it is meaningless to plot its input characteristic curve, so its transfer characteristic curve is plotted. Figure 1 shows the MOSFET transfer characteristic curve mapping circuit. Ideally[10], the measurement of the transfer characteristic curve requires a constant drain voltage. The current limiting resistor cannot be added. However, if the current limiting resistor is not added, the drain current cannot be measured by the resistor divider[11]. Here, the resistance of R is selected to be 0.1 Ω, the

resistance is small, and the voltage division is small, so that the drain voltage can be approximately considered to be constant. During measurement, CH4 directly collects the gate voltage as the X-axis physical quantity; the difference between CH1 and CH2 is divided by R to obtain the drain current as the Y-axis physical quantity.

The MOSFET output characteristic curve is shown in Figure 2[12]. It is basically the same as the BJT mapping method. The difference is that the MOSFET gate is applied with a step voltage signal. During measurement, CH2 directly collects the drain voltage as the X-axis physical quantity; the difference between CH1 and CH2 is divided by R to obtain the drain current as the Y-axis physical quantity.

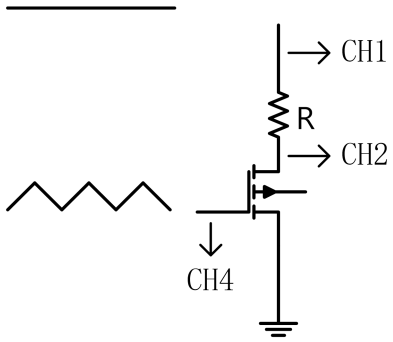

Figure 1 MOSFET transfer characteristic mapping

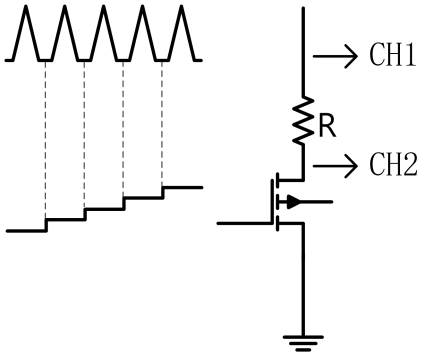

Figure 2 MOSFET output characteristics mapping

The entire test system can be divided into three parts: signal generator, signal acquisition, and graphic display[13].

Signal generator: mainly produces two kinds of waveforms, step wave and triangle wave, and the amplitude is about plus or minus 10V. Generated using a stm32 microcontroller and an external amplifier circuit[14-15].

Signal Acquisition: The acquisition card selected in this design is the Smikehua USB-4220 data acquisition card. This series is for channel synchronous sampling, and the acquisition card has ultra-low noise and high precision. The USB-4220 model has 12-bit resolution and a sampling rate of up to 500K[16-17] , which is sufficient for design needs.

Graphic display: use labview to design the required front panel, and directly display the data transmitted from the acquisition card into a characteristic curve.

III. OVERALL MODEL

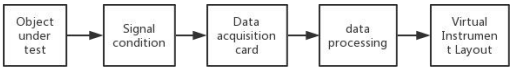

Figure 3 overall model

IV. TEST RESULTS

A. *Signal waveform*

Figure 4 step wave

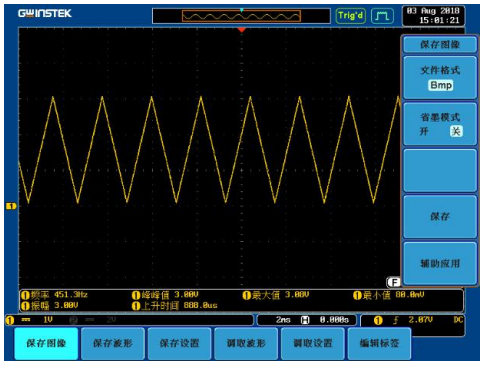

Figure 5 triangle wave

B. *Characteristic curve*

N-channel depletion

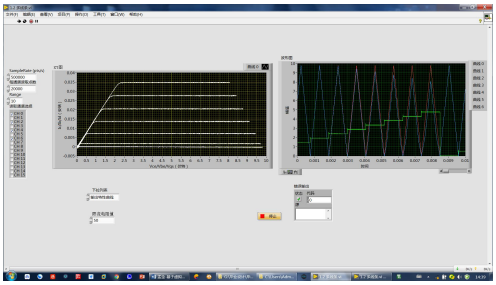

Figure 6 output characteristic curve

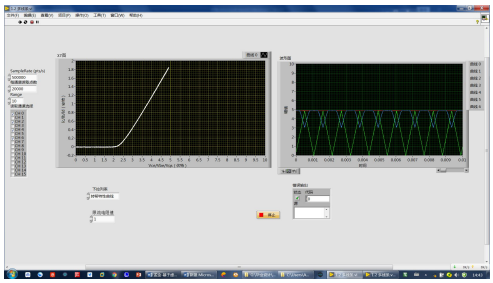

Figure 7 transfer characteristic curve

N-channel enhancement

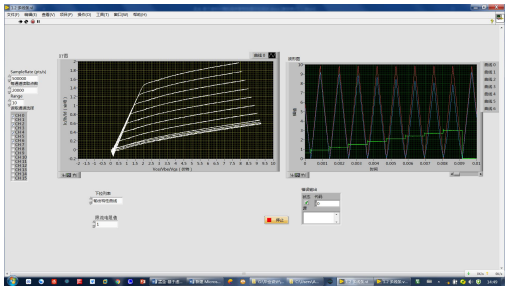

Figure 8 output characteristic curve

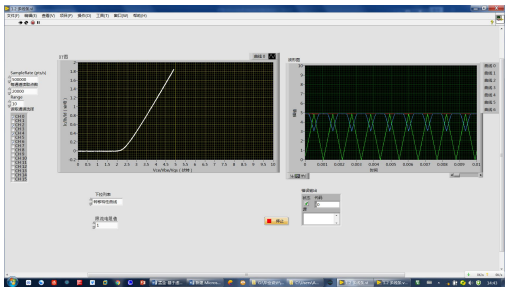

Figure 9 transfer characteristic curve

V. CONCLUSION

Through the design of the VI-based FET tester, the display of the FET characteristic curve is basically realized, but the test accuracy and range need to be improved. The whole test system can also be simplified to make the test more convenient and quick. Meet the accuracy requirements. Thanks to Professor Bingren Zhang for his guidance.

References

[1] Fang Shang-xia.Virtual Transistor Diagram Based on LabVIEW and USB Interface.Chengdu.University of Electronic Science and Technology of China.2006.

[2] LIU Jun.Study on Transistor Characteristic Tester Based on Virtual Instrument [D]. Chongqing: Chongqing University, 2008.

[3] Zhao Zhongyi. Semiconductor tube characteristics of the principle of the instrument, maintenance, testing and application [M]. Beijing: Electronic Industry Press, 1994.

[4] Yuan Yuan,Gu Jun.Virtual Instrument Basic Tutorial[M].Chengdu.University of Electronic Science and Technology Press.2002.

[5] Liu Jun.Study on Transistor Characteristic Intrument based on Virtual Instrument[D].Chongqing.Chongqing University.2008.

[6] Hou Guo-ping,Ye Qi-xin.LabVIEW7.1.LabVIEW7.1 programming and virtual instrument design[M].Beijing.Tsinghua University Press.2003.

[7] Mukesh Kumar，Mansav Joshi，Sanjeev Sharma. Design and Implementation of Embedding Web Server for Real Time Data Acquisition and Logging System[J]. International Journal of Computer Applications,2012,42(11):13-16.

[8] National Instruments Corporation. LabVIEW User Manual. Reference Materials, 2003

[9] DAI Yi-song. Noise of Electronic System and Method of Low Noise Design [M]. Changchun: Jilin People Publishing House, 1984.

[10] Deshpande S G,Jenq-Neng H. A real-time interactive virtual classroom multimedia distance learning system[J]. Multimedia,IEEE Transactions on. 2001,3(4):432-444.

Intelligent infusion speed control system

Hou jie, Lv Chunxu, Zhang Jinwei
（jilin university instrument science and engineering institute,changchun,130021）

***Abstract*—Nowadays, with the rapid development of society and the development of technology, the automation in many aspects of life is getting higher and higher.However, nowadays, there is no automatic system to control the infusion speed automatically to prevent the danger caused by too fast infusion, nor can it realize remote control.Nurses can only adjust the infusion speed themselves, which is not only inefficient, but also limited.Our team aims to finish a system that can automatically detect the infusion speed and detect whether the infusion speed is too fast according to the patient's heart pulse, automatically adjust the infusion speed, finally realize remote control.**

***keywords*—Infusion speed control；Remote control**

I. PREFACE

THE speed of infusion is a key physical quantity in the process of infusion. When the infusion speed is appropriate, the efficacy of drugs can be guaranteed; when the infusion speed is too fast or too slow, the effect of intravenous infusion will be affected, and sometimes even threaten the safety of patients. For some medicines with adverse side effects, the infusion speed should be reduced appropriately, so as to effectively reduce the side effects of medicines on the body of patients. If the speed of intravenous drip is too fast, it will increase the burden of heart and lung, and easily cause problems such as heart failure and pulmonary edema [1-5].

At present, most of our country still adopts the traditional infusion method. Medical staff need to monitor the infusion situation of patients regularly and control the drip rate manually by relying on their own experience and patients' feedback. This method of infusion has the following unavoidable shortcomings: infusion usually lasts for several hours, while patients and medical personnel tend to neglect to observe the infusion during a long process. When the infusion speed is not appropriate or the medicine is about to run out and the situation can not be dealt with timely, it may delay the patient's recovery and even cause medical accidents [10-14].

Li zhe et al., he xiao rong et al., and li hetai et al., all designed their own infusion monitoring equipment or system, all realized the function of infusion speed detection, liquid residual warning, but did not realize the control of infusion speed, can only be used as a monitoring system, speed adjustment depends on the medical personnel. Hui-fang zeng et al. The infusion control system were designed, can realize the less liquid remaining automatic stop infusion, but still not implemented infusion process for the control of the infusion speed, also did not realize the remote control. Compared with other low-cost infusion methods, this system realizes infusion speed monitoring, automatic speed adjustment and remote control, which increases the safety and convenience of infusion and reduces the pressure on medical personnel [6-9].

II. OVERALL SYSTEM PLAN

In order to realize the integration of the system, the STM32 core must be connected with a number of peripherals,including remote communication, information acquisition and control devices, in order to achieve the function of the whole system. The specific functions are as follows:

(1) collect heart rate data and drip rate data through each module and input them into the control core for software analysis.

(2) after the software analysis, change the status sign in the control core, and then output the hardware control signal through the port.

(3) the stepper motor rotation is controlled by hardware control signal to change infusion speed, and data collection is continued.

The overall operation scheme of the above system is shown in figure 1.

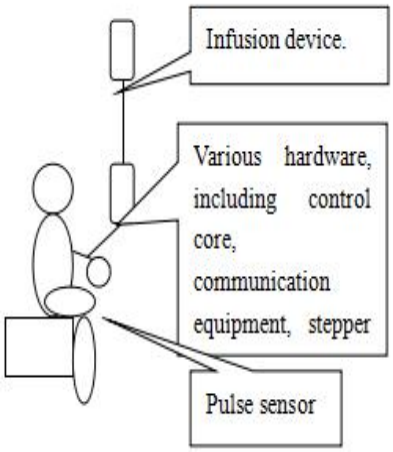

Fig.1 System Overall Scheme

III. SYSTEM HARDWARE IMPLEMENTATION

The whole system should be practical, stability, economic, rapid as the main target. According to various requirements, STM32 chip has the advantages of high performance, low power consumption, high frequency, low price and multiple I/O ports, which makes it more suitable for use as the control core in this system.

Design the hardware architecture according to the overall scheme of the system:

(1)Connecting with mobile terminal through Bluetooth module and remote control.

(2)Connect the droplet velocimeter to detect the infusion speed and display the data.

(3) Connecting the pulse heart rate sensor to detect the patient's heart rate and feedback control the speed.

(4) The rotation of the motor is directly controlled by STM32 and stepper motor driver, and the infusion speed is controlled by transmission device.

According to the above design, the hardware architecture is shown in figure 2.

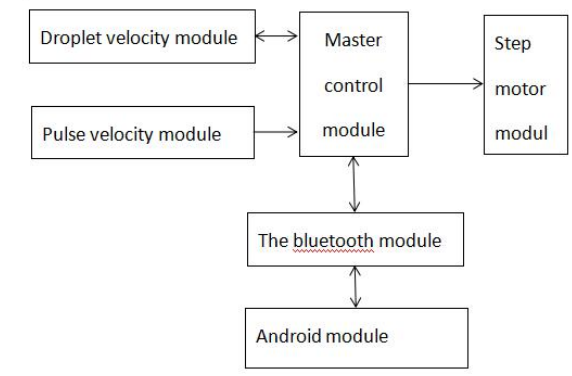

Fig.2 Hardware Structure

Pulse sensor is used to measure pulse and heart rate. The photoelectric volume method is used to measure pulse, which ensures the convenience of measurement, and the measurement accuracy can also meet the requirements when the conditions are satisfied. Pulse sensor pulse heart rate sensor can transmit data only by connecting the S-terminal output to the ADC of STM32. Figure 3 shows the hardware connection of Pulse Sensor.

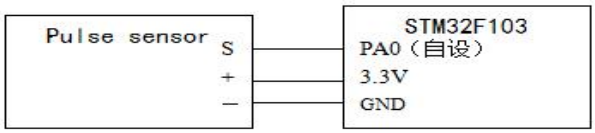

Fig.3 Connection Diagram Of Pulse Sensor

The bluetooth module USES the BT06 bluetooth module, which is a commonly used bluetooth module with high sensitivity in sending and receiving, simple hardware connection, and can be equipped with bluetooth 2.0 protocol. Only four pins need to be connected to complete the communication task, which is more suitable for the connection between STM32 and the mobile terminal of the system. Figure 4 for BT06 with STM32 hardware connection.

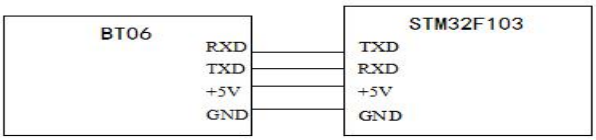

Fig.4 Connection Diagram Of BT06

Stepper motor driven by stepping motor drives for control of a total of only three port, on the STM32 set three I/O port, input square wave respectively, enabling signal and direction control signal can complete control of the stepper motor.

According to the above analysis, the hardware connection is carried out, and the final hardware connection is shown in figure 5.

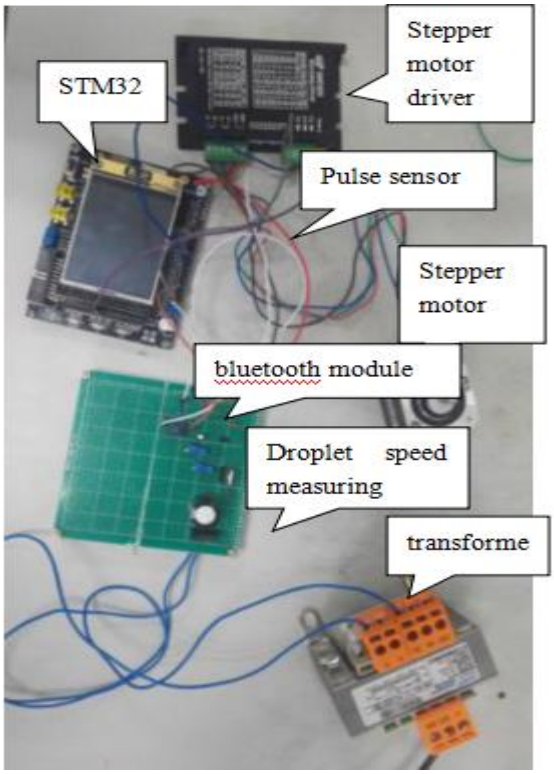

Fig.5 The Picture Of Final Hardware Connection

IV. SOFTWARE IMPLEMENTATION

When the system starts, it sets a target drip speed. After the system starts, it receives drip speed data, heart rate data and data sent by mobile terminal continuously. Whenever there is a data problem, it calls the speed regulating function, drives the stepping motor and controls the drip speed. As long as the infusion is not completed, it continues to receive data and controls the infusion speed according to the requirement until the infusion is completed.

For stepper motor control, in order to accurately control the dripping speed, we finished design of PWM wave frequency and time delay start a stepper motor control program turn a quarter circle.

Pulse sensor can output waveform signals through the serial port. After the collection of STM32, switch is required to convert the human heart rate signal, so as to further monitor the infusion safety.

Setting up the communication between Bluetooth module and STM32, and installing Bluetooth communication software on the mobile terminal or Android platform terminal, the system can be controlled by Bluetooth remote terminal.

According to the above requirements for system operation, the design system flow chart is shown in figure 6.

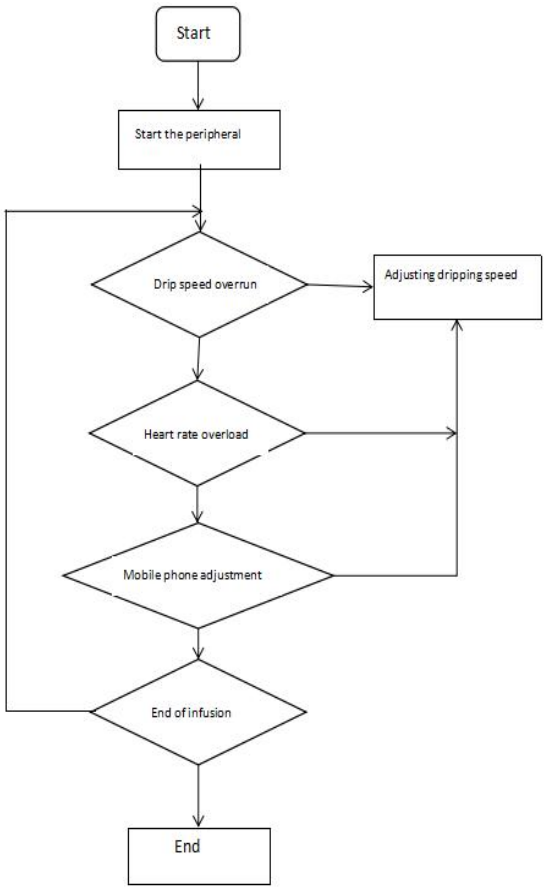

Fig.6 System Flow Chart

V. RESULTS AND CONCLUSIONS

Burn the written software program code into stm32 MCU, place the system in the room, turn on the power supply, open the regulating valve to let the liquid drop drop, and debug and verify the system function.

When the beginning of the whole system run normally, name of the screen above will display system, real-time dripping speed, the default rate of alarm information. Figure 7 shows the LCD data.

Fig.7 Picture Of LCD

Testing process that can be set at a steady speed, when set through a screen or cell rate, equipment can set in a relatively short period of time to adjust speed. In case of emergency, the emergency brake device can brake in a relatively fast time.

On the whole, the accurate measurement and accurate control of injection speed, but at present there are still some problems, control device still need to improve the sensitivity and stability of the equipment and convenience to ascend, and so on.

References

[1] Wang yiwang, design of intelligent infusion monitoring system based on wireless sensor network, measurement and control technology. 2015，NO.11

[2] Diao huimin, application of monitoring system of intravenous infusion in individualized intravenous infusion, journal of nursing.2013,NO.10

[3] Zhang aihua, zhang keping, zhu liang. Research on capacitive sensor for detecting medical infusion level [J]. Sensor technology; 08, 2014.

[4] Wang hong, Yang xiaowen, Chen hongyu, hu June, ni lirong; Investigation and analysis of infusion drop rate problems and countermeasures [J]; Journal of nursing; 21, 2014.

[5] Wang yuanqing; 5. Detection of infusion volume in infusion monitoring system [J]. Measurement and control technology; The year is 2004.

[6] Li zhe, yu xuefei, Chen guangjie, lu guangwen; Design of

infusion monitoring system based on single chip microcomputer [J]. Medical device information; 06, 2006

[7] Zeng huifang, liao neng. Design of medical drop infusion control system based on single chip microcomputer.2006 (08Z)

[8] He xiaorong, wu fuxiang, kong ruodagger, yan qingfu, shen xiaodong. Infusion speed monitoring system.

[9] Li hetai, zhao xin, li xin, xia jiakuan. Development of intelligent infusion monitoring system. Journal of shenyang university of technology.2006, 28 (3)

[10] LinderA.Global.Telemedicine and Telehealth Networks. Journal of Telemedicine andTelecare, 1996, 2 (5):

[11] Carelse X F. An introduction to the industrial applications of microcontrollers[J].Physica Scripta, 2002, 2002 (T97).

[12] Wale J D, Pollock C. Hybrid stepping motors and drives[J].Power Engineering Journal,2001, 15 (1):

[13] Hoffmann W. Computer controlled titration with piston bu rette or peristaltic pump a comparison[J]. Fresenius' journ al of analytical chemistry, 1996 356 (3-4)

[14] Pratondo BUSONO. Design and Implementation of Fuzzy Logic Controller for Peristaltic Blood Pump[A]. Science and Engineering Research Center.Proceedings of 2015 Int ernational Conference on Informatics, Control and Autom ation(ICA 2015)[C].Science and Engineering Research Ce nter:,2015:5.

[15] X.S.Che. A Peristaltic Pump Controller Design with Wirel ess Communication[A]. Science and Engineering Researc h Center.Proceedings of 2015 International Conference on Computer Information Systems and Industrial Application s(CISIA2015)[C].Science and Engineering Research Cent er:,2015:4.

Design of Positioning and Display Module for Three-Component Magnetic Measurement System

Chen Zhonghua
（*College of materials Science and Engineering, Jilin University,Changchun 130022,China*）

***Abstract*—The three-component magnetic measuring device needs a reference direction as the initial reference direction in the measurement. The reference direction affects the measurement accuracy of the system, while the true north direction is a better choice. By combining GPS module, GSM module and benchmarking method, the angle between the measuring point and the connecting line of the benchmarking and the true north direction can be solved, so as to locate the true north direction and improve the measurement accuracy of the system.**

***keywords*—GPS True north direction Benchmarking Three-component**

0. INTRODUCTION

THE three-component magnetic measurement system uses fluxgate sensors to measure the geomagnetic field in wells and to search for deep mineral resources. Firstly, it is necessary to convert the three-component magnetic field value of the well axis coordinate system into the three-component magnetic field value of the geodetic coordinate system. The accuracy of this conversion involves the accuracy of the system's magnetic and gravity measurement, as well as the correction accuracy of orthogonality and coincidence with the coordinate axis[1].

The positioning and display module of the three-component magnetic measurement system designed in this paper is to improve the accuracy in the starting datum direction[2]. The traditional way of measurement is to direct the direction of the north-pointing direction as the reference direction, but it will be affected by the geomagnetic field, not the correct North direction, resulting in errors[3]. The module designed in this paper is to find the correct North direction, so as to reduce the error.

1. OVERALL DESIGN SCHEME

The overall design plan of the positioning and display module of the three-component magnetic measurement system is shown in Figure 1. By using the GPS module based on STM32 development board, the longitude and latitude, altitude, time, satellite and other information of the measuring point can be read out on the display screen of the development board[4]. After GPS gets the information, it sends the information to the system through GSM module. The method of benchmarking is used to calculate the angle between the measuring point and the connecting line of the benchmarking and the correct north direction through GPS information of two points on a measuring point and a nearby benchmarking. At this time, the system will then export this information and send it back to the measuring area through the GSM module, while the people in the measuring area can use the correct north direction as the reference direction to start the measurement of the three-component magnetic measurement system[5].

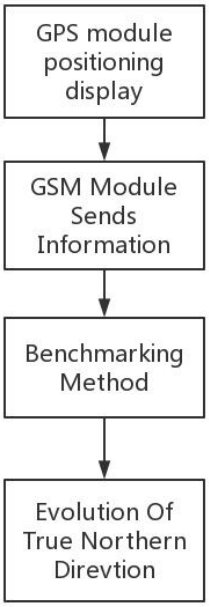

Fig1. Overall schematic diagram of module design

2. HARDWARE CIRCUIT DESIGN

Select to use the ATK-NEO-6M Module shown in Figure 2 for positioning. The GPS module is a high performance module with 50 channels, tracking sensitivity of - 161dBm and measuring output frequency of 5Hz. The module has five controllable

pins: VCC, GND, TXD, PPS, RXD. The design principle is shown in Fig. 2.

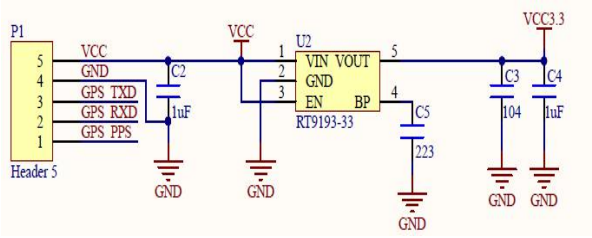

Fig2. GPS Partial schematic diagram

It is driven by supplying 3.3V voltage to the chip. Through two pins TXD and RXD, the measured information is input into STM32 development board. The pin connection diagram of the development board and the GPS module is shown in Figure 3.

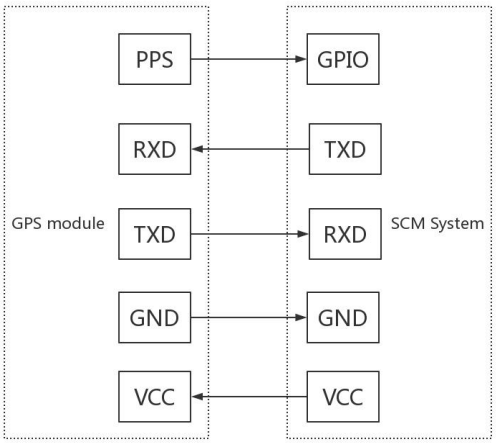

Fig3. Connection Chart of GPS Module and Single Chip Microcomputer Pipe Pin

VCC module supplies power to GPS module, GND grounding, PPS clock control pin, RTD, TXD pin controls information transmission between GPS module and single chip computer[6].

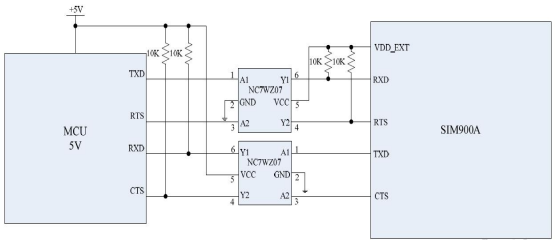

Fig4. Connection Diagram of MCU and GSM Module of Single Chip Microcomputer

Fig. 4 is the connection diagram between the SCM system and the GSM module. Among them, NC7WZ07 chip is designed to supply the 5V voltage converter provided by MCU to the GSM module and make it work. The pin connection mode of GPS module is similar to that of GPS module.

3. SOFTWARE DESIGN

At the beginning of programming, the basic parameters such as baud rate are set, and the GPS chip is activated by giving high-level signals. Then, whether the GPS chip works or not is judged. When the indicator light is on, it indicates that the GPS chip is working normally and data can be transmitted. MCU receives information and transmits it to the display screen. The content program displayed on the display screen makes the next judgement at this time. If the power supply is always in power supply, the display screen will be updated continuously, otherwise the display will stop. Thus the program can realize the function of real-time display of GPS measurement data[7]. The programming block diagram is shown in Figure 5.

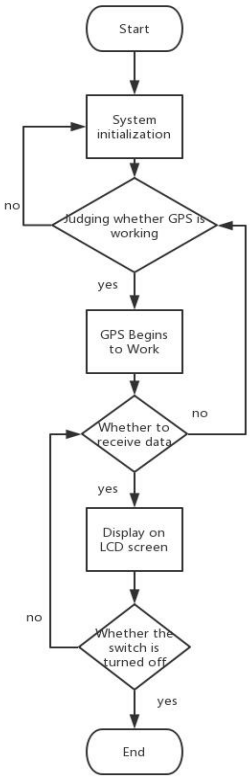

Fig5. Design block diagram of GPS information display

When using GSM module to send information to remote system, debugging software is used. This way of sending information using SIM card is suitable for the situation that there is no network in the field. By debugging the software, input the information to be sent according to the rules and send it. In the system, mobile phones can be used to receive. After obtaining the data, the angle between the angles can be calculated by benchmarking method[8].

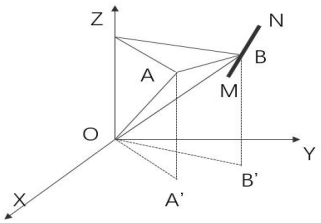

Fig6. Map of GPS and benchmark position

As shown in Figure 6, the programming idea in MATLAB is to ask for the angle between AB and AC in Figure 6. The longitude and latitude of points A, M and N in geodetic coordinate system can be measured by GPS module. Planar intersection of MN at point B and OZ at point C parallel to XOY can be made by point A. Then the coordinates of point C can be calculated by A. By solving the intersection point of plane ABC and MN, the coordinates of point B can be obtained. At this time, the coordinates of point A, B and C are known, and the angle between AB and AC can be calculated. The system sends the calculated results back to the measurement area through the GSM module. After receiving the information, the person in the survey area can begin to measure the three-component magnetic measurement system according to the correct North direction[9].

4. TEST RESULTS AND ANALYSIS

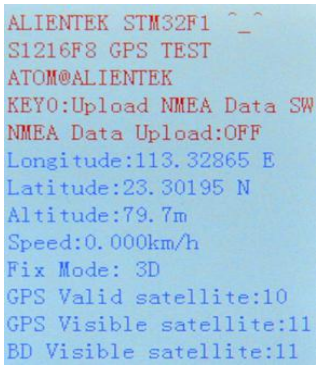

Fig7. LCD screen display

Figure 7 is a LCD display on STM32 development board, which can display the coordinates of the measuring points and other related information.

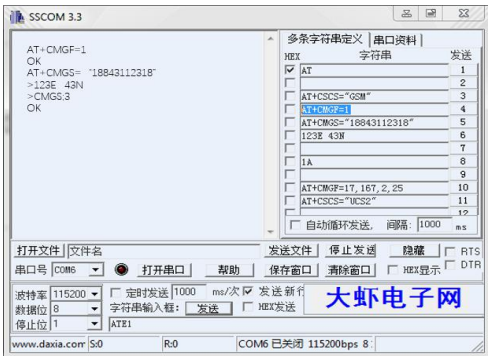

Fig8. Debugging Software Diagram

Figure 8 shows the information transmission diagram of the GSM module. The message 123E, 43N is sent to the mobile phone through the program, and OK indicates that the sending is successful.

Figure 9 shows the coordinates of the measured points and the benchmark, and the calculation results of the angle between the measured points and the benchmark. It can be seen that by inputting point A coordinates (N43.00000, E123.0000), point M coordinates (N43.88155, E125.30003) and point M coordinates (N43.88104, E125.30087), the angle can be calculated to be 62.8240 degrees, which is more accurate than the result of using the North finger pin. But when measuring the M and N coordinates of two points on the benchmark, we can see that there is a little error in longitude and latitude between M and N points on the benchmark perpendicular to the ground, which leads to the error in the angle between M and N points. We can take the method of increasing the number of benchmarks and solving the correct north direction of the measuring points many times to eliminate the error caused by the accuracy of the GPS module itself.

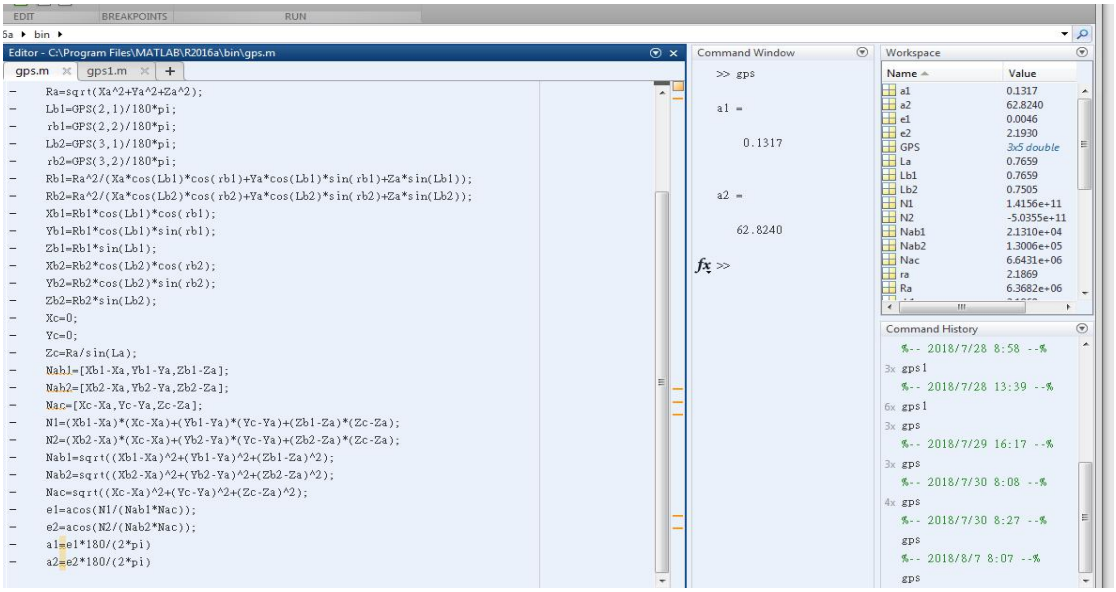

Fig9. Graph of Angle Calculations

5. CONCLUSION

The positioning and display module of the three-component magnetic measurement system introduced in this paper is based on GPS module, GSM module, MATLAB software and STM32 development board. The purpose is to find the reference direction needed by the magnetic measurement system to improve the measurement accuracy. Experiments show that the whole module can achieve the desired results, and the module can be used in non-network areas such as the field. By displaying the coordinates of each measuring point, the correct north direction of the measuring point position can be found accurately, and the reference direction can be found for the three-component magnetic measurement system, which can improve the measurement accuracy. But there are many points to be measured, and the operation can be simplified by more advanced equipment. At the same time, GSM modules and receivers for sending information are needed in both the measuring area and the remote system, which requires a lot of equipment for experiment.

References

[1] Meng Qiang, Xu Hui, Wan Qingmiao. Design of data acquisition and display system based on STM32 [J]. Computer knowledge and technology, 2013, 9 (13): 3183-3186.

[2] Yang Yuanyuan. Design and implementation of three-component geomagnetic field detection system [D]. Southeast University, 2016.

[3] Wang Qingyi, Qiu Gang. High Precision of Three-component Magnetic Survey in Well [J]. Geological Equipment. 2013 (01).

[4] Guo Wenjian, Fengli, Hao Guangcheng. Error analysis and accuracy improvement scheme of three-component magnetic survey in borehole [J]. Land and resources of Shandong Province. 2014 (10).

[5] Edited by Chen Kaizhou. Calculating Method [M]. Northwest Telecommunication Engineering Institute Press, 1985.

[6] Shao Qing. LCD Display Design Scheme Based on STM32F4x9 [J]. Application of Single Chip Microcomputer and Embedded System, 2014, 14 (06): 82-83.

[7] Wang Chenhui, Wu Yue, Yang Kai. Design of multi-channel data acquisition system based on STM32 [J]. Application of electronic technology, 2016,42(01): 51-53+57.

[8] Yao Jing, Pan Ping, Yang Huaijie, Wang Xiuqi. The method of determining the orientation and spatial position of ore body by three-component magnetic survey in borehole [J]. Geophysical and geochemical exploration, 2017, 41 (01): 35-44.

[9] Huang Zongsheng, Wang Shangshu, Qin Shiqiao. Research on high-precision azimuth measurement method based on differential GPS [D]. Journal of Electronic Surveying and Instruments, 2006.

Design of self-balancing sphere robot for finding

Shan-chao Gong, Feng Li, Yi-fan Liu
(College of Instrumentation and Electrical Engineering, Jilin University, Changchun 130012, China)

***Abstract*—Designed a tumbler self-balancing spherical robot with the ability to achieve the acquisition of information around, wireless transmission of data, wireless charging and other functions. The spherical robot can adapt the complex terrain and the radius is about 5cm. In order to control its motion accurately, incremental PID, integration limiting and Kalman filtering algorithms are used. While keeping the center of gravity stable, the white noise of Gao Si can be suppressed, and it can always output the image information from horizontal view. The reliability of collecting data is also improved. According to the text, the robot was able to recover its balance within three seconds of being disturbed. It can also realize the function of multiple cooperative control and super large area searching. And combined with the image acquisition and recognition function of the camera, the object seeking can be realized finally. Moreover, compared with the wheeled robot, the spherical robot has stronger anti-interference ability and higher robustness.**

Keywords—spherical robot; self-balancing; Low power consumption; PID algorithm.

I. INTRODUCTION

SPHERE robot is a kind of robot with special shape that is able to adapt complex terrain environment. Compared with wheeled robot, it has better athletic ability and environmental adaptive capacity, therefore, it has become a research hotspot in recent years [1-2]. In Japan, a sphere robot is designed by Toshiaki Otani who used gyroscope to drive and combining with the principle of conservation of angular momentum. The research of sphere robot in China haven't been long. Beijing University of Posts and Telecommunications developed BYQ-1 to BYQ-4 series robots. Based on two-motor drive under wireless control, the spherical mobile robot could realize omni-direction motion and obstacle navigation [3-6]. But now the spherical robot on the market is mainly aimed at the toy market, which consumes a lot of power, and is too expensive. The practicality of the robot cannot be fully utilized.

This paper presents the design of a sphere robot aimed at object-finding function. The mechanical structure and control circuit of the spherical robot are designed for this robot system. A camera is placed in the middle of the robot to achieve the goal of object finding, which combines the image recognition function and the invariance of the center of gravity of the sphere robot. The sphere self-balancing object-seeking robot has the characteristics of small size, low power consumption, low cost and high practicability.

II. HARDWARE DESIGN

The hardware circuit of the system includes main controller, camera, wireless transmission module, motor drive module, power management module and wireless charging module. BPI-D1 camera supports 1280x720p high-definition image. The capture rate of video is 30 frames per second. It has the advantages of light weight, small volume and supporting WIFI transmission. It can be installed inside the sphere and implement real-time image transmission function over a long distance. STM32F103 produced by STMicroelectronics is chosen as the main controller. It uses Cortex-M3 core and the highest frequency is 72MHz. It can process data quickly and realize multi-sensor data fusion.

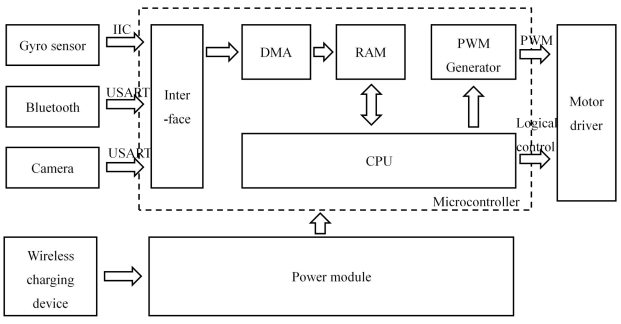

Fig.1. System hardware block diagram.

In order to improve the speed of gyroscope inclination data acquisition, IIC interface is chosen for communication. The highest transmission speed can up to 400 Kbit/s. By using the DMA function in the main controller, the data can be transmitted to the internal RAM directly, which reduces the burden of CPU. The BDI-PI camera transmits the image information to the host computer through WIFI directly. The image processing is completed by the host computer, then the result is transmitted back to the main controller, which

can realize the real-time video monitoring function. The control signal of motors is generated by motor driver. The TB6612 chip of Toshiba Semiconductor Company is selected as the motor driver. In each channel the maximum output driving current is 1.2A. Four modes can be selected by logical control, which makes the switch of motor states easier and more convenient.

The mechanical diagram of the spherical robot is shown in Fig. 2. The whole mechanical structure is divided into three layers. The first layer is composed of control board, including motion control module, data transmission module and other core control modules. Two DC motors are placed symmetrically on second layer and their axis are connected to each other. A rechargeable battery is fixed on the third layer and it connects with control board by wire. The charging coil is also placed on third layer. When the battery is charging, the spherical robot needs to be placed on the charging base. Without opening the spherical shell, the robot can charge under the principle of electromagnetic induction.

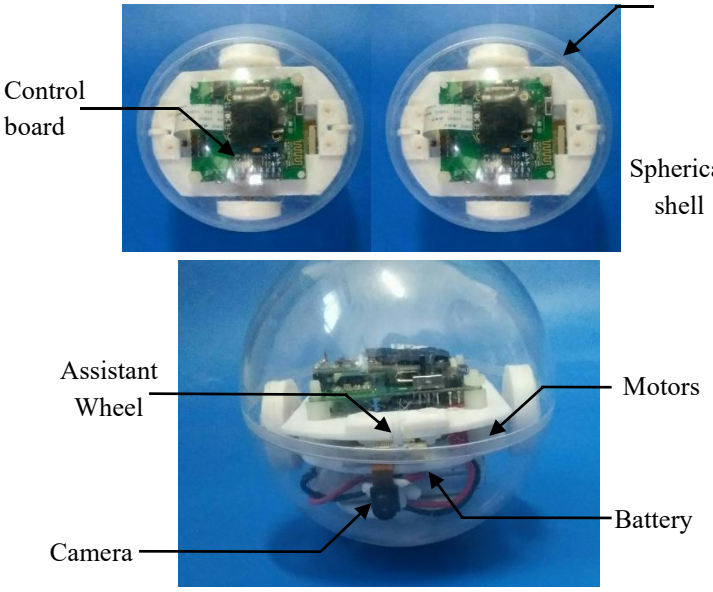

Fig.2 Spherical robot physical map

In the initial state, the spherical robot is in stable state, the barycenter of the system maintains on the central line, which is at the lower part of the system. The built-in wheel point contacts with the spherical shell. When the motor turns to drive the wheel, the wheel rubs against the spherical shell and a turning torque is generated, which moves the spherical shell while the internal device keeps its horizontal state. Thus, the rolling of the robot is realized [7-8].

III. ALGORITHM DESIGN

The primary goal of the spherical robot is to maintain self-balance. According to the design of the actual structure of the robot, the expected state of the system is to keep the roll angle of the robot θ near the expected value θ_0. In response to this situation, this system chooses incremental PID control algorithm [9-10]. A closed-loop system is formed by feeding the data of angular velocity and acceleration, collected by gyroscope in real time to the controller.

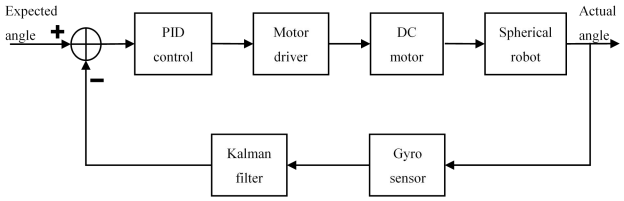

Fig.3. PID control flow chart.

Set the real-time angle data collected by gyroscope as follows $\theta_1,\theta_2,\ldots,\theta_k$, so the current deviation from the expected value is:

$$E_k = \theta_k - \theta_0 \tag{1}$$

Set the historical deviation between the angle data sampled by gyroscope and the setting value as follows: $E_1,E_2,\ldots,E_k$, so cumulative historical deviation, two adjacent deviations and digital PID difference equation are respectively as follows:

$$S_k = \sum_{i=0}^{k} E_i \tag{2}$$

$$D_k = E_k - E_{k-1} \tag{3}$$

$$Q = K_p E_k + K_i S_k + K_d D_k \tag{4}$$

The integral effect exists in the PID controller of the system. Although the static error of the control system can be eliminated, it may cause integral saturation [11]. While the deviation always exists, it is easy to cause excessive integral, which delays the adjustment of integral and makes the overshoot of the system. In order to overcome the saturation of integration, the system chooses the integral limit method. When the integral output reaches the limited amplitude, the operation of the integral term is stopped, and the integral term keeps the output as the limited value.

$$I_{out} = \begin{cases} I_{out} & I_{out} \le I_{max} \\ I_{out} & I_{out} \ge I_{max} \end{cases} \tag{5}$$

Dead zone of the motor rotation is S_q, There is an upper limit Q_{max} for PWM output, so the revised

PWM output value is:

$$Q = \begin{cases} Q + S_q & Q \le Q_{max} \\ Q & Q \ge Q_{max} \end{cases} \quad (6)$$

IV. SOFTWARE DESIGN

The Software flow chart is shown in Fig. 4, in which (a) is the overall process design of the system and (b) is the sub-process design of the balance control.

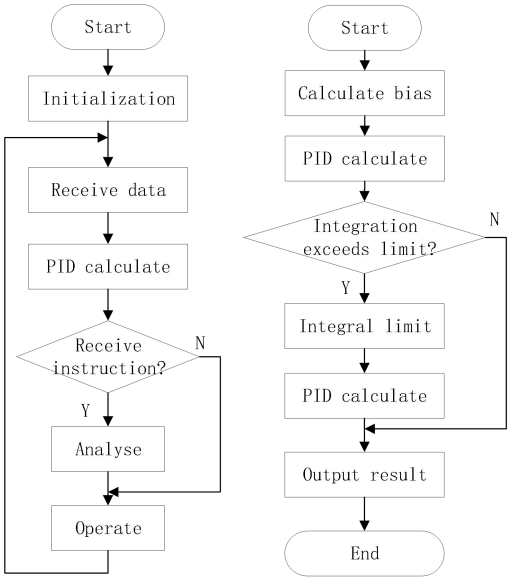

Fig.4. Software flow chart.

After the system is powered on, initialization begins immediately. STM32 completes the initialization of Bluetooth, motor driver and MPU 6050, and BDI-PI completes the initialization of the camera. Firstly, the raw data of the gyroscope are generated, and then the Gauss white noise is suppressed by Kalman filter[12]. The filtered data are compared with the equilibrium point of the sphere structure. If it meets the balance requirement, image data is acquired, image processing is implemented, and the movement of the sphere is under control. If the balance is not reached, the PID calculation is processed to make the sphere reach the equilibrium state. In actual operation, STM32 generates motor drive signal, collects gyroscope data and carries out PID calculation, and receives commands via Bluetooth. BDI-PI collects images and sends them back to PC via WIFI. After recognition, PC sends commands to STM32 via Bluetooth.

V. TESTING AND ANALYSIS

During the test the system is powered on, the spherical robot maintains the initial state of self-balance. When searching for objects, the controller receives action commands via Bluetooth, and the robot executes the corresponding forward, backward and turn actions. The change of pitch angle of the spherical robot is recorded after a period of operation, and the image is as follows:

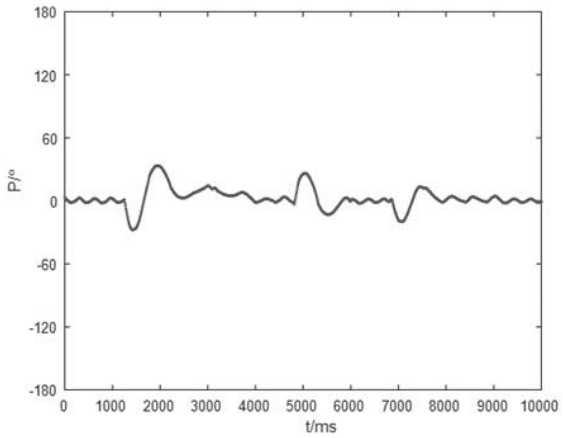

Fig.5. Angle in operating state.

Through many experiments, the maximum deviation angle of the robot when it executes the corresponding action commands in a period of time is obtained via Bluetooth. The experimental data were recorded in the following table:

TABLE I Maximum deviation angle in operating state.

Times	Angle/°
1	12.7
2	33.5
3	20.8
4	26.3
5	14.6
6	11.5
7	13.8

TABLE I (CONTINUED) Maximum deviation angle in operating state.

Times	Angle/°
8	20.4
9	14.9
10	13.2
11	16.4
12	15.3
13	15.7
14	19.5
15	17.1

After calculation, comparing the spherical robot in searching function with the setting self-balancing angle, the average maximum deviation angle is about 17.1°.

When a slight disturbance is applying to the spherical robot, the angle information of the robot during the process of rebalancing is changed as shown in the following figure.

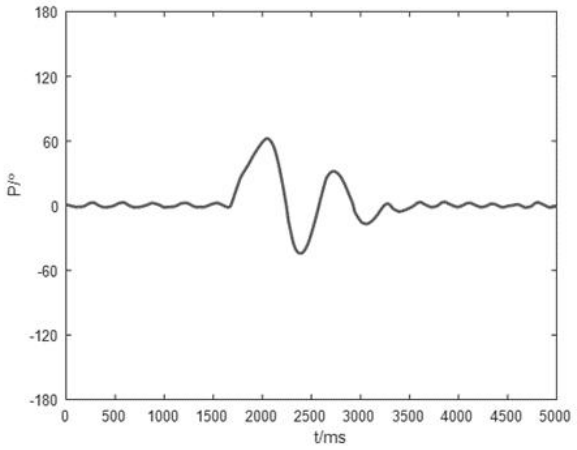

Fig.6. Angle after applying disturbance.

The restoring equilibrium time and the maximum deviation angle of several groups of spherical robots after disturbance are applied. The data are recorded as follows.

TABLE II Restoring equilibrium time and angle change after applying disturbance.

Times	Cost Time/s	Angle/°
1	1.15	12.4
2	1.42	13.8
3	2.25	11.5
4	2.01	12.7
5	2.12	11.6
6	1.75	13.9
7	1.64	23.4
8	1.87	18.7
9	1.17	20.6
10	1.21	14.2
11	1.87	11.4
12	1.42	14.6
13	1.65	17.7
14	1.58	12.5
15	1.98	16.4

After calculation, the average time of restoring equilibrium after disturbance is 1.67 s, and the average maximum deviation angle is about 54.67 degrees.

VI. CONCLUSION

In this paper, a spherical self-balancing object-finding robot is designed. The camera is placed inside the spherical shell of the robot, which can recognize the surrounding objects directionally and transmit the search content to the host computer after finding the target object. The robot designed in this paper is low-cost and high-utility with a radius of about 5 cm for specific tasks. It can restore balance within 3 seconds after being disturbed. Under the background of low efficiency of spherical robot, It has great exploitable market value.

Reference

[1] ZHAO Peng, AN Qiang, Research on a Visual Positioning System for Spherical Robot [J]. Mechanical Manufacturing and Automation, vol.47, no.3, 2018, pp.184-186+193. (in Chinese with English abstract)

[2] LIN Xing-ling, CHEN Jian-yi, Structural Design of a New Kind of Spherical Robot[J]. Combined machine tools and automated machining technology, vol.5, 2015, pp. 104-106. (in Chinese with English abstract)

[3] Otani, T., Urakubo, T., Maekawa S, et al. Position and attitude control of a spherical rolling robot equipped with a gyro[C]//IEEE International Workshop on Advanced Motion Control.2006:416-421.

[4] WAN Yue, YANG Li-jian, Jing Tao, Two-wheel drive spherical robot[J]. Automated application, vol.10, 2006, pp.416-421. (in Chinese)

[5] SUN Han-xu, WANG Liang-qing, JIA Qing-xuan, LIU Da-liang, Dynamic Model of the BYQ-3 Spherical Robot [J]. Journal of Mechanical Engineering, vol.45, no.10, 2009, pp.8-14. (in Chinese with English abstract)

[6] ZHAO Kai-liang, The Kinetic Characteristics And Operational Task of BYQ-4 Spherical Robot[D], Beijing University of Posts and Telecommunications, 2009. (in Chinese with English abstract)

[7] Li Xuan, Development of small multi-purpose spherical unmanned vehicles[J]. Science and technology, vol.14, 2017, pp.32. (in Chinese)

[8] P. Frankovský, L. Dominik, A. Gmiterko, I. Virgala, P. Kurylo, O. Perminova, Modeling of Two-Wheeled Self-Balancing Robot Driven by DC Gearmotors[J]. International Journal of Applied Mechanics and Engineering,2017,22(3).

[9] XIONG Chao-wei, Everett WANG, JIE Yun-fei, ZHI Kai-xuan, LI Xue-yi, Research on Self-balancing System for Robotic Bicycle Based on PID Control[J]. Computer knowledge and technology, vol.14, no.19, pp.274-275. (in Chinese with English abstract)

[10] S. Dettori, V. Iannino, V. Colla, A. Signorini, An adaptive Fuzzy logic-based approach to PID control of steam turbines in solar applications[J]. Applied Energy,2017.

[11] Song Chang-bao, Song Jin-ze, Zheng xiao-yuan, Li

Yi-chen, Li Jun-long, Feng, Lei, Simulation Research of Robot Motion Control Based on Fuzzy Adaptive PID Control[J], Journal of Changchun Institute of Technology (Natural Science Edition), vol.19, no.03, 2018, pp.107-110. (in Chinese)

[12] Liu X, Yu Y, Li Z, et al. A novel constant gain Kalman filter design for nonlinear systems[J]. Signal Processing, 2017, 135:158-167.

Design of Gain and Phase Position Measurement System

Li Zihao, Zhao Shuo, Wang Feng

(College of materials Science and Engineering, Jilin University,Changchun130022,China)

***Abstract*—This system is a gain and phase position measurement system. It includes a signal generator module, a band pass filter module, a gain meter module, a phase meter module and a display module.The STM32 MCU produces a regularly varying voltage, which controls the signal generator module to output frequency periodic sine wave.After the sine wave is adjusted and filtered by amplitudes, the phase meter module is used for waveform transformation and linear phase discrimination to measure phase position .The gain meter module uses the AD637 to measure the signal RMS and pass the data to the MCU, then calculates the gain. The results are displayed by the serial screen.**

***Key words*—phase meter signal generator gain meter**

I. INTRODUCTION

AS a necessary electronic measuring tool [1], digital gain and phase meter have been widely used measurement and detection methods.It use scurrent-coupled, high-impedance input to check the phase difference of the track circuit and the polarity of adjacent segments. Many types of phase meters can be purchased on the market today, but most manufacturers are increasing their accuracy and the price is becoming more and more expensive. Therefore, a simple gain phase meter can be designed to meet the requirements of stability, convenience and digital display[2], low price and measurement accuracy requirements.

II. BASIC PRINCIPLE

According to the workflow of the phase measurement system, the whole system is divided into signal conditioning module, data acquisition and processing module, data transmission and liquid crystal display module, and then divided into modules with single function, and then these modules are designed and debugged separately.

In order to obtain the test signal, the signal generating circuit and the conditioning circuit are designed, which are a signal generating portion and a band pass filter composed of a stm32 and an ICL8038 chip, respectively.

The gain phase meter realizes the reading of the amplitude of different signals, and sets the gain meter to realize the adjustment. The two equal-amplitude signals are transmitted into the phase detecting circuit to obtain the voltage value, and the phase difference is displayed by numerical conversion.

III. THEORETICAL ANALYSIS AND CALCULATION

3.1 The analysis and calculation of Signal generator

3.1.1 Basic principle of signal generation circuit

The signal generator needs to output a wide frequency output range, while the ICL8038 chip has a frequency output range of 0.001 Hz to 1 MHz, and the working change period is wide, and the distortion is low, the frequency drift caused by the temperature change is small, and the use is simple, only need There are very few external conditions, so theICL8038 chip can be used to adjust the frequency of the output signal by adjusting the capacitance and charging current of the ICL8038 chip. After the sine wave output, a voltage divider circuit is connected to achieve voltage regulation of the signal.

3.1.2 Design and calculation of signal generation circuit

Using a single-chip design to output a voltage-increasing signal, control the 8 pin of ICL8038, control the current of the capacitor charge and discharge, thereby controlling the charge and discharge time of the capacitor to adjust the signal frequency, and can realize the signal of 100LZ to 100kHZ frequency gradient of ICL8038 chip output. Then, after the sine wave output is connected to a resistor divider circuit, and a voltage follower is designed with an operational amplifier, a signal circuit with adjustable frequency and voltage can be obtained.

3.1.3 Signal generation circuit calculation

Supply voltage:

In dual power supply, the voltage range of 8038 is V+, V-=±5V~±15V. When V+, V-=±10V, the power supply efficiency is high, the ripple is small, and the output signal amplitude of 8038 is large, so V+ and V-=±10V are designed.

The Selection of Resistance R_A :

$1\mu A < I_A < 25mA$ $5V < V_R < 10V$, so R_A =500Ω

The selection of Capacitor C_2 :

$$V_B - V_A = \frac{1}{3}(V^+ - V^-) \quad (1\text{-}1)$$

That is, V_C changes between V_A and V_B.

Because $V_C = \frac{1}{3}\int_0^t I_C d\tau$ (1-2)

recharging current: $I_C = I_A$, Discharge current: $I_C = 2I_B - I_A$

So $T = \frac{20C}{3}\frac{2R_A}{V^+ - V_B} = \frac{40R_AC}{3(V^+ - V_B)}$ (1-3)

Oscillation frequency: $f = \frac{1}{T} = \frac{3(V_+ - V_B)}{40R_AC_2} = \frac{3(10 - V_R)}{20000C_2}$ (1-4)

Since the frequency is greater than 100 kHz, it can be seen that the 3nF capacitor can meet the design requirements.

3.2 Bandpass filter design and calculation

3.2.1 Principle of bandpass filter

Second-order bandpass filter formula:

$$K(S) = \frac{A_{VP}\frac{\omega_n}{Q}S}{S^2 + \frac{\omega_n}{Q} + \omega_n{}^2} \quad (1\text{-}5)$$

$\alpha = \frac{1}{Q}$ Q is quality factor; is damping coefficient;

ω_n is characteristic angular frequency, It is the center frequency for bandpass and bandstop filters; When $\alpha = \sqrt{2}$, for the low-pass filter, it is the high-frequency cutoff frequency ω_H , For the high pass filter, it is the low frequency cutoff frequency ω_L , A_{VP} is Passband gain （The quality factor is equal to the ratio of center frequency to bandwidth）[3].

3.2.2 Bandpass filter design and calculation

The biquadratic filter circuit has a simple structure and the center frequency can also be adjusted[4], so a double quadratic filter is used. The circuit diagram is as follows:

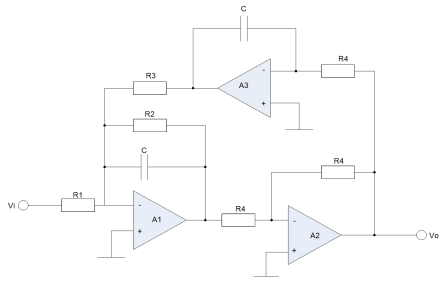

Fig.1 bandpass filter circuit

$$\begin{cases} V_o = -V_{o1} \\ V_{o3} = -\frac{1}{R_4CS}V_o \\ V_{o1} = -(\frac{V_i}{R_1} + \frac{V_{o3}}{R_3})(R_2 // \frac{1}{SC}) \end{cases} \Rightarrow \begin{cases} f_0 = \frac{1}{2\pi C\sqrt{R_3R_4}} \\ Q = \frac{R_2}{\sqrt{R_3R_4}} \\ A = \frac{R_2}{R_1} \end{cases}$$

Centre frequency is 3kHz， bandwidth is 1kHz， Passband Gain is 10db. According to the above formula, the calculation can be obtained:C=0.01uF， R4=10kΩ， R1 is a 10kΩ potentiometer，R2 is a 100kΩ potentiometer and R3 is a 10kΩ potentiometer.

3.3 Design and calculation of gain meter

3.3.1 Principle of the gain meter

Calculating the gain can compare the effective value, peak-to-peak value, and average value. If the peak-to-peak value of the AC voltage is converted into an effective value, the comparison can be measured by the single-chip microcomputer.

3.3.2 Design and calculation of gain meter

The AD637 is a complete high-precision, single-chip rms-to-dc converter. The AD637 chip is used. The AD637 chip can be used to obtain a DC voltage proportional to the rms value of the AC voltage. After adjusting the coefficient, the RMS value can be obtained. Collected into the STM32 microcontroller system, the voltage values are compared to calculate the gain.

The resistance between pin 6 and pin 9 can be seen as a scale factor adjuster, which is located between the VOUT pin and the denominator input pin to reduce the denominator input voltage and thus increase the scale factor of the device.

A resistor connected to pin 4, which is used to fully reduce the scale factor of the rms converter so that when the regulator R1 (approximately) is set at the center of its range, the change of the scale factor is zero because sensitive voltage values and comparisons are required. For small currents, choose a larger 50kΩ potentiometer and connect a protective resistor in series.

3.4 phase meter design

3.4.1 Principle of the phase meter

When measuring the phase, the waveform is first converted into a high-low-level rectangular wave circuit,

and the exclusive-OR operation of the circuit is realized by the trigger design. The high level obtained by the exclusive OR in the actual circuit is equivalent to taking out a pulse signal, and the width of the pulse signal is divided. The phase difference of the signal can be obtained by performing the radians operation in cycles.

3.4.2 Design of the phase meter

The shaping circuit composed of the zero-crossing comparator can convert the sine wave into a square wave signal. By using the capacitor charging and discharging effect, the square wave can be converted into a sharp pulse, and the diode can filter out the negative half-axis signal. In order to realize the circuit comparison function, R4 The difference from R5 is large, and 100Ω and 200kΩ are selected respectively.

The hysteresis comparator is then used to convert the pulse into a square wave. This circuit consists of an op amp with the forward side of the op amp.

Adjust the reference voltage and reverse the input signal. When a pulse large enough is encountered, the waveform jumps and the pulse signal is converted into a rectangular wave. Then the rectangular wave is subjected to third-order passive filtering to obtain the effective value, and the voltage value linearly related to the phase is obtained, and the scale coefficient of the two can be obtained by fitting the data.

IV. HARDWARE CIRCUIT DESIGN

4.1 signal generator circuit diagram

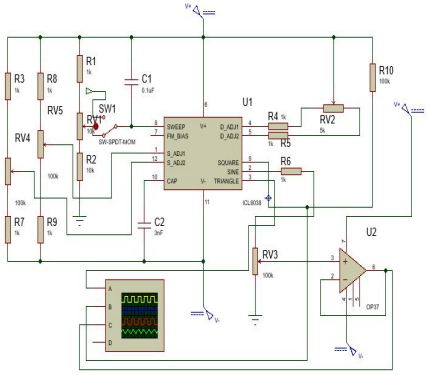

Fig.2 Signal generator circuit

Connect a switch at the 8 pin in the figure. You can choose to adjust the frequency by the sliding rheostat or directly control the voltage with the STM32 microcontroller system D/A.

4.2 Gain meter design block diagram and circuit diagram

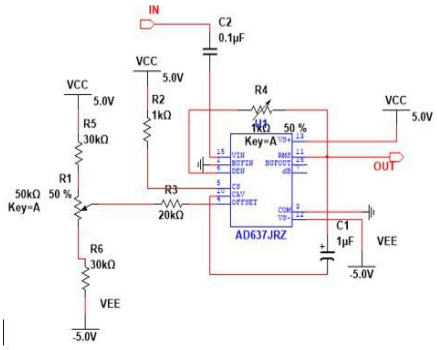

Fig.3 gain meter circuit

Using the AD637 chip, the chip measures the effective value of the signal and uses the STM32 A/D channel acquisition for data processing.

4.3 phase meter design block diagram and circuit diagram

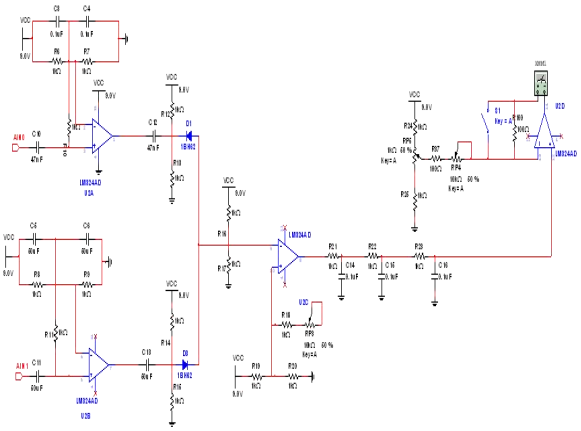

Fig.4 phase meter circuit

The sine wave is converted into a square wave by two op amps, and the phase is phase-detected by the capacitor and the circuit built by the diode and the operational amplifier. The phase can be read by the effective value of the final output waveform, so the waveform is low-pass filtered and will be read. The data is passed to STM32 to convert the phase[5].

4.4 overall system block diagram

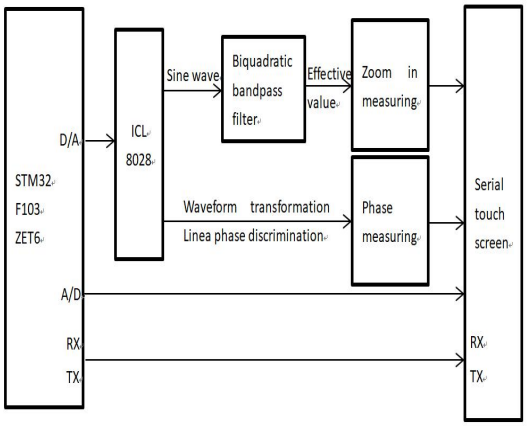

Fig.5 system block diagram

V. TEST PLAN AND RESULTS

5.1 test plan

Powered by a DC power supply, the signal generator provides an input sine wave, the oscilloscope observes the output waveform detection signal generator and the bandpass filter portion; it is powered by a DC power supply, and the oscilloscope is used to observe the output. The measurement bandpass filter is partially displayed. The gain measurement gain meter is displayed. And the phase meter section[6].

5.2 Test results

Signal generator module: adjust the slip: 97Hz-103kHz; program control: 200Hz-120kHz.

Table1 bandpass filter circuit test result

Center frequency /Hz	Center frequency/Hz	Passband gain/dB
3k	1.002k	10

Table2 gain meter and phase meter test result Table

frequency/Hz	gain/dB	phase/
1k	-20-+20	-90-+90
30k	-20-+20	-90-+90
60k	-20-+19	-90-+90
100k	-20-+19	-80-+75

5.3 Analysis of results

It can be seen from the test results that the whole system can realize the functions of phase discrimination and measurement gain, but there are also some disadvantages. For example, the signal generator program control part is stepped by 10Hz, but because the correspondence between voltage and frequency is not linear, it cannot be accurately achieved; because the high frequency characteristic of the LM324 is poor in the phase meter, the rising edge of the waveform is not steep enough. When the frequency is high, the linear phase discrimination result is wrong; the phase meter part has different capacitive reactance at different frequencies, so the phase value of the high frequency signal measurement also has an error.

References

[13] Kang Huaguang. Electronic Technology Foundation·Simulation Part (Fifth Edition) [M]. Beijing: Higher Education Press, 2006.1.

[14] Ma Qungang. Principle and Design of TFT-LCD [M]. Electronic Industry Press (first edition), 2011.12.

[15] Chang Yimin, Dai Yongsheng. Design and implementation of high harmonic suppression LTCC filter[J]. Journal of Functional Materials and Devices, 2018, 24(03): 169-173.

[16] Chen Shaorong, Liu Yulin, Wang Kai, Xu Wei. Design of IIR digital bandpass filter based on Chebyshev type I low-pass filter[J].Communication Technology, 2019, 52(01):1-10.

[17] Liu Sijie, Xu Min, Zhang Chenyu, Zhao Yali. Temperature and Humidity Measurement System Based on HMI Intelligent Serial Screen Display [J]. Science and Technology Journal (late), 2018 (08): 59-60+84.

[18] Joseph Yiu. The Definitive Guide to the ARM Cortex-M3 [M]. Beijing: Aerospace University Press, 2009.

Design of Ball Rolling Control System based on PID Algorithm

Yan Fuxue, Li Qingyan, Hao Xin

（Jilin university College of Instrumentation & Electrical Engineering,,changchun,130021）

***Abstract*—In this paper, the rolling ball control system is designed and implemented, and the overshoot of the moving ball is calculated by establishing the PID model and simulation, which provides important theoretical support for the regulation of the program. This design adopts orthogonal rocker ARM support structure, uses OpenMV to collect image information and calculate the position of the ball, the controller handles the position information, uses the position PID to judge and output the PWM wave, then controls the steering angle of the rudder, so that the ball reaches the specified position and realizes the problem requirement. After the test, the system can control the ball in 7 seconds on the plate to achieve rolling to the specified position and stability.**

***keywords*— Positional PID OpenMV Auto-control**

I. INTRODUCTION

WITH the requirements of the control system, especially the improvement of control accuracy, the camera is indispensable for high precision control according to real-time information, which is of great significance for automatic control and large-scale mechanical production[1-2]. Cricket system is a kind of complex open-loop unstable system, which can provide a solution for nonlinear problems in practical problems, introduce PID regulation, and realize closed-loop control with camera.

The rolling ball control system is a system based on the 2017 Nations B entitled Foundation. It can control where the ball stops anywhere in the smooth plate or draw a fixed graphic. According to the requirements of the topic, the camera is used to capture the image, and the image is processed in real time to obtain the position of the ball movement, the controller according to the location information, in the x-axis and y-axis direction respectively according to the PID algorithm adjustment output PWM wave, two rudder rotation and drive the plate in two directions independently tilt the corresponding angle, The ball scrolls toward the target point.

II. OVER ALL SYSTEM DESIGN

The control system can be controlled by the tilt of the plate, so that the diameter of not more than 2.5cm of the ball can be specified according to the side length of 65cm smooth square plate to complete a variety of actions, and from the beginning of the action after the timing of the display, in seconds. 9 circular areas with an outer diameter of 3cm evenly distributed on the plate, numbered 1~9, and the position is shown in Figure 1

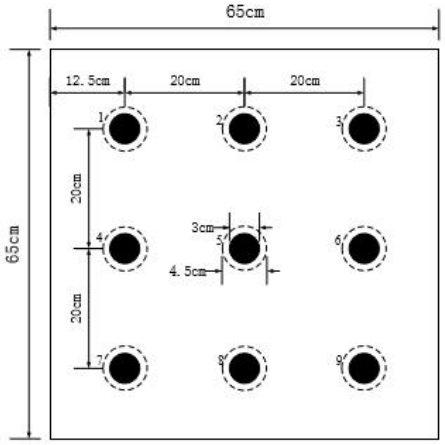

Fig.1 Plate Position Distribution Diagram

The whole system is divided into 4 subsystems: Acquisition system, execution system, power supply system, control and processing system. The overall block diagram of the system is shown in Figure 2.

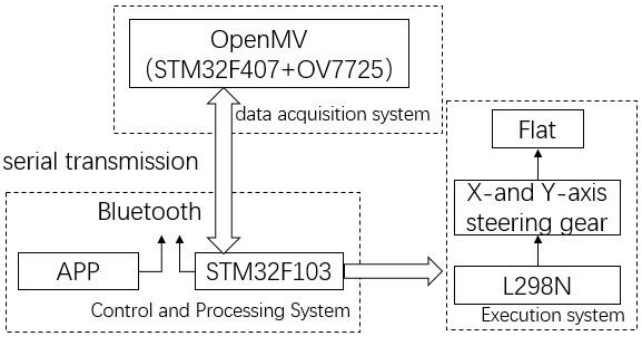

Fig.2 System general block diagram

In the process of controlling the movement of the ball2, use OpenMV1 to obtain the position information of the ball and pass through the serial port to the STM32f103 controller. In the controller, the current position of the ball

is compared with the target position, the output of different PWM waves, and then the rudder becomes different angles, the plate inclination changes, thus forming a closed feedback loop to achieve the system requirements. The OpenMV1, which captures the image itself, is equipped with a STM32F407 chip that can be captured and processed, with a lens OV7725 frame rate of up to 60FPS on it, in order to make the real-time better, the grayscale graph is used to capture the pellet image [3-6]. Using STM32F103 series single-chip microcomputer as the control chip, the single-chip microcomputer controls are more complex, and the internal timer, IIC，SPI interface and other resources are abundant, the operation processing speed is fast, very suitable for the real-time control of the system. The rudder has the characteristics of large torsion, low cost, fast response speed and small jitter, so long as the appropriate control information can be achieved to achieve the system requirements.

The hardware design of the system focuses on the control of the tablet3. In this system, the lightweight wood strip is fixed diagonally in the bottom of the plate to ensure the flattening of the plate. Upright supporting rod5 is used in the middle to make the center of gravity of the plate easy to control. Adjacent sides with servos4 fixed, the other side of the use of spring6 buffer, plate and rudder and support between the universal joint con-nection7, fixed support rod so that the plate center of gravity does not offset, control is simpler[7]. Its hardware architecture profile is shown in Figure 3.

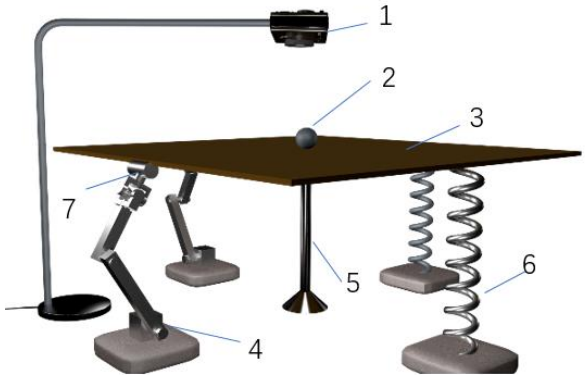

Fig.3 Schematic diagram of hardware structure

Note：1-OpenMV；2-ball；3-tablet；4-servo；5-supporting rod；6-spring；7-universal joint

III. HARDWARE ARE DESIGNED ON THE SYSTEM

A. Calculation of orthogonal rocker ARM support data

A simplified schematic diagram of the system is shown in Figure 4, and the plate with the ball motion is set to a square plate with a edge length of 65cm, with a smoother surface. In order to achieve the ball can do directional movement on the flat plate, in the lower plate below the edge of the vertical placement of a rudder, each rudder installed by acrylic material made of the rocker arm to the plate for a single direction of lifting, thus changing the flat and horizontal inclination, and then give the ball acceleration to move. The current length of R of the rudder connector in the rudder rotation led to draw a circle, angle a with a certain range of changes, requiring a maximum angle of 30°, there is the following formula:

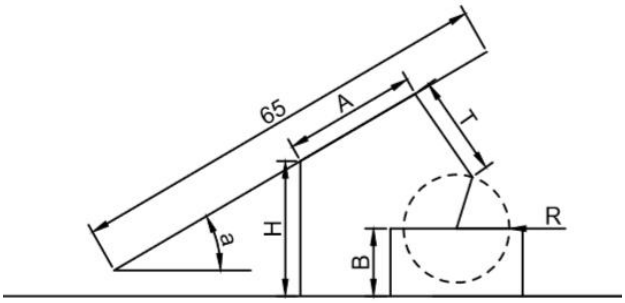

Fig.4 System Axial Model

$$(B+R+T-H)/A=\sin 30° \quad (1)$$

$$(H-B-T+R)/A=\sin 30° \quad (2)$$

On account that the tablet cannot touch the ground, we get

$$\sin 30°*L/2<H \quad (3)$$

Thus T=12cm,H=20cm,A=20cm,B=10cm,R=8cm.

B. Calculation of positional PID

In order to complete the task of the specified movement of the ball, it is necessary to continuously change the inclination of x and y direction of the two rudder and accept the position information from the camera feedback back to the ball, and then make the appropriate adjustment, and finally bring the motion state closer and stable, so the PID algorithm can be selected to complete the conversion of feedback to the control amount.

The PID controller includes two forms: position type and incremental formula, and the position PID is calculated by the current state and the past state difference, such as inverted pendulum. Incremental PID is the calculation of the amount of control increment for integral related components, such as stepper motors. Because of the reatime change of rolling ball coordinates and the use of rudder control, the system adopts position PID algorithm to adjust the stability of the system more advantages. The formula looks like this:

$$u(k) = k_p e(k) + k_i \sum_{i=0}^{k} e(i) + k_d[e(k) - e(k-1)] \quad (4)$$

Among them, K_P is the coefficient of the proportional element of the controller, and the increase of K_P will

increase the response speed of the system, reduce the steady state error and improve the control accuracy. However, if the General Assembly leads to a reduction in the stability of the system, the stability of the system is destroyed, resulting in increased oscillation. Simply putted, for a rolling ball system, K_P is the system's response to the difference between the current position of the ball and the previous position, the larger the K_P, the same displacement of the ball, the greater the plane inclination, the advantage is that the ball response speed will be very fast, but the disadvantage is that the ball is more difficult to control.

K_I is the coefficient of the integral part of the controller, which is related to the steady state characteristics of the system, but if the integral coefficient reduces the stability of the system and causes the system oscillation when it is serious, it will sometimes use the integral link to add the proportional link to the coordinated adjustment [8]. This coefficient is not used to adjust in this rolling ball control system. K_D is the coefficient of the differential item of the controller, its main feature is the dynamic control effect, can speed up the dynamic response, usually with the proportional link with the use of PD adjustment, so that the system into a stable state as soon as possible [8]. In this rolling ball control system, this parameter is responsible for controlling the time to enter the steady state, that is, when the ball tends to stabilize the position, because of the deviation effect, will make the ball in the preset position near the constant movement is to produce oscillation, the appropriate adjustment parameters can reduce the oscillation at the same time so that the ball gets into a stable state faster.

The control chart of PID is as follows：

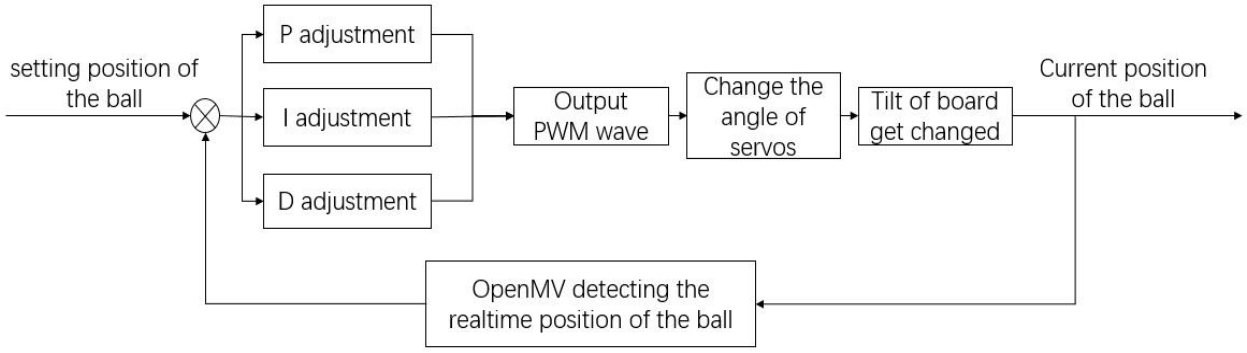

Fig.5 PID flow block diagram

IV. SYSTEM SOFTWARE DESIGN

The whole system collects and processes the position of the ball through OpenMV, and sends it to STM32 MCU to output PWM wave to control the servos through PID algorithm; Bluetooth remote control microprocessor of mobile phone to choose the movement mode of the ball. The current position and movement time of the ball will be displayed on OLED display screen for easy observation. Each part is designed as follows:

1) OpenMV image acquisition: OV7725 is used to capture the image, and STM32F407 is used to process the image. OpenMV is programmed by Python to select gray model to distinguish the sphere from the plate and the surrounding environment. It also lock the threshold of recognition range and the size of the capture object, so as to prevent the mistaken acquisition of objects outside the flat plate or some other objects that can cause interference. After the acquisition is completed, X and Y coordinates are sent to the serial port of MCU for further processing.

2) Control of the servos: After the ball is processed by serial communication, the PWM wave is output by the PID algorithm to control the steering gear's inclination. The servos in both horizontal and vertical directions can work at the same time to make the ball move unilaterally or obliquely. In practical system, because the working plate is not absolutely flat, the PWM wave required by the servos may be different when the ball is stable in each position of the plate, so it is necessary to test the data of each point in order to provide data for the displacement difference in the PID algorithm.

3) Bluetooth remote control function: use Bluetooth module to pair with the mobile phone. When pressing the corresponding button on the mobile phone, the serial port of the controller can receive the data sent by the mobile phone. Press the signal generated by different buttons to specify the system to complete different functions, including the basic part and the play part of the game.

4) OLED display part: The X and Y coordinates of the small ball sent from OpenMV will be displayed on the OLED screen, and the time of executing the task will be displayed at the same time.

Fig6 is the main program flow chart. When pressing the button, it detects the status of the button and achieves the corresponding functional requirements. The process is as follows: OpenMV detects the trajectory of the ball, after processing, outputs PWM wave to control the servosrotation angle, and OpenMV detects the status of the ball movement and determines whether it reaches the designated area. If not, continue to adjust the steering until it reaches the designated area.

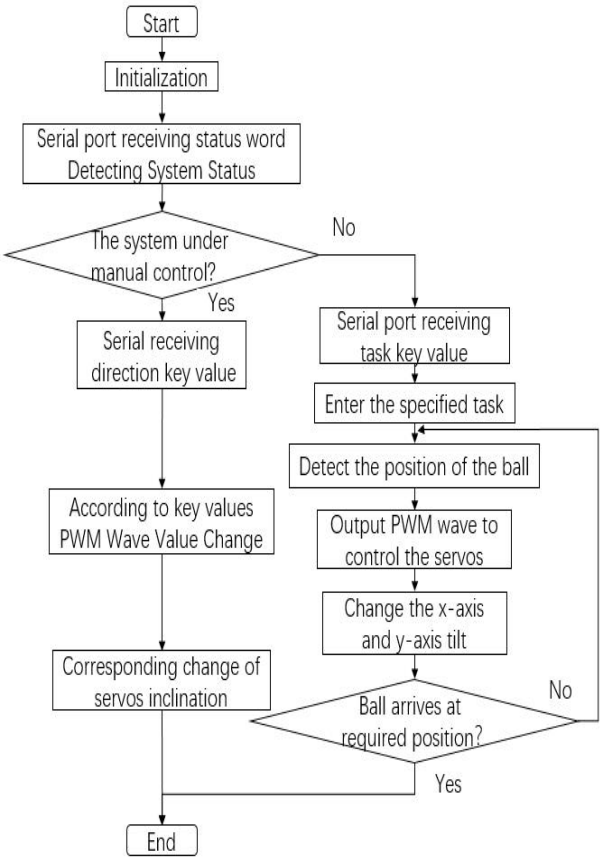

Fig.6 System flow block diagram

V. CONCLUSION

Before measurement, signal generator and DC regulated power supply are used to detect whether the servos is working properly, and oscilloscope is used to detect whether the output of PWM wave is normal. During the measurement, the stopwatch was used to measure the movement time and residence time of the ball, and the experimental results were observed.

1) The stability time test results from the surrounding points to the central point are shown in Table1 (time in s).

2) Draw an octagon with a diagonal length of 40 cm. The test results are shown in Table2(time in s).

Table 1 Test data of the basic part

T P	1	2	3	4	6	7	8	9
1	5.29	5.40	5.66	4.06	5.23	6.48	5.43	4.77
2	7.13	7.57	6.30	5.81	3.40	6.40	5.95	6.35
3	5.34	6.32	5.48	5.60	4.48	5.89	6.15	5.43
4	5.45	5.96	5.78	4.97	3.79	6.17	6.24	5.32
5	5.89	5.75	6.74	5.17	4.93	5.76	4.37	6.48
Avg	5.82	6.21	5.99	5.12	4.36	6.14	5.63	5.67

P. S.: P is the target; T is the number of times

Table 2 Test data of the extra part

Type	1	2	3	4	5	Avg
Time	41.40	39.81	40.90	41.58	38.91	40.72

After testing, the system can fully meet the requirements of the indicators. OpenMV is used to collect the position information of the ball and send it to the controller. After processing by the controller, the PWM wave is output to control the tilt angle of the servosand change the direction of the plate so that the ball reaches the designated position. In 7 seconds, the ball can reach the designated position from any position on the board, and its error is within ±5 pixels. The ball motion detection and processing are completed by parameter calculation, and the control algorithm and driving mechanism are implemented.

References

[1] Liu Baomin, Fang Shibo, Zhao Haibo, Geng Chunli. Design of ball rolling control system [J]. Electronic technology and software engineering, 2018 (12): 114.4654

[2] Design and Implementation of Rolling Ball Control System by Lu Fang, Zhang Chenhe and Zheng Hao [J]. Electronic Technology and Software Engineering, 2018 (12): 129.

[3] Su Jingya, Fan Penghui, Cai Kaiyuan. Nonlinear PID attitude control of quad-rotor aircraft [J]. Journal of Beijing University of Aeronautics and Astronautics, 2011, 37 (09): 1054-1058.45

[4] Mark Lutz. Learning Python, Forth Edition[M]. Beijing: Machinery Industry Press, 2009.1

[5] He Yu. Edge Detection and Algorithmic Analysis of Image Based on Python Language [J]. Computer Products and Circulation, 2018 (06): 147.545

[6] Liu Jie, Jiang Qinhong. OpenMV-based search car [J]. Electronic technology and software engineering, 2018 (14): 74.456

[7] Wang Dong. Theoretical analysis and experimental study on stability bearing capacity of fastener-type steel tube formwork support [D]. Tianjin University, 2009.

[8] Wang Chunmin, Luanhua. Continuous and Discrete Control Engineering [M]. Beijing: Beijing University of Posts and Telecommunications Press, 2015.8

[9] Wang Shuyan, Shiyu, Feng Zhongxu. Control method research based on fuzzy PID controller [J]. Mechanical Science and Technology, 2011, 30 (01): 166-172.

[10] Zhang Shiqi. Design and Research of Fuzzy Self-tuning Cascade PID Cricket Control System [J].Automation Technology and Application, 2019,38(01): 1-4.

Design of a Simple Gain Phase Meter

Sun Yubing, Geng Yingyi
（jilin university the college of instrumentation and electrical engineering ,changchun,130061）

***Abstract*—This design is based on the simple gain phase meter of item E of the 2017 college students electronic design competition in Jilin province. It consists of a signal source, a band pass filter, a gain meter and a phase meter. The controller displays the gain characteristic curve and the phase frequency characteristic curve of the signal. Signal source part of the manual adjustment of the signal frequency, with automatic frequency sweep function. The band pass filter can partially achieve the required center frequency, bandwidth and gain within the allowable error range. The phase meter consists of waveform transform circuit, phase detector circuit and low pass filter circuit. By the determination of phase difference within the range - 90 ° ~ 90 ° measurable, error is about 1 °, gain within 20 dB ~ + 20 dB measurable, the error of about 0.001 dB.**

I. INTRODUCTION

PHASE meter is an instrument to measure the phase difference between two signals of the same frequency[1]. The earliest research on phase is in mathematical vector analysis, physical circular motion and physics. With the development of electronic technology and computer technology, phase measurement technology has gradually matured[2]. Traditional phase meters are based on analog electronic technology knowledge to achieve the purpose of simple phase measurement.

This design is based on the principle of RMS detection, filter and phase detection.

II. Test Method and Scheme

A.Design of Signal Source Module

Digital function signal generator mostly uses DDS technology to produce sine wave, square wave and triangle wave.[3][4] Because of the requirement of the subject, DDS chip is forbidden to be used in this design, so single chip computer and function signal generator are used to realize sine wave output of different frequencies. ICL8038 chip adopts advanced technology such as Schottky barrier diode, can produce sinusoidal wave from 0.001 HZ to 300 kHz, and has the advantages of low frequency drift and low distortion.

B.Design of Phase Shift Measurement Circuit

By using phase-voltage conversion method, sinusoidal wave is shaped into square wave, and rectangular wave can be generated by phase detector. Its duty cycle is proportional to the phase difference of input signal, and the voltage value obtained by low-pass filter is proportional to the phase angle, thus realizing phase-voltage conversion [5].

C.Design of Gain Measurement Circuit

The peak-to-peak detection circuit is composed of AD637 integrated detector chip and RMS detector to measure gain. AD637 is a true RMS response power detector with a wide detection range and a maximum non-linear distortion of (+0.25dB). It has the advantage of measuring any complex RMS without considering waveform distortion and low power consumption[6][7][8].

D.Design of Bandpass Filter Circuit

Biquadratic band-pass filter and operational amplifier with high voltage swing ratio are used to adapt to high frequency. Biquadratic circuit adopts sliding rheostat to adjust central frequency, bandwidth and gain.[9]

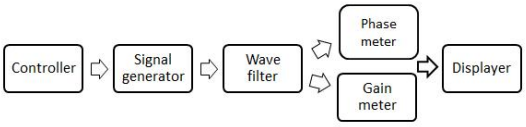

Figure 1. System block diagram

III. Circuit Design

A.Design of Signal Source Circuit

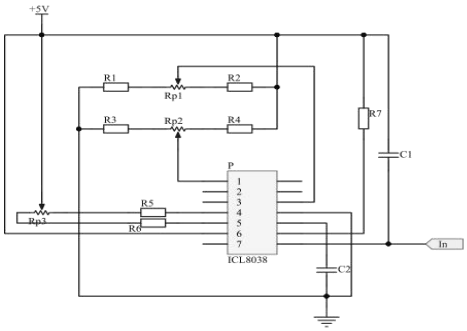

Figure 2. Principle diagram of 8038 signal generator

MCU controls ICL8038 to output sinusoidal wave of different frequencies by output sawtooth wave of certain amplitude and frequency through DAC0832, realizes automatic scanning with certain step length,

and realizes manual setting of step length of 10 Hz by key control.

In order to make ICL8038 work properly, the input voltage VP of 8 legs should be between 5V and 10V, and the input current should be between 1muA and 1mA. Therefore, it is necessary to ensure that the resistance RA of four legs is 5.1k and the oscillation frequency is:

$$f = \frac{1}{T} = \frac{3(10 - V_P)}{40 R_A C} \tag{1}$$

In order to make the frequency meet the requirements of the subject 100 Hz to 100 kHz, the capacitance C should be less than 7nF; in order to make the scanning frequency step satisfy 10Hz, the minimum difference of input voltage is 0.00476V.

B.Design of Bandpass Filter

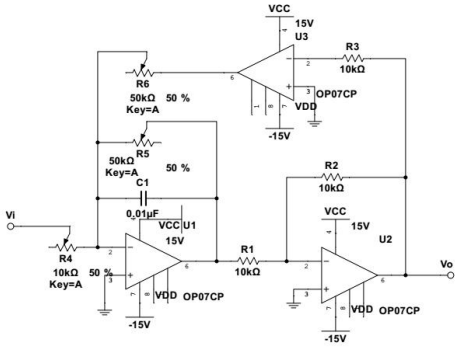

Figure 3. Schematic diagram of biquadratic bandpass filter

The bandpass filter circuit is shown in Figure 3. Operational amplifier OP07 is used to construct a bandpass filter. Potentiometers are used to regulate the performance of R4, R5 and R6.

The transfer function of the bandpass filter is:

$$K(S) = \frac{A_{vp}\frac{\omega_n}{Q}S}{S^2 + \frac{\omega_n}{Q}S + \omega_n{}^2} \tag{2}$$

By comparing the circuit schematic diagram with the transfer function of the filter, it can be obtained that:

$$V_O = -V_{O1}; \tag{3}$$

$$V_{O3} = -\frac{1}{R_4 sC} V_O \tag{4}$$

$$V_{O1} = -(\frac{V_i}{R_1} + \frac{V_{O3}}{R_3})(R_2 // \frac{1}{sC}) \tag{5}$$

By introducing the transfer function, we can get:

$$f_0 = \frac{1}{2\pi C\sqrt{R_3 R_4}} \tag{6}$$

$$Q = \frac{f_0}{BW} = \frac{R_2}{\sqrt{R_3 R_4}} \tag{7}$$

$$A_{vp} = \frac{R_2}{R_1} \tag{8}$$

In order to meet the requirements of the title, C = 0.01 F; R4 = 10k; R3 = 2.814 k; R2 = 15.9 k; and R1 = 5.033 K are selected.

C.Circuit design of AD637 geophone

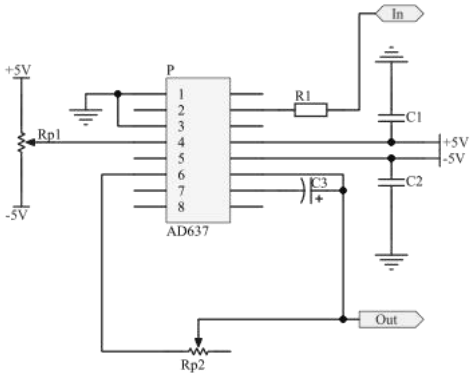

Figure 4. Schematic diagram of biquadratic bandpass filter

The RMS detection circuit is shown in Figure 4. The output value of the two geophones is sent to ADC for voltage acquisition, and the gain value is displayed on the display after internal processing.

D.Design of Phase Shift Circuit

After shaping sinusoidal wave into square wave, impulse signal is generated by differential circuit, rectangular wave is obtained by hysteresis comparator, DC component is generated by seven-order passive low-pass filter and sent into ADC for voltage acquisition[10][11], and phase value is displayed on display.

Pulse amplitude: Pulse height at 500 Hz is (6.8, 3.4). Through hysteresis comparator formula:

$$V_{T+} = \frac{R_1 * V_{ref}}{R_1 + R_2} + \frac{R_2 * V_{oh}}{R_1 + R_2} \tag{9}$$

$$V_{T+} = \frac{R_1 * V_{ref}}{R_1 + R_2} + \frac{R_2 * V_{ol}}{R_1 + R_2} \tag{10}$$

Two resistance values can be calculated.

IV. Test Results and Comparison

A.Test plan

1. Two signals with different peaks and phases are output by signal generator. Gain measurement device and phase measurement device are connected respectively, and current gain and phase value are displayed by display screen.

2. The frequency of sinusoidal wave generated by

self-made signal generator is tested by oscilloscope, and the reading step is adjusted and displayed by keys according to the frequency reading before and after keys.

3. The gain characteristic curve and phase characteristic curve of the filter are tested by the oscilloscope, and compared with the display curve of the display screen.

B.Test Result

Table 1. Partial Test Results of Bandpass Filters

Center Frequency /Hz	Bandwidth /Hz	Passband Gain /dB
2.98k	1.03k	10

Central frequency error: 0.6%; Bandwidth error: 3%; Passband gain error: 0.

Table 2. Gain meter and phase meter test results

Frequency /Hz	Gain /dB	Phase /°
100	-20-+20	-90-+90
20k	-20-+20	-90-+90
100k	-20-+20	-90-+90

Signal frequency range: 100Hz-106 kHz; Step: about 1kHz

C.Error Analysis

1. Based on the above test data, the following conclusions can be drawn:

(1) The work achieves the functions of phase measurement and gain measurement, but the indicators are slightly inadequate. The accuracy of the phase meter is about 1 degree.

(2) The scanning frequency range of the self-made signal source is 100Hz-106 kHz, the step is 1kHz, and the scanning measurement time is less than 2 minutes.

2. Existing problems and improvement measures:

(1) The rectangular wave generated by the phase detector in the phase-shifting measurement device has a problem with the DC component after the active low-pass filtering, which can be eliminated by passive low-pass filtering, and then the influence of the subsequent load can be avoided by connecting the voltage follower.

(2) AD637 RMS detection circuit can eliminate the influence of DC component by zero resistance and improve the accuracy of gain measurement device.

V. Conclusion

In the process of analog circuit design, phase detection and gain detection are very important contents. There are many methods for phase detection and gain detection. This design can generate signals with its own signal source in a larger frequency range, and can measure phase difference and gain more accurately. It is convenient to carry. Combining theory with practice, it enhances the design ability of analog circuit. and the ability of comprehensive practice and innovation.

References

[1] Zhang Xiang. Design and Realization of High Precision Phase Meter Based on FPGA [J]. Digital Technology and Applications, 2016, (02), 151-152

[2] Wu Zhirui. Research and Design of Digital Phase Meter [D]. Harbin: College of Underwater Acoustic Engineering, Harbin Engineering University, 2009:1-80

[3] Meng Fanping. Design and Implementation of Digital Signal Source [D]. Nanjing: Nanjing University of Posts and Telecommunications, 2018:1-76

[4] Shang Yalei, Yu Jun. Design of function generator based on ICL8038 [J]. Technological innovation, 2017, 65-135

[5] Gao Jixiang. Electronic Instrument Design [M]. Beijing: Electronic Industry Press, 2007.6

[6] Alan. V. Oppenheim, Alan. S. Willsky, S. Hamid. Nawab. Signalsand. Systems, Second. Edition [M]. Beijing: Electronic Industry Press, June 2009

[7] Kang Huaguang. Basic Simulation of Electronic Technology [M]. Wuhan: Higher Education Press, 2013

[8] Guo Zongping. Design and Implementation of Peak Detection Circuit in Signal Acquisition [J]. China Testing, 2011, 37 (3): 63-88

[9] Zhang Ya, Huang Keping. Design of Active Analog Bandpass Filter [J]. Electronic Science and Technology, 2009, 22 (1): 9-12

[10] Ren Guanzhong, Ning Yonglan. Phase measurement technology [J]. Electrical measurement and instrumentation, 1990, 9:41-60

[11] Wu Chun'e, Wei Tingcun. Discussion on A/D [J]. Science and Technology and Engineering, 2007, 7 (9): 1882-1898

Design of Simple Phase Meter Based on Operational Amplifier

Shen Mengxian, Liu Qiankun, Yan Yan
（jilin university instrument science and engineering institute,changchun,130021）

***Abstract*—Operational amplifier Linear phase detector circuitAbstract: Phase is one of the basic measurements in electrical signal measurement, so phase measurement is essential in circuit signal measurement. In this paper, the hardware circuit is used to realize the phase measurement by a quad op amp chip LT1814CS and related peripheral circuits. After testing, the scheme realizes the detection of the phase difference of the signal by the ammeter, and can detect the lead lag state of the phase difference. By fitting the test result, the phase difference between the measurement result and the input signal has a good linear relationship.**

***Key words*—Operational amplifier Linear phase detector circuit Phase measurement**

I. INTRODUCTION

PHASE measurement is one of the basic measurements of electrical signal measurement and is widely used. Usually, digital circuit logic gates, single-chip microcomputers and FPGAs are used to measure the phase, but the cost is high. Besides, the result of the phase detection circuit output is the absolute value of the phase difference, so the lead or hysteresis characteristics of the phase need to be judged separately, which is very inconvenient and error-prone. The phase difference between the output voltage and the input signal is non-linear, and requires later data processing, which also causes a large error in the measurement results. In this paper, the analog circuit is used to fabricate the phase meter. The waveform of the sinusoidal signal with different input phases is transformed into a square wave signal [1]. Then, the linear phase-detection circuit is input to obtain a square wave signal corresponding to the phase difference, which is transformed by passive filtering. After the DC component, use a multimeter to measure the phase difference between the two input signals. The phase meter circuit designed in this paper is simple in circuit, low in cost, small in size, and easy to operate. It is convenient and quick to detect and read the phase difference of two sinusoidal signals only through a four-operating amplifier chip and multimeter.

II. DESIGN PRINCIPLES AND SOLUTIONS

The principle of phase measurement is based on the time interval measurement method. The difference time width of the two signals is taken out as a voltage pulse by differential processing, and the phase difference between the two signals is expressed by the duty ratio of the pulse in the entire pulse sequence. After converting the sinusoidal signal into a square wave signal , the phase is calculated by measuring the duty ratio of the square wave after the square wave signals A and B are subtracted [2-3]. The formula is:

$$\Delta\varphi = 360^{\circ} \cdot \Delta t/T \tag{1}$$

The overall design of the phase meter is shown in Figure 1. After the two sinusoidal signals are converted into square waves by the waveform conversion circuit, they are converted into pulse signals by the differential circuit, and the positive signals of the diodes are used to obtain the positive signals of the two pulse signals. The pulse and the negative pulse are converted into a square wave signal after the hysteresis comparator. Then, the DC component is retained by the passive low-pass filter, and the voltage-current conversion circuit is used to adjust the phase difference between the two signals by the potentiometer. Finally, output a significant proportional relationship of the current signal.

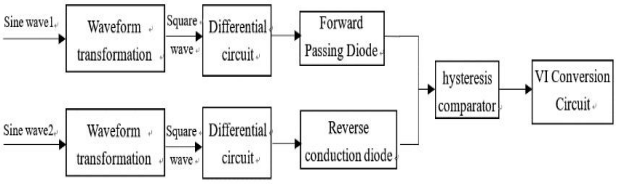

Fig.1 System overall design block diagram

III. SYSTEM THEORY ANALYSIS AND CALCULATION

A. Analysis of Waveform Conversion Circuit

The two sinusoidal signals generated by the signal source with the same frequency and different phases, through the zero-crossing comparator, can be converted into two square-wave signals with phase difference. When the sine wave voltage is greater than 4.5V, a square

wave is obtained at the output end. In the positive direction part, when the sine wave voltage is less than 4.5V, the square wave voltage is less than zero. This facilitates the measurement of the phase difference of the signal, and the circuit is simple and sensitive.

B. Analysis and calculation of linear phase detector circuit[4-6]

The square wave signal is differentiated into a sharp pulse signal after being differentiated by the differential circuit. The two pulse signals are respectively passed through diodes placed in opposite directions in two directions, and the upper pulse signal and the lower pulse signal are respectively retained by the principle of diode forward conduction. Next, the two signals are input to the hysteresis comparator circuit to output a rectangular wave. The waveform of each point conversion is shown in Figure 2. The relationship between the duty cycle of a rectangular wave and the phase difference is:

$$V_O = \frac{1}{T}(V_{\max}(\Delta t + \frac{T}{2}) + V_{\max}(\Delta t - \frac{T}{2})) \quad (2)$$

$$V_O = \frac{\phi}{360}(V_{\max} - V_{\min}) + \frac{1}{2}(V_{\max} + V_{\min}) \quad (3)$$

$$V_O = k\phi + b \quad (4)$$

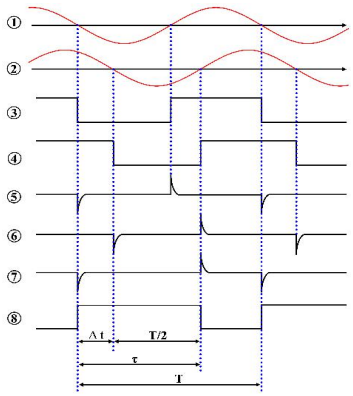

Fig.2 Schematic diagram of waveform conversion of phase detector circuits

C. Analysis of passive low-pass filters

The square wave signal outputted by the hysteresis comparator is filtered by a fourth-order RC passive low-pass filter, in order to retain the DC component and filter out the excess fundamental component [7]. A voltage signal that is linear with respect to the phase difference can be obtained.

D. Analysis and calculation of voltage-current conversion circuit

The voltage signal is converted into a current signal, and by adjusting the potentiometer, the output current signal has a clear linear relationship with the actual phase difference, and can be directly read. If the phase difference is 45°, the output current signal is 4.5 mA, 0.45 mA, and the like. Its calculation formula is as follows:

$$V_1 = \frac{R_1 + W_2}{R_1 + R_2 + R_3} V_{cc} \quad (5)$$

$$I = \frac{V_i - \frac{R_1 + W_2}{R_1 + R_2 + R_3} V_{cc}}{W_1 + R_3} \quad (6)$$

When V_1=b, the current signal is proportional to the phase difference.

IV. HARDWARE CIRCUIT DESIGN

A. Waveform Conversion Circuit Design

The waveform conversion circuit is shown in Figure 4. The sine wave is converted into a square wave by two identical waveform conversion circuits, and the voltages of the non-inverting terminal and the inverting terminal of the operational amplifier are equalized by a resistor, and a clamp circuit is added to make the circuit operate in a stable state.

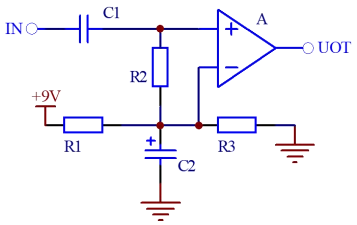

Fig.3 Waveform conversion circuit

B. Linear phase detector circuit design

The linear phase discrimination circuit includes a differential circuit, a diode and a hysteresis comparator, and the circuit thereof is as shown in FIG. 5. Since it is a single-supply operation, it is still necessary to add a clamp circuit to reduce the zero drift caused by the op amp before the signal is input to the hysteresis comparator, so that the zero point is always maintained at 4.5V. In addition, the threshold voltage of the hysteresis comparator can be changed by adjusting to prevent the threshold voltage of the comparator from being reached due to the voltage of the input signal being too small, so that the pulse signal cannot be converted into a square wave signal.

Fig.4 Linear phase detector circuit

C. Voltage-current conversion circuit design

The voltage-current conversion circuit is shown in Figure 5. By adjusting W_1, the proportional relationship between the output current signal and the phase difference can be changed, that is, adjust k, and b can be adjusted by adjusting W_2 to improve the linearity of the phase meter.

Fig.5 Voltage-current conversion circuit

V. TEST PLAN AND TEST RESULTS

A. Test plan

Two signals with a frequency range of 1.5 kHz to 100 kHz and an amplitude of 1 to 5 V are input to the phase meter circuit. After the power is turned on, the multimeter is used to detect the voltage output after the low-pass filtering of the phase-detecting circuit, and the signal generator is guaranteed. When the output frequency is constant, change the phase difference between the two signals multiple times, and the result is recorded to observe whether the phase difference between the output voltage and the input is linear.

B. Tset result

The phaser output voltage results are shown in Table 1.

Table1 Linear relationship between phase difference and output voltage

	100Hz	*1.5kHz*	*5Hz*	*10kHz*	*20Hz*	*50kHz*	*100kH*
-90°	2.48V	6.08V	5.92V	6.08V	6.16V	6.16V	6.16V
-60°	3.12V	5.44V	5.44V	5.52V	5.52V	5.52V	5.52V
-30°	3.68V	4.80V	4.88V	4.88V	4.88V	4.64V	4.80V
0°	4.16V	4.32V	4.32V	4.32V	4.32V	4.32V	4.32V
30°	4.80V	3.84V	3.68V	3.76V	3.76V	3.84V	3.92V
60°	5.44V	3.12V	3.12V	3.12V	3.12V	3.12V	3.20V
90°	6.00V	2.48V	2.58V	2.56V	2.48V	2.48V	2.48V

According to the data of Table 1, a curve as shown in Fig. 6 can be obtained, and it can be seen that the input phase difference and the output voltage linearity are good.

According to the data of Table 1, a curve as shown in Fig. 6 can be obtained, and it can be seen that the input phase difference and the output voltage linearity are good.

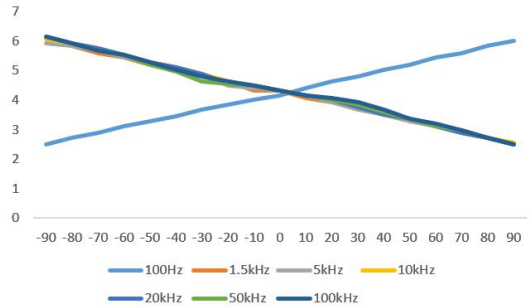

Fig.6 Linear relationship between phase difference and output voltage

Use MATLAB to fit the curve in Table 1. When the frequency range of the signal is 1.5kHz~100kHz, the obtained functional relationship is:

$$y = -0.02x + 4.28 \quad (7)$$

When the frequency range of the signal is lower than 1.5 kHz, taking 100 Hz as an example, the obtained functional relationship is:

$$y = 0.02x + 4.24 \quad (8)$$

By adjusting potentiometer W_1 and potentiometer W_2, let b = 0, k = 0.1, the relationship between current and phase difference can be changed to y = 0.1x, this adjustment mode is simple to operate, and the error of the obtained result is small.

C. Test result analysis test result

Through the above data analysis, the following conclusions can be drawn:

(1) There is a good linear relationship between the output voltage and the phase difference, which basically realizes the function of phase measurement, and can judge the lead and lag of the phase according to the positive and negative of the output data.

(2) The frequency requirement of the phase meter for the output signal is in the range of 1.5 kHz to 100 kHz. In addition to zeroing and calibrating the phase meter during the first use, it can be used normally with a measurement accuracy of about 1°. This is due to the error caused by manual adjustment of the potentiometer. The use of higher potentiometers and op amp chips with higher slew rate can reduce measurement errors and improve accuracy.

(3) If the frequency of the input signal is lower than 1.5 kHz, between 100 Hz and 800 Hz, the phase meter needs to be recalibrated, and the k and b values in equation (4) are changed to meet the measurement needs.

(4) If the frequency of the input signal is between 800 Hz and 1.5 kHz, there is no obvious linear relationship between the output voltage and the phase difference, so it cannot be used normally. Through experimental debugging analysis, it is believed that the reason for this problem is that when the square wave signal after the waveform transformation is changed into a pulse signal by the differential circuit in the phase-detection circuit, the improper selection of the resistor and the capacitor has

an influence on the subsequent circuit.

VI. CONCLUSION

This article uses an analog circuit design and produces a phase meter with an accuracy of 1°. The device is simple and low cost, and the phase difference can be directly displayed using a multimeter. However, due to the error caused by the analog circuit itself, the accuracy and the phase meter using the digital circuit design still have certain errors.

References

[1] Kang Huaguang. Fundamentals of Electronic Technology·Analog part（The Sixth Edition）[M].Beijing：Higher Education Press,2006.1

[2] Alan V.Oppenheim，Alan S.Willsky，S.Hamid Nawab. Signals and Systems，Second Edition[M]. Beijing：Electronic Industry Press，2009.6

[3] Hu Renjie,Du Guoliang,Huang Huichun. Selection of Excellent Works Design Report for National Undergraduate Electronic Design Competition

[4] Phase difference detection circuit [EB/OL]. https://wenku.baidu.com/view/144831315a8102d276a22f35.html/2018.8.20

[5] Phase detector circuit [EB/OL]. https://wenku.baidu.com/view/a8ca2bdf960590c69fc3764f.html/2018.8.2

[6] Yu Li，Fan Junhua，Gao Zhongyuan. Optimization method based on the traditional phase measurement [J]. Electrical Measurement & Instrumentation,2016,53(15A):47-49.

[7] PENG Xiaofeng，WAN Wenlue. Multiple Configuration Simulation Based on Operational Amplifier Circuit Design [J]. Experiment Science and Technology, 2016, 14(3):25-29.

Propeller-type obstacle-crossing trolley

Xiao Lan, Zhang Zibo
（college of instumentation and elctrical engineering,changchun,130061）

***Abstract*—With the advent of the era of robotics, people's demand for obstacle-crossing cars is increasing. At present, common obstacle-crossing cars can not cross steeper obstacles. For slopes larger than 45 degrees, they can not cross when the friction coefficient between tire and ground is less than 1. The propeller car in this paper redefines the structure of the car body. On the basis of the traditional four-wheeled car, the propeller is added to provide part of the power. Through the change of the propeller angle, the support and traction of the car will change during the climbing process, and then the obstacle will be overcome**

***keywords*—Propeller Car Structure**

I. INTRODUCTION

IN order to cope with complex terrain, traditional cars usually adopt increasing wheel radius or caterpillar structure, but when the terrain gradient is greater than 45 degrees, it is difficult to achieve crossing again. In order to overcome this problem, we design a new propeller car from the body structure itself. It adjusts the propeller angle by PID algorithm so as to provide suitable pressure and thrust at high slope, thereby increasing the maximum static friction and traction force, making the car easier to cross obstacles[1].

The new mobile platform designed by this research institute can be used in many fields, because the propeller-type obstacle-crossing car can work on rugged roads and even on walls. In the military field, it can be used to detect and detect in complex terrain, and can do mine clearance and other work, thus largely avoiding personnel injuries. In scientific research, the car can operate on complex terrain in the field and be applied to different research purposes, thus carrying different measurement systems to complete data collection; in safety search and rescue, forestry and mining, it can overcome various obstacles to terrain and complete various instructions. As far as entertainment is concerned, on the basis of this car and remote control device, it can be used as a product of mass entertainment.

This research can not only accomplish social work, but also enrich social life, with a wide range of positive significance.

II. OVERALL PLAN

The system consists of four parts: state detection module, height prediction module, angle control module and motion platform.Two kinds of sensors are used in the state detection module, laser range sensor is used in the distance detection part and gyroscope module is used in the inclination detection part. Both of them transmit the required distance and angle information to the main control STM32F103 through serial port. The angle determination module uses mechanism modeling to predict the current body angle and the running speed of the car, and calculate the appropriate propeller inclination motion. The platform controls the car to achieve obstacle crossing. The design block diagram is shown in Figure 1[2-3].

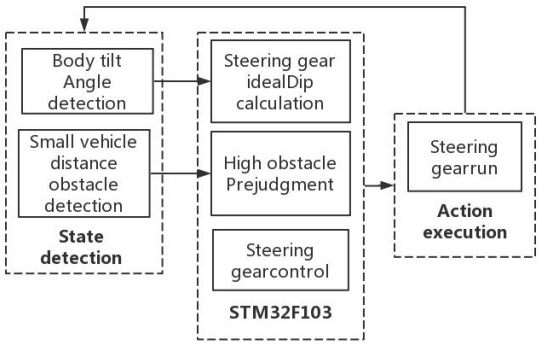

Fig.1 Design block diagram

III. DESIGN SCHEME AND IMPLEMENTATION

A.Design and Implementation of High Prediction Module

The state detection module is composed of two kinds of sensors. The distance detection part requires that the distance of the obstacle in front of the vehicle can be identified, and the height of the obstacle can be predicted by cooperating with the steering gear. The angle detection part requires the gyroscope to recognize the current body angle information. Both of them transmit information to STM32F103 through serial port.

The height prediction module is realized by laser ranging module. The flow chart of the height prediction of the obstacle is shown in Figure 2. The distance of obstacles in front is analyzed and processed by the cooperation of laser ranging and steering gear, the effective position information is intercepted, the height of obstacles is calculated, and the car mode is judged by serial port transmission to STM32F103.

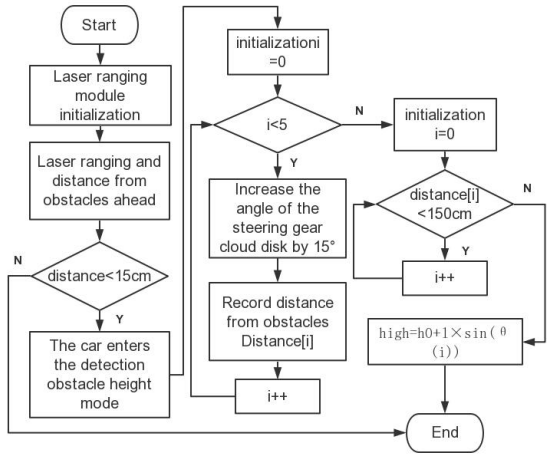

Fig.2 Flow chart of identification, detection and location module

As shown in Figure 3, the laser range finder module is fixed on the steering gear. The distance between the steering gear and the obstacle in front is collected once and saved at 15 degrees per turn. The data is collected and processed, and the maximum available value is calculated by formula

$$h = h_0 + l \sin \theta'$$

,estimate obstacle height.

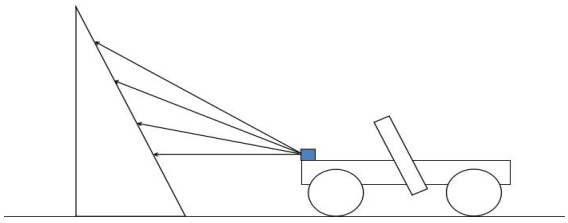

Fig.3 Prediction Diagram of Obstacle Height

B.Design and Implementation of Motion Platform

If you want to submit your file with one column electronically, please do the following:The speed reducer motor uses the speed converter of gears to reduce the number of rotations of the motor to the desired number of rotations and to obtain a larger torque mechanism. In this design, the speed requirement of the system is not high. In the case of large slope of obstacles, the force of gravity along the slope is larger, the traction force of the car is larger, and the torque requirement of the motor is as large as possible.

Propeller blade selection should take into account the relationship between vehicle volume and propeller lift. The propeller lift is related to diameter D (cm), pitch L (cm), slurry width h (cm), speed v (rad/s), and atmospheric pressure.

$F = \mathrm{d} \times l \times h \times v \times 1 \times 0.00025$, The unit F is g.The motor speed is 22000 rad/s (input voltage is 10V). According to the formula, the force of 8040 propeller is about 1.2 kg (the speed of propeller is 12000 rad/s), and that of 7040 propeller is about 1.1 kg (the speed of propeller is 12000 rad/s). The diameter of 8040 propeller is 20.32 cm, 7040 propeller is 17.78 cm and tyre is 13 cm. When only the propeller is installed, the propeller provides forward thrust. At this time, the distance between the center point of the propeller and the ground is 9 cm. 7040 propeller can provide 1.1 kg thrust, while 8040 propeller can provide 1.08 kg force. Considering comprehensively, 7040 propeller is chosen.

For a sports car, the position of traction force is at the wheel of the car. The change of the support force at the wheel will directly affect the maximum static friction that the car can bear. The larger the maximum static friction force, the less easy the car will skid, which is beneficial to the climbing of the car. In order to make the car more conducive to crossing obstacles, it is necessary to install the propeller directly above the wheel. Propeller rotation will directly change the wheel support force, and install a rudder at both ends of the propeller. The direction of the propeller can be changed. Try to provide traction for the car[3].

C.Design and Implementation of Angle Control Module

Angle control module needs to be able to use the measured body inclination information and car speed, information for mathematical calculation, to get the optimal propeller inclination value.

As shown in Figure 4, the angle control module is modeled and analyzed. The force analysis of the car at the current moment is carried out. According to the experiment, the car can cross the obstacle of 30 degrees without the partial force provided by the propeller. The slope inclination angle of the car is modeled as theta > 30 degrees. At this point, the propeller needs to provide downward force to increase its maximum static friction so that it will not slip, and properly provide forward thrust to help the car cross the obstacle.

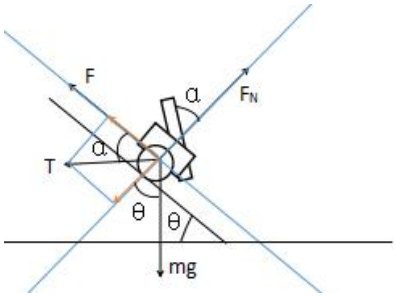

Fig.4 Modeling and Analysis of Angle Control

From the above figure, the equation can be listed as follows:

$$F + T \times \cos\alpha - mg \times \sin\theta = m\frac{dv}{dt}$$

$$T \times \sin\alpha + mg \times \cos\theta = F_N$$

$$\mu \times F_N > T$$

According to the above formula, we can know when we climb a slope, $\mathrm{m}\dfrac{dv}{dt} \geq 0$, $\mu \times F_N > T$.

According to this condition, the range of propeller inclination angle can be solved by mathematical modeling based on MATLAB. The inclinable angle range of the propeller is shown in Fig. 5. According to this figure, the range of propeller inclination can be limited to 17-63.

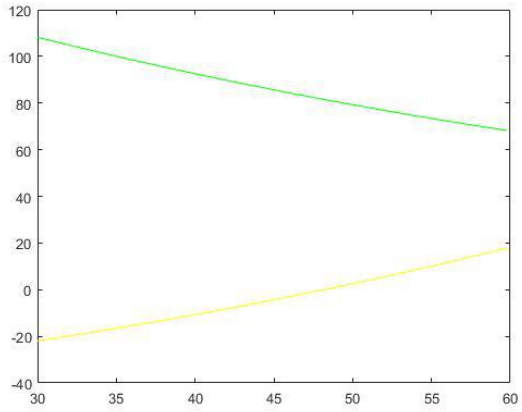

Fig.5 Propeller inclinable angle range

Figure 6 shows the PID control block diagram.The ideal position of the current moment is imported and adjusted by proportional P, integral I and differential D(Fast response can be achieved by proportional link, static error can be reduced by integral link, overshoot can be reduced by differential link, and dynamic response can be accelerated),The motion state of the car is changed, and the current state detection module value is fed back to make the car reach the exact position quickly.

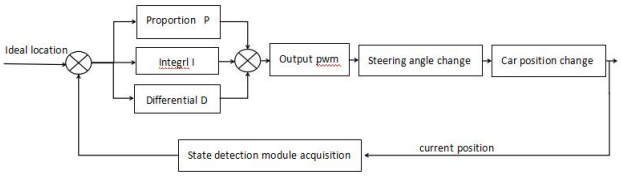

Fig.6 Pid control block diagram

The flow chart of the angle control module is shown in Figure 7. The optimal propeller inclination angle is obtained by introducing the current car inclination and acceleration value into the calculation formula obtained by mechanism modeling. The optimal propeller inclination angle is adjusted by PID control, and the motion state of the car is changed. The current state detection module value is fed back to realize the vehicle crossing obstacles.

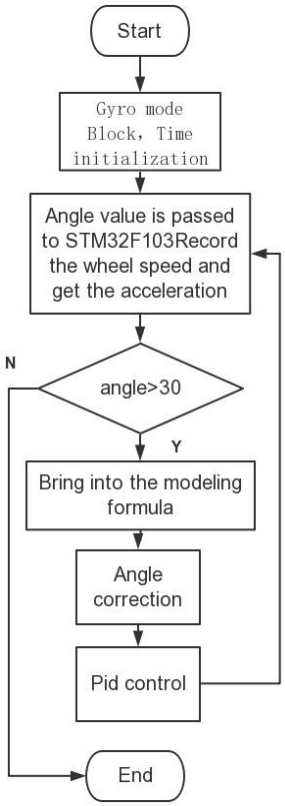

Fig.7 Flow chart of angle control module

IV. TEST SCHEME AND RESULTS

A.System Test Flow

The device is mainly used to overcome obstacles with high inclination. The flow chart of the system program is shown in Fig. 8. Waiting for system initialization, car running, entering normal mode mode mode = 0 to change propeller angle in real time according to body inclination angle, and judge the distance of obstacles ahead. When the distance of obstacles is less than 15 cm, car running speed

decreases, and the height of obstacles ahead is predicted, and the height value is sent to mobile phone through Bluetooth module. When the height judges lodging, the car enters mode 1 and climbs mode, the ranging module is invalid. The optimum propeller angle is calculated by formula based on the angle value of gyroscope feedback, and the propeller inclination angle is adjusted by three parameters of pid. Record the angle value of the car each time. When the inclination value of the car is equal for five consecutive measurements, the car exits mode 1 and enters normal mode mode = 0. Bluetooth module connects the mobile phone and receives the current car mode in real time, as well as the operation of the car. The mobile phone sends the number 1 and the car stops running[5]

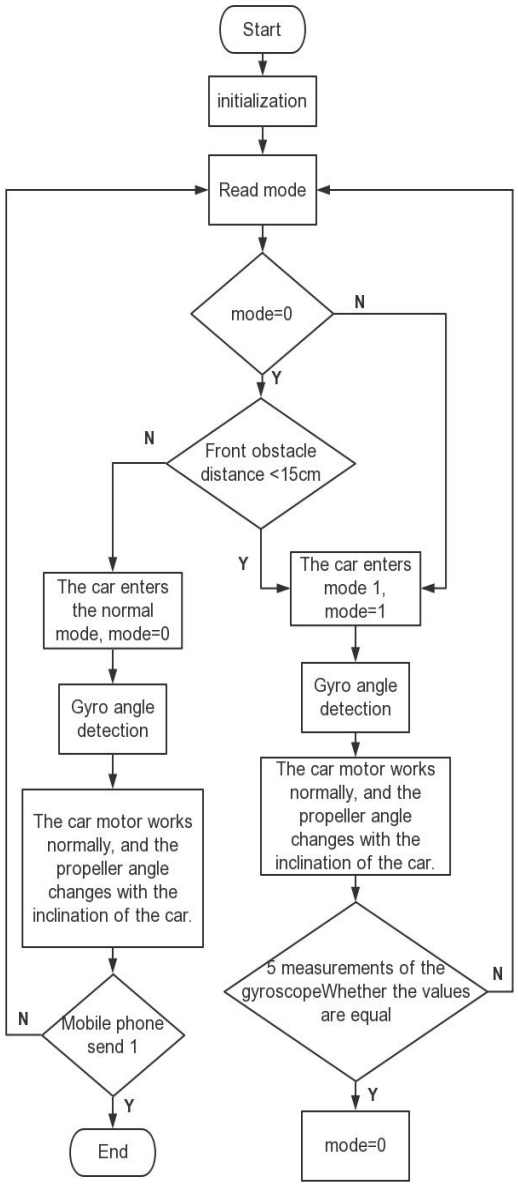

Fig.8 Program flow chart

B. System Test Conclusion

The test results are shown in Table 1

Table 1 Test result

Inclination of inclined plane	First (s)	Second (s)
30°	34	31
45°	54	52
60°	70	76

From the above test data, the system can fully meet the requirements of the indicators.

V. CONCLUSION

The propeller car has reasonable structure design and high stability. The angle of the propeller is adjusted by the body attitude and the inclination of obstacles in real time, so that the ideal crossing state can be achieved easily. The feedback of body attitude is real-time feedback by gyroscope, and the inclination of obstacles is judged by height prediction module. The reasonable configuration of the system can make the car cross the obstacle with the inclination of 17-63 degrees.

This new mobile platform can be applied in many fields, and has certain research significance and expansion value.

References

[1] Chen Wuyang. Application of Variable Universe Fuzzy PID Control in DC Motor [D]. Northern University of Technology, 2017.

[2] Mao Ying. Realization of PID algorithm of self-balancing vehicle based on myRIO controller [J].Fujian Computer, 2016, 32 (12): 107-109.

[3] Song Xingguo. Modeling of mobile system and tracking control based on model learning for wheeled robots [D]. Harbin University of Technology, 2015.

[4] Wang Yuchen. Software and hardware design and system control of intelligent wheeled robot platform [D]. Chongqing University, 2016.

[5] Wang Lei. Design and implementation of STM32-based micro Four-rotor aircraft [J]. Innovation and application of science and technology, 2017 (24): 113-114

Item sorting and handling device based on Ant Colony Algorithm

Li Ang, Wang Fan, Xiao Lan

（*College of Instrument Science and Electrical Engineering, Jilin University, Changchun 130022, China*）

***Abstract*—In recent years, with the development of Internet technology, online shopping has increased, and the logistics industry has developed rapidly. The sorting and transportation of express delivery has become an important part of the logistics industry. In order to improve the sorting efficiency of articles and improve production efficiency, intelligent sorting should be developed rapidly. The automatic sorting and transporting device designed in this paper detects the object of the target color size based on the image processing technology, optimizes the transport path through the ant colony algorithm, and uses the X-Y dual-axis slide table and the mechanical arm as the execution device. After many experiments, the device can automatically detect the items being transported, and realize automatic sorting and handling functions.**

***keywords*—Item sorting Ant Colony Algorithm X-Y double axis slide table Image Identification**

I. INTRODUCTION

IN recent years, with the advancement of Internet technology, the behavior of online shopping has increased, and the logistics industry has developed rapidly. The sorting and transportation of express delivery has become an important part of the logistics industry. The device which can intelligently sort and convey can greatly increase production efficiency[1].

II. DESIGN GOAL

The automatic sorting and conveying device designed in this paper has the function of recognizing the target object, and can realize the function of automatically grasping and carrying objects according to the user setting. According to the functional requirements of the automatic sorting and handling device, the handling device is reasonably simplified in the project to verify the feasibility of the intelligent sorting and handling device based on image recognition and two-dimensional rail movement[2].

A square area of 80 cm × 130 cm was set in the transport area, and a 30 cm × 30 cm area at any corner of the square was used as the area to be transported, and the yellow and black square cubes with a side length of 4 cm were used as the object of transport to verify the system. The system is required to automatically detect the items being transported, and realize the function of automatically sorting and moving the target color wood blocks.

III. DESIGN AND IMPLEMENTATION

The system consists of four parts: identification detection and positioning module, route planning module, grab handling module and motion platform. The item identification module adopts the OPENMV camera, which is responsible for collecting the color and position of the wooden block, and transmits the extracted item position information to the controller with STM32F103 as the core through the serial port; the route planning module adopts the ant colony algorithm to carry out the moving path of the moving platform. Planning; grab the handling module to calculate the steering angle of the robot arm when performing push and grab motions, and control the movement of the robot arm to realize the handling of the test wooden block; the motion platform controls the mechanical arm to move in the XY plane; the power module is the above module Provide the required power. The diagram is shown in Figure 2.1.

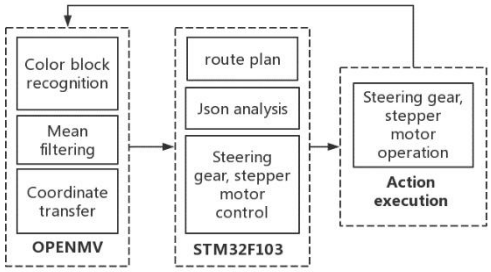

Fig2.1 Design block diagram

A. Design and Implementation of Identification Detection and Positioning Module

The recognition detection and positioning module is required to be able to identify image information in the work site, and to identify and filter the carried item by image analysis of the color information of the object, and generate coordinates for transmission to the route planning module[2-4].

The identification detection and positioning module is

implemented by OPENMV, and the flow chart of the identification detection and positioning module is shown in Figure 2.1.1. The OPENMV is used to analyze and process the real-time image information of the workplace, intercept the effective position, perform filtering processing, and then extract the position information of the effective object color, and transmit it to the route planning module of STM32F103 through the serial port for processing.

As shown in Figure 2.1.2, the block information extracted by OPENMV ensures the measurement accuracy by constraining the number of pixels included in the measured color block and the range of the center coordinates of the patch. In the recognition of OPENMV, in order to improve the reliability of recognition, the pixels are averaged, the size of the identified pixel blocks is judged, and the smaller pixel interference is filtered out. After obtaining the pixel coordinates, the coordinate point list data is wrapped by json, and the same json decoding program is matched on the STM32F103 controller side, and the coordinates of each wooden block are saved in a two-dimensional array as input data for subsequent path optimization. And the target position of the sports platform.

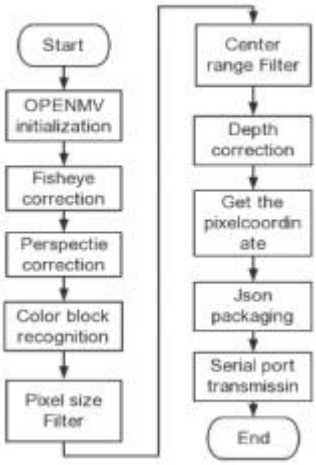

Fig.2.1.2 Identification detection and positioning module flow chart

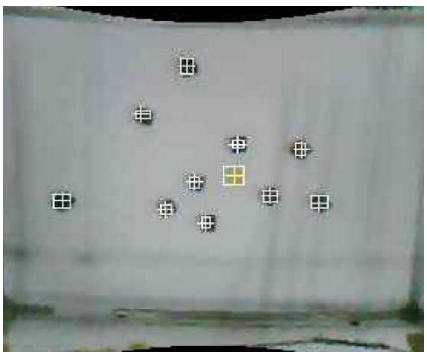

Fig.3.1.2 Block information extracted by OPENMV

B. Design and implementation of path planning module

The path planning module requires that the coordinate information can be received for path planning to obtain an optimal transport path.

Figure 3.2.1 shows the flow chart of the path planning part algorithm. In this module, the coordinates of each position are imported, and the distance between each position is calculated. Using the ant colony algorithm, 50 ants are released each time, the starting point and the end point are fixed, the pheromone on the path is iteratively updated, and roulette is utilized to determine the coordinates of the next unvisited position, after 200 iterations, the coordinate order of the optimal path is obtained.

After mathematical modeling analysis, the manipulator pushes 3 wooden blocks at a time compared with 61% of the time each time, pushing 4 wooden blocks at a time compared with 68.6% for each push, as shown in Fig 3.2.2, Fig 3.2.3 and Fig 3.2.4 show the path planning situation of pushing 1, 3, and 4 wooden blocks at a time, and the required moving length. Considering the size and time of the manipulator, it is more appropriate to push three at a time. When the system performs the block transport mode, in order to prevent the direction from being unable to be reversed due to the existence of the loop, the route loop needs to be re-planned. If the loop path reaches the farthest point first, the loop path sequence is not changed, otherwise the loop is reversed[6].

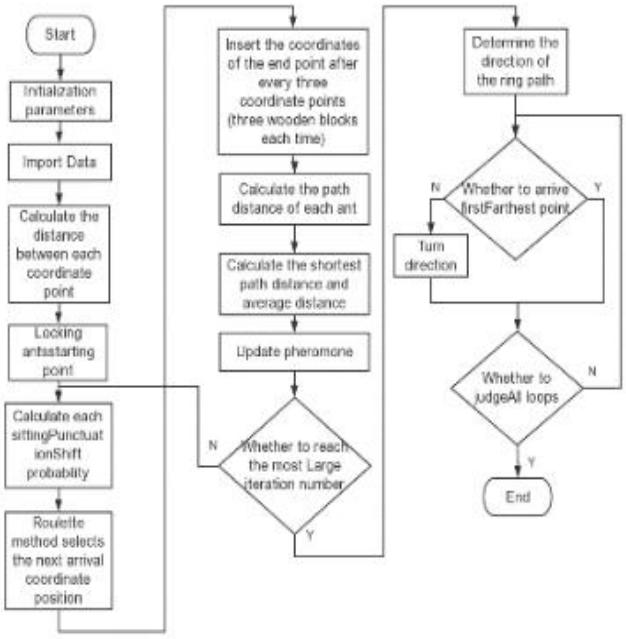

Fig.3.2.1 Path planning part algorithm flow chart

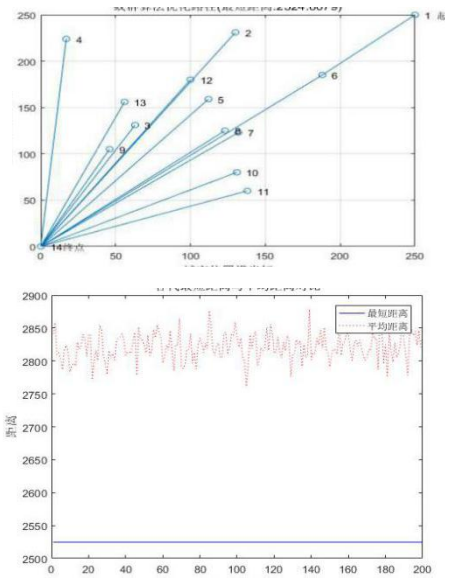

Fig.3.2.2 Push 1 block at a time

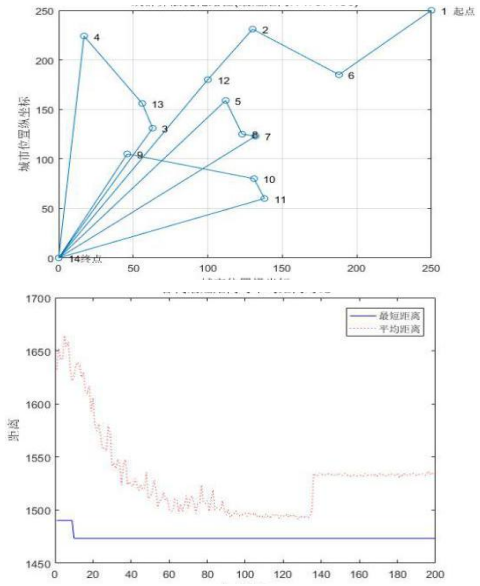

Fig.3.2.3 Push 3 wooden blocks at a time

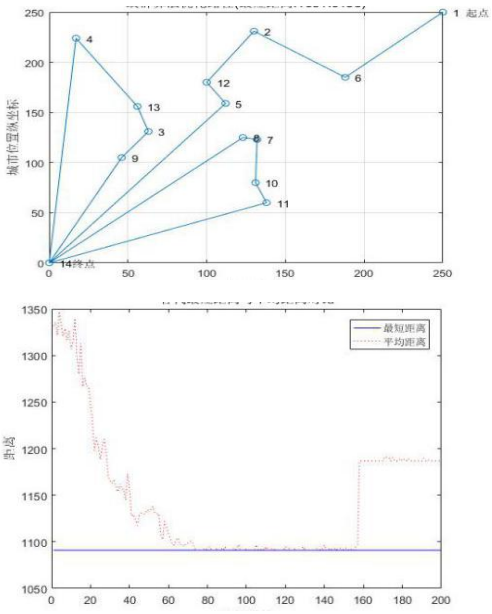

Fig.3.2.4 Push 4 blocks at a time

C Design and implementation of motion processing part

The motion processing part requires that the optimal handling path can be converted into the positional movement of the motion platform, and the target object can be grasped and transported by coordinating with the mechanical arm, and the wood block to be transported is transported to a designated position.

Stepper motors have the advantage of enabling open-loop control with no feedback signals and high-precision control. The system uses stepping motors as power source for X-Y direction movement. The motion platform is modified by a 3D printer structure, using a conveyor shaft and a conveyor belt as a conveyor. The stepping motors travel one turn and the moving length is fixed. The accuracy and moving speed can meet the requirements without off teeth.

The motion processing part is implemented by the STM32F103 chip. By taking the points of different coordinates, the pixel coordinates and the actual physical coordinates corresponding to them are obtained, and the correspondence between the two is obtained by Least Squares Method. The target path obtained by the path planning module obtains the actual physical coordinates through the above relationship, and controls the operation of the two stepping motors to reach the target position, thereby realizing the precise operation of the grabbing platform.

The robot arm is fixed to the mobile platform and its rotation angle is controlled. According to the positional relationship between the arrival point and the current point, the coordinate system is established with the current position as the center. When $\Delta y > 0$, the angle is converted by the formula to obtain the ideal angle.

$$\theta = \arctan\frac{\Delta y}{\Delta x}$$

And use the following formula to convert the angle information into the steering gear control information, and send the grabbing and carrying action to the robot arm through the Bluetooth module to realize the grasping and handling of the target object[6].

$$k = 1500 - \theta \times \frac{100}{9}$$

IV. SYSTEM TEST

A System test process

This device is mainly for scattered, sorting and handling of different types of items. The system program flow chart is shown in Figure 3.1.1. Press the button, monitor the button, judge the color of the object

to be moved, the camera monitors the object in real time and passes the coordinate position to the STM32F103 for path planning, and passes the path planning result to the driving platform to realize the grasping and handling of the specified color object. , again, check the number of objects in the area to be transported. If there is an object to be transported, continue to carry it; if it does not exist, end the transport. It is required that the overall system can complete the picking and handling of 12 wooden blocks randomly placed in the site within 3 minutes.

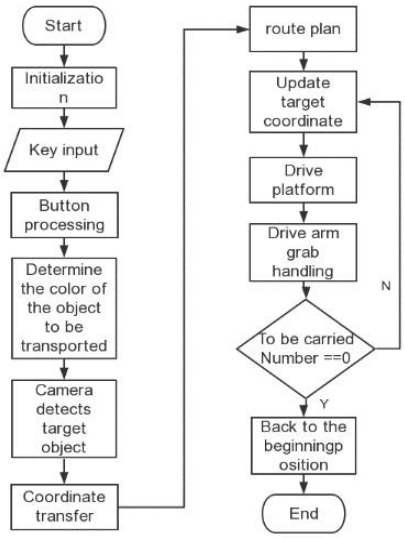

Fig 4.1.1 Program flow chart

B System test result

The test results are shown in Table 4.2.1.

Table 4.2.1 Test Results

Type	12black/12yellow		6black+6yellow	
	First(s)	Second(s)	Third(s)	forth(s)
Move black	103	94	116	121
Move yellow	89	98	124	135

V. CONCLUSION

From the above test data, the system can fully fulfill the index requirements, and the actual exercise time is controlled within the target requirement range, and the designated color wood block can be transported as required.

References

[1] Janzugen, Li Ming, Xu Kefei, Sun Xiaohua, Shi Peng, Sun wisdom. High-speed robot sorting Research on system machine Vision technology [J]. Packaging & amp; food Machinery, 2014,32 (01)

[2] Liuzhenyu, Li Zhong, Zhao Xue, Shan. Industrial robot sorting based on machine vision Technical research [J]. Manufacturing Automation, 2013,35 (17): 25-30.

[3] Liuzhenyu, Zhao Bin, Shan. Application of machine vision technology in workpiece sorting [J]. Computer applications and software, 2012,29 (11): 87-91.

[4] Giongon, Duong. Realization of industrial robot sorting technology [J]. Combination machine tool and automation processing technology, 2010 (02): 84-87.

[5] Lu Shaoping, Zhang, Wu Yaohua, Wu Yingying. Automatic sorting system parallel partition picking Optimization strategy [J]. Journal of Shenzhen University (Polytechnic edition), 2010,27 (01): 120-126.

[6] Qiming H . Analysis of Automatic Sorting System and Its Application Prospect[J]. Val Ngnrng, 2010.:17-18.

Research on non-contact control of mobile phones based on sEMG

Xiaolu Liu, Yiming Song, Chao Wang
（*College of Instrument Science and Electrical Engineering, Jilin University,Changchun 130021*）

***Abstract*—A system of mobile phone manipulation through gestures is established. Two-channel surface electromyography (sEMG) signal was collected and processed.Activity segment detection is through short-time energy and zero-crossing rate.Feature extraction uses IEMG, RMS, MPF, and MF, and the BP neural network classifier was used for pattern recognition. Finally the automated scripting tool is used to manipulate the phone. The test results are in good agreement with the expected results.**

***keywords*—Surface electromyography signal;Feature extraction;Artificial neural network;Gesture control**

I. INTRODUCTION

ELECTROMYOGRAPHIC signals (EMG) are an important bioelectrical signal that is associated with muscle activity. The surface electromyography (sEMG) sensor captures muscle activity on the skin surface of the corresponding muscle group and reflects information on the state of flexion and extension, the shape and position of the limb during movement[1]. Gesture recognition through surface EMG signals can provide an effective way for human-computer interaction, and has important application value in the fields of prosthetic control, mobile device manipulation, and medical rehabilitation.

In this paper, the sEMG signal collected by the arm is applied to the non-contact control mobile phone. The research content includes the following aspects: Firstly, the sEMG signal is collected on the appropriate forearm muscle group, preprocessed by the conditioning circuit and transmitted to the computer; then by the computer Algorithm processing, classification of gesture signals, involving signal noise reduction, active segment detection, feature extraction and pattern recognition; finally, the gesture is used to control the mobile phone.

II. SYSTEM HARDWARE DESIGN

The hardware part is mainly used for acquisition, preprocessing and signal transmission of sEMG. The hardware block diagram is shown in Figure 1.

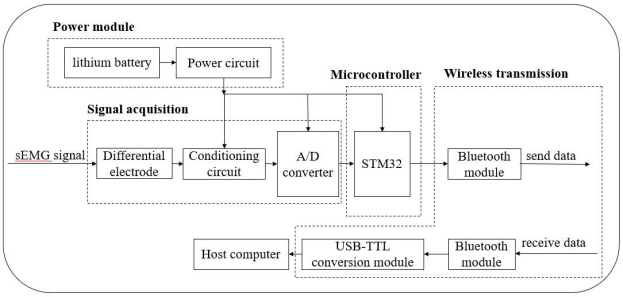

Fig.1 Hardware block diagram

A.Power module

The system is powered by a 12V rechargeable lithium battery. It provides 12V voltage to the sEMG acquisition module and 3.3V to the STM32 microcontroller via two sets of DC regulated power supply modules.

B.sEMG acquisition module

Signal acquisition: The electrode material of the sensor uses Ag-AgCl, and its low polarization voltage makes it possible to quickly obtain a stable EMG signal. The electrode form uses a bipolar type to form a differential input terminal and is added to the reference electrode to reduce noise interference and improve common mode rejection. In order to eliminate common mode noise from power lines, a differential amplification method is employed. Since the signal is detected by two electrodes, any noise that is far away from the detection point will appear as a "common mode" component at the detection point, which is eliminated, and the signal near the detection surface (mainly the desired sEMG signal) appears as The "differential mode" component is amplified, effectively improving the signal-to-noise ratio[2].

Electrode placement: According to the relationship between forearm muscle and hand movement, two sets of bipolar electrodes were placed in the right forearm

and ulnar flexor muscles of the tester, and the reference electrode was attached to the bulge of the wrist. The electrode itself should have a large enough contact area with the skin, and the electrode spacing should not be too small. The electrode patch used is square and the center is a circular electrode. Considering that the electrode patch itself has a certain size (36*25mm), The electrode patch is then placed in close proximity and fixed in the direction of the muscle fibers. as shown in Figure 2.

Fig.2 sEMG signal acquisition module - electrode placement

Signal acquisition and conditioning circuit: Use the dual-channel sEMG acquisition circuit produced by Zhituo Company. The power input is 12V DC. After being processed by the self-contained buck regulator circuit, it outputs ±5V DC for subsequent acquisition and conditioning circuits, including amplification and filter circuit.

TABLE 1 Specific parameters of sEMG acquisition circuit

Number of channels	2
Signal amplification	1000
Frequency range of bandpass filter circuit	10Hz≤f≤1000Hz
Range of signal output voltage	-1.5V≤Vo≤1.5V

C.Microcontroller module

The STM32 microcontroller is used to perform A/D conversion on the acquired two-channel analog signal. The serial communication method is used, and the signal is transmitted by the Bluetooth module. The receiving end receives the signal by using the paired Bluetooth module and transmits the signal to the computer. The Matlab software of the computer completes the subsequent algorithm processing.

III. SOFTWARE DESIGN

A.Digital filtering

The acquisition device has amplified and filtered the signal through the hardware circuit, and also needs to perform software denoising, and further filters the obtained data by using a filter. As can be seen from Figure 3, the 50,000 points taken from the signal constitute a plurality of sets of actions. As can be seen from Figure 4, the frequency of the set of signals is between about 20 and 500 Hz. Select FIR low-pass filter (set passband cutoff frequency 500Hz, stopband cutoff frequency 600Hz) and high-pass filter (set passband cutoff frequency 5Hz, stopband cutoff frequency 2Hz) to filter high frequency noise and baseline drift signal, The filtered signals are shown in Figures 3 and 4, respectively. The noise cancellation quality meets the requirements and can be processed in the next step.

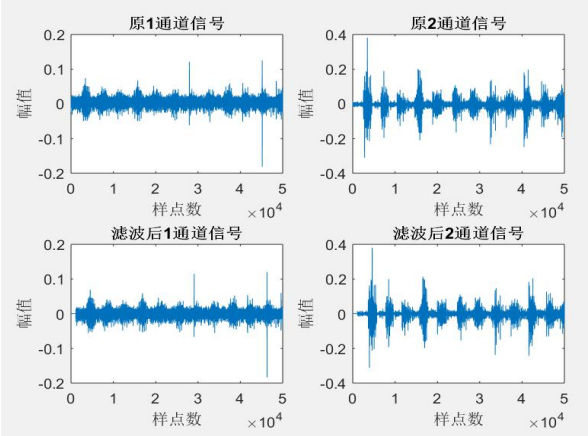

Fig.3 Time-domain waveform of signal before and after filtering

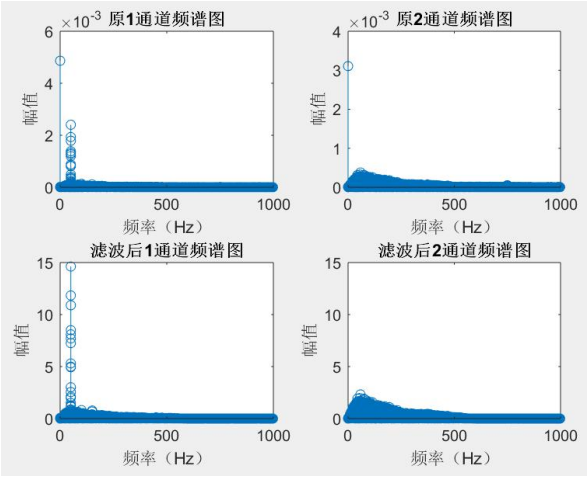

Fig.4 Frequency-domain analysis of signal before and after filtering

B.Active segment detection

The current myoelectric signal is a continuously obtained signal that includes both a stop state and an action execution state, and the two appear alternately. Now it is necessary to find a signal corresponding to the execution of the action, which is called active segment detection.

Select two parameters: short-time energy and short-term average zero-crossing rate, limit high and low values, and find the starting and ending points of the active segment by threshold method. Segments that are too short in length are considered as noise and discarded.

1) short-term average zero-crossing rate

$$Z_n = \sum_{m=-\infty}^{\infty} |\operatorname{sgn}[x[m]] - \operatorname{sgn}[x(m-1)]|\, w(n-m)$$

For continuous time signals, the zero crossing rate refers to the case where the time domain waveform passes through the time axis. For discrete-time signals, the sign of two adjacent samples is called a "zero-crossing", meaning that the time waveform of the signal passes through the horizontal axis of zero level, so that zero crossing can be calculated. Number, the number of times the sample changes the symbol. At the same time, the zero crossings per unit time is the average zero crossing rate. Short-term zero-crossing analysis is often used as an endpoint detection method to estimate the starting and ending points of an active segment[3].

2) short-time energy

$$E_m = \sum_{m=-\infty}^{\infty}[x(m)w(n-m)]^2 = \sum_{m=n-N+1}^{n}[x(m)w(n-m)]^2$$

The energy of the dynamic signal changes with time. Compared with the active segment, the energy of the stop segment tends to approach zero, and the energy difference between the two is quite significant. Therefore, the short-term energy of the signal is analyzed, and the threshold can be set according to the amplitude of the short-time energy, and the threshold is automatically adjusted by using an algorithm to perform the active segment detection.

Figure 5 shows the results of obtaining the short-term energy and the average zero-crossing rate for the signal. The activity segment detection result is shown in Figure 6.

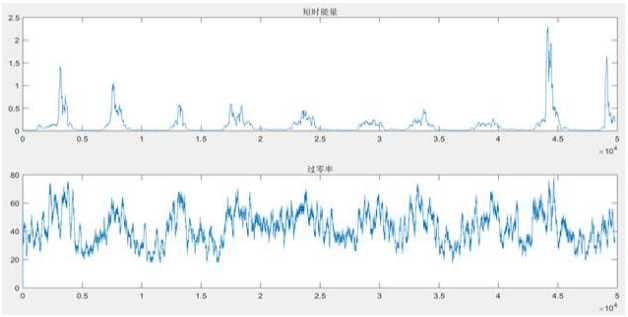

Fig.5 Short-term signal energy and zero-crossing rate

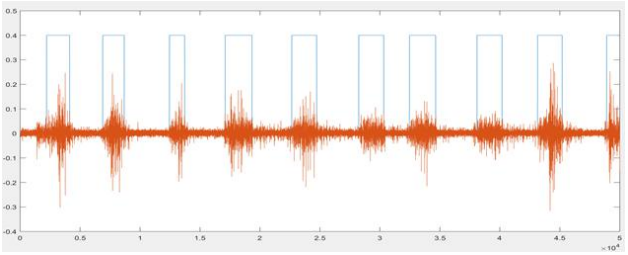

Fig.6 Detection of active segment

C.Feature extraction

Feature extraction is to extract the components of the sEMG signal that are most effective and can distinguish the other actions from the sEMG signal when the action is performed. It is the basis of pattern recognition and has a great influence on the correct rate of action classification. At present, the widely used sEMG signal feature extraction methods are mainly time domain analysis, frequency domain analysis, time-frequency domain analysis and chaos analysis[4].

Considering the simplicity and effectiveness of the algorithm, this paper uses time domain analysis and frequency domain analysis to extract the feature quantities of sEMG signals, using integral electromyography (IEMG), root mean square (RMS), and average power frequency (MPF). And the four characteristic quantities of the median frequency (MF). After finding the feature value, the two-two joint cooperative scatter plot is shown in Fig. 7. The red, yellow and blue colors respectively represent the sEMG signal characteristic values of three different actions. It can be seen from the figure that the characteristic values of the three kinds of motion signals are respectively distributed within a certain interval range and are easily distinguishable from each other, so the above four feature quantities can be used as feature extraction.

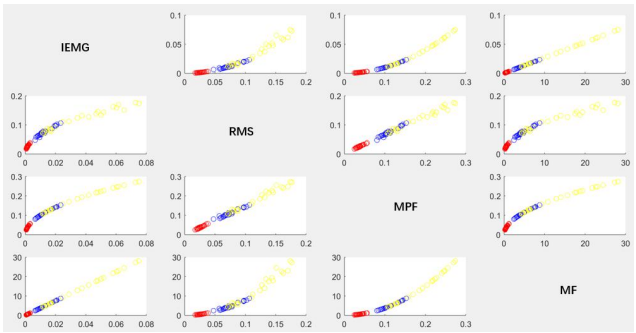

Fig.7 Scatter plot of eigenvalue

D.Pattern recognition

Pattern recognition uses a BP neural network classifier. The BP (Back Propagation) neural network is a multi-layer feedforward network, that is, there is only a feedback signal during the training process, and in the classification process, the data can only be forwarded until it reaches the output layer. As one of the most widely used NN models, BP neural network can learn and store a large number of input-output mode mapping relationships without the need to reveal the mathematical equations describing this mapping relationship[5]. The characteristics of sEMG signals make Pattern recognition of sEMG signals is a type of problem that neural network classifiers are good at solving.

The structure of the BP neural network model is divided into an input layer, an implicit layer, and an output layer. Each neuron signal is in the feedforward network, starting from the input layer, receiving the

previous stage input, and outputting to the next stage until the output layer, which has higher discrimination ability and pattern recognition intensity. The entire network can be represented by Figure 8. Here, a three-layer BP neural network is used, and a logarithmic S-shaped transfer function is selected as the transfer function of the intermediate layer, and a general linear function can be used as a transfer function of the output layer.

According to the research in this paper, three kinds of gesture actions need to be identified, namely, GLPM, TIWR, and TLWR. The four feature quantities of the sEMG signals of each action are respectively extracted to form a feature vector, and the feature vectors of the three actions are combined into one feature vector set. The feature vector set is then divided into two groups, one of which serves as a training sample for the neural network and the other as a test sample with 100 samples for each action in each group. Use these training samples to train a forward network. The input to this network is 4 features, and each element of the output is the probability that a certain sample belongs to a certain action. The action corresponding to the highest absolute value among the three output values of the same sample is the classification result of the sample. The training performance of the BP neural network is shown in Fig. 9, and the convergence is achieved after about 300 trainings.

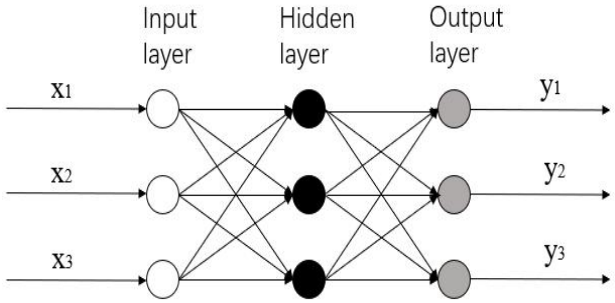

Fig.8 Structural chart of neural network

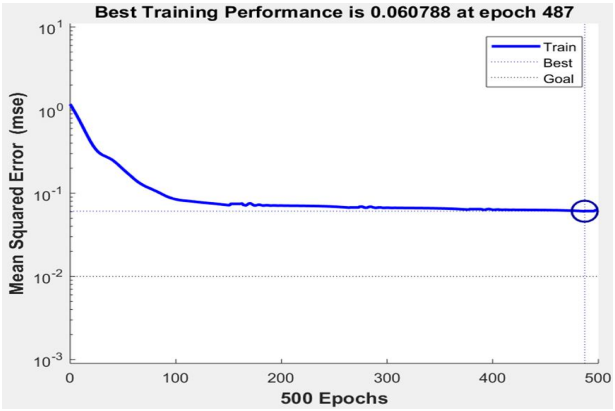

Fig.9 Training performance of neural network

The test samples are sent to the mature neural network for identification, and the results of the identification are given in Table 2.

TABLE 2 Recognition results of 3 gestures and recognition rate

Three kinds	GLPM	TIWR	TLWR	Recognition rate /%
GLPM	97	3	0	97%
TIWR	12	84	4	84%
TLWR	1	4	95	95%
Time/s： 1.3s		Average recognition rate /%： 92%		

It can be seen from Table 2 that the average recognition rate of the three gestures reaches 92%, and the recognition rate of the palm-sliding (GLPM) action is the highest, which is 97%; the total time of the neural network training and inspection is 1.3s, and the recognition speed is fast; The training sample and the test sample are different in time, indicating that the neural network classifier also has good stability. In summary, the BP neural network classifier basically recognizes the three gesture actions to meet the system design requirements.

E.Output and results

The result is output as a file in the form of an action classification label, an automatic script tool is used to read the recognition result file, and a corresponding operation is performed according to the content of the read gesture to control the mobile phone. The apk installation package that is created requires the phone to gain superuser privileges, that is, to fully control the underlying system and system files. The simulator was used for debugging in the research test.

The three types of gesture actions and the corresponding operations are shown in Figure 10.

a. GLPM-to bring up the upper sidebar

b. TIWR-to adjust volume

c. TLWR-to slide left

Fig10 Gestures and control results

IV. CONCLUSIONS

A system based on sEMG to non-contact control mobile phone is designed. The system successfully recognizes 3 kinds of gesture actions, the recognition success rate reaches 92%, the recognition speed and stability basically reach the expected level, and the realization and application of software functions are reasonable. The operation is feasible, with the characteristics of fast response, high recognition accuracy, good portability, and convenient use, which lays a foundation for further recognition of more actions.

References

[1] Zhao Zhangwei. Research on several key technologies in surface EMG signal detection and processing [D]. University of Science and Technology of China, 2010.

[2] Geng Guansheng, Yang Peng, Guo Xin, Chen Lingling.Design of Digital Sensor for Surface EMG Signal[J].Control of Microcomputer,2007(25):123-124.

[3] Lu Weiqiang, Huang Wei. Real-time speech endpoint detection method based on short-time energy plus zero-crossing rate[J]. Ordnance Automation, 2009, 28(09): 69-70+73.

[4] Liu Jian, Zou Renling, Zhang Dongheng, Xu Xiulin, Hu Xiuzhen. Research and Development Trend of Surface EMG Signal Feature Extraction Method[J]. Progress in Biomedical Engineering, 2015, 36(03): 164-168.

[5] Chen Ming, Hu Huiping, Yang Minhua. Classification of BP Neural Networks Based on Object-Oriented Feature Extraction——Taking Wulingyuan Area as an Example[J]. Modern Surveying,2017,40(03):17-20.

Gesture Recognition Means Based on Variable Capacitance Sensor

Gao Xinyu, Li fuhao, Gao jinxiao
（Jilin university instrument science and engineering institute,changchun,130021）

***Abstract*—The device uses the specific capacitive sensor FDC2214 series as the core to complete the gesture recognition and judgment of the guessing game and the fist-rowing game. After training, any tester can make a gesture decision. The change of capacitance is mainly caused by the change of the front end of the sensor, and then the controller acquires information, mathematical analysis, algorithm processing and judgment of the gesture feature information fed back by the controller, and displays the posture of the current gesture according to the judgment result to achieve a specific function. After testing, in the judgment mode, the decision of the designated person's fist-rowing and guessing can be realized, the correct rate is 100% and the judgment time is not more than 1s. In the training mode, the number of training for any person is 3 times, the guessing gesture The training time is less than 40s, the training time of the fist-rowing is less than 1min, the correct rate is higher, and the judgment time is not more than 1 second.**

Keywords—Gesture Recognition Layered template matching FDC2214

I. INTRODUCTION

GESTURE recognition is an important part of human-computer interaction technology in the field of artificial intelligence. It is a more natural way of interacting with human communication habits. The development of gesture recognition technology has made it possible for people to interact with machines or other smart devices. With broad application prospects, the related gesture recognition technology can be used in smart home, VR (Virtual Realit), sign language intelligent translation, unmanned system control and other occasions. At present, there are mainly the following mainstream methods for recognizing gestures at home and abroad: Gesture recognition based on wearable sensors [4] [5], gesture recognition based on visual sensors [6], gesture recognition based on acceleration sensors [7], gesture recognition based on special markers [8].In October 2015, Texas Instruments introduced the FDC2214 series of capacitive sensing integrated circuits[9]. Achieve reliable object and human sensing in industrial, automotive and consumer electronics applications in any environment based on low-cost capacitive methods [10]. This paper will adopt a technical solution different from the mainstream gesture recognition method. Based on the principle of LC resonant circuit produced by TI, high-resolution, high-speed, multi-channel FDC2214 capacitive sensor [11] as the core, design a cost-effective, high anti-interference The ability of the gesture recognition device (hereinafter referred to as "device") completes the recognition and judgment function of the one-hand gesture.

II. SYSTEM DESIGN

The design goal of the system is to make a gesture recognition device to realize the judgment of the guessing game and the boxing game, and at the same time, it has two working modes of training and judgment. The judgment of the guessing game here refers to the judgment of the gestures "stone", "scissors" and "cloth". The judgment of the boxing game refers to the gestures "1", "2", "3", "4" and " 5" decision, and each decision time is no more than 1 second. In the training mode, any tester can be trained in gestures and the recognition decision is completed, and the training time of the guessing gesture is no more than 1 minute, and the training of the punching gesture is no more than 2 minutes. The system uses the FDC2214 capacitance detection sensor to realize the gesture detection of the front-end variable capacitance. The STM32F103ZET6 controller performs mathematical analysis, algorithm processing and judgment on the gesture feature information fed back by the sensor, and displays the posture of the current gesture according to the judgment result combined with the OLED liquid crystal display to achieve a specific function, and at the same time, the mode is switched by the button; The OLED display screen displays the current gesture and posture information; wireless transmission is performed through Bluetooth, and the front end feedback data and the controller processing result are uploaded to the computer and displayed by the upper computer, as shown in FIG. 1 .

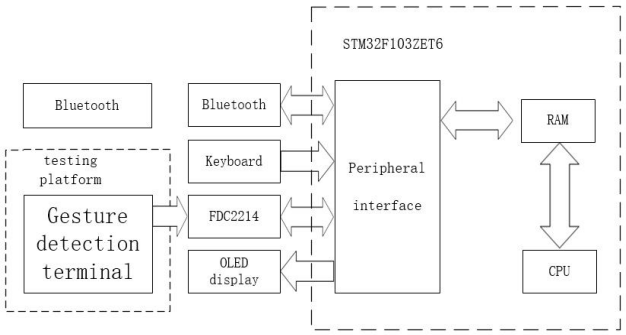

Fig.1 Overall system design block diagram

III. HARDWARE DESIGN

A.Controlling

The control part uses the STM32F103ZET6 minimum system as the master. The chip can provide a series of rich peripherals including external crystal oscillator, A/D converter, voltage regulator module, basic I/O port module, etc. The chip is rich in resources and can be directly programmed by library function. The large amount of data storage and data processing required by the system design is cost-effective and low-power.

B.Detection

The schematic diagram of the detection part is shown in Fig. 2. When the human hand approaches the detection plane, the capacitance of the sensing end will change, thereby reflecting the posture change of the gesture, and the MCU obtains the gesture determination by performing data processing on the collected data.

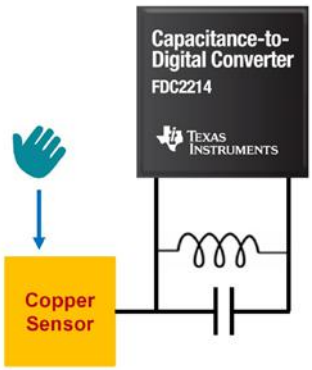

Fig.2 Gesture sensing diagram

The gesture detection platform is a variable capacitance module. This design uses a metal copper plate as one of the plates of the variable capacitor, and the other plate is used by the human hand. When the gesture changes, the effective area of the plate changes to change the capacitance value, as shown in Figure 3.

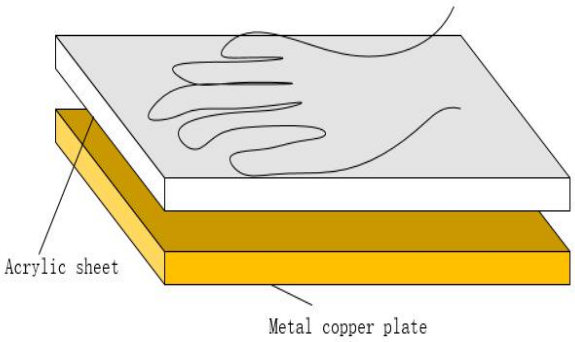

Fig.3 Test platform schematic diagram

Since the FDC2214 sensor is a capacitance-to-digital converter with 4 channels and a resolution of up to 28 bits, it has strong anti-noise ability. We divide the metal copper plate of the front-end gesture variable capacitance sensor into 4 equal-area parts, respectively using the FDC2214 sensor. The data is collected by the channel. It is verified by experiments that the corresponding capacitance value is changed when the gesture is changed. This change is obvious, the sensitivity is high, the data is reliable, the feature analysis and data processing are easy, and the test is convenient. As shown in Figure 4.

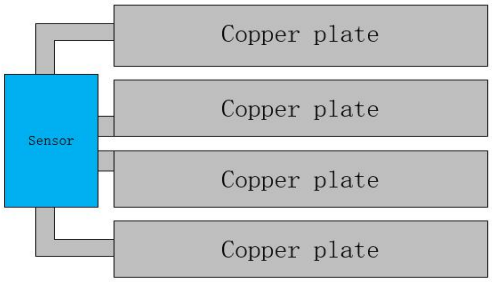

Fig.4 Metal plate inspection platform

IV.SOFTWARE DESIGN

A.General programming

The first design of the sensor and controller I2C interface subroutine. After the FDC2214 conversion data is completed, the MCU issues an interrupt instruction through the interrupt, and the MCU reads the data through the I2C bus and stores it in the built-in RAM of the MCU. Secondly, a sample library program is established for the sample storage in the training mode and the matching judgment of the gesture gesture. Next, a keyboard scanning subroutine, an OLED display program, a serial communication, and a Bluetooth wireless communication module are designed to select and present the game mode and game type. Finally, the overall logic design and adjustments are made in the main function.

B.Decision pattern design ideas

First, the collected data is processed by data, and then the obtained data is processed with the standard or the sample library to take residuals, and the three sets of data are compared with the standard or the sample library for the sum of the absolute values of the residuals, and the absolute value is The smallest one is the closest to the gesture of the standard library, that is, the gesture, the program flow chart is shown in Figure 5.

The algorithm steps are as follows:

a. Take the three sets of data δ_{ij} and the gesture standard or sample library α_{ij} for the sum of the absolute values of the residuals calculation:

$$\Delta_{11}=\left|\delta_{11}-\alpha_{11}\right|+\left|\delta_{12}-\alpha_{12}\right|+\left|\delta_{13}-\alpha_{13}\right|+\left|\delta_{14}-\alpha_{14}\right| \quad \text{(I)}$$

$$\Delta_{12}=\left|\delta_{21}-\alpha_{21}\right|+\left|\delta_{22}-\alpha_{22}\right|+\left|\delta_{23}-\alpha_{23}\right|+\left|\delta_{24}-\alpha_{24}\right| \quad \text{(П)}$$

$$\Delta_{13}=\left|\delta_{31}-\alpha_{31}\right|+\left|\delta_{32}-\alpha_{32}\right|+\left|\delta_{33}-\alpha_{33}\right|+\left|\delta_{34}-\alpha_{34}\right| \quad \text{(Ш)}$$

...

$$\Delta_{li}=\left|\delta_{ij}-\alpha_{ij}\right|+\left|\delta_{i(j+1)}-\alpha_{i(j+1)}\right|+\left|\delta_{i(j+2)}-\alpha_{i(j+2)}\right|+\left|\delta_{i(j+4)}-\alpha_{i(j+4)}\right| \quad \text{(I)}$$

Explanation: i-- Inter-group ordinal number;
j-- The order of data within a group
l--Sample library order, sample "scissors", "stones", "cloth" and "1", "2", "3", "4", "5";

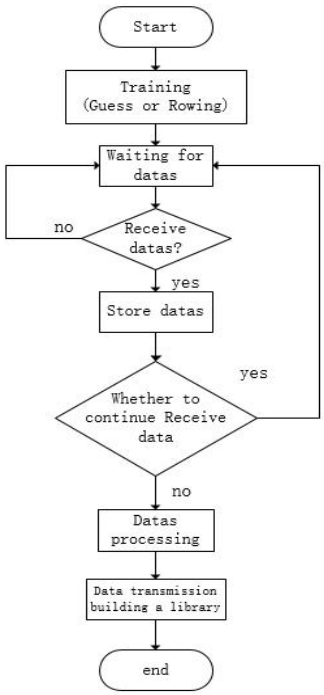

Fig.5 Training mode flow chart

b. The obtained Δ_li are compared and arranged in size, and the position of the minimum value is returned;

c. The retrieved Δ_l1 (the minimum value of each library) is compared and arranged according to the above size, and the library in which the minimum value is located is the gesture represented by the library.

C.Training mode design ideas

In the training mode, unlike the decision mode, the sample library is obtained after training. We will sample the different gestures 4 times/group in the training mode for a total of 3 groups. The subsequent processing method is the same as the judgment mode. The program flow chart is shown in Figure 6.

After actual verification, the correct rate is as high as 98%, and in different environments, as long as the gestures are collected according to the rules, they can be correctly identified, and the interference from the environment is relatively small.

V. TEST PLAN AND RESULT ANALYSIS

A.Test plan

In order to facilitate the training and judgment test, the recommended test plan of the competition is adopted, as shown in Figure 7. The distance between the gesture and the FDC2214 sensor is not less than 1 cm. At the same time, in addition to the device designer, random testers participate in the test

B.Test results and analysis

The test data is started according to the above indicators, and the test results are shown in Table 1 and Table 2. After comparing the arguments, the following conclusions are drawn:

1. The device works in the judgment mode, and can realize the judgment of the punching and guessing of the designated personnel, the correct rate is 100%, and the judgment time is not more than 1 s, which satisfies the design requirements;

2. The device works in the training mode, the number of trainings for any person is 3 times, the training time for guessing gestures is less than 40s, and the training time for punching is less than 1 minute, all meeting the design requirements;

3. The device is switched from the training mode to the judgment mode, and the decision of punching and guessing for any person can be realized, the correct rate is high, and the judgment time is not more than 1 s, which satisfies the design requirements.

4. The device can send device function information in real time through Bluetooth and send gesture information data, which enhances the system's observability and user interface.

TABLE I Guessing game training and judgment test results

Num.	Testers	Training mode duration (s) rock	paper	scissors	result
1	Person A	10.3	8.6	7.6	correct
2	Person B	11.4	11.9	10.8	correct
3	Person C	7.6	6.8	8.8	correct
4	Anyone 1	11.5	10.6	9.8	correct
5	Anyone 2	12.3	11.4	12.6	correct
6	Anyone 3	11.2	9.6	10.6	correct

TABLE II Guessing game training and judgment test results

num	Testers	Training mode duration (s) One	Two	Three	Four	Five	result
1	Person A	6.5	10.2	11.2	7.6	8.9	correct
2	Person B	11.6	11.7	11.2	10.9	10.8	correct
3	Person C	10.8	10.9	11.5	9.7	9.6	correct
4	Anyone 1	11.4	8.7	10.7	10.9	9.8	correct
5	Anyone 2	10.9	8.7	11.2	12.4	14.3	correct
6	Anyone 3	10.7	9.6	11.4	13.5	12.5	correct

VI.CONCLUSION

This design is based on the FDC2214 capacitive sensor. It uses a multi-channel technology and uses a unique mathematical algorithm to solve the problem of incomplete data information using single and dual channels [12] and a slightly lower gesture matching rate. The gesture recognition device was designed to achieve the desired goals.The implementation of the device provides new ideas and new solutions for gesture recognition technology, and has certain reference value.

References

[1] Wang yanfeng. Research on gesture recognition algorithm based on multi-modal input[D]. University of Science and Technology of China, 2017.

[2] Fan Xueqiao. Research on interactive experience evaluation based on gesture recognition VR system [D]. Harbin Institute of Technology, 2017.

[3] Zhao Xiaochuan. Research and Application Prospect of Gesture Recognition Technology[A]. Intelligent Information Processing Industrialization Branch of China Hi-Tech Industrialization Research Association, Signal Processing Expert Committee of China High-tech Industrialization Research Association. The 11th National Signal and Intelligent Information Processing and Application Academic conference special issue [C]. China High-tech Industrialization Research Association Intelligent Information Processing Industrialization Branch, China High-Tech Industrialization Research Association Signal Processing Expert Committee: China High-Tech Industrialization Research Association, 2017: 4.

[4] Wang Yuan, Tan Yongming, Wang baoping. Non-fixed grip gesture recognition based on mixed Gaussian model[J].Journal of Southeast University(Natural Science Edition),2014,44(02):239-243.

[5] User independent hand gesture recognition by accelerated DTW. Hussain Shah M A. International Conference on Informatics, Electronics and Vision . 2012

[6] Chen Yi, Yang Ping, Chen Xuguang. A gesture recognition method based on acceleration feature extraction[J].Journal of Transduction Technology,2012,25(08):1073-1078.

[7] Yao Yuan, Zhang Linjian, Qiao Wenbao. RGB Hand sample mark and gesture recognition in GB-D images[J]. Journal of Computer-Aided Design & Computer Graphics,2013,25(12):1810-1817.

[8] Anti-noise capacitance sensing series [J]. Today Electronics, 2015 (12): 63-64.

[9] Datongda Youshang Group launched an object (human) sensing application solution based on TI technology [J]. Microcontroller and Embedded Systems Application, 2016, 16 (06): 88.

[10] Yu Yanxiu, Mou Fupeng, Chen Yang, Gai Lei. Non-contact gesture recognition device based on FDC2214[J]. Industrial Technology Innovation,2018,05(05):76-81.

[11] Guo Xia, Tan Yali, Shen Miao. Gesture Recognition System Based on FDC2214[J].Sensors and Microsystems,2018,37(12):90-92

Design of Wind Pendulum Control System

Zhang zibo, Teng zeyuan, Li ziqun
（jilin university instrument science and engineering institute,changchun,130061）

Abstract-Wind pendulum system is the subject requirement of the National Electronic Design Competition in 2015. The speed of motor is controlled by PID algorithm, and the trajectory of wind pendulum is planned and controlled. The system consists of control module, power module, driver module, sensor module, measurement module and human-computer interaction module. The motion device is cross-symmetrical distributed by four hollow cup motors. The gyroscope real-time monitors the angle of the pendulum rod and inputs it to the controller. The duty cycle of the two-way PWM signal is adjusted by using the PID algorithm. The signal is sent to the hollow cup motor to realize the trajectory movement. After testing, the wind pendulum system draws a circle of 30-70 cm in diameter within 15 seconds, with an accuracy of (+2.5 cm), which meets the requirements of the competition.

Keywords **PID PWM attitude angle**

I. INTRODUCTION

THE pendulum is a kind of equipment which uses wind as power to control objects. It involves many knowledge such as control theory, automation, embedded system, programming. The control idea and control theory used can be applied in many aspects [1]. PWM technology is a technology that modulates the pulse width and outputs the expected voltage. PWM technology is a basic technology. PWM technology is needed in wind power generation, motor speed regulation, DC power supply and other fields. The PID arithmetic is calculated according to the proportion of deviation (P), integral (I), differential (D), and is applied to the PID controller [2]. PID controller is an automatic controller widely used in the control process.

II. SYSTEM DESIGN

A.Overall plan

By controlling the fan's rotation, the system can complete all kinds of trajectory movement in a square area of 80 cm, and has a certain anti-interference ability. The whole system is mainly divided into four modules: angle acquisition module, control module, execution module and power module. The overall block diagram is shown in Figure 1.

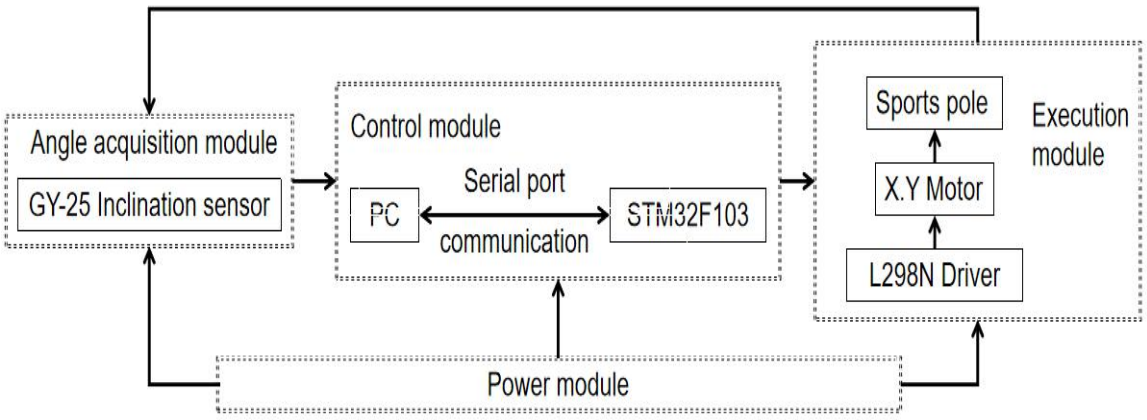

Fig.1 System block diagram

In the process of controlling the motion of the wind pendulum, the attitude angle of the wind pendulum is obtained by using GY25 and sent to the STM32 controller through the serial port. According to the angle returned by the serial port, different PWM waves are output, and then the speed of the motor is changed. After the wind force changes, the wind pendulum moves to the expected position. In this process, the attitude of the wind pendulum changes, and the return value of the GY25 sensor changes, thus forming a closed feedback loop. This is a servo control system. In order to improve the rapidity of the system, the system needs a large bandwidth. The bandwidth of the wind pendulum control system is mainly limited by the inertia of the control object and the actuator. The greater the inertia, the narrower the bandwidth. We

need to design a control system with a bandwidth greater than 0.77Hz. According to Nyquist sampling theorem, angle sampling rate can be selected as FS > 2F theoretically. In order to reduce the maximum adjustment time of the system and achieve better control effect, it is necessary to take FS > 10F or *higher*. STM32 clock frequency 72 MHz, power consumption 36 mA, is a high-performance low-power microprocessor, supporting external interrupts and serial data transmission, on-chip resource-rich, strong data processing capabilities. The motor chooses the hollow cup motor. Hollow cup is a kind of motor with small mass, thrust-weight ratio of 3 to 8, frequency response of 4 to 8 Hz, high mobility and weak anti-interference ability. It has the advantages of small inertia, high flexibility and easy control. Four hollow cup motors constitute a cross-shaped structure. The two hollow cup motors are divided into two groups. When drawing a straight line, two groups of hollow cup motors are controlled respectively. One group gives sinusoidal data to make it draw a straight line, and the other group controls the linearity of the trajectory. When drawing a circle, two groups of hollow cup motors are controlled, and sinusoidal data with phase difference of 90 degrees are given to two groups of hollow cup motors respectively. According to the principle of Lissajou figure, the circular trajectory can be drawn.

B.System Hardware Design

The wind pendulum is mainly composed of rod, universal joint, four hollow cup motors and laser pen. The upper part of the rod is fixed with a beam through universal joint so that it can swing freely. The lower part of the pole is connected with a hollow cup motor which is symmetrical with two pairs of crosses, as shown in Fig. 2. The hollow cup motor works to push the rod to move. A laser pen is installed directly below the rod to show the curve drawn by the wind pendulum. Wind pendulum usually moves freely or conically.

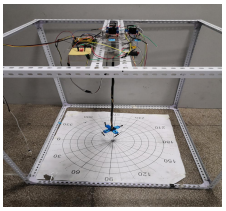

Fig.2 Physical Diagram of Wind Pendulum

C.System Software Design

Fig. 3 is the flow chart of the main program. After power-on and reset, the specified trajectory curve can be drawn. GY25 detects the current attitude angle. After the controller's PID arithmetic processing, it outputs PWM wave to control the speed of the hollow cup motor. At the same time, GY25 detects the attitude angle to judge whether it reaches the specified angle or not. If not, it continues to adjust until it reaches the specified angle..

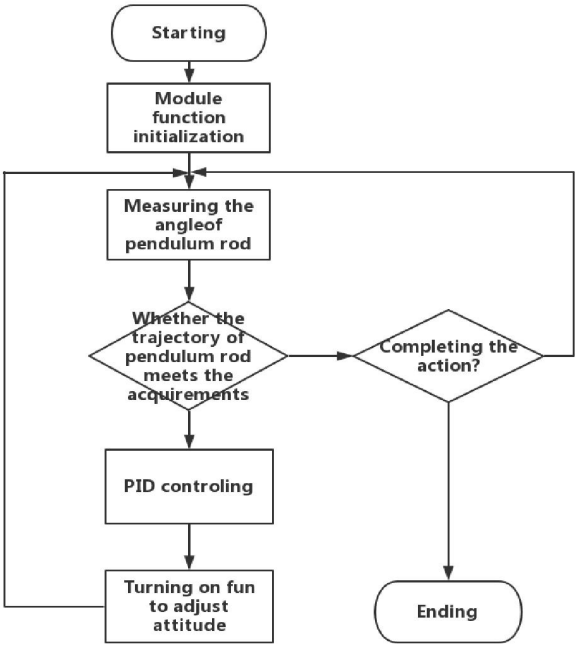

Fig.3 System Flow Chart

III. Analysis of Model and Algorithms

A.Model Analysis

Assuming that the wind pendulum moves freely and ignores the loss, the gravitational potential energy and kinetic energy can be converted to each other in the whole process of the motion of the wind pendulum by using the principle of conservation of mechanical energy. However, due to the loss of wind pendulum movement will eventually stop, can not meet the requirements of continuous line drawing. Therefore, by controlling the hollow cup motor to provide a positive power to the wind pendulum system to offset the loss. Setting PWM produces a sinusoidal wave voltage, which makes the thrust force of the hollow cup change approximately sinusoidally, so that the variable force can work to offset the loss. Adjust the PWM so that the wind pendulum can draw straight lines. Based on Lissajous graph principle, the phase difference of PWM is 90 degrees in X and Y directions. Adjust the value of PWM so that the wind pendulum can draw a circle.

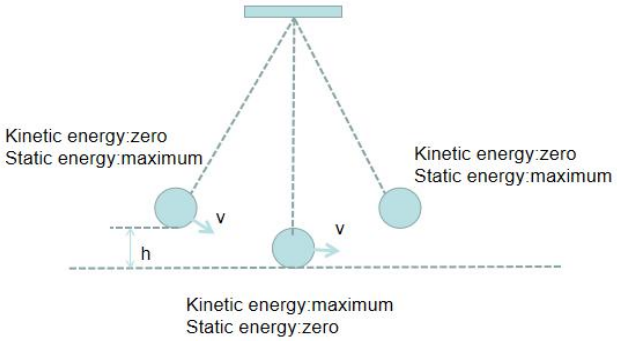

Fig.4 Theoretical analysis diagram

GY25 collects the current attitude angle of the wind pendulum. The expected attitude angle is a = arctan (2*h/l), h is the height and l is the scribed length. The difference between the current attitude angle and the expected attitude angle is deviated. The duty cycle of output PWM_is adjusted by PID arithmetic to control the working state of four fans so as to realize the control of the wind pendulum.

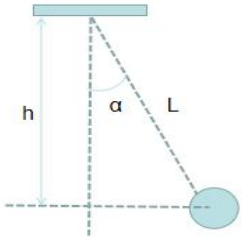

Fig5 Angle analysis diagram

B.Algorithm Analysis

PID_algorithm, proportional P is to adjust the wind swing angular speed, that is, to adjust the rotation speed of the hollow cup. The value of proportional P is positively correlated with the value of adjusting speed. It is hoped that the P value is larger for the system to be fast and stable, but excessive P value may lead to excessive regulation and unstable working state of the system. Integral I improves the accuracy and eliminates the steady-state error of the system. But the integration regulation will reduce the stability of the system and prolong the dynamic response time. The wind pendulum system needs to control the wind pendulum quickly and steadily. Therefore, the integral regulation part of the system should be very weak, that is, it needs very little or even no I. Differential D is to differentiate the angle of the wind pendulum, that is, the angular velocity of the angle change of the wind pendulum. Differentiation has predictability, that is to say, it can advance the control of the system, which can improve the dynamic performance of the system and reduce the adjustment time.

U(t)=Kp*e(t)+Ki_e(t)+u0;

U (t) - output; Kp - proportional amplification factor; Ki - integral amplification factor; e (t) - error; U0 - control reference value (base deviation).

IV. *Test scheme and results*

(1) Starting from stationary, control the wind pendulum to do free pendulum motion within 15 seconds, and let the laser pen draw a straight line not less than 50 cm in length on the ground. The repeatability is good, and the linearity deviation is not more than (+2.5 cm).

Table 1 Linear Trajectory Testing

Test times	1	2	3	4	5	6
Length/cm	50.3	50.2	49.8	49.6	50.0	50.1
Linearity /cm	±1.7	±1.5	±1.8	±1.6	±1.7	±1.7
Completion time/s	10.7	11.0	10.5	10.7	10.8	11.0

(2) Starting from the rest, complete the swing with controllable amplitude within 15 seconds, draw the line segments which can be set between 30 and 60 cm in length, the deviation is not more than (+2.5 cm), and the repeatability is good.

Table 2 Requested Line Length Test

Test times	1	2	3	4	5	6
Setted length /cm	30	35	40	45	50	60
Length deviation /cm	±0.8	±1.0	±1.3	±1.4	±1.7	±1.9
Completion time/s	10.3	10.5	10.7	10.7	10.8	11.2

(3) Pull the wind pendulum to a certain angle (30 ~45) and open it, and restore it to a static state within 5 seconds.

Table 3 Implementing interference to restore stability test

Test times	1	2	3	4	5	6
Interference angle/°	25	30	35	40	45	50
Completion time/s	1.4	1.7	1.8	2.0	3.2	4.1

(4) Driving the wind pendulum to draw a circle on the ground with the laser pen at rest, the radius of the circle can be set in the range of 15-35 cm, and the trajectory drawn should fall in the circle with the specified radius (+2.5 cm). The wind pendulum can restore its original motion state within 5 seconds by artificial disturbance.

Table 4 Drawing circles and applying interference to restor

Test times	1	2	3	4	5	6
Setted radius/cm	30	35	40	45	50	60
Radius deviation /cm	±0.8	±1.0	±1.3	±1.4	±1.7	±1.9
Recovery time/s	10.3	10.5	10.7	10.7	10.8	11.2

V. *Conclusion*

The wind pendulum adopts the PID algorithm to control the motor speed to realize the trajectory motion. The system has a small adjustment time and can track the normal wave motion quickly. Structural design is reasonable, stability is relatively good, anti-jamming ability is strong, can complete the requirements of the straight line and circular trajectory.

It has certain reference significance for the measurement and control system, PID and attitude control.

References

[1] Li Zhengqing. Design and Test of Wind Pendulum Control System [J]. Shanxi Electronic Technology, 2018 (01): 36-38.

[2] Xu Guanyu, Zhou Yefan, Huang Yipeng. Double closed-loop PID control based on wind pendulum control system [J]. Computer knowledge and technology, 2016, 12 (30): 253-255.

[3] Chen Xuhui, Yang Hongyun. Design of multi-serial parallel transmission system based on STM32 [J]. Computer measurement and control, 2019, 27 (01): 166-170.

[4] He Yali, Guo Yanhua, Gao Rongdeng. Design of wind pendulum control system based on STM32F103 [J]. Intelligent computer and application, 2017, 7 (04): 76-78.

[5] Xia Tong, Ye Xiaohan, Hu Ting, Sui Zhucui. Research and application of wind pendulum experimental platform based on ARM [J].Experimental Science and Technology, 2017,15(04): 34-38+79.

[6] Zhang Wei. Reliability analysis of SCM automatic control system [J/OL]. Integrated circuit applications, 2019 (03): 54-55 [2019-03-05].

[7] Jin Dongzi, Zhu Jun. Wind Pendulum Control System Based on STM32 [J]. Computer Knowledge and Technology, 2016, 12 (23): 180-182+194.

[8] Xu Wenqi, Chen Jiaying, Yuan Juming. Research on wind pendulum control system based on improved PID algorithm [J]. Computer knowledge and technology, 2016, 12 (11): 256-257.

[9] Wang Kexin. Simple control equipment based on MPU6050 [J]. Electronic production, 2018 (11): 86-89.

[10] Liu Tuosheng. Design of Inverted Pendulum Control System Based on STM32 [J]. Computer Knowledge and Technology, 2018, 14 (36):

3D Laser Scanner Design And Scan Data Processing

Wang Fan, Xu Linlin, Quan Wenjun
(College of Instrumentation & Electrical Engineering, Jilin University, Changchun 130000)

***Abstract*—Based on 2D laser radar and 1D pan-tilt device, a 3D laser scanner is designed as a data acquisition device. At the same time, the scanning control and data processing system was designed on the host computer. The scanning control system realizes the control of the scanning range and the scanning precision. The data processing system converts the coordinates into the global coordinate system through the mapping relationship of the collected data, and converts the data into a standard point cloud format file for storage. In order to further improve the accuracy of the data, after designing the filter to eliminate the outliers, a three-dimensional model is constructed to realize discrete point cloud data visualization. The results show that the system can reconstruct the three-dimensional space better.**

***Key words*—2D laser radar; control system; point cloud filtering; 3D reconstruction**

I. INTRODUCTION

IN recent years, with the development of computer graphics and computer vision, 3D scanning reconstruction technology has gradually demonstrated its advantages in various fields, such as industrial measurement, topographic mapping, automatic navigation, drone aerial photography, and gob area survey.

Traditional 3D scene reconstruction methods include active modeling and passive modeling. Active modeling is a point cloud imaging by collecting scene information at a time[1]. Passive modeling is based on a single image, or multiple images, directly using the image for 3D modeling. The latter does not need to calibrate the global coordinates relative to the former, avoiding the geometric complexity in the real scene, but the computational complexity is high, and there are major defects in reducing the geometric accuracy and obtaining the integrity of the three-dimensional information. With the rapid development of laser radar scanning technology, it has the characteristics of fast measurement speed, high precision, non-contact, and greatly reduced application cost, making it possible to perform 3D reconstruction through laser radar. Therefore, the application of active modeling is more and more extensive[2].

The laser radar used in active modeling realizes the measurement of a single plane through the rotation of the steering gear and the single point ranging of infrared rays. The returned data includes both the measurement distance and the measured orientation, and is less affected by the external environment under the operating state. But a single 2D laser radar can only get information on a section. In order to obtain three-dimensional data for modeling, if the three-dimensional laser radar with the same accuracy and measurement range is used, the cost will be ten times higher than that of the two-dimensional laser radar, which limits the application in the general scene. Therefore, this paper extends the original two-dimensional to three-dimensional through a self-designed mechanical device to realize three-dimensional scene reconstruction.

In recent years, many researchers have modified 2D laser radar in a variety of ways to achieve 3D scanning. However, most of the mechanical structures are complex or the measurement range is limited, which makes the calibration of the global coordinates difficult, and the overall design system scheme for the 3D laser scanning system is lacking[3]. The existence of these problems also pointed out the direction for the later study of the use of two-dimensional laser radar to achieve three-dimensional reconstruction.

Based on two-dimensional laser radar and one-dimensional rotating pan/tilt, this paper designs a three-dimensional laser scanner as the acquisition device. At the same time, the mechanical control and data processing system of the upper computer is designed to realize the three-dimensional reconstruction of the scanning scene.

II DESIGN OF COORDINATE ACQUISITION SYSTEM

A Scanning schemes

Since the 2D laser radar uses a point laser to scan, in the case of one week of scanning, only a set of distance information in a set of polar coordinates in a single section can be acquired. If you need to expand to a 3D scanner, there are generally two ways, one is "change point to line", change the point laser to linear laser, get the distance information of one section at the current angle at one time, and the other is to add mechanical structures, such as rotating devices which are added as extension axes to obtain information on the third dimension[5].

Applying the first method does not affect the scanning rate, but the brightness of the laser increases with the increase of the distance, the measurement speed is limited, and the measurement distance of the original 2D laser radar is large. Besides, the use of the camera is more demanding. The workload increases, and the installation accuracy of the scanning device is high. Applying the second method, it is necessary to control the axis of rotation with additional degrees of freedom, introducing a new error, and the scanning speed is reduced, but the second method is to measure the distance. When the accuracy of the shaft meets the requirements, the introduced error can be artificially reduced. The reduction of the original 2D laser radar is reduced, and only the rotating device needs to be designed. Therefore, in the experiment, the 3D scanner was designed by adding a rotating shaft.

In the project, a 3D laser scanner was built by using the HLS-LFCD2 model 2D laser radar and the RDS3115 digital steering gear controlled camera platform device. The mechanical structure is shown in Fig.1.

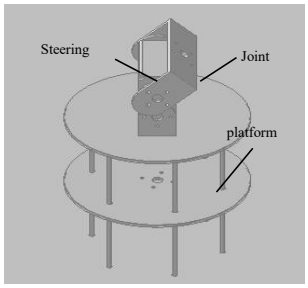

Fig.1 Mechanical structure diagram

The steering gear drives the rotation of the mechanical joint 1, and the 2D radar is fixed at the joint 1, and the laser radar continuously scans the plane of the laser. Taking the O point of the geometric center of the steering shaft of the steering gear as the origin, a space rectangular coordinate system is established as shown in Fig.2 below.

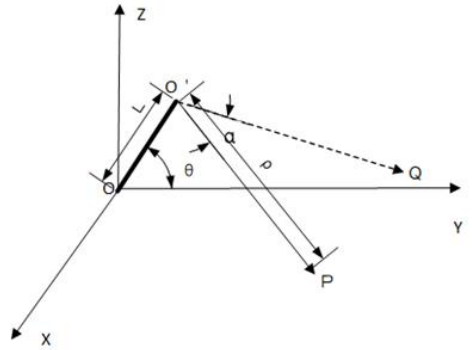

Fig.2 Coordinate system diagram

O ' is the geometric center of the radar, the plane O ' QP is the radar scanning plane, the XOY plane is parallel to the reference level surface, according to the current measurement angle α of the 2D laser radar, the deflection angle θ of the mechanical joint, and the distance ρ from the measured point P to the radar center， we knows that the coordinates (x, y, z) of the point P to be measured can be calculated by the following formula:

$$\begin{aligned} x &= \rho\sin(\alpha) \\ y &= \rho\cos(\alpha)\sin(\theta) + L\cos(\theta) \\ z &= \rho\cos(\alpha)\cos(\theta) + L\cos(\theta) \end{aligned} \quad (1)$$

The azimuth angle α and the distance ρ are obtained by decoding the data outputted by the laser radar serial port, and the deflection angle θ is obtained according to the relationship between the PWM output of the controller and the physical deflection amount of the steering gear.

B Mechanical control

As shown in Fig. 1 of the above mechanical structure, the mechanical control portion is mainly for the operation of the steering gear, and the accuracy of the steering gear determines the accuracy of the above-mentioned deflection angle θ. The RDS3115 digital steering gear is used in the project, and the STM32ZET6 of ARM is used as the controller to output PWM wave for control. The main control characteristics of the steering gear are shown in Table 1.

Table 1 Main control specification of steering gear

No.	Item	Specification
1	Control System	PWM
2	Pulse with range	500~2500μsec
3	Neutral position	1500μsec
4	Running degree	180°
5	Dead band width	3μsec
6	Operating frequency	50~330Hz
7	Rotating direction	Counterclockwise

A 20 ms time base pulse is generated by the controller, and the high level portion of the pulse is in the range of 0.5 ms to 2.5 ms, and the maximum interval is 2 ms. According to Table 1 and the servo's data sheet, within this range, the angular value of the output is linear with the width of the high level. The steering output angle value θ is calculated as follows:

$$\theta = \frac{N_{set} - 500}{2500} \times 180 \quad (2)$$

The unit of θ is degree, and N_{set} is set by the controller, and the range is between 500 and 2500, so that the steering angle can be deflected within the range of 0 to 180 degrees.

Since there is a deadband when the steering gear is controlled, during the control process, the minimum interval between two adjacent deflection angles θ is:

$$\Delta\theta = \frac{3\mu\text{sec}}{(2500-500)\mu\text{sec}} \times 180 = 0.27^\circ \quad (3)$$

Therefore, during the control process, the set step spacing is an integer multiple of 0.27°.

III SOFTWARE CONTROL AND RECONSTRUCTION SYSTEM DESIGN

A The design of the control system.

The host computer control system of this paper is based on the Win 10 development platform on the PC. The MFC in Visual Studio 2015 is used as the development environment. By writing the message response function of the main interface control, the scanner control and scan data storage functions are realized. MFC contains a large number of Windows handle wrapper classes, as well as a variety of Windows built-in controls and wrapper classes for components[4]. Rich built-in controls facilitate the design of visual interfaces,and the system design block diagram is shown in Fig 3.

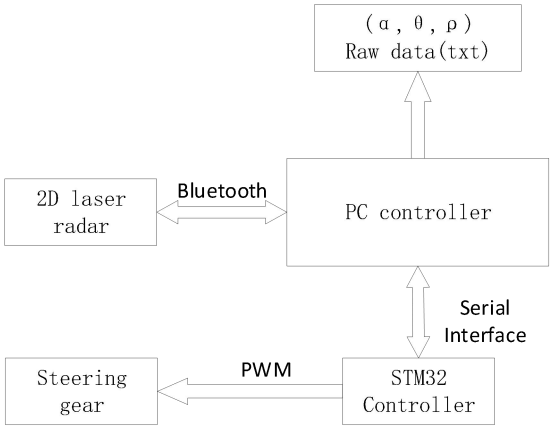

Fig.3 Coordinate system diagram

As can be seen from the above figure, the tasks of the host computer PC include communication with the 2D laser radar and control of the steering gear by the lower computer STM32. Since the data transmission interface of the laser radar is in the UART format, in order to avoid the interference of the transmission line to the scanning process, the HC-06 wireless Bluetooth module is used for communication between the upper computer and the radar. Communication includes controlling the start and stop of the radar and acquiring ρ and θ in the radar scan plane. Since the radar has been packaged into simple components, the operation of transmitting data to the radar is mainly to decode each frame of data transmitted by the radar, and to preserve the angle and distance information in each frame of data. At the same time, the host computer communicates with the STM32 through the serial line RS232, and controls the steering gear to realize the rotation of the joint. There is also a set of communication command protocol between the host computer and the STM32 controller for command control. In the upper computer interface, by selecting and setting the initial scanning position, the scanning interval and the ending scanning position in the relative coordinate system, the scanning path setting is ensured.Besides, while controlling the joint rotation, the form of buffer-response is used to ensure that the steering gear is completed after the steering task is completed. The overall scanning progress is displayed in the form of a progress bar on the upper computer interface, so that the user can observe the scanning progress in real time.

The flow chart of the upper computer control system is shown in Fig. 4. According to the requirements of the project, the multi-threading method is adopted in the MFC design, in which the main thread is used to respond to the user's operation, and the user requirements instructions such as opening the serial port, opening the file, saving the file, etc. are converted into program instructions for execution, judgment, and feedback execution result. The designed MFC interface is shown in Fig.5 below. Both the accept box and the send box in the interface operate on the serial port of the servo. The send box displays the setup command or the manual edit command, and the acceptance box displays the response of the lower computer. As the lower computer, the function of the STM32 controller is mainly to communicate with the host computer, receive the data sent by the host computer, and set the starting angle, step interval and end angle of the servo. According to the command of the host computer, the step servo is driven and the host computer is returned to execute the result. The system will decode the received data from the radar to obtain the azimuth angle α and the distance ρ and the deflection angle θ controlled from the steering gear.The three datas are stored in the format of (θ, α, ρ) in the txt file set by the user as the original file of the subsequent data processing system.

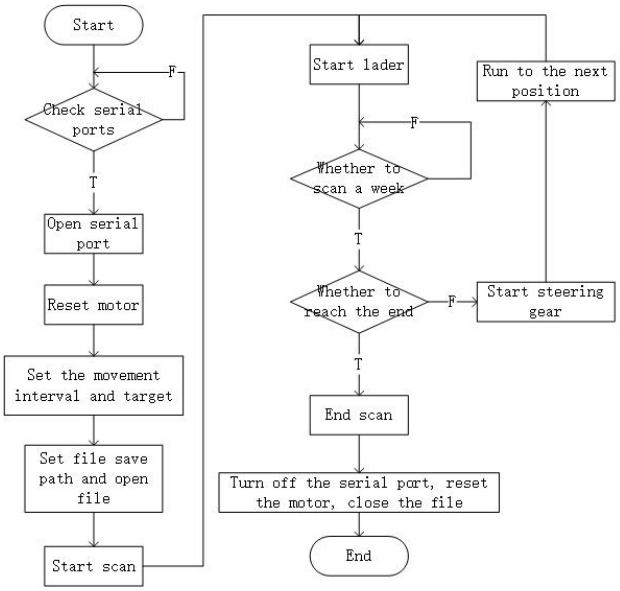

Fig.4 Control system flow chart

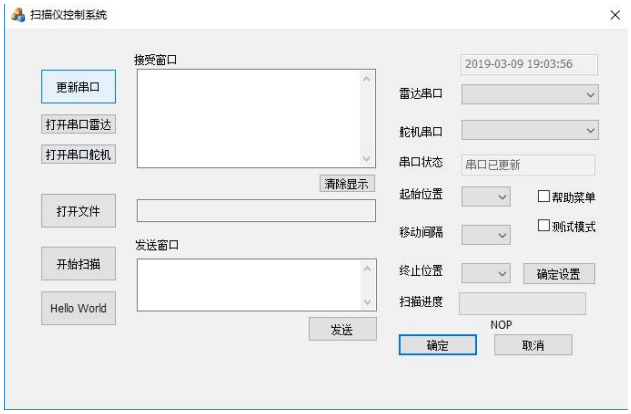

Fig.5 Control system main interface

B. Point cloud processing design

In order to improve the speed of data processing, the calculation process of point cloud processing is simplified, and the visualization of discrete point cloud data is performed. In the project, the MATLAB GUI platform has established a small system dedicated to the project's coordinate transformation, point cloud data processing and data imaging. The composition of the point cloud processing system is shown in Fig.6 below.

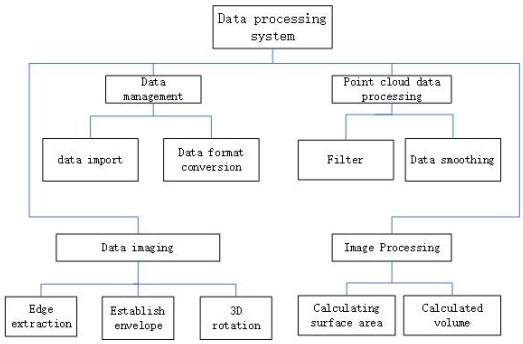

Fig.6 Control system main interface

In the project, import the txt text file stored in the form of (α, θ, ρ) in the previous stage, and then convert it into the form of three-dimensional data coordinates (X, Y, Z) according to the formula (1.1), and respectively the output is saved in txt and pcd format. At this time, the pcd stores the original standard point cloud data.

The number of point clouds obtained by the scanner is extremely large, and the measurement data will reach tens of thousands or even hundreds of thousands of points. In addition to the normal data points, the huge amount of data also contains unpredictable noise points. The source of the noise point is mainly the error caused by the laser scanning hardware itself. In addition, it is related to the actual situation of the acquisition, such as the presence of smoke, particles, corners, etc. in the scanning area, which is obviously unfavorable for the later work such as point cloud matching. Therefore, it is necessary to perform a series of data denoising on the data points to filter out the noise points.

For removing the noise points present in the data, the field of each point is statistically analyzed in the project to delete some points that do not meet the requirements.

The main method of deletion is to calculate the distance distribution between the point and the adjacent point for each point in the point cloud, to find the average value of the distance, and compare the average value with the global mean and standard deviation to determine whether the point is an outlier. The standard C++ library provided by Point Cloud Library (PCL) is referenced in the project. By using the StatisticalOutlierRemoval filter, the number of neighboring points and the distance threshold of each point are set. When the distance between all neighboring points and the point exceeds the threshold, it is considered to be an outlier and is clipped, and the filtered result is finally saved and used for subsequent three-dimensional imaging.

After filtering, import the file again, obtain the point cloud contour, call the volume() and surfaceArea() functions provided by Matlab to find the volume and surface area of the point cloud contour, and display it on the main interface. In order to enable the user to further observe the final imaging, three sliders are added to the interface, and the sliding slider can rotate the point cloud data imaging results in three directions of X, Y and Z. When the slider is moved, the callback function is called to obtain the position of the current slider then convert into an angle value. A 4×4 transition matrix is created according to the rotation axis and the angle value.Get the current point cloud location at the same time and the MATLAB function pctransform() is called to get the new point cloud data after rotation and refresh the display.

The main interface of the system is shown in Fig .7. The callback function of the button "file processing" implements the conversion data format and stores it according to the pcd format. The "data processing" contains the main processing algorithms for visual display. The "filtering" points for the standard format. filtering and generating filtered results which are saved in txt format. The drop-down bar can operate on the left image area, including "clear", "display original 3D point map", "display point cloud map", and "display point cloud envelope map" for the right image area. Since the envelope map is the result of the final rendered image, it is displayed separately in the right column for visual comparison with other imagery.

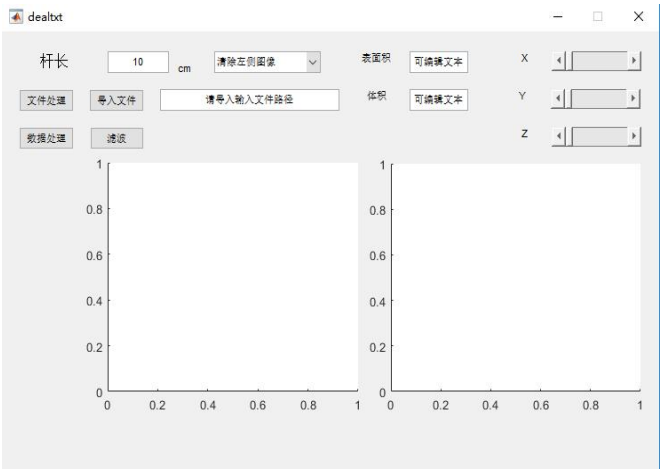

Fig.7 Data processing system main interface

IV Experimental Verification

The test was carried out in a fixed rectangular body of 50 cm × 45 cm × 28 cm, first with a fixed deflection angle α, let α = 90 °, and subjected to 2D laser radar test with a scanning section of 50 cm × 45 cm. The obtained three-dimensional point data imaging results are shown in Fig.8.

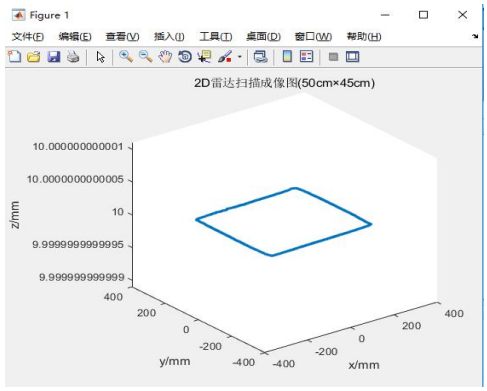

Fig.8 2D lidar scanning test diagram

The calculated length is Ly = 495.88 mm, Lx = 457.19 mm.

Partial testing is performed on a cuboid of a certain size. The filtering result shows that the number of original data is 4581, and the filtered data is 4513. The results before and after filtering are as shown in Fig.9 below.

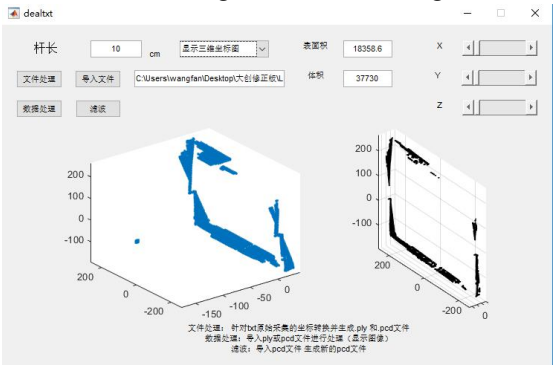

Fig.9 3D lidar scanning test chart

It can be clearly seen from the figure that after filtering, the noise points are removed. The image on the right shows the contour of the final point cloud and the image on the left shows the initial data.

V Conclusion

This paper introduces a method of 3D data acquisition based on 2D lidar and pan-tilt device. With the control system based on MFC design, the three-dimensional points in the specified area are collected, and the coordinate transformation relationship is derived, and the coordinates are converted into the global coordinate system to realize the collection and storage of the three-dimensional data. At the same time, through the GUI tool in MATLAB software, the collected raw data is preprocessed, and the outliers in the point cloud are removed by the filter to realize the noise reduction filtering, and the point cloud contour is drawn.According to the preprocessed data,the 3D reconstruction is finally displayed on the interface of data processing. The results of actual acquisition and reconstruction show that the device can perform three-dimensional reconstruction better in a less complex environment.

References

[1] Shang Tao, He Huichao, Wang Wei, Gong Wenbin, Dai Yongqiang.An Algorithm for 3D Imaging of 2D Lidar[J].Journal of Jilin University:Engineering Science,2012,42(S1):91-95

[2] Zou Xinci, Guo Zhe, Qi Xin, Zhang Han.Study on preprocessing method of indoor positioning data for 2D laser radar[J].Mine Surveying,2017,45(03):77-81.

[3] Huang Fengshan, Ma Shuai, Xue Ze. Rotating two-dimensional lidar measurement system and its calibration method [J]. Optoelectronics•Laser, 2018, 29(09): 987-995.

[4] Li Lin. 3D reconstruction system of indoor environment based on laser scanning [D]. Harbin Institute of Technology, 2016.

[5] Wang Zenglan. Research on 3D reconstruction based on 2D lidar data [D]. Northeastern University, 2013.

Circuit delay and frequency measuring device design

Gao Xing, Zhang Chenggang, Liu He
(College of Instrument & Electrical Engineering, Jilin University,Changchun 130022,China)

***Abstract*—The circuit delay and frequency measuring device uses STM32 as the main controller, and converts the analog quantity into digital quantity through the waveform conditioning circuit, and combines the FPGA to accurately delay the input signal. The delay interval step value is less than 10 ns, and the step process control is adjustable. The frequency measurement uses the timing counting method. The phase-locked loop is used to multiply the reference clock source of the FPGA to 200MHz, and the set gate time is 0.5s. The FPGA communicates with the main controller through SPI, and the main controller obtains the frequency of the signal to be tested after decoding and data calculation. In the frequency range required by the title, the relative error of the frequency measurement is not more than 2.1%, so as to achieve accurate delay and frequency measurement of the circuit, and display the input signal and the delayed signal in the form of a curve.**

***keywords*—RMS detection delay circuit frequency measurement SPI communication**

I. FOREWORD

With the advent of the information age, delay and frequency measurement have been widely used in many fields of the country. For example, politics, military, technology, and the economy. Frequency measurement systems are widely used in industrial control, transportation, and electronic information. Timing, industrial control, positioning and navigation, digital technology and computers are all inseparable from frequency measurement and quantity control technology [1].

Commonly used frequency measurement methods include timing counting method and equal precision measurement method[2]. The equal-precision measurement method is suitable for occasions with large frequency variation range. The actual frequency measurement start time is the synchronous gate opening time, which is related to the system clock and The measured signals are synchronized, and the frequency does not affect the error caused by the frequency measurement. After calculating the ±1 error, it can be known that the frequency measurement low frequency band error of the timing counting method is within the allowable range, so the frequency measurement is performed by this method.

The delay module can use the analog method RC circuit for delay, but this delay method cannot adjust the delay time program control, and the delay time is difficult to control. The conditioning signal is converted into a digital signal by using a conditioning circuit, and then the unit step value delay is performed by using the FPGA, and a plurality of step values are superimposed to realize a long time delay, and the delay precision requirement can also be met.

II.DETECTION CIRCUIT DESIGN

RMS detection using the AD8361 chip: The AD8361 is a true rms response power detector for high frequency signals with a detection range of LF-2.5 GHz and a maximum nonlinear distortion of ±0.25 dB. The advantage is that it can measure the effective value of various complex waveforms without regard to the degree of waveform distortion, and can be powered by a single power supply with low power consumption.

The effective value of the voltage is defined as

$$U_{\text{rms}}=\sqrt{\frac{1}{T}\int_0^T U^2(t)dt} \qquad ①$$

Therefore, in order to obtain the rms response, there must be a volt-ampere characteristic of the square-law detection [3]. The amplitude-frequency characteristic test device uses the integrated detection chip AD8361 for detection, and the output is a DC voltage representing the effective value of the input signal, and is converted into a peak-to-peak value of the input signal according to the crest factor of the sine wave.

$$V_{p-p}=2.828U_{\text{rms}} \qquad ②$$

The rms detection circuit is shown in Figure 1. The input is buffered using the ADA4817, which is used to prevent the output characteristics of the preamplifier from being affected by load variations. The output of the AD8361 detector is followed by the RC circuit. The first-order RC circuit is used for anti-aliasing filtering, and the output signal is sent to the ADC for voltage acquisition

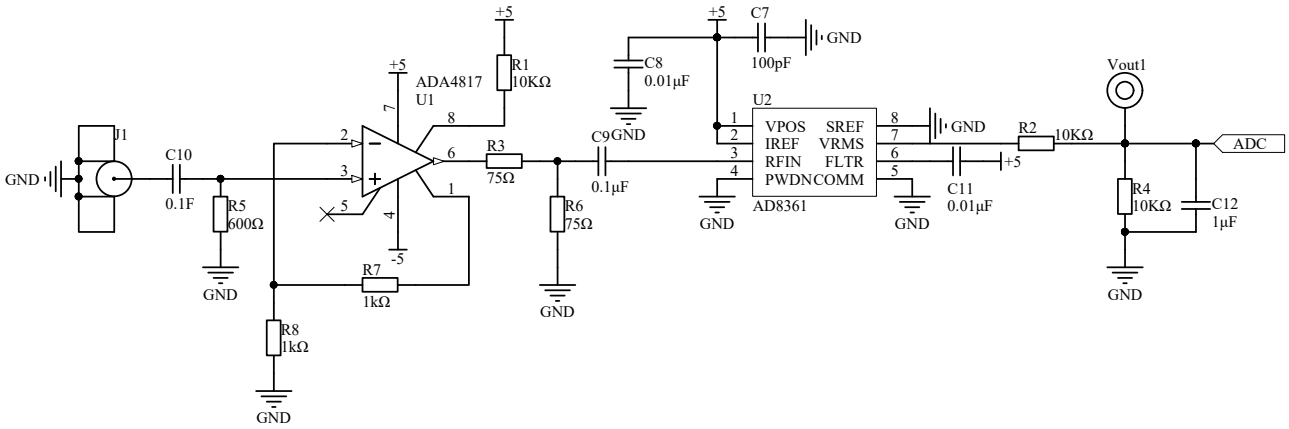

Fig .1. Circuit diagram of AD8361 geophone

III. DELAY CIRCUIT MODULE

The signal is converted into a digital signal through the pre-conversion process, and the high-frequency digital signal is processed into a digital signal. The high-frequency digital signal is processed and analyzed by FPGA. The FPGA is used to implement the delay circuit and the signal frequency measurement circuit, and the SPI communication protocol and the main The controller completes the transfer of control signals and data.

The delay circuit chip uses the Cyclone2 series to delay the square wave signal generated by the signal conditioning circuit, so that the time difference of the time interval can be adjusted between the input and output of the square wave signal, thereby achieving the delay effect on the input signal [4] [5]. The high rate of FPGA processing of digital signals ensures the accuracy and stability of the delay time. The core idea of the delay program [6]: When the rising edge of the clock comes, the input signal and the latter signal are logically operated to complete the delay of the input signal, thereby completing the delay of the reference clock frequency, the reference clock frequency. For 50MHz, the delay step is 20ns. Did not achieve the expected results [7].

Calling the analog phase-locked loop (PLL) inside the chip to multiply the reference clock, it can reduce the step value of the delay [8][9]. It is calculated that if the reference frequency is multiplied to 300MHz, the step value of the delay is too small, the delay efficiency is not high, and the logic gate is occupied too much. Multiplying to 100MHz will cause the clock frequency to be too low to meet the clock frequency required by the frequency measurement circuit. The accuracy of the frequency measurement is not high enough. Therefore, the frequency multiplication to 200MHz, the minimum step size of the delay is 5ns, which can satisfy the problem. The step size is 10 ns. The clock frequency can meet the requirements of the frequency measurement clock, and the theoretical frequency measurement accuracy can meet the requirements of the title.

The delay time is set by using four peripheral buttons, that is, how many steps are set. The program monitors the four independent buttons in real time to determine if the button is pressed, thereby determining the delay time of the input. In order to prevent the wrong touch of the button and repeated presses, the input delay time is incorrect. The button is added to the jitter program. After the input is completed, press the confirm button to ensure the accuracy of the external input delay time.

After the actual test, the actual delay step is 5 ns, which can meet the step requirement in the problem. It is feasible to use the external button to input the delay time. There is no key time reading error, and the input is in the range of 100Hz-20MHz. The signal is delayed to achieve the desired result.

IV.FREQUENCY MEASUREMENT MODULE

Common frequency measurement methods include measurement cycle frequency measurement, legal time counting method and equal precision frequency measurement. The measurement period method is often used to measure the low-frequency signal frequency. The frequency range measured by the equal-precision frequency measurement is wide, and the measurement accuracy of the high and low frequency bands is consistent [10].

The frequency range to be tested is 100Hz-20MHz, the step value is 10Hz, and the method of frequency measurement [11] is relatively complicated. After calculation, the frequency can be measured by the timed counting method. Therefore, the frequency of the

input signal is measured by the timed counting method.

The reference frequency of the FPGA is 50MHz, and the phase-locked loop 4 times the frequency is 200MHz. Assuming that the gate time is 1s, the hardware resources are too much, and the real-time performance of the frequency measurement will be affected. If the gate time is too short, the ±1 error of measuring the low frequency band will have a large influence. After the actual test, setting the gate time to 0.5s can ensure the measurement accuracy and reduce the influence of ±1 error [12].

The data obtained by the FPGA frequency measurement is a binary number, and the obtained frequency cannot be displayed. The SPI communication protocol is used for data transmission between the FPGA and the main controller. While the main controller (STM32) sends the command, the FPGA transmits the acquired binary number to the main controller [13], and the main controller obtains the frequency of the signal to be tested through decoding and mathematical operations.

After the actual test, the communication between the FPGA and the main controller is normal, and the binary number sent by the frequency measurement module to the main controller is decoded, and the result is the frequency of the input signal. Compared with the frequency measured by the oscilloscope, the frequency measurement result is accurate, the real-time line is good, and the error is within the allowable range, which can meet the requirements of the title.

V. TEST PLAN AND TEST RESULTS

A.test plan

(1) Link and control the DDS frequency control word and amplitude control word to output any sine wave with amplitude between 10mV and 200mV and frequency between 100Hz and 20MHz. Use the oscilloscope to detect the delay and frequency of the device. performance.

(2) Verify the accuracy of the frequency measurement module by comparing the frequency measurement module with the oscilloscope.

(3) Verify the accuracy of the delay module by comparing the set delay time with the oscilloscope display.

(4) Verify the accuracy of the detector module by comparing the set amplitude with the oscilloscope display

B.Test results

After the hardware circuit is built, the detection circuit, the delay circuit module and the frequency measurement module all achieve the expected goals. The stability of each circuit module is high and can meet the design requirements. After the cascade debugging of each circuit module, the detection effect of the detection module in each frequency range, the delay time interval of the delay circuit, and the frequency measurement data of the frequency measurement circuit are shown in Tables 1, 2 and 3..

Table 1 Detection Accuracy Test

Set valid value(mV)	1KHz output amplitude（mV）	1KHz relative error (%)	100KHz output amplitude(mV)	100KHz relative error (%)	20MHz output amplitude (mV)	20MHz relative error (%)
20	21.6	8.0	21.6	8.0	20.6	3
40	40.8	2.0	40.8	2.0	41.6	4
60	60.8	1.3	60.0	0.0	61.5	2.5
80	80.0	0.0	80.0	0.0	82.0	2.5
100	100.0	0.0	100.0	0.0	104.0	4

Table 2 Delay Circuit Test

Input square wave frequency	Setting delay	Measured value	Absolute error
1KHz	100ns	95.000ns	5.000ns
1KHz	100us	99.993us	0.007us
100KHz	100ns	93.600ns	6.400ns
100KHz	100us	99.973 us	0.027us
20MHz	100ns	99.000ns	1.000ns
20MHz	100us	99.960us	0.040us

Table 3 Frequency measurement module test

Setting frequency	Output frequency	Relative error(%)
1 kHz	1.021kHz	2.1
10 kHz	10.00kHz	0
100 kHz	100.156kHz	0.16
1 MHz	999.031kHz	0.1
10 MHz	9.999MHz	0.1
20MHz	19.986MHz	0.1

VI.CONCLUSION

The circuit delay and frequency measuring device has been tested and found that there is no obvious distortion when the peak-to-peak value of the output signal is 8mV, and there is no obvious distortion in the signal band. The signal with peak-to-peak value less than 200mV and frequency 1kHz-100kHz can be shaped into square wave. The amplitude is 3±0.5V. The delay module delay time range is 100ns-100ms, the program control is adjustable, and the adjustment step size is less than 10ns. The measuring device has a resolution of 0.1 μs, an absolute error of 1 μs, and can display waveforms before and after the delay. After actual testing, the designed circuit delay and frequency measuring device meets the requirements of the problem. The design won the second prize of the 2018 Jilin Province Electronic Design Competition.

References

[1] Zhang Yingping, Ji Jiahao, Li Guojun. Research and Design of Simple Circuit Delay Measurement Device Based on Single Chip Microcomputer——Study on Students' Practice Training[J].Digital Technology and Application,2018,36(12):129-130.

[2] Huang Zhiwen, Lu Meiji, Zhong Xujie, Wang Chunmei, Wei Shanyu. Design of Digital Frequency Measurement Device Based on FPGA[J]. Electronic Technology, 2018, 47(12): 78-79+66.

[3] Alan V. Oppenheim, Alan S. Willsky, S. Hamid Nawab. Signals and Systems, Second Edition [M]. Beijing: Publishing House of Electronics Industry, 2009.6

[4] Kang Huaguang. Electronic Technolo Foundation·Simulation Part (Sixth Edition) [M]. Beijing: Higher Education Press, 2006.1

[5] Lin Chang, Pang Hui, Chang Bin, Liu Dong, Qi Xuebing, Gao Lu, Yan Heming. Simulation Modeling and Delay Compensation Algorithm of DC Circuit Breaker Based on FPGA[J]. Power System Technology, 2018, 42(05): 1417-1423.

[6] Ling Jiajun, Dong Yinghui. Research and Design of Signal Delayer Based on FPGA[J].Information Communication,2015(09):73-74.

[7] Ma Fei, Liu Qi, Wang Peng, Zheng Xianguo. A Micro-delay Method for Signals Based on FPGA[J]. Computer Measurement & Control, 2015, 23(08): 2868-2870+2874.

[8] Geng Liangfeng, Chen Zili. Design and Implementation of Delay Block LMS Equalizer Based on FPGA[J]. Computer Measurement & Control, 2013, 21(01): 184-187.

[9] Wang Pengxiang, Zhou Wei, Lai Jinmei. FPGA IO Delay Management Circuit Based on Digital Delay Phase-Locked Loop[J]. Journal of Fudan University(Natural Science), 2013, 52(04): 497-504.

[10] Wang Yandong, Shao Ying, Wang Liming, Xiao Xiongbo. Intelligent and High Precision Frequency Measurement Design Based on FPGA[J].The Chinese Test,2014,40(04):119-12.

[11] Xu Deren, Huang Ming, Wang Can, Jixiang. Design of Broadband and Other Precision Digital Frequency Measurement System[J].Electronic Science and Technology,2016,03(06):685-688.

[12] Liu Meiying. Design and Implementation of Frequency Measurement Instrument Based on FPGA[J]. Electronic Technology and Software Engineering, 2017(23): 84-85.

[13] Pan Yu. Pulse width measurement method based on FPGA and STM32[J].Laboratory Research and Exploration, 2017, 36(02): 83-86

Design of Mutual Inductance Current Signal Detection Device Based on FFT

He Liu, Qianxin Hu, Xiaofei Huang
（college of instumentation and elctrical engineering,changchun,130061）

Abstract **—Current is an important parameter that reflects the characteristics of the circuit and is therefore of great value for the detection of current signals. In this paper, a set of FFT-based mutual inductance current signal detection device is designed. The device achieves non-contact measurement of the loop current signal, and is composed of hardware and software. The hardware circuit includes a mutual inductance current sensor and a detection circuit, and the software part is mainly composed of STM32, and the frequency of the signal is obtained by Fourier transform. Amplitude information. After detection, the frequency resolution can be achieved, the amplitude resolution can be achieved, the measurement current signal frequency error is less than, the amplitude error is less, and the measurement accuracy is high.**

Keywords**—Mutual inductance current signal detection Non-contact measurement FFT**

I. INTRODUCTION

AT present, the method of current signal detecting device is relatively mature [1], both the pyroelectric method and the bolometer method can measure the high-frequency current [2] [3]. In the traditional current measurement method, usually the measured object and the measuring instrument are connected in series, resulting in a large circuit load effect, and the measurement difficulty is also increased [4]. With the rapid development of electronic technology, microprocessor-based current detection devices can communicate with computers to transmit data, complete automatic detection of measurement objects, and promote innovation in the field of measurement and control instruments [5] [6]. The device is designed with the insufficiency of the current current measurement technology to be connected in series. Combined with the microprocessor current detection technology, an algorithm-based mutual inductance current detecting device is designed, which adopts the non-contact current measurement method to reduce The impact on the circuit under test.

II. DESIGN IDEAS

The current signal detecting device is composed of a current sensor, a detector, a controller, and a display. The mutual inductance current sensor module is fabricated by winding an enameled wire on a ferrite magnetic ring. The detection circuit uses OP07 to design a filter circuit and an amplifying circuit, and DC biases the output signal. The STM32 microprocessor integrates an analog-to-digital converter to collect the pre-stage circuit. The output voltage signal is subjected to FFT to obtain the frequency and amplitude characteristics of the signal, and the amplitude and frequency information of the signal are displayed on the OLED screen. Figure 1 is a block diagram showing the overall design of the current signal detecting device.

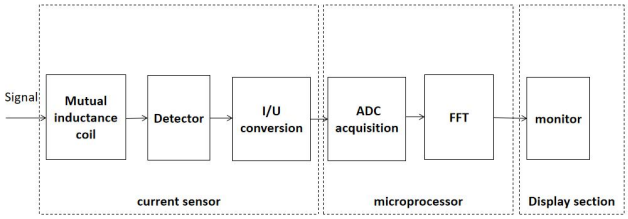

Fig.1 Current signal detection device overall block diagram

III. THEORETICAL ANALYSIS AND CALCULATION OF THE SYSTEM

The mutual inductance current sensor is based on Faraday's law of electromagnetic induction [8]. The theoretical formula is as follows:

$$E = n\frac{\Delta\phi}{\Delta t} = nfSB \tag{1}$$

A change in the coil current causes a change in the magnetic flux in the core, and a varying voltage can be induced in the secondary coil according to the Faraday electromagnetic induction principle.

Analogy transformer works, if there is no magnetic field leakage:

$$\frac{E_2}{E_1} = \frac{N_2}{N_1} \tag{2}$$

The frequency range of the sine wave signal measured by the device is that the peak-to-peak range is better than the current measurement accuracy, and the frequency

measurement accuracy is better than 1%, so:

$$\delta A = A_{\min} \cdot \gamma_A = 10mA \cdot 5\% = 0.5mA \quad (3)$$

$$\delta f = f_{\min} \cdot \gamma_f = 50Hz \cdot 2\% = 1Hz \quad (4)$$

Since the frequency calculation uses FFT [10], the frequency resolution formula is as follows:

$$f = f_s / N \quad (5)$$

According to the sampling theorem:

$$f_s > 2 * f_{\max} \quad (6)$$

In order to facilitate the measurement, the output voltage of the mutual-inductance current sensor is amplified and then collected, so the current resolution is converted (the voltage is adjusted to):

$$\delta A' = \delta A * 3 = 1.5mA \quad (7)$$

$$b = A' \max / \delta A' = 2000 \quad (8)$$

In summary, the AD bit is selected to be 12 bits, the sampling frequency is set to 4 kHz, and the number of sampling points is 4000.

IV. HARDWARE CIRCUIT DESIGN

A. Mutual inductance current sensor circuit

The mutual inductance current sensor is formed by winding an enameled wire on a magnetic ring, and the number of turns of the enameled wire is the number of turns of the circuit under test passing through the magnetic ring.

B. Detection circuit

The current induced by the mutual current sensor has a certain noise interference and a certain attenuation, so filtering and amplification are required. The input offset voltage of the 0P07 op amp is low, and its input bias current is low [9], which is very suitable for the weak signal of the measuring device and the amplified sensor. Therefore, the detection circuit selects OP07. The signal induced by the coil flows through the active filter composed of OP07 for low-pass filtering. The filtered signal is amplified by the non-inverting amplifier formed by OP07 [7, 8]. Finally, the signal is DC biased by the potentiometer to satisfy STM32. The microprocessor's ADC collects voltage requirements. The circuit diagram is shown in Figure 2 and Figure 3.

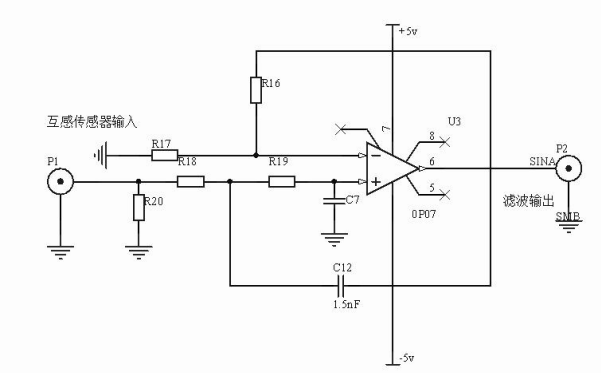

Fig.2 Filter circuit diagram

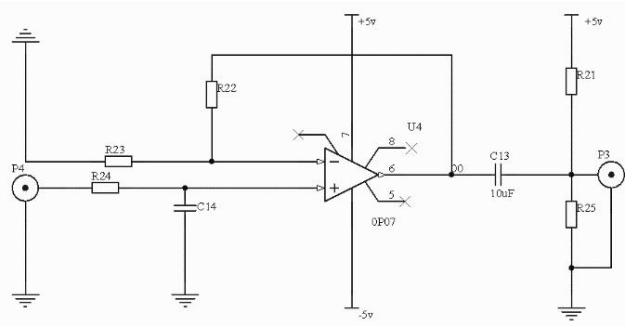

Fig.3 Amplification and DC bias circuit diagram

V. SOFTWARE PROGRAMMING

The main task of the software part is to read back the voltage signal from the sensor, analyze the signal by fast Fourier transform, analyze the frequency and amplitude of the signal, and display it on the host computer and OLED. The programming flow chart is shown in Figure 4.

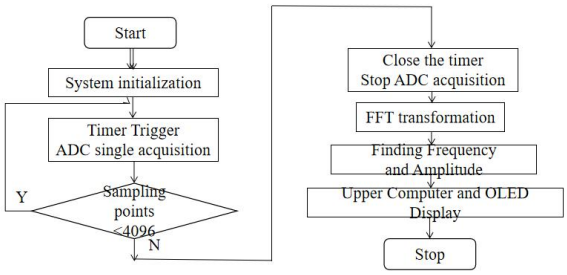

Fig.4 Current signal detection program flow chart

In the actual measurement, the frequency and amplitude will affect the inductance of the coil. The data is calibrated using the current test data as shown in Figure 5. Available, the calibration function for amplitude and frequency is:

$$A = 53023 \cdot f^{-1.196} \cdot A_0 \quad (9)$$

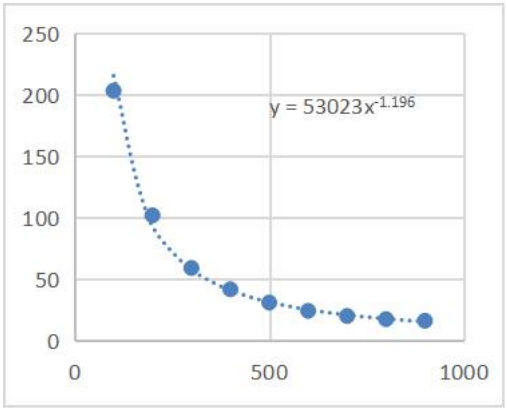

Fig.5 Data acquisition and image fitting

VI..TEST SCHEME AND TEST RESULT

A. Test Plan

The measurement loop is routed to the TDA2030A audio power amplifier and load resistor to ensure that the loop current is large enough to be detected by the sensor. The power amplifier circuit is shown in Figure 6.

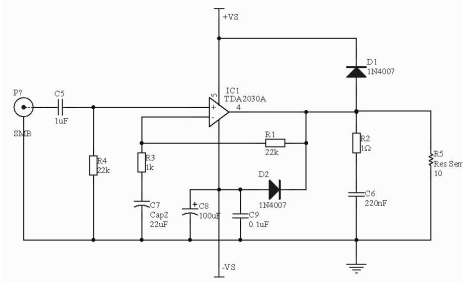

Fig.6 Circuit Diagram of Power Amplifier

Any signal output by the signal generator is input to the in-phase amplifying circuit of TDA2030 through J1 (two diodes are used for output voltage positive and negative limiting protection; R2 and C6 are used to stabilize the frequency), and the amplified current flows through the load. The peak value of R5 peaks up to 1A.

2) verify the accuracy of measuring the sinusoidal signal by comparing the signal generator indication value and the measurement display result;

3) Verify the accuracy of the measured triangular wave signal by comparing the signal generator indication value, the theoretically calculated Fourier series and the measurement display result.

B. Test results and analysis

Power amplifier performance test is shown in Table 1:

Table1 Power Amplifier Test Table

Frequency (Hz)	Input Peak-to-Peak (mV)	Output Current (mA)
50	52	10
50	5000	1000
100	25	10
100	2800	1000
500	6	10
500	700	1000
750	4.5	10
750	500	1000
1000	3.5	10
1000	400	1000

It can be seen from Table 1 that the signal current peak-to-peak value can reach 1A after the signal is passed through the power amplifier circuit.

Table2 Sinusoidal Signal Detection Test Table

Set Frequency (Hz)	Detection Frequency(Hz)	Frequency Relative Error (%)	Set Current Value (mA)	Detection Peak (mV)	Peak Relative Error (%)
100	101	1	500	515	3
500	502	0.4	500	458	8.4
800	803	0.375	500	460	8

Table3 Triangular Wave Signal Detection Test Table

Frequency (Hz)	Set Amplitude (mA)	Primary Harmonic frequency (Hz)	Detection of First Harmonic Peak-peak (mA)	Detection of Third Harmonic Frequency (Hz)	Third Harmonic Peak-to-peak (mV)	Detection of Five Harmonic Frequencies (Hz)	Detection of the Peak and Peak (mV) of the Fifth Harmonic Wave
60	273	59.88	206.56	180.6	60.837	240.92	27.82
100	390	100.44	360.4	301.02	54.892	501.15	23.633
200	689	200.89	679.1	601.7	171.47	-	-

It can be seen from Tables 2 and 3 that the device can detect and analyze the current signal, the frequency detection error is less than 2%, and the amplitude detection error is less than 5%.

C. Test Analysis and Conclusion

Based on the above test data, the following conclusions can be drawn:

1) The device has high cost performance under the premise of ensuring measurement accuracy, the frequency detection error is less than 2%, and the amplitude detection error is less than 5%. Moreover, it can communicate with the computer to transmit data, and realize automatic debugging and verification of the measurement object. The microprocessor-based measurement device realizes measurement automation and functional diversification.

2) The signal detected by the current sensor is non-linear, and the microprocessor can correct the nonlinear signal, such as linear compensation. Not only can it improve accuracy, but debugging is quick and easy.

3) The device measures a large dynamic range, measuring the frequency range of the sine wave signal, and the peak-to-peak range is . The passband is adjustable, and the gain of the amplifying circuit is adjustable. When the low frequency and low amplitude signals are detected, the gain multiple can be adjusted to amplify the input signal to the range that can be collected, and the filter circuit can be adjusted according to the input signal frequency to reduce external interference.

References

[1] Kang Huaguang. Electronic Technolo Foundation Simulation Part (Sixth Edition) [M]. Beijing: Higher Education Press, 2006.1

[2] Alan V.Oppenheim， Alan S.Willsky S.Hamid Nawab. Signals and Systems， Second Edition[M]. Beijing: Electronic Industry Press，2009.6

[3] Hu Renjie, Du Guoliang, Huang Huichun. Selection of Excellent Works Design Report for National College Students Electronic Design Competition

[4] Li Yanjun, Zhao Fan. Current Signal Detection Device Based on MSP430 Single Chip Microcomputer [J]. Computer Fans,2018(11):95.

[5] Zhang Xinyi, Guan Wenliang, Mei Zheng, Li Gang. Current Signal Detection Device [J]. Electronic Production,2018(21):62-64.

[6] Huang Ping, Zhang Yufei. Design of Current Signal Detection Device [J].Southern Agricultural Machinery,2018,49(20):134.

[7] Wang Shisheng, Zhou Ying. Measurement circuit of mutual inductance sensor with interference adaptive filter [J].Journal of Xiamen University (Natural Science Edition),2001(S1):167-171.

[8] Liu Hong, Li Yukun, Liu Yanjun. Design of Harmonic Component Detection System for Current Signal Based on STM32 [J].Journal of Xiamen Institute of Technology,2018,26(05):25-30.

Research on Monocular Ranging Method of Soccer Robot

Li Jing, Han Run ze, Yu Bin
（jilin university instrument science and engineering institute,changchun,130021）

***Abstract*—In recent years, with the continuous development of intelligent robot technology. The related technology of soccer robots has gradually become a research hotspot. In the robot soccer game, the robot must measure the target and use the visual information of the robot to measure the feature points composed of the field line and the goal post and the position where the ball may exist. Based on the Darwin robot development platform, this paper establishes and analyzes the monocular ranging model, and obtains an effective method for monocular ranging through specific experiments, and studies the monocular ranging of soccer robots in the competition environment.**

***keywords*—Monocular ranging Soccer robot vision**

I. FOREWORD

THE soccer robot has the functions of sensing environment, positioning navigation, autonomous movement, etc. It is easy to operate, powerful and has broad application prospects. It is a research hotspot in the field of robotics. In the soccer robot vision system, in addition to being able to accurately detect the target object in the recognition field, an important goal is to calculate the distance from the identified target object in the external space. An effective method is to use the visual ranging of the robot to calculate the target distance from the feature points formed by the field line and the goal foot and the position where the ball may exist. Darwin Robot is a high-performance open source intelligent humanoid robot platform developed by a Korean company. It has advanced computing power, multiple replica sensors, high load capacity and balance of motion, which is very suitable for the research of humanoid robots. Based on the imaging of the camera, this paper systematically analyzes and studies the target recognition part of Darwin robot.

II . CAMERA OBSERVATION MATHEMATICAL MODEL

A. Camera Aperture Imaging Model

The imaging model of the camera can be divided into two types: linear model and nonlinear model [1]. The Darwin robot head is equipped with two cameras, which can be assumed to be a linear aperture imaging model [2][3]. Under this model, there is a linear relationship between object space coordinates and image coordinates, and camera parameters. The solution can be transformed into a solution to a system of linear equations. In the process of mapping a target object in the external environment onto an image through a camera system, four coordinate systems need to be defined.

(1) External world coordinate system: (O, X_W, Y_W, Z_W) This is the absolute coordinates of the external world. This coordinate system is used as the reference coordinate system to describe the camera position.

(2) Camera coordinate system: (O, X_C, Y_C, Z_C); This coordinate system is also called the optical center coordinate system, and the origin of the coordinate system is the lens optical center of the camera, wherein the Z axis is the optical axis of the camera.

(3) Camera imaging plane coordinate system: (O, X, Y); the origin of the coordinate system is the center point of the imaging plane. Its X and Y axes are parallel to the vertical sides of the image plane. This is a plane coordinate system in which the pixel position in the image is expressed in physical units, usually in millimeters.

(4) Image pixel point coordinate system: (O, u, v); The coordinate origin of the coordinate system is the vertex of the upper left corner of the image. Its two axes are parallel to the coordinate axes of the camera imaging plane coordinate system. In this coordinate system, it is measured in units of pixels. To achieve a correspondence between a pixel in an image and a corresponding object in the external world, a conversion relationship between the four coordinate systems is required. The internal parameters and external parameters of the corresponding camera formally implement the parameters of this conversion. Under the aperture imaging model, the relationship between the above four coordinate systems is shown in Figure1 and Figure2.

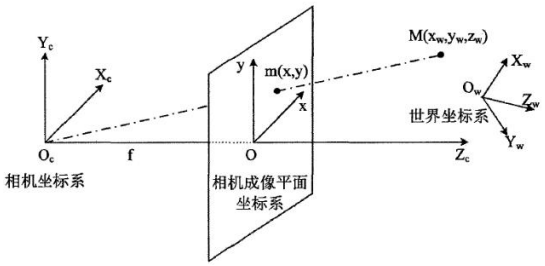

Fig. 1 relationship diagram between four coordinates of pinhole imaging

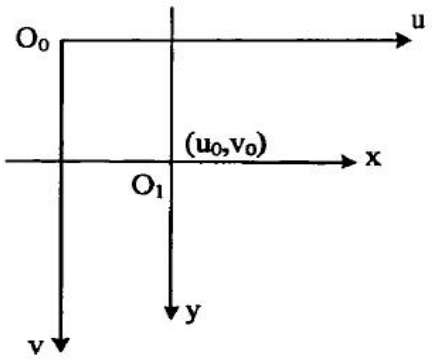

Fig. 2 relationship between image pixel coordinate system and camera imaging plane coordinate system

The relationship between the image pixel coordinate system (O_0, u, v) and the camera imaging plane coordinate system (O_1, x, y) is shown in Fig. 2. (u_0, v_0) in the figure represents the coordinates of the origin of the imaging plane coordinate system (the camera's optical point) in the image pixel point coordinate system. Let: d_x, $d_y$represent the physical size of each pixel in the imaging plane, respectively, then the conversion between the two coordinate systems can be expressed by:

$$\begin{cases} u = \frac{x}{d_x} + u_0 \\ v = \frac{y}{d_y} + v_0 \end{cases} \quad (1.1)$$

In the form of homogeneous coordinates and matrix, the above equation can be expressed as:

$$\begin{vmatrix} u \\ v \\ 1 \end{vmatrix} = \begin{vmatrix} 1/d_x & 0 & u_0 \\ 0 & 1/d_y & v_0 \\ 0 & 0 & 1 \end{vmatrix} \begin{vmatrix} x \\ y \\ 1 \end{vmatrix} \quad (1.2)$$

As shown in Figure 1, since the camera imaging plane coordinate system is parallel to the camera coordinate system, the geometric relationship between them can be derived:

$$\begin{cases} x = \frac{fX_c}{Z_c} \\ y = \frac{fY_c}{Z_c} \end{cases} \quad (1.3)$$

Where f is the focal length of the camera (the distance between the camera plane and the imaging plane of the camera). The form converted to homogeneous coordinates and matrix is:

$$Z_c \begin{vmatrix} x \\ y \\ 1 \end{vmatrix} = \begin{vmatrix} f & 0 & 0 & 0 \\ 0 & f & 0 & 0 \\ 0 & 0 & 1 & 0 \end{vmatrix} \begin{vmatrix} X_c \\ Y_c \\ Z_c \\ 1 \end{vmatrix} \quad (1.4)$$

The transformation of points in the world coordinate system into the camera coordinate system can be thought of as a process of rotation and translation:

$$\begin{vmatrix} x_c \\ y_c \\ z_c \\ 1 \end{vmatrix} = \begin{vmatrix} R & t \\ o^T & 1 \end{vmatrix} \begin{vmatrix} X_w \\ Y_w \\ Z_w \\ 1 \end{vmatrix} \quad (1.5)$$

Where R is a 3x3 orthogonal rotation matrix, and t is a three-dimensional translation vector, which is obtained by (1.2), (1.4), (1.5):

$$Z_c \begin{vmatrix} u \\ v \\ 1 \end{vmatrix} = \begin{vmatrix} 1/d_x & 0 & u_0 \\ 0 & 1/d_y & v_0 \\ 0 & 0 & 1 \end{vmatrix} \begin{vmatrix} f & 0 & 0 & 0 \\ 0 & f & 0 & 0 \\ 0 & 0 & 1 & 0 \end{vmatrix} \begin{vmatrix} R & t \\ o^T & 1 \end{vmatrix} \begin{vmatrix} X_w \\ Y_w \\ Z_w \\ 1 \end{vmatrix} = \begin{vmatrix} f_x & 0 & u_0 & 0 \\ 0 & f_y & v_0 & 0 \\ 0 & 0 & 1 & 0 \end{vmatrix} \begin{vmatrix} R & t \\ o^T & 1 \end{vmatrix} \begin{vmatrix} X_w \\ Y_w \\ Z_w \\ 1 \end{vmatrix} = KM_1 \begin{vmatrix} X_w \\ Y_w \\ Z_w \\ 1 \end{vmatrix} \quad (1.6)$$

among them:

$$f_x = \frac{f}{d_x}, f_y = \frac{f}{d_y}, \mathrm{K} = \begin{vmatrix} f_x & 0 & u_0 & 0 \\ 0 & f_y & u_0 & 0 \\ 0 & 0 & 1 & 0 \end{vmatrix},$$

$$M_1 = \begin{vmatrix} R & t \\ o^T & 1 \end{vmatrix}$$

f_x and f_y are respectively called scale factors on the u-axis and v of the image. The matrix only contains information related to the focal length of the camera and the coordinates of the optical axis, which are determined by the internal structure of the camera, called the internal parameter matrix that is, the formula (1.6).

f_x, f_y, u_0, v_0 in the equation are called internal parameters. The matrix M_1 contains a rotation matrix R and a translation vector t. These parameters are related to the camera coordinates and the relative position

of the world coordinate system, and are called external parameter matrices.

B. Ground plane-based constraint model [4].

In this model, it is known that the distance between the camera and the plane of the target object to be measured (i.e., the height at which the camera is located) is known, and the target object is observed at a 'looking angle' and the viewing angle of the camera is known. After calibration, the camera internal parameters are obtained, and the distance between the camera and the measured object on the plane can be obtained through a simple geometric relationship derivation. The model is shown in Figure 3. In the soccer robot system, the target of the ball and the field line feature point in the same field is on the field plane, and the camera is in the head position of the Darwin robot, which is consistent with the constraint of the ranging model, so this can be used. The constraint model constructs the monocular ranging function of the Darwin robot.

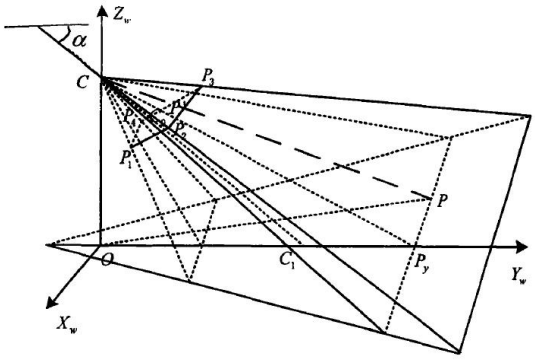

Fig. 3 constraint model based on ground plane

C. Monocular Ranging Mathematical Model

A monocular ranging model is constructed based on a ground plane-based constraint model. The soccer robot is set to be in the same horizontal plane as the target object, and the mounting position of the robot camera is fixed, and the height from the horizontal plane can also be obtained by measurement. According to the principle of small hole imaging, the geometric relationship can be used to estimate the same in the two-dimensional image. The distance between a horizontal object and the robot. Let the camera installation position be at a height from the horizontal plane, A is the angle between the camera's optical axis and the plane. A point P on the horizontal plane of the external world coordinate system is the measured point, and the horizontal distance between P and the camera lens is d. According to the principle of small hole imaging, the geometric relationship between the point and the optical imaging of the camera can be represented by Figure4.

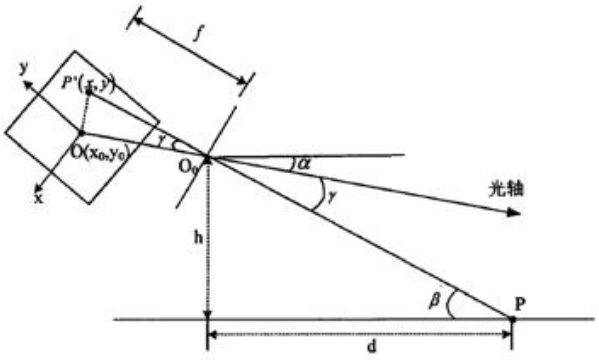

Figure 4 Schematic Diagram of Single Visual Distance

Where O_0 is the origin of the camera coordinate system, O is the origin of the camera imaging plane coordinate system, and the distance between O and O_0 is the focal length f of the camera. P (x, y) is the projection point of the measured point in the camera imaging plane coordinate system. The following geometric relationships can be derived from the graph:

$$\beta = \alpha + \gamma$$

$$\tan\beta = \frac{h}{d}$$

$$\tan\gamma = \frac{OP'}{f}$$

$$d = \frac{h}{\tan\left[\alpha + \arctan\sqrt{\left[\frac{(u-u_0)}{f_x}\right]^2 + \left[\frac{(v-v_0)}{f_y}\right]^2}\right]}$$

Among them, the camera position height A and the camera's pitch angle α are available, then: $OP'^2 = (x^2 + y^2)$

Let (u, v) be a point coordinate in the image pixel point coordinate system, and O (u_0, v_0) is the coordinate of the camera optical axis and the phased imaging plane intersection O(x_0, y_0) in the image pixel point coordinate system. P (u,v) is the coordinate of P (u,v) in the image pixel point coordinate system. Let the actual physical size of a pixel point in the X-axis and y-direction of the image pixel point coordinate plane be d_x and d_y, respectively:

$$\begin{vmatrix} u \\ v \\ 1 \end{vmatrix} = \begin{vmatrix} 1/d_x & 0 & u_0 \\ 0 & 1/d_y & v_0 \\ 0 & 0 & 1 \end{vmatrix} \begin{vmatrix} x \\ y \\ 1 \end{vmatrix}, \text{ 即 } \begin{cases} x = (u-u_0)d_x \\ y = (v-v_0)d_y \end{cases}$$

$$OP'^2 = [(u-u_0)d_x]^2 + [(v-v_0)d_y]^2$$

make $f_x = \frac{f}{d_x}, f_y = \frac{f}{d_y}$, then there are:

$$\left(\frac{OP'}{f}\right)^2 = \left[\frac{(u-u_0)}{f_x}\right]^2 + \left[\frac{(v-v_0)}{f_y}\right]^2$$

Then the distance d between the measured point and the camera can be expressed as:

$$d = \frac{h}{\tan\left[\alpha + \arctan\sqrt{\left[\frac{(u-u_0)}{f_x}\right]^2 + \left[\frac{(v-v_0)}{f_y}\right]^2}\right]}$$

Among them, f_x, f_y, u_0, v_0 are the internal parameters of the camera, which can be obtained by offline calibration of the camera. α is the angle between the camera's optical axis and the horizontal plane of the camera. It can be added by camera mount angle and head pitch value headpitch. get. The height of the camera mounting position from the horizontal plane is also available, so the distance information can be quickly obtained. In this model, in order to ensure the accuracy of ranging, it is necessary to keep the target to be measured in the middle of the field of view image.

III. MONOCULAR DISTANCE TEST METHOD AND EXPERIMENTAL SCHEME

A. Experiment Method

a. This paper calibration experiment (preparatory experiment)

In a general monocular ranging system, in order to make the calculation of the constructed monocular ranging model more accurate, the Darwin robot camera needs to be calibrated to obtain the internal parameters of the Darwin camera. In this article, Zhang Zhengyou's calibration method [5] is adopted. The calibration method is a traditional calibration method, which is widely used, requires little equipment, has high practicability, and the calibration accuracy can also meet the requirements. In this experiment, the Darwin camera was calibrated using the MATLAB toolbox based on Zhang Zhengyou's calibration method. The calibration plate is printed on A4 paper as shown in Figure 5. The shape of the checkerboard is 14x10, and each square has a length and width of 20mm.

The resolution of the Darwin robot camera is set to 640x480. Figure 5 and Figure 6 show the calibration plate images collected in the experiment, which are collected by the camera at different angles. Since Darwin has two cameras in the upper and lower parts, Darwin's upper and lower cameras are to be calibrated in the experiment, just to name a few examples.

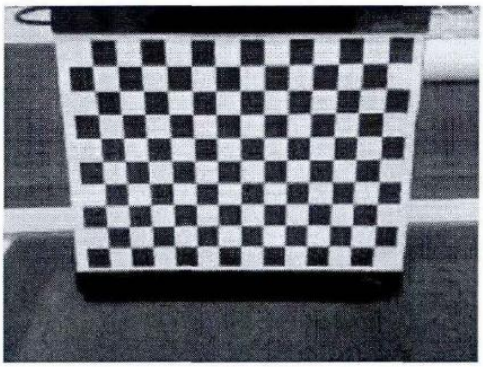

Fig. 5 physical diagram of calibration board

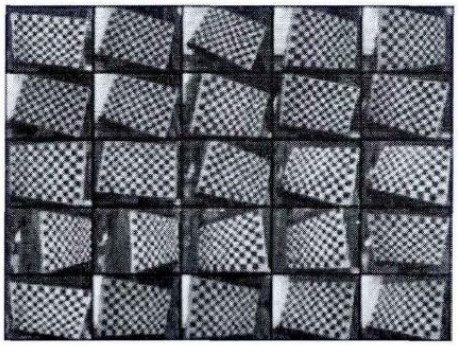

Fig. 6 calibration plate image acquired by camera

Place the captured calibration plate image in the calibration toolbox directory, run the calibration tool, import all images into the program, manually calibrate the calibration plate area, and calibrate the calibration plate corner point detection example as shown in Figure 7(a) and (b) show.

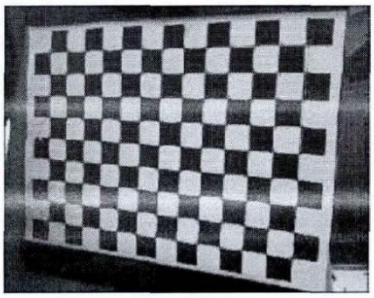

Fig. 7(a) selected detection area

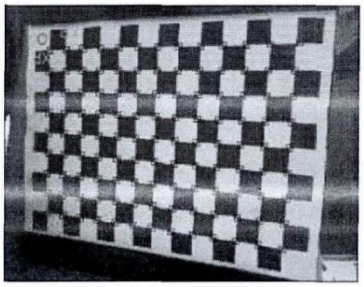

Fig. 7(b) corner detection result diagram

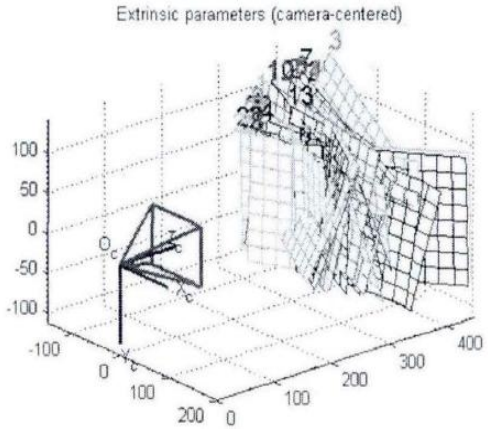

Fig. 8(a) relative pose diagram of camera and calibration plate

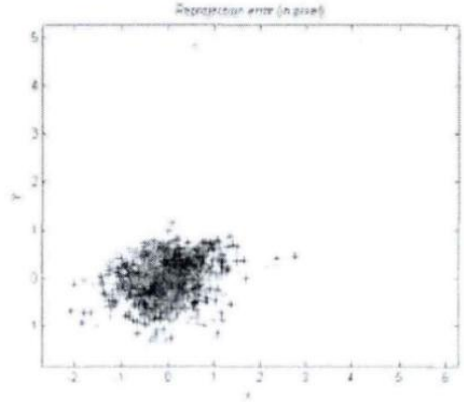

Figure 8(b) Error Diagram of Calibration Results

Figures 8(a) and (b) show the relative pose space image of the generated camera and the calibration plate. The final reference matrix of the Darwin camera is:

$$M_1 = \begin{vmatrix} f_x & 0 & u_0 \\ 0 & f_y & v_0 \\ 0 & 0 & 1 \end{vmatrix}$$

$$= \begin{vmatrix} 632.1350 & 0 & 327.128599 \\ 0 & 637.503655 & 244.690310 \\ 0 & 0 & 0 \end{vmatrix}$$

The coefficient of change is:

Kc=[0.11371 0.39486 0.00072 0.00319 0.00000]

b.Ranging experiment:

In the ranging experiment, the control robot is in a stationary standing position. At this time, it can be determined that the distance of the upper camera from the ground is h1=38.99 cm, and the distance of the lower camera from the ground is h2=34.41 cm. According to the robot's head camera installation structure, the camera's elevation angle at the top of the head can be expressed as α=headpitch+1.2°, and the camera's pitch angle at the lower part of the head can be expressed as; α=headpitch+39.7°, headpitch can be Obtained in real time through library functions. The marker used is a red ball. The group ball is placed directly in front of the robot. Starting from the toe of the robot, a monocular distance measurement is performed every 10 cm. The experimental scene is shown in Fig. 9(a). First find the center of gravity of the ball and control the angle of the robot's headpitch so that it is near the center of the field of view, as shown in Figure 9(b). In the experiment, since the red ball used was about 6 cm in diameter, the robot camera height h should be reduced by 3 cm. In each ranging, the upper and lower cameras are used to separately measure the distance (the target does not appear in the upper camera field of view at close range).

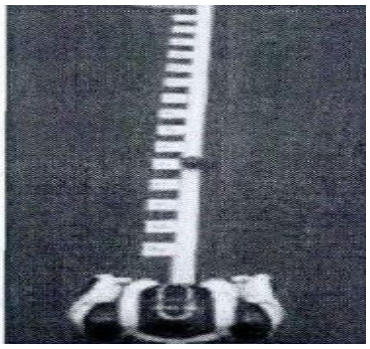

Fig. 9(a) ranging experiment scene

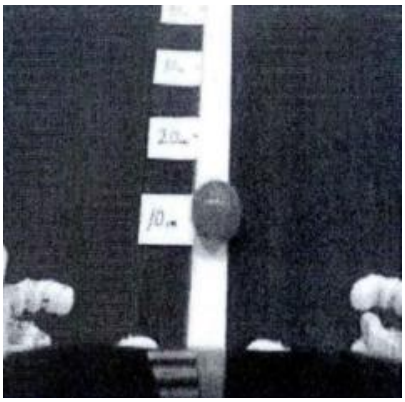

Fig. 9(b) image captured by robot

IV. CALCULATION results AND COMPARISON

A. Monocular ranging based on triangular model

In order to ensure accuracy as much as possible during the measurement, five distances were made at each distance, and the average of the five distances was taken as the final value. The distance measurement results calculated according to the formula are shown in Table 1.

Table 1 Single Visual Distance Results Based on Triangle Model

Real distance（cm）	Estimated distance（cm）		Absolute error（cm）		Percentage error（cm）	
	Upper camera	Upper camera	Upper camera	Lower camera	Upper camera	Lower camera
10	Unobserved	13.32	Unobserved	3.32	Unobserved	33.20
20	Unobserved	24.17	Unobserved	4.17	Unobserved	20.85
30	Unobserved	34.65	Unobserved	4.65	Unobserved	15.50
40	Unobserved	41.79	Unobserved	1.79	Unobserved	4.48
50	Unobserved	51.67	Unobserved	1.67	Unobserved	3.34
60	62.72	62.62	2.27	2.62	3.78	4.37
70	73.24	71.34	3.24	1.34	4.63	1.91
80	83.35	83.12	3.35	3.15	4.19	3.94
90	94.65	93.12	4.65	3.12	5.17	3.47
100	105.32	104.15	5.32	4.15	5.32	4.15
110	116.31	115.12	6.31	5.12	5.74	4.65
120	128.28	127.43	8.28	7.43	6.90	6.19
130	139.57	138.96	9.57	8.96	7.36	6.89
140	149.78	149.09	9.78	9.09	6.98	6.49
150	161.15	160.15	11.15	10.94	7.43	7.29

V. CONCLUSION

The future world will be the world of artificial intelligence, and football robots are still in the early stages of development. Ranging is an indispensable part of football robot research. Based on the Darwin robot development platform, this paper establishes and analyzes the monocular ranging model and obtains an effective method for monocular ranging through specific experiments. After verifying the results of multiple experiments, it can be concluded that the camera position is 34.41cm. It is more suitable. When the detection distance is between 40cm and 110cm, the data percentage error is within 5%, and the data is more reliable.

References

[1] Xu G, Shi Y Q. Camera Model Identification Using Local Binary Patterns[J].2012:392-397.

[2] Moldovan D , Wada T. A calibrated pinhole camera madel for single viewpoint omnidirectional imaging systems[C]//International Conference on Image Processing. IEEE, 2004:65-71

[3] Xu Bo, Liu Lu, Liu Yihui, et al. A correction and calibration method for fisheye camera with extended aperture imaging model [J].Journal of Automation, 2012,40(4):653-659.

[4] Cao Jian, Chen Hongqian, Mao Dianhui, Li Haisheng and Cai Qiang. A review of image target recognition based on local features [J]. Journal of Central South University (Natural Science Edition),2013,44(S2): 258-262

[5] Li Wanyi, Wang Peng and Qiao Hong. A review of target tracking methods introducing visual attention mechanism [J].Journal oAutomation,2014,40(04): 561-576

Application of multi-task timing control algorithm in automated farm

LiuHanqing, LiRuoyv, LiuSuxian

（jilin university instrument science and engineering institute,changchun,130021）

***Abstract*—Based on the algorithm of time series control in embedded system design, many functions needed by automatic breeding sites are realized. After analysis, four sets of control algorithms with different characteristics for timing control in embedded system are obtained. Choose the most suitable algorithm to make the program easy to maintain. It can also reduce the operating pressure of embedded system, effectively save system resources, and meet the requirements of controlled peripherals, and provide necessary software conditions for automatic breeding.**

***Key words*—Embedded system Timing control algorithm**

I. PREFACE

THE scale of aquaculture in China is large, but the level of automation of aquaculture is still insufficient, compared with the developed countries, there are high cost, low efficiency and so on[1]. Automated aquaculture is the development trend of aquaculture industry nowadays. Through automatic control to realize the automation and intelligence of the breeding system, can effectively save manpower and material resources, improve the efficiency of breeding. In recent years, automation farms have sprung up quietly, but there are still shortcomings in the control algorithm. In the control process of the breeding system, it is often necessary to control multiple tasks of multiple devices in real time, and it is easy to make changes to the task execution time and the number of task execution without changing the program. Embedded system is generally a single-core processor, only able to line up the processing program. If the control program designs the single task algorithm directly according to the process requirements, it is difficult to control the various tasks at the same time, and it is not convenient for the task to be adjusted[2]. In order to solve this problem, it is necessary to decompose the task in time, and take advantage of the extremely high execution speed of the CPU to design a multi-task parallel algorithm, so that all tasks can run at the same time, be controlled in real time, and can be easily adjusted [2].

II．.PROBLEM ANALYSIS

In the breeding system, often a large number of equipment, in order to analyze the simple assumption of the existing three equipment: feeding equipment, water injection equipment and cleaning equipment, respectively, recorded as A,B,C. In fact, the number of devices does not affect the design of the algorithm. The feeding equipment needs to ta1 open the feed gate at a specified time, conveying the specified feed quantity, that is, after a period of time Δta1 the gate is closed. The opening and closing processes are recorded as Ha1,Ha2 respectively. The water delivery process is similar, its designated time is recorded as ta1, the time interval is recorded as Δtb1, and the task of opening the sluice and the off-water gate is recorded as Hb1,Hb2respectively. Cleaning up the device requires tb1 to start cleaning at a specified time, that is, the cleaning brush forward movement, after the interval Δtc1 reverse return, after the interval Δtc1 stop movement. The forward motion, backward motion, stopping three operations are recorded as Hc1,Hc2,Hc3[4].

Three devices need to do this multiple times in a day at different times. Tasks may be performed at the same time, and data transferred to the embedded system only through external communication devices can be easily changed without changing the program. At the same time, the embedded system can accept the external random transmission of data at any time, and timely processing to control the equipment.

The number of devices controlled in the actual farming system is larger and the tasks performed are more complex Obviously, it is difficult to complete the above tasks by using the algorithm writing program of a single process.

For example, the time interval for δta1 is achieved using the delay process. Embedded system is controlling the operation of feeding equipment, in the delay time Δta1, now need to open the water injection process, the embedded system must complete the feeding operation before the implementation of water injection. If a string of

data comes from a communication device at this point, it is difficult to complete the reception and processing.

In order to accomplish the above tasks, it is also possible to set the timer for time control, such as setting a timer to the device a A,B,C, and controlling the task execution time by taking into account the value, so that the corresponding task is performed when the corresponding timer is interrupted. However, in the breeding system, an embedded system often needs to control a lot of devices, so the writing program needs to calculate a large number of timer count values, which for programmers is a lot of work. And in this way, the number of timers may not be sufficient to use. If you try to avoid this behavior while you are programming, you will make the program design very complex, and there are many factors to consider, making debugging and maintenance programs very difficult.

In order to make programming simple, with standardized, modular characteristics, the following decomposition of tasks. On this basis, the scheme one can easily control the equipment through the delay process, in the case of not receiving external information can still be controlled in real time. Scenario II is improved on the basis of scenario one, using a single timer to control multiple tasks while having the ability to receive information in real time Scenario III makes programming simpler and has the advantage of modularity[3].

III.ALGORITHM ESTABLISHMENT

3.1 Programme I

Below to solve the above problems, we can use the following methods. Still taking the process control described above as an example, we first consider a fixed mode control system that does not involve random changes. That is, in the above problems, ta1,tb1,tc1 and Δta1,Δtb1,Δtc1 do not need to change throughout the control process. Let's finish the task in the simplest way. From the above analysis, it is concluded that the use of delay algorithm is unfavorable for stochastic systems where requirements are controlled in real time. For non-random algorithms, using a delay algorithm can also cause a lot of trouble with programming if there are too many peripherals and more tasks need to be performed for each peripheral, but it is still possible to do so. The following algorithm is to accomplish this task through the delay program, and can make the programming standardized and simplified.

First, ignore the differences of the device and simply use the task as the control object of our programming so that each task of each peripheral is considered unified throughout the program. The absolute execution time of the task is recorded as T, so the task Ha1 execution time for peripheral A is recorded as T1, and the execution time of the task Ha2 is recorded as T2, apparently

T2=t1+Δta1.

Similarly, the tasks of peripheral B,C are recorded as T3,T4,T5,T6,T7

T3=tb1,T4=tb1+Δtb1,T5=tc1,

T6=t3+Δtc1,T7= t3+2*Δtc1. A set of data T1,T2,T3,T4,T5,T6,T7 is derived from this.

In programming, this set of data can be recorded as a set of arrays:

{T1,T2,T3,T4,T5,T6,T7}

Write to the array G2.

Record the task Ha1,Ha2 as Hk1,Hk2. The task Hb1,Hb2 is recorded as Hk3,Hk4. The task Hc1,Hc2,Hc3 is recorded as Hk5,Hc6,Hc7.

Get the following array:

{Hk1,Hk2,Hk3,Hk4,Hk5, Hk6,Hk7} Remember to make an array of HK.

In actual programming, elements in array Hk can be replaced by numbers, or they can be replaced with other characters, as long as the program can be recognized.

Now the task Hk[i] is G2[i] The task that needs to be performed at all times.

Integrate it together to get the matrix:

$$\begin{bmatrix} T1 & T2 & T3 & T4 & T5 & T6 & T7 \\ Hk1 & Hk2 & Hk3 & Hk4 & Hk5 & Hk6 & Hk7 \end{bmatrix}$$

By using the simple sorting algorithm, the logarithmic group G2 can be sorted sequentially, and the Elementary column transformation of the above matrix is carried out, so that a certain point in time still corresponds to the task that it should accomplish. The sorted array G2 is recorded as: { Th1,Th2,Th3,Th4,Th5,Th6,Th7 } , and the transformed HK is an array of H. According to our expectations, the program will complete the corresponding task at each point in time of the array.In order to use the delay function for control, we need to get the time interval between each adjacent point in time, which is still represented by an array and recorded as an array G3:

{Δth1, Δth2, Δth3, Δth4, Δth5, Δth6, Δth7}

which

Δth1=Th1,Δth2=Th2 −Th1,

Δth3=Th3 −Th2,Δth4=Th4 −Th3,

Δth5=Th5 −Th4,Δth6=Th6 −Th5,

Δth7=Th7 −Th6.

The algorithm used by this method to write the program is shown in Figure 3.1.1.

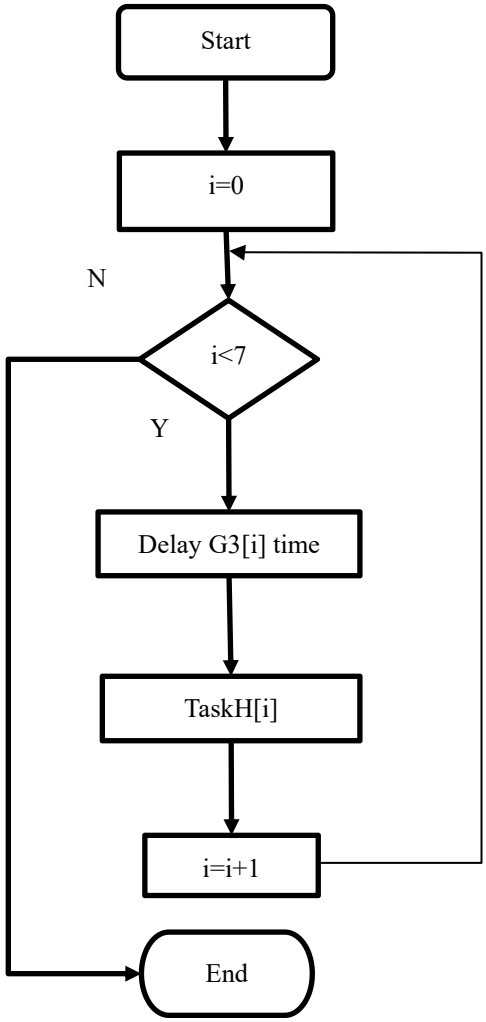

Fig. 3.1.1 (Schemes 1 Algorithmic Flow Chart)

3.2 Programme II

According to the above analysis, the algorithm in 3.1 can meet the control requirements of the system, and become the process standardization, reduce the programming burden and the program is conducive to modification and maintenance. However, because the above algorithm uses the delay process, according to the discussion of problem analysis, it is not suitable for use in stochastic control, and it results in the waste of CPU computing resources. The following is still based on the above analysis, and the delay process is no longer used to discuss more practical algorithms.

The above algorithm ultimately plays a role in the array G3. The following algorithm is consistent with the aforementioned algorithm to obtain the G3 method, so it will not be repeated. In order to solve the adverse effect of the delay process on the whole control process, the timer is used instead of the delay process. In the problem analysis has been concluded that the allocation of a timer for each peripheral has caused a great waste of resources, and programming is more complex, not conducive to maintenance. In 2.1, the tasks performed by all peripherals are unified, so you can use only one timer to complete the control of multiple peripherals. That is, use a timer instead of the full delay process of the above algorithm.

The specific process is as follows:

Configure the timer to convert the value of the Δth1 into the count value of the timer, load the timer, and wait for the timer to break.

Perform the Th1 corresponding task in the interrupt function, load the ΔTH2 value into the timer, interrupt before performing the Th2 corresponding task, and then transfer the value of the Δth3 ...

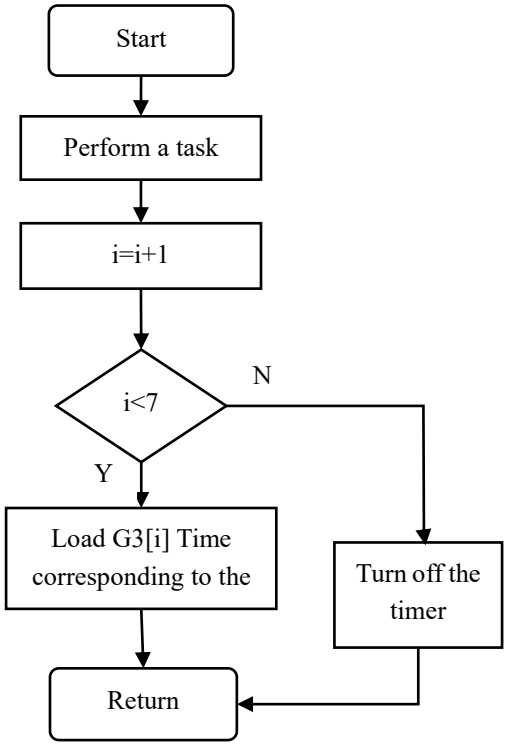

Fig. 3.2.1 (Scheme2 interrupt subroutine flow chart)

Until the completion of the task Th7 corresponding to the task end algorithm. It must be taken into account that in many cases the maximum timing time of the timer may be less than the required timing time. The solution to this problem is also very simple, so that the timer multiple times timing, time overlay [5].This is done as follows: Assuming the required time is influence, the timer maximum timing time is Tmax. Sets a count to change the i,j. The value of I is the downward rounding of the Δth/tmax. Sets the time variable Tp,tp=Δth,-tmax. In the interrupt program, each time an interrupt occurs, J plus one, and load the Tmax corresponding count value, until the value of j is equal to I, load the timer TP corresponding to the timer count value. The flowchart of the timer interrupt program is shown in Figure 3.2.1, as shown in Figure 3.2.2 of the algorithm's main program.

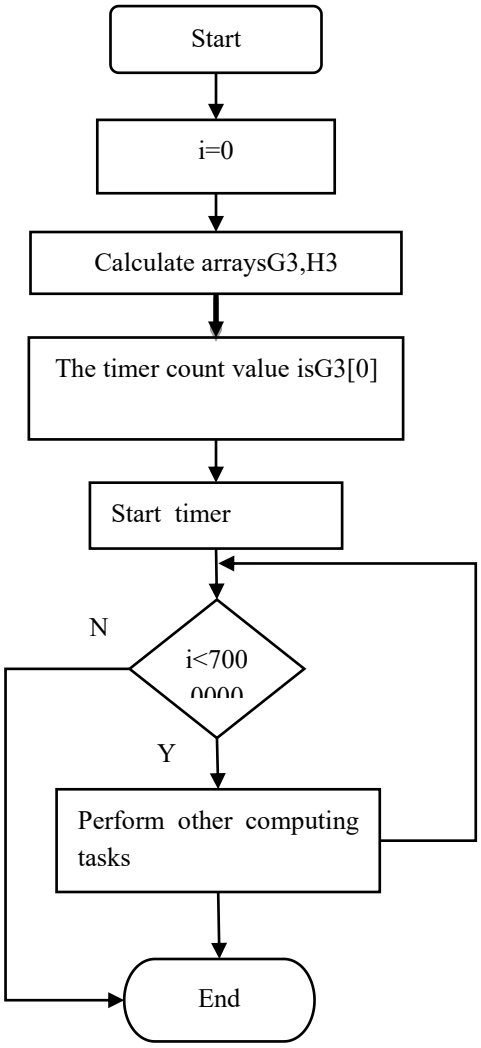

Fig. 3.2.2 (Schemes 2 Algorithmic Flow Chart)

After the above analysis, it can be concluded that the algorithm can complete the control of the system, the effect achieved is consistent with the algorithm in 3.1.However, because the delay program is not used, the algorithm does not consume the CPU for a long time during the extension process, so the tasks in the whole program can be completed in real time, and when the system receives the information, it can be processed in a timely manner.

3.3 Programme III

However, the algorithm needs to calculate the more complex timer count value, although such a calculation can be done in the embedded processor by writing a program, but there is still a certain amount of work to write such a program. And we expect the design of the program to be modular, such decomposition, although effectively solve the problem of time control, but obviously make the task performed by each module in the program is scattered and irregular embodiment.

And in the execution of each task sometimes need to get the time information, the algorithm in 3.1,3.2 to complete this task will need to set up another set of clock program. The following algorithm can replace this algorithm in a more concise way.

First set up a system clock to timing the system from the start to the end of the run. This allows you to get running from the system to the current time at any run point in the system. The program that needs to be executed to control each device, as a module throughout the program, can be written in the C language as a function, in other programming languages can be written in the form of a sub-function. Putting aside the design of the program, we expect each module to be able to monitor time at all times and perform the appropriate tasks at a time when it needs to perform tasks, which can be seen as the presence of a CPU to service the module at any time. Assuming that there are three tasks within device A that need to be performed, the time to execute is t1,t2,t3. The program for the module is designed according to the following algorithm: Check whether the current moment is equal to the expected execution time, t1,t2 or t3, if equal to perform the corresponding time corresponding to the task, if not equal to continue the check. The corresponding algorithm flowchart is shown in Figure 3.3.1.

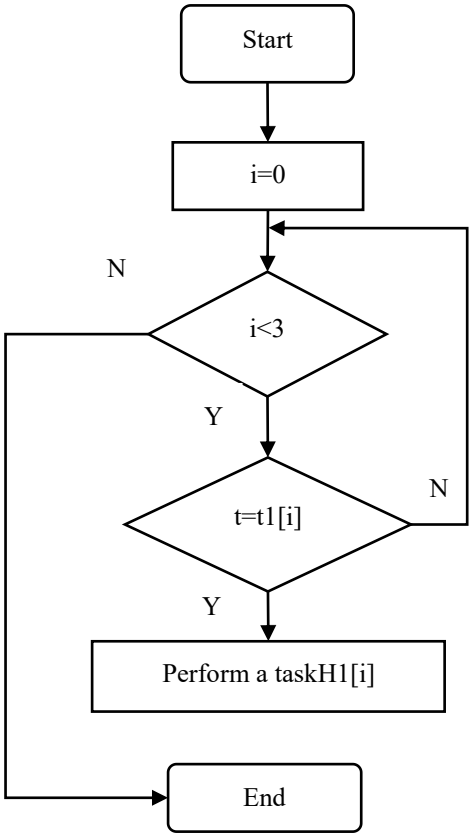

Fig. 3.3.1 (Algorithmic Flow Chart)

For the lower narrative it is convenient for us to represent the above block diagram as a whole block diagram part, which is recorded as M. As mentioned earlier, it is represented as a function or subroutine in the actual program design. For peripheral A, it is recorded as Ma, as shown in Figure 3.3.2.

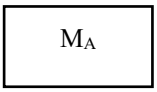

Fig. 3.3.2 (Representation diagram of peripheral A subroutine)

The above analysis requires that each task be seen as having a CPU at its service at any time, and obviously, because the CPU executes instructions very quickly, its execution time is negligible relative to the peripherals. Furthermore, when using a single embedded system to control multiple peripherals, this can be achieved as long as C loops through the program modules of all peripherals in the program.

This way, although a program designed with a single core CPU is actually a one-way program, because the CPU executes instructions fast enough relative to the peripherals, the program appears to be multi-process for peripherals, so it meets our requirements [6].

As mentioned earlier, in order to be able to get the time from the start of the system operation to the current moment, there needs to be a program module in the program that acts as a clock. Time information can be stored and passed through a variable, and the value of the variable is the time information, where the variable is recorded as n. In order to obtain the basic time signal, first set a small counting variable on the timer, resulting in a smaller time signal, which is recorded as the specific selection of ts, ts will be discussed below. The initial value of n is recorded as 0, and when the timer is interrupted, the value of n is added one. Therefore, when the starting time of the current time distance from the system is recorded as ti, then when the value of ts is small enough for the task expected by the peripheral, it can approximate the ti with the value of the nts. Due to the use of nts approximate ti, in the case of TS values have been determined, the corresponding n value needs to be required, which is represented by N. Set N0=ti/ts, because the actual N0 value is not an integer, in order to approximate the time, the value of the contract n is N0 upward rounding, that is, n=[n0+1]. Suppose peripheral a requires three tasks, Ha1,Ha2,Ha3, and the execution time for each task is t1,t2,t3. The n value obtained by the T1,T2,T3 is recorded as N1,N2,N3. Record the maximum value of the N1,N2,N3 as Nmax. Then, the procedure runs as follows: N has an initial value of 0, the timer interrupts the time of TS at each interval, the value of n is added one, the program constantly compares the values of N and N1,n2,n3, and if N=N1 performs the tasks that should be performed at the T1, for n2,n3 the same. Until n is greater than Nmax ends. This process is the process of the algorithm 2.3.1 discrete, specifically the algorithm 3.3.1 T change to n,ta[i] into na[i]. The rest is the same as in 3.3.1, so no specific block diagrams are drawn.

The whole as a segment of the process, recorded as D_A, its overall representation diagram as shown in Figure 3.3.3.

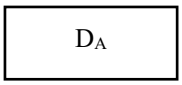

Fig. 3.3.3 (Subprocess diagram of peripheral A)

For other peripheralsB,Cin the same way, the child process is recorded as DB,DC. The flowchart of the program that can draw the main program algorithm according to the above analysis is shown in Figure 3.3.4. The algorithm flow chart of the timer interrupt subroutine is shown in Figure 3.3.5.

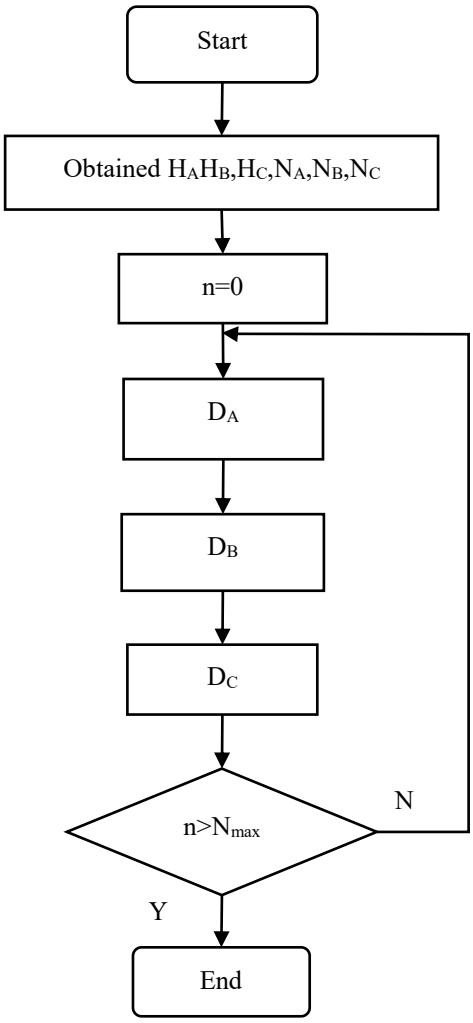

Fig. 3.3.4 (Main Program Algorithmic Flow Chart)

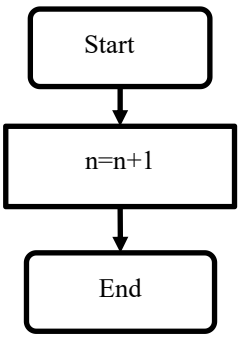

Fig. 3.3.5 (Interrupt subroutine flow chart)

The above algorithm is based only on A1,A2,A3, three peripherals and their tasks, and the program is written in the same way as the other number of peripherals and peripherals that need to complete different numbers of tasks.

IV.Applicability analysis of Algorithms

The applicability analysis of the algorithm focuses on the following two points:

(1)For peripherals, whether the control accuracy of the algorithm can meet the requirements of each peripheral;

(2)For embedded systems, whether the system performance can meet the needs of the algorithm.

For the algorithm in 3.1, it is assumed that the minimum influence in the peripheral operation is Δthmin, and the relative error is s%. In theory, the minimum delay time of the delay function is a clock period of the embedded system, and the frequency of the crystal vibration is F, and the clock period is 1/f. It is not necessary to execute some other instructions during the execution of the actual program, and the number of bars executing the instructions in the above algorithm is small, and the above process is difficult to calculate concretely, so the Δthmin >100/f is set. For STM32 series Embedded systems, the crystal frequency can reach 72MHZ, so Δthmin >1.4μs. For relative error, its value is affected by Δthmin, and Δthmin=0.01ms is set, in fact, this event can meet the requirements of most systems.

So s%≈2/fΔthmin≈0.2%.

This is sufficient for the control accuracy of the culture system.

For the algorithm in 3.2, the delay process is replaced by timer interrupt. The above process of the specific error analysis process is similar, and the scope of application is the same in quantity and on. So no more narration. The difference is that the algorithm in 3.2 does not consume too much CPU time, and can be applied when other analytical operations are required, as well as in random control. For the algorithm in 3.3, the value of TS must be selected reasonably in order to meet the requirements of peripherals and embedded systems.

As long as there is a TS algorithm 3.3 that can meet both of these requirements, it is applicable. For the time control of the equipment, we first assume that the execution speed of the embedded system can meet the requirements. A task in a peripheral expects the execution time to be TN. Allow error s%.

The selection range of TS is determined by the following formula: There is a positive integer n, which makes

((NTs-Tn))/tn≤s%

Due to min (nts-tn) ≤ts

So, Ts≤s%tn The upper limit of TS can be determined by requiring only the TS range corresponding to all tasks and taking the minimum value. Suppose a tn=30min,s%=2% of a task in a system.

Then the ts≤s%tn=36s to meet this requirement.

For embedded systems, we expect the time of the program execution to be ignored relative to ts, and the time required to meet the program execution is much less than ts.

Since the program is a loop to control the peripherals, the maximum execution time of a circular program can be compared with ts.

As long as the tc<ts is met, the requirements can be met.

For actual programming, it is extremely cumbersome to be accurate to tc, which requires an accurate analysis of the program execution process, as well as the number of execution cycles per instruction. Moreover, we do not need such accurate data, we just expect the program execution time to be negligible. For ease of analysis, we assume that the maximum number of instruction bars for a program is 100,000. This is enough for most embedded system programs. Still take the STM32 series embedded system as an example, the crystal frequency 72Mhz, the average instruction speed is 1.25mips/Mhz, in order to set aside the margin, each cycle as the execution of a directive. Then the execution time of each instruction is approximately 14ns. So tc≈1.4ms. Therefore, as long as the ts>1.4ms, the embedded system can meet the requirements of the algorithm. This is fully responsive to the requirements of the breeding system.

V.Comparison of programmes

From the above analysis, it can be seen that the algorithm control accuracy in scenario One and Scenario II is relatively high. Scenario one is not suitable for systems that need to receive random information from the outside world. Scenario III will design modularization, reduce the workload of programming, and be able to respond to data in real time, effectively solve the time control problem. Modular programming also makes the program easy to maintain and add new features. Although compared with the first two schemes, the control accuracy is slightly lower, but it is sufficient for the breeding system. Table 1 shows a comparison of the advantages and disadvantages of the three schemes.

Table 1 Scheme comparison

	Programme I,	programme two,	programme III
The advantages	Relatively high accuracy	relatively high accuracy, timely processing of information	suitable for receiving random information easy to maintain
The disadvantages	Not suitable to accept random information	writing more complex	control accuracy slightly lower

VI. CONCLUDING REMARKS

In this paper, the importance of multi-task sequential control algorithm in automated farms is briefly described, three different schemes are designed, and why each scheme is chosen is analyzed and explained. Finally, the advantages and disadvantages of the three schemes are obtained through comparative analysis. In practical engineering, it can be selected according to the needs. Generally, the third scheme in the aquaculture system is more conducive to programming and function realization.

Reference

[1] Tang Chaojie. Distributed control farm automation [J]. Science and Technology Innovation Guide, 2018, 15(11):6+8.

[2] Zhang Qiuju, Wang Fenghe. Application of Multitask Scheduling Algorithm in Single Chip Microcomputer Control System[J]. Photoelectric Countermeasure and Passive Interference,2002(03):23-25.

[3] Cao Qiong. Modular design of single chip programming[J]. Journal of Anhui Vocational College of Electronics & Information Technology,2017,16(03):51-53+63.

[4] Huang Xijun, Chen Huijin, Li Baosheng, Zhang Long.Design of intelligent farm control system[J]. Heilongjiang Animal Husbandry and Veterinary Medicine,2017(12):73-75.

[5] Qin Yumeng, Wang Yanan, Qiu Chunling. Design and Implementation of an Efficient Software Timer[J]. Laboratory Research and Exploration, 2015, 34(09): 94-97+106.

[6] Du Longzhen, Fang Bing, Zheng Jun. 51 single-chip cycle polling multi-task programming [J]. Computer age, 2018(10): 1-4.

Independent measurement design of three-dimensional trajectory in space

Shen Yihan, Cui Tiancheng, Bai Yunfei
（jilin university college of instrumentation and electrical engineering,changchun,130021）

***Abstract*—This document will use MATLAB programming to make the error compensation and filter the data obtained by the sensor and make the attitude algorithm by the quaternion method. The calculated data will be fused with the output data of the sensor. The sensor data will be converted into the spatial position data of the moving object. The trajectory of a moving object in three - dimensional relative space will be obtained by integrating the acceleration value of the sensor. At the last,a set of algorithms with sufficient precision and able to display the target object's motion trajectory in the three-dimensional space coordinate system will be designed.**

***keywords*—MATLAB error compensation filter quaternion attitude algorithm fusion trajectory three-dimensional**

I. INTRODUCTION

WITH the development of modern science and technology, 3d technology has important theoretical and applied significance for the research of aerospace and military.With the development of advanced microelectronics technology, it will also have a broad application prospect in the field of civil consumption. It is expected to be applied in some new fields, such as vehicle navigation system, astronomical telescope, industrial robot technology, computer mouse, camera, robot toys and other low-end application demand products.Unlike regular trajectory capture technology based on two-dimensional image, the project design of the system can be in 3 d space to independent measurement of trajectory, the space 3 d trajectory independent measuring system combined with the computer interface, can record the location of the target, describing the movement of the target by MATLAB software, using computer to study trajectory analysis. [1]

After the technology of this project is improved, it has wide application and high practicability. It can be used together with the traditional GPS system to provide navigation services in the urban areas with very weak satellite signal, high-rise buildings, or indoor or subway environment with no signal at all.When spraying paint in automobile industry, it can be used to detect whether the track of paint sprayer covers the surface of automobile.In the absence of reference, inaccurate magnetic field and unavailability of GPS, the research results of this project can be used to record trajectory in a short term.

II. PROJECT IMPLEMENTATION PLAN

A.Research idea

Based on the MEMS sensor to the target object's acceleration, angular velocity and other basic information acquisition, using the principle of integral and differential, the obtained acceleration, angular velocity signal analysis and processing to obtain the velocity and trajectory.Carry out filtering influenced by irrelevant factors, such as gravity acceleration component filtering, remove the error caused by the target object's rotation in irregular motion, carry out accurate processing, and improve the accuracy.

B.Implementation plan

Is given priority to with calculation method of system research, and analysis of the data processing, using integral theorem and quadratic integral gyro sensor collected data can be processed, to get movement displacement, to build axis from the direction of mine, analysis, using the proceeds from the Angle, euler Angle analysis, list the iterative matrix solution.

C.Technical route

Algorithm, MEMS sensor, gyroscope application, Matlab data analysis.

III. DESIGN PROCESS

A.Set up the coordinate system

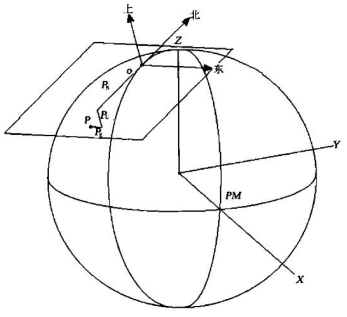

Fig. 1. ENU coordinate system.

Firstly, the reference coordinate system is determined, and the northeast sky coordinate system (ENU) as shown in the figure is selected. After the coordinate system is established, the initial position of the target object coordinate system (o-xyz) and the reference coordinate system (O-XYZ) coincides.

B.Coordinate transformation

Since the rotation order of sensor output data is z-x-y order, also known as 3-1-2 order.Therefore, it is equivalent to the following rotation: the rotation of the target object's coordinate system around the z axis with a φ Angle into o-$x_1y_1z_1$ coordinate system, o-$x_1y_1z_1$ coordinate system around the x_1 axis with a β Angle into o-$x_2y_2z_2$ coordinate system, o-$x_2y_2z_2$ coordinate system around the y_2 axis with a ψ Angle into o-$x_3y_3z_3$ coordinate system.The transformation matrix corresponding to each basic rotation of coordinate system o-xyz is:

$$C_0^1 = \begin{bmatrix} \cos\varphi & \sin\varphi & 0 \\ -\sin\varphi & \cos\varphi & 0 \\ 0 & 0 & 1 \end{bmatrix} \tag{1}$$

$$C_1^2 = \begin{bmatrix} 1 & 0 & 0 \\ 0 & \cos\beta & \sin\beta \\ 0 & -\sin\beta & \cos\beta \end{bmatrix} \tag{2}$$

$$C_2^3 = \begin{bmatrix} \cos\psi & 0 & -\sin\psi \\ 0 & 1 & 0 \\ \sin\psi & 0 & \cos\psi \end{bmatrix} \tag{3}$$

After three consecutive rotations, the attitude matrix from the coordinate system of the target object to the reference coordinate system can be obtained by (1), (2) and (3) :

$$C_0^3 = C_2^3 C_1^2 C_0^1 = \begin{bmatrix} \cos\psi & 0 & -\sin\psi \\ 0 & 1 & 0 \\ \sin\psi & 0 & \cos\psi \end{bmatrix} \begin{bmatrix} 1 & 0 & 0 \\ 0 & \cos\beta & \sin\beta \\ 0 & -\sin\beta & \cos\beta \end{bmatrix} \begin{bmatrix} \cos\varphi & \sin\varphi & 0 \\ -\sin\varphi & \cos\varphi & 0 \\ 0 & 0 & 1 \end{bmatrix}$$

$$= \begin{bmatrix} \cos\psi\cos\varphi - \sin\psi\sin\beta\sin\varphi & \cos\psi\sin\varphi + \sin\psi\sin\beta\cos\varphi & -\sin\psi\cos\beta \\ -\cos\beta\sin\varphi & \cos\beta\cos\varphi & \sin\beta \\ \sin\psi\cos\varphi + \cos\psi\sin\beta\sin\varphi & \sin\psi\sin\varphi - \cos\psi\sin\beta\cos\varphi & \cos\psi\cos\beta \end{bmatrix} \tag{4}$$

Accordingly, the matrix from the reference coordinate system to the carrier coordinate system is the transpose of the attitude matrix:

$$C_3^0 = (C_0^3)^T = \begin{bmatrix} \cos\psi\cos\varphi - \sin\psi\sin\beta\sin\varphi & -\cos\beta\sin\varphi & \sin\psi\cos\varphi + \cos\psi\sin\beta\sin\varphi \\ \cos\psi\sin\varphi + \sin\psi\sin\beta\cos\varphi & \cos\beta\cos\varphi & \sin\psi\sin\varphi - \cos\psi\sin\beta\cos\varphi \\ -\sin\psi\cos\beta & \sin\beta & \cos\psi\cos\beta \end{bmatrix} \tag{5}$$

Therefore:

$$\begin{bmatrix} x_0 \\ y_0 \\ z_0 \end{bmatrix} = C_3^0 \begin{bmatrix} x_3 \\ y_3 \\ z_3 \end{bmatrix} \tag{6}$$

In this way, the theoretical basis of coordinate transformation is completed.

C.Get the data

Connect the sensor with PC and obtain the acceleration value, angular velocity value and euler Angle value obtained after the sensor is connected with PC as shown in figure 1, with the value frequency of 100Hz.

After data query, it is known that the gravity acceleration value of changchun area is about 9.8066 m/s2, the unit of the acceleration value is converted to m/s2, the angular velocity value and euler Angle value are converted into the arc system, and the numerical range of the pitching Angle and yawing Angle is unified as [-π, π].

Using the euler Angle value output by the sensor and substituting into (4), the attitude matrix of the target object at each moment can be obtained.

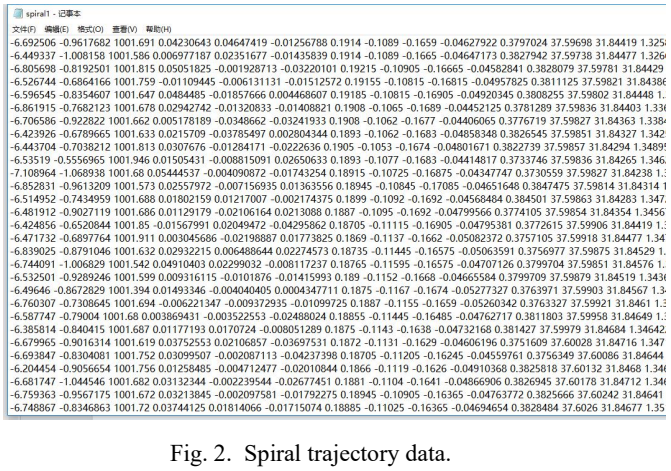
spiral1 - 记事本

文件(F) 编辑(E) 格式(O) 查看(V) 帮助(H)

-6.692506 -0.9617682 1001.691 0.04230643 0.04647419 -0.01256788 0.1914 -0.1089 -0.1659 -0.04627922 0.3797024 37.59698 31.84419 1.325
-6.449337 -1.008158 1001.586 0.006977187 0.02351677 -0.01435839 0.1914 -0.1089 -0.1665 -0.04647173 0.3827942 37.59738 31.84477 1.326
-6.805698 -0.8192501 1001.815 0.05051825 -0.01928713 -0.03220101 0.19215 -0.10905 -0.16665 -0.04582841 0.3828079 37.59781 31.84429
-6.526744 -0.6864166 1001.759 -0.01109445 -0.006131131 -0.01157572 0.19155 -0.10815 -0.16815 -0.04957825 0.3811125 37.59821 31.84386
-6.596545 -0.8354607 1001.647 0.0484485 -0.01857666 0.004468607 0.19185 -0.10815 -0.16905 -0.04920345 0.3808255 37.59802 31.84448 1.
-6.861915 -0.7682123 1001.678 0.02942742 -0.01320833 -0.01408821 0.1908 -0.1065 -0.1689 -0.04452125 0.3781289 37.59836 31.84403 1.33
-6.706586 -0.922822 1001.662 0.005178189 -0.0348662 -0.03241933 0.1908 -0.1062 -0.1677 -0.04406065 0.3776719 37.59827 31.84363 1.338
-6.423926 -0.6789665 1001.633 0.0215709 -0.03785497 0.002804344 0.1893 -0.1062 -0.1683 -0.04858348 0.3826545 37.59851 31.84327 1.342
-6.443704 -0.7038212 1001.813 0.0307676 -0.01284171 -0.0222636 0.1905 -0.1053 -0.1674 -0.04801671 0.3822739 37.59857 31.84294 1.3489
-6.53519 -0.5556965 1001.946 0.01505431 -0.008815091 0.02650633 0.1893 -0.1077 -0.1683 -0.04414817 0.3733746 37.59836 31.84265 1.346
-7.108964 -1.068938 1001.68 0.05444537 -0.004090872 -0.01743254 0.18915 -0.10725 -0.16875 -0.04347747 0.3730559 37.59827 31.84238 1.3
-6.852831 -0.9613209 1001.573 0.02557972 -0.007156935 0.01363556 0.18945 -0.10845 -0.17085 -0.04651648 0.3847475 37.59814 31.84314 1
-6.514952 -0.7434959 1001.688 0.01802159 0.01217007 -0.002174375 0.1899 -0.1092 -0.1692 -0.04568484 0.384501 37.59863 31.84283 1.347
-6.481912 -0.9027119 1001.686 0.01129179 -0.02106164 0.0213088 0.1887 -0.1095 -0.1692 -0.04799566 0.3774105 37.59854 31.84354 1.3456
-6.424856 -0.6520844 1001.85 -0.01567991 0.02049472 -0.04295862 0.18705 -0.11115 -0.16905 -0.04795381 0.3772615 37.59906 31.84419 1.3
-6.471732 -0.6897764 1001.911 0.003045686 -0.02198887 0.01773825 0.1869 -0.1137 -0.1662 -0.05082372 0.3757105 37.59918 31.84477 1.34
-6.839025 -0.8791046 1001.632 0.02932215 0.006488644 0.02274573 0.18735 -0.11445 -0.16575 -0.05063591 0.3756977 37.59875 31.84529 1.
-6.744091 -1.006829 1001.542 0.04910403 0.02299032 -0.008117237 0.18765 -0.11595 -0.16575 -0.04707126 0.3799704 37.59851 31.84576 1.
-6.532501 -0.9289246 1001.599 0.009316115 -0.0101876 -0.01415993 0.189 -0.1152 -0.1668 -0.04665584 0.3799709 37.59879 31.84519 1.343
-6.49646 -0.8672829 1001.394 0.01493346 -0.004040405 0.0004347711 0.1875 -0.1167 -0.1674 -0.05277327 0.3763971 37.59903 31.84567 1.3
-6.760307 -0.7308645 1001.694 -0.006221347 -0.009372935 -0.01099725 0.1887 -0.1155 -0.1659 -0.05260342 0.3763327 37.59921 31.8461 1.3
-6.587747 -0.79004 1001.68 0.003869431 -0.003522553 -0.02488024 0.18855 -0.11445 -0.16485 -0.04762717 0.3811803 37.59958 31.84649 1.3
-6.385814 -0.840415 1001.687 0.01177193 0.0170724 -0.008051289 0.1875 -0.1143 -0.1638 -0.04732168 0.381427 37.59979 31.84684 1.34642
-6.679965 -0.9016314 1001.619 0.03752553 0.02106857 -0.03697531 0.1872 -0.1131 -0.1629 -0.04606196 0.3751609 37.60028 31.84716 1.347
-6.693847 -0.8304081 1001.752 0.03099507 -0.002087113 -0.04237398 0.18705 -0.11205 -0.16245 -0.04559761 0.3756349 37.60086 31.84644
-6.204454 -0.9056654 1001.756 0.01258485 -0.004712477 -0.02010844 0.1866 -0.1119 -0.1626 -0.04910368 0.3825818 37.60132 31.8468 1.34
-6.681747 -1.044546 1001.682 0.03132344 -0.002239544 -0.02677451 0.1881 -0.1104 -0.1641 -0.04866906 0.3826945 37.60178 31.84712 1.34
-6.759363 -0.9567175 1001.672 0.03213845 -0.002097581 -0.01792275 0.18945 -0.10905 -0.16365 -0.04763772 0.3825666 37.60242 31.84641
-6.748867 -0.8346863 1001.72 0.03744125 0.01814066 -0.01715074 0.18885 -0.11025 -0.16365 -0.04694654 0.3828484 37.6026 31.84677 1.35

Fig. 2. Spiral trajectory data.

D.Independent component removal

Given that the gravitational acceleration always exists and has components on the x, y and z axes of the target object coordinate system, it is an independent component. If we want to find the trajectory of the moving object, we need to remove the gravitational acceleration.Since the gravitational acceleration is always the vertical downward acceleration, in the

reference coordinate system it is always the vector in the Z axis, namely:

$$\boldsymbol{g} = \begin{bmatrix} 0 \\ 0 \\ 1 \end{bmatrix} g \tag{7}$$

$$\begin{bmatrix} G_{px} \\ G_{py} \\ G_{pz} \end{bmatrix} = \begin{bmatrix} \cos\psi\cos\varphi - \sin\psi\sin\beta\sin\varphi & \cos\psi\sin\varphi + \sin\psi\sin\beta\cos\varphi & -\sin\psi\cos\beta \\ -\cos\beta\sin\varphi & \cos\beta\cos\varphi & \sin\beta \\ \sin\psi\cos\varphi + \cos\psi\sin\beta\sin\varphi & \sin\psi\sin\varphi - \cos\psi\sin\beta\cos\varphi & \cos\psi\cos\beta \end{bmatrix} \begin{bmatrix} 0 \\ 0 \\ 1 \end{bmatrix} g \tag{8}$$

After simplifying (8), we can get:

$$\begin{bmatrix} G_{px} \\ G_{py} \\ G_{pz} \end{bmatrix} = \begin{bmatrix} -\sin\psi\cos\beta \\ \sin\beta \\ \cos\psi\cos\beta \end{bmatrix} g \tag{9}$$

This gives the component of the acceleration of gravity in the coordinate system of the target object at each moment.

Before removing the gravity acceleration, the temperature drift can be removed first. Take the first 20 data of the acceleration value and the gravity component output by the sensor respectively and then take the average value. Then, the temperature drift of the acceleration and the gravity component can be calculated.When these independent variables are solved, the independent variables can be removed from the original acceleration value.

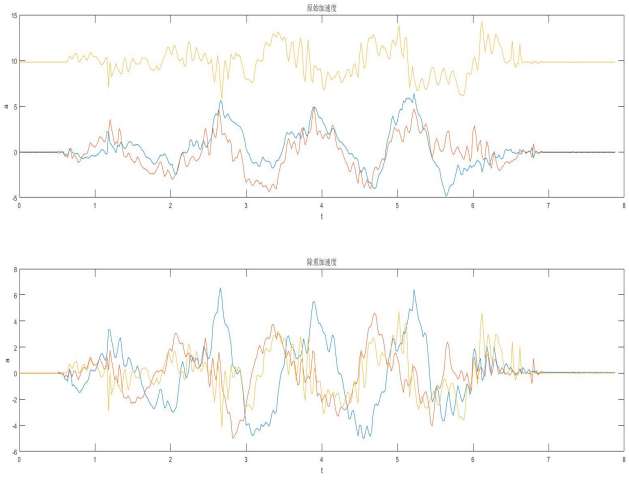

Fig. 3. The initial acceleration and the acceleration after removing the independent components.

Due to the acceleration output data of the sensor have drift, after integral calculation in the process, accumulate the drift error, lead to the velocity and displacement results of integral amplifies the drift phenomenon, using the least squares method, can be obtained to remove the influence of gravity acceleration to remove linear trend, can be found by comparing the speed curve is a smooth.

is the unit vector of gravity acceleration, in the rotation order of z-x-y, we can get:

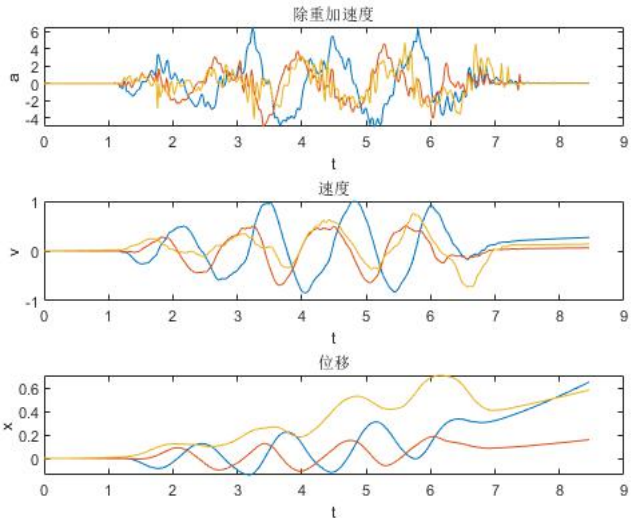

Fig. 4. Data before temperature drift.

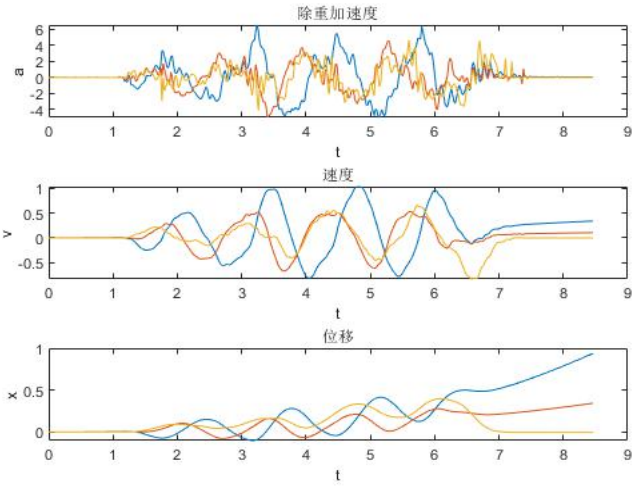

Fig. 5. Data after temperature drift.

By comparing figure 3 and figure 4, it can be found that the integral error can be reduced after the temperature drift is removed, and finally more accurate and stable data can be obtained.

E.Get trajectory

Since the acceleration value output by the sensor is the projection value of each coordinate axis in the coordinate system of the target object, it needs to be transformed to the reference coordinate system through the attitude matrix. After the transformation is completed, the obtained acceleration value can be integrated twice to obtain the trajectory of the moving

object.

F.Attitude algorithm

The attitude solution is to find out the current attitude of the sensor, the change of the carrier coordinate system relative to the reference coordinate system, and there are three ways to express the attitude matrix, which are euler Angle, direction cosine and quaternion respectively.The euler Angle method has singularity because of the universal joint lock, and the direction cosine method has a large amount of calculation, so the quaternion method has no singularity and the calculation amount is not large. [2]

Euler Angle is solved by quaternion method.Quaternions are simple supercomplex Numbers. [3]The complex number is composed of real number plus imaginary unit i, and the quaternion is composed of real number plus three imaginary units i, j and k, which can be expressed as: $\mathbf{Q} = q_0 + q_1\boldsymbol{i} + q_2\boldsymbol{j} + q_3\boldsymbol{k}$, the quaternion can also be used to express the rotation relation in the coordinate system: $\mathrm{r}' = \mathrm{Q} \otimes \mathrm{r} \otimes \mathrm{Q}'$, where r 'is the rotated vector and r is the rotated vector. [4]

According to the $\begin{cases} \mathbf{q}_z = \cos\frac{\varphi}{2} + \mathbf{k}\sin\frac{\varphi}{2} \\ \mathbf{q}_x = \cos\frac{\beta}{2} + \mathbf{j}\sin\frac{\beta}{2} \\ \mathbf{q}_y = \cos\frac{\psi}{2} + \mathbf{i}\sin\frac{\psi}{2} \\ \mathbf{Q} = \mathbf{q}_z\mathbf{q}_x\mathbf{q}_y \end{cases}$ it can be concluded that:

$$\begin{bmatrix} \cos\psi\cos\varphi - \sin\psi\sin\beta\sin\varphi & \cos\psi\sin\varphi + \sin\psi\sin\beta\cos\varphi & -\sin\psi\cos\beta \\ -\cos\beta\sin\varphi & \cos\beta\cos\varphi & \sin\beta \\ \sin\psi\cos\varphi + \cos\psi\sin\beta\sin\varphi & \sin\psi\sin\varphi - \cos\psi\sin\beta\cos\varphi & \cos\psi\cos\beta \end{bmatrix}$$

$$= \begin{bmatrix} q_0^2 + q_1^2 - q_2^2 - q_3^2 & 2(q_1q_2 + q_0q_3) & 2(q_1q_3 - q_0q_2) \\ 2(q_1q_2 - q_0q_3) & q_0^2 - q_1^2 + q_2^2 - q_3^2 & 2(q_2q_3 - q_0q_1) \\ 2(q_1q_3 + q_0q_2) & 2(q_2q_3 - q_0q_1) & q_0^2 - q_1^2 - q_2^2 + q_3^2 \end{bmatrix} \quad (10)$$

Assume that $C_0^3 = \begin{bmatrix} T_{11} & T_{12} & T_{13} \\ T_{21} & T_{22} & T_{23} \\ T_{31} & T_{32} & T_{33} \end{bmatrix}$ then:

Through $\begin{cases} q_0^2 + q_1^2 - q_2^2 - q_3^2 = T_{11} \\ q_0^2 - q_1^2 + q_2^2 - q_3^2 = T_{22} \\ q_0^2 - q_1^2 - q_2^2 + q_3^2 = T_{33} \\ q_0^2 + q_1^2 + q_2^2 + q_3^2 = 1 \end{cases}$, we can get the quaternion from (10) $\begin{cases} q_0 = \frac{1}{2}\sqrt{1 + T_{11} + T_{22} + T_{33}} \\ q_1 = \frac{1}{4q_0(T_{23} + T_{32})} \\ q_1 = \frac{1}{4q_0(T_{31} + T_{13})} \\ q_1 = \frac{1}{4q_0(T_{12} + T_{21})} \end{cases}$.

Thus, the initial value of euler Angle output by the sensor can be assigned to the quaternion.

Next, the angular velocity value and quaternion differential equation output by the sensor are used:

$$\begin{bmatrix} \dot{q}_0 \\ \dot{q}_1 \\ \dot{q}_2 \\ \dot{q}_3 \end{bmatrix} = \frac{1}{2}\begin{bmatrix} 0 & -\omega_x & \omega_y & -\omega_z \\ \omega_x & 0 & \omega_z & -\omega_y \\ \omega_y & -\omega_z & 0 & \omega_x \\ \omega_z & \omega_y & -\omega_x & 0 \end{bmatrix}\begin{bmatrix} q_0 \\ q_1 \\ q_2 \\ q_3 \end{bmatrix} \quad (11)$$

The first-order runge-kutta method[4] is adopted, as shown in equation (12), to perform iterative recursion and update quaternions:

$$\begin{bmatrix} q_0 \\ q_1 \\ q_2 \\ q_3 \end{bmatrix}_{t+\Delta t} = \begin{bmatrix} q_0 \\ q_1 \\ q_2 \\ q_3 \end{bmatrix}_t + \frac{\Delta t}{2}\begin{bmatrix} -\omega_x q_1 - \omega_y q_2 - \omega_z q_3 \\ \omega_x q_0 + \omega_z q_2 - \omega_y q_3 \\ \omega_y q_0 - \omega_z q_1 + \omega_x q_3 \\ \omega_z q_0 + \omega_y q_1 - \omega_x q_2 \end{bmatrix} \quad (12)$$

After the quaternion is obtained, the data is normalized, and a new attitude matrix represented by quaternion can be obtained through the relationship between quaternion and attitude matrix (10).

$$\begin{cases} \Phi = \sin^{-1} T_{23} \\ \psi = \tan^{-1} - \frac{T_{21}}{T_{22}} \\ \beta = \tan^{-1} - \frac{T_{13}}{T_{33}} \end{cases} \quad (13)$$

With the new attitude matrix, the new euler Angle data can be obtained through the relationship between euler Angle and attitude matrix (4).It lays a foundation for obtaining the optimal estimation Angle later.

G.Data preprocessing

Firstly, the sensor is set for 10s to obtain data, and then the static data is preprocessed.Here using AR model is established to error compensation, AR model is a kind of linear prediction, namely known N data, can be launched by the model N points in front of or behind the data (a launch point P), so its nature is similar to the interpolation, its purpose is to increase the effective data, just a bit AR model was made by N recursion, and the interpolation is composed of two (or a few points) to derive more, so the AR model is better than the interpolation method.

Filtering mode selection Kalman filtering is an algorithm that USES linear system state equation to optimize the system state estimation through system input and output observation data. [5]Since the observed data include the influence of noise and interference in the system, the optimal estimation can also be regarded as a filtering process. The five basic formulas of kalman filter are:

$$\begin{cases} X(k|k-1) = A\,X(k-1|k-1) + B\,U(k) \\ P(k|k-1) = A\,P(k-1|k-1)\,A' + Q \\ X(k|k) = X(k|k-1) + Kg(k)\,(Z(k) - H\,X(k|k-1)) \\ Kg(k) = P(k|k-1)\,H' / (H\,P(k|k-1)\,H' + R) \\ P(k|k) = (I - Kg(k)\,H)\,P(k|k-1) \end{cases}$$

Kg is Kalman Gain.

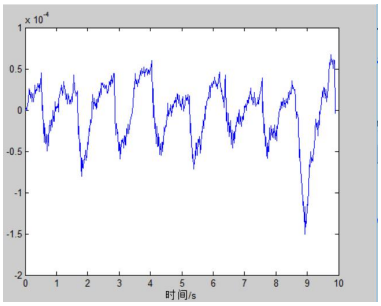

Fig. 6. The error estimate curve for a set of data.

H.Data fusion

Now there are two sets of data, one is the euler Angle value output by the sensor, and the other is the euler Angle value obtained by the inverse solution of quaternion. The fusion of the two data can obtain the euler Angle value with higher accuracy, so as to improve the accuracy of the final trajectory.

The euler Angle of the sensor output is taken as the estimated value, the euler Angle of the quaternion inverse solution is taken as the measured value, and the optimal estimated Angle is obtained by using kalman filter algorithm.

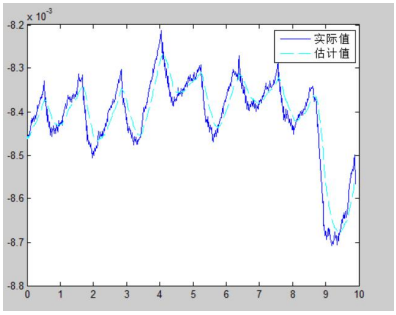

Fig. 7. The actual and estimated values of a set of data.

IV. EXPERIMENTAL VERIFICATION

A.Two-dimensional

Firstly, the trajectory is acquired by using the unfiltered data through quadratic integration, and then the 2d image trajectory is acquired.Use the sensor to place a rectangular track on the desktop, obtain data and import MATLAB software.

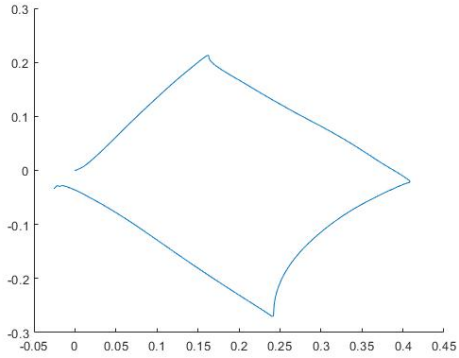

Fig. 8. 2d graph obtained from un-processed data.

The image obtained with the processed data is shown in figure 6, which shows that it is obviously more regular and accurate.

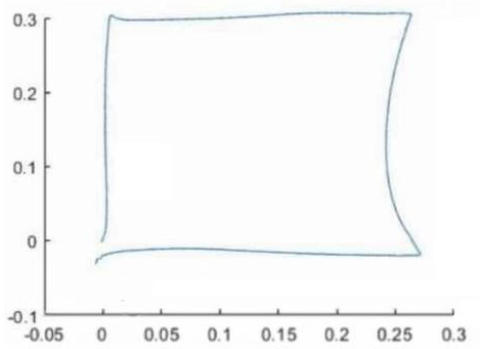

Fig. 9. The 2d graph obtained from processed data.

Use form in the following table to summarize the result of the experiment, it can be seen that is effective for data processing, precision reached: point of ±5 °, ±5 cm distance.

TABLE I Experimental results of rectangular trajectories

Edge1	Actual value	30cm	Angle1	Actual value	90°
	Before processing	38cm		Before processing	78°
	After processing	33cm		After processing	89°
Edge 2	Actual value	30cm	Angle2	Actual value	90°
	Before processing	37cm		Before processing	108°
	After processing	31cm		After processing	87°
Edge 3	Actual value	30cm	Angle3	Actual value	90°
	Before processing	42cm		Before processing	70°
	After processing	36cm		After processing	85°
Edge 4	Actual value	30cm	Angle4	Actual value	90°
	Before processing	24cm		Before processing	84°
	After processing	29cm		After processing	85°

B.Three-dimensional

After the experiment on the two-dimensional trajectory, the experiment on the three-dimensional trajectory is attempted.Hold the sensor, swing the spiral trajectory, obtain data, import MATLAB software.

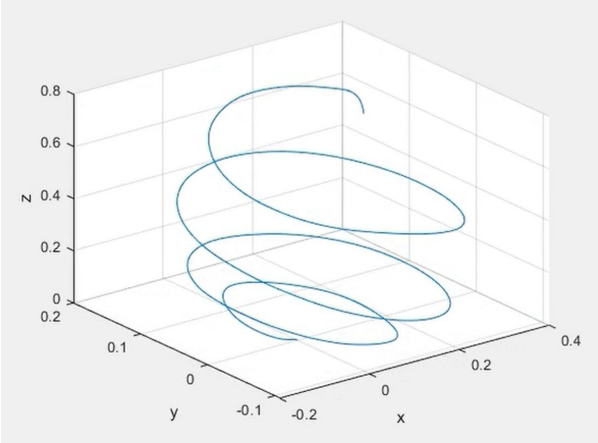

Fig. 10. The 3d graph obtained from processed data.

We can see that the trajectory of the spiral is basically consistent with the trajectory of the swinging hand.

V. CONCLUSION

This article describes the use of MATLAB to design a set of independent space three-dimensional measurement algorithm, including the theoretical part, design part and experiment part, the final accuracy reached: point of ±5 °, ±5 cm distance.The contents mentioned in this paper are summarized and reflected as follows:

(1) the rotation order of coordinate transformation should be consistent with the rotation order of sensor output data.

(2) the obtained data shall firstly unify the unit and numerical range.

(3) in the attitude solution, the euler Angle method of quaternion method has singularity due to the universal joint lock, and the direction cosine method requires a large amount of calculation, while the quaternion method has no singularity and requires a small amount of calculation.

(4) some error factors can be removed, such as gravity acceleration, temperature drift and random drift of the sensor.

(5) if more complex algorithms are adopted, such as the fusion of data obtained by extended kalman filter (EKF) and untracked kalman filter (UKF), more accurate results can be obtained.

References

[1] 2012(1): 294-298. Chen wei. Research and application of attitude Angle estimation algorithm based on quaternion and kalman filter [D]. Yanshan university,,2015.

[2] Ping Han, Haoliang Gan, Weikun He. Aircraft attitude estimation based on central difference Kalman filter[C]. Proceeding of 2012 IE EE 11th International Conference on Signal Processing, 2012(1): 294-298.

[3] Du hailong, zhang ronghui, liu ping, et al. Realization of attitude calculation module of strapdown inertial navigation system [J]. Optical precision engineering, 2008, 16(10): 1956-1962.

[4] Liu haiying, wang huinan. Research on low cost attitude measurement system [J]. Journal of nanjing university of science and technology, 2007, 31(2): 233-237.

[5] Ma ruiping, wei dong, zhang minglian. An improved adaptive kalman filter and its application in integrated navigation [J]. Chinese journal of inertial technology, 2006(12): 37-40..

Design of Pulse Signal Parameter Measurement System

Hou Xiaochun, Cui Meng, Bai Dongxu, Xin Shibo
(jilin university instrument science and engineering institute,changchun,130021)

***Abstract*--Pulse signal is not only a common signal, but also a very important signal. Therefore, it is very important to accurately measure the characteristics of pulse signal. This paper designs a pulse signal parameter measuring instrument, which can measure the basic parameters of the input pulse signal，including frequency, duty cycle, amplitude and rise time. Its frequency measurement range is from 10Hz to 2MHz, duty cycle measurement range is from 10% to 90%, amplitude measurement range is from 0.1V to 10V, rise time is from 50ns to 999ns. The whole design can be divided into analog and digital parts. The analog part is composed of amplifiers, comparators, adders, subtractors and differentiators, which are built by operational amplifiers and other chips. The digital part is composed of FPGA and MSP430 for measurement and display respectively. In addition, a standard signal source consisting of a FPGA and a comparator is attached to the design, which can generate a pulse signal with a frequency of 1MHz, a pulse width of 100ns, an amplitude of 5V and a rise time of no more than 30ns.**

***Key words*--Pulse signal, signal parameters, signal source.**

I. INTRODUCTION

PULSE signals are of great significance both in production and life and in scientific experiments. Pulse signals can be used not only to transmit information, but also as carriers[1]. For a system, the characteristics of the system can also be analyzed by analyzing its response to a pulse signal. Therefore, it is of great significance to measure the characteristics of pulse signals. Pulse signal measurement device is a pulse parameter measurement technology based on transient signal in time domain. It is widely used in many fields such as computer, laser, remote sensing, biology, medical electronics and so on[2]. With the development of science and technology, the research methods of pulse parameter measurement technology will be more perfect, the research means will be more advanced, and the basic role of technology will be more obvious.

II. CONCEPTUAL DESIGN

A. Demonstration And Comparison of Schemes

Scheme 1: A medium-scale digital circuit is adopted, which consists of a comparator, a function selection, a range selection, a counter and a control module[3]. The circuit is complex in design, narrow in frequency band and weak in function, which makes it difficult to realize. Therefore, no such scheme is adopted.

Scheme 2: A scheme combining FPGA and MCU is adopted. The main measurement module is composed of the FPGA. The advantages of this circuit are: relatively few peripheral components, high speed signal processing, high accuracy, and flexible control. However, the measurement accuracy of this scheme is difficult to guarantee. After the input signal passes through attenuation and amplification circuit, the details such as the rising time of the input signal will be seriously destroyed, resulting in the low correlation between the characteristics of the final measured signal and those of the original signal, which makes it difficult to accurately measure the characteristics of the measured signal. Therefore, no such scheme is adopted.

Scheme 3: The scheme of combining FPGA with MCU is also adopted. The difference is that after attenuation, the signals are first divided into three channels which do not affect each other. A signal is converted into TTL level by a comparative amplifier and a voltage comparator, and the frequency and duty cycle of the signal are measured by subsequent circuits. A signal is sent directly to a high-speed AD chip to measure the amplitude of the signal. One signal passes through a differentiator, which converts the rise time to the pulse width, which is then measured by the FPGA. The measurement and display part is composed of a FPGA and a MSP430. The frequency, duty cycle, amplitude and rise time are measured by the FPGA through programming. Finally, the data are transmitted to MSP430, and the measured data are displayed after calculation[4]. Although this scheme is slightly troublesome, its accuracy and stability are guaranteed. Therefore, choose option 3.

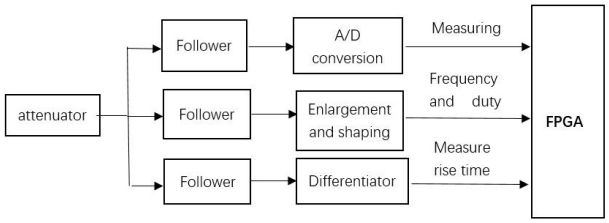

Fig.1 Scheme 3 System design block diagram

B. Overall Design Scheme

Because this design is a combination of digital signal and analog signal, the overall idea of this design is: first, the analog circuit is designed to convert the input signal into TTL level, and then the digital circuit is designed to collect, calculate and display the converted signal.

The design idea of the analog circuit is as follows. First, the input signal passes through a attenuator, which attenuates about three times and satisfies the requirement of input resistance 50. After that, the signal is divided into three circuits, each of which is isolated by a voltage follower to ensure that the subsequent measurement circuits do not affect each other. The first signal is converted into TTL level by a comparative amplifier and a voltage comparator, and the frequency and duty cycle of the signal are measured by subsequent circuits. The second signal is directly fed into a high-speed AD chip to measure the amplitude of the signal. The third signal first passes through a differentiator, which converts rise time into pulse width, making the measurement more convenient and accurate.

The digital circuit is composed of a FPGA and a MSP430. The frequency, duty cycle, amplitude and rise time are measured by the FPGA through programming. Finally, the data are transmitted to MSP430, and the measured data are displayed after calculation.

III. OVERALL DESIGN SCHEME

A. Frequency Measurement Method

In this design, the indirect measurement method is adopted, that is, the period of the signal is measured first, and then the frequency is calculated by the reciprocal method. The reason why this measurement method is adopted is that the measurement frequency range is from 10HZ to 2MHz, and the main body of the measurement range is in the low frequency range[5]. Therefore, the measurement error can be reduced by using the method of measuring period. Specific methods are as follows: Firstly, the measured frequency is divided into two segments. The internal clock is counted directly from 10Hz to 10KHz in one cycle. The counting value is n1, and the internal clock is 50MHz.

The calculated signal period is n1/50M (unit s). The signal frequency can be obtained by the reciprocal. The signal above 10KHz is first divided into 1000 frequencies, and then the calculation process is the same as above.

B. Duty Cycle Measurement Method

Since the input signal is a square wave and the period of the signal has been obtained in the previous step, the duty cycle can be obtained by directly measuring the duration of the high level. The specific method is to count the internal clock when the input signal is high, and the count value is n2. The duty cycle is (n2/n1)*100%.

C. Amplitude Measurement Method

Since the highest frequency of the signal is only 2 MHz, high-speed A/D chip is directly used to collect the voltage value of the measured signal, and then the amplitude can be extracted. The specific method is that the enabling clock is output by the FPGA, and the data sent by the A/D module is received by the I/O port. A/D module has a controllable attenuator, which can control whether the attenuation is 10 times, adjust the attenuation multiples according to the range of data in time, and finally get the correct amplitude.

D. Rising Time Measurement Method

Because the amplitude and frequency of the signal to be measured vary widely, it is not easy to obtain the analog value of the signal amplitude in real time, so the method of window comparator is not very suitable[6]. In this design, the rise time of the measured signal is differentiated into a low level by using a differentiator, and then through a comparator, the information of the rise time can be transferred to the duty cycle of the measurement, which can be achieved by using the method mentioned above. The advantage of this method is that the rise time is a very easily affected feature. Once the circuit is amplified, it will suffer a lot of losses and is not easy to handle. When converted into duty cycle, this feature is not easy to be destroyed, which is convenient for subsequent circuit processing.

IV. CIRCUIT AND PROGRAMMING

A. Design of Front-end Signal Processing Circuit

Fig. 2 shows that the input signal is attenuated three times, then connected with three comparators and divided into three non-interference signals. Frequency and duty cycle measurement, amplitude measurement and rise time measurement are carried out respectively through the post-circuit.

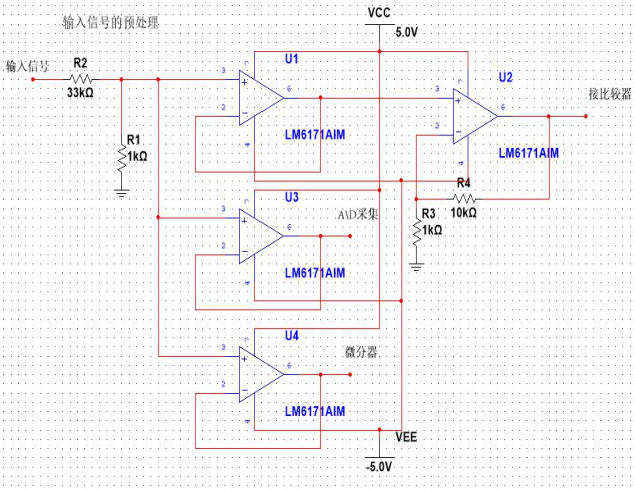

Fig.2 Front-end signal processing circuit

B. Circuit Design of Comparator Part

As shown in Fig. 3, in the process of generating pulse signal with FPGA, the pulse signal will jitter, so a hysteresis comparator is needed to stabilize the pulse. In addition, the comparator is also used in AD acquisition and differentiator conversion to regulate the waveform.

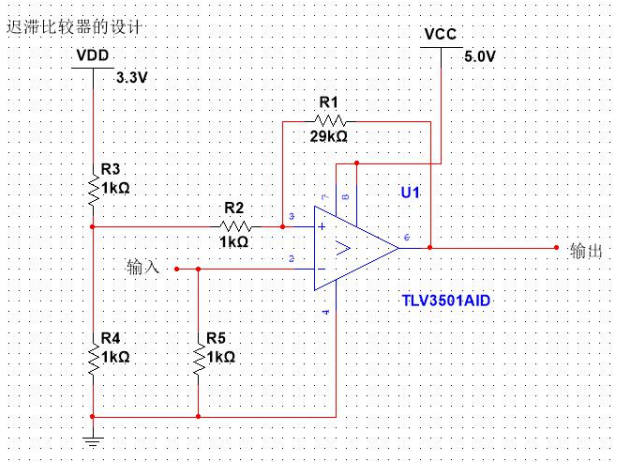

Fig.3 Schmitt

C. Circuit Design of AD Part

As shown in Fig. 4, since the highest frequency of the collected signal is 2MHZ, the attenuated signal is input into the high-speed AD acquisition chip to collect the amplitude of the signal, and the amplitude is calculated and displayed by the FPGA.

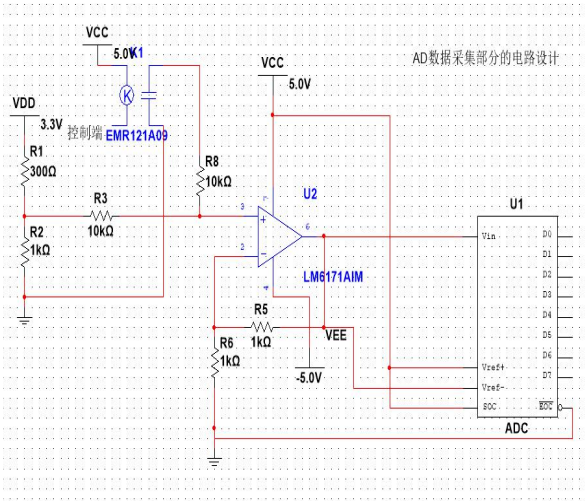

Fig.4 AD acquisition circuit

D. Circuit Design of Differentiator Part

In the measurement of the rising time of pulse signal, the rising edge of the signal should be converted to the level and measured by the FPGA. Therefore, the differentiator shown in Fig. 5should be used to convert the signals, and the signal after conversion will also be jittery. Therefore, the hysteresis comparator shown in Fig. 5 should be used to eliminate the jitter.

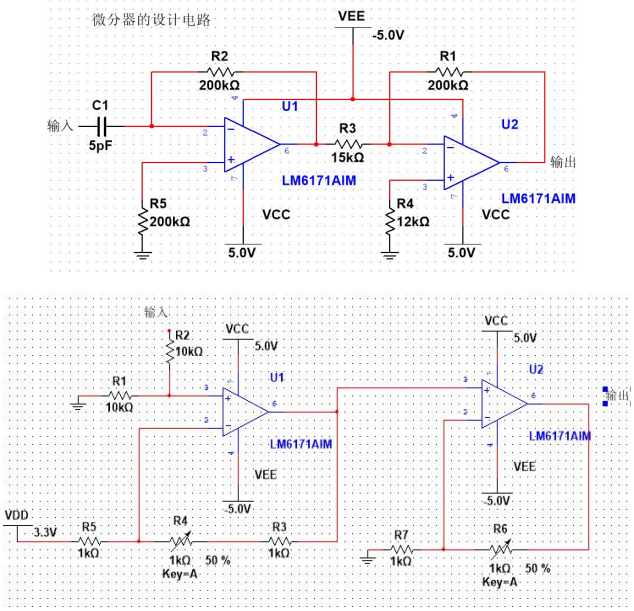

Fig.5 Differentiator Circuit Design

E. Other Circuit Design of Signal Generator

Pulse signal generator is realized by means of FPGA comparator. The rectangular signal with 1 MHZ and 10% duty cycle is programmed by FPGA. At this time, the output signal is slightly inadequate in both amplitude and shape. Therefore, the shape of the signal and the amplified signal are regulated by the hysteresis comparator shown in Fig. 5, in order to realize the generation of a standard rectangular signal.

The idea of programming is to count the period of the input signal to get the periodic value of the input signal, count the high level of the corresponding period,

and then get the duty ratio of the input signal compared with the periodic value. The output enabling clock drives the A/D module and reads the returned digital value. The rising time of the input signal is also obtained by measuring the duty cycle. Finally, all the data are packaged and sent to MCU for display.

The chip is initialized, and two input pins are defined as data line and clock line. The interrupt enable is opened. The interrupt condition of P1 port is defined as rising edge trigger. Except for the first check bit, other checks are correctly cleared and recalculated and displayed. Finally, the integer is forced to be transformed into a pointer-type symbolic string and the display function is called for display. Different data units are displayed by checking bits.

V. TEST SCHEME AND TEST RESULTS

After testing, all parts work normally and the measurement error is small. The specific indicators are shown in Table 1.

Table1 Test Result Table

Measuring Characteristic Quantity	measuring range	measurement error
frequency	10Hz—2MHz	0.1%
Duty cycle	10%—90%	2%
amplitude	0.1V—10V	1%
rise time	50ns—999ns	5%

VI. CONCLUDING REMARKS

In this paper, the significance of pulse signal is briefly described, and a pulse signal measuring device is given. The scheme selection, scheme design, specific circuit and programming are introduced in detail. Finally, the measurement results and indicators of the design are given. From the results, it can be seen that the design has the advantages of good measurement effect and wide application range.

References

[1] Zhang Yongrui, Yang Linyao, Zhang Yalan. Fundamentals of Circuit Analysis (Second Edition) [M]. Xidian University Press, 1987.

[2] Kang Huaguang. Electronic Technology Foundation, Digital Part. 4th Edition [M]. Higher Education Press, 2000.

[3] Li Lei. Pulse signal parameter measuring instrument. [EB/OL].https://wenku.baidu.com/view/5afbf23fb94ae45c3b3567ec102de2bd9705de6c?pcf=2&tdsourcetag=s_pcqq_aiomsg&qq-pf-to=pcqq.group.2019.03.04

[4] Kang Huaguang. Electronic Technology Foundation, Simulation Part [M]. Higher Education Press, 1988.

[5] Zhang Yubo. Signals and Systems [M]. China Electric Power Press, 2012.

[6] LI Yuan-yuan, CAI Wei, GAO Xu-rong. Retinal vessel segmentation algorithm based on fusion phase feature[J]. Journal of Computer Applications, 2018, 38(7): 2083-2088.

[7] Shi Yongbin, Yu Meng, Li Di. Uncertainty Analysis and Evaluation of Measurement Results of Oscilloscope Measurement Pulse Signals[J]. Foreign Electronic Measurement Technology, 2016, 35(3): 50-53.

[8] Hu Song, Jiang Xiaowei, Yang Guang, et al. Application of Moving Average Filtering in Weak Pulse Signal Detection[J]. Computer and Digital Engineering, 2007, 35(10): 169-171.

Design of simple circuit delay measuring device

Zhao Delin, Chen Hao, Shi Yunfei
（jilin university, instrument science and electrical engineering institute,changchun,130021）

***Abstract*—In this paper, a simple circuit delay measuring device is designed. The device consists of signal source, signal shaping circuit, delay circuit, measuring circuit and human-machine interface. It is used to measure a square wave with amplitude range of 3V, frequency range of 1kHz~20MHz and delay time of 1000ns~100ms. The resolution of measurement is less than 0.01μs. The signal source uses DDS to generate a sinusoidal signal, and the signal shaping circuit converts the sine wave into a square wave, and uses FPGA to delay and measure the signal. After testing, the simple circuit is extended. The time measuring device can meet the requirements.**

***Keywords*—Anti-interference high frequency delayed**

I. INTRODUCTION

THE time delay measuring device is widely used in production practice. The time delay relay unit in time relay[1] can be used for automatic control, and the precision delay circuit plays an important role in the radar system[2]. These delay measuring devices use a combination of a single-chip microcomputer and a CPLD to form a digital frequency meter[3-5]. This type of scheme has many combined devices and low system integration, and the use of the same precision frequency measurement inside the FPGA can effectively improve the measurement accuracy. Integration with the system.

This design uses DDS9910 chip as the signal source, with low power consumption and small size, suitable for full digital circuit design [6][7]. With STM32F103ZET6 as the main controller, the FPGA module is responsible for delay and frequency measurement [8]. Using the principle of equal-precision frequency measurement, the measured signal is accurately frequency-measured, and the minimum 50 ns delay is realized, which ensures measurement accuracy and reliability. It includes signal source circuit, signal shaping circuit, delay circuit measurement circuit and human-machine interface, which realizes system integration and miniaturization.

II. OVERALL DESIGN OF THE DEVICE

The program-controlled adjustable signal generated by the DDS is used as a self-made signal source, and is filtered to generate a sine wave with a peak-to-peak range of 0V~1V from 1 kHz to 20 MHz. The output of the signal source can be manually adjusted by the TFT screen, and the control signal is transmitted through the STM103ZET6. The output signal is conditioned and shaped to output a square wave, and then the real-time display is performed after the voltage regulator circuit reaches the amplitude specified by the square wave. Finally, the FPGA square wave circuit is used for delay, and the data information of the acquisition delay circuit is displayed on the TFT screen.

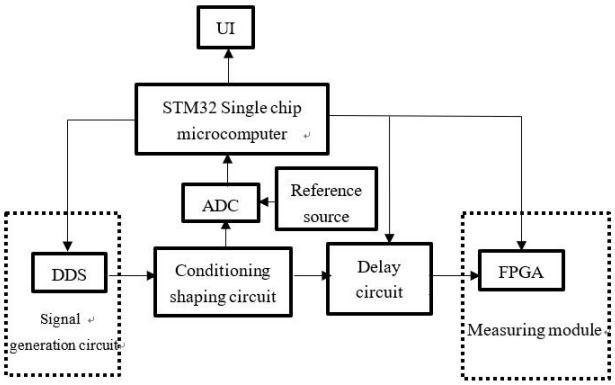

Fig 1 System block diagram

III. OVERALL DESIGN OF THE DEVICE SYSTEM MODULE ANALYSIS

A. Waveform generating circuit

It is required to generate voltage peak-to-peak range from 0 to 1000mV, frequency range from 1kHz to 20MHz, amplitude and frequency program control adjustable, peak-to-peak adjustment step size ≤10mv, frequency adjustment step size ≤10Hz, based on ARM microcontroller and DDS chip design signal source generation circuit DDS uses a stable reference clock source to specify the sampling time (up to 400MHz analog output). The frequency resolution is high, the frequency switching speed is fast, the frequency range can meet the requirements of the signal source frequency range, and the full digital technology facilitates the monolithic integration of the system. Using the single-chip microcomputer to control the

DDS program, use the TFT screen to input the waveform information to the single-chip microcomputer, the waveform information to be displayed by the single-chip microcomputer is written into the DDS chip, and the DDS outputs the corresponding waveform signal.

B. Conditioning plastic circuit

Anti-jamming is the most important part of the overall system, including the handling of power supplies, as well as higher requirements for chip and device selection. Integrating the whole system The device focuses on the comprehensive anti-interference performance of the system in design, and performs amplification and shaping processing on small high-frequency signals.

First, the OPA657 is used to perform secondary amplification of the weak signal of the signal source to reach the voltage range that the comparator can recognize. For the shaping circuit, the LT1711 high-speed comparator is used to form a hysteresis comparator. The hysteresis comparator removes most of the pulse interference, making the resulting square wave more accurate. The LT1711 is powered by ±5V and has an output range of 4.5V to 4.8V. The maximum switching frequency reaches 100MHz, which meets the basic requirements of the circuit. Finally, the Zener amplitude is limited to 3.3V using a Zener diode.

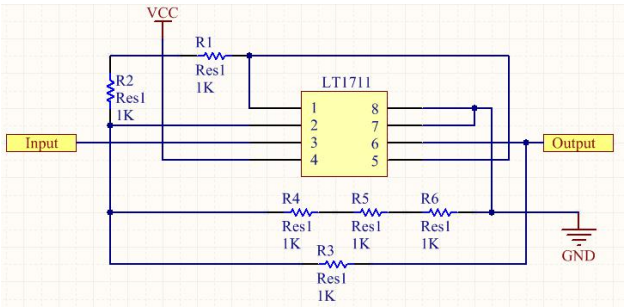

Fig2 Part of the shaping circuit

C. Delay circuit

The delay circuit requires the delay of the square wave signal, the delay time range is 100ns~100ms, and the program control is adjustable, and the adjustment step length is ≤100ns. After multiplying the FPGA, a high-speed clock can be generated. At the same time, the internal shift register of the FPGA is easy to write. By collecting the level value of the port, accurate delay output can be realized. Therefore, the Cyclone II series EP2C5T144C8 can be selected as the delay processing unit. The frequency is 100MHz, which can meet the requirements of adjustment step and delay time. For different frequency signals, CLK is divided to meet different delay time requirements. For low frequency signals, the frequency-divided clock signal is used for delay control, and the high-frequency signal is controlled by 100MHz clock signal.

Write the FPGA shift register, using the clock signal or the divided clock as the counting unit, when the frequency is not divided, the minimum delay time T_{min} is $10ns$. After dividing by 200, minimum delay time T_{min} is $2\mu s$ .Thereby the delay requirement of square wave signals of different frequencies is fulfilled.

D. Frequency measuring circuit

Using the equal-precision frequency measurement method, by setting a gate synchronized with the signal under test, the measured signal and the time base pulse are simultaneously counted. The ratio of the two count values is equal to its frequency ratio. The equal-precision frequency measurement strictly corresponds to the corresponding relationship between the rising edge and the falling edge of the measuring gate, so that the measurement error is only related to the reference clock frequency, eliminating the error of the positive and negative one pulse of the measured counter, so that the error is independent of the measured frequency. Achieve equal precision frequency measurement.

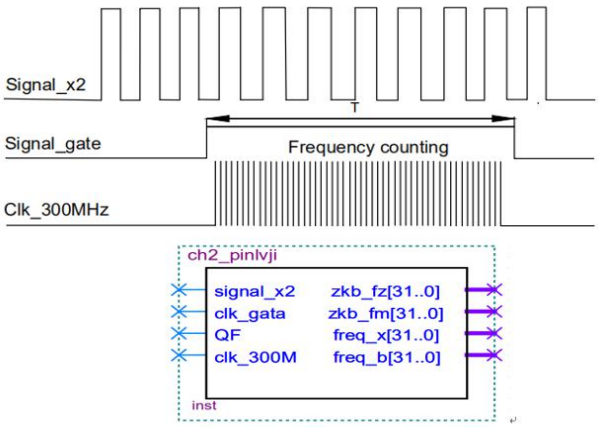

Fig3 Equal precision frequency measurement principle

Let n1 be the number of pulses of the reference clock recorded by counter 1 in the gate time, and n2 be the number of pulses of the measured signal recorded by counter 2 in the gate time, then the measured signal frequency

$$f_x = \frac{N_2}{N_1} \times f_c$$

When designing the delay measurement part, it is required to measure the delay time of the delay circuit, the resolution is ≤0.1μs, the absolute error is ≤1μs, and the square wave after conditioning and shaping and the square wave waveform after delay can be displayed. Therefore, the EP2C5T144C8 is multiplied to obtain a 300MHz clock signal, and the square wave before and after the delay is compared and operated, and the number of clock pulses in the high-level time of each

cycle is measured, thereby calculating the delay time and satisfying the problem. Precision requirements. Let N be the number of reference clocks in one cycle obtained after the operation, then the delay time

$$T_x = 10ns \times N = 10Nns$$

The frequency measurement result and the delay time measurement result are transmitted to the main controller through the SPI, and the waveform of the waveform and the delay time are displayed by the serial port screen connected by the main controller.

E. Display circuit

By using the TFT liquid crystal screen as a human-machine interface, not only waveform data can be drawn on the display screen, but also a touch input control signal can be performed. The auxiliary power supply is used to provide a +5V supply voltage to the display, which is connected to the RX and TX pins on the microcontroller for easy programming.

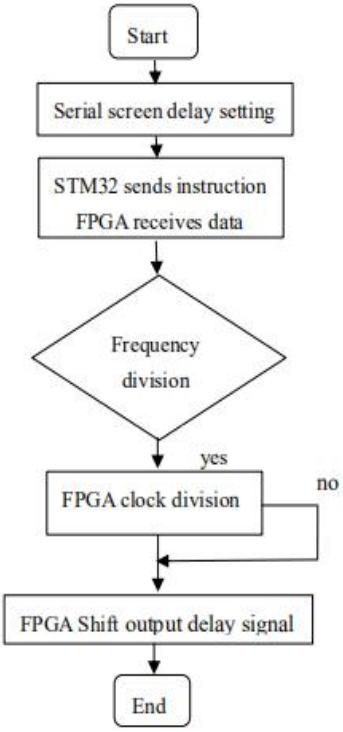

Fig4 software process design

IV. OVERALL PROGRAMMING

A. Test scheme

1) Perform real-time testing on the signals at all levels, first observe whether the signal has obvious distortion.

2) Compare the pre-determined data indicators with the actual test values, and whether the test can meet the requirements and make further adjustments.

B. Test results and analysis

The test results are shown below:

Table1 Signal Generator Signal Detection

Vpp	f/Hz	Vpp step/mv	Frequency step/Hz
5mv	20MHz	1	1
50mv	10MHz	1	1
700mv	100MHz	1	1

As can be seen from Table 1, the DDS can fully meet the requirements, and can adjust the small step size to make the output signal more accurate.

Table2 Test data of shaping and conditioning circuit

	Vpp	f/Hz	Duty cycle
Input	50mv	500Hz-20MHz	50%
Amplified signal	545mv	500-13MHz	51%
Square wave	3450mv	500-20MHz	53.4%

The shape adjustment data is obtained by oscilloscope measurement, and the waveform has not much distortion, which basically meets the requirements, and the amplitude error of the comparator output signal is 0.15V to meet the error requirement.

Table3 Test data of delay circuit

Theoretical value/μs	1000	1500	3000	6000	8000
Measured value/μs	990.453	1482.354	2988.232	6012.125	8015.231
Absolute error/μs	9.547	17.646	22.768	60.125	15.231
Relative error	0.95%	1.18%	2.35%	1.02%	0.62%

It can be seen from Table 3 that the measurement accuracy of the delay measurement circuit meets the requirements of the problem, and the measurement resolution is less than 0.01 μs.

V. CONCLUSION

This paper mainly designs a simple delay circuit measuring device. It can be known from the test data that the device can generate a frequency range of 0~20MHz.

The sinusoidal signal source with peak-to-peak range of 0~1000mV can obtain a square wave with a frequency range of 1kHz~20MHz after conditioning and shaping. The delay can be 1000us~100ms, the program control can be adjusted, and the step size can satisfy <100ns. The device can be correct. The delay time of the delay circuit is measured, and the integration degree is high. The design won the first prize of the 2018 Jilin Province Electronic Competition.

References

[1] Menglin Yang. Research and Design of Relay Delay Time

Measurement Circuit[J]. Electronic design engineering. 2014, 22(13):120-122.

[2] Yingping Zhang,Jiahao Ji,Guojun Li.Research and Design of Simple Circuit Delay Measurement Device Based on Single Chip Microcomputer Student practice training results[J].Digital technology and application. 2018, 36(12): 129-130.

[3] Lina Wang,Xusen Yang,Ran Xu,Wei Xu,Jing Wu,Mingchen Shi.Wideband signal generation and frequency measurement circuit based on FPGA[J].modern electronic technology. 2018,41(17):107-111.

[4] BenGang Bao,Xiangping Zhu.ASIC design for implementing DDS signal source for instrumentation with FPGA[J].MCU and embedded system applications. 2017, 17(11):60-63.

[5] Zheng Zhang,Ting Hu.Design of Multifunctional High Precision DDS Signal Source Based on AD9854[J]. Electronic technology. 2017,30(03):182-184.

[6] Lili Shen.Frequency measurement circuit design in DDS signal source[J].Industrial control computer. 2014, 27(10): 165-166.

[7] Ji Zhang,Yun Zeng,Zheng Wang,Qiuju Li,Jifang Lv,Jinyuan Wu.Implementation of High Precision Time Measurement Circuit Based on FPGA[J].Nuclear Electronics and Detection Technology. 2011, 31(05): 508-512.

[8] Huaguaung Kuang.Electronic circuit foundation(Sixth edition)[M].Beijing.2013.12.

Lens Design for the Spacecraft Rendezvous and Docking

Yawen Wang, Mengyang Shi, Ziyi Zhao
（Jilin university instrument science and engineering institute,Changchun,130061）

***Abstract*—This study focuses on the lens design for the imaging sensor baffle used in spacecraft rendezvous and docking which includes two parts. One is used to detecting the attitude of the spacecraft when docking. The other one offers the help to measure the relative orbital position and attitude angle of the two spacecraft. This paper describes the optical prescription, lens materials and thermal analysis for the camera lenses.**

***keywords*—lens design; spacecraft rendezvous and docking (RVD); aerial camera; near infrared**

I. INTRODUCTION

SPACECRAFT rendezvous and docking (RVD) is a critical spaceflight operation required for many missions involving more than one spacecraft. [1] With the continuous development of manned space technology, space rendezvous and docking technology has begun to evolve to automatic operation, and if necessary, with the direction of ground remote control. For autonomous and automatic rendezvous and docking, different navigation sensors are usually used according to different stages of RVD and different navigation information requirements. In the final approximation phase, a CCD optical imaging sensor is generally used as the main navigation sensor to obtain the relative position and relative attitude navigation information of the two spacecraft. Due to the existence of the external disturbances and safe constraint in the process of rendezvous and docking, it is difficult to present lens designs for spacecraft proximity relative motion. Therefore, the research on the measurement of autonomous rendezvous and docking considering safety and accuracy has become a significant research subject. [2]

In China, the research on visible/infrared dual-band imaging technology started late, and most of the research focuses on the optical system with limited focal length. There are few reports on the visible/ infrared dual-band dual-field optical system.[3]

According to what has been mentioned above, we focus our study on the lens design for the CCD optical imaging sensor. Compared with former study, the innovations of the paper are shown as follows:

A. The improvement in accuracy

Because of the employment of the “telecentric beam path” technology, the aperture is located at the focal plane of the parallel to the axis of light, consequently promote the object, and the principal ray of an outgoing beam is ranging accuracy during the rendezvous and docking process;

B. near infrared lens design

This device was specially designated to improve the image quality as it is capable to adapt to complex environment such as low light situation in outer space.[4]

II. ABERRATION THEORY

The diffractive hybrid zoom optical system contains both a refractive lens and a diffractive lens. When considering a diffraction device, its refractive index can be considered $n_d = \infty$, that is its dielectric constant $\mu_d = \frac{1}{n_d}$. After this transition, the primary aberration of the system can be expressed as:

$$\begin{cases} \text{primary spherical aberration coefficient:} S_1 = \sum hP \\ \text{primary coma coefficient:} S_2 = \sum h_z p - J\sum W \\ \text{primary astigmatism coefficient:} \\ S_3 = \sum \frac{h_z}{h} P - 2J\sum \frac{h_z}{h} W + J^2 \sum \phi \end{cases}$$

$$\begin{cases} \text{primary distortion coefficient:} \\ S_4 = \sum \frac{h_z^3}{h} P - 3J\sum \frac{h_z^2}{h} W + J^2 \sum \frac{h_z}{h} \varphi(3\varphi + \mu_r \varphi_r) \end{cases}$$

For a coaxial rotationally symmetric optical system, its primary axial chromatic aberration and primary vertical chromatic aberration can be expressed as:

$$\begin{cases} \text{primary axial chromatic aberration and number:} \\ S_{1c} = \sum h^2 c \\ \text{primary heavy axis color difference and number:} \\ S_{2c} = \sum h h_z c \end{cases}$$

$$c = \sum \frac{\varphi}{\mu}$$

III. Structure design

The double Gauss lens and its anamorphic lens are common objective lenses developed for many years. The six-piece four-group double Gauss lens is the most typical lens of all double Gauss lenses. It can correct almost all aberrations, especially for asymmetry. Aberrations such as coma, distortion, and chromatic aberration of magnification are well corrected, and the correction for on-axis aberrations is due to other types of lenses. The double Gauss lens and its anamorphic lens are mostly used in the design of objective lenses with medium to large aperture and medium to large field of view. Telephoto, anti-distance objective and fixed-focus projection objective with special performance are also from double Gauss lens. It has evolved. Therefore, the initial structure of this subject uses six four-group dual Gauss lenses.

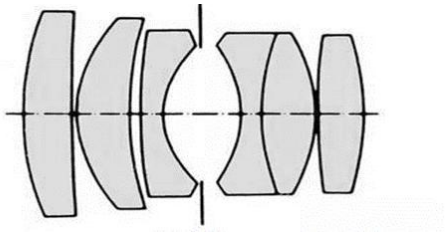

Fig.1 The fundamental structure of double-Gauss

In aberration theory, it can be shown that radii have a dominant influence on aberrations of optical system. Glasses aren't varied because they are discrete variables taken from the glass database, and evolutionary algorithms use only continuous variables such as radii and distances. Due to their stochastic nature, every evolutionary method was conducted five times. [5]

IV. Temperature characteristic analysis

The performance of optical systems is affected by environmental factors such as temperature and pressure, mainly for the following three aspects: 1) The refractive index of glass depends on temperature and wavelength; 2) Glass expands and contracts with temperature, which changes the radius and thickness of the lens; 3) The spacing between the lens elements changes, because material is changed by thermal expansion and cold contraction. As a result, we choose glass materials with small temperature change, such as H-LAK1 and H-ZF11, etc. In addition, the thermal effect is further eliminated by ZEMAX on the previously optimized optical system. Using titanium alloy as the tube materials (Thermal expansion coefficient 8.9*10-6/K), analyzing from -30 degree to 50 degree without focusing lens, imaging quality change of the system.

V. Lens design for surveillance optical system

A. System parameters

Spectrum: 480~800nm
Inlet diameter: 5.5mm
Field of view 2ω: 40°
Focal length: 22mm
Distortion: <1%
F#: 4

B. Light path design result

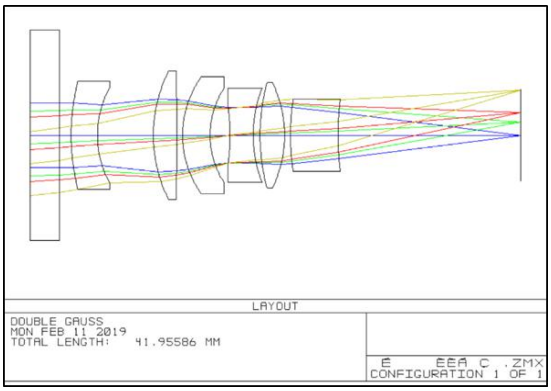

Fig.2 Light path design results of monitor lens.

As shown in Fig.2, the surveillance lens consists of seven lenses, including six spherical lenses and one quartz protective glass. The entire optical path is approximately 42 mm long. Lens materials are commonly used glass grades, all of which are spherical.

C. Optical system evaluation

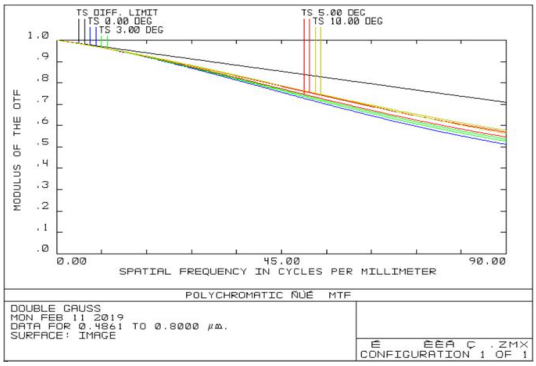

Fig.3 MTF of the system

Figure 3 is a system MTF curve at 90lp/mm cut off during imaging. From the curve, we can see that the system's full field average transfer function is better than 0.5.

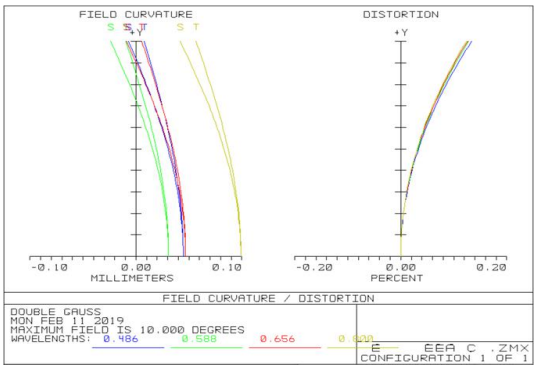

Fig.4 Field curvature distortion curve of the system

It can be seen from Fig. 4 that the distortion of the most edge field of view of 20° is better than 0.2%.

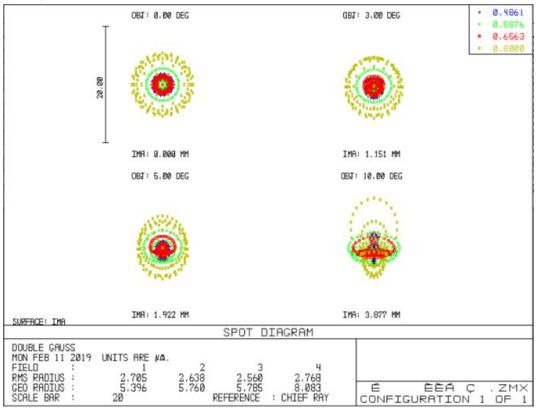

Fig.5 The spot diagram of the system

Figure 5 is a spot pattern of four fields of view of the optical system when focusing on infinity, with an RMS radius of at most 2.8 μm.

D. Temperature characteristic analysis

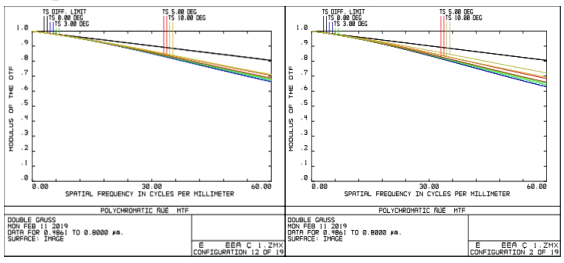

Fig.6 MTF curve of the system at -30 ° C and 50 ° C

VI. LENS DESIGN FOR MEASURING OPTICAL SYSTEM

A. System parameters

Spectrum: 900~920nm
Inlet diameter: 7.5mm
Field of view 2ω: 20°
Focal length: 32mm
Distortion: <1%
Telecentric beam path in image space

B. Light path design result

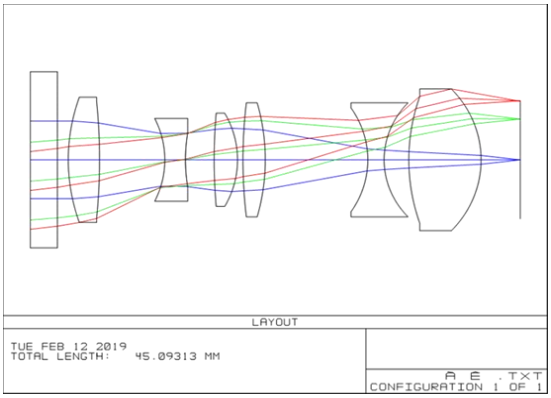

Fig.7 Light path design results of measuring lens

As shown in Fig.7, the system consists of 6 lenses, of which 5 are spherical lenses and 1 is fused silica protective glass. The total length of the system optical path is 45.1 mm.

C. Optical system evaluation

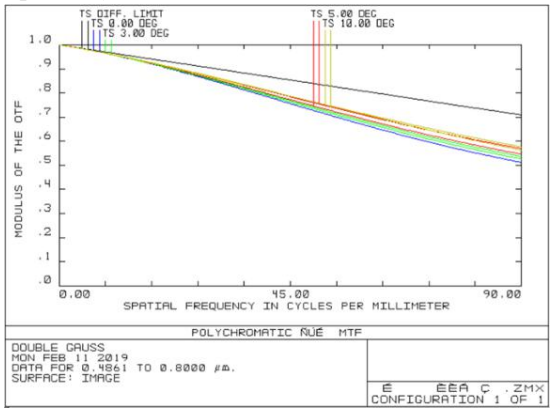

Fig.8 MTF of the system

Figure 8 is a system MTF curve at 90lp/mm cutoff during imaging. When imaging the target, MTF is slightly low at 90 lp/mm, but the system's full field average transmission is better than 0.4.

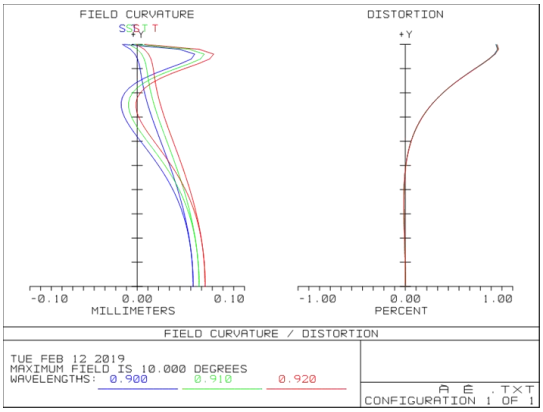

Fig.9 Field curvature distortion curve of the system

It can be seen from Fig.9 that the maximum distortion of the full field of this optical path is better than 1%.

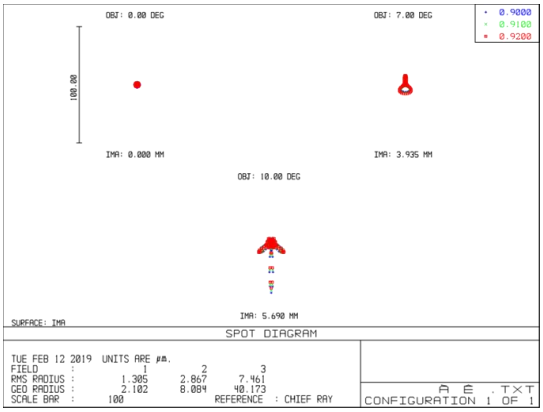

Fig.10 The spot diagram of the system

Figure 10 is a spot pattern of four fields of view of the optical system when the measuring lens is used to image the infinity target, including the central field of view, 0.7 field of view, and 1 field of view. The maximum dispersion radius is less than 8 μm.

D. Temperature characteristic analysis

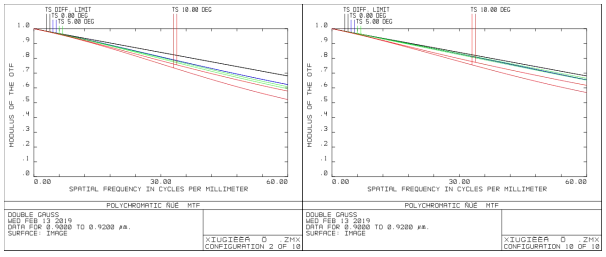

Fig.11 MTF curve of the system at -30 ° C and 50 ° C

VII. CONCLUSION

This paper designs a two-lens optical system for space rendezvous and docking based on the double-Gauss structure.

The surveillance lens is in the visible light range of 480 nm to 800 nm, the field of view is 40°, the effective focal length is 22 mm, and the full field of view MTF is higher than 0.5 at a spatial frequency of 60 lp/mm, and the total field of view is lower than 1%. The measuring lens is in the near-infrared band of 900 nm to 920 nm, the field of view is 20°, the effective focal length is 32 mm, and the full field of view MTF is higher than 0.5 at a spatial frequency of 60 lp/mm, and the total field of view distortion is 1%. The aberrations of the system are well corrected to meet technical specifications. And after the thermal analysis, the optical system without focusing does not change the image quality in the range of -30 ° C ~ 50 ° C.

References

[1] Yijing Zhang, Yongzhong Xu, Zhizhong Li, Jie Li, Su Wu. Influence of Monitoring Method and Control Complexity on Operator Performance in Manually Controlled Spacecraft Rendezvous and Docking[J].Tsinghua Science and Technology,2008(05):619-624.

[2] Guan-qun Wu, Shen-min Song. Attitude and Orbit Coupled Control for Spacecraft Rendezvous and Docking Considering Safe Constraint[A]. China Automation Society Control Theory Committee. Proceedings of the 37th China Control Conference（C）[C], 2018:6.

[3] ZHU Haibin;ZHANG Yuanjian;ZHOU Liang;XU Zhigang; ZHU Dalue;Jilin Dongguang Factory of Precision and Ma chinery;The Military Representative Office in Changchun of Armoured Forces Military Representative Bureau of Ch inese People's Liberation Army;;The optical system desig n of double-band/double-field of view of panoramic aerial camera[J]; Optical Instruments;2017-02

[4] Zhou Chao, Yang Hongbo, Wu Xiaoxia, et al. Structural analysis of ground-based large telescope [J]. Optics and

[5] Precision Engineering, 2011, 19(1): 138-145.

[6] S Bakic, D Vasiljevic. Optimization of the double-Gauss objective with the various evolution strategies and the damped least squares[J].Physica Scripta, T162(2014) 014034

Design of Simple Circuit Delay Measuring Device

Jinlong Chen, Dongxu Bai, Fei Liu
(Jilin University Instrumentation and Electrical Engineering institution, Changchun 130061)

***Abstract*—This design is a simple device for measuring the delay of periodic signals. This device can measure the delay of signals quickly under the condition of guaranteeing the accuracy. This device has a wide measuring range, and achieves a controllable and precise delay of signals with a peak value range of 0 to 1000mV and a frequency range of 1 KHz to 20 MHz. The delay time can be adjusted from 100 ns to 100 ms. Finally, the delay time of signals can be measured simultaneously and drew the corresponding waveform. In addition, the measurement error of the device is small, only 1%, and it has high stability and wide application range, which is of great significance to scientific research and other work.**

***Key words*—Periodic signal delay Fast and accurate measurement**

I. INTRODUCTION

DIGITAL circuit has a wide range of applications in life. In digital circuit, delay is used to achieve stable control, while delay is used to change phase in analog circuit. Sometimes in order to synchronize signal, they also try to set equal delay lines, so delay is of great significance to digital and analog systems. In this paper, how to measure the delay accurately and how to reduce the cost, miniaturization and intellectualization of the delay measurement device are described in detail, and a new design method of the signal delay measurement device is given.

II SYSTEM STRUCTURE AND THEORY

The device is composed of DDS, integer conditioning circuit, delay circuit, ADC, FPGA and STM32. The system block diagram is shown in Figure 1. DDS is used as a signal source to generate the sinusoidal signal needed. STM32 communicates with DDS by SPI mode, and controls the amplitude, frequency and waveform of the sinusoidal wave output by DDS. Under the control of STM32, DDS generates sinusoidal signal and sends it into the conditioning circuit, which can transform the input sinusoidal wave into square wave. On the one hand, the square wave obtained after shaping is fed into the delay circuit composed of shift registers to get the delayed square wave, on the other hand, it is fed directly into ADC to measure the amplitude of the signal. Finally, two signals are input to the FPGA for frequency measurement. Then the delay time of the two signals is obtained by comparing them. Finally, all the data are sent to STM32 by the FPGA for processing, and after processing, the data is sent to the TFT screen for display. At the same time, DDS is further adjusted to increase the stability of the system.

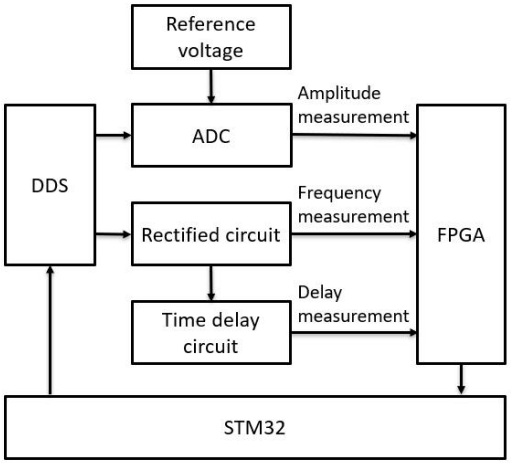

Fig.1 System Chart

The operation process of the system is relatively simple. After receiving the start signal, the system first undergoes a series of initialization activities, then input the selection signal by the TFT screen, and select the function to be performed. After processing by STM32, the control signals of each part are generated and the corresponding functions are executed. The optional functions include outputting the original signal and the delay signal, and measuring the delay time of the delay signal. After the execution of the corresponding functions, determine whether termination, if not termination, it will be returned as a interrupt, so that the system into the cycle, to achieve the purpose of continuous control of all parts of the system.

III THEORETICAL ANALYSIS AND CALCULATION

A. Plastic conditioning circuit

The shaping and conditioning circuit adopts hysteresis comparison circuit. The formula is given below.

$$V_{T+} = R_1 V_{REF}/(R_1 + R_2) + R_2 V_{OH}/(R_1 + R_2) \quad (1)$$

$$V_{T-} = R_1 V_{REF}/(R_1 + R_2) + R_2 V_{OL}/(R_1 + R_2) \quad (2)$$

$$\Delta V_T = V_{T+} - V_{T-} = R_2(V_{OH} - V_{OL})/(R_1 + R_2) \quad (3)$$

According to the above formulas, when we know V_{T-}、V_{T+}、V_{REF}, the resistance value can be selected appropriately.[1][2]

B. Delay circuit

The selection of delay circuit is based on rich logic gates and high frequency timing of FPGA.

After signal input, every time it passes through a shift register, the signal is delayed by a system clock cycle. After a certain number of registers, the signal is delayed to a specified period of time. Different number of registers are pre-equipped in the FPGA. The clock of these registers will change according to the frequency of the measured signal. The time delay of different frequency signals can be controlled by STM32, and the time delay of signals can be controlled.

$$T = t \cdot N \quad (4)$$

T represents the total delay time, T represents the system clock cycle, and N represents the number of shift registers.

C. Delay time measure

For the measurement of delay, first of all, the input square wave signal and the delay signal should be exclusively or, so that the time difference between the two signals will be generated as a pulse signal, and the delay time can be obtained by measuring the width of the pulse. The pulse width measurement module first generates a high frequency square wave as the reference signal by the system, and uses the pulse signal generated before as the gate signal. When the pulse signal rises, the counter begins to count. The level of the pulse signal is checked while counting. Once the pulse signal becomes low, the counting stops. After obtaining the counter count value, the delay time of the signal can be measured by using the following formula.

$$T = N_m/N_x \cdot t \quad (5)$$

In the above formula, T represents the delay time to be measured, N_m represents the total number of rising edges of the system clock at high level of the pulse signal in the gate, N_x represents the number of rising edges of the signal to be measured in the gate, and T represents the period of the system clock.[4]

The principle is shown in Figure 2.

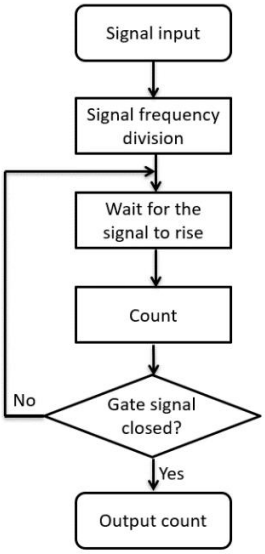

Fig.2 Principle Diagram of Delay Measurement

In order to measure the frequency of the signal, the counting time of the counter can be set to the time of several signal cycles. In this design, eight signal cycles are selected as counting time. After counting, the counting value is taken to calculate eight signal cycle time, and then the period and frequency of the signal can be calculated.

IV Test Results and Analysis

The testing process is divided into two steps. Firstly, the performance of each module is tested. Finally, all modules are combined to test the whole system. The test results are shown in Table 1-3.

TABLE1 Frequency Test of Signal Generator

Set frequency	Actual frequency	relative error
100Hz	100Hz	0%
1KHz	10-5Hz	0.5%
10KHz	10.1KHz	1%
1MHz	1.005 MHz	0.5%
20MHz	20.2 MHz	1%

TABLE 2 Amplitude Test of Signal Generator at Different Frequencies

Amplitude（mV）	Frequency（Hz）			
	1k	100k	1M	10M
10	9.2	9.4	10.0	10.4
50	50.5	47.8	56.3	55.8
100	98.2	89.6	99.1	106.7
500	504.8	508.6	497.5	489.5
1000	700.7	689.7	649.9	694.6

TABLE 3 Delay Setting and Measurement

Delay settings	Delay measurements	Oculographic value
100ns	105ns	110ns
100 s	101 s	1s
1ms	1.005ms	1.007ms
50 s	50 s	52 s
50ns	54ns	56ns

V RESULT

Delay plays an important role in both analog and digital circuits. It is particularly important to ensure the accuracy of delay. The device designed can meet the detection task under certain conditions. This design uses a series of simple methods to realize the rapid detection of signals. At the same time, through the software method, the accuracy of measurement can meet the requirements. It is a highly adaptable measuring equipment.

References

[1] FU Zhihong, ZHOU Luowei, SU Xiangfeng, DU Xiong. Two Novel Quasi-resonant Steep Current Impulse Rectifying Circuits [J]. Proceedings of the CSEE,2 006(05): 70-75.

[2] Zhao Xiang. Practical Voltage-Booster and Pulse Shaping Circuit Design for Pulsed-Laser[J]. Optics & Optoelectronic Technology,2014,12(03):67-71.

[3] Lan Dechun. Long Delay Circuit [N]. Electronic Newspaper,2015-05-17(010).

[4] Ma Kai, Wang Yanwen. Design of programmable digital control precision timing circuit [J]. China Measurement & Test,2014,40(01):93-96.